Facially Polarized Cyclohexanes and Orthoesters as Building Blocks in Host-Guest Architectures and Functional Materials

Dissertation zur Erlangung des Doktorgrades Dr. rer. nat. der

Fakultät für Naturwissenschaften der Universität Ulm

vorgelegt von

Oleksandr Shyshov

geboren in Sumy, Ukraine

Ulm, 2021

Amtierender Dekan: Prof. Dr. Thorsten Bernhardt

1. Gutachter: Prof. Dr. Max von Delius

2. Gutachter: Prof. Dr. Alexander Kühne

Tag der Promotionsprüfung: 04.02.2021

Universität Ulm, Fakultät der Naturwissenschaften, 2021

Contents

Preface I

List of Abbreviations III

1. State of the Art ..... - 1 -

1.1 Key Building Blocks Used in This Study ..... - 1 -

1.1.1 Orthoesters ..... - 1 -

1.1.2 All-*cis* 1,2,3,4,5,6-Hexafluorocyclohexane and its Derivatives ..... - 3 -

1.2 Key Processes Carried Out in This Thesis ..... - 9 -

1.2.1 Dynamic Combinatorial Chemistry ..... - 9 -

1.2.2 Orthoester Exchange ..... - 26 -

1.2.3 Supramolecular Polymerization ..... - 32 -

2. Aims and Achievements ..... - 54 -

2.1 Adaptive Behaviour of Dynamic Orthoester Cryptands ..... - 54 -

2.2 Ammonium Complexes of Orthoester Cryptands are Inherently Dynamic and Adaptive ..... - 57 -

2.3 Long–Chain Polyorthoesters as Biodegradable Polyethylene Mimics ..... - 60 -

2.4 Anion-binding of All-*cis* Hexafluorocyclohexane in Solution and Solid State ..... - 64 -

2.5 Living Supramolecular Polymerization of Fluorinated Cyclohexanes ..... - 67 -

3. Summary and Outlook ..... - 72 -

4. Publications ..... - 75 -

4.1 Adaptive Behaviour of Dynamic Orthoester Cryptands ..... - 75 -

4.2 Ammonium Complexes of Orthoester Cryptands are Inherently Dynamic and Adaptive ..... - 184 -

4.3 Long-Chain Polyorthoesters as Degradable Polyethylene Mimics ..... - 265 -

4.4 Evidence for Anion-Binding of all-*cis* Hexafluorocyclohexane in Solution and Solid State ..... - 304 -

4.5 Living Supramolecular Polymerization of Fluorinated Cyclohexanes ..... - 330 -

References ..... - 426 -

List of Publications ..... - 433 -

List of Talks and Conference Contributions ..... - 434 -

Curriculum Vitae ..... - 435 -

Acknowledgments ..... - 436 -

Statement ..... - 437 -

Preface

This thesis is based on two seemingly different types of organic building blocks: orthoesters and all-*cis* multifluorocyclohexanes. However, both compound classes have in common that prior to this doctoral thesis they have not been used to meet objectives related to supramolecular chemistry (self-assembly, anion and cation binding, and supramolecular polymerization).

The first part deals with the orthoester exchange. Orthoester exchange is an acid-catalysed dynamic covalent reaction between orthoesters and alcohols that was re-discovered six years ago in the Delius group. In 2015, Delius and coworkers demonstrated the application of the orthoester exchange to the self-assembly of small hosts for sodium ions. The first big goal of this thesis was to expand the scope of orthoester exchange to more complex architectures using different cations and anions and to use the lability of orthoesters to create new (bio)degradable polymers. The first project describes the self-assembly of orthoester cryptates using different alkali metal cations. We could demonstrate the adaptive behaviour of orthoester cryptands, obtained after metal-ion removal, via subcomponent exchange in response to the addition of alkali metal ions. The second project presents the development of the first-ever fluxional supramolecular system – ammonium orthoester cryptates – in which ammonium cation acts both as a catalyst for orthoester exchange and as a template, thus leading to constant intramolecular rearrangements. The fourth orthoester project describes the development of high-density polyethylene mimetics bearing labile orthoester groups that impart the ability to degrade in acidic medium.

The second part describes pioneering studies on the supramolecular properties of all-*cis* 1,2,3,4,5,6-hexafluorocyclohexane. All-*cis* $C_6H_6F_6$ is unique because it is the most polar aliphatic compound reported to date. Its high dipole moment allows to form strong dipole-dipole and dipole-ion interactions that are among the most important and abundant non-covalent interactions. However, until 2017 the synthesis of all-*cis* $C_6H_6F_6$ had been extremely tedious, precluding nearly all experimental investigations. In the first project, we demonstrate moderate affinities of all-*cis* $C_6H_6F_6$ in solution toward simple inorganic anions. In the second project, we present an unprecedented platform for living supramolecular polymerization based on all-*cis* $C_6H_6F_6$ derivatives.

The first chapter of this thesis consists of two sections. Section 1.1 introduces key building blocks used in this study: orthoesters and all-*cis* hexafluorocyclohexanes. Section 1.2 describes key processes used in this thesis: dynamic combinatorial chemistry (with particular focus on the dynamic orthoester exchange) and supramolecular polymerization. Chapter 2 is a synopsis on the aims and achievements of all research projects that have been carried out. Chapter 3 is presented in the form of articles that have recently been published or under peer-review. Section 3.1 (**Project 1**) describes the self-assembly and dynamic behaviour of orthoester cryptates. Section 3.2 (**Project 2**) presents the first-ever fluxional supramolecular assembly where ammonium serves both as a template and as a catalyst for the orthoester exchange. Section 3.3 (**Project 3**) introduces a new synthetic route towards biodegradable polymers containing orthoesters in the main chain that have some properties reminiscent to the common high-density polyethylene. Section 3.4 (**Project 4**) presents pioneering studies on host-guest properties of all-*cis* $C_6H_6F_6$ and its derivative in solution and solid state. Section 3.5 (**Project 5**) describes how the outstanding dipole moment of all-*cis* $C_6H_6F_6$ can be used to create a new system for living supramolecular polymerization. Chapter 4 contains closing remarks about the significance of the presented work as well as further ideas that can be tested or currently under investigation.

List of Abbreviations

AFM	atomic force microscopy
all-*cis* $C_6H_6F_6$	all-*cis* 1,2,3,4,5,6-hexafluorocyclohexane
Ar	aryl
ATR-IR	attenuated total reflectance infrared spectroscopy
BArF	tetrakis[3,5-bis(trifluoromethyl)-phenyl]borate
BCP	block copolymer
BOC	tert-butoxycarbonyl
BTA	1,3,5-benzenetricaroxamide
br	broad
CAAC	cyclic alkyl amino carbene
CD	circular dichroism
CH	cyclohexane
COD	1,5-cyclooctadiene
DCC	dynamic combinatorial chemistry
DCL	dynamic combinatorial library
DCM	dichloromethane
DEG	diethylene glycol
DFT	density functional theory
DIPEA	N,N-diisopropylethylamine
DLS	dynamic light scattering
DMAP	4-dimethylaminopyridine
DMSO	dimethyl sulfoxide
DNA	deoxyribonucleic acid
DOSY	diffusion-ordered NMR spectroscopy
DTT	dithiothreitol
EDC	1-ethyl-3-(3-dimethylaminopropyl)carbodiimide
ESI	electrospray ionization
EtOAc	ethyl acetate
EXSY	exchange spectroscopy
GPC	gel permeation chromatography
HBC	hexa-*peri*-hexabenzocoronene

HDPE	high-density polyethylene
HOESY	heteronuclear Overhauser effect spectroscopy
HOPG	highly oriented pyrolytic graphite
HPLC	high-performance liquid chromatography
HR-TEM	high-resolution transmission electron microscopy
LDA	lithium diisopropylamide
LSP	living supramolecular polymerization
MCH	methylcyclohexane
MD	molecular dynamics
MeCN	acetonitrile
MS	mass spectrometry
NDI	naphtalene diimide
NMR	nuclear magnetic resonance
NOE	nuclear Overhauser effect
NT	nanotube
PBI	perylene bisimide
PDI	polydispersity index
PFPA	perfluoropentanoic acid
PFP	2,3,4,5,6-pentafluorophenol
PHA	polyhydroxyalkanoate
PMMA	poly(methyl methacrylate)
PS	polystyrene
PVDF	polyvinylidene fluoride
PXRD	powder x-ray diffraction
PZT	lead zirconate titanate
RNA	ribonucleic acid
SEC	size exclusion chromatography
SEM	scanning electron microscopy
SIM	structured illumination microscopy
TBA	tetrabutyl ammonium
TEA	triethylamine
TEG	triethylene glycol
TFA	trifluoroacetic acid

THF	tetrahydrofurane
TLC	thin-layer chromatography
TPP	tetraphenylphosphonium
TREN	tris(2-aminoethyl)amine
UHPLC	ultra-performance liquid chromatography
UV-Vis	ultraviolet-visible
VT	variable temperature

1. State of the Art

1.1 Key Building Blocks Used in This Study

1.1.1 Orthoesters

An orthoester is a functional group bearing three alkoxy groups attached to one sp^3-hybridized carbon atom. There are many routes towards orthoesters, and Robert H. DeWolfe gives an extensive review on this topic.[1] Some useful methods include: 1) reaction of nitriles with anhydrous hydrogen chloride and alcohols (Fig. 1a) known as Pinner reaction;[2,3] 2) Williamson ether synthesis from 1,1,1-trichloro compounds with alkoxides or phenoxides (Fig. 1b; this approach is usually used in industry);[4] 3) acid-catalysed transesterification (Fig. 1c) , which allows the synthesis of more complex orthoesters from simple commercially available orthoesters.[5,6] Since the reaction is reversible, the removal of the released alcohol is required. This procedure is not efficient with secondary and tertiary alcohols; 4) Treatment of orthocarbonates with Grignard reagents (Fig. 1d) similar to Bodroux-Chichibabin synthesis.[7]

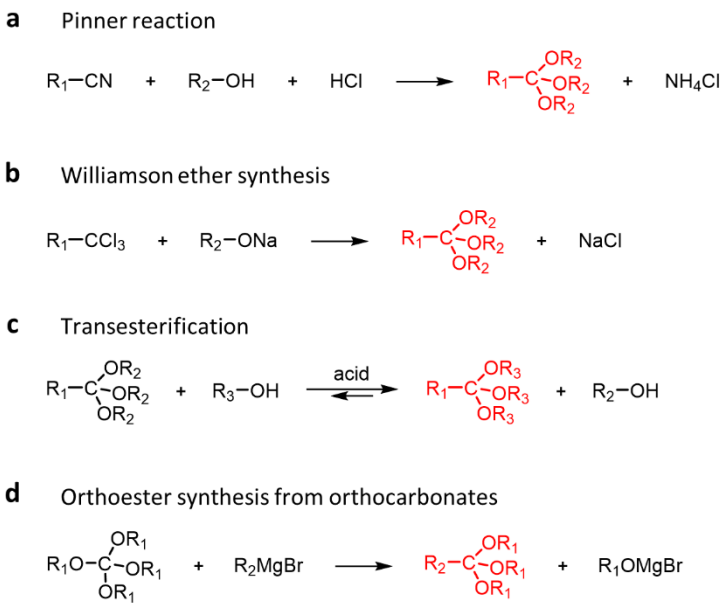

Figure 1. Orthoester synthesis by (**a**) Pinner reaction, (**b**) Williamson ether synthesis, (**c**) transesterification, (**d**) reaction between orthocarbonates and Grignard reagents.

The most important reaction of orthoesters is the general acid-catalysed formation of oxonium ion that can be attacked by various nucleophiles (Fig. 2a,b). Both Lewis and Brønsted

acids can be used as a catalyst.[8] Highly reactive oxonium intermediates make orthoesters valuable alkylating[9] and acylating[10] reagents, as well as C1 building blocks in the synthesis of heterocycles (Fig. 2c).[11] Orthoesters are well-known protecting groups in carbohydrate chemistry (Fig. 2d), where they are typically used when two or three facial hydroxyl groups need to be protected simultaneously.[12]

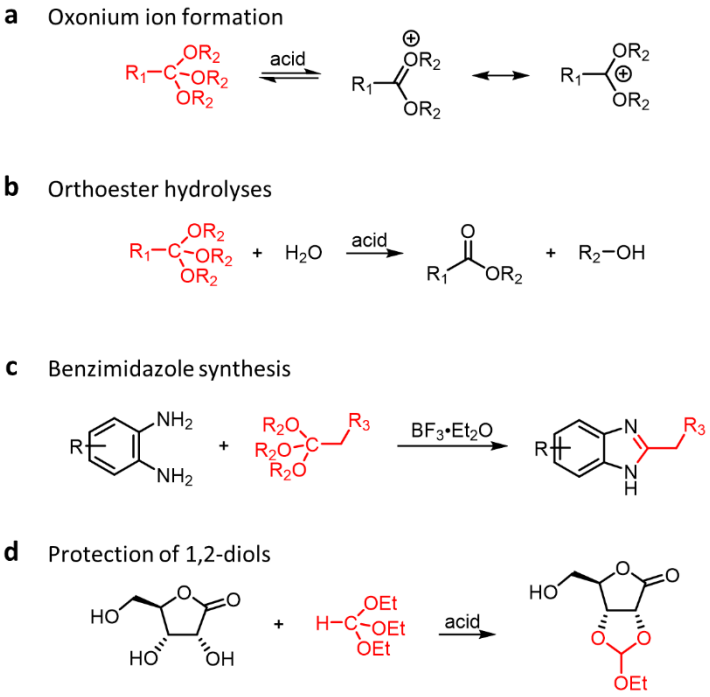

Figure 2. **a**, Acid-catalysed formation of the oxonium ion. **b**. Acid-catalysed aqueous hydrolysis. **c**, Benzimidazole synthesis by the reaction of orthoesters with 1,2-diamines. **d**, Representative example of alcohol protection with orthoesters.

A large part of this thesis is focused, however, on completely different applications of orthoesters – in dynamic combinatorial and supramolecular chemistry.

1.1.2 All-*cis* 1,2,3,4,5,6-Hexafluorocyclohexane and its Derivatives

According to the Pauling scale, fluorine has the highest electronegativity value among all elements (χ = 4), making the C–F bond the strongest and the most polarized in organic chemistry.[13] C–F bond has a relatively large dipole moment, however, three lone electron pairs are held tightly and, as a result, rarely get involved in hydrogen bonding.[14,15] In linear alkanes, C–F bonds positioned on alternate carbons tend to align in opposite directions to minimize dipolar repulsion.[16,17] However, if fluorines are placed on a structurally rigid core, which maintains the orientation of the C–F bond in the same direction, highly polar organic molecules and materials can be created.

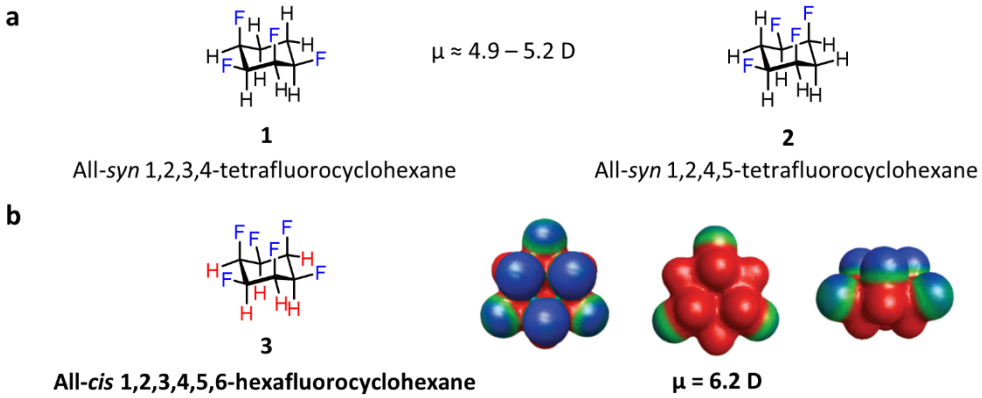

Figure 3. a, All-*syn* tetrafluorocyclohexanes. **b**, All-*cis* 1,2,3,4,5,6-hexafluorocyclohexane and its electrostatic potential surface map, reproduced from [20] with permission from the Nature Publishing Group, copyright (2015).

The extreme case of polarized aliphatic compounds is represented by facially polarized fluorinated cyclohexanes pioneered by O'Hagan and coworkers. In 2011 and 2012, they reported on the first synthesis of all-*syn* 1,2,3,4-tetrafluorocyclohexane **1** and all-*syn* 1,2,4,5-tetrafluorocyclohexane **2** (Fig. 3a),[18,19] demonstrating that ring conformation can override repulsive 1,3-C–F interactions. Obtained compounds had unusually high calculated dipole moments (μ ≈ 4.9 – 5.2 D), which was experimentally confirmed by single-crystal X-ray analyses. The crystal packing arrangement revealed weak electrostatic hydrogen to fluorine contacts between the upper "fluorine" faces and lower "hydrogen" faces.

The all-*cis* 1,2,3,4,5,6-hexafluorocyclohexane **3** bears six fluorine atoms pointing up and six hydrogen atoms pointing down, resulting in an enormous dipole moment μ = 6.2 D (Fig. 3b). The first synthesis was achieved only in 2015 by the same group in 12 linear steps yielding only

a few milligrams of the target molecule, leaving this appealing molecule only a subject of theoretical investigations (Fig. 4a).[20]

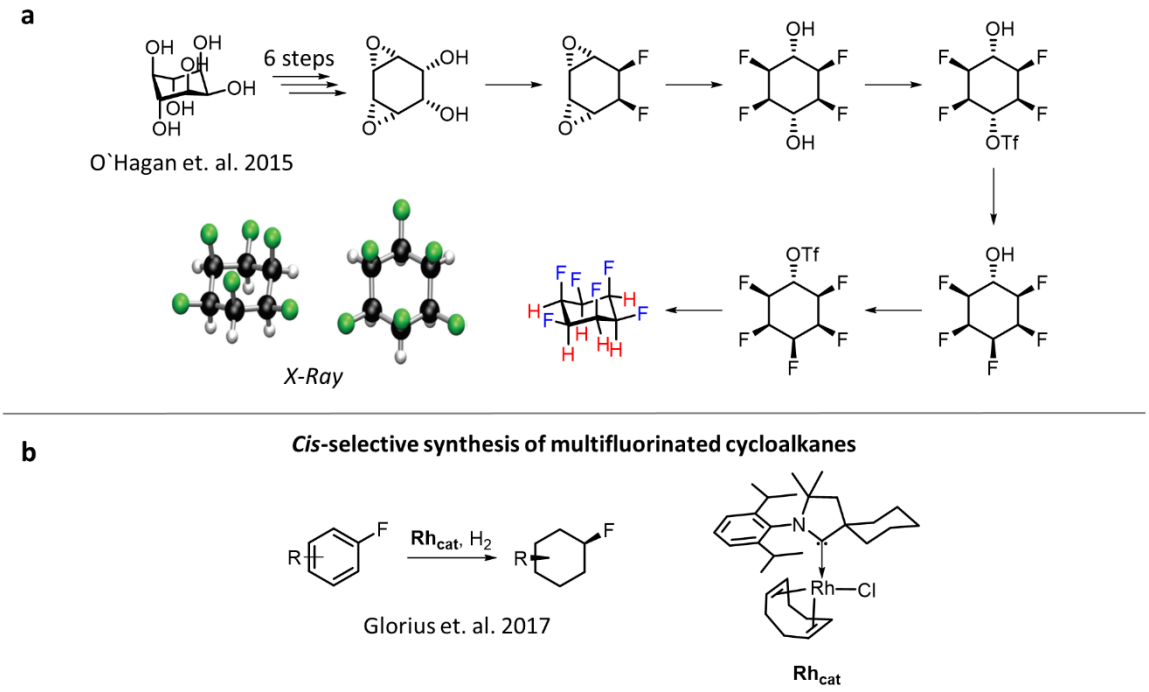

Figure 4. a, First synthesis of all-*cis* 1,2,3,4,5,6-hexafluorocyclohexane reported by O'Hagan and coworkers. Adapted from [20] with permission from the Nature Publishing Group, copyright (2015). **b**, *Cis*-selective synthesis of multifluorinated cycloalkanes. Adapted from [21] with permission from the American Association for the Advancement of Science, copyright (2017).

The synthetic breakthrough came from Germany two years after. Glorius and coworkers described a one-step chemoselective, *cis*-selective, and scalable synthesis of all-*cis*-(multi)fluorinated cycloalkanes (Fig. 4b).[21] They established direct high-pressure hydrogenation of fluoroarenes catalysed by complexes of rhodium with a strongly electron-donating cyclic alkyl amino carbene (CAAC) ligand[22] making all-*cis* 1,2,3,4,5,6-hexafluorocyclohexane and its derivatives synthetically available.

Dipole-dipole and dipole-ion interactions are among the most important and abundant non-covalent interactions in supramolecular, biological chemistry, and materials science. One of the examples are ferroelectric materials. Ferroelectrics have spontaneous macroscopic polarization that reverts by using an external electric field. Ferroelectrics are widely used in data storage, electro-optical devices, actuation, sensing, and energy harvesting, to name a few.[23,24] Most ferroelectrics are inorganic salts, for example, $BaTiO_3$ and $Pb(Zr_xTi_{1-x})O_3$ (PZT).

Organic ferroelectric materials are relatively rare, and their design is more challenging. However, they have certain advantages over inorganic such as solution processability, low density, and cost.[25–27] One possible requirement for the molecular design of organic ferroelectrics is a large dipole moment. The work-horse of organic ferroelectrics is polyvinylidene fluoride (PVDF).[28] Polarization in PVDF comes from the polarity of the CF_2 group, which has 2.1 D dipole moment.[29] It is not surprising that a molecule with three times larger dipole moment immediately attracted the attention of researchers.

Theoretical studies on its interactions with 2D materials,[30] aromatic surfaces,[31] alkali metals,[32] and ions[33,34] rapidly followed the first synthesis of all-*cis* 1,2,3,4,5,6-hexafluorocyclohexane.

In 2015 Bühl, O'Hagan and coworkers disclosed the ability of all-*cis* $C_6H_6F_6$ to form particularly strong C–H···π interactions (ca. 6 – 8 kcal mol^{-1}) with benzene.[31] In the following report, Datta and coworkers studied the ability of all-*cis* $C_6H_6F_6$ to form C–H···π and C–H···F–C interactions with planar molecules and materials: benzene, pyrene, coronene, graphene (Fig. 5). Interestingly, structural and optical properties of such complexes could be tuned by applying an external electric field.[30]

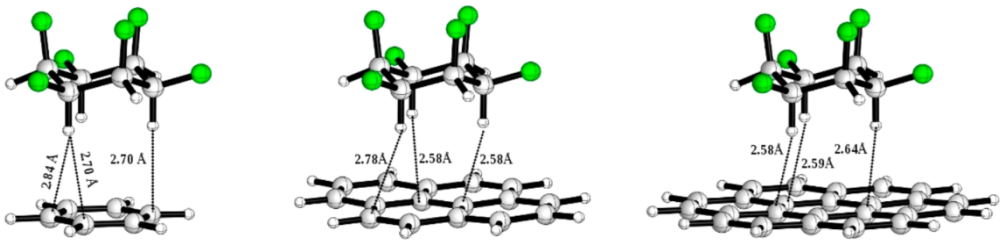

Figure 5. C–H···π interactions with all-*cis* 1,2,3,4,5,6-hexafluorocyclohexane. Reproduced from [30] with permission from the American Chemical Society, copyright (2017).

Two particular research articles laid the foundation for the big part of this thesis. The large dipole moment of all-*cis* $C_6H_6F_6$ naturally leads to the expectation that it should strongly bind anions to its positively charged hydrogen face and cations to the negatively charged fluorine face. A combined experimental and computational approach confirmed this hypothesis. McMahon and coworkers carried out electrospray ionization – ion trap mass spectrometry coupled with infrared multiple photon dissociation spectroscopy on the mixture of all-*cis*

$C_6H_6F_6$ and sodium chloride.[33] They could detect both mono- and di-coordinated adducts of all-*cis* $C_6H_6F_6$ with both Na^+ and Cl^- (Fig. 6a,b). Thermochemistry of binding was studied using DFT and *ab initio* methods (Table 1). In all cases, binding enthalpies were impressively large. For example, binding enthalpy of all-*cis* $C_6H_6F_6$ to Na^+ concedes only cyclic ethers: 12-crown-4, 12-crown-5, and 18-crown-6. In the case of chloride binding situation is even more impressive: the binding enthalpy of 156.5 kJ mol^{-1} is comparable only to very strong gas-phase Lewis and Brønsted acid species,[35] thus making all-*cis* $C_6H_6F_6$, arguably, the strongest gas-phase chloride binder.

In all cases, the formation of 2:1 complexes was thermodynamically much less favourable, which one can expect for ion-dipole complexes.

Upon binding of the second molecule of all-*cis* $C_6H_6F_6$, the contact distance between Na^+ (Cl^-) to axial fluorine (hydrogen) only slightly increased. The magnitude of this change was relatively similar for Na^+ and Cl^- (0.06 Å for Na^+ and 0.07 Å for Cl^-), while changes in binding enthalpies were somewhat larger for Cl^- (42 kJ mol^{-1}) than for Na^+ (30 kJ mol^{-1}). Bond internal lengths and angles of all-*cis* $C_6H_6F_6$ remained relatively unchanged despite the very strong energies of binding. These results indicate that interaction of all-*cis* $C_6H_6F_6$ with ions is electrostatic in origin and involves ion-dipole and ion-induced–dipole interactions.

Table 1. Energetics of association reactions. Reproduced from [33] with permission from the American Chemical Society, copyright (2016).

	$Na^+ + C_6H_6F_6 \rightarrow [C_6H_6F_6]Na^+$		(1)
	$[C_6H_6F_6]Na^+ + C_6H_6F_6 \rightarrow [C_6H_6F_6]_2Na^+$		(2)
	$Cl^- + C_6H_6F_6 \rightarrow [C_6H_6F_6]Cl^-$		(3)
	$[C_6H_6F_6]Cl^- + C_6H_6F_6 \rightarrow [C_6H_6F_6]_2Cl^-$		(4)
Eq.	ΔH^0_{298} kJ mol^{-1}	ΔH^0_{298} J mol^{-1} K^{-1}	ΔG^0_{298} kJ mol^{-1}
1	-175.9	-116.3	-141.3
2	-145.4	-132.9	-105.8
3	-156.5	-97.2	-127.5
4	-114.5	-112.5	-81.0

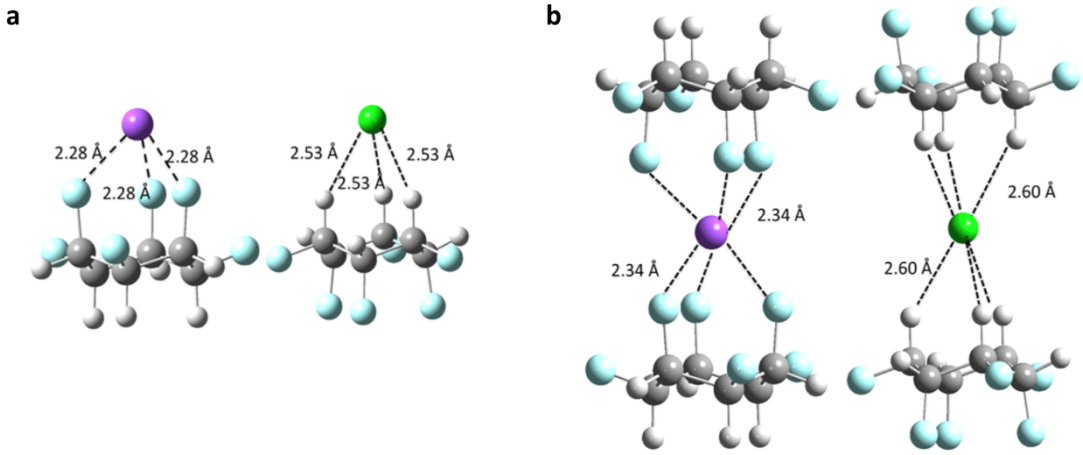

Figure 6. a, Structures of Na^+ and Cl^- coordinated to one molecule of all-*cis* $C_6H_6F_6$. **b**, Structures of Na^+ and Cl^- coordinated to two molecules of all-*cis* $C_6H_6F_6$. Reproduced from [33] with permission from the American Chemical Society, copyright (2016).

Datta and coworkers studied different arrangements of all-*cis* $C_6H_6F_6$ in the solid-state.[36] They found that perfect parallel stacking of all-*cis* $C_6H_6F_6$ units gives rise to energetically the most stable complexes (Fig. 7 and Table 2). This stability is a result of a strong C–H···F hydrogen bonding network of approximately 2.40 Å.

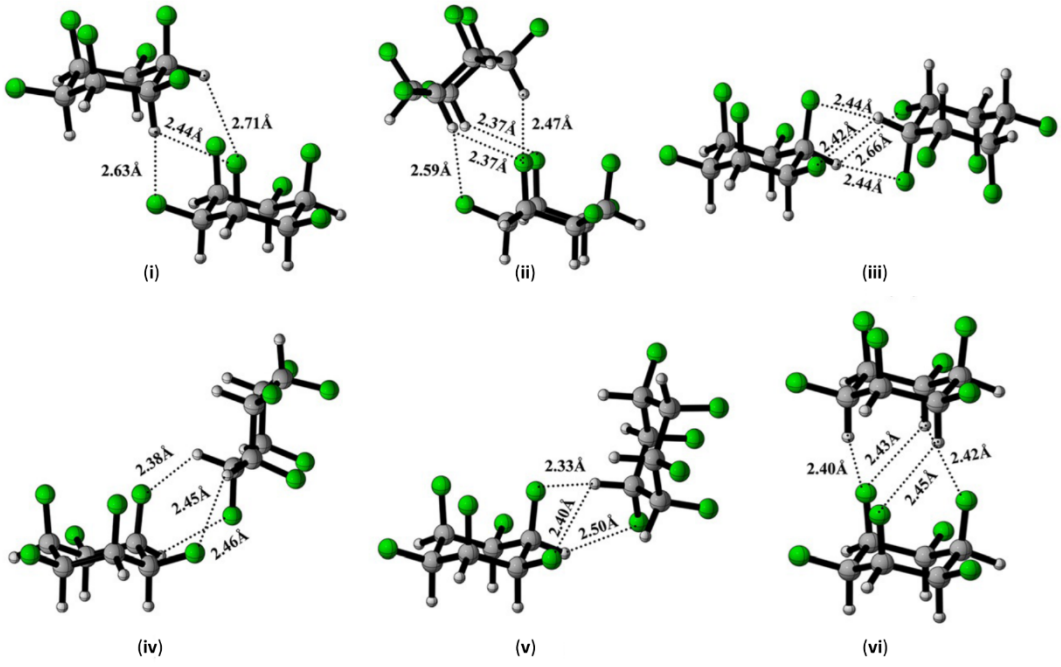

Figure 7. Optimized geometries of all-*cis* $C_6H_6F_6$ dimers in different arrangements. Reproduced from [35] with permission from Wiley-VCH, copyright (2016).

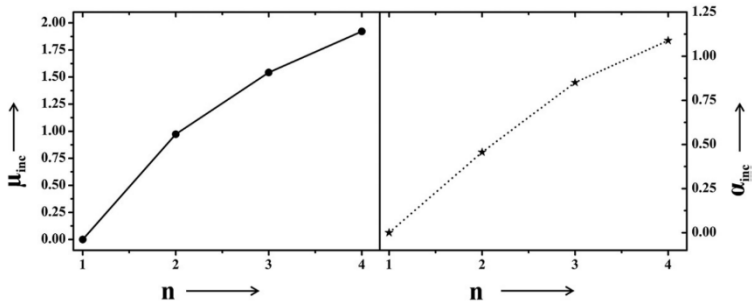

Figure 8. Increase of the dipole moment (μ) and polarization (α) with respect to the number of molecules of **3** in parallel stacks. Reproduced from [35] with permission from Wiley-VCH, copyright (2016).

The cooperative nature of these intermolecular interactions leads to huge cooperative enhancement of the dipole moment and macroscopic polarization. The parallel one-dimensional stack of four all-*cis* $C_6H_6F_6$ units has a total dipole moment 32.9 D, which corresponds to 8.2 D per unit against 6.2 D for all-*cis* $C_6H_6F_6$ itself. The total dipole moment monotonically increases from the dimer to the tetramer and ultimately reaches the limit in a 1D crystal as predicted by calculations (Fig. 8).

Table 2. Binding energies for the dimers of $C_6H_6F_6$ in different arrangements (Fig. 7). Reproduced from [35] with permission from Wiley-VCH, copyright (2016).

Binding mode	ΔE (E_{dimer} - 2×$E_{monomer}$) kcal mol^{-1}
Slipped parallel stack (**i**), 5.56	-4.7
Slipped parallel stack (**ii**), 5.84	-7.1
Linearly arranged (**iii**), 6.37	-3.8
Slipped perpendicular stack (**iv**), 6.70	-4.6
Slipped perpendicular stack (**v**), 6.82	-5.9
Parallel stack (v**i**), 4.90	-8.2

1.2 Key Processes Carried Out in This Thesis

1.2.1 Dynamic Combinatorial Chemistry

Based on a personal impression, for a chemist not well familiar with the field of supramolecular chemistry, the first association that comes to mind when he/she hears or sees "supramolecular chemistry" is probably a large, scary-looking molecule, very often macrocyclic, that requires many synthetic steps to achieve and which can bind other molecules, often relatively small and simple, forming host-guest complexes. This conception is true to a large part of the early research on supramolecular chemistry. For example, even synthesis of the simple 2.2.2-cryptand, which efficiently binds simple cations, took Lehn and coworkers five steps to accomplish.[37] The construction of effective receptors capable of selective recognition is a task that is sometimes difficult to address using straightforward synthesis. However, what if guest molecules could select their own most efficient hosts or facilitate their formation? This idea was realized in the 1990s and became a fundamental concept of the dynamic combinatorial chemistry (DCC).

DCC operates libraries of complex structures that are under thermodynamic equilibrium known as dynamic combinatorial libraries (DCLs). They contain different building blocks that can react with one another via reversible covalent reactions or non-covalent interactions, giving mixtures of increasingly complex, constantly interconverting molecules (library members). Because all reactions are reversible, the distribution of library members will correspond to the thermodynamic minimum of the system; in other words, DCL is in thermodynamic equilibrium. Thermodynamic equilibrium (lowest energy state) is a goal that every DCL aims to achieve; therefore, an external stimulus that can alter the stability of any library member will influence the product distribution. For example, if we add a compound that can bind a certain library member particularly strongly, it will lead to its amplification on the expense of other components to achieve thermodynamically the most stable state of the system.[38,39]

Substrate-induced expression of the barbiturate receptor is a simple but very illustrative example of DCC.[40] Condensation of 5,5-dimethyl-1,3-cyclohexanedione **4** and 2-hydrazino pyridine **5** in chloroform forms an equilibrated mixture of eight compounds (Fig. 9). The

mixture contains monohydrazones **7** and **8** (*E* and *Z* isomer), dihydrazones **9**, **10**, and **11** (*Z*/*Z*, *E*/*E* and *E*/*Z* isomers), and hydrazine-enone tautomers **12** and **13** that are continually interconverting and therefore dynamic. The gradual addition of dibutylbarbiturate **14** leads to quantitative amplification of *Z*/*Z* dihydrazone **10** because it efficiently binds barbiturate via four complementary hydrogen bonds and thus is a new thermodynamic minimum of the system.

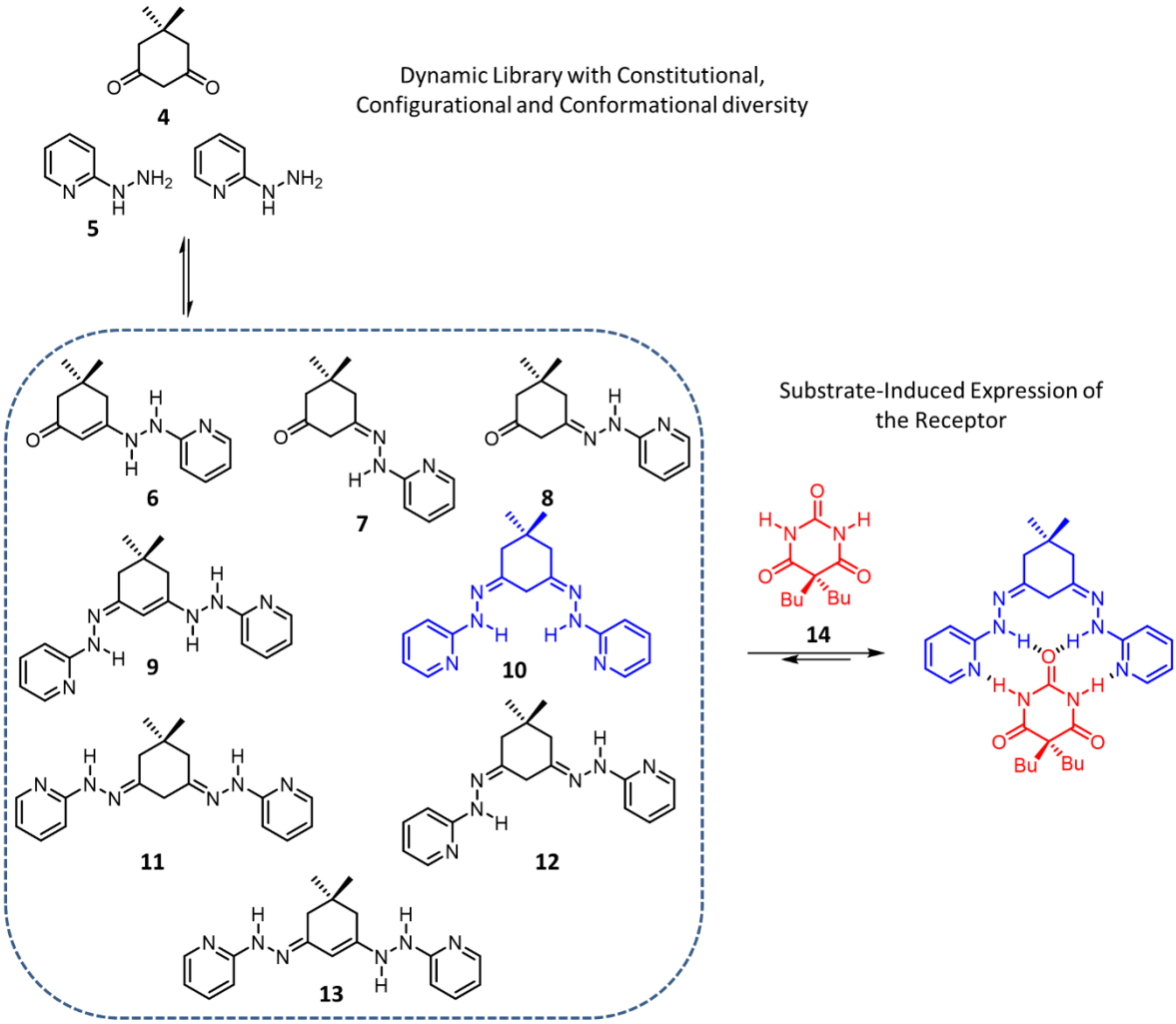

Figure 9. Barbiturate receptor amplification from the dynamic combinatorial library. Adapted from [40] with permission from Wiley-VCH, copyright (1999).

1.2.1.1 Dynamic Combinatorial Reactions

New dynamic combinatorial reactions are continuously discovered. They can be covalent (e.g., disulfide exchange) or non-covalent (e.g. hydrogen bonding). A good DCC reaction ideally has to fulfil the following requirements:[41]

1) Interactions must be reversible.
2) To reach the thermodynamic equilibrium in a reasonable time frame, all interactions should be relatively fast. This is particularly important for the selection process of a molecular host or guest and less important for dynamic materials, where fast kinetics can impact materials` properties. This requirement is often achieved using a catalyst.
3) The reaction conditions. Harsh reaction conditions, for instance, high temperature, can destroy all weak non-covalent interactions. Mild reaction conditions (for example, water and low temperature) are highly desired for DCLs of biomolecules.
4) There needs to be a way to terminate the exchange process to isolate selected library members. This can be achieved by changing pH, removal of the catalyst, temperature control, or kinetic trapping of the library member.

Figure 10 shows some of the most commonly used DCC reactions.

DCC allows the discovery of new receptors, catalysts, inhibitors, materials, interactions, and systems behaviour some examples of which will be discussed in the following chapters.

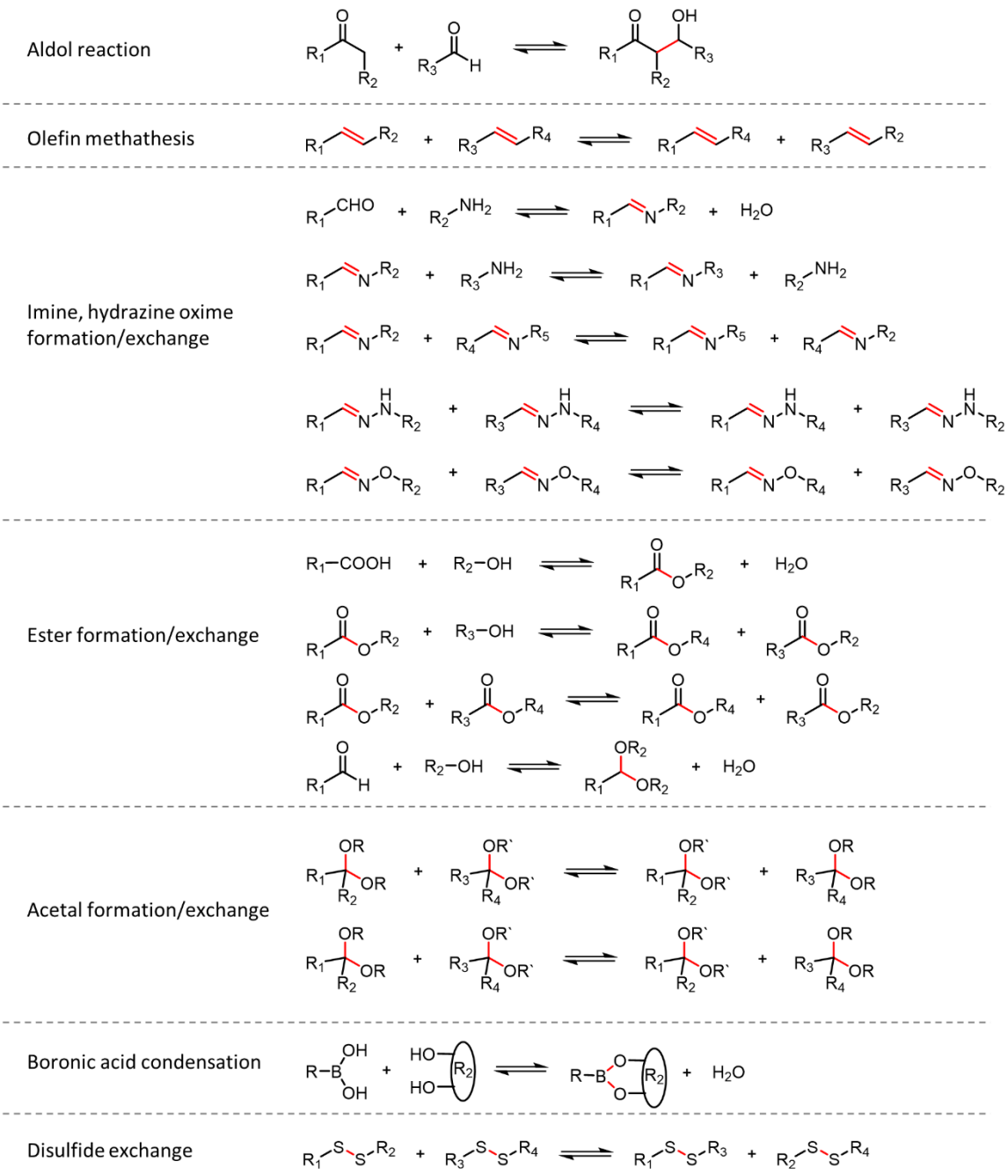

Figure 10. Examples of DCC reaction. Dynamic bonds are coloured in red. Adapted from [41] with permission from the Royal Society of Chemistry, copyright (2013).

1.2.1.2 Self-assembled Molecular Cages

The reversible nature of DCC reactions imparts the ability of error-correction, therefore, DCC is a method of choice for the synthesis of large three-dimensional structures: cages and covalent/metal-organic frameworks. Main factors fuelling the interest in cage compounds are the following:

1) Cages possess internal cavities that can encapsulate different guests. This ability can be used for storage and separation applications.
2) Encapsulated molecules are in a confined environment. This, combined with interactions with the cage itself, can cause unusual reactivities.
3) The emergence of complex behaviour, for example, structural changes upon the addition of external stimuli.

Fujita and coworkers reported the first self-assembled metal-organic cage in 1995.[42] They used reversible coordination of Pd(II) complexes with pyridyl ligands to assemble in one step ten molecules into a nanometer-sized organic framework **15** with a cavity able to encapsulate hydrophobic guests (e.g., adamantly carboxylate). In 2006 Fujita and coworkers demonstrated that cage **15** encapsulates anthracene **16** and phthalimide **17** (Fig. 11a) derivatives and catalyses Diels-Alder reaction with unusual regioselectivity.[43] Instead of adding to the central anthracene ring, the fixed orientation of the encapsulated guests promoted addition to the terminal ring leading to the *syn* isomer of 1,4-adduct **18** (Fig. 11b,c).

Since then, the field of coordination cages has been among the most quickly growing in supramolecular chemistry. Metal-organic cages with various geometries and topologies[44] have been synthesized that can encapsulate a large number of different guests[45], for example, anions,[46,47] organic molecules,[48,49] fullerenes,[50] and even a small protein[51] imparting, often, unusual reactivities.[52–54] The ultimate power of reversible coordination bonding for the self-assembly of complex molecules was demonstrated in the 144 (!) component self-assembly of Goldberg polyhedron with size rivalling natural peptides.[55]

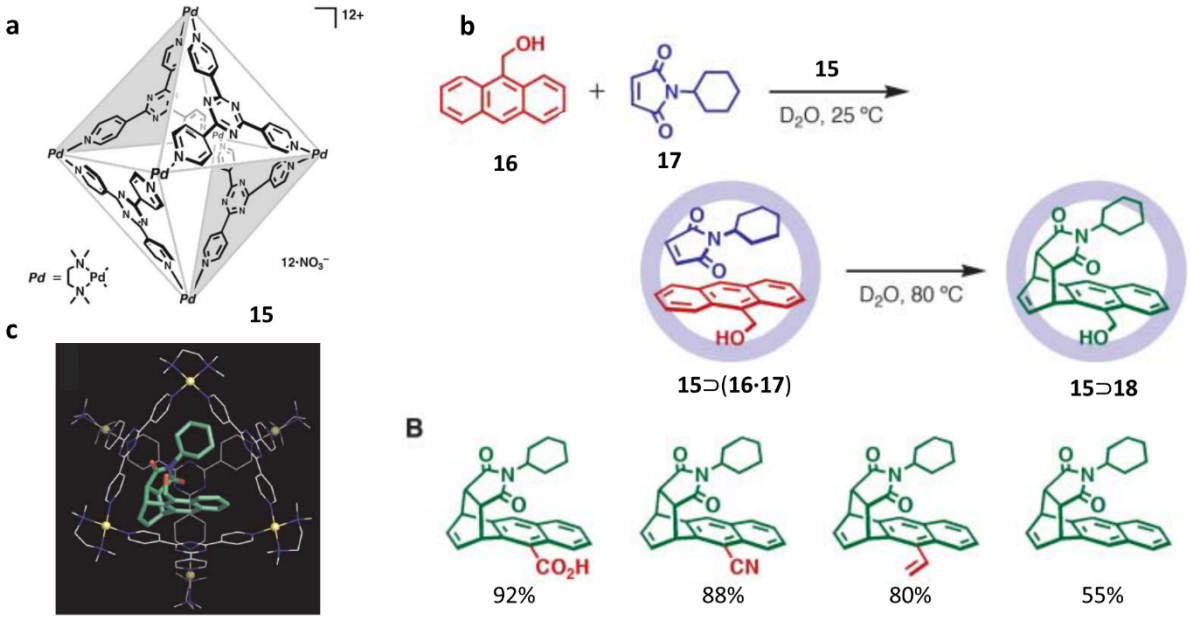

Figure 11. a, Self-assembled coordination cage **15**. Reproduced from [42] with permission from the Nature Publishing Group, copyright (1999). **b**, Unusual regioselectivity of the Diels-Alder reaction. **c**, Crystal structure of **18** encapsulated in the **15**. Adapted from [43] with permission from the American Association for the Advancement of Science, copyright (2006).

Initially, most purely covalent organic cages were synthesized in a stepwise manner that was often very low yielding. In 1988, MacDowell and Nelson reported the first covalent self-assembled cage using dynamic imine exchange. They utilized Schiff-base condensation of the tris(2-aminoethyl)amine with various aromatic dialdehydes to produce [2+3] imine cages.[56] The rise of porous self-assembled cages started in the 2010s with works from Mastalerz[57] and Cooper[58] groups and continues ever since. The most widely used reactions for the self-assembly of porous organic cages currently are imine and boronic ester formation between rigid organic molecules that bear preprogrammed information about the structure of the final cage. From the practical point of view, these compounds are promising for the storage and separation of volatile compounds.

One particularly interesting research finding that is possible thanks to DCC is porous liquids. Normal porous materials, for example, zeolites, are typically crystalline solids, the robustness of which allows containing permanent porosity. Liquids, in contrast, have limited porosity due to fluid structure. In 2015, Cooper and coworkers prepared the first porous liquid.[59] Scientists synthesized the porous imine-based organic cage **21** (Fig. 12a), equipped with crown-ether-like side chains, and dissolved it in 15-crown-5. Because solvent molecules were too large to

enter the cavity, the obtained free-flowing liquid had permanent porosity (Fig. 12b). The fractional void volume of porous liquids was estimated as 0.7%, not much, but it was enough to change the solubility of gases significantly. The porous liquid had enhanced ability to solubilize N_2, CH_4, CO_2, and Xe. However, the addition of a better-fitting guest, e.g., chloroform, readily displaced dissolved gasses leading to their liberation (Fig. 12c).

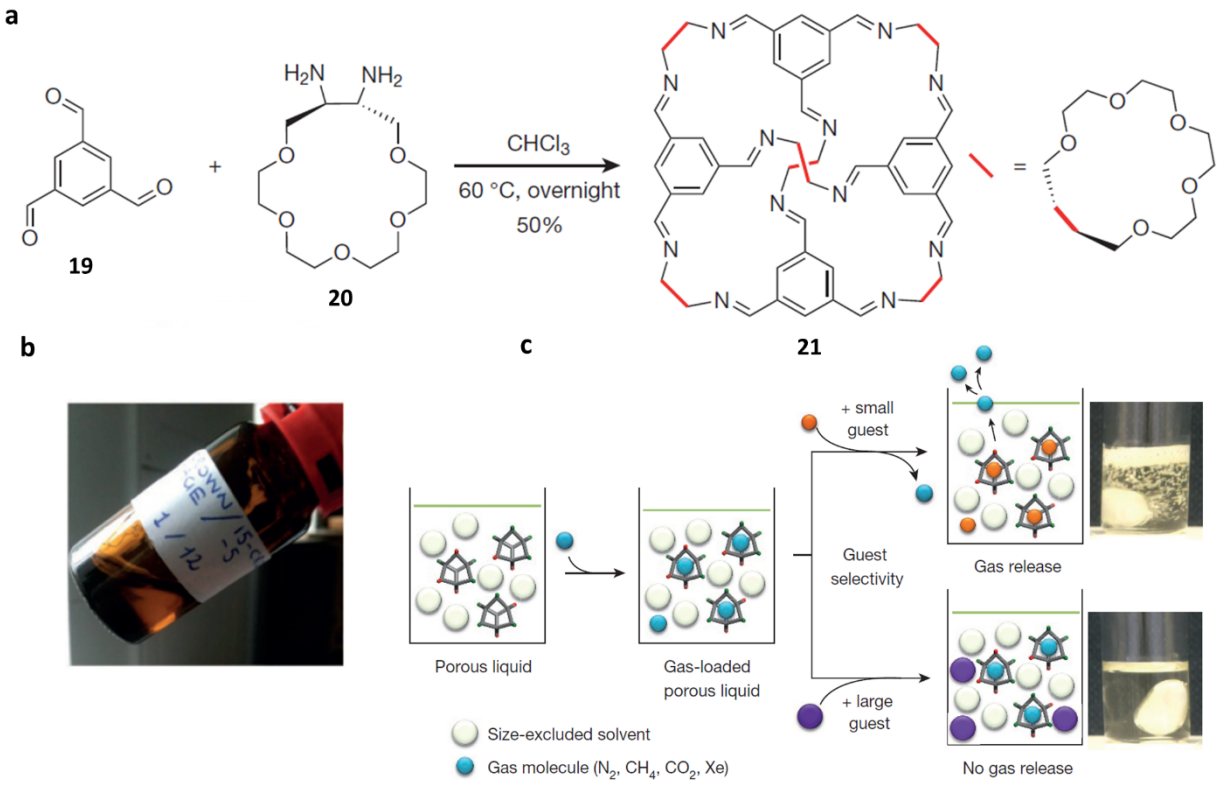

Figure 12. a, Synthesis of the crown-ether cage **21**. **b**, Free-flowing concentrated solution of **21** in 15-crown-5 solvent (porous liquid). **c**, The porous liquids show enhanced solubilities for nitrogen, methane, xenon, and carbon dioxide. The addition of small, good-fitting guest $CHCl_3$ liberates xenon gas from a saturated porous liquid. Adapted from [59] with permission from the Nature Publishing Group, copyright (2015).

1.2.1.3 Mechanically Interlocked Compounds

The most common and historically the first rational strategy towards mechanically interlocked molecules relies on metal coordination.[60] Sanders and coworkers showed that DCC allows the stereoselective synthesis of extremely complex molecular topology: trefoil knot[61] – the most sophisticated mechanically interlocked compound synthesized using DCC.[62] Sanders and his team used building block **22** composed of three hydrophobic electron-deficient NDIs connected by flexible hydrophilic amino acids and terminated at both ends by L-cysteine, which provides a thiol for disulfide exchange (Fig. 13a). After equilibration in water at pH 8 DCL contained mainly the closed monomer and dimer with trace amounts of the trimer, which appeared to be the trefoil knot (Fig. 13b). The equilibration in the presence of high concentrations of $NaNO_3$ nearly quantitatively amplified the knotted trimer (Fig. 13 c-f). This result proved that the driving force in the formation of the trefoil knot is the hydrophobic effect that forces the hydrophobic surfaces to be buried, in order to minimize water exposed area, and the hydrophilic side chains to be exposed to the solvent (Fig. 13g).

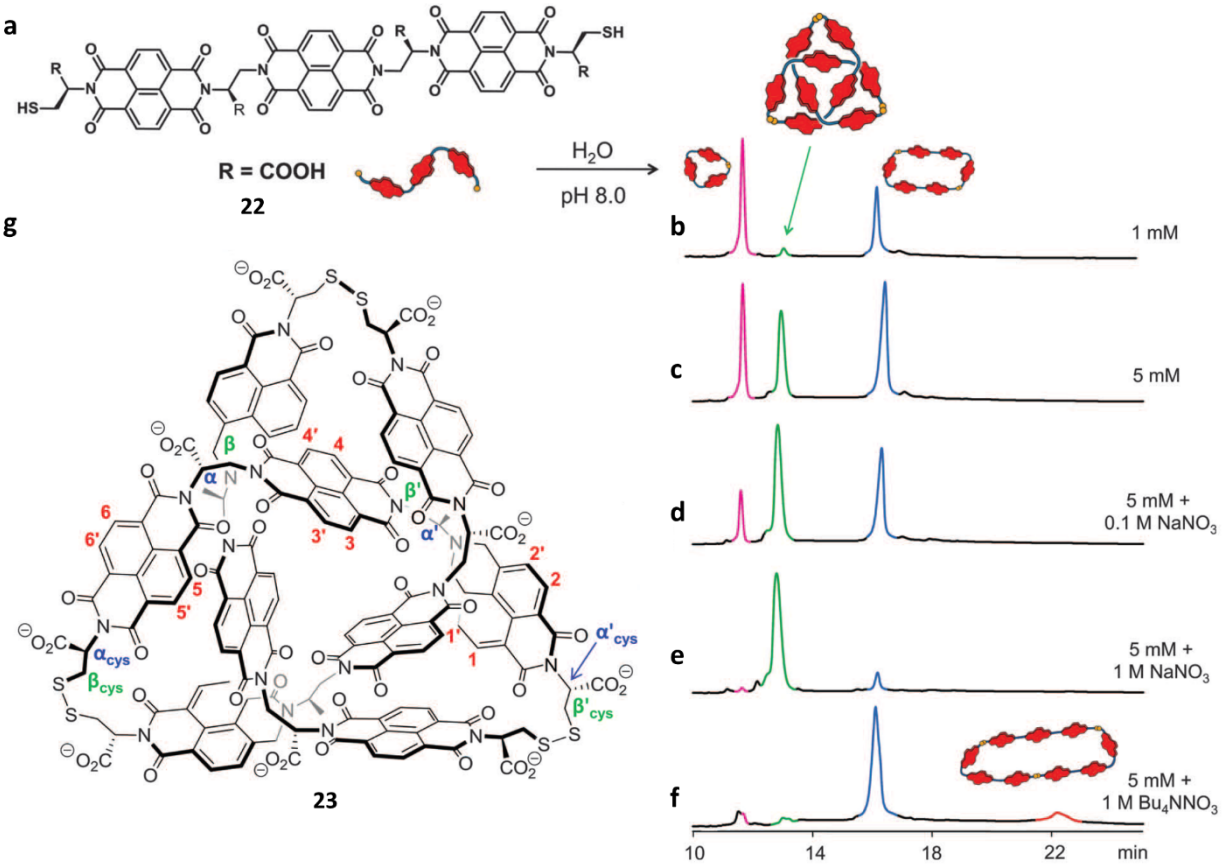

Figure 13. a, The structure of NDI building block **22**. **b**, **c**, HPLC analysis of DCLs formed at 1 mM and 5 mM concentration of **22**. **d**, **e**, **f**, Salt effect on the product distribution in DCLs of **22**. **g**,

Chemical structure of the trefoil knot **23**. Adapted from [61] with permission from the American Association for the Advancement of Science, copyright (2012).

1.2.1.4 Synthetic Receptors and Ligands for Biomolecules

In 2006, Otto and coworkers used DCC to create a receptor for a biologically active compound - spermine.[63] Spermine **24** is a polyamine that plays a key role in many biological processes. For instance, it facilitates the formation of nucleosomes by condensing DNA and chromatin.[64] To study its biological functions, there is a need for synthetic receptors that can efficiently sequester polyamines. However, binding affinities of synthetic receptors are usually several orders of magnitude lower than those of biomolecules, thus preventing the efficient removal of polyamines.[65]

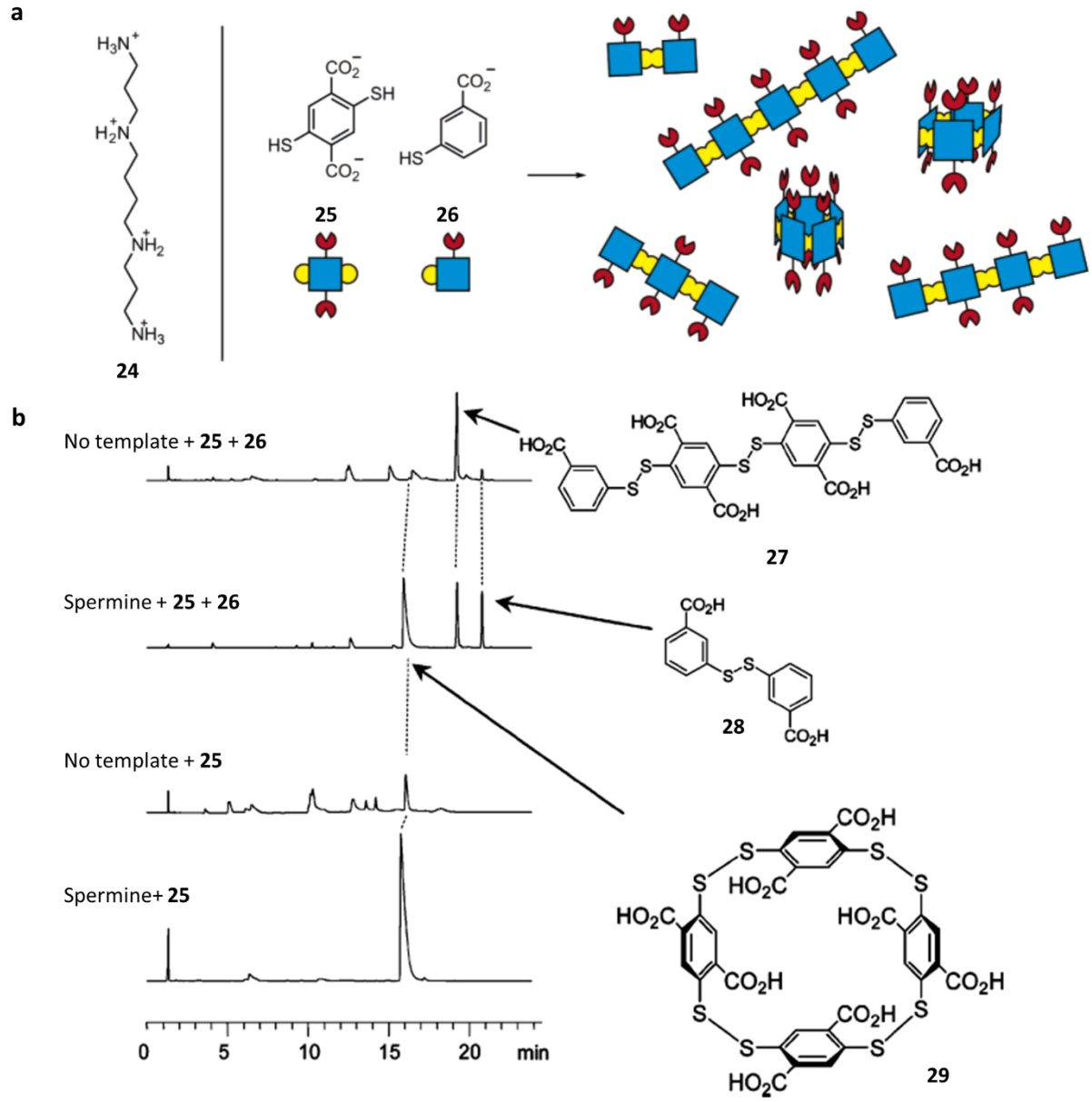

Figure 14. a, Schematic illustration of the DCL produced by oxidation of thiols **25** and **26**. **b**, HPLC analysis of the influence of spermine on DCLs of **25** and **26**. Adapted from [63] with permission from the American Chemical Society, copyright (2006).

To find an efficient spermine binder, Otto and coworkers generated a DCL by disulfide exchange between thiol derivatives of benzoic and terephtalic acids **25** and **26** (Fig. 14a). Library members were tailored to recognize protonated spermine through hydrogen bonding and electrostatic interactions. Without spermine, the major component was linear tetramer **27**. The addition of the spermine amplified cyclic tetramer **29** (Fig. 14b). Tetramer **29** binds spermine with a dissociation constant 22 nM forming a pseudorotaxane complex. The binding affinity was high enough to compete with biomolecules. It was demonstrated in experiments where **29** was able to unbind spermine from DNA and thereby control the helicity of DNA.

DCC is also useful in discovering new anion receptors. As one example, the self-assembled sulfate receptor reported by Sessler and coworkers.[66] Imine condensation of diformylbipyrrole **31** and 2,6-dicarboxamidopyridine derived diamine **30** led to the DCL of different macrocycles and linear oligomers. When sulfuric acid was used as a catalyst, [2+2] macrocycle **32** was amplified nearly free of other side products (Fig. 15). Upon treatment with TEA free macrocycle **33** was isolated in 75 % yield and single-crystal X-ray analysis confirmed its structure. UV/Vis spectroscopic titrations revealed that **33** has high affinity towards tetrahedral anions HSO_4^- (1:1, K_{a1} = 63500 M^{-1}) and $H_2PO_4^-$ (2:1, K_{a1} = 191000 M^{-1}, K_{a2} = 60200 M^{-1}) and relatively weakly binds acetate (1:1, K_{a1} = 26000 M^{-1}). Almost no interactions were observed with all other tested anions: chloride, bromide, and nitrate.

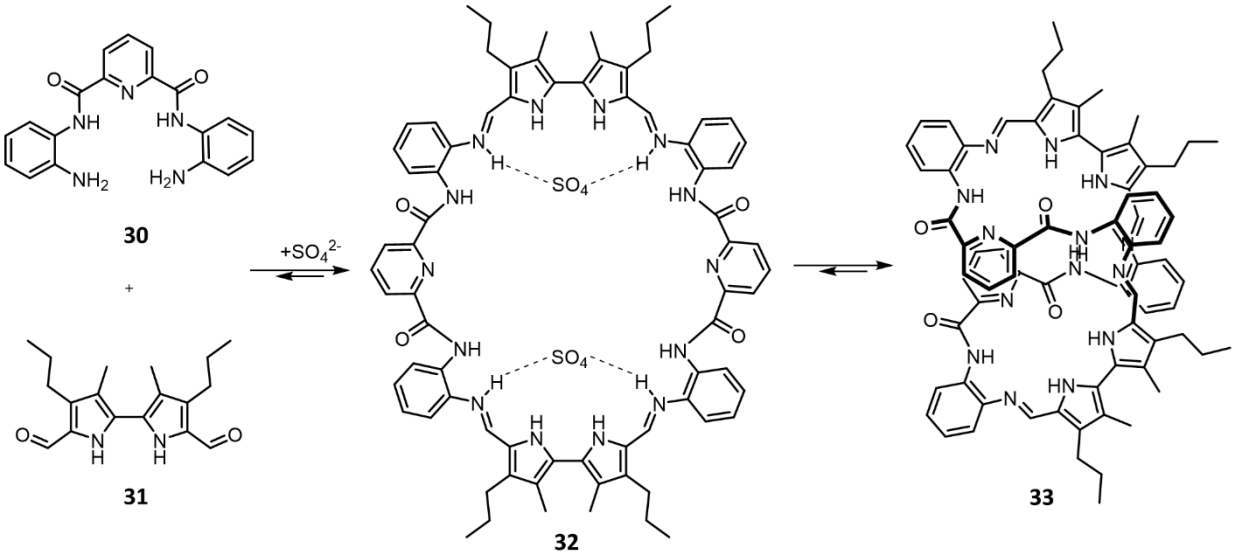

Figure 15. a, Dynamic amplification of the anion binding macrocycle **32** templated by sulfate anion. Adapted from [66] with permission from Wiley-VCH, copyright (2005).

A very important application of DCC is the discovery of ligands for biological receptors.[67] Combinatorial chemistry is an important instrument in medicinal chemistry. It is a potent technology for creating collections of structurally related compounds that may be subsequently screened for desired biological activity. Components of chemical combinatorial libraries are usually synthesized using a straightforward synthetic approach. They are usually prepared as discrete, stable entities nearly insensitive to environmental changes. Drug discovery using combinatorial chemistry is a trial-and-error method, and the success highly depends on the number of compounds synthesized and screened. An alternative approach to simplifying the drug discovery is to allow biological targets to select an active ligand directly from a library pool. This can be achieved by generating DCLs in the presence of a biological target that amplifies the most efficient binder. This approach has been successfully demonstrated for a number of biological targets: trypsin,[68] carbonic anhydrase,[69] kinases,[70] DNAs, and RNAs,[71–73] to name a few.

In a representative example, DCC was used to discover an inhibitor of the influenza A virus neuraminidase – an enzyme playing an important role in the propagation of the virus.[74] The DCL was generated via imine exchange between diamine **34** and several different aldehydes that can react, forming imines and hemiaminals (Fig. 16a). The potential diversity level of such system is very high; for example, the set of 20 aldehydes potentially yields over 40000 stable components – the number that is not achievable in reality using straightforward synthesis (Fig. 16b). Incubation of the DCL in the presence of neuraminidase followed by reduction, to stop the exchange, resulting in a striking amplification of selected library components with amplification factors up to 200 (Fig. 16c). Amplified compounds had enhanced inhibitory activity against neuraminidase.

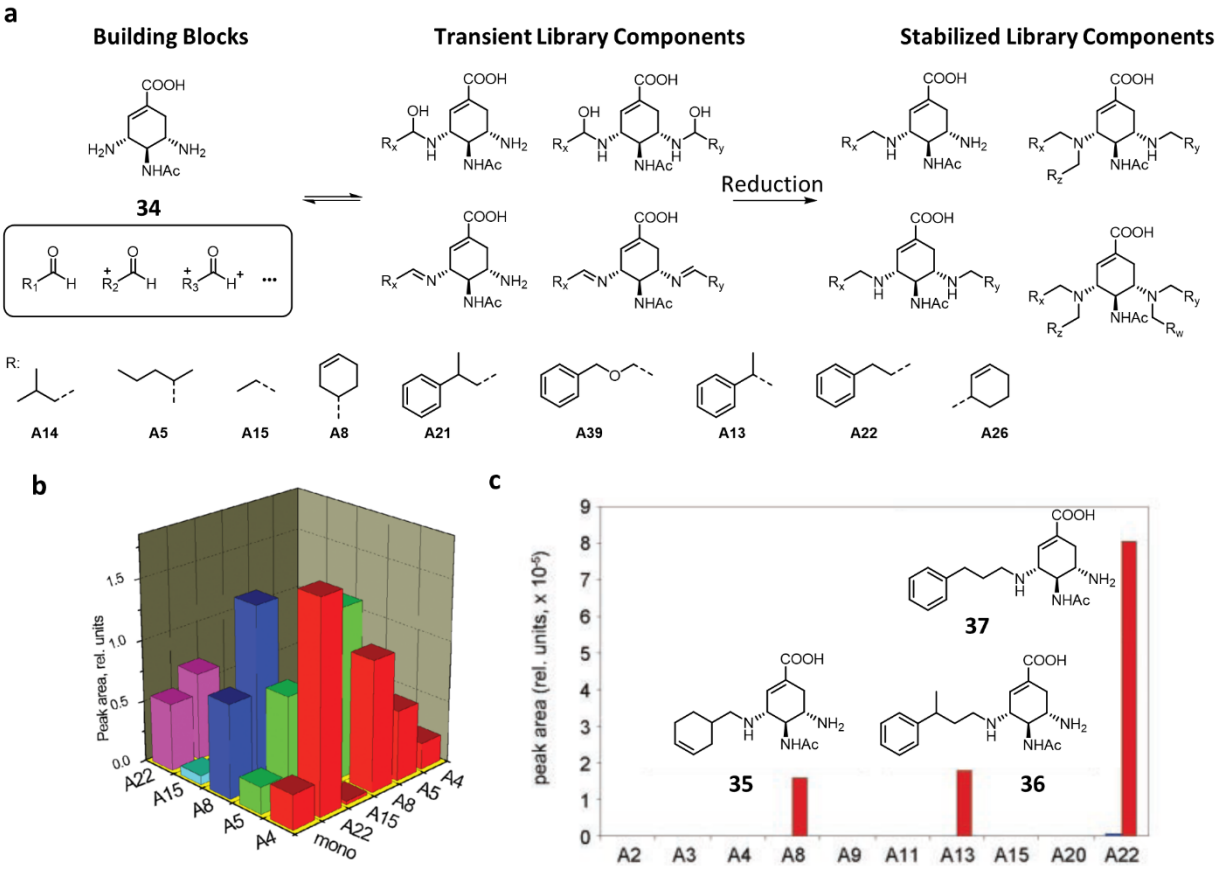

Figure 16. **a**, Possible members of DCL obtained via imine formation between **34** and aldehydes. **b**, Mono- and disubstituted components detected in a static library of potential inhibitors. **c**, Library members formed in the presence (red bars) and the absence (blue bars) of neuraminidase. Reproduced from [74] with permission from the National Academy of Sciences (USA), copyright (2015).

1.2.1.5 Adaptive Materials

The key elements of DCC are diversity, reversibility, and molecular recognition. A combination of these three elements in polymeric systems can lead to new functional polymers that are self-healable and responsive to external stimuli.[75]

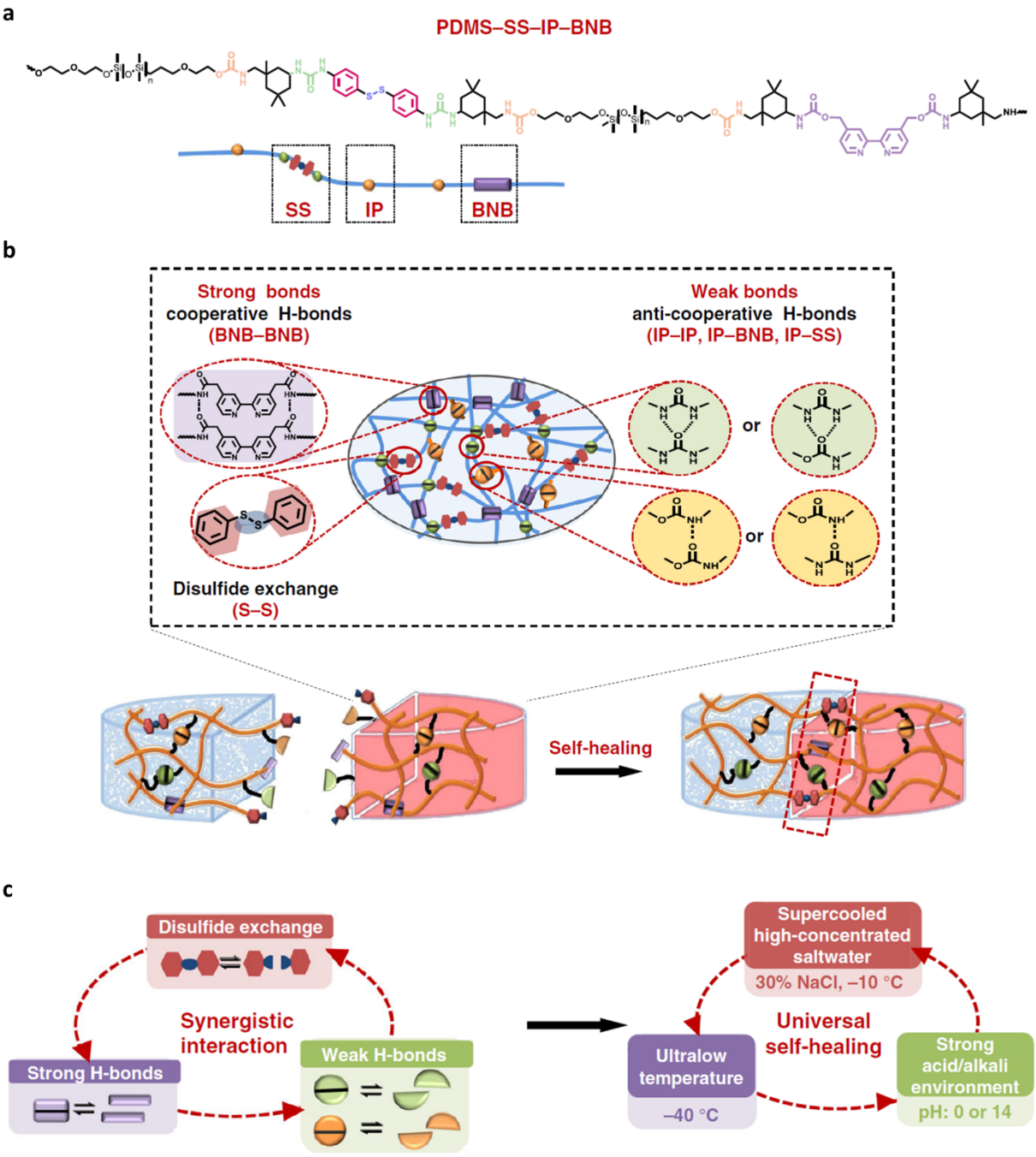

Figure 17. **a**, Chemical structure of the dynamic polymer. **b**, The structure of the supramolecular polymer network based on strong crosslinking H-bonds (BNB-BNB), weak crosslinking H-bonds (IP-IP, IP-BNB, IP-SS), and disulfide metathesis (S–S). **c**, Universal self-

healing capability of the elastomer as a result of multiple synergistic interactions. Adapted from [76] with permission from the Nature Publishing Group, copyright (2020).

For example, Zhang and coworkers synthesized a dynamic polymer network (Fig. 17a) that contains different covalent and non-covalent dynamic bonds, including disulfide metathesis (S–S) and strong and weak crosslinking H-bonds (Fig. 17b).[76] The synergy of these interactions resulted in a supramolecular elastomer with high stretchability and universally autonomous self-healing capabilities in ambient conditions and harsh conditions including underwater, at freezing or even ultralow temperatures (-20 °C or -40 °C), in supercooled salt-water, or under strongly acidic or alkali conditions without external stimuli or additives (Fig. 17c).

Liebler and coworkers managed to create a vitrimer with backbones solely made of carbon-carbon single bonds using dynamic metathesis of dioxaborolanes that takes place without any catalyst and at relatively low temperature (60 °C).[77] Dioxaborolanes were incorporated in polymers either by copolymerization with monomers containing pendant dioxaborolanes (Fig. 18a) or by reactive processing of commercial thermoplastics (Fig. 18b). The first approach was demonstrated for polystyrene and poly(methyl methacrylate). The latter approach is very useful for the preparation of vitrimers directly from commercial thermoplastics, for example, HDPE. PS and PMMA vitrimers at room temperature were transparent and colorless solids with mechanical properties comparable to homopolymers. All vitrimers could be processed and reprocessed by extrusion or injection molding several times, just like commercial thermoplastics. Due to dynamic covalent bonding, vitrimers were also endowed with enhanced adhesive abilities. The adhesion between PMMA and HDPE was so strong that in mechanical tests bulk PMMA ruptured (Fig. 18d).

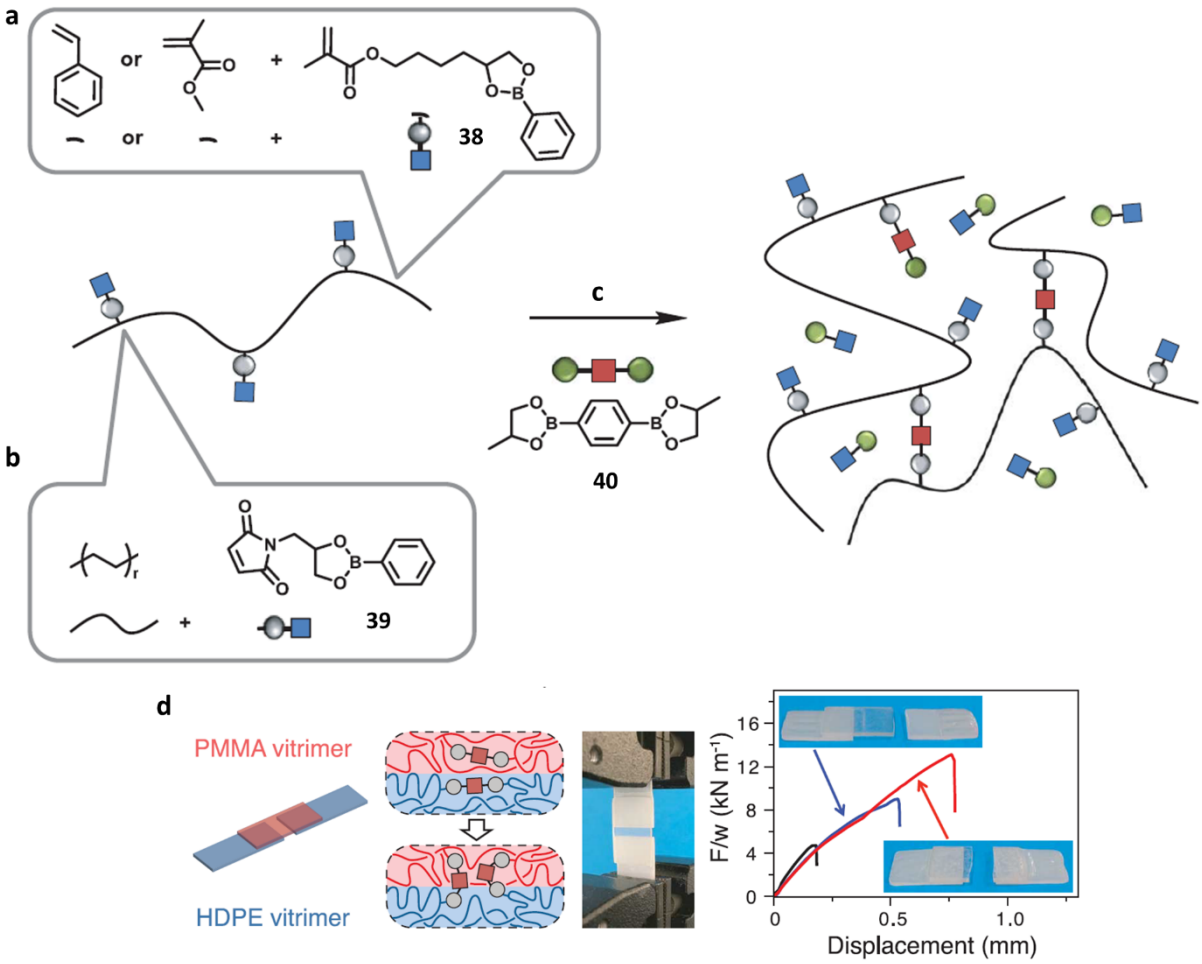

Figure 18. a, Formation of the vitrimer by copolymerization of styrene or methyl methacrylate with monomer **38** bearing dioxaborolanes. **b**, Formation of the vitrimer by reactive processing of commercial polyethylene. **c**, Schematic illustration of the dynamic polymer network. **d**, Enhanced adhesion of PMMA and HDPE vitrimers. Shown are schematic illustration, photo, and lap-shear testing of double lap joints of PMMA/HDPE dioxaborolane thermoplastic precursors and PMMA/HDPE vitrimers for two contact times, 10 min and 20 min. Adapted from [77] with permission from the American Association for the Advancement of Science, copyright (2017).

Helms and coworkers created a fully recyclable and reusable polymer using dynamic diketoenamine bonds.[78] Poly(diketonamine)s (PDKs) were prepared via polycondensation reaction between β-triketones (e.g., **41**) and amines using a ball mill (Fig. 19a). PDKs hydrolyze in strong aqueous acid (0.5 – 5.0 M H_2SO_4) in less than 12 h to starting diketones and amines. From the resulting mixture, triketones could be easily removed by basic extraction and subsequent precipitation upon re-acidification. Amines were separated using a regenerative resin-based process (Fig. 19a). The utility of the proposed approach was demonstrated using

colored polymers, polymers reinforced with carbon nanofibers, TiO_2, and additives that endow flame-retardant properties (Fig. 19b).

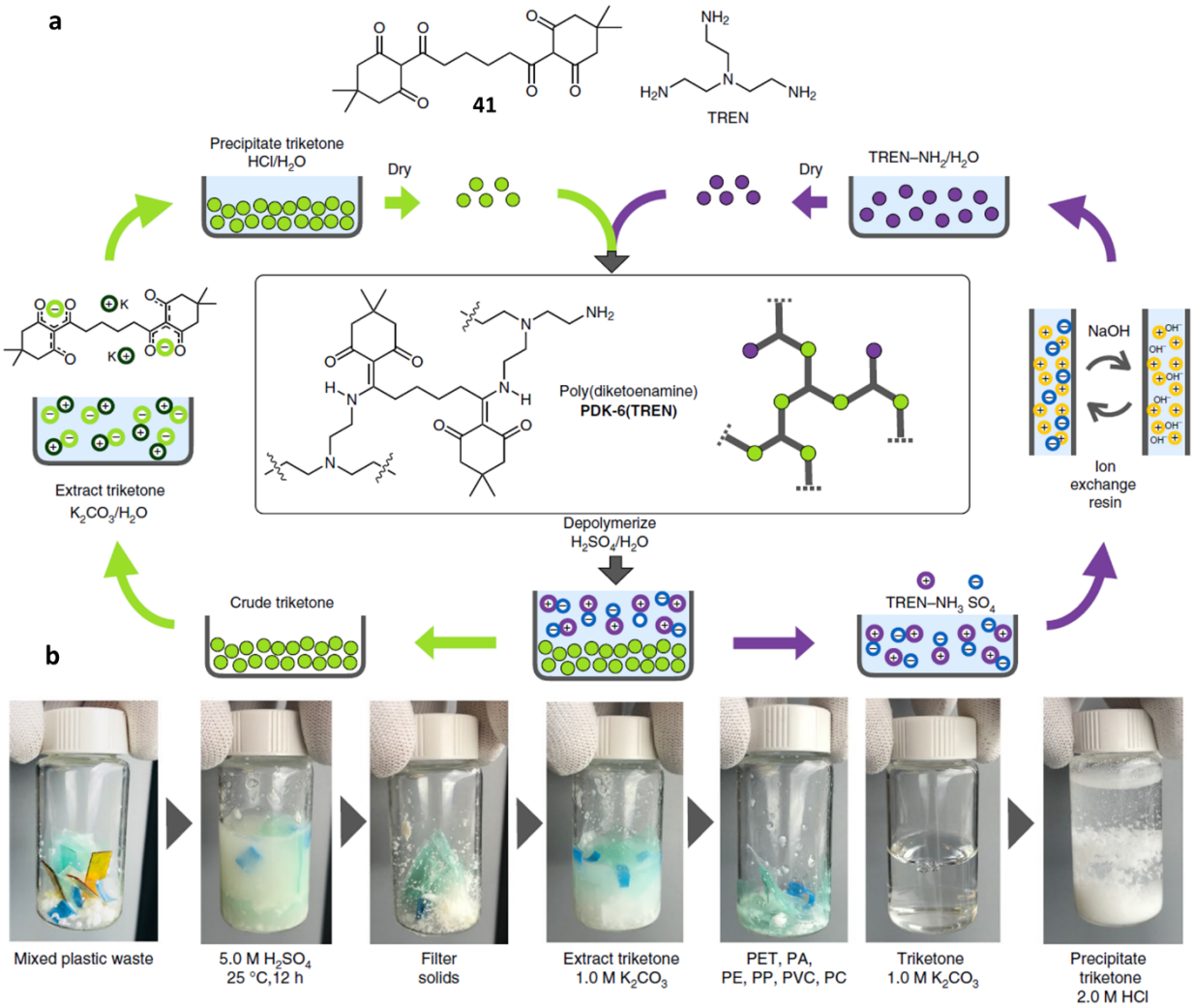

Figure 19. a, Schematic illustration of the formation and recycling of the PDK network. **b**, Photographs showing different steps of the triketone **41** monomer recovery from mixed plastic waste containing poly(ethylene terephthalate), nylon-6,6, polyethylene, poly(vinyl chloride) and polycarbonate. Adapted from [78] with permission from the Nature Publishing Group, copyright (2019).

1.2.2 Orthoester Exchange

In 2015, von Delius and Brachvogel introduced a new dynamic covalent reaction – acid-catalysed exchange of *O,O,O*-orthoester.[79] In terms of reaction mechanism, orthoester exchange is related to the ester and the acetal exchange by general acid catalysis and is characterized by occurrence of sp^2-hybridized oxonium ion intermediates. The exchange of orthoesters with alcohols occurs under mild conditions in various solvents when the catalytic amount of acid is present (typically 0.1 – 5%).

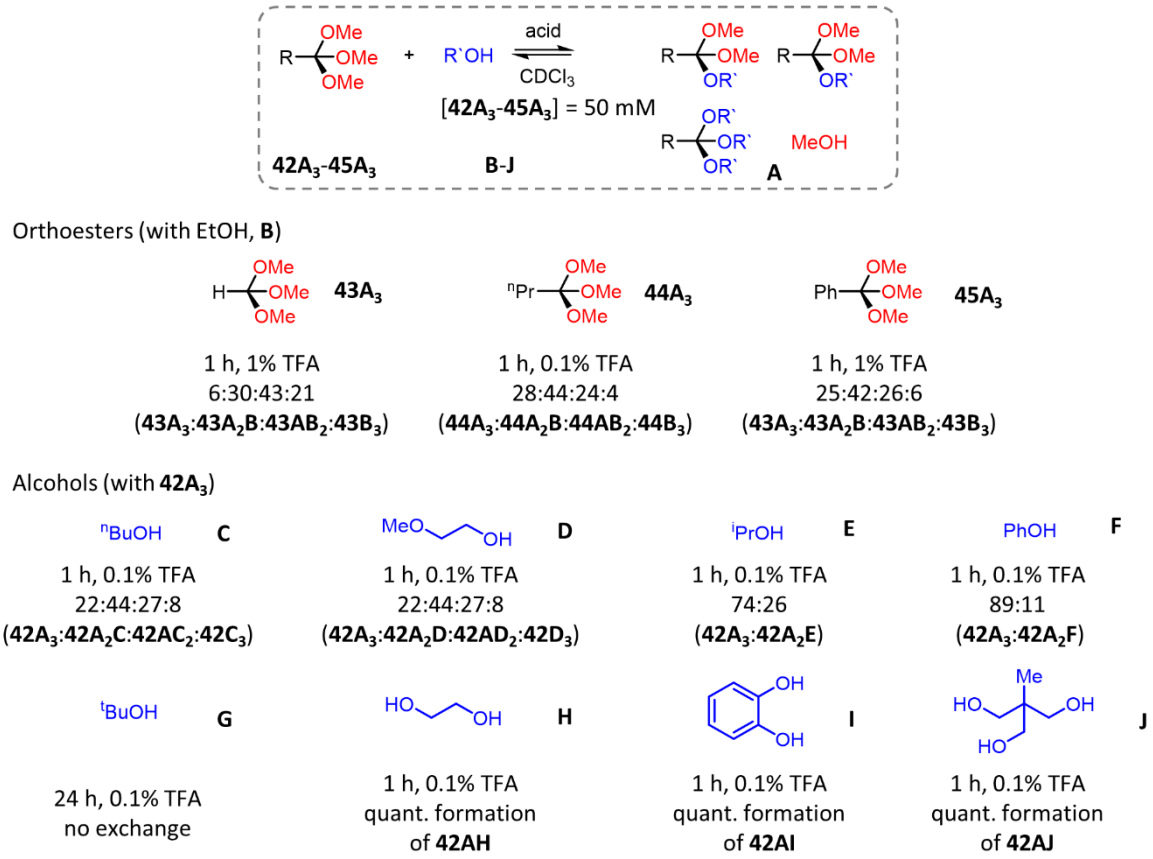

Figure 20. Scope studies on orthoester exchange. Adapted from [79] with permission from the Royal Society of Chemistry, copyright (2015).

As an example, trimethyl orthoacetate reacted with ethanol forming a statistically distributed mixture of four orthoesters. When starting from triethyl orthoacetate and methanol, identical product distribution was reached, confirming that the reaction outcome corresponded to the system's thermodynamic minimum. Different alcohols and phenols could be used for the orthoester exchange. However, the nature of the substrate affects the final distribution of products. Bulk isopropanol and phenol formed only orthoesters featuring only one secondary

alcohol, likely due to significant steric crowding in the products. Triisopropyl orthoacetate could be obtained following this route only if methanol was continuously removed under vacuum to shift the equilibrium to the side of products. *Tert*-butanol gave no products of exchange. Due to the chelate effect, diols and triols formed quantitatively cyclic products (Fig. 20). This property is well-known and has been widely exploited in synthetic chemistry for the face-selective protection of polyols.[80]

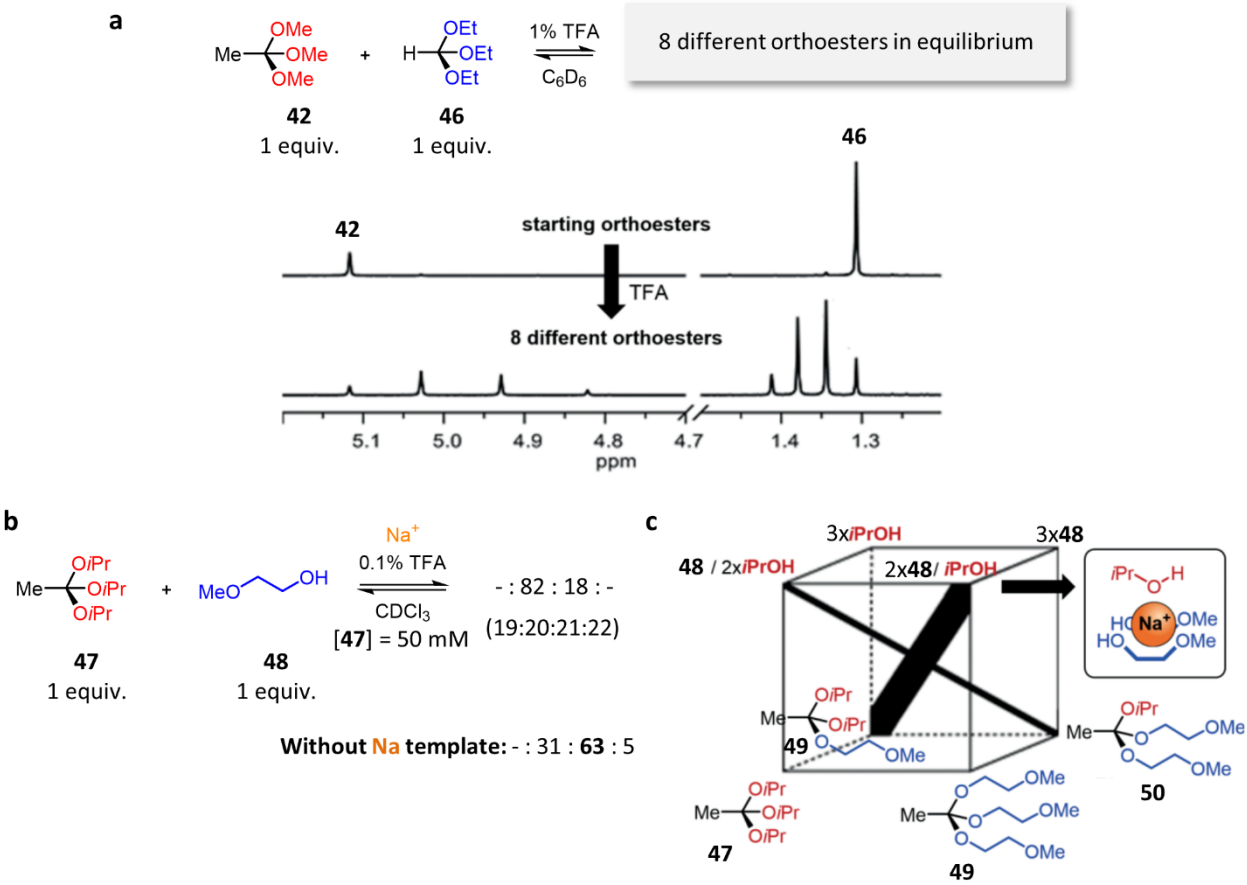

Figure 21. a, ^{1}H NMR monitoring of orthoester metathesis reaction ([**42**]$_0$ = 50 mM, C_6D_6, 400 MHz, 298 K). **b**, Exchange experiment illustrating influence of Na^+ on the equilibrium distribution in dynamic orthoester library ([**47**]$_0$ = 50 mM, $CDCl_3$, 400 MHz, 298 K). **c**, Graphical analysis of the reaction outcome in the presence of Na^+ based on agonistic relationships. Adapted from [79] with permission from the Royal Society of Chemistry, copyright (2015).

The possibility of the orthoester exchange between two different orthoesters was also demonstrated. In the presence of an acid, an equimolar mixture of trimethylorthoacetate and triethylorthoformate formed a mixture of eight different orthoesters (Fig. 21a). In terms of complexity, namely the number of DCL members produced by two monofunctional compounds, orthoester exchange is by far the most efficient DCC reaction.

External stimuli can shift product distribution in orthoester DCLs. In a model reaction between "high-energy" triisopropyl orthoacetate **47** and 2-methoxyethanol **48**, a two-fold exchange product was the major component of the DCL. However, in the presence of NaBArF, another exchange product – **49** – was amplified (Fig. 21b). This observation was rationalized based on agonistic and antagonistic relationships in DCL. The agonist pair 3 × **48** and **47** can efficiently stabilize the naked sodium ion. However, high ground state energy of **47** precludes the formation of this pair. The second best solution would be the agonist pair 2 × **48** × **iPrOH** and **49**, which is the major product (Fig. 21c).

The main disadvantage of the dynamic orthoester exchange is the hydrolytic instability of orthoesters that decompose to corresponding esters in the presence of acid and water. This property complicates the separation and purification of amplified orthoester DCL members, and all orthoester exchange reactions must be carried out with thorough exclusion of any moisture. Due to relative instability, one would wish to manipulate orthoesters as little as possible. However, this disadvantage could potentially be a huge benefit for some applications e.g. in drug delivery, when irreversible hydrolysis could lead to guest release.[81,82] These applications would require control over the rate of hydrolysis.

In 2018, von Delius and coworkers demonstrated that the nature of orthoester substituent can tune the rates of hydrolysis and the orthoester exchange.[83] They studied orthoesters bearing electron-donating substituents (e. g. $–CH_3$, $–nC_3H_7$), which stabilize the oxonium intermediate, and electron-withdrawing groups ($–CH_2Cl$, $–CCl_3$, triazole, and triazolium). The kinetics of hydrolysis was studied in buffered aqueous solutions in the pH range 8 – 1. Kinetics of the exchange was studied in chloroform with ethanol and different amounts (0.01 to 100 mol. %) of organic acids (TFA or TfOH). In both cases, electron-rich orthoesters had faster kinetics of both exchange and hydrolysis. For instance, trimethyl orthoacetate had 10 min half-life of hydrolysis at pH 7, whereas electron-deficient orthoesters (R_1 = -triazolium, $–CCl_3$) were stable for hours even at pH 1 (Table 3). The observed reactivity trend correlates well with the Taft parameter for R_1 group.[84] The authors also proposed that alkylation of the triazole into triazolium can be used to enhance the stability of orthoesters towards hydrolyses.

Table 3. Kinetics of orthoester hydrolysis. R_1 corresponds to the orthoester substituent, in all cases trimethyl orthoesters were used. Reproduced from [83] with permission from the Royal Society of Chemistry, copyright (2016).

R_1		pH 8	pH 7	pH 6	pH 5	pH 4	pH 3	pH 1
$-CH_3$	$t_{1/2}$ [min],	60,	10,	2,	<1			
	k_{obs} [s^{-1}]	1.8×10^{-4}	1.3×10^{-3}	6.1×10^{-3}				
–H	$t_{1/2}$ [min],	>1000	510,	70,	20,	7,	<1	
	k_{obs} [s^{-1}]		2.5×10^{-5}	1.6×10^{-4}	8.8×10^{-4}	2.0×10^{-3}		
$-CH_2Cl$	$t_{1/2}$ [min],		>1000	660,	120,	30,	<1	
	k_{obs} [s^{-1}]			1.7×10^{-5}	8.6×10^{-4}	2.9×10^{-4}		
–Triazole	$t_{1/2}$ [min],							<1
	k_{obs} [s^{-1}]							
–	$t_{1/2}$ [min],						Inert	>10000
Triazolium	k_{obs} [s^{-1}]							
$-CCl_3$	$t_{1/2}$ [min],							>1000
	k_{obs} [s^{-1}]							

In 2015, the same group described a one-pot synthesis of monometallic cryptates using orthoester exchange.[85] Orthoester exchange between trimethyl orthoacetate and diethylene glycol with NaBArF, serving as a source of naked sodium ions, in chloroform after one hour of reaction time formed a complex mixture of different orthoester products. Upon addition of 4 Å molecular sieves, which remove released methanol and serve as a thermodynamic sink, complex mixture converged into one single product – [**Na^+⊂*o*-Me_2-1.1.1**]**$BArF^-$** – that was isolated by passing its solution in chloroform through a short silica plug (Fig. 22). Single crystal X-ray analysis revealed that sodium ion is bound in the centre of the cavity to all nine oxygens via dipole-ion interaction. Competition experiments performed with Lehn's 2.2.1 cryptate afforded ***o*-Me_2-1.1.1** cryptand.[37] ***o*-Me_2-1.1.1** upon addition of catalytic TFA transformed into orthoester products featuring eight-membered rings, thus proving that ***o*-Me_2-1.1.1** does not represent a thermodynamic minimum and cannot be prepared without a template from trimethyl orthoacetate and diethylene glycol via reversible orthoester exchange.

***o*-Me$_2$-1.1.1** cryptand could also be obtained by treating a chloroform solution of [**Na$^+$⊂*o*-Me$_2$-1.1.1**]**BArF$^-$** with anion exchange resin Lewatit® MP-64, which leads to precipitation of NaCl. Titration experiments with Li^+, Na^+, and K^+ salts in CD_3CN were performed to determine the corresponding binding constants.[86] Na^+ and Li^+ formed *endo* complexes with binding constants 1330 and 2750 M^{-1} respectively. K^+ had binding constant one order of magnitude lower (75 M^{-1}) and, being too large for *endo* binding, binds *exo* instead. This difference was also expressed in the kinetics of cation binding. 1D EXSY NMR measurements showed that degenerate hopping of Na^+ and Li^+ from one cryptand to another is relatively slow (ca. 1 Hz) whereas for K^+ it was several orders of magnitude faster.

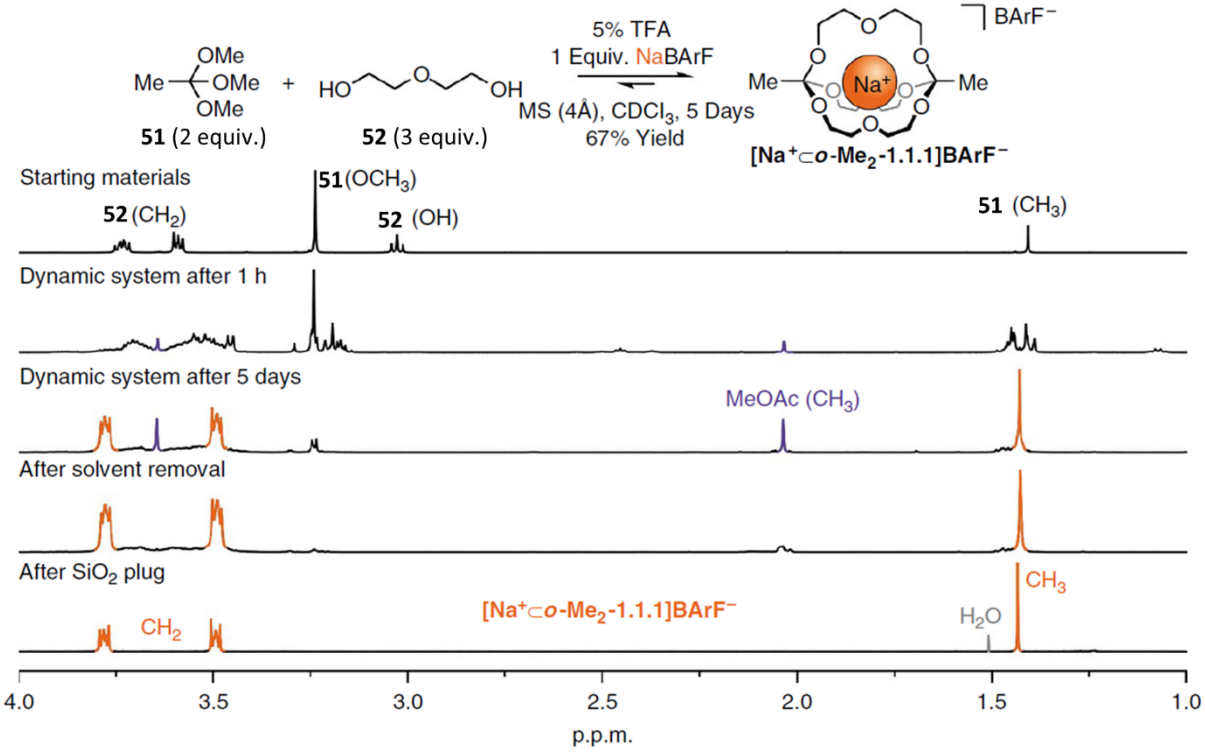

Figure 22. ^{1}H NMR monitoring of the self-assembly of orthoester cryptates templated by Na^+. Reproduced from [85] with permission from the Nature Publishing Group, copyright (2015).

Until recently, it was believed that the self-assembly of orthoester cryptates requires the presence of a suitable alkali metal template. Recently, von Delius and coworkers serendipitously found that the polar C–H bond of the bridgehead orthoformate orthoester can form intramolecular hydrogen bonds with the central oxygen atoms in the DEG chain, driving the formation of orthoformate cryptands ("self-templation").[87] The reaction of trimethyl orthoformate and DEG with catalytic amount of TFA unexpectedly furnished ***o*-(H$_{in}$)$_2$-1.1.1** in ca. 50% yield (Fig. 23a). This finding was very unusual because normally metal-free orthoester

exchange leads to the predominant formation of eight-membered ring products. ***o*-(H$_{in}$)$_2$-1.1.1** could be crystallized to give a single crystal suitable for X-ray analysis. The solid-state structure revealed the presence of two four-center C–H···O hydrogen bonds with the approximate H···O distances 2.4 and 2.5 Å below the sum of van der Waals radii (2.6 Å) (Fig. 23b). The addition of Li^+ to trimethyl orthoformate and DEG afforded [**Li^+⊂*o*-(H)$_2$-1.1.1**] that could be transformed into ***o*-(H)$_2$-1.1.1** by treatment with anion exchange resin. Addition of catalytic amount of TFA to ***o*-(H)$_2$-1.1.1** resulted in the bridgehead inversion with the quantitative formation of ***o*-(H$_{in}$)$_2$-1.1.1** within 5 min. Attempts to perform thermal (homeomorphic) inversion failed even at 200 °C, demonstrating that the DEG chain cannot be just pulled through to invert the configuration of the bridgeheads. Addition of the equimolar amount of Li^+ to ***o*-(H$_{in}$)$_2$-1.1.1** in the presence of catalytic TFA quantitatively yielded [**Li^+⊂*o*-(H)$_2$-1.1.1**]. However, an identical experiment but with Na^+ did not cause the transformation to the corresponding [**Na^+⊂*o*-(H)$_2$-1.1.1**] cryptate. This result was explained by a low affinity of Na^+ towards ***o*-(H)$_2$-1.1.1**. These experiments confirmed the thermodynamic stabilization of ***o*-(H$_{in}$)$_2$-1.1.1** by intramolecular hydrogen bonds.

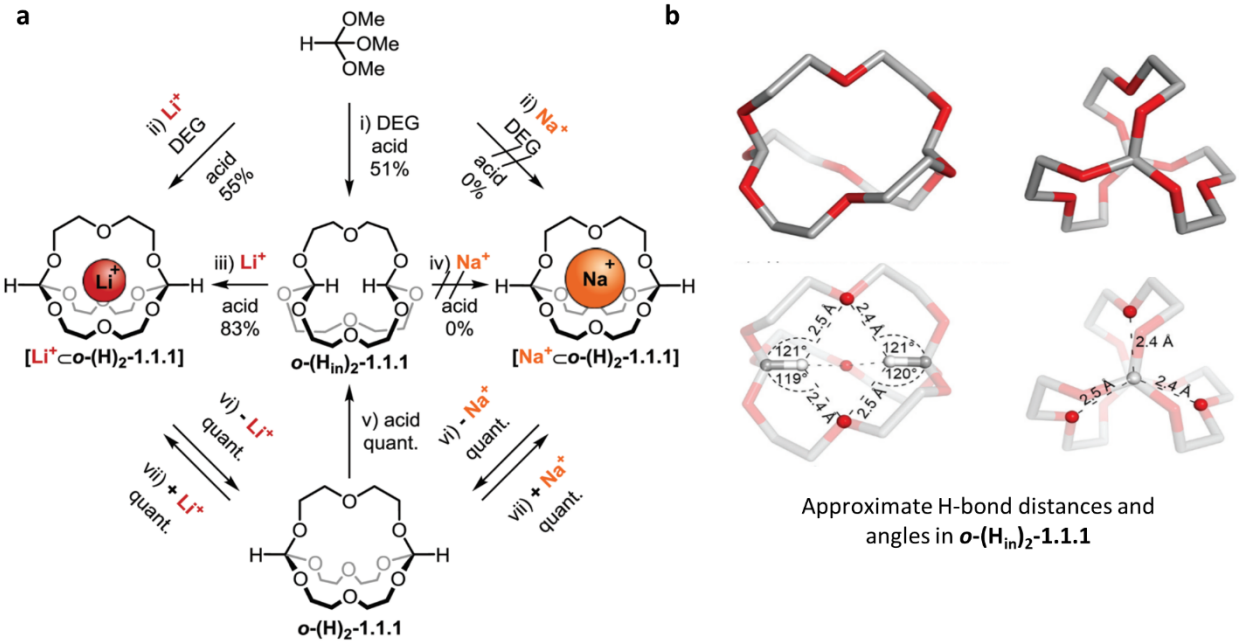

Figure 23. **a**, Interconversion of self-templated *in*,*in*- and metal-templated *out*,*out*-orthoformate cryptands. **b**, Solid-state structure of self-templated orthoformate cryptand. Adapted from [87] with permission from the Royal Society of Chemistry, copyright (2019).

1.2.3 Supramolecular Polymerization

1.2.3.1 Classification and Mechanisms of Supramolecular Polymerization

Synthetic covalent polymers find vast applications in all areas of human life: from space exploration to baby diapers. In fact, they are so important that entire industries would not exist in the current form without synthetic polymers: for example, electronics where most insulating materials are made of polymers. However, the industrial future of polymers with noncovalent monomer connections – supramolecular polymers – is yet to come and it is difficult to predict what advancements to science and society it could bring.

Meijer and coworkers proposed the following definition of supramolecular polymers: "Supramolecular polymers are defined as polymeric arrays of monomeric units that are brought together by reversible and highly directional secondary interaction, resulting in polymeric properties in dilute and concentrated solutions as well as in the bulk. The directionality and strength of the supramolecular bonding are important features of systems that can be regarded as polymers and behave according to well-established theories of polymer physics."[88]

Different supramolecular polymers can be classified based on various types of interactions driving the formation of large supramolecular assemblies. These interactions include but not limited to 1) *hydrogen bonds*, with the most famous examples being 2-ureido-4[1H]-pyrimidinone **53**[89] and benzene-1,3,5-tricarboxamides **54** (Fig. 24a) ;[90–92] 2) *π-π interactions*, e.g. supramolecular polymers of porphyrins **55**,[93,94] perylene bisimides (PBIs),[95,96] and bis(merocyanines) (Fig. 24b);[97–100] 3) *hydrophobic interactions*, e. g. supramolecular polymers of cyclodextrins with hydrophobic guests;[101] 4) *metal-ligand interactions* (e.g. **56**; Fig. 24c).[102]

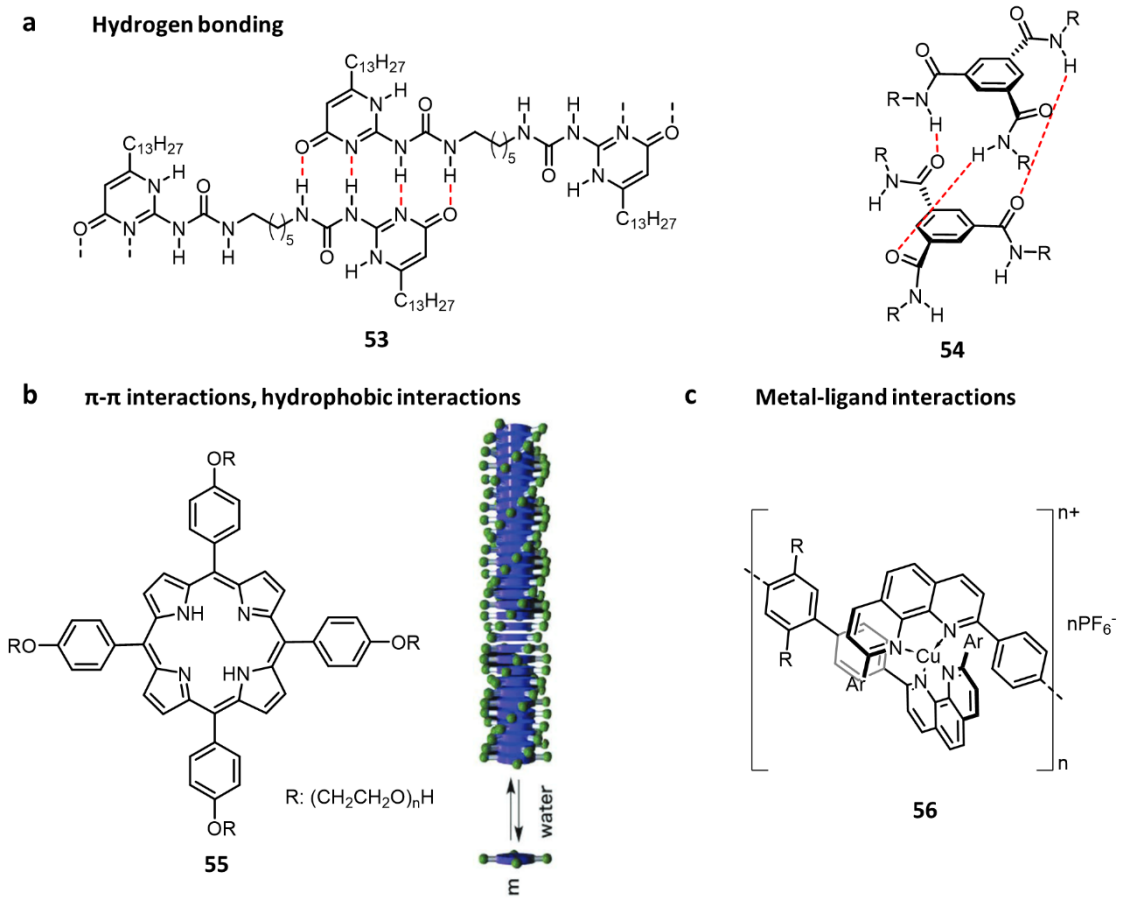

Figure 24. Examples of supramolecular polymers formed by (**a**) hydrogen bonding; (**b**) π-π interactions, and hydrophobic interactions. Reproduced from [93] with permission from the Royal Society of Chemistry, copyright (1988); (**c**) by metal-ligand interactions.

Another classification of supramolecular polymers is based on the evolution of Gibbs free energy during polymerization from monomeric to polymerized states (Fig. 25). There are three most common mechanisms: 1) *isodesmic* polymerization, 2) *cooperative* polymerization, and 3) *anticooperative* polymerization.

If each addition of a monomer to the growing end of supramolecular polymer leads to a constant decrease of free energy and characterized by the same binding constant K_E (elongation constant) it is called *isodesmic* supramolecular polymerisation. In isodesmic polymerisation, the system consists of growing polymers, oligomers, and monomers. The covalent counterpart of isodesmic supramolecular polymerization is the step-growth polymerization. This mechanism often takes place in 1) systems that polymerize by π-π interactions only; 2) supramolecular polymers built by monomers containing electronically

noncoupled end groups; 3) supramolecular polymers based on inclusion complexes; 4) supramolecular polymers based on metal-ligand interactions

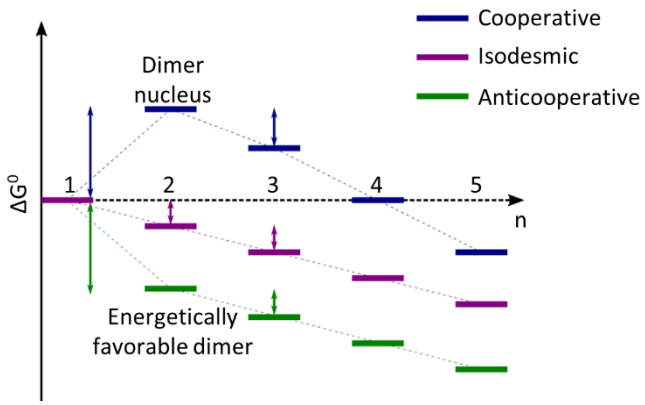

Figure 25. Qualitative energy diagram of a cooperative (blue), isodesmic (purple), and anticooperative supramolecular polymerization. X-axis represents the number of monomers n in hypothetical aggregate. Adapted from [129] with permission from the Nature Publishing Group, copyright (2020).

Cooperative supramolecular polymerization is also known as the nucleation-elongation. In cooperative supramolecular polymerisation, the first step is the formation of nuclei – a non-covalent assembly of n monomers – by the isodesmic mechanism with a lower association constant called nucleation constant K_N. After the nucleus of critical size is formed, elongation proceeds with a higher association constant – elongation constant – K_E, such that $K_E/K_N>1$. Importantly, during the elongation, the system consists only of growing polymer chains and free monomers. The covalent counterpart of the cooperative supramolecular polymerization is the chain-growth polymerization. It normally occurs when there is electronic communication between polymerizable groups, for example, in systems that polymerize via hydrogen bonding or dipole-dipole interactions.

For *anticooperative* supramolecular polymerization, initial oligomerization is more favourable than subsequent elongation ($K_E/K_N<1$). Anticooperative polymerization is expected for systems in which repulsive forces from steric interaction build-up with the increasing aggregate size or where particularly strong electrostatic interactions are strongly reduced after the formation of a centrosymmetric dimer unit (e.g. merocyanine dyes)[99].

1.2.3.2 Supramolecular Polymerization under Kinetic Control

Self-assembly of biological systems often proceeds under kinetic control, in other words, thermodynamic properties of final states do not play the major role. In contrast, self-assembly pathways, kinetic barriers, and energy influx are the key determinants of the system properties. Kinetics plays an important role in the formation of amyloid aggregates,[103,104] actin filaments,[105] and flagellae,[106] to name a few.

Despite significant progress in understanding and characterization of thermodynamically controlled supramolecular polymerization, supramolecular polymerization under kinetic control is still in its infancy.

Here, I will focus only on kinetic processes that involve kinetically stable/trapped monomers, because it is directly related to some key achievements of this thesis. I will not, however, discuss the formation of different polymorphs controlled by kinetic processes.[107]

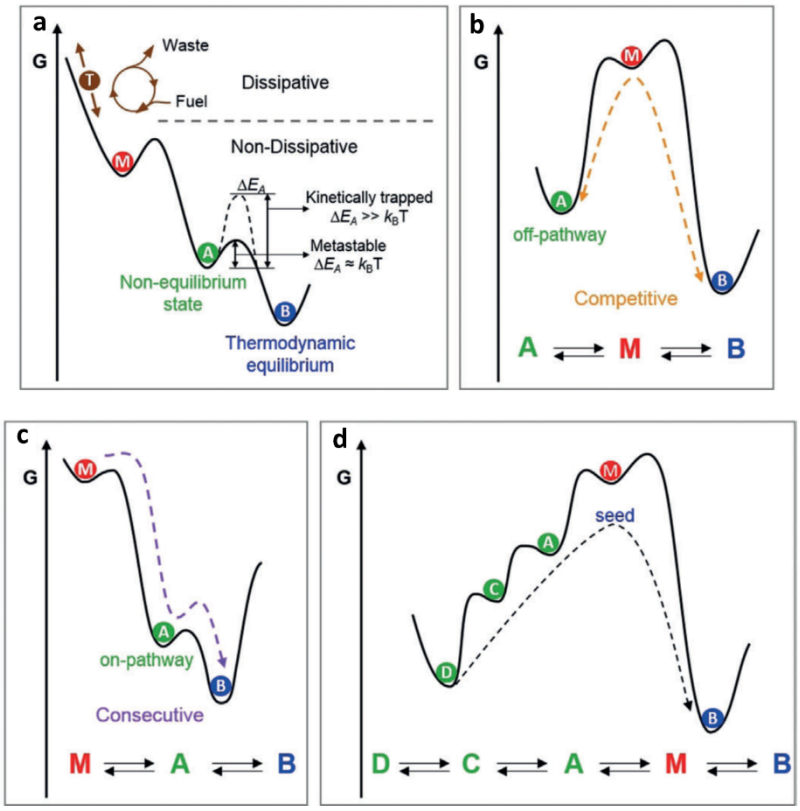

Figure 26. Energy landscapes demonstrating different pathways of supramolecular polymerization. **a**, Dissipative versus non-dissipative. **b**, Competitive pathway. **c**, Consecutive pathway. **d**, Hierarchical kinetic pathway with the possibility of seeded living supramolecular polymerization (LSP). Reproduced from [107] with permission from Wiley-VCH, copyright (2019).

Figure 26 schematically illustrates four common self-assembly pathways in the kinetically controlled supramolecular polymerization. The thermodynamic equilibrium of the system is represented by the global energy minima (states B). The transformation from the monomeric state (M) to a thermodynamic minimum can involve transitions through several local minima on the energy landscapes that are stable on the experimentally observable time scale and separated from thermodynamic minimum by small but not negligible activation barriers. These states are called metastable non-dissipative states. However, if the activation energy barrier leading from a metastable state to thermodynamic minimum is significantly higher than the thermal energy, only a tiny fraction of the substance in state A will be able to surmount it. In this case, we say that A is the kinetically trapped state.

Depending on the relative position of the monomeric state on the energy diagram, local minima, and thermodynamic minimum, we can differentiate two elementary self-assembly pathways: *competitive* (off-pathway) and *consecutive* (on-pathway).

Competitive pathways occur when several self-assembled structures compete for the monomer (Fig. 26b). In the competitive pathway, species can be interconverted only by disassembly to monomeric state M. Energy barrier leading from the state M to non-equilibrium state A is lower than to thermodynamic minimum B. In such systems, monomer concentration is buffered in the form of kinetically favourable state A. In consecutive pathway M transforms directly into equilibrium state B going through local minimum A (Fig. 26c). In real life, however, often a mix of these pathways can be observed (Fig. 26d). Off-pathway aggregation can be proven by studying the kinetics of spontaneous polymerization. If the lag time of the process leading to the thermodynamic minimum increases upon the increase of the monomer concentration, that indicates that metastable off-pathway aggregates are present.

Understanding of the energy landscapes and kinetics of supramolecular polymerization has led to the development of *living supramolecular polymerization* (LSP).

1.2.3.3 Living Supramolecular Polymerization

In living supramolecular polymerization, spontaneous polymerization of monomers via cooperative nucleation-elongation mechanism is kinetically suppressed. However, it can be initiated when an initiator or seeds, acting as preformed nuclei, are added, and polymer chains continue to elongate when a fresh portion of the monomer is added.

To achieve LSP, a system has to meet two crucial requirements:

1) Nucleation-elongation mechanism of polymerization.
2) Spontaneous polymerization has to be kinetically retarded.

Nucleation-elongation polymerization is required to ensure that propagation occurs only at the termini of the supramolecular polymers and continue when the fresh feed of the monomer is added.

Kinetically trapped states guarantee that no nucleation starts in the absence of an initiator or active polymer termini. However, once the initiator is added, these species are transformed into aggregates of lower energy, and the length of the obtained supramolecular polymers is determined by the feed ratio of the monomer to the initiator. Kinetically delayed supramolecular polymerization can easily be noticed by the presence of a thermal hysteresis between the heating and cooling cycles, since it occurs when there is a large kinetic barrier in the assembly or disassembly pathway.

Sugiyasu, Takeuchi, and coworkers reported the first example of LSP in 2014.[108] They designed Zn porphyrin **57** (Fig. 27a) that self-assembled through two competitive pathways. Upon cooling in methylcyclohexane (MCH), **57** formed nanoparticles of J-aggregate $\mathbf{57}_{\mathbf{J\text{-}Agg}}$ with slipped stacking of porphyrins. Over a few days, J-aggregate transformed into fibers of H-aggregate $\mathbf{57}_{\mathbf{H\text{-}Agg}}$. The lag time for this transformation increased with the concentration of **57**, suggesting that transformation proceeded via the free monomer, and the nanoparticles are the off-pathway aggregate. Sonication of the H-aggregate solution yielded seeds $\mathbf{57}_{\mathbf{H\text{-}Seeds}}$ with narrow length polydispersity. The addition of $\mathbf{57}_{\mathbf{H\text{-}Seeds}}$ to $\mathbf{57}_{\mathbf{J\text{-}Agg}}$ solution caused the transformation of J-aggregate nanoparticles into H-aggregate fibers with kinetic features identical to covalent chain-growth polymerization (Fig. 27b). Polymer termini remained active

and continued to elongate upon the addition of more J-aggregate solution (Fig. 27c). Polymers obtained by this method had narrow polydispersities with sizes controlled by the amount **57**$_{\text{H-Seeds}}$ added.

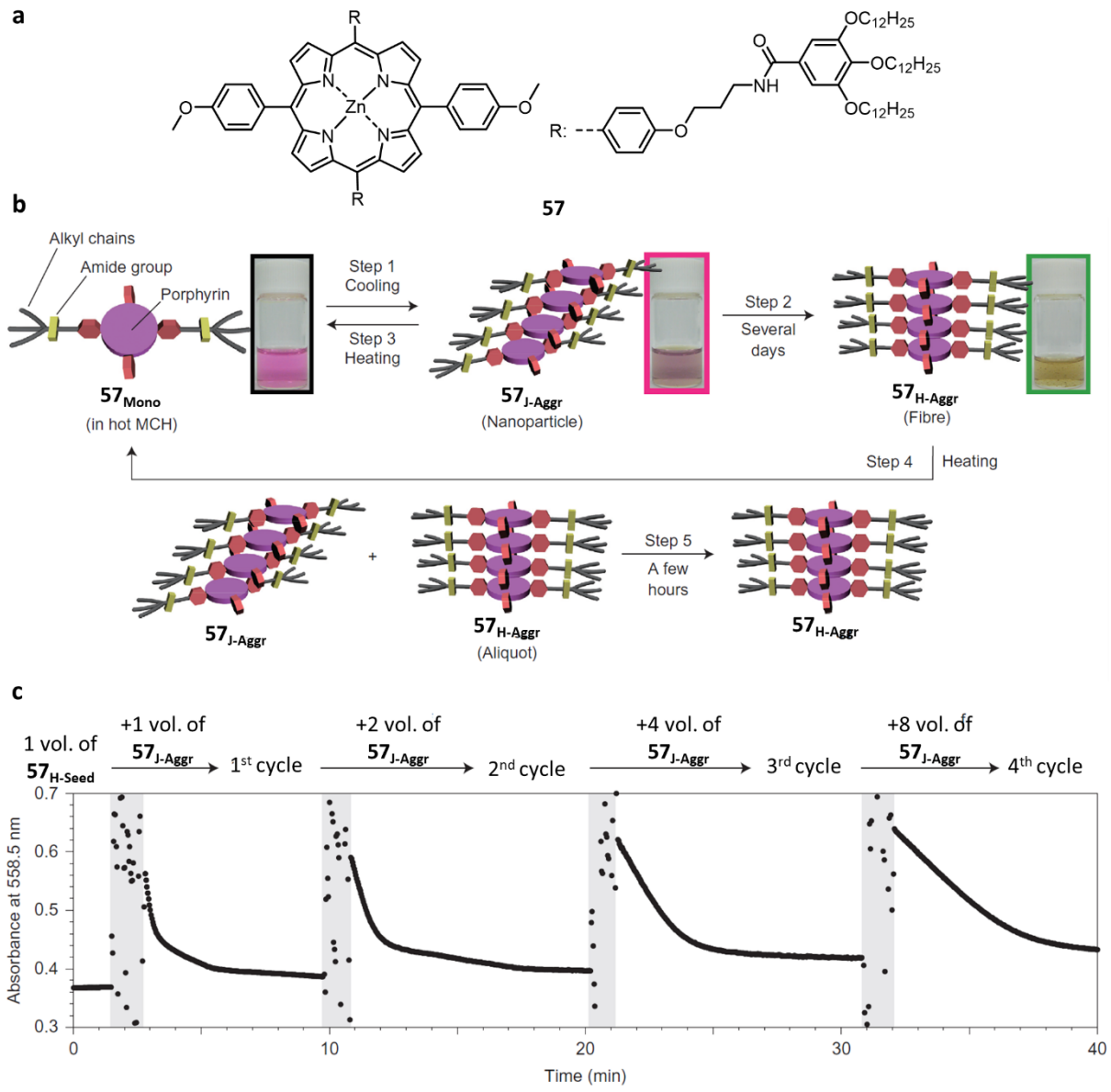

Figure 27. a, Chemical structure of the monomer **57**. **b**, Schematic representation of the self-assembling behaviour of **57** in MCH. **c**, UV-Vis cycling experiment showing repeated polymerization on each addition of **57**$_{\text{J-Agg}}$ with increasingly slower rates indicating the living nature of polymerization. Adapted from [108] with permission from the Nature Publishing Group, copyright (2014).

The same year, De Cola and coworkers reported amphiphilic platinum (II) complex **58** that can be engaged in hydrophobic interactions, H-bonding, and metallophilic interactions.[109] Upon fast injection of dioxane solution of **58** into water, complex **58** formed kinetically trapped metastable off-pathway nanoparticles **A**, where monomers were held together via

hydrophobic effect, Pt-Pt interactions and π-π stacking. Nanoparticles were remarkably kinetically stable: only after three months they spontaneously interconverted into the thermodynamically stable isomorphic nanofibers **C** (Fig. 28a). When seeds of **C**, obtained by sonication, were added to kinetically stable state **A**, it caused immediate transformation into **C** without lag time via LSP mechanism (Fig. 28b) forming blue-emissive rods with the uniform length that increased on decreasing the amount of seeds (Fig. 28c). Interestingly, thermodynamic form **C** could be photochemically transformed into a transient state **B**, with different monomer arrangement, upon laser irradiation at λ_{exc} = 405 nm (Fig. 28d). All isomorphs had different optical properties allowing monitoring the polymerization using an electron-multiplying charge-coupled device camera.

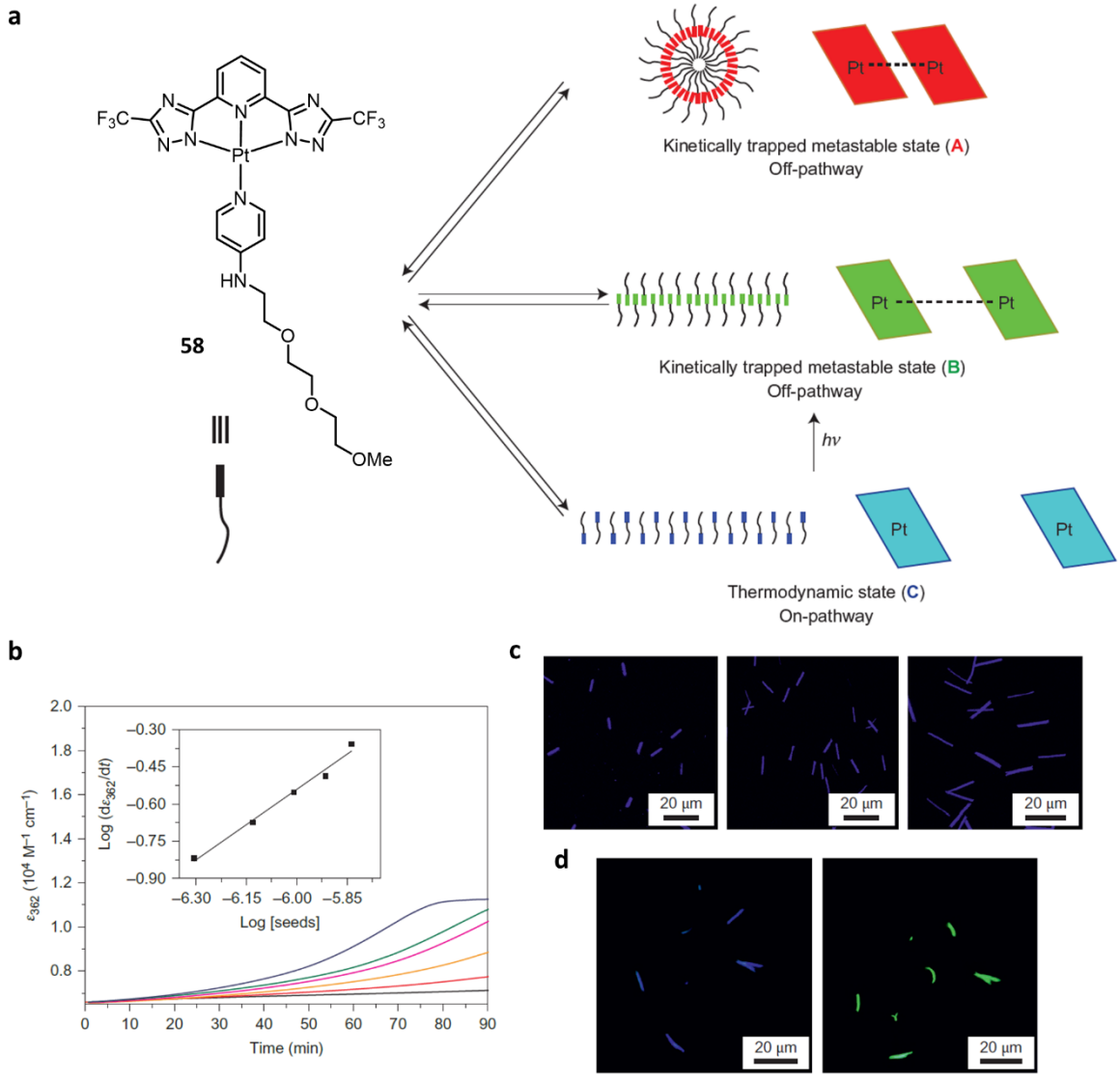

Figure 28. a, Left, chemical structure, and schematic representation of the monomer **58**. Right, Schematic illustration of the assemblies A, B, and C. **b**, Time course of the supramolecular polymerization of assembly A, when [**A**]/[**C**] = 200:1 (black line), 200:2 (red line), 200:3 (orange

line), 200:4 (magenta line), 200:5 (green line), and 200:6 (blue line). Inset shows the log-log of the initial rate of polymerization against the amount of seed added. **c**, Confocal images of the fibres obtained from the seeded polymerization using [**A**]/[**C**] = 200:3 (left), 200:2 (middle), 200:1 (right). **d**, Confocal images of the fibers before (left) and after (right) five minutes of laser irradiation at λ_{exc} = 405 nm. Adapted from [109] with permission from the Nature Publishing Group, copyright (2016).

In 2017, Würthner and coworkers described LSP of the bay-modified PBIs **59** that can also form kinetically trapped off-pathway aggregates (Fig. 29).[110] In weakly polar solvents, **59** forms intramolecular hydrogen bonds between amide hydrogen and imide oxygen. The "closed" form self-assembled following isodesmic mechanism into metastable H-aggregate nanoparticles. The addition of seeds of the thermodynamically stable J-aggregate led to the growth of thermodynamically stable, emissive nanofibers with J-type exciton coupling with feature characteristic to LSP.

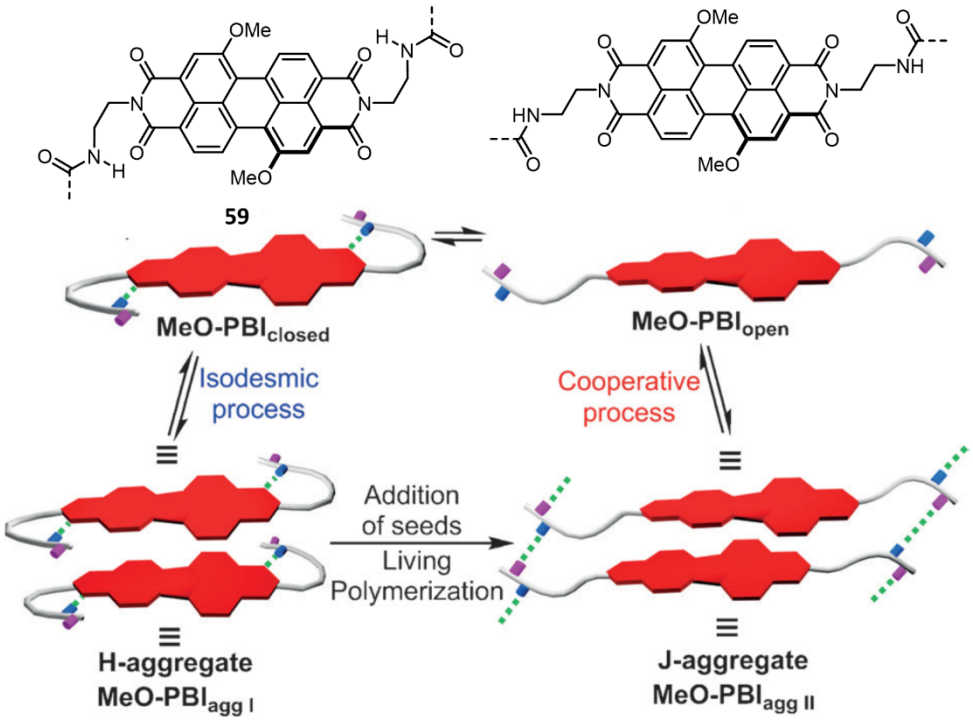

Figure 29. Chemical equilibria between open and closed forms of **59** and formation of the metastable H-aggregate and the thermodynamically stable J-aggregate. Reproduced from [110] with permission from Wiley-VCH, copyright (2017).

Since then, other groups used off-pathway aggregates to perform living supramolecular polymerization of rylene dyes,[111–115] N-heterotriangulenes,[116] Aza-BODIPY dyes,[117] and diketopyrrolopyrroles.[118]

The formation of the off-pathway aggregates remains the most common method to achieve LSP. Another approach utilizes the ability of tailor-made monomers to fold in solution into inactive conformations due to the formation of multiple strong intramolecular non-covalent interactions such as hydrogen bonds. This folding can significantly delay or even completely suppress spontaneous polymerization.

In 2015, Würthner, Aida, and Miyajima's groups introduced examples of monomers where spontaneous polymerization is inhibited by the formation of intramolecular hydrogen bonds instead of off-pathway aggregates.

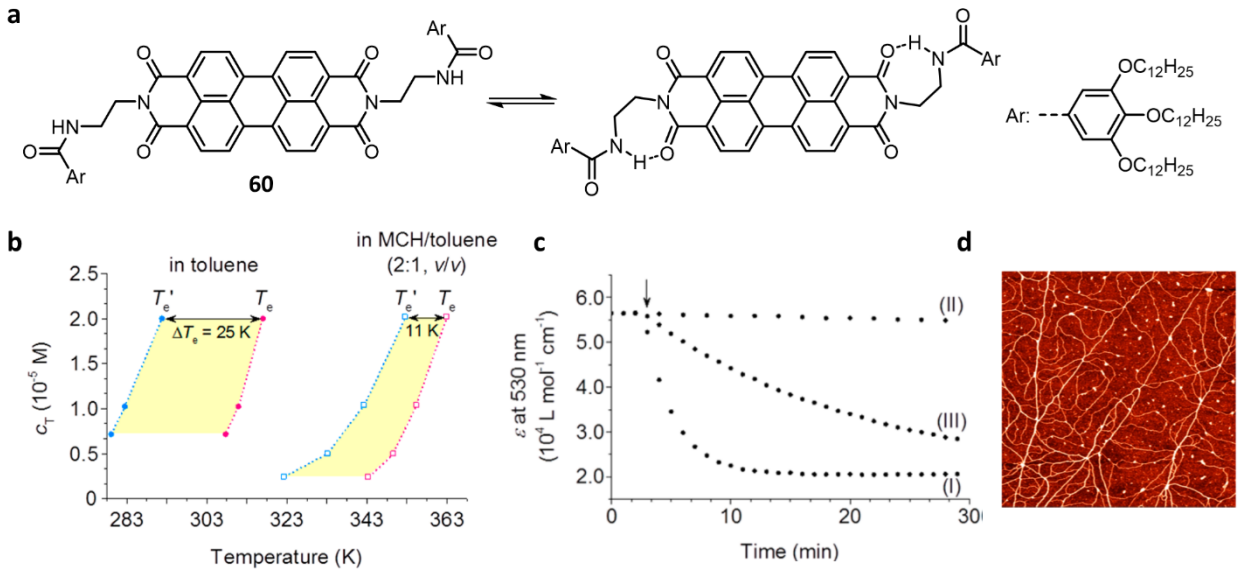

Figure 30. a, Chemical equilibrium between a reactive open form and a trapped closed conformation of **60**. **b**, Hysteresis observed during heating-cooling cycles of **60** in toluene and MCH/toluene (2:1, v/v) mixture. **c**, Time course of the change in absorbance before and after addition of either $\mathbf{60}_{\mathbf{Seed}}$ (I), no **60** (II) or $\mathbf{60}_{\mathbf{Agg}}$ (III) to the solution of **60** in toluene at a certain time indicated by an arrow. **d**, AFM height image of the aggregate sample obtained after the seeded polymerization of **60** initiated by the addition of $\mathbf{60}_{\mathbf{Seed}}$. Adapted from [119] with permission from the American Chemical Society, copyright (2015).

In the amide-appended PBI **60**, amide-imide intramolecular hydrogen bonds prevent spontaneous nucleation (Fig. 30a).[119] This resulted in a pronounced hysteresis in both pure toluene and MCH:toluene (2:1) (Fig. 30b). The addition of polymer seeds $\mathbf{60}_{\mathbf{Seed}}$ induced transformation of **60** into the thermodynamically stable supramolecular polymer (Fig. 30c,d). In this study, however, authors did not demonstrate so far the "living" character of polymerization in multicycle experiments, so it cannot be characterized as LSP. The influence of the linker between amide and imide on LSP was investigated as well. Monomers with longer

butylene-tethered amides self-assemble into kinetically trapped amorphous aggregates instead of forming intramolecular hydrogen bonds.[120]

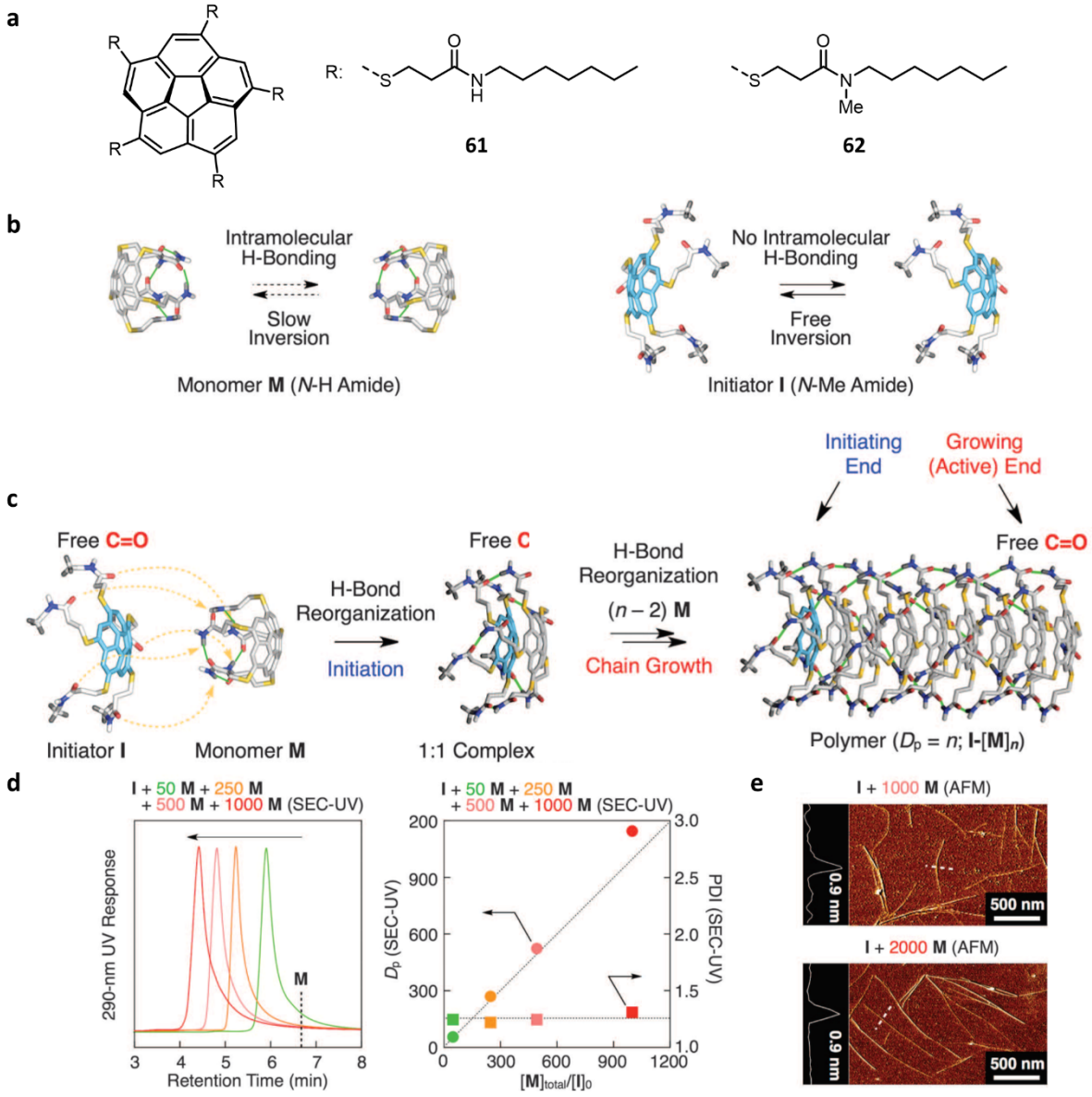

Figure 31. a, Structures of the monomer **61** (**M** in the figure), and the initiator **62** (**I** in the figure). **b**, Formation of the intramolecular H-bonded network by **61** and no intramolecular H-bonding in **62**. **c**, Initiation of the supramolecular polymerization of **61** by the molecular initiator **62** and subsequent chain growth. **d**, SEC traces, degrees of polymerization, and PDIs of supramolecular polymers obtained with different monomer-to-seed ratios. **e**, AFM images of polymers formed at 1000 and 2000 **61**/**62** ratios. Adapted from [121] with permission from the American Association for the Advancement of Science, copyright (2015).

A unique example of LSP initiated by a molecular initiator was reported by Aida and Miyajima.[121] In their studies on liquid crystals, they noticed that C_5-symmetric coranulene derivative **61** (Fig. 31a), carrying amide-appended thioalkyl side chains, adopts a cage-like

closed conformation in low-polarity media such as MCH (Fig. 31b).The reason for that is the bowl-like shape of corannulene orientating the side-chain amide units to facilitate their intramolecular hydrogen bonding interactions.[122] Monomer **61** does not self-assemble at room temperature in solution, however, it spontaneously polymerizes upon heating in MCH. Such behaviour is very unusual for supramolecular polymers, but resembles temperature-induced covalent polymerization. This observation prompted authors to investigate the possibility of triggering supramolecular polymerization using a chemical initiator. They discovered that compound **62** - N-methylated derivative of **61**, cannot form intramolecular hydrogen bonds and self-assemble but serves as a hydrogen bond acceptor. **62** forms intermolecular hydrogen bonds with **61**, which "opens" to form further intermolecular amide-amide bonds (Fig. 31c). It led to the formation of 1D nanofibers with low PDIs (between 1.2 and 1.3). The supramolecular polymer continuously grew upon the addition of fresh **61**, which was verified by DLS, SEC, and DOSY NMR (Fig. 31d).

Ogi and Yamaguchi described another example of a kinetically retarded monomer. They demonstrated that amino-acid-based diamide **63** (Fig. 32a) forms intramolecular hydrogen bonds in a low-polar medium.[123] This resulted in hysteretic behaviour and lag times during spontaneous polymerization that disappeared when seeds of polymer were added to the system (Fig. 32b,c). In this example of seeded supramolecular polymerization, however, authors did not demonstrate the necessary features to qualify it as LSP.

In 2016, Sugiyasu, Takeuchi, and coworkers proposed a new elegant approach conceptually different from those mentioned above. They combined supramolecular polymerization and photoisomerization of azobenzene chromophore **64** (Fig. 33a) into one energy landscape.[124] *Cis* form of azobenzene **64** corresponds to a very deep energy trap and does not polymerize spontaneously. The *trans* form of **64**, which can be obtained from *cis* form upon light irradiation, polymerizes following cooperative mechanism (Fig. 33b). When the dormant *cis* monomer was irradiated with light in the presence of seeds of the supramolecular polymer, the activated free monomer was polymerized at the termini of the seed in a chain-growth manner. Obtained supramolecular polymers had controlled length and narrow polydispersities (Fig. 33c,d).

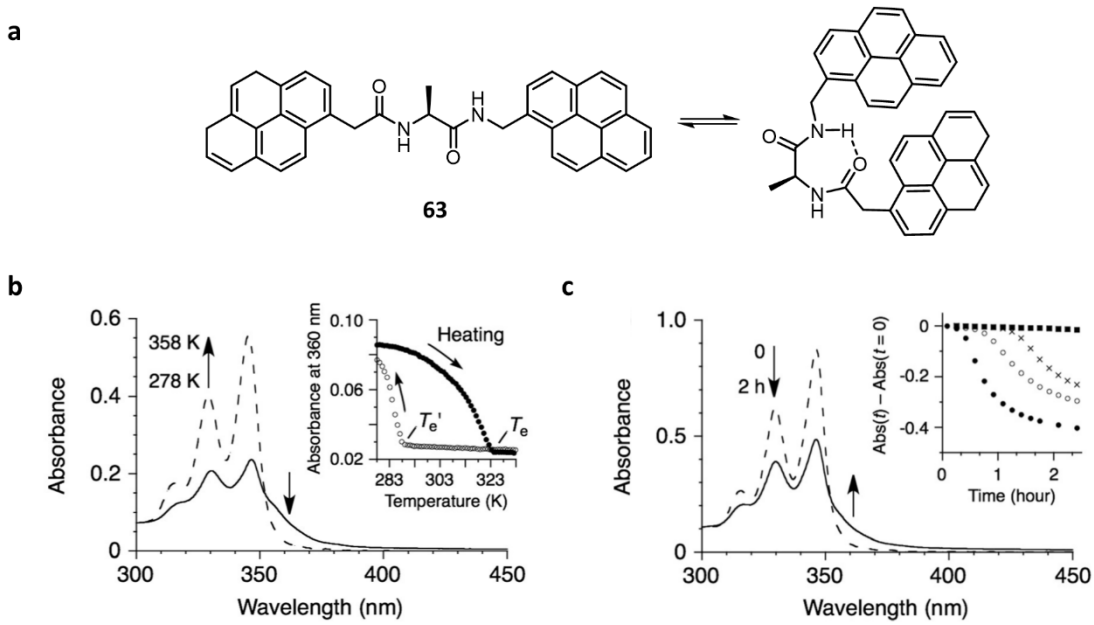

Figure 32. a, Chemical structure of the pyrene-substituted diamide **63** in its folded and unfolded states. **b**, Changes in the UV absorption of **63** during heating from 278 K to 358 K. Inset shows thermal hysteresis observed during slow cooling and heating of 0.1 mM solution of **63** in toluene. **c**, Time-dependent changes in the UV absorption of **63** observed after fast cooling. Inset shows the time course of the absorbance for different total concentrations of **63**. Adapted from [123] with permission from Wiley-VCH, copyright (2018).

Other examples of LSP include Pd^{II}-isocyanide complexes, where the nature of counteranion modulates polymerization;[125] seed induced LSP of phosphate receptor-functionalized monomers controlled biomimetically by the consumption of the chemical fuel ATP;[126] the living growth of a charge-transfer amphiphile constructed from a potassium coronene salt donor and a methyl viologen-derived acceptor, modulated by the addition of amines;[127] and trapping of an active monomer using “dummy” monomers incapable of 1D supramolecular polymerization.[128]

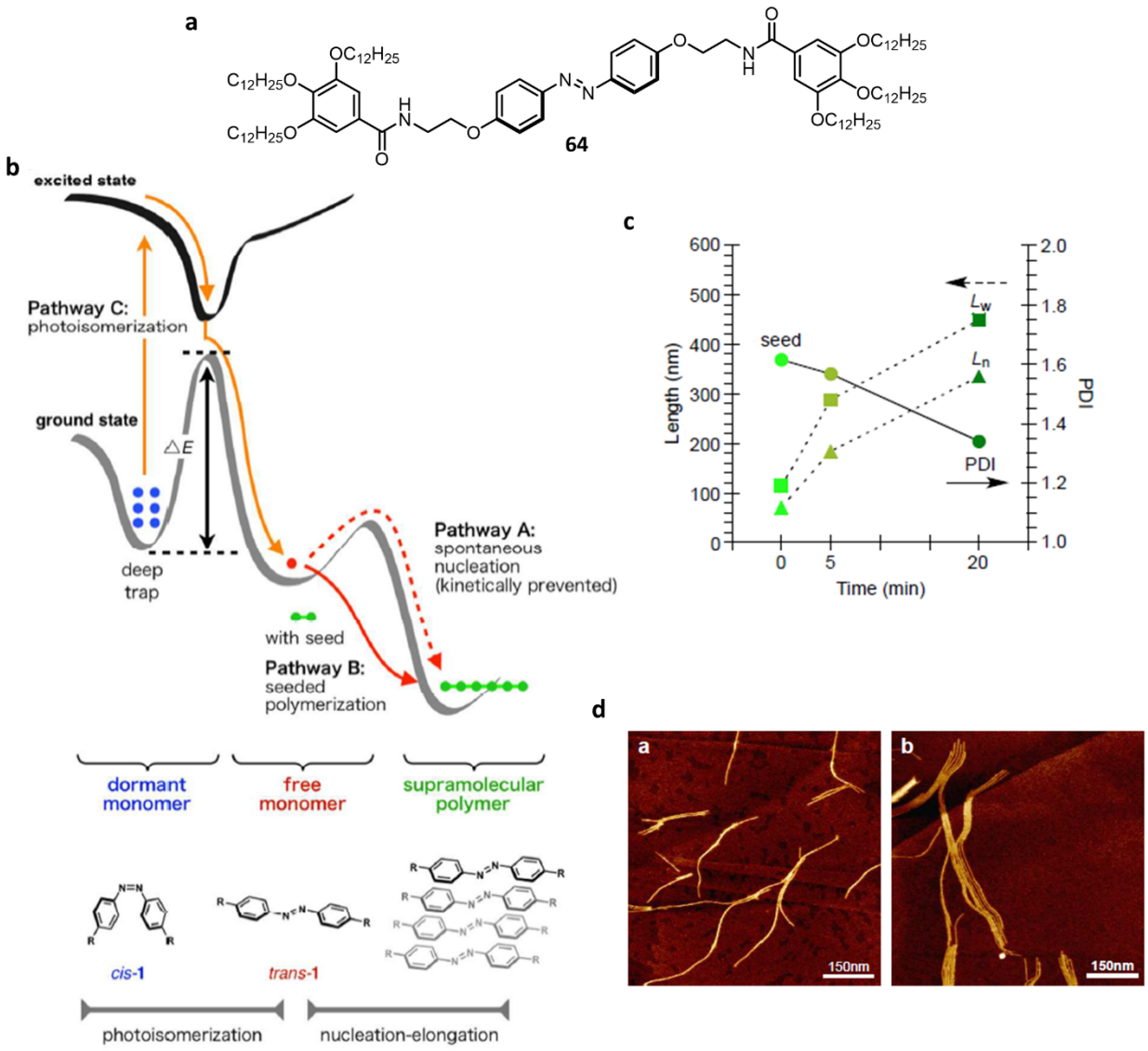

Figure 33. **a**, Chemical structure of the azobenzene monomer **64**. **b**, Energy landscape of supramolecular polymerization coupled with the photoisomerization process used to create the kinetic trap and the mechanism of living supramolecular polymerization. **c**, Number-averaged length (L_n), weight-averaged length (L_w), and PDI (L_w/L_n) of seeds and supramolecular polymers. **d**, AFM height images of supramolecular polymers obtained through photo-regulated living supramolecular polymerization conducted for 5 (left) and 20 (right) min. Adapted from [124] with permission from the American Chemical Society, copyright (2016).

1.2.3.4 Supramolecular Block Copolymers

Developments in the field of LSP allowed chemists to study supramolecular block copolymers (BCPs). Supramolecular BCPs are polymeric architectures in which long sequences (blocks) of individual monomers are connected by intermolecular interaction. Because of relative weakness and high dynamics of non-covalent interactions, supramolecular polymers are highly sensitive to the solvent nature, environmental parameters (temperature) and constantly undergo *inter*chain and *intra*chain exchange, thus making the control of the microstructure of supramolecular BCPs challenging.[129] Currently, supramolecular BCP synthesis requires tailor-made monomers that have similar thermodynamic and kinetic properties. To make things even more complicated, techniques commonly used to characterise covalent polymers and block copolymers, such as GPC, are usually inapplicable to supramolecular polymers. The formation of supramolecular BCPs can be experimentally proven either indirectly, studying the kinetics of polymerization and physical properties of BCPs (e.g., thermodynamic, electronic and optical properties), or using high-resolution microscopic techniques (AFM, TEM, and fluorescent microscopy).[130]

Manners and Winnik have pioneered the field of non-covalent block assemblies using epitaxial crystallization driven self-assembly of poly(ferrocenyldimethylsilane) based micelles. However, these examples can not be considered as truly supramolecular polymers because they are not one dimensional and are related more to nanocrystals.[131–135]

The history of supramolecular BCPs started in 2011. Aida and coworkers studied nanotubular self-assembly of Gemini-shaped HBC amphiphiles.[136] HBC **65** carries two bipyridine units that can efficiently coordinate copper ions (Fig. 34a). HBC **66** bears four electron-withdrawing fluorine substituents and can adhere electronically to HBC **65**. HBC **65** self-assembled into bundled nanotubes $\mathbf{NT_1}$ (Fig. 34a) that, upon treatment with $Cu(OTf)_2$, coordinated copper, and became well-dispersed due to electrostatic repulsion (Fig. 34b). The addition of $\mathbf{NT_{1\cdot Cu}}$, serving as seeds, to acetone solution of HBC **66** at 50 °C followed by cooling to 25 °C resulted in the formation of *block*-$\mathbf{NT_{1\cdot Cu}/NT_2}$ supramolecular BCP (Fig. 34c,d). Blocks in supramolecular BCPs electronically communicated at the heterojunctions and displayed characteristic excitation energy transfer and charge transport properties not present in a mixture of homotropically assembled nanotubes.

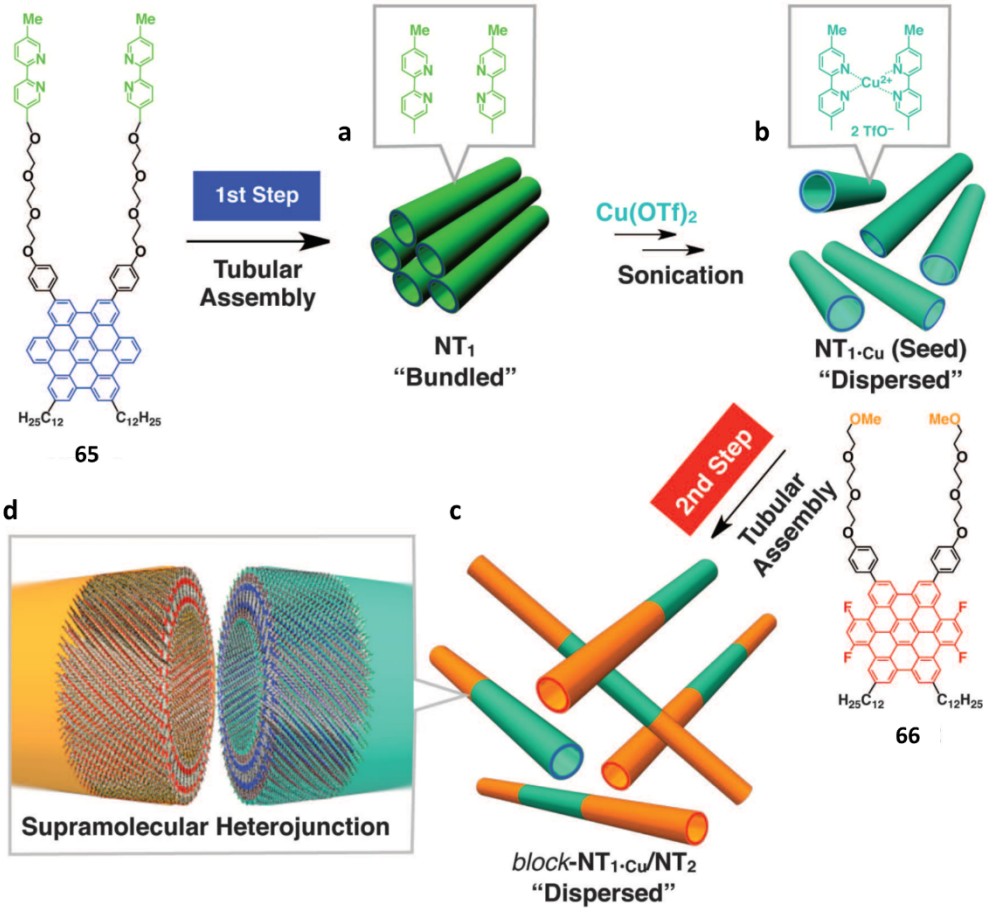

Figure 34. Molecular structures of HBCs **65** and **66**. **a**, Formation of supramolecular nanotubes by HBC **65**. **b**, Seeds of $\mathbf{NT_{1\cdot Cu}}$ dispersed after postfunctionalisation of $\mathbf{NT_1}$ with $Cu(OTf)_2$. **c**, Formation of block-$\mathbf{NT_{1\cdot Cu}/NT_1}$ by cooling acetone solution of HBC **66** in the presence of $\mathbf{NT_{1\cdot Cu}}$ (**Seed**). **d**, Schematic illustration of the idealized heterojunction. Adapted from [136] with permission from the American Association for the Advancement of Science, copyright (2011).

In 2015, Otto and co-workers reported the first examples of supramolecular A-B-A BCPs synthesized via LSP.[137] Oxidation of peptide-functionalized dithiol **66** led to the formation of an equilibrium mixture of different sized macrocyclic disulfides dominated by trimers and tetramers that do not self-assemble, whereas hexamer can form the supramolecular polymer (Fig. 35a), thus the concentration of non-polymerized monomer is buffered in the form of dormant macrocycles. When fibers, assembled from the hexamer, were added to the equilibrated mixture, they shifted the distribution towards the formation of more of the self-assembling library member, giving rise to a self-synthesizing material (Fig. 35b). Polymer seeds could be obtained either by mechanical shearing in a Couette cell or by chemical disassembly of fibers by reduction of the disulfide bonds of the macrocycles at the fiber ends mediated by dithiothreitol (DTT). The addition of seeds $\mathbf{67_{Seed}}$ to the equilibrated mixture of macrocycles

caused their elongation by LSP, giving supramolecular polymers with low PDIs (< 1.1). Using dithiol **68** bearing cyclohexyl instead of phenyl in the side chain and cross-seeding it with **67$_{Seed}$,** they could obtain the A-B-A supramolecular BCP. The formation of the A-B-A BCPs was confirmed by partial reduction of the ends with DTT and monitoring the sample composition using UHPLC. Upon gradual increase of the extent of reduction from 0 to 20%, the chromatographic peak area for **68** decreased steadily, while that of **67** remained unchanged.

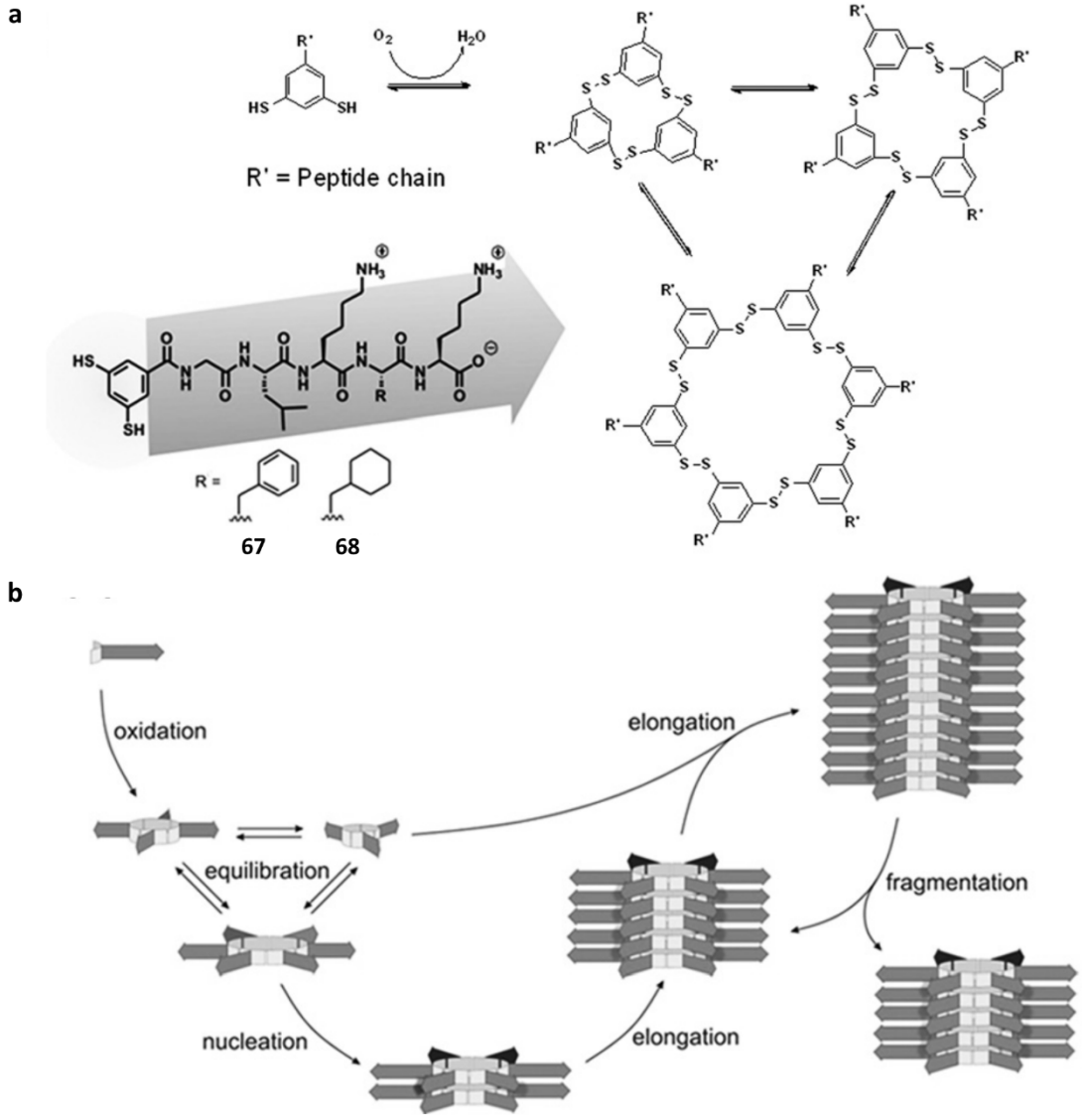

Figure 35. a, Molecular structure of disulfides **67** and **68** and DCL components obtained by oxidation of **67** or **68**. **b**, Schematic illustration of amplification of the hexameric macrocycle from the DCL and subsequent chain-growth leading to supramolecular BCPs. Adapted from [137] with permission from Wiley-VCH, copyright (2015).

In 2015, Sugiyasu and Takeuchi reported A-B-A BCP formation using previously mentioned porphyrin-based monomers **57**.[138] That system tolerated only tiny structural changes,

namely, they could achieve BCPs formation using two homologous monomers, which differed only by one methylene group.

Three years later, the same group described A-B-A BCPs using zinc- and copper-porphyrins **69$_{Zn}$** and **69$_{Cu}$** as building blocks (Fig. 36). They demonstrated that compartmentalization of **69$_{Zn}$** zinc-porphyrin-block between **69$_{Cu}$** copper-porphyrin-blocks led to enhanced stability of the **69$_{Zn}$** zinc-porphyrin against DMAP.[138]

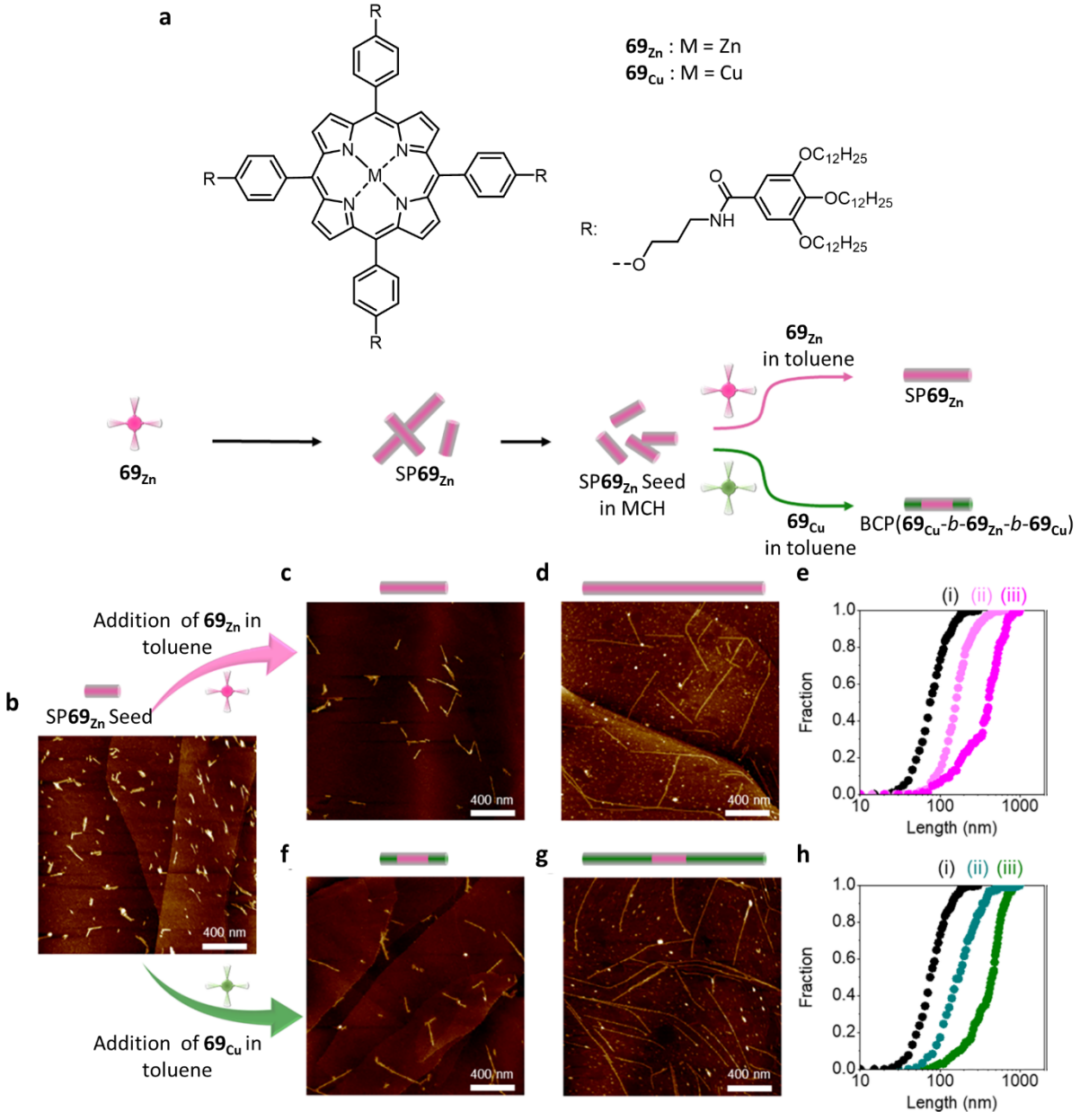

Figure 36. a, Structure of porphyrin-based monomers **69** and schematic representation of its seeded LSP. **b**, AFM image of seeds of SP**69$_{Zn}$**. **c**, **d**, AFM images of SP**69$_{Zn}$** prepared according to the scheme shown in **a** with ratios between the seed SP**69$_{Zn}$** and monomeric **69$_{Zn}$** 1:1 (**c**) and 1:5 (**d**). **e**, Cumulative histograms of the seeds of SP**69$_{Zn}$** (i), SP**69$_{Zn}$** prepared with 1:1 (ii),

and 1:5 (iii) ratios of seed SP**69**$_{Zn}$ to SP**69**$_{Zn}$. **f**, **g**, AFM images of BCP(SP**69**$_{Cu}$-*b*-SP**69**$_{Zn}$-*b*- SP**69**$_{Cu}$) prepared according to the scheme shown in **a** with ratios between the seed SP**69**$_{Zn}$ and monomeric **69**$_{Cu}$ 1:1 (**f**) and 1:5 (**g**). **e**, Cumulative histograms of the seeds of SP**69**$_{Zn}$ (i) and BCP(SP**69**$_{Cu}$-*b*-SP**69**$_{Zn}$-*b*- SP**69**$_{Cu}$) prepared with 1:1 (ii) and 1:5 (iii) ratio of seed SP**69**$_{Zn}$ to SP**69**$_{Cu}$. Adapted from [138] with permission from the American Chemical Society, copyright (2018).

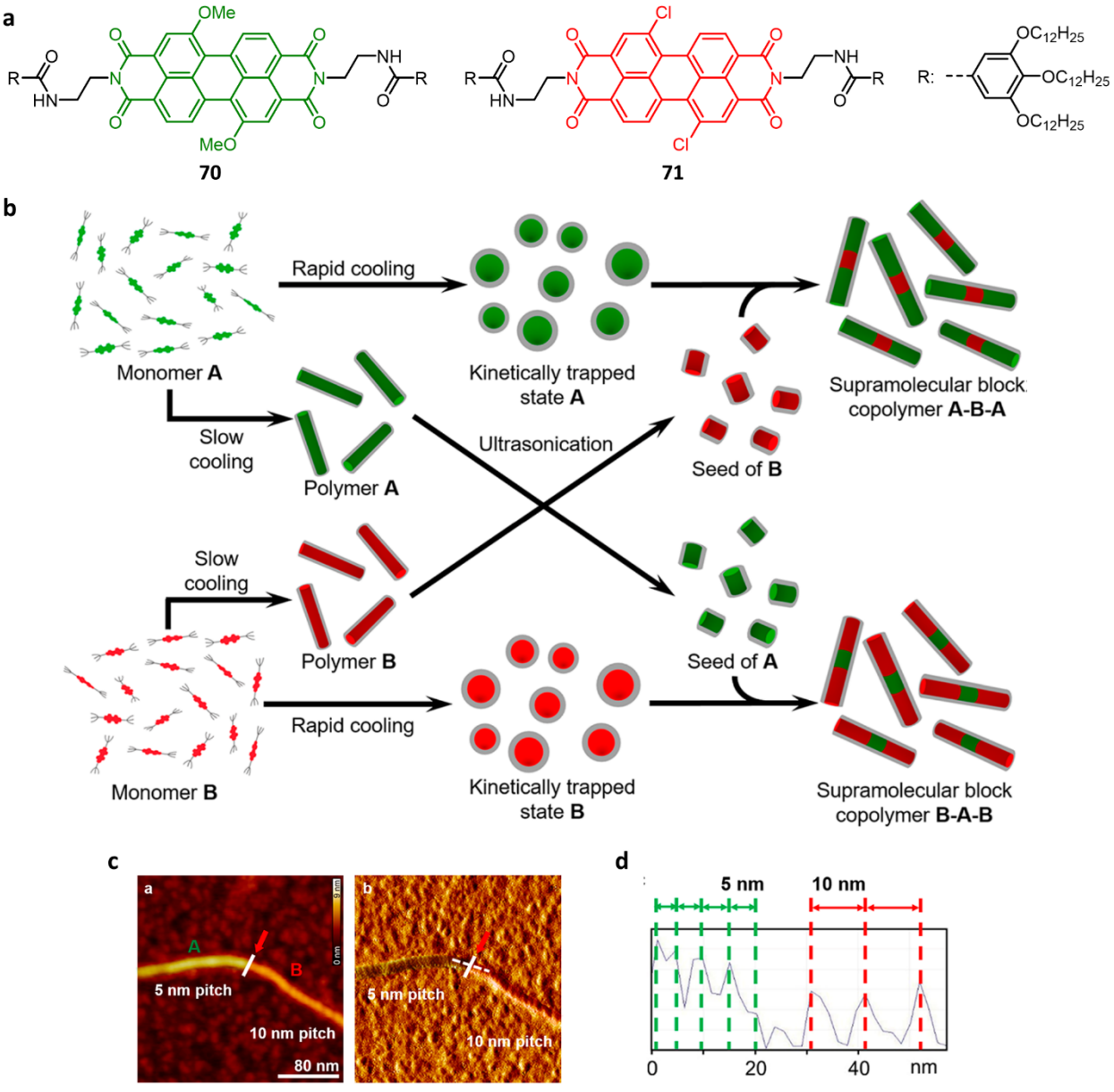

Figure 37. a, Structures of 1,7-disubstituted PBIs **70** and **71**. **b**, Schematic illustration of the two-component seeded LSP to obtain A-B-A and B-A-B supramolecular BCPs. **c**, AFM height (left), and phase (right) images of the supramolecular BCPs prepared. AFM profile analyses laong the white lines in panel **c**. Adapted from [139] with permission from the American Chemical Society, copyright (2019).

Results from Aida's, Sugiyasu's, Takeuchi's, and Otto's labs for the first time demonstrated that incorporation of different molecules into supramolecular BCP architecture has an impact on chemical as well as physical properties relevant to the area of organic photovoltaics.

In several reports, chemists used LSP of rylene dyes to make supramolecular BCPs. Würthner and coworkers used PBIs substituted in 1,7 bay-positions that contain methoxy (MeO-PBI **70**) and chloro (Cl-PBI **71**) substituents (Fig. 37a).[139] Both **70** and **71** self-assemble into metastable off-pathway aggregates that, upon addition of seeds of opposite species, obtained by sonication of corresponding supramolecular polymer, transformed into A-B-A or B-A-B supramolecular BCPs (Fig. 37b). Core substitution influences the helical pitch of the supramolecular polymers, thus making it possible to observe supramolecular BCPs by AFM directly (Fig. 37c,d).

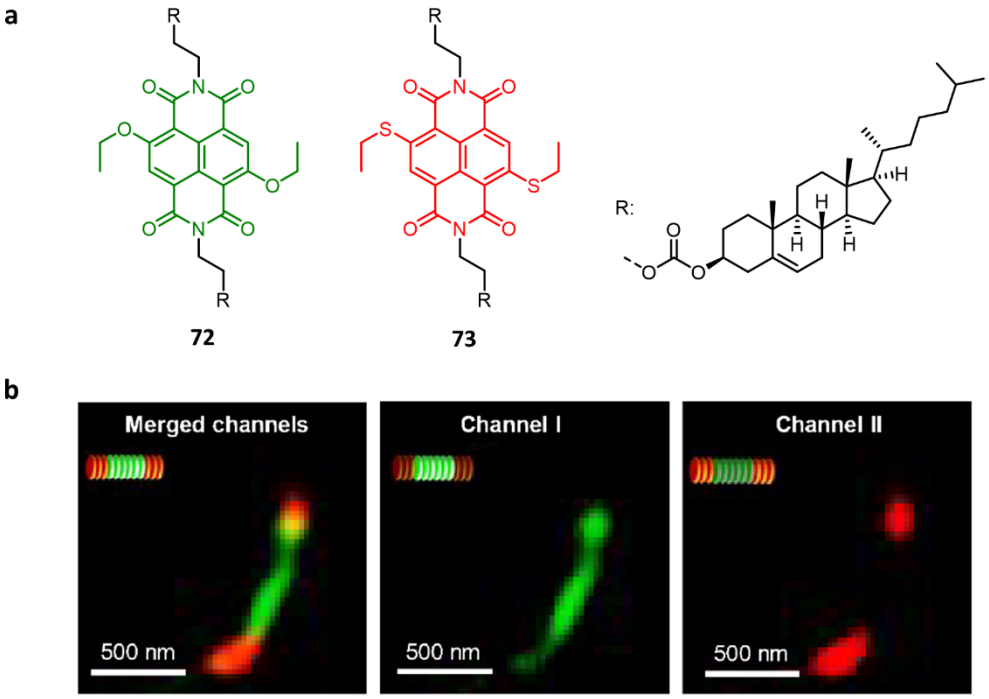

Figure 38. a, Structures of disubstituted NDIs **72** and **73**. **b**, SIM images demonstrating supramolecular BCPs of **72** and **73**. Adapted from [140] with permission from the American Chemical Society, copyright (2020).

Direct visualization of the formation of supramolecular BCPs is possible for fluorescent monomers using high-resolution fluorescent microscopy. George's group used symmetrically disubstituted NDIs with ethoxy groups **72** and ethanethiol **73** (Fig. 38a).[140] The monomers have very distinct absorption and emission profiles, which was used to visualize the blocks directly using super-resolved fluorescence microscopy (Fig. 38b).

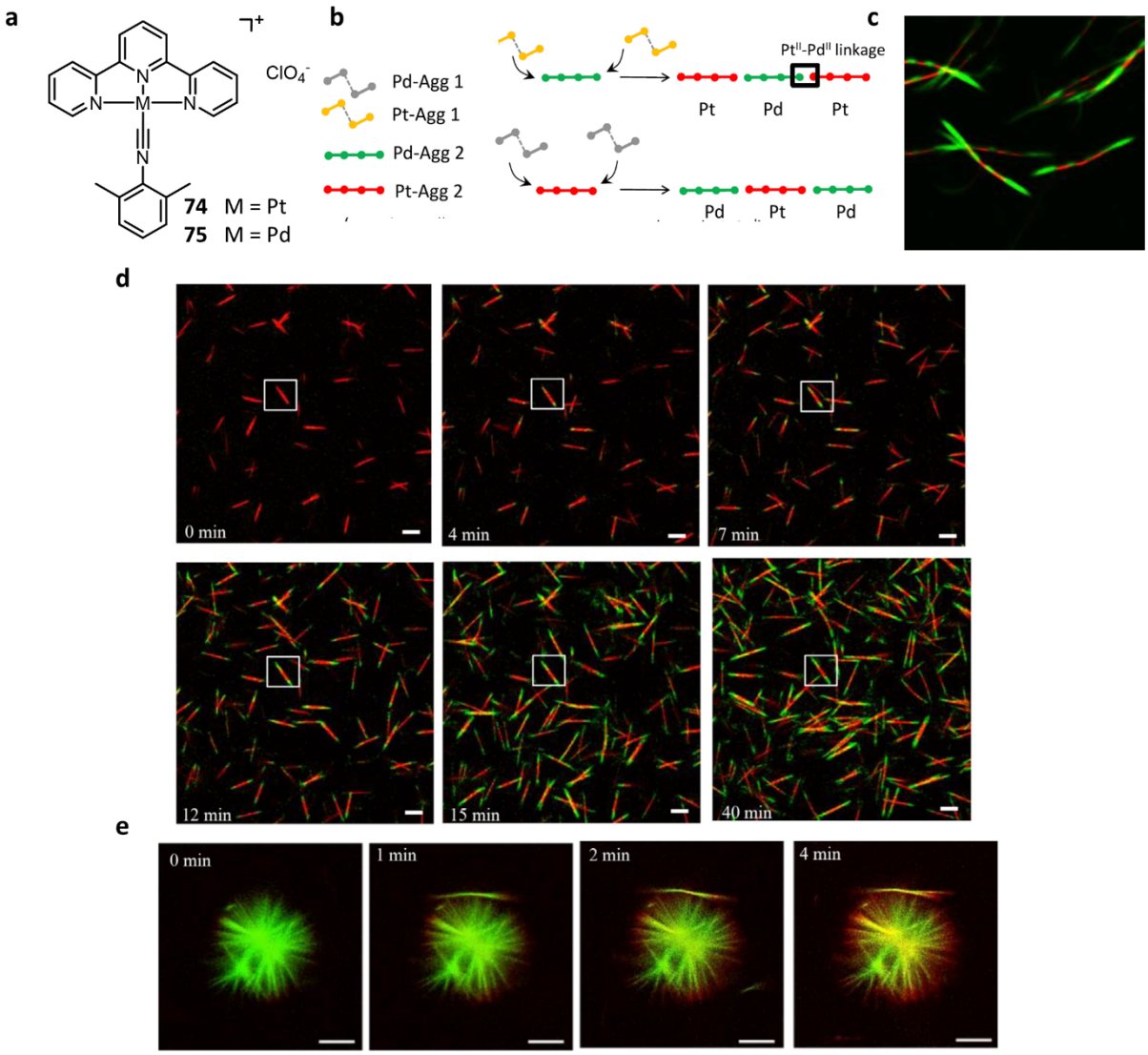

Figure 39. a, Structures of organometallic complexes **74** and **75**. **b**, Schematic representation of the preparation of multi-block Pt^{II} and Pd^{II} supramolecular BCPs. **c**, Confocal image of 7-block supramolecular BCP. **d**, Real-time elongation process of **75** at the ends of **74**. **e**, Real-time elongation of **74** around three-dimensional seed of **75**. Adapted from [141] with permission from the Cell Press, copyright (2020).

In 2020, Che and co-workers reported the most elaborate supramolecular BCPs that exhibit long-lived phosphorescence. Che and co-workers used organometallic Pt^{II} and Pd^{II} tweezer complexes **74** and **75** (Fig. 39a).[141] They form slip-stacked aggregates with counteranions between metal complexes that are kinetically trapped and stable in solution up to one week (Agg1). By breaking electrostatic interactions between counteranions (PF_6^-, ClO_4^-) kinetic aggregates gradually transform into the thermodynamic product (Agg2) with infinite linear parallel stacking of the monomers (Fig. 39b). Agg2 complexes of Pt^{II} and Pd^{II} could act interchangeably as seeds to convert Agg1 into Agg2,thus allowing Che and his team to make

3-block, 5-block, and 7-block copolymers (Fig. 39c,d). Interestingly, seeds of Agg2 could be prepared by adding poor solvent (water) to the solution of **74** (or **75**) in acetonitrile without sonication or any other mechanical stimuli. By changing the water content or temperature during seed preparation, it was possible to obtain multi-dimensional seeds that were used to prepare two- and three-dimensional BCPs (Fig. 39e). All assemblies exhibited bright fluorescence that allowed real-time observation of BCP growth. Che also found that the phosphorescence of supramolecular polymers could be tuned by doping with Pt^{II}.

To conclude this chapter, up to date all supramolecular BCPs were synthesized using kinetically-trapped off-pathway aggregates. Monomers are limited in structure and tolerate only tiny structural changes usually not more than a few atoms. None of the current systems could potentially offer a platform to systematically study supramolecular BCPs.

2. Aims and Achievements

2.1 Adaptive Behaviour of Dynamic Orthoester Cryptands

The second decade of the 21st century is marked by rapid growth of the field of systems chemistry.[142,143] In this context, macrocyclic compounds bearing dynamic bonds represent a valuable playground for the investigation of the adaptive behaviour and complex molecular networks.[144–149] Most such examples reported to date are based on the adaptive behaviour of metal-ligand cages and dynamic combinatorial macrocycles.[38,150–158] However, in most cases, different macrocyclic species compete for guest binding. Examples of systems where the exchange of the building blocks between different hosts leads to adaptive behaviour in response to the guest present remain relatively rare.[159–163] We envisioned that dynamic orthoester cryptands could undergo adaptive structural changes in response to the presence of potential guests – alkali metal cations. Therefore, we decided to study subcomponent exchange in systems consisting of orthoester cryptands, ethylene glycols, and alkali metal cations – probably the smallest conceivable three-dimensional platform for studying molecular complexity.[164]

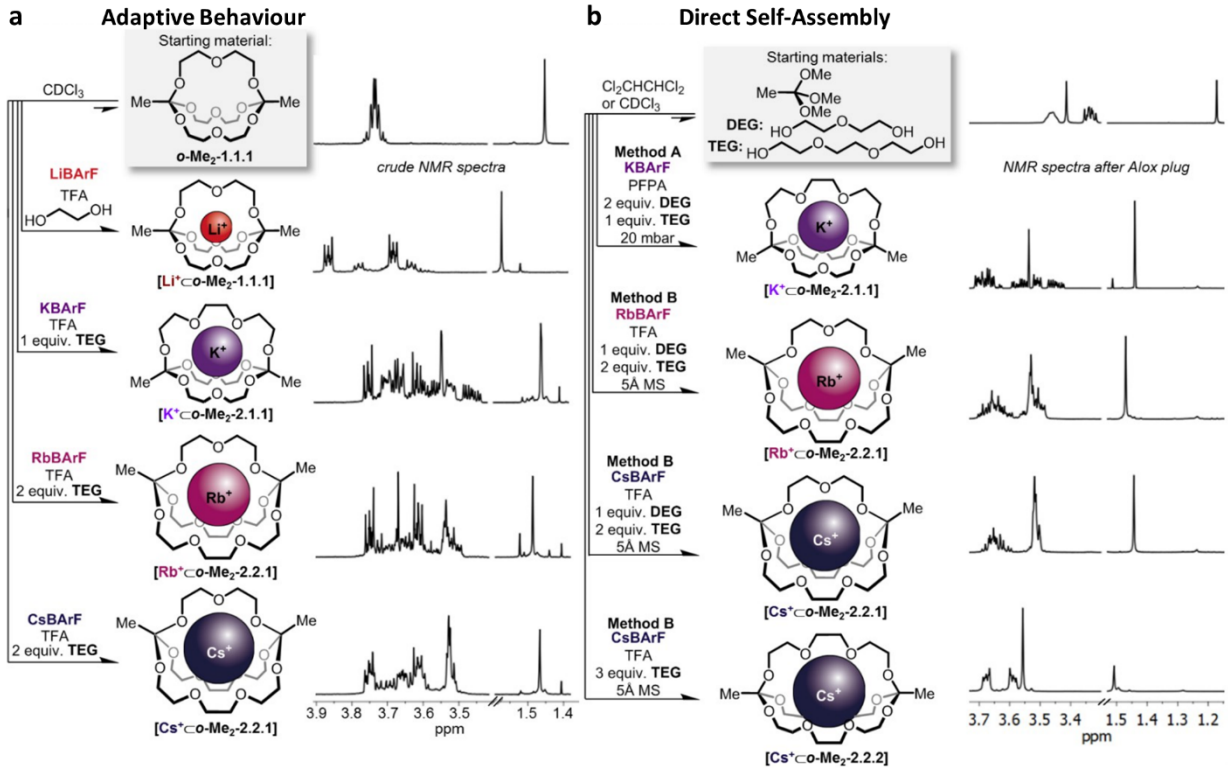

Figure 40. a, Adaptive behaviour of the dynamic orthoester cryptands. **b**, Self-assembly of the orthoester cryptates. Reproduced from [164] with permission from Wiley-VCH, copyright (2017).

The first goal of this project was the synthesis of unsymmetric orthoester cryptands. The preparation of unsymmetric cryptands usually requires tedious multistep synthesis.[37] Therefore, we decided to use direct self-assembly using dynamic orthoester exchange and alkali metal ions (K^+, Rb^+, Cs^+) as templates (Fig. 40a). We could identify conditions under which self-assembly proceeds in good yields. In the case of K^+, we could not use molecular sieves because they can serve as a source of Na^+ that competes with K^+,[85] therefore, self-assembly was carried out under reduced pressure (20 mbar) to remove methanol using perfluoropentanoic acid as a nonvolatile analogue of TFA. The self-assembly templated by Rb^+ and Cs^+ was carried out using a slightly modified previously reported procedure.[85] For all cryptates, we were able to grow single crystals suitable for X-ray analysis, thus unambiguously characterizing all compounds (Fig. 41). Interestingly, X-ray analysis of [**Cs^+⊂*o*-Me_2-2.2.1**]BArF revealed the formation of the helical structure with fluorine-decorated channels. When only TEG was present, Cs^+-templated self-assembly yielded large [**Cs^+⊂*o*-Me_2-2.2.2**]BArF cryptate lacking one Cs-O contact in solid state; that was not observed in experiments on adaptive behaviour.

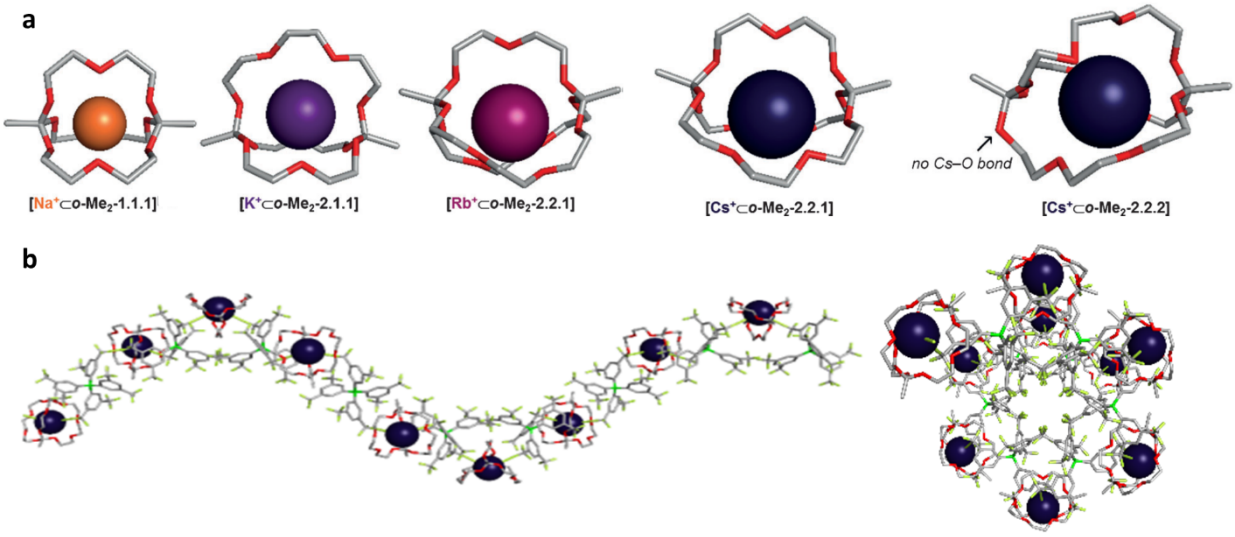

Figure 41. a, Solid-state structures of five orthoester cryptates. **b**, Helical structure of [**Cs^+⊂*o*-Me_2-2.2.1**]BArF with fluorine-decorated channel. Adapted from [164] with permission from Wiley-VCH, copyright (2017).

Removal of metal ions using ion exchange resin provided orthoester cryptands. Having at hand orthoester cryptands, we demonstrated that they can shrink or expand via subcomponent

exchange in response to the addition of alkali metal ions. For example, ***o*-Me$_2$-1.1.1** cryptand responded to the addition of mismatched metal guests, in the presence of different amounts of triethylene glycol, by the dynamic covalent expansion forming bigger metal cryptates: [**Na$^+$⊂*o*-Me$_2$-1.1.1**], [**K$^+$⊂*o*-Me$_2$-2.1.1**], [**Rb$^+$⊂*o*-Me$_2$-2.2.1**], [**Cs$^+$⊂*o*-Me$_2$-2.2.1**] (Fig. 40b). Big cryptands could also shrink: for instance, ***o*-Me$_2$-2.2.2** formed predominantly [**Cs$^+$⊂*o*-Me$_2$-2.2.1**] upon addition of Cs$^+$ and diethylene glycol. NMR titration experiments and DFT calculations, performed by our collaborators, rationalized observed reactivities.

Because certain host-guest pairs represented pronounced thermodynamic it allowed us to carry out an unprecedented "cryptate metathesis" reaction. The equimolar mixture of mismatching [**K$^+$⊂*o*-Me$_2$-1.1.1**] and [**Cs$^+$⊂*o*-Me$_2$-2.2.2**], both of which are suboptimal guests for corresponding metals, upon addition of catalytic amounts of acid reorganized, forming the equimolar mixture of [**Cs$^+$⊂*o*-Me$_2$-2.2.1**] and [**K$^+$⊂*o*-Me$_2$-2.1.1**] cryptates (Fig. 42).

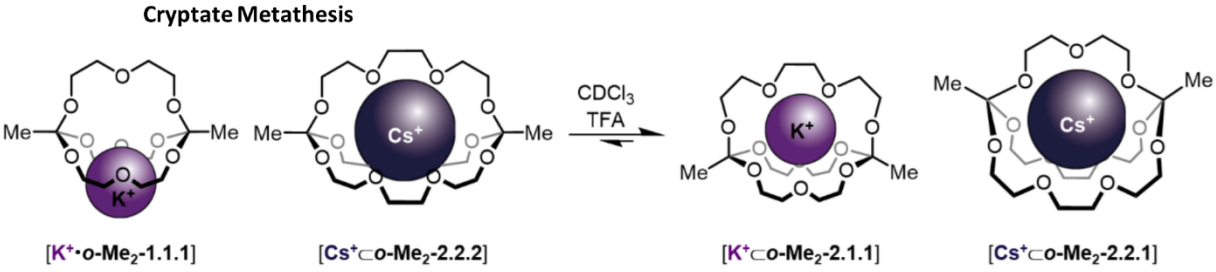

Figure 42. Cryptate metathesis. Adapted from [164] with permission from Wiley-VCH, copyright (2017).

In summary, we have demonstrated that the self-assembly of different orthoesters proceeds in one step, from cheap reagents, under mild conditions and in high yields. The cryptates and cryptands, obtained after metal removal, can shrink, expand, and undergo cryptate metathesis upon the addition of suitable alkali metal guests and/or diols. Thus, orthoester cryptates represent the smallest and simplest example of metal-organic cages with adaptive behaviour and could be used in the future as a new tool for systems chemistry to study complexity in chemical reaction networks under thermodynamic control.

2.2 Ammonium Complexes of Orthoester Cryptands are Inherently Dynamic and Adaptive

During our studies on the self-assembly and dynamic behaviour of alkali metal orthoester cryptates, we noticed that ammonium, not surprisingly, is also a good guest. However, all our attempts to isolate ammonium cryptate failed. We wondered whether ammonium could be a good host but, at the same time, acidic enough to catalyse orthoester exchange (Fig. 43a), thus precluding purification. In this case, oxonium ion at the orthoester bridgehead would be ceaselessly forming and reacting, leading to a continuous subcomponent exchange.

Similar behaviour is known for covalent systems with the most studied example being bullvalene, which above certain temperature exists as a mixture of numerous, rapidly interconverting degenerate isomers – such systems are called fluxional.[165,166] Another example is degenerate 1,2,6-hydride shifts in the nonclassical 2-norbornyl cation.[167]

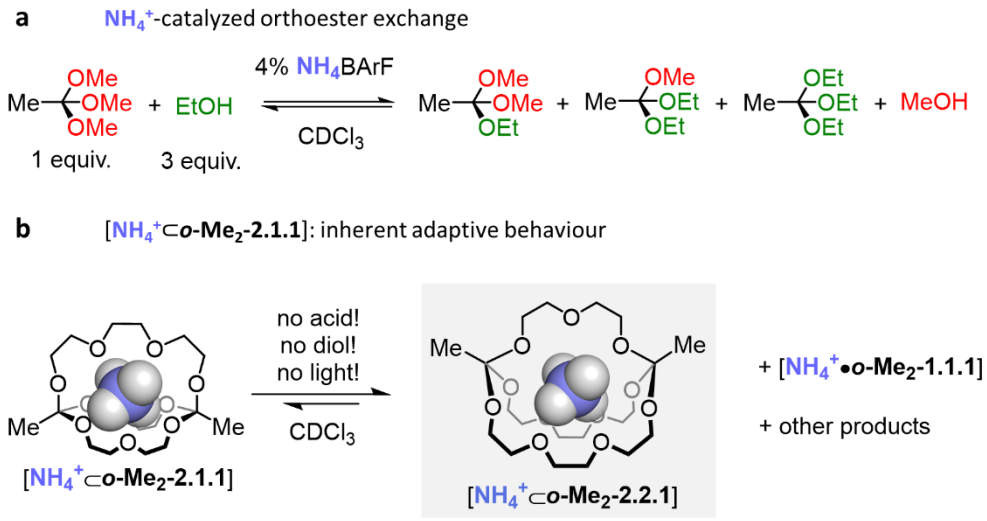

Figure 43. **a**, NH_4BArF-catalysed orthoester exchange. **b**, Inherent adaptive behaviour of orthoester [$\mathbf{NH_4^+}\subset\boldsymbol{o}$-$\mathbf{Me_2}$-**2.1.1**]$BArF^-$ cryptate. Adapted from [170] with permission from the American Chemical Society, copyright (2019).

Apart from the purely scientific interest, it was recently demonstrated that fluxionality of "shape-shifting" bullvalone could be used as an analytical fingerprint readout for components of complex food products such as carbohydrates, flavanols, and sialic acid.[168,169]

The fluxional ammonium cryptates would represent the first example of a fluxional supramolecular system.

We could demonstrate experimentally that nonsymmetrical cryptate [**NH_4^+⊂*o*-Me_2-2.1.1**] in the absence of acid, in the dark spontaneously rearranges into the thermodynamically more stable cryptate [**NH_4^+⊂*o*-Me_2-2.2.1**] by intermolecular subcomponent exchange (Fig. 43b).[170]

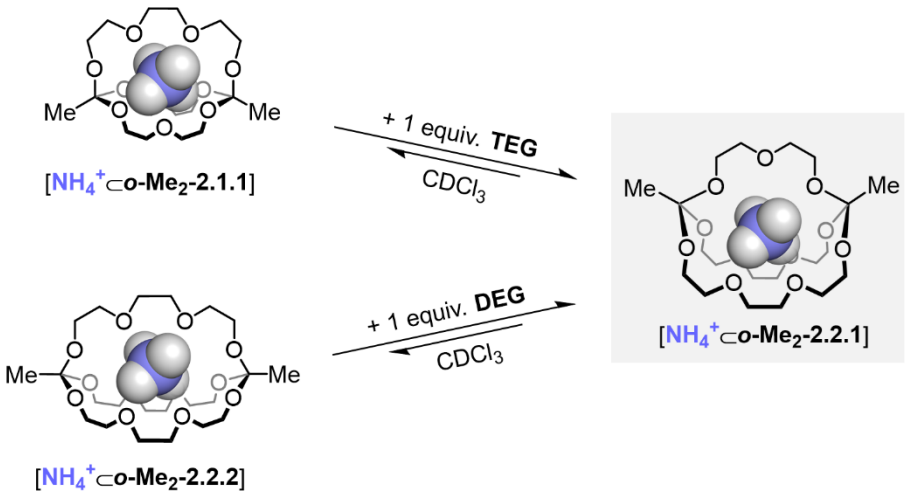

Figure 44. Adaptive behaviour of [**NH_4^+⊂*o*-Me_2-2.1.1**] and [**NH_4^+⊂*o*-Me_2-2.2.2**] cryptates in the presence of 1 equiv. of TEG or DEG, respectively. Reproduced from [170] with permission from the American Chemical Society, copyright (2019).

Relative thermodynamic stability of [**NH_4^+⊂*o*-Me_2-2.2.1**] was further proven in the experiments where [**NH_4^+⊂*o*-Me_2-2.2.2**] shrinks upon the addition of DEG and [**NH_4^+⊂*o*-Me_2-2.1.1**] expands into [**NH_4^+⊂*o*-Me_2-2.2.1**] upon addition of TEG (Fig. 44). In all cases all possible measures were taken to make sure that there is no acid present or formed, for example from chloroform. Finally, we could obtain a single-crystal X-ray structure of [**NH_4^+⊂*o*-Me_2-2.2.1**] (Fig. 45).

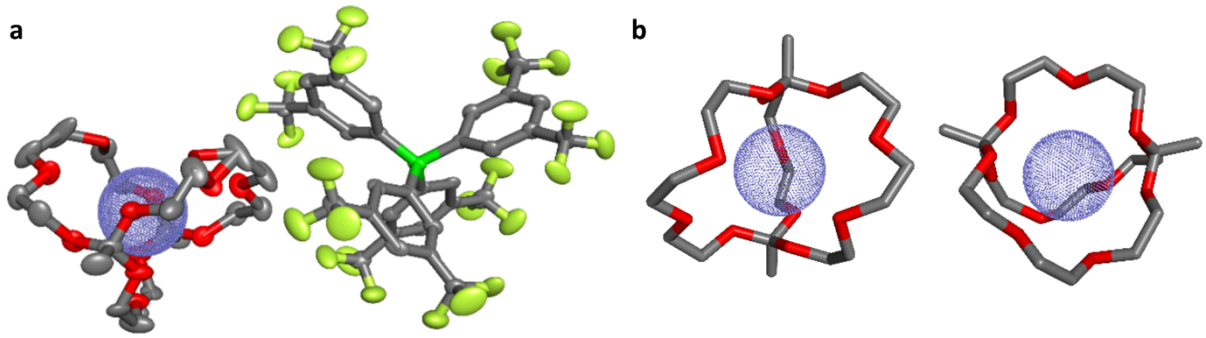

Figure 45. a, Single crystal X-ray structure of [**NH_4^+⊂*o*-Me_2-2.2.1**]$BArF^-$. **b**, Top view and side view of cryptate complex [**NH_4^+⊂*o*-Me_2-2.2.1**]. Colour code: carbon: grey, nitrogen: purple, oxygen: red, fluorine: yellow, boron: green. Adapted from [170] with permission from the American Chemical Society, copyright (2019).

Computational studies using QM/MM and DFT calculation revealed that the formation of the oxonium ion is hindered by ammonium ion's ability to strongly bind to the cryptands through multiple hydrogen bonds and the associated complexation-induced pK_a shift. Calculations confirmed that our host-guest system is fluxional and that intramolecular degenerate rearrangements accompany experimentally observed intermolecular rearrangements (Fig. 46).

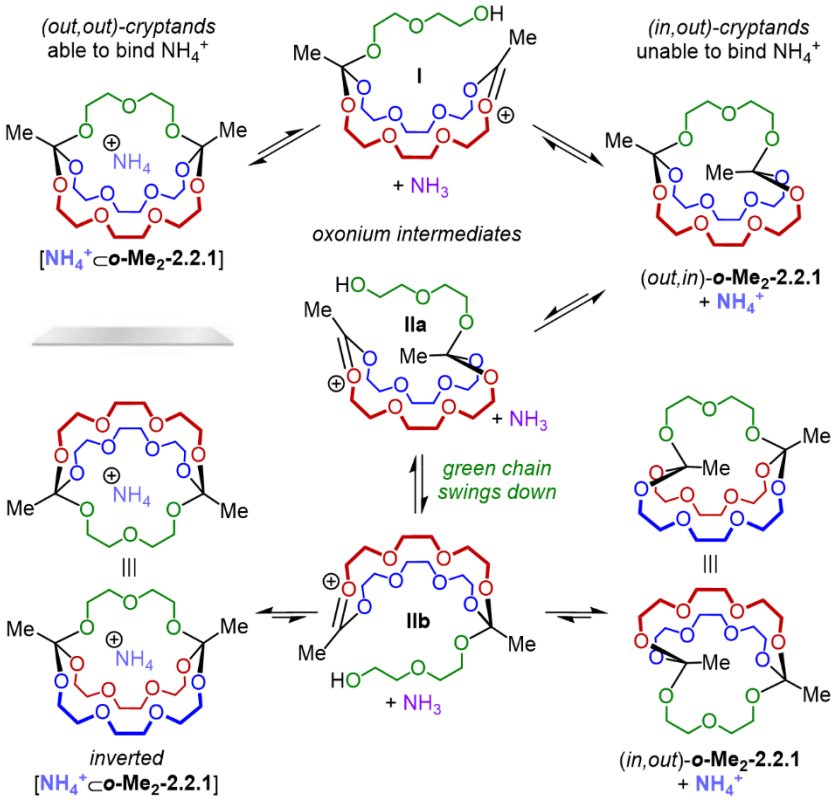

Figure 46. Reaction sequence of a "fluxional" intramolecular rearrangement leading to the exchange of the two triethylene glycol chains. Adapted from [170] with permission from the American Chemical Society, copyright (2019).

In conclusion, we have presented here the first fluxional supramolecular system, where ammonium cation serves simultaneously as a template and as a catalyst leading to degenerate *intra*molecular rearrangements. The results of this study are of fundamental interest and now it is difficult to predict any practical applications, however it lays a methodological foundation and can lead in the future to the further development of new fluxional supramolecular systems.

2.3 Long–Chain Polyorthoesters as Biodegradable Polyethylene Mimics

Plastics are used in all areas of life, from food storage to electronics. The annual production of plastics is over 250 millions of tons. They are long-lasting and persistent in the environment and when disposed in an uncontrolled way plastics accumulate in nature for decades endangering entire ecosystems.[171,172]

Approaches to fight plastic pollution include 1) responsible handling and recycling of plastic waste; 2) development of new eco-friendly methods to chemically decompose plastics, e.g., artificial enzymes that can digest synthetic polymers;[173] 3) substitution of common plastics with biodegradable analogues (e.g., starch, cellulose); 4) supramolecular polymers.

Polyethylene is one of the most widely used polymers.[174] However, low biodegradability leads to constantly increasing plastic pollution of our environment, therefore, there is a need for biodegradable alternatives.

Biodegradable polymers are designed to degrade by the action of living organisms or under ambient conditions.[175] Polyhydroxyalkanoates (PHAs; e.g., polyhydroxybutyrate, polylactic acid, polybutylenesuccinate, polycaprolactone) are one of the first biodegradable polymers produced. PHAs can be obtained directly from renewable sources by bacteria and degrade when disposed of in bioactive environments such as soil.[176,177]

Another approach towards degradable polymers involves the incorporation of water-labile groups in the polymer chain e.g., acetals and esters.[178] However, long-chain polyesters and polyacetals do not always show required enzymatic or hydrolytic degradation because water is hindered from penetrating into the material due to high crystallinity and hydrophobicity.[179]

An alternative would be the incorporation of orthoesters, that have higher hydrolysis rate.[180] Heller and coworkers synthesized the first polyorthoester in the 1970s by transesterification.[181] Dove and coworkers described the synthesis of polyorthoesters by the addition of diols to diketene acetals.[182] However, these methods require tedious synthesis of precursors, involve long reaction times and are very difficult to scale up.

In this project, we aimed to develop a new method of synthesis of polyorthoesters using ring-opening metathesis copolymerization of cyclic orthoesters with cyclodienes and evaluate their (bio)degradability.

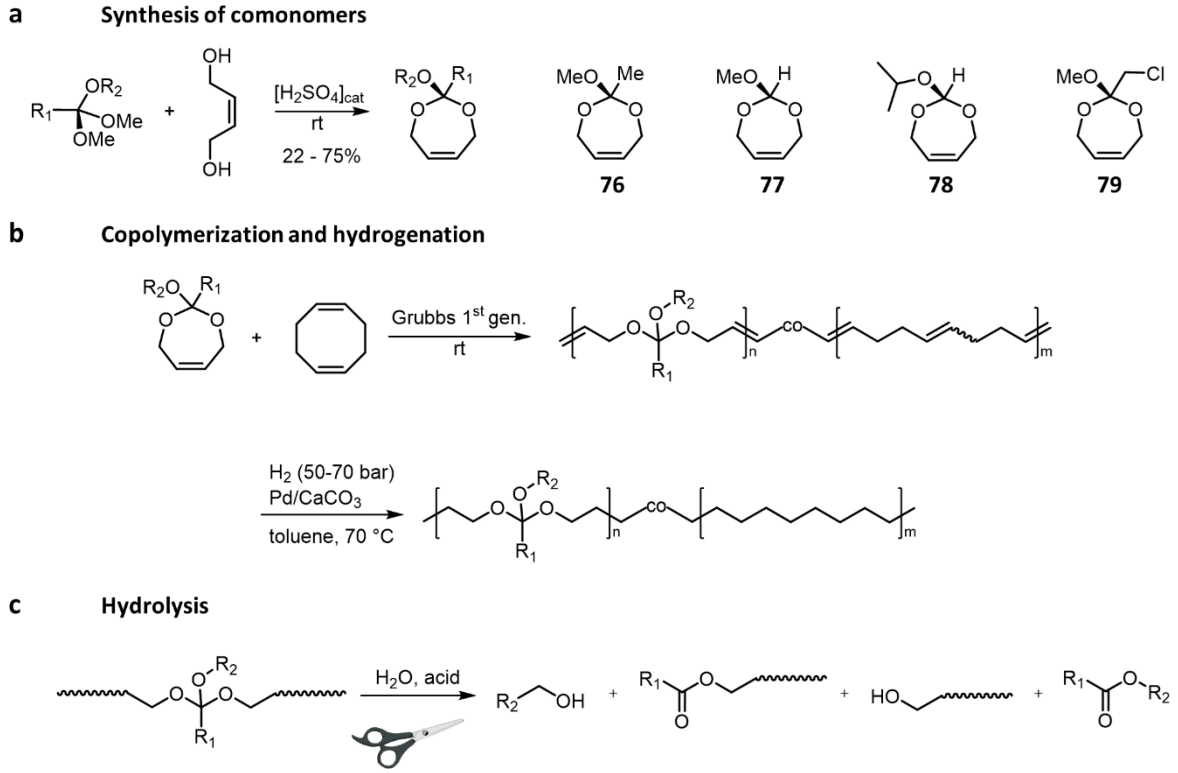

Figure 47. a, Structures of the orthoester monomers. **b**, Copolymerisation of cyclic orthoesters and 1,5-cyclooctadiene. **b**, Aqueous hydrolysis of the copolymers. Adapted from [183] with permission from the American Chemical Society, copyright (2019).

We synthesized orthoester monomers **76** - **79** by reacting corresponding orthoesters with *cis*-2-butene-1,4-diol. Orthoester monomers bear different substituents in order to study their influence on the degradation rate of the final copolymers (Fig. 47a).[183]

In our initial attempts, we tried to carry our homopolymerization of orthoesters **76** – **79** in the presence of the Grubbs catalyst. Since this approach was not successful, we decided to introduce labile point modifications into the polymer chain.

To this end, we carried out ring-opening metathesis polymerization to co-polymerize cyclic orthoester monomers with 1,5-cyclooctadiene in different ratios to give unsaturated polymers with molecular weights up to 38000 g mol^{-1}. Hydrogenation of obtained polymers yielded hard solid materials (Fig. 47b). Unfortunately, polymer brittleness precluded studies on some

mechanical properties. Obtained polymers were semicrystalline with melting points 85 – 110 °C. All copolymers had similar crystal structure as common polyethylene as was evident from the diffraction studies.

Orthoester groups in the polymer chain impart the ability to slowly degrade when exposed to atmospheric moisture (Fig. 48). We observed that the rate of polymer degradation under acidic aqueous conditions could be adjusted by changing R_1 group. For example, more electron-deficient orthoesters (R_1 = CH_2Cl, $t_{1/2}$ = 111 h) hydrolyse slower than orthoformates (R_1 = H, $t_{1/2}$ = 10 h), which in turn are less stable than electron-rich orthoacetates (R_1 = CH_3, $t_{1/2}$ = 3 min). The copolymers could also be anaerobically biodegraded using activated sludge from sewage treatment plants.

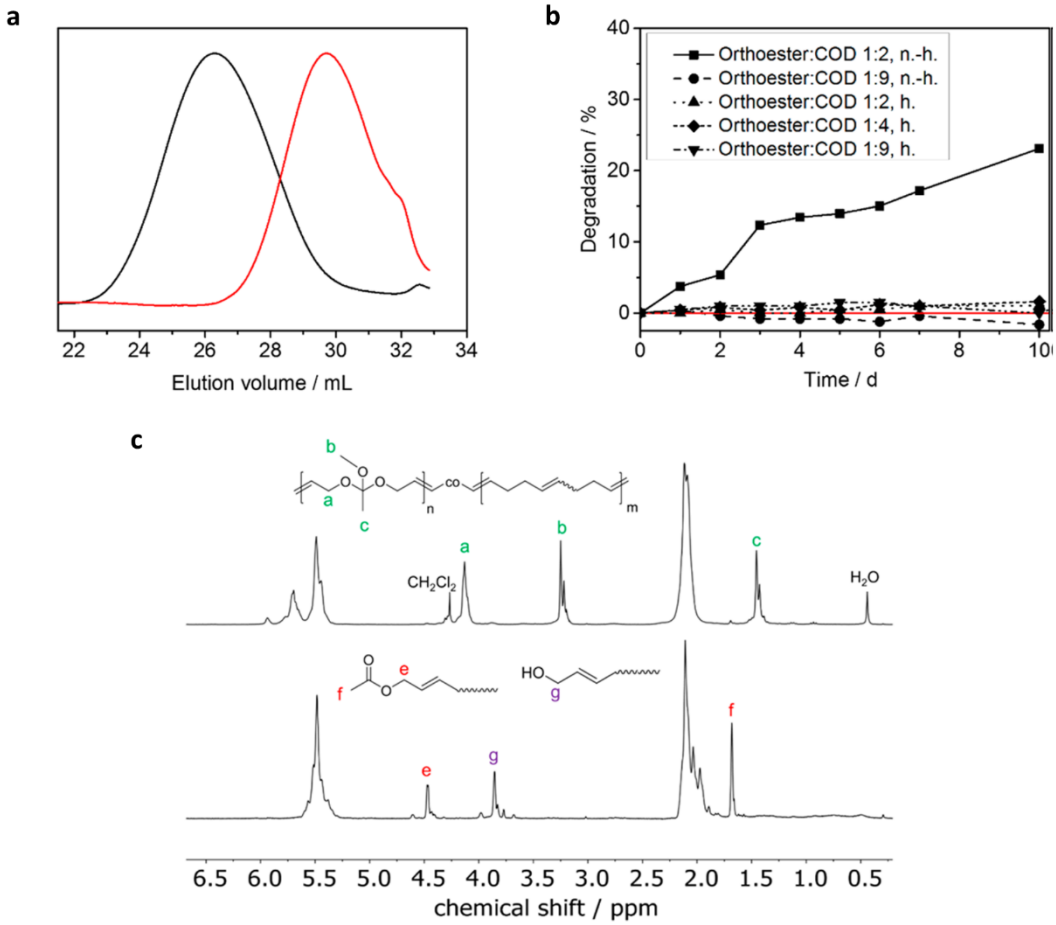

Figure 48. a, Representative SEC elugram (in THF) of the orthoester copolymer before (black) and after (red) degradation by hydrolysis. **b,** Manometric respiratory biodegradation test of hydrogenated (h.) and non-hydrogenated (n.h.) orthoester copolymers using activated sludge from a local sewage plant. **c**, ^{1}H-NMR spectrum (300 MHz, 298 K, C_6D_6) of the orthoester copolymer before and after hydrolysis. Adapted from [183] with permission from the American Chemical Society, copyright (2019).

In conclusion, we have presented a new synthetic route towards orthoester-containing polymers that have structural features similar to high-density polyethylene but can degrade in common biological environment. Due to the facile synthesis of orthoester comonomers, further developments of such polymers could potentially lead to practically valuable (bio)degradable polymers. Further studies can be focused on different diene comonomers (for example norbornene derivatives) to tune the physical and mechanical properties of the polymers.

2.4 Anion-binding of All-*cis* Hexafluorocyclohexane in Solution and Solid State

Anion recognition is one of the long-standing challenges of supramolecular chemistry due to generally higher solvation energy compared to cations, bigger size, often non-spherical shape and narrow pH-windows in which anions often exist. Nevertheless, during the past two decades, considerable progress has been made regarding the synthesis of effective anion receptors.[184–186]

Receptors for inorganic anions such as chloride, fluoride, sulfate or nitrate have recently received considerable attention because of their vast potential for applications in sensing,[187–189] catalysis,[190] and medicinal chemistry.[82,191] Well-known motifs for anion binding include (thio)ureas,[192] triazoles,[193,194] and pyrroles.[195,196]

In this project, we wanted to investigate the supramolecular properties of all-*cis* $C_6H_6F_6$, which due to large dipole moment and co-facial orientation of C–H bonds promised a huge potential as a new motif for anion binding. At that time, there were no reports on solution or solid-state studies of supramolecular properties of all-*cis* $C_6H_6F_6$, even though some interesting theoretical results were present. McMahon and O`Hagan demonstrated that in the gas phase, all-*cis* $C_6H_6F_6$ could bind anions with enthalpies exceeding all anion binding motifs (ΔH^0_{298} = -156.5 kJ mol^{-1}, ΔS^0_{298} = -97.2 J mol^{-1} K^{-1}, ΔG^0_{298} = -127.5 kJ mol^{-1} which corresponds to logK_a = 22).[33] Encouraged by the theoretical results, we expected to achieve high K_a values also in solution. High anion affinities combined with polar hydrophobicity of C–F bonds[197] could lead to a new class of anion binding motifs, extremely promising in the area of transmembrane anion transport.[82] To probe the anion binding affinities, we carried out ^{1}H and ^{19}F NMR titrations in acetone-d_6, acetonitrile-d_3, and DMSO-d_6. These solvents differ significantly in hydrogen bond accepting abilities and dielectric constants. Titrations were carried out with halide anions, nitrate (NO_3^-) and hexafluorophosphate (PF_6^-) as a weakly coordinating anion.

All-*cis* $C_6H_6F_6$ exhibits moderate binding constants with halides (Table 3) (K_a = 100 – 500 mol^{-1}) in acetone-d_6. When we compare solvents, binding affinities were ca. one order of magnitude lower in acetonitrile-d_3 and below NMR detection limit in DMSO-d_6. The formation of 2:1

complexes was much less favourable than in the gas phase studies. Inside the halide series binding in acetone-d_6 drops from small F^-, which has the largest electron density, to big I^-. These results demonstrate that the anion binding of all-*cis* $C_6H_6F_6$ in solution is electrostatic in nature.

Table 3. Association constants for the interaction of all-*cis* $C_6H_6F_6$ with simple anions. Reproduced from [198] with permission from the Royal Society of Chemistry, copyright (2018).

Anion	**Acetone-d_6** K_a (1:1 fit)	**CD_3CN** K_a (1:1 fit)	**DMSO-d_6** K_a (1:1 fit)
F^-	600 ± 400 M^{-1}	HF elimination	
Cl^-	400 ± 40 M^{-1}	19 ± 8 M^{-1}	-
Br^-	150 ± 40 M^{-1}	13 ± 5 M^{-1}	-
I^-	38 ± 7 M^{-1}	<10 M^{-1}	-
NO_3^-	37 ± 7 M^{-1}	<10 M^{-1}	-
PF_6^-	-	-	-

To demonstrate the possibility of the incorporation of all-*cis* $C_6H_6F_6$ into more complex architectures, we prepared its derivative bearing a methoxy group, which can be easily chemically modified, to see how this substitution would impact binding affinities. Less polar all-*cis* $C_6H_6F_5OMe$ had ca. three times lower affinity to Cl^- than all-*cis* $C_6H_6F_6$.[198]

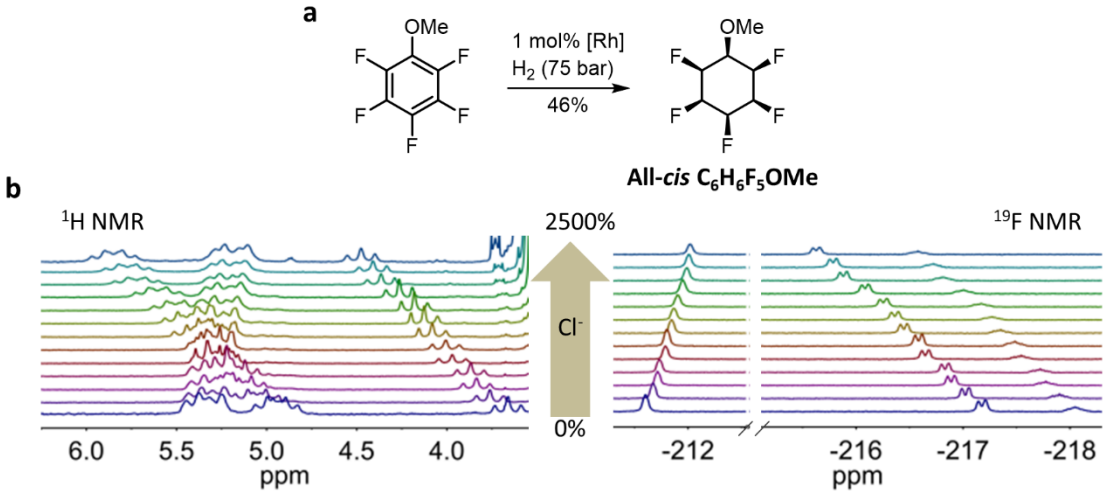

Figure 49. a, Synthesis of all-*cis* $C_6H_6F_5OMe$. **b**, Partial ^1H and ^{19}F NMR (acetone-d_6, 400 MHz, 293 K) stacked plots for titration of all-*cis* $C_6H_6F_5OMe$ with TBACl. Reproduced from [198] with permission from the Royal Society of Chemistry, copyright (2018).

Anion affinities in solution are much lower than in gas phase. This can be explained by the electrostatic screening of the solvent and the solvation of all components.[199]

Finally, we were able to co-crystallize all-*cis* $C_6H_6F_6$ with tetraphenyl phosphonium chloride (Fig. 50a). All-*cis* $C_6H_6F_6$ co-crystallized with Cl^- in 1:1 ratio and chloride forming $(Cl^-)_2(H_2O)_2$ cluster where Cl^- forms two hydrogen bonds to each water molecule. Each $(Cl^-)_2(H_2O)_2$ cluster is surrounded by four all-*cis* $C_6H_6F_6$ molecules that stabilize the cluster by C–H···Cl and C–H···O interactions (Fig. 50b).

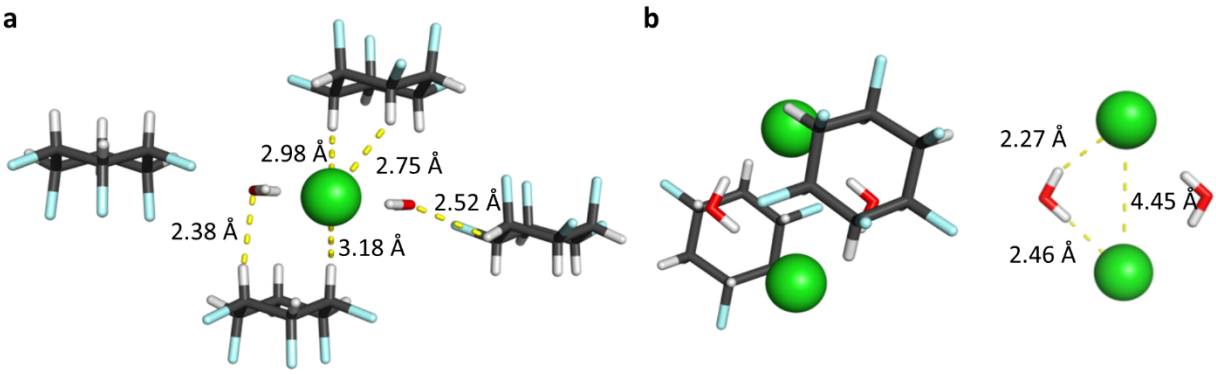

Figure 50. a, Solid-state structure of the c-crystal of all-*cis* $C_6H_6F_6$ with tetraphenylphosphonium chloride (cations omitted for clarity). **b**, Structure of $(Cl^-)_2 \cdot (H_2O)_2$ cluster stacked between two molecules of all-*cis* $C_6H_6F_6$. Colour code: carbon – dark grey, oxygen – red, fluorine – blue, chlorine – green. Reproduced from [198] with permission from the Royal Society of Chemistry, copyright (2018).

In conclusion, we have demonstrated the ability of all-*cis* $C_6H_6F_6$ to bind anions electrostatically in solution and in solid-state, forming predominantly 1:1 complexes. This study suggests that all-*cis* multifluorocyclohexanes constitute a promising new type of anion binding motifs. In the future, it can be incorporated into more complex architectures or used to create materials with simultaneous cationo- and anionophilicity for application as a solid electrolyte in lithium batteries. Simultaneous incorporation of these two effects in solid electrolytes is a new and promising approach to reduce dendrite growth in Lithium-ion batteries.[200]

2.5 Living Supramolecular Polymerization of Fluorinated Cyclohexanes

In ferroelectric materials, individual molecules are organized into ordered lattices that are dynamic under the influence of external electric fields. The source of polarization is either an intrinsic molecular dipole or an induced dipole from supramolecular interactions between molecules. In all cases, they must reside in a noncentrosymmetric lattice.[27] Although we did not manage to implement all-*cis* $C_6H_6F_6$ into this concept, our failed result has led to much more interesting discovery – a new system for living supramolecular polymerization.

Our initial goal was to organize dipoles of all-*cis* $C_6H_6F_6$ around rigid noncentrosymmetric polymeric carcass – poly(isocyanide)[201] – to make new ferroelectric materials. However, when we saw the report by Datta and coworkers[36] we realized that all-*cis* $C_6H_6F_6$ must stack very well in a low polar medium. We decided to use this property to make supramolecular polymers with potentially macroscopic polarization.

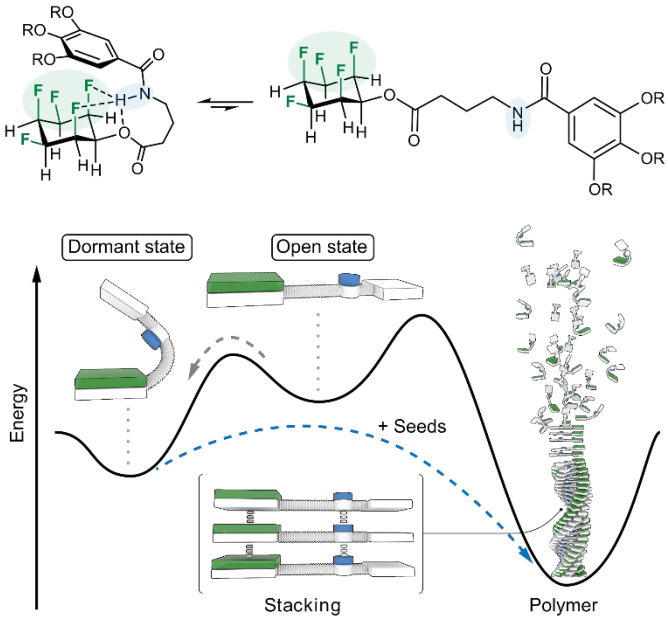

Figure 51. Molecular structure of the monomer in the folded (top left) and unfolded (top right) states and schematic illustration of the partial energy profile of supramolecular polymerization. Reproduced from [203] with permission from the Nature Publishing Group, copyright (2021).

We synthesized a monomer **M₃** with all-*cis* $C_6H_6F_5$ connected by a short flexible linker to an amide (Fig. 52). In solution, this monomer is kinetically stable and does not polymerize spontaneously, although the polymerized state is thermodynamically favourable. We could

demonstrate that the reason behind kinetic stability is the folding of the monomer into the dormant C-shaped conformations, where all-*cis* $C_6H_6F_5$ coordinates onto the amide and aromatic ring. Folding was proven by HOESY, VT-NMR, kinetic experiments, and high-level MD calculations. We could identify the conditions under which the monomer was stable for hours but polymerized when ultrasound was applied or pre-formed supramolecular polymer was added.

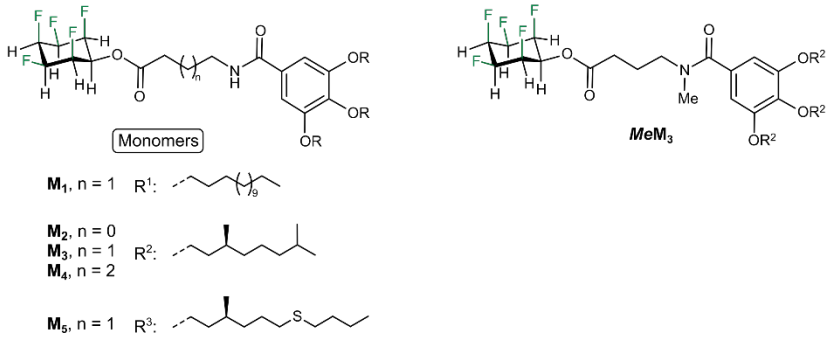

Figure 52. Structures of the studied compounds. Adapted from [203] with permission from the Nature Publishing Group, copyright (2021).

The kinetically stable monomer is the key prerequisite for living supramolecular polymerization, so we started to look for an initiator. Unfortunately, quasi monotopic *N*-methylated monomer ***Me*M$_3$** did not initiate polymerization by itself. However, we could use it to prepare well-defined seeds. The methylated monomer was sonicated with the non-methylated monomer at 0 °C for 20 min to give uniform seeds with weight-averaged length approximately 100 nm and narrow polydispersity. In this procedure, methylated monomer helps to control the final length of the seeds acting as a sequestrator (Fig 53b,c).[202]

Upon addition of the seeds to the monomer solution in cyclohexane:chloroform 84:16 v/v, polymerisation starts immediately without lag time, and the rate of polymerization is first order with respect to the seed concentration, indicating chain-growth mechanism (Fig. 53d,e). Obtained polymers remained active and continued to elongate upon the addition of fresh portions of the monomer, which was proven by multicycle dilution experiments.

In AFM studies of supramolecular polymers, we observed separate fibers with narrow polydispersity, and the length of the fibers was proportional to the amount of the seeds added, and they continued to grow upon the addition of fresh portions of the monomer. Thus, we could achieve living supramolecular polymerization.

The next big challenge was the synthesis of supramolecular block copolymers. We wondered whether it would be possible to carry out kinetically controlled LSP of monomers with different side chains. This approach would be reminiscent of the very common covalent living chain-growth polymerization of acrylates, where a molecule of interest is transformed into acrylate or acrylamide that undergoes living polymerization.

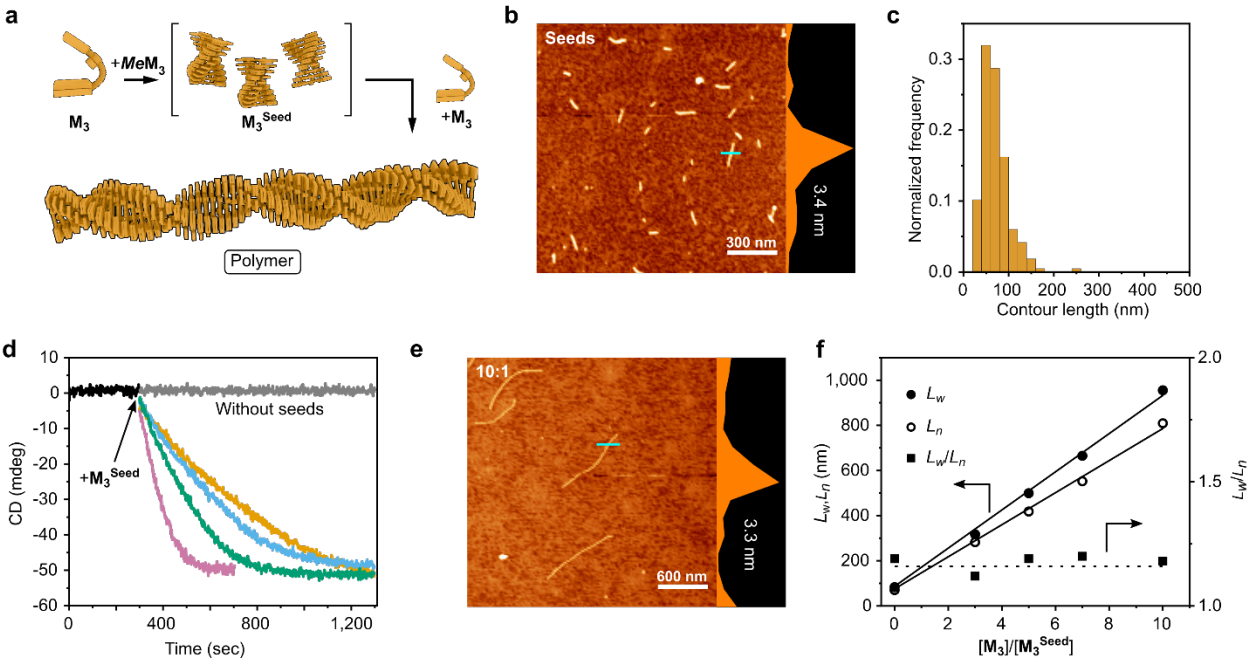

Figure 53. **a**, Schematic illustration of the seeded living supramolecular polymerization. **b**, AFM height image of $\mathbf{M_3^{Seed}}$ spin-coated on silicon wafer. Cross-section was measured along the blue line. **c**, Histogram of the length distribution of $\mathbf{M_3^{Seed}}$. **d**, Time course of supramolecular polymerization of $\mathbf{M_3}$ initiated by addition of different amounts of $\mathbf{M_3^{Seed}}$ ([$\mathbf{M_3}$]/[$\mathbf{M_3^{Seed}}$] = 50/1 (pink line), 100/1 (green line), 150/1 (blue line), 200/1 (yellow line) v/v). **e**, Representative AFM height images of supramolecular polymers obtained with different [$\mathbf{M_3}$]/[$\mathbf{M_3^{Seed}}$] = 10:1 (v/v) ratio spin-coated on silicon wafer. **f**, Weight-average length (L_w), number-average length (L_n) and PDI (L_w/L_n) obtained with different [$\mathbf{M_3}$]/[$\mathbf{M_3^{Seed}}$] ratios (3/1, 5/1, 7/1, 10/1 v/v) plotted against [$\mathbf{M_3}$]/[$\mathbf{M_3^{Seed}}$] v/v. Solid lines represent linear fit. Dashed line is to guide the eye. Adapted from [203] with permission from the Nature Publishing Group, copyright (2021).

Current approaches towards kinetically controlled synthesis of supramolecular block copolymers by LSP mainly rely on the modification of the polymerisable core: synthetically laborious attachment of different substituents onto the perylene diimide core or use of different porphyrin-metal complexes. Our approach, owing to its modularity, could offer a playground for further research on supramolecular block copolymer synthesis. Moreover, it would be the first example of a supramolecular BCP synthesized using kinetically trapped monomers rather than off-pathway aggregates.

We prepared a new monomer by replacing the terminal isopropyl group with the thiobutyl group. The idea behind was to modify the periphery of the molecule with minimal changes to the polymerizable core.

The new monomer had increased kinetic stability with similar overall behaviour. The polymerisation kinetics similar to the seeded-growth of **M₃** was observed, indicating chain-growth polymerization mechanism. The size and PDI of **M₅-M₃-M₅** supramolecular polymer obtained with 3/1 and 5/1 [**M₅**]/[**M₃**^{Seed}] ratios perfectly matched the corresponding **M₃** homopolymer (Fig. 54e).

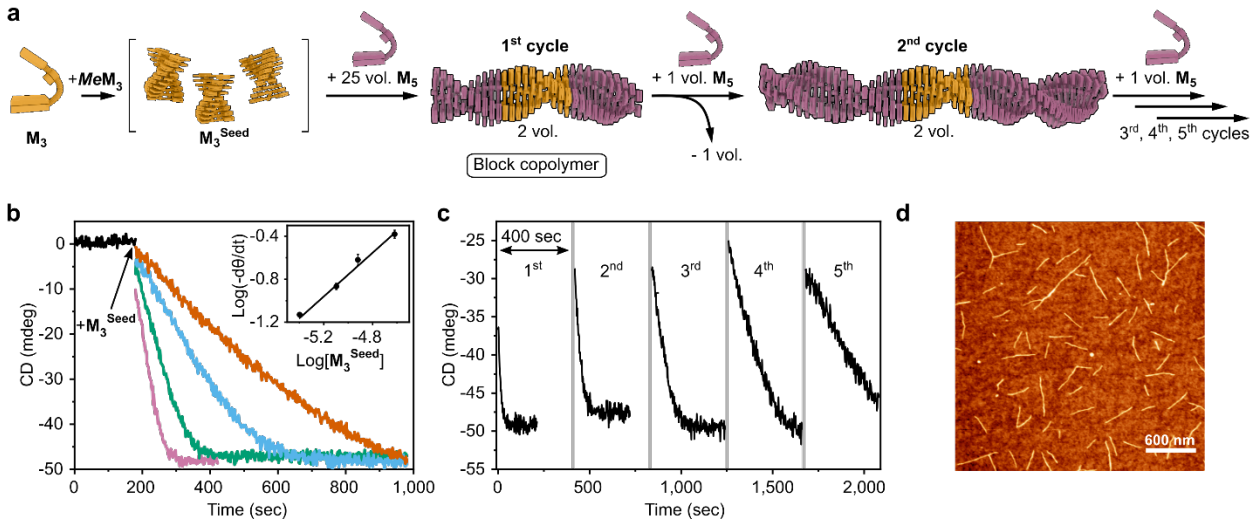

Figure 54. a, Schematic illustration of the synthesis of block copolymers by seeded LSP. **b**, Time course of supramolecular polymerization of **M₅** initiated by addition of different amounts of **M₃**^{Seed}: [**M₅**]/[**M₃**^{Seed}] = 50/1 (pink curve), 100/1 (green curve), 150/1 (blue curve), 300/1 (orange curve) v/v. Inset shows log-log plot of the rate of polymerisation as a function of **M₃**^{Seed} concentration. **c**, Time course of change of the CD signal at 260 nm while **M₅-M₃-M₅** supramolecular block copolymer, obtained using [**M₅**]/[**M₃**^{Seed}] = 25/1 ratio (1st cycle), was diluted with **M₅**. **d**, Representative AFM height image of **M₅-M₃-M₅** supramolecular block copolymers obtained using [**M₅**]/[**M₃**^{Seed}] = 3/1 ratio, spin-coated on silicon wafer. Adapted from [203] with permission from the Nature Publishing Group, copyright (2021).

Finally, we were able to visualize supramolecular block copolymers using AFM directly. AFM height profiles along the fibers of **M₅-M₃-M₅** supramolecular copolymers spin-coated on the silicon wafer revealed the presence of thinner middle parts with z-displacement of 3.1 nm, corresponding to **M₃** block, and thicker termini with z-displacement of ca. 4.2 – 4.3 nm, corresponding to **M₅** block.

In summary, we have discovered a new platform for living supramolecular polymerisation that offers high control over the self-assembly of supramolecular polymers and synthesis of supramolecular block copolymers. We expect that our system due to its simplicity, lack of extended π-system and metal centres might become a system of choice for the investigation of supramolecular block copolymer synthesis and their properties.

3. Summary and Outlook

In the first part of this thesis, it is demonstrated that the orthoester exchange is a useful tool for the self-assembly of cryptates that have unique dynamic properties. We could also demonstrate that incorporation of water-labile orthoesters into a polymer chain, using ring-opening metathesis polymerization, can lead to biodegradable polymers.

The future work could pursue two goals. From a fundamental point of view, it would be interesting to demonstrate the scope of dynamic orthoester exchange by assembling anion-binding and ion-pair binding cryptates, as well as carceplexes.

One application where orthoesters could shine is polymers. For example, one could imagine polymersomes with orthoesters in the main chain that will exhibit an increased rate of hydrolysis in an acidic environment. At the same time, because orthoesters will be partially buried inside the vesicle, hydrolyses might be slowed down. Such polymersomes could be used in drug delivery with controlled release in the acidic environment.

In the second part of this thesis, we demonstrated the emergent supramolecular properties of facially polarized fluorinated cyclohexanes. We could demonstrate that all-*cis* $C_6H_6F_6$ derivatives can be potent anion binding motifs. We also designed a new, simple, metal-free, platform for living supramolecular polymerization lacking extended π-systems.

Future research on properties of all-*cis* $C_6H_6F_6$ might be: 1) investigation of novel potential ferroelectric materials by appending all-*cis* $C_6H_6F_6$ to a polymer core; 2) investigation of novel solid-state electrolytes for lithium-ion batteries that have simultaneously high anion and cation mobilities that could suppress the formation of dendrites; 3) bifunctional organocatalysts based on all-*cis* $C_6H_6F_6$ that can stabilize both anionic and cationic transition states; 4) investigation of non-covalent functionalization of 2D materials (for example graphene) based on the ability of all-*cis* $C_6H_6F_6$ to form strong CH···π interactions.

The development of the new platform for LSP opens up a large number of possible follow up studies.

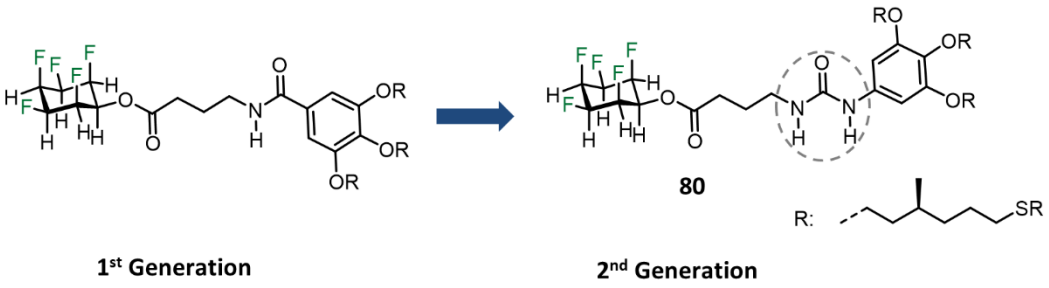

Figure 55. Substitution of the amide with more polar urea can improve folding.

First of all, we need to explore whether it is possible to optimize our design to create a universal platform for LSP with truly predictable properties. In order to minimize the influence of the side chains on the thermodynamic profile and kinetics of supramolecular polymerisation, it is desirable to increase the energy of folding and stacking by substitution of the amide with more polar urea (Fig. 55). Next, the core structure of the monomer needs to be improved in order to minimize the number of synthetic steps that lead to supramolecular monomers allowing us easy access to the library of monomers. A library of monomers would allow us to explore chemical space, drawing relationships between structure and supramolecular properties.

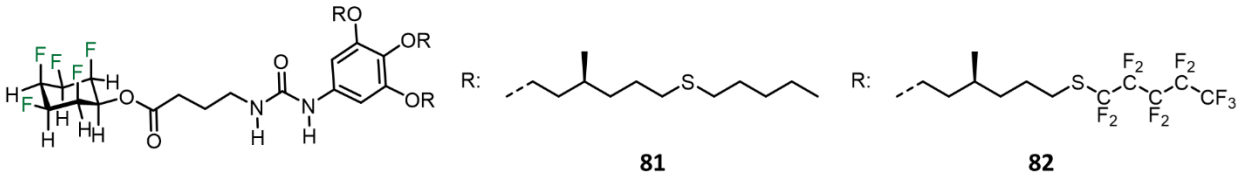

Figure 56. Possible structures of the monomers that can be used to study microphase separation in supramolecular BCPs.

Another big goal that has not been achieved by supramolecular polymer chemists would be the investigation of the microphase separation in supramolecular BCPs. It is well known that conventional covalent block copolymers in bulk often form microphase-separated structures. However, it is unknown whether supramolecular BCPs can form microphase-separated structures in bulk or they will self-sort, giving the mixture of homopolymers. Two possible monomers that could be used to test this hypothesis are shown in Figure 56.

Finally, it would be extremely interesting to try to create supramolecular polymers with different morphologies, e.g. star-shaped polymers. To this end, one could envision using star-shaped auxiliary compounds for the synthesis of star-shaped seeds.

4. Publications

4.1 Adaptive Behaviour of Dynamic Orthoester Cryptands

Shyshov O, Brachvogel RC, Bachmann T, et al. Adaptive Behavior of Dynamic Orthoester Cryptands. *Angew. Chem. Int. Ed*. **2017**, 56(3), 776-781.
DOI: 10.1002/anie.201609855.

Reprinted with permission from John Wiley and Sons and Copyright Clearence Center.

Abstract:

The integration of dynamic covalent bonds into macrocycles has been a tremendously successful strategy for investigating noncovalent interactions and identifying effective host-guest pairs. While numerous studies have focused on the dynamic responses of macrocycles and larger cages to various guests, the corresponding constitutionally dynamic chemistry of cryptands remains unexplored. Reported here is that cryptands based on orthoester bridgeheads offer an elegant entry to experiments in which a metal ion selects its preferred host from a dynamic mixture of competing subcomponents. In such dynamic mixtures, the alkali metal ions Li^+, Na^+, K^+, Rb^+, and Cs^+ exhibit pronounced preferences for the formation of cryptands of certain sizes and donor numbers, and the selection is rationalized by DFT calculations. Reported is also the first self-assembly of a chiral orthoester cryptate and a preliminary study on the use of stereoisomers as subcomponents.

Comments on own contributions:

Prof. Max von Delius had the original idea. I performed synthesis and characterization of orthoester cryptates and cryptands via self-assembly and experiments on the adaptive behaviour of large cages: cage shrinkage and cryptate metathesis. I obtained most of the single-crystal X-ray structures (for Rb and Cs cryptates). Dr. Brachvogel performed experiments on adaptive behaviour, titration studies, and prepared figures for the manuscript. Our collaborators in Erlangen carried out DFT calculations and isothermal titration calorimetry studies. I participated in all discussions, manuscript writing, and writing of the supporting information.

Supramolecular Chemistry

International Edition: DOI: 10.1002/anie.201609855
German Edition: DOI: 10.1002/ange.201609855

Adaptive Behavior of Dynamic Orthoester Cryptands

*Oleksandr Shyshov[+], René-Chris Brachvogel[+], Tobias Bachmann, Rubitha Srikantharajah, Doris Segets, Frank Hampel, Ralph Puchta, and Max von Delius**

Abstract: *The integration of dynamic covalent bonds into macrocycles has been a tremendously successful strategy for investigating noncovalent interactions and identifying effective host–guest pairs. While numerous studies have focused on the dynamic responses of macrocycles and larger cages to various guests, the corresponding constitutionally dynamic chemistry of cryptands remains unexplored. Reported here is that cryptands based on orthoester bridgeheads offer an elegant entry to experiments in which a metal ion selects its preferred host from a dynamic mixture of competing subcomponents. In such dynamic mixtures, the alkali metal ions Li^+, Na^+, K^+, Rb^+, and Cs^+ exhibit pronounced preferences for the formation of cryptands of certain sizes and donor numbers, and the selection is rationalized by DFT calculations. Reported is also the first self-assembly of a chiral orthoester cryptate and a preliminary study on the use of stereoisomers as subcomponents.*

The unique feature of dynamic covalent bonds, their stability or dynamics depending on the reaction conditions, has led to diverse applications in chemistry and adjacent disciplines.[1] In supramolecular host–guest chemistry, the integration of dynamic covalent bonds into macrocycles,[2] their combination with metal–ligand interactions,[3] and the structural response of macrocyclic systems to (ionic) guests have recently attracted considerable interest.[4]

The majority of constitutionally dynamic metal-ligand cages are rigid and positively charged, a property which makes them an ideal platform for the binding and recognition of anions. The groups of Nitschke,[5] Clever,[6] and others[7] have recently reported impressive examples of adaptive cage transformations in response to different anions. Besides metal-ligand cages, there have been numerous studies on the adaptive behavior of dynamic combinatorial macrocycles in response to guests.[1f,8] However, in most examples reported to date, the selection occurs between oligomeric species, for example, dimeric and trimeric species compete for guest binding. Studies in which adaptive behavior is based on subcomponent selection and subtle architectural differences between competing organic hosts are rare.[2c,9]

As the smallest three-dimensional hosts, dynamic cryptands represent an attractive, yet practically unexplored[10] area of chemical (host–guest) space. We have recently reported the first dynamic covalent self-assembly of a monometallic cryptate[11] (**[Na^+⊂*o*-Me_2-1.1.1]**), which was based on the reversible, acid-catalyzed reaction of a simple orthoester with diethylene glycol (Scheme 1a).[12] Herein, we report the adaptive behavior of orthoester cryptands in response to cationic guests (Scheme 1b).

In a first series of experiments, we tested whether the orthoester cryptand ***o*-Me_2-1.1.1** would respond to the addition of mismatched metal guests by either a dynamic covalent shrinkage or expansion event (Scheme 2a). The combination of one equivalent of LiTPFPB (lithium tetrakis(pentafluorophenyl)borate), ethylene glycol, and acid catalyst, for instance, should lead to the formation of the shrunken cryptate **[Li^+⊂*o*-Me_2-1.1.0]**, if this host-guest pair repre-

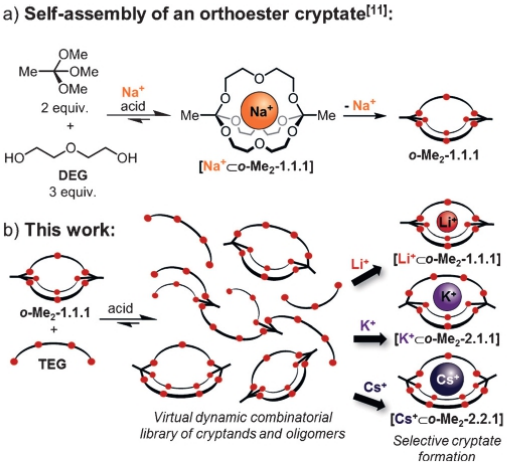

Scheme 1. a) Sodium-templated self-assembly of the orthoester cryptate **[Na^+⊂*o*-Me_2-1.1.1]** and subsequent preparation of cryptand ***o*-Me_2-1.1.1**. b) Adaptive behavior of ***o*-Me_2-1.1.1** in the presence of triethylene glycol (TEG), catalytic acid, and selected guest ions. DEG = diethylene glycol.

[*] O. Shyshov,[+] R.-C. Brachvogel,[+] Prof. Dr. M. von Delius
Institute of Organic Chemistry and Advanced Materials
University of Ulm
Albert-Einstein-Allee 11, 89081 Ulm (Germany)
E-mail: max.vondelius@uni-ulm.de
R. Srikantharajah, Dr. D. Segets
Institute of Particle Technology (LFG) and
Interdisciplinary Center for Functional Particle Systems (FPS)
Friedrich-Alexander Universität Erlangen-Nürnberg (FAU)
Cauerstrasse 4, 91058 Erlangen (Germany)
T. Bachmann, Dr. F. Hampel, Priv.-Doz. R. Puchta
Department of Chemistry and Pharmacy, Institute of Organic Chemistry, and Computer Chemistry Center (CCC)
Friedrich-Alexander Universität Erlangen-Nürnberg (FAU)
Henkestrasse 42, 91054 Erlangen (Germany)
[+] These authors contributed equally to this work.
Supporting information and the ORCID identification number(s) for the author(s) of this article can be found under http://dx.doi.org/10.1002/anie.201609855.

 © 2017 Wiley-VCH Verlag GmbH & Co. KGaA, Weinheim

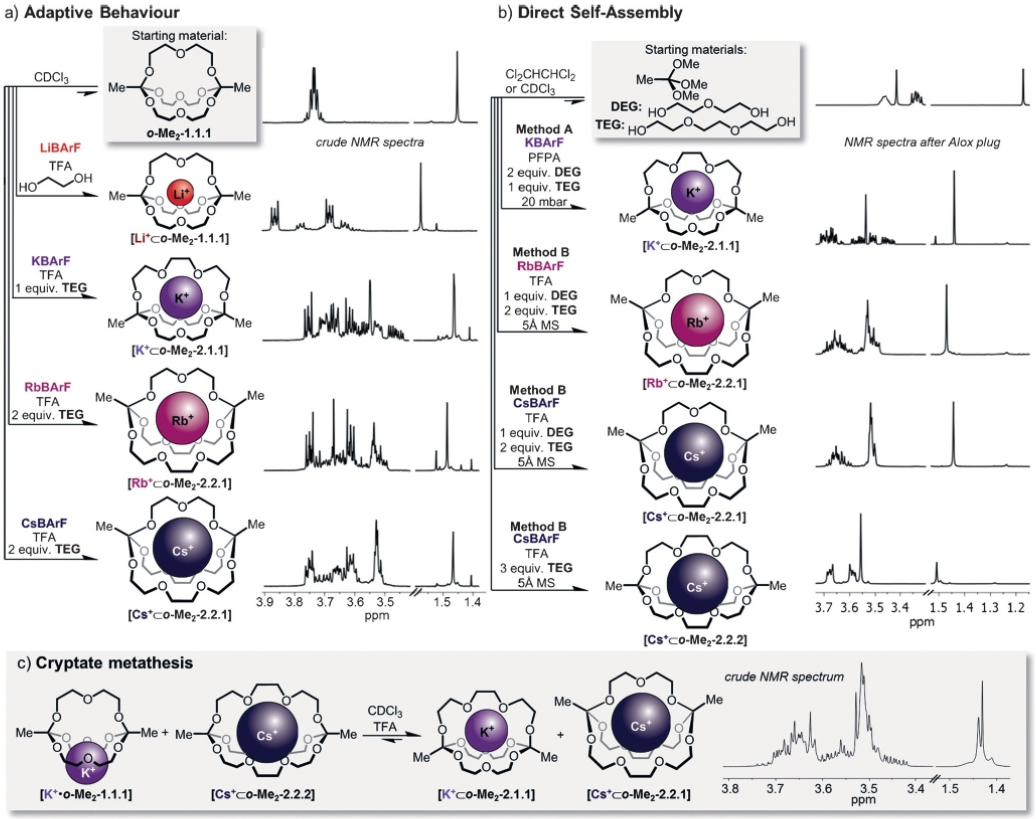

Scheme 2. a) Adaptive behavior of ***o*-Me$_2$-1.1.1** in the presence of different diols and metal ions. Reaction conditions: 5 mmol ***o*-Me$_2$-1.1.1**, 5 mmol metal salt, 5–10 mmol **TEG**, and 0.5 mmol TFA in $CDCl_3$; equilibration time: 3–6 hours, yields (NMR) 20–83% (for further experiments see Supporting Information). b) Direct self-assembly of the different orthoester cryptates. Method A: 5 mmol metal salt, 5–10 mmol **TEG**, 5–10 mmol DEG, 1.5 mmol PFPA, 1,1,2,2-tetrachloroethane, 20 mbar, yield (isolated) 39–55%. Method B: 5 mmol metal salt, 0–5 mmol TEG, 10–15 mmol DEG, 1.5 mmol TFA, 1.5 mL $CDCl_3$, 5 Å M.S. (ca. 0.5 g), yield (isolated) 27–49%. BArF = tetrakis[3,5-bis(trifluoromethyl)phenyl]borate, DEG = diethylene glycol, PFPA = perfluoropentanoic acid, TEG = triethylene glycol, TFA = trifluoroacetic acid.

sented the thermodynamic minimum. In the corresponding experiment, we found that the dynamic system remained mainly at the **[Li$^+$⊂*o*-Me$_2$-1.1.1]** state, thus indicating that the cryptand ***o*-Me$_2$-1.1.0** is either too small to accommodate Li^+ or that binding to a host with one additional oxygen donor atom outweighs a possible preference for the smaller host. It is worth noting that **[Li$^+$⊂*o*-Me$_2$-1.1.1]** does not only outcompete the alternative host ***o*-Me$_2$-1.1.0**, but also five-membered ring products derived from an addition of both alcohol functions in ethylene glycol to the orthoester.[12a]

When we studied larger alkali metal ions in combination with longer diol triethylene glycol (TEG), we observed that these metals exhibit pronounced preferences for the formation of certain orthoester hosts. The selectivity becomes evident by the appearance of only one predominant signal in the methyl region of the ^{1}H NMR spectra of the crude mixture in each of these experiments (Scheme 2a). For example, potassium directs the dynamic system almost exclusively towards the formation of the cryptand ***o*-Me$_2$-2.1.1**, whereas both rubidium and cesium direct towards ***o*-Me$_2$-2.2.1**. All these experiments were independently conducted with zero, one, two, and three equivalents of TEG, because the quantity of this subcomponent represents a bias for the formation of certain species. Throughout these experiments we found preferences for the same cryptates, even in cases where the amount of TEG should favor other reaction products (see the Supporting Information for all experiments).

These template-based desymmetrization reactions are also remarkable from a synthetic perspective, because conventional unsymmetric cryptands require multistep syntheses.[13] However, having to synthesize a symmetric cryptand en route to an unsymmetric one, does not meet the requirements of any modern metric of synthesis efficiency.[14]

 © 2017 Wiley-VCH Verlag GmbH & Co. KGaA, Weinheim

As a result, we focused our efforts on the direct self-assembly of unsymmetric orthoester cryptates. To achieve this, we needed to identify reaction conditions under which methanol could be slowly removed from equilibrium, while no source of sodium ions [e.g. 4 Å molecular sieves (M.S.)] is present, because the latter would lead to the formation of the symmetric cryptate **[Na$^+$⊂*o*-Me$_2$-1.1.1]**.[11] As shown in Scheme 2b, two such methods, based on either reduced pressure or 5 Å M.S. (containing Ca^{2+} ions) could be identified, thus leading to the preparation of the desired unsymmetric cryptates in yields of 27–55%.

In light of possible applications it is worth noting that all cryptands can conveniently be prepared in quantitative yield from the corresponding cryptates by treatment with ion-exchange resin (see the Supporting Information). We were also able to prepare the symmetric cryptate **[Cs$^+$⊂*o*-Me$_2$-2.2.2]**, which interestingly, was not observed in previous experiments, where this compound would have been a possible product. The preference of Cs^+ for the cryptand ***o*-Me$_2$-2.2.1** was confirmed by a shrinkage experiment, in which **[Cs$^+$⊂*o*-Me$_2$-2.2.2]**, under reaction conditions for orthoester exchange was treated with DEG, and **[Cs$^+$⊂*o*-Me$_2$-2.2.1]** was observed as predominant product (see the Supporting Information).[16]

Adaptive behavior at a higher level of complexity was observed in the multi-metal/multi-cryptand exchange experiment illustrated in Scheme 2c. The symmetric cryptands ***o*-Me$_2$-1.1.1** and ***o*-Me$_2$-2.2.2** were combined with mismatched[17] metal ions K^+ and Cs^+, and orthoester exchange was initiated by addition of acid. The NMR spectrum of the crude mixtures after equilibration and the ESI$^+$ mass spectrum after work-up (see the Supporting Information) clearly demonstrate that a 1:1 mixture of the unsymmetric cryptates **[K$^+$⊂*o*-Me$_2$-2.1.1]** and **[Cs$^+$⊂*o*-Me$_2$-2.2.1]** was formed. Even though we cannot deduce from our data which one of the two host–guest pairs provides the main thermodynamic driving force, this cryptate metathesis is nevertheless a remarkable case of adaptive behavior.

To shed further light on the underlying noncovalent interactions, we grew single crystals from all cryptates which represented preferred species in self-assembly experiments. The resulting X-ray structures are depicted in Figure 1a, along with the structure of previously reported **[Na$^+$⊂*o*-Me$_2$-1.1.1]**. Relatively symmetric coordination geometries are adopted in the cryptates **[K$^+$⊂*o*-Me$_2$-2.1.1]**, **[Rb$^+$⊂*o*-Me$_2$-2.2.1]**, and **[Cs$^+$⊂*o*-Me$_2$-2.2.1]**, while the unique combination of orthoester bridgeheads with glycol side chains results in the formation of up to eleven metal–oxygen bonds. An apparent limit for binding is reached with the cryptand ***o*-Me$_2$-2.2.2**, which only forms eleven out of twelve possible Cs–O bonds. This observation might explain why **[Cs$^+$⊂*o*-Me$_2$-2.2.1]** is the preferred species in experiments where ***o*-Me$_2$-2.2.1** and ***o*-Me$_2$-2.2.2** compete for Cs^+. An unusual type of anisotropic long-range order was observed in the crystal structure of **[Cs$^+$⊂*o*-Me$_2$-2.2.1]**: the presence of Cs–F bonds between counteranion and cryptates results in the formation of a helical coordination polymer (see the Supporting Information for the packing diagram).

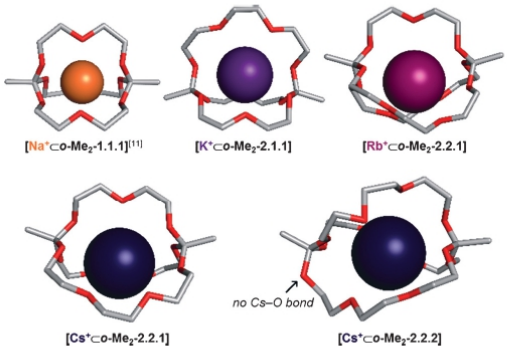

Figure 1. a) Solid-state structures of five orthoester cryptates.[21] The structure of **[Na$^+$⊂*o*-Me$_2$-1.1.1]** was reported previously[11] and is shown for comparison. Single crystals of **[K$^+$⊂*o*-Me$_2$-2.1.1]** were obtained by the vapor diffusion method (cyclopentane/ chloroform). Single crystals of **[Rb$^+$⊂*o*-Me$_2$-2.2.1]**, **[Cs$^+$⊂*o*-Me$_2$-2.2.1]**, and **[Cs$^+$⊂*o*-Me$_2$-2.2.2]** were obtained by the layering method (*n*-heptane/ chloroform). Hydrogen atoms, anions, solvent, and disorder (where applicable) are omitted for clarity. Metal ions are displayed at 100% of effective ionic radius.[15] Selected bond length ranges: Na–O: 2.5–2.6 Å; K–O: 2.8–3.0 Å; Rb–O: 3.0–3.3 Å; Cs–O: 3.2–3.3 Å in **[Cs$^+$⊂*o*-Me$_2$-2.2.1]**; Cs–O: 3.1–3.7 Å (binding) and 4.4 Å (nonbinding) in **[Cs$^+$⊂*o*-Me$_2$-2.2.2]**.

Because some of our experiments represent a stoichiometrically unbiased[18] competition between two dynamic cryptands for a metal ion, we wanted to test, whether the observed trends could be rationalized by theory. In a first set of DFT-based (B3LYP/LANL2DZp) model equations (see the Supporting Information for details), we determined complexation energies for the combination of the cryptands ***o*-Me$_2$-1.1.0**, ***o*-Me$_2$-1.1.1**, ***o*-Me$_2$-2.1.1**, ***o*-Me$_2$-2.2.1**, and ***o*-Me$_2$-2.2.2** with five alkali metal ions.[19] We also carried out NMR titrations for all 20 host-guest combinations, as well as one representative isothermal titration calorimetry (ITC) study, which revealed that sodium binding to ***o*-Me$_2$-1.1.1** is driven both enthalpically and entropically (see the Supporting Information).

With the exception of two outliers (**[Li$^+$⊂*o*-Me$_2$-1.1.1]** and **[Rb$^+$⊂*o*-Me$_2$-1.1.1]**), we observed good agreement between the trends in experiment (Figure 2a) and theory (Figure 2b). More importantly, the relative binding energies do indeed allow rationalizing our findings on adaptive behavior. For instance, K^+ represents a clear minimum for ***o*-Me$_2$-2.1.1** (Figure 2a and 2b), thus explaining the predominant formation of **[K$^+$⊂*o*-Me$_2$-2.1.1]** in the experiment shown in Scheme 2a. It is also evident from the data that binding of Rb^+ and Cs^+ only becomes favorable for the larger cryptands ***o*-Me$_2$-2.2.1** and ***o*-Me$_2$-2.2.2**. The flat line observed in the computational binding energies for ***o*-Me$_2$-1.1.0** (Figure 2b) suggests that no alkali-metal ion fits into this host, and would explain why not even the small Li^+ template led to its formation.

A second set of model equations was designed to more adequately mimic the competition of two cryptands for cation binding. For each metal ion, these calculations revealed

 © 2017 Wiley-VCH Verlag GmbH & Co. KGaA, Weinheim

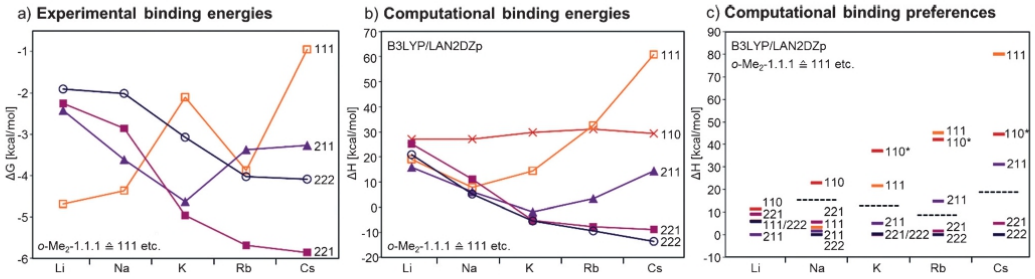

Figure 2. a) Experimental binding energies determined by ^{1}H NMR titrations and data fitting ([D$_3$]acetonitrile, 298 K). b) Computational binding enthalpies (B3LYP/LANL2DZp; gas phase) based on a model equation that mimics the transfer of a metal ion from sixfold water coordination to the orthoester cryptand. c) Computational binding enthalpies (B3LYP/LANL2DZp; gas phase) based on a model equation that mimics the transfer of a metal ion from one orthoester cryptand to another. *: metal was expelled from cage as a result of DFT calculation. See the Supporting Information for experimental/computational details and a discussion of the limitations of the DFT calculations.

energy differences between five host-guest species (Figure 2c). Although these calculations fail to correctly predict all experimental outcomes (for example, ***o*-Me$_2$-2.1.1** should represent the minimum in the case of K^+), they do reveal relatively large energy cutoffs above which a metal ion seemingly is too large to fit into the cavity of the host (highlighted by dashed lines).

Finally, we turned our attention to more complex subcomponents, from which stereochemical insights could be gained.[20] When enantiopure diol *SS*-**1** was subjected to standard self-assembly conditions, the corresponding homochiral cryptate **[Na$^+$⊂*o*-Me$_2$-*SS*,*SS*,*SS*]** formed as the predominant product (Scheme 3a). Interestingly, the corresponding *meso* diastereomer *RS*-**1** failed to produce detectable quantities of the corresponding cryptate under identical reaction conditions (Scheme 3b). A complex mixture of species formed instead (see the Supporting Information), thus indicating that the self-assembly is highly sensitive to conformational differences between diastereomers.

To study a racemic mixture of diols, we prepared the deuterated compound d$_4$-*RR*-**1**, which was subsequently mixed (1:1) with *SS*-**1** to form a pseudo-racemate (Scheme 3c). Because orthoester cryptands comprise an uneven number of diol building blocks, we wondered whether only the homochiral cryptates would form or if opposite enantiomers could be incorporated into the bicyclic structure. Analysis of the reaction outcome by NMR spectroscopy and mass spectrometry revealed that the latter is the case: all four possible cryptate species were formed in roughly statistical mixture.

In conclusion, we have demonstrated that dynamic orthoester cryptands can shrink or expand by subcomponent exchange in response to the addition of alkali-metal ions. We found that certain host-guest pairs represent pronounced thermodynamic minima, which allowed us to use spherical metal templates for the desymmetrization of symmetric cryptands and to carry out an unprecedented cryptate metathesis reaction. We now plan to extend this concept to the combination of transition metals with diols featuring heteroatoms other than oxygen, where added selectivity based on the HSAB principle and applications in sensing and delivery might become viable.

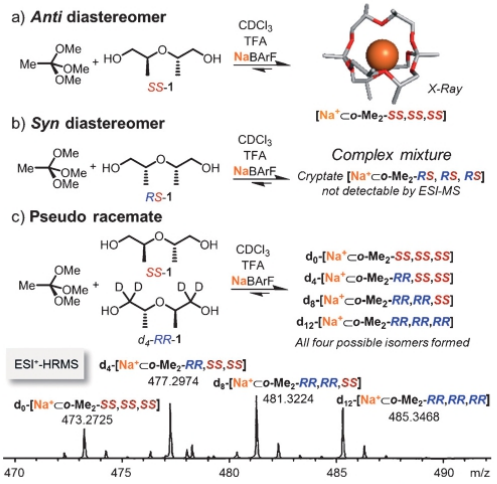

Scheme 3. a) Self-assembly of a chiral cryptate based on diol *SS*-**1**. Solid-state structure of **[Na$^+$⊂*o*-Me$_2$-*SS*,*SS*,*SS*]**.[21] Single crystals were obtained by the vapor diffusion method (CDCl$_3$/ cyclopentane). Hydrogen atoms, anions, and solvent are omitted for clarity. Na—O bond length range: 2.4–2.8 Å. b) Attempted self-assembly based on the *meso* diol *RS*-**1** (no cryptate formation observed by either NMR spectroscopy or ESI$^+$-MS). c) Self-assembly based on pseudo-racemate: 1:1 mixture of *SS*-**1** and deuterated enantiomer d$_4$-*RR*-**1**. Formation of a statistical mixture of all four cryptate stereoisomers, as indicated by ESI$^+$-HRMS (bottom). Reaction conditions: trimethyl orthoacetate (0.12 mmol, 2.0 equiv), diol (0.18 mmol, 3.0 equiv), NaBArF (0.06 mmol, 1.0 equiv), TFA (trifluoroacetic acid, 1.2 µmol, 2 mol%) in 6 mL CDCl$_3$ with 5 Å M.S. Yields: 15–53 %.

Acknowledgments

This work was supported by the Fonds der Chemischen Industrie (FCI doctoral fellowship for R.-C.B.) and the

 © 2017 Wiley-VCH Verlag GmbH & Co. KGaA, Weinheim

Deutsche Forschungsgemeinschaft (Emmy-Noether grant DE1830/2-1). We would like to thank Margarete Dzialach, Wolfgang Donaubauer, Dr. Harald Maid, and Dr. Svetlana Begel for assistance with mass spectrometry, X-ray crystallography, NMR spectroscopy and the analysis of DFT calculations, respectively. Prof. Wolfgang Peukert is acknowledged for providing access to an isothermal titration calorimeter. D.S. and R.S. acknowledge funding from the Deutsche Forschungsgemeinschaft (DFG) through the Cluster of Excellence "Engineering of Advanced Materials" (EAM). R.P. thanks Prof. Tim Clark for hosting this work at the CCC and the Regionales Rechenzentrum Erlangen (RRZE) for a generous allotment of computer time.

Conflict of interest

The authors declare no conflict of interest.

Keywords: cryptands · dynamic combinatorial chemistry · host–guest chemistry · NMR spectroscopy · supramolecular chemistry

How to cite: *Angew. Chem. Int. Ed.* **2017**, *56*, 776–781
Angew. Chem. **2017**, *129*, 794–799

[1] a) E. Moulin, G. Cormos, N. Giuseppone, *Chem. Soc. Rev.* **2012**, *41*, 1031–1049; b) Y. Jin, C. Yu, R. J. Denman, W. Zhang, *Chem. Soc. Rev.* **2013**, *42*, 6634–6654; c) J. Li, P. Nowak, S. Otto, *J. Am. Chem. Soc.* **2013**, *135*, 9222–9239; d) Y. Jin, Q. Wang, P. Taynton, W. Zhang, *Acc. Chem. Res.* **2014**, *47*, 1575–1586; e) G. Zhang, M. Mastalerz, *Chem. Soc. Rev.* **2014**, *43*, 1934–1947; f) A. Herrmann, *Chem. Soc. Rev.* **2014**, *43*, 1899–1933; g) A. G. Slater, A. I. Cooper, *Science* **2015**, *348*, aaa8075.

[2] a) S. J. Rowan, P. A. Brady, J. K. M. Sanders, *Angew. Chem. Int. Ed. Engl.* **1996**, *35*, 2143–2145; *Angew. Chem.* **1996**, *108*, 2283–2285; b) S. J. Rowan, D. G. Hamilton, P. A. Brady, J. K. M. Sanders, *J. Am. Chem. Soc.* **1997**, *119*, 2578–2579; c) S. Otto, R. L. E. Furlan, J. K. M. Sanders, *Science* **2002**, *297*, 590–593.

[3] a) B. Hasenknopf, J.-M. Lehn, N. Boumediene, A. Dupont-Gervais, A. Van Dorsselaer, B. Kneisel, D. Fenske, *J. Am. Chem. Soc.* **1997**, *119*, 10956–10962; b) K. S. Chichak, S. J. Cantrill, A. R. Pease, S.-H. Chiu, G. W. V. Cave, J. L. Atwood, J. F. Stoddart, *Science* **2004**, *304*, 1308–1312; c) D. Schultz, J. R. Nitschke, *Proc. Natl. Acad. Sci. USA* **2005**, *102*, 11191–11195; d) D. A. Leigh, R. G. Pritchard, A. J. Stephens, *Nat. Chem.* **2014**, *6*, 978–982.

[4] a) B. de Bruin, P. Hauwert, J. N. H. Reek, *Angew. Chem. Int. Ed.* **2006**, *45*, 2660–2663; *Angew. Chem.* **2006**, *118*, 2726–2729; b) F. B. L. Cougnon, J. K. M. Sanders, *Acc. Chem. Res.* **2012**, *45*, 2211–2221; c) J.-F. Ayme, J. E. Beves, C. J. Campbell, D. A. Leigh, *Chem. Soc. Rev.* **2013**, *42*, 1700–1712; d) M. Zhang, X. Yan, F. Huang, Z. Niu, H. W. Gibson, *Acc. Chem. Res.* **2014**, *47*, 1995–2005; e) S. Zarra, D. M. Wood, D. A. Roberts, J. R. Nitschke, *Chem. Soc. Rev.* **2015**, *44*, 419–432.

[5] a) I. A. Riddell, M. M. J. Smulders, J. K. Clegg, Y. R. Hristova, B. Breiner, J. D. Thoburn, J. R. Nitschke, *Nat. Chem.* **2012**, *4*, 751–756; b) J. K. Clegg, J. Cremers, A. J. Hogben, B. Breiner, M. M. J. Smulders, J. D. Thoburn, J. R. Nitschke, *Chem. Sci.* **2013**, *4*, 68–76; c) I. A. Riddell, Y. R. Hristova, J. K. Clegg, C. S. Wood, B. Breiner, J. R. Nitschke, *J. Am. Chem. Soc.* **2013**, *135*, 2723–2733; d) W. Meng, T. K. Ronson, J. K. Clegg, J. R. Nitschke, *Angew. Chem. Int. Ed.* **2013**, *52*, 1017–1021; *Angew. Chem.* **2013**, *125*, 1051–1055; e) I. A. Riddell, T. K. Ronson, J. K. Clegg, C. S. Wood, R. A. Bilbeisi, J. R. Nitschke, *J. Am. Chem. Soc.* **2014**, *136*, 9491–9498; f) I. A. Riddell, T. K. Ronson, J. R. Nitschke, *Chem. Sci.* **2015**, *6*, 3533–3537.

[6] a) S. Freye, J. Hey, A. Torras-Galán, D. Stalke, R. Herbst-Irmer, M. John, G. H. Clever, *Angew. Chem. Int. Ed.* **2012**, *51*, 2191–2194; *Angew. Chem.* **2012**, *124*, 2233–2237; b) S. Freye, R. Michel, D. Stalke, M. Pawliczek, H. Frauendorf, G. H. Clever, *J. Am. Chem. Soc.* **2013**, *135*, 8476–8479; c) S. Löffler, J. Lübben, L. Krause, D. Stalke, B. Dittrich, G. H. Clever, *J. Am. Chem. Soc.* **2015**, *137*, 1060–1063; d) R. Zhu, J. Lübben, B. Dittrich, G. H. Clever, *Angew. Chem. Int. Ed.* **2015**, *54*, 2796–2800; *Angew. Chem.* **2015**, *127*, 2838–2842; e) M. Frank, M. D. Johnstone, G. H. Clever, *Chem. Eur. J.* **2016**, *22*, 14104–14125.

[7] R. Custelcean, *Chem. Soc. Rev.* **2014**, *43*, 1813–1824.

[8] a) G. R. L. Cousins, R. L. E. Furlan, Y.-F. Ng, J. E. Redman, J. K. M. Sanders, *Angew. Chem. Int. Ed.* **2001**, *40*, 423–428; *Angew. Chem.* **2001**, *113*, 437–442; b) B. Fuchs, A. Nelson, A. Star, J. F. Stoddart, S. Vidal, *Angew. Chem. Int. Ed.* **2003**, *42*, 4220–4224; *Angew. Chem.* **2003**, *115*, 4352–4356; c) A. González-Álvarez, I. Alfonso, F. López-Ortiz, Á. Aguirre, S. García-Granda, V. Gotor, *Eur. J. Org. Chem.* **2004**, 1117–1127; d) P. T. Corbett, J. Leclaire, L. Vial, K. R. West, J.-L. Wietor, J. K. M. Sanders, S. Otto, *Chem. Rev.* **2006**, *106*, 3652–3711.

[9] a) S. Otto, S. Kubik, *J. Am. Chem. Soc.* **2003**, *125*, 7804–7805; b) H. Y. Au-Yeung, F. B. L. Cougnon, S. Otto, G. D. Pantos, J. K. M. Sanders, *Chem. Sci.* **2010**, *1*, 567–574; c) J. A. Berrocal, R. Cacciapaglia, S. D. Stefano, *Org. Biomol. Chem.* **2011**, *9*, 8190–8194; d) Y. Zhang, Y.-M. Legrand, A. van der Lee, M. Barboiu, *Eur. J. Org. Chem.* **2016**, 1825–1828.

[10] Lehn and Nelson reported imine-based, bimetallic cryptates, yet their dynamic behavior was not explored. a) J. Jazwinski, J.-M. Lehn, D. Lilienbaum, R. Ziessel, J. Guilhem, C. Pascard, *J. Chem. Soc. Chem. Commun.* **1987**, 1691–1694; b) D. MacDowell, J. Nelson, *Tetrahedron Lett.* **1988**, *29*, 385–386; c) Q. Lu, J.-M. Latour, C. J. Harding, N. Martin, D. J. Marrs, V. McKee, J. Nelson, *J. Chem. Soc. Dalton Trans.* **1994**, 1471–1478; d) O. W. Howarth, G. G. Morgan, V. McKee, J. Nelson, *J. Chem. Soc. Dalton Trans.* **1999**, 2097–2102.

[11] R.-C. Brachvogel, F. Hampel, M. von Delius, *Nat. Commun.* **2015**, *6*, 7129.

[12] a) R.-C. Brachvogel, M. von Delius, *Chem. Sci.* **2015**, *6*, 1399–1403; b) R.-C. Brachvogel, M. von Delius, *Eur. J. Org. Chem.* **2016**, 3662–3670.

[13] N.-D. H. Gamage, Y. Mei, J. Garcia, M. J. Allen, *Angew. Chem. Int. Ed.* **2010**, *49*, 8923–8925; *Angew. Chem.* **2010**, *122*, 9107–9109.

[14] a) P. A. Wender, V. A. Verma, T. J. Paxton, T. H. Pillow, *Acc. Chem. Res.* **2008**, *41*, 40–49; b) T. Gaich, P. S. Baran, *J. Org. Chem.* **2010**, *75*, 4657–4673.

[15] R. D. Shannon, *Acta Crystallogr. Sect. A* **1976**, *32*, 751–767.

[16] We also explored the ammonium ion as a possible nonspherical template. Preliminary results indicate that ammonium cryptates such as **[NH_4^+⊂*o*-Me_2-2.1.1]** are intrinsically dynamic, which merits comprehensive experimental and computational studies that are beyond the scope of this manuscript.

[17] R.-C. Brachvogel, H. Maid, M. von Delius, *Int. J. Mol. Sci.* **2015**, *16*, 20641–20656.

[18] By "stoichiometrically unbiased" we refer to potential mass balance effects, which can override thermodynamic preferences in DCLs, but do not play a role in experiments such as **[K^+-*o*-Me_2-1.1.1]** + TEG ↔ **[K^+⊂*o*-Me_2-2.1.1]** + DEG (assuming perfect stoichiometry control and negligible oligomer formation). For seminal contributions on mass balance effects see: a) K. Severin, *Chem. Eur. J.* **2004**, *10*, 2565–2580; b) P. T. Corbett, J. K. M. Sanders, S. Otto, *Chem. Eur. J.* **2008**, *14*, 2153–2166.

[19] a) S. Begel, A. Scheurer, R. Puchta, *J. Coord. Chem.* **2015**, *68*, 3374–3387; b) S. Begel, A. Scheurer, R. Puchta, R. van Eldik, *Z.*

 © 2017 Wiley-VCH Verlag GmbH & Co. KGaA, Weinheim

Anorg. Allg. Chem. **2016**, *642*, 395 – 402; c) S. Begel, R. Puchta, R. van Eldik, *J. Mol. Model.* **2014**, *20*, 1 – 11; d) S. Begel, R. Puchta, R. van Eldik, *Beilstein J. Org. Chem.* **2013**, *9*, 1252 – 1268.

[20] a) M. Ziegler, A. V. Davis, D. W. Johnson, K. N. Raymond, *Angew. Chem. Int. Ed.* **2003**, *42*, 665 – 668; *Angew. Chem.* **2003**, *115*, 689 – 692; b) C. Gütz, R. Hovorka, G. Schnakenburg, A. Lützen, *Chem. Eur. J.* **2013**, *19*, 10890 – 10894; c) W. Meng, T. K. Ronson, J. R. Nitschke, *Proc. Natl. Acad. Sci. USA* **2013**, *110*, 10531 – 10535; d) C. Gütz, R. Hovorka, C. Klein, Q.-Q. Jiang, C. Bannwarth, M. Engeser, C. Schmuck, W. Assenmacher, W. Mader, F. Topić, K. Rissanen, S. Grimme, A. Lützen, *Angew. Chem. Int. Ed.* **2014**, *53*, 1693 – 1698; *Angew. Chem.* **2014**, *126*, 1719 – 1724; e) A. M. Castilla, W. J. Ramsay, J. R. Nitschke, *Acc. Chem. Res.* **2014**, *47*, 2063 – 2073; f) L.-L. Yan, C.-H. Tan, G.-L. Zhang, L.-P. Zhou, J.-C. Bünzli, Q.-F. Sun, *J. Am. Chem. Soc.* **2015**, *137*, 8550 – 8555; g) A. Schaly, Y. Rousselin, J.-C. Chambron, E. Aubert, E. Espinosa, *Eur. J. Inorg. Chem.* **2016**, 832 – 843; h) X. Wang, Y. Wang, H. Yang, H. Fang, R. Chen, Y. Sun, N. Zheng, K. Tan, X. Lu, Z. Tian, X. Cao, *Nat. Commun.* **2016**, *7*, 12469.

[21] CCDC 1505902 (**[K$^+$⊂*o*-Me$_2$-2.1.1]**), 1505906 (**[Rb$^+$⊂*o*-Me$_2$-2.2.1]**), 1505905 (**[Cs$^+$⊂*o*-Me$_2$-2.2.1]**), 1505904 (**[Cs$^+$⊂*o*-Me$_2$-2.2.2]**), and 1505903 (**[Na$^+$⊂*o*-Me$_2$-*SS*,*SS*,*SS*]**) contain the supplementary crystallographic data for this paper. These data can be obtained free of charge from The Cambridge Crystallographic Data Centre.

Manuscript received: October 8, 2016
Revised: November 22, 2016
Final Article published: December 13, 2016

 © 2017 Wiley-VCH Verlag GmbH & Co. KGaA, Weinheim

Angewandte Chemie
Eine Zeitschrift der Gesellschaft Deutscher Chemiker

Supporting Information

Adaptive Behavior of Dynamic Orthoester Cryptands

*Oleksandr Shyshov[+], René-Chris Brachvogel[+], Tobias Bachmann, Rubitha Srikantharajah, Doris Segets, Frank Hampel, Ralph Puchta, and Max von Delius**

anie_201609855_sm_miscellaneous_information.pdf

Contents

1. General Experimental Section ... 3

2. Preparation of Metal Salts with BArF Counteranion ... 5

3. Synthetic Procedures and Characterization Data ... 6

3.1 Synthesis by Adaptive Behaviour ... 6

Synthesis of $[Na^+\subset o\text{-}Me_2\text{-}1.1.1]BArF^-$ ... 6

Synthesis of $[K^+\subset o\text{-}Me_2\text{-}2.1.1]BArF^-$ ... 6

Synthesis of $[Rb^+\subset o\text{-}Me_2\text{-}2.2.1]BArF^-$ ... 12

Synthesis of $[Cs^+\subset o\text{-}Me_2\text{-}2.2.1]BArF^-$ ... 12

3.2 Direct Synthesis ... 17

Synthesis of $[K^+\subset o\text{-}Me_2\text{-}2.1.1]TCPB^-$ ... 17

Synthesis of $[Rb^+\subset o\text{-}Me_2\text{-}2.2.1]BArF^-$ ... 19

Synthesis of $[Cs^+\subset o\text{-}Me_2\text{-}2.2.1]BArF^-$ ... 22

Synthesis of $[Cs^+\subset o\text{-}Me_2\text{-}2.2.2]BArF^-$ ... 23

3.3 Synthesis of Cryptands ... 28

4. Adaptive Behavior Experiments ... 32

General experimental procedure ... 322

Experiment of [*o*-Me$_2$-1.1.1] with LiTPFPB and EG ... 33

Experiment of [*o*-Me$_2$-1.1.1] with LiTPFPB and PG ... 34

Experiment of [*o*-Me$_2$-1.1.1] with NaBArF and TEG ... 35

Experiment of [*o*-Me$_2$-1.1.1] with KBArF and TEG ... 36

Experiment of [*o*-Me$_2$-1.1.1] with RbBArF and TEG ... 37

Experiment of [*o*-Me$_2$-1.1.1] with CsBArF and TEG ... 38

Experiment of [*o*-Me$_2$-2.1.1] with CsBArF and TEG ... 39

Experiment of [*o*-Me$_2$-2.2.2] with CsBArF and DEG ... 40

Cryptate metathesis: *o*-Me$_2$-1.1.1 and *o*-Me$_2$-2.2.2 with KBArF and CsBArF ... 41

5. Synthesis of Chiral/Meso Diols and Cryptates ... 43

Synthesis of *S*,*S*-2,2‘-Oxydi-1-propanol (*S*,*S*-1) ... 44

Synthesis of Ethyl (L)-lactate triflate (*S*-3) ... 46

Synthesis of *R*,*S*-Dilactic acid diethyl ester (*R*,*S*-2) ... 47

Synthesis of *R*,*S*-2,2‘-Oxydi-1-propanol (*R*,*S*-1) ... 49

Synthesis of *R*,*R*-Dilactic acid diethyl ester (*R*,*R*-2) ... 50

Synthesis of d$_4$-*R*,*R*-2,2‘-Oxydi-1-propanol (d$_4$-*RR*-1) ... 52

General procedure for chiral cryptate synthesis 54
Synthesis of [$Na^+ \subset o$-Me_2-*SS*,*SS*,*SS*]$BArF^-$ 54
Synthesis of d_{12}-[$Na^+ \subset o$-Me_2-*RR*,*RR*,*RR*]$BArF^-$ 56
Overview of self-sorting experiments with chiral Diols (*SS*-1, *RS*-1 and d_4-*RR*-1) 58
6. Crystallographic Data 59
7. Computational Chemistry 71
8. Experimental Binding Studies 78
8.1 Results of Experimental Binding Studies 78
8.2 Determination of Binding Constants by NMR Titrations 78
8.2 ITC Titration 99
9. References 100

1. General Experimental Section

Reagents and instruments

All commercially available reagents were purchased from Sigma Aldrich, Alfa Aesar, Acros Organics or TCI and were used without further purification. Molecular sieves were dried for 3 days at 150 °C under reduced pressure (10^{-2} mbar) before use. $CDCl_3$, was dried for at least 3 days and stored over molecular sieves. All solvents were dried over molecular sieves for at least 24 hours. 1,1,2,2-tetrachloroethane was refluxed for 4h with phosphorus pentoxide (30% mass) and distilled on activated 3 Å molecular sieves. All orthoester exchange reactions (catalyzed by TFA) were carried out under nitrogen. Aluminum oxide (activated, basic, Brockman grade I) was dried for 1 day at 180°C under reduced pressure (10^{-2} mbar). NMR spectra were recorded on Bruker Avance 300 (^{1}H: 300 MHz), Bruker Avance 400 (^{1}H: 400 MHz), Jeol EX 400 (^{1}H: 400 MHz) and Jeol Alpha 500 (^{1}H: 500 MHz) spectrometers at 298 K and referenced to the residual solvent peak (^{1}H: $CDCl_3$, 7.24 ppm; ^{13}C: $CDCl_3$, 77.16 ppm). Coupling constants (*J*) are denoted in Hz and chemical shifts (δ) in ppm. Mass spectra were obtained on Bruker micro TOF II and Bruker Maxis 4G or Bruker SolariX (HRMS-ESI$^+$-TOF, Solvent: Toluene or Acetonitrile) instruments. IR spectra were recorded on a Bruker Tensor 27- IR spectrometer as solids in ATR-mode.

Preparation of stock solutions

To achieve a high level of stoichiometric accuracy and adequate exclusion of moisture, diethylene and triethylene glycol were added from stock solutions that were dried over molecular sieves.

To obtain the **stock solution of diethelene glycol (DEG)** ca. 100 µl of DEG were dissolved in 1 mL of dry $CDCl_3$ and 3Å molecular sieve were added. The **stock solution of triethleneglycol** was prepared in a similar way. Concentration of the stock solutions was determined using an internal standard (NMR, 1,4-dinitrobenzene, error: ±5%).

To obtain the **acid stock solutions**, trifluoroacetic acid (TFA, 327 µmol, 25 µL) was topped up with $CDCl_3$ to obtain a total volume of 1 mL. Perfluoropentanoic acid (PFPA, 324 µmol, 50 µL) was topped up with $CDCl_3$ to obtain a total volume of 1mL.

To obtain the **trimethyl orthoacetate stock solution** for **Method A:** trimethyl orthoacetate (250 µl, 1.96 mmol), perfluoropentanoic acid (PFPA, 389 µmol, 60 µL) were dissolved in 1,1,2,2-tetrachloroethane (TCE, 12 mL) and the obtained concentration was determined using 1,4-dinitrobenzene as an internal standard. For **Method B:** trimethyl orthoacetate (25 µL, 196 µmol) was topped up with $CDCl_3$ to obtain a total volume of 1 mL. Concentration of the stock solutions was determined using an internal standard (NMR, 1,4-dinitrobenzene, error: ±5%).

General procedures

Method A:

For drying of the metal salts, 60 µmol of the corresponding salt were placed in a heat-gun dried 10 mL Schlenk tube equipped with Teflon-coated stir bar, dry acetonitrile (400 µl), trimethyl orthoacetate (298 µmol, 5 equiv., 38.1 µL) and trifluoroacetic acid (131 µmol, 2.2 equiv, 10 µL). The solution was stirred for 1 h at room temperature and the solvent was removed under reduced pressure.

To the Schlenk tube containing the pre-dried salt, diethylene glycol, triethylene glycol, trimethyl orthoacetate and PFPA (5 mol%) were added from stock solutions under an atmosphere of dry nitrogen. The tube was tightly closed with a stopper, greased with PTFE paste, and the joint was additionally isolated with PTFE tape to prevent any leakage of moisture into the reaction vessel. The Schlenk tube was attached to a membrane pump and the reaction mixture was stirred under reduced pressure (20mbar). Reaction progress was monitored using ^{1}H NMR spectroscopy. Upon completion, the solvent was removed under reduced pressure (10^{-2} mbar), dry chloroform (ca. 300 µL) and triethylamine (20 mol%) were added and the crude mixture was passed through a 10 mm plug of basic aluminum oxide to remove non-reacted alcohols and products of hydrolysis. The plug was washed with ca. 2 mL of dry chloroform. Removal of the solvent under reduced pressure gave the corresponding salts as white powder.

Method B:

For drying of the metal salts 60 µmol of the corresponding salt were placed in a 15 mL screw-cap vial. Dry acetonitrile (400 µl), trimethyl orthoacetate (298 µmol, 5 equiv., 38.1 µL) and trifluoroacetic acid (131 µmol, 2.2 equiv., 10 µL) was added and the solution was shaken by hand for 1 min and left to stand for 1 h at room temperature. The solvent was removed under reduced pressure.

To the vial containing the dried salt were added the corresponding amounts of diethylene glycol, triethylene glycol, trimethyl orthoacetate, chloroform (1 mL), TFA (5 mol%, 36 µmol) and molecular sieves 5 Å (ca. 0.25 g) from stock solutions under an atmosphere of dry nitrogen. The reaction mixture was shaken and left to stand at room temperature. Every 24 h, 2.5 mol% TFA (18 µmol) from the acid stock solution (were added to keep the exchange reaction active (molecular sieves slowly transform the acid catalyst into inactive anhydride and/or esters) and the reaction progress was monitored regularly by ^{1}H NMR spectroscopy. Upon completion, the solution was transferred into a dry clean vial, molecular sieves were rinsed with additional chloroform (1 mL) and the solutions were combined. Triethylamine (5 equiv. in respect to total amount of added TFA) was added to the reaction mixture and the solvent was removed under vacuum. Dry chloroform (ca 300 µL) was added to the residue and the obtained mixture was passed through a plug of basic aluminum oxide (ca. 10mm) to remove non-reacted alcohols, products of hydrolysis and triethylammonium salts. The plug was washed with ca. 2 mL of dry chloroform. Removal of $CHCl_3$ under reduced pressure gave the corresponding salts as a white powder.

2. Preparation of Metal Salts with BArF Counteranion

MBArF salts were prepared from AgBArF and corresponding metal halides.

Synthesis of AgBArF

AgBArF was prepared according to a published procedure:[1] NaBArF (493 mg, 1 equiv., 556 μmol) was dissolved in diethyl ether (20 mL) and vigorously shaken for 5 min in a separatory funnel wrapped in aluminum foil with silver nitrate (190 mg, 2 equiv., 1.12 mmol) dissolved in 10 mL of water. The organic layer was separated and evaporated to give AgBArF as white solid (460 mg, 85%), which was directly used for the preparation of MBArF salts.

Synthesis of MBArF salts

AgBArF (460 mg, 1 equiv., 476 μmol) was dissolved in 10 mL of acetonitrile. The corresponding metal chloride (2 equiv.) was added and the reaction mixture was stirred overnight under exclusion of light. The precipitate was filtered off and the solvent was removed under reduced pressure to give the corresponding MBArF salt as a white crystalline solid, which was used without further purification (the purity of each batch was determined by ^{1}H NMR analysis with internal standard; see section 4).

3. Synthetic Procedures and Characterization Data

3.1 Synthesis by Adaptive Behaviour

Synthesis of [Na^+⊂*o*-Me_2-1.1.1]BArF$^-$

The synthesis of **[Na^+⊂*o*-Me_2-1.1.1]BArF$^-$** was reported previously.[2]

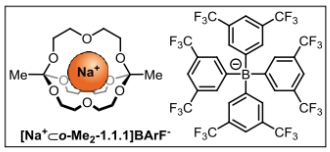

Synthesis of [K^+⊂*o*-Me_2-2.1.1]BArF$^-$

9.47 mg KBArF (10 µmol) and triethylene glycol (10 µmol) were added from a stock solution to o-Me_2-1.1.1 (10 µmol) in 0.6 mL $CDCl_3$. The solvent was evaporated under vacuum. The white solid was dissolved in 0.6 mL dry $CDCl_3$ and 10 mol% TFA was added to the sample. After one hour, 10 mol% NEt_3 was added to quench the reaction. The complete solvent was evaporated under vacuum.

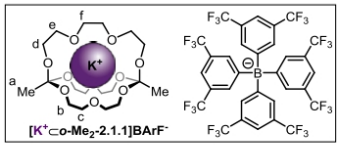

The white solid was dissolved in 0.6 mL $CDCl_3$ and passed through a plug (SiO_2) to remove residual diol and decomposition products. **[K^+⊂*o*-Me_2-2.1.1]BArF$^-$** was obtained as a colourless solid in 57% yield.

M. p.: 210 °C.

^{1}H NMR (400 MHz, $CDCl_3$): δ = 7.68 (s, 8H), 7.51 (s, 4H), 3,71–3.69 (m, 4H, d), 3,69–3.63 (m, 8H, b), 3.59–3.54 (m, 4H, c), 3.54 (s, 4H, f), 3.52–3.50 (m, 4H, e), 3.47– 3.42 (m, 4H, c), 1.44 ppm (s, 6H, a).

^{13}C {^{1}H} NMR (100 MHz, $CDCl_3$): δ = 162.6, 162.0, 161.6, 161.1, 134.9, 129.6, 129.2, 128.9, 128.8, 128.6, 126.0, 123.3, 120.6, 117.6, 114.0, 70.3, 69.7, 69.3, 62.7, 62.3, 16.9 ppm.

HRMS (ESI$^+$): *m*/*z* = 449.1780 $[M+K]^+$ (calcd. 449.1784 for $C_{18}H_{34}O_{10}K$).

^{1}H NMR spectrum (400 MHz, $CDCl_3$, 298 K):

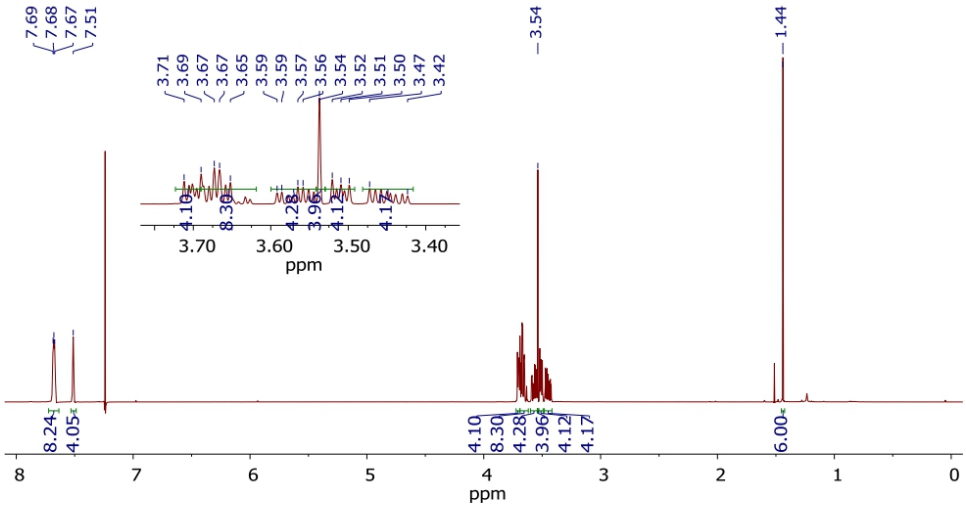

^{13}C {^{1}H} NMR spectrum (100 MHz, $CDCl_3$, 298 K):

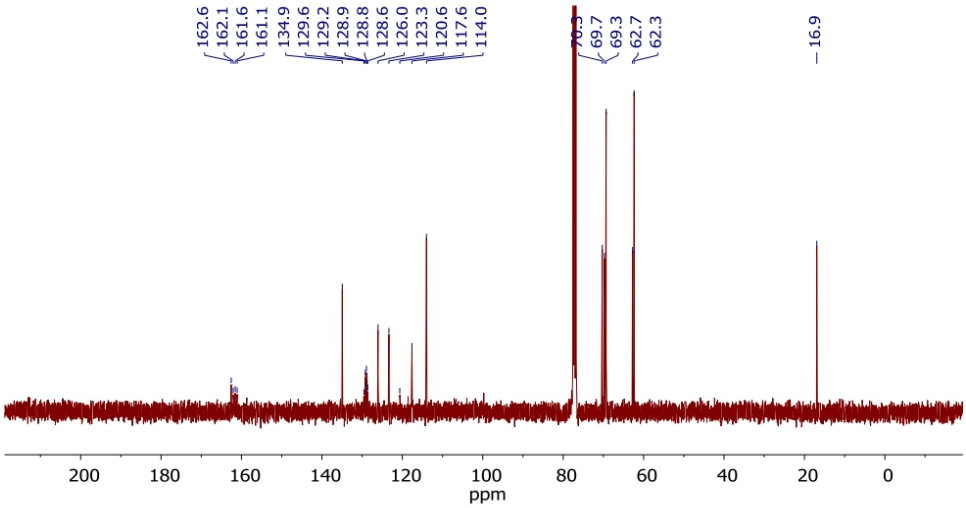

2D-^{1}H/^{1}H-COSY-NMR spectrum (400 MHz, $CDCl_3$, 298 K):

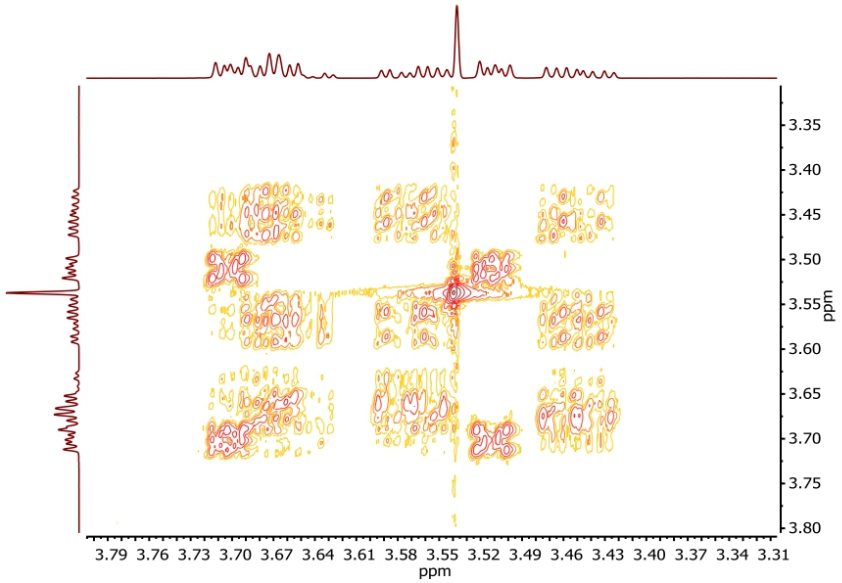

1D-NOESY-NMR spectrum (400 MHz, $CDCl_3$, 298 K):

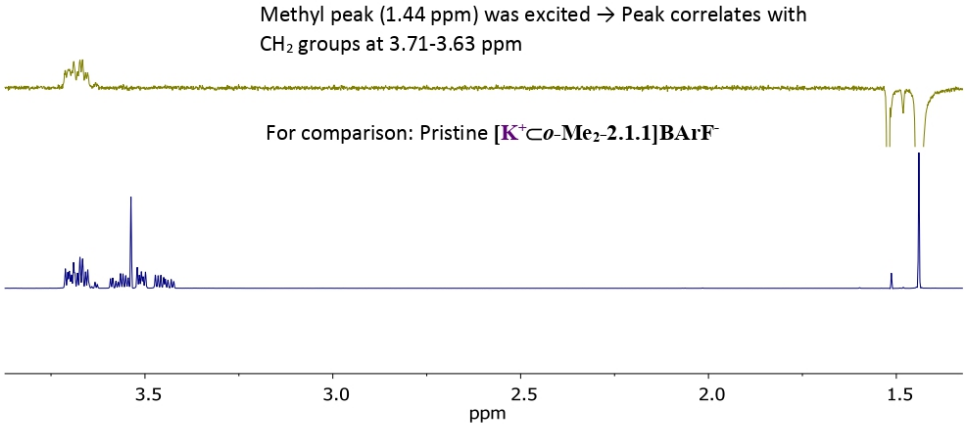

2D-$^{1}H/^{13}C$-HSQC-NMR spectrum ($CDCl_3$, 298 K):

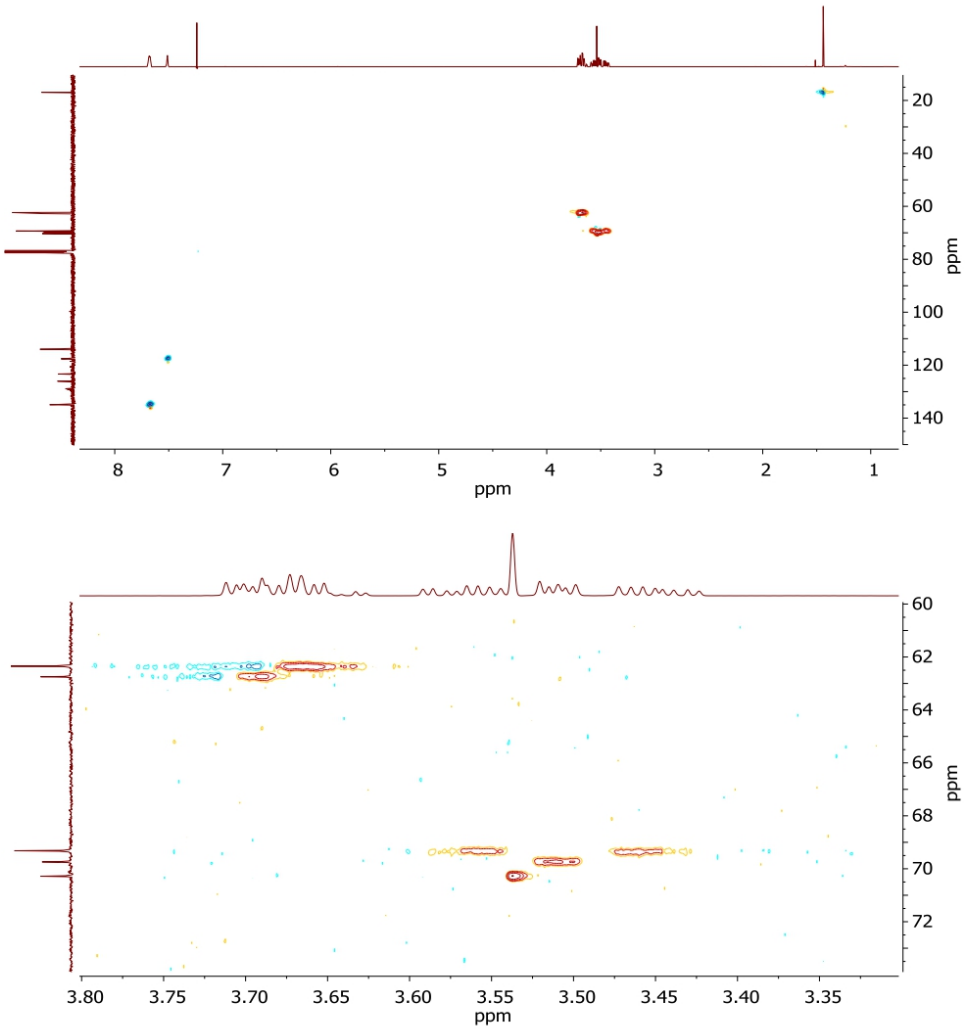

2D-$^{1}H/^{13}C$-HMBC-NMR spectrum ($CDCl_3$, 298 K):

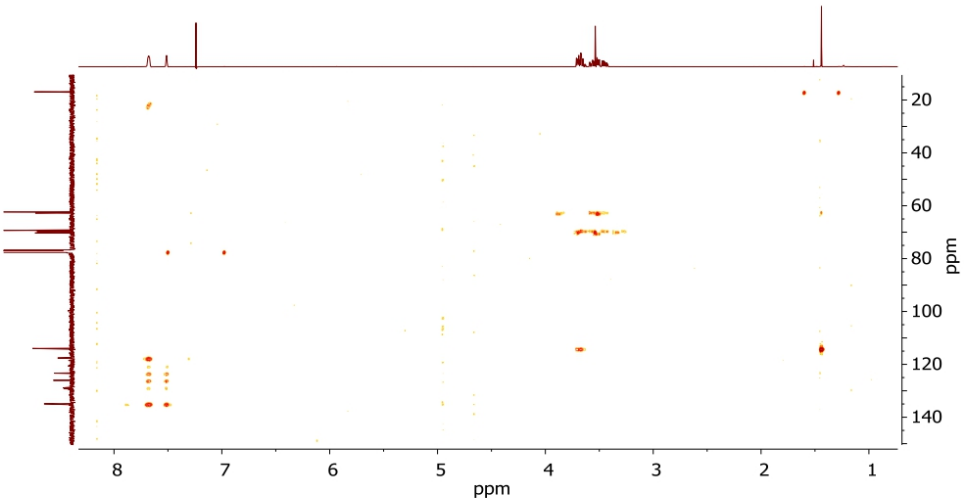

HighRes-MS-Spectrum (ESI^{+}):

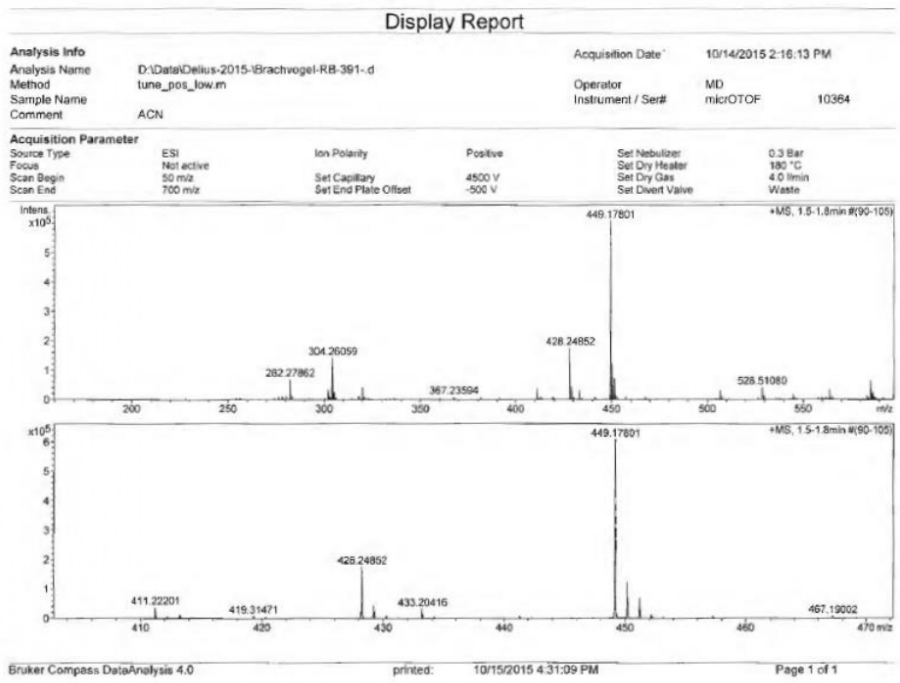

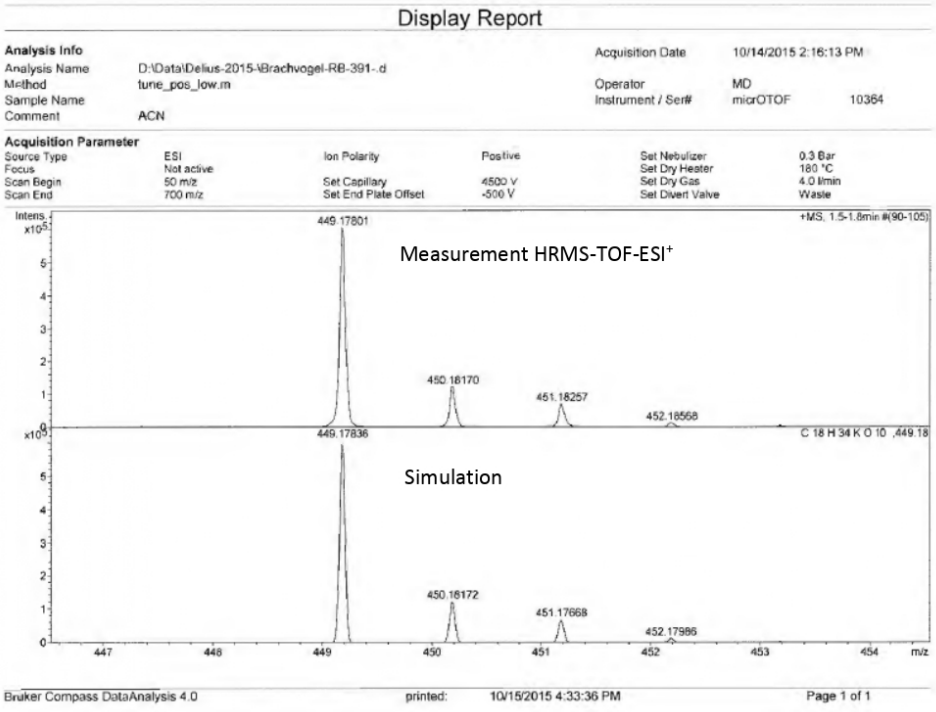
Display Report
Analysis Info
Analysis Name D:\Data\Delius-2015-\Brachvogel-RB-391-.d
Method tune_pos_low.m
Sample Name
Comment ACN
Acquisition Date 10/14/2015 2:16:13 PM
Operator MD
Instrument / Ser# micrOTOF 10364
Acquisition Parameter
Source Type ESI
Focus Not active
Scan Begin 50 m/z
Scan End 700 m/z
Ion Polarity Positive
Set Capillary 4500 V
Set End Plate Offset -500 V
Set Nebulizer 0.3 Bar
Set Dry Heater 180 °C
Set Dry Gas 4.0 l/min
Set Divert Valve Waste
Intens.
x10^5
449.17801
+MS, 1.5-1.8min #(90-105)
Measurement HRMS-TOF-ESI+
450.18170
451.18257
452.18568
x10^5
449.17836
C 18 H 34 K O 10 ,449.18
Simulation
450.18172
451.17668
452.17986
447
448
449
450
451
452
453
454
m/z
Bruker Compass DataAnalysis 4.0
printed: 10/15/2015 4:33:36 PM
Page 1 of 1

S11

Synthesis of [Rb^+⊂*o*-Me_2-2.2.1]$BArF^-$

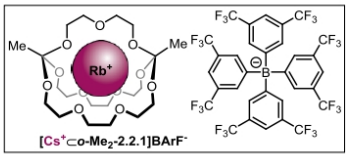

RbBArF (10 µmol) and triethylene glycol (20 µmol) were added from stock solutions to o-Me_2-1.1.1 (10 µmol) in 0.6 mL $CDCl_3$. The solvent was evaporated under vacuum. The white solid was dissolved in 0.6 mL dry $CDCl_3$ and 10 mol% TFA was added to the sample. After three hours, 10 mol% NEt_3 was added to quench the reaction. The complete solvent was evaporated under vacuum. The white solid was dissolved in 0.6 mL $CDCl_3$ and passed through a short plug of silica to remove residual diol and decomposition products. **[Rb^+⊂*o*-Me_2-2.2.1]$BArF^-$** was obtained as a colourless solid in 31% yield.

^{1}H NMR (400 MHz, $CDCl_3$): δ = 7.68 (t, *J* = 2.6 Hz, 8H), 7.51 (s, 4H) 3.69–3.59 (m, 15H), 3.53-3.49 (m, 17H), 1.47 ppm (s, 6H).

HRMS (ESI$^+$): *m*/*z* = 539.1538 $[M+Rb]^+$ (calcd. 539.1527 for $C_{20}H_{38}O_{11}Rb$).

Spectroscopic data was identical to those obtained via direct synthesis (see chapter 3.2).

Synthesis of [Cs^+⊂*o*-Me_2-2.2.1]$BArF^-$

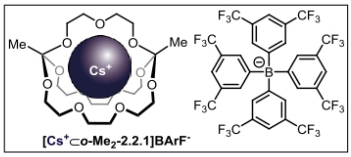

CsBArF (10 µmol) and triethylene glycol (20 µmol) were added from stock solutions to o-Me_2-1.1.1 (10 µmol) in 0.6 mL $CDCl_3$. The solvent was evaporated under vacuum. The white solid was dissolved in 0.6 mL dry $CDCl_3$ and 10 mol% TFA was added to the sample. After one hour, 10 mol% NEt_3 was added to quench the reaction. The complete solvent was evaporated under vacuum. The white solid was dissolved in 0.6 mL $CDCl_3$ and passed through a short plug of silica to remove residual diol and decomposition products. **[Cs^+⊂*o*-Me_2-2.2.1]$BArF^-$** was obtained as a colourless solid in 26% yield.

^{1}H NMR (400 MHz, $CDCl_3$): δ = 7.68 (t, *J* = 2.6 Hz, 8H), 7.51 (s, 4H), 3,68–3.60 (m, 12H), 3.53–3.49 (m, 20H), 1.44 ppm (s, 6H).

^{13}C {^{1}H} NMR (100 MHz, $CDCl_3$): δ = 162.6, 162.0, 161.6, 161.1, 134.9, 129.5, 129.2, 128.9, 128.8, 128.6, 126.0, 123.3, 120.6, 117.6, 114.3, 70.4, 70.1, 70.1, 63.1, 62.9, 17.3, 17.1 ppm.

^{133}Cs NMR (132 MHz, $CDCl_3$): δ = 34.0 ppm.

HRMS (ESI$^+$): *m*/*z* = 587.1460 $[M+Cs]^+$ (calcd. 587.1463 for $C_{20}H_{38}O_{11}Cs$).

^{1}H NMR spectrum (400 MHz, $CDCl_3$, 298 K):

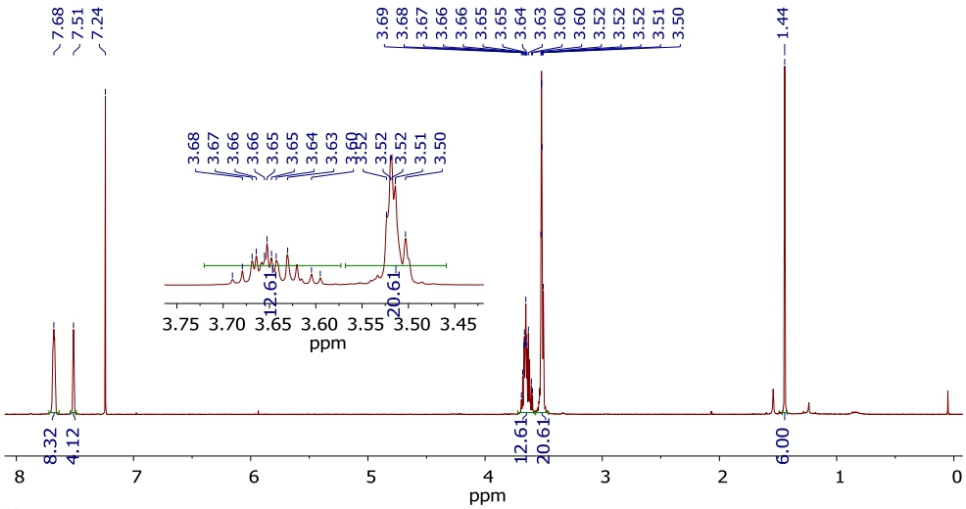

^{13}C {^{1}H} NMR spectrum (100 MHz, $CDCl_3$, 298 K):

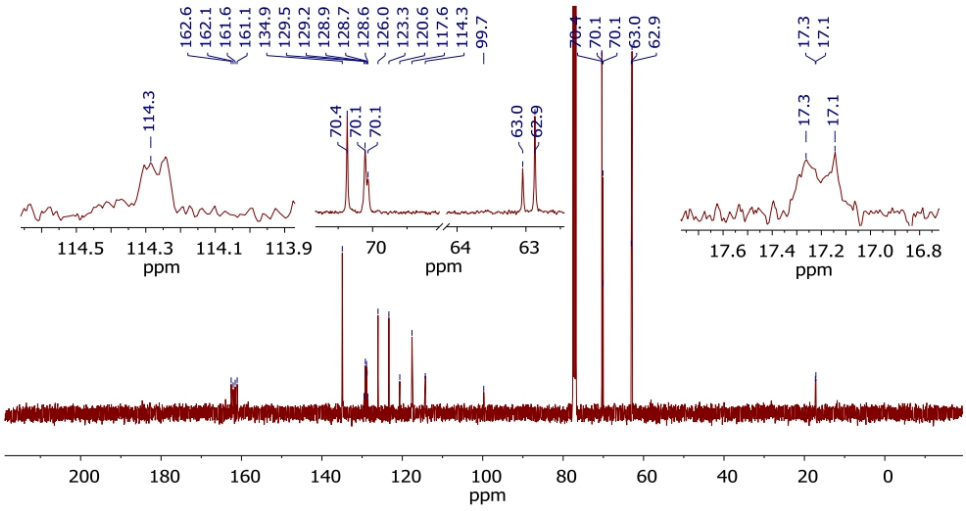

1D-NOESY-NMR spectrum (400 MHz, $CDCl_3$, 298 K):

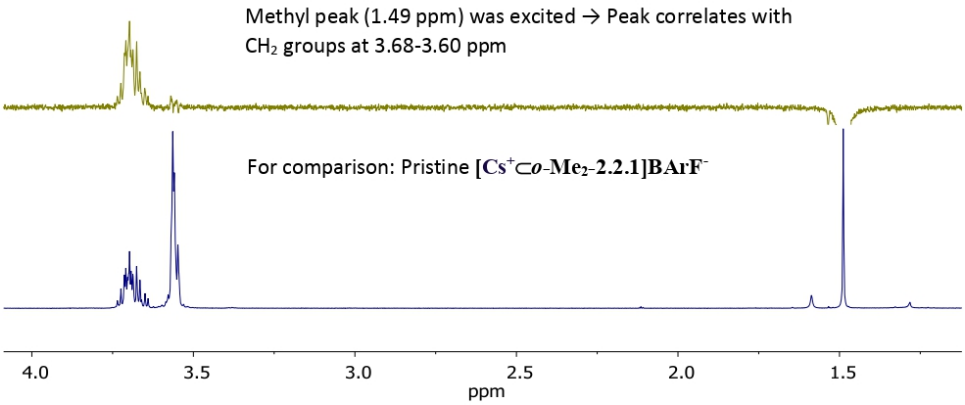

2D-$^{1}H/^{13}C$-HSQC-NMR spectrum ($CDCl_3$, 298 K):

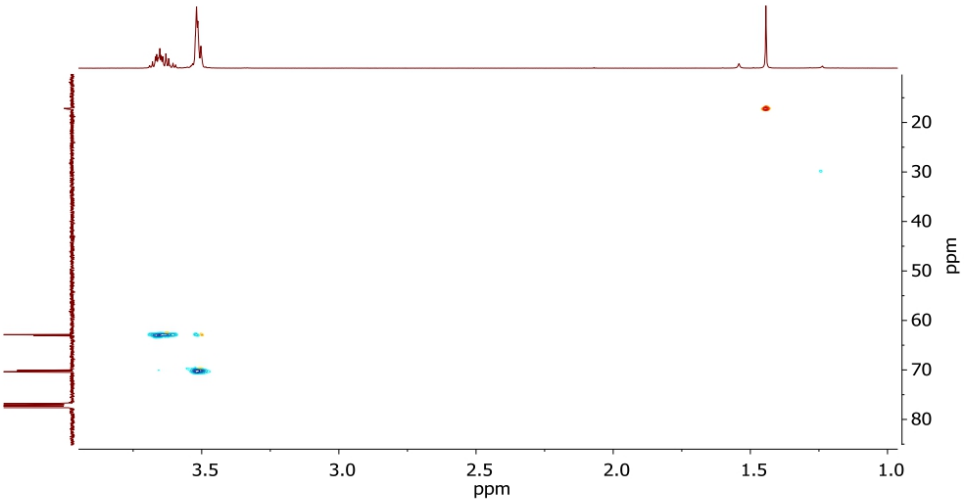

2D-$^{1}H/^{13}C$-HMBC-NMR spectrum ($CDCl_3$, 298 K):

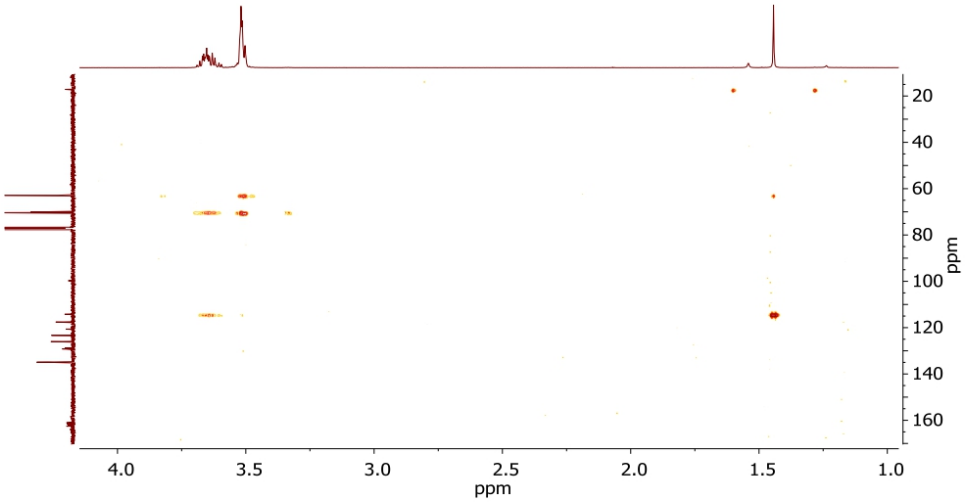

^{133}Cs NMR spectrum (66 MHz, $CDCl_3$, 298 K):

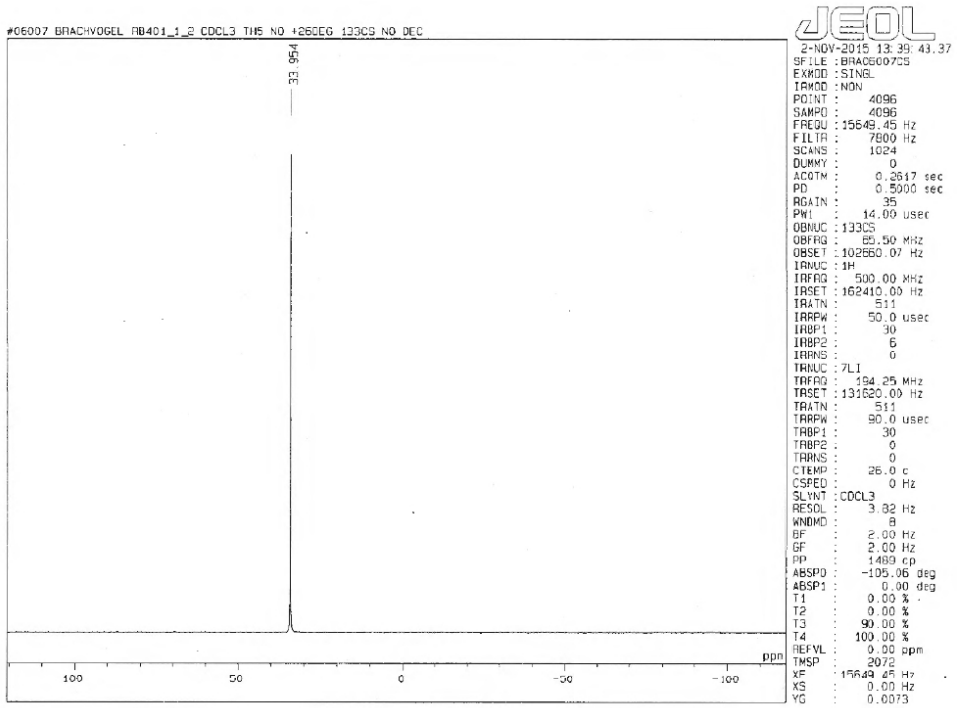

S15

HighRes-MS-Spectrum (ESI$^+$):

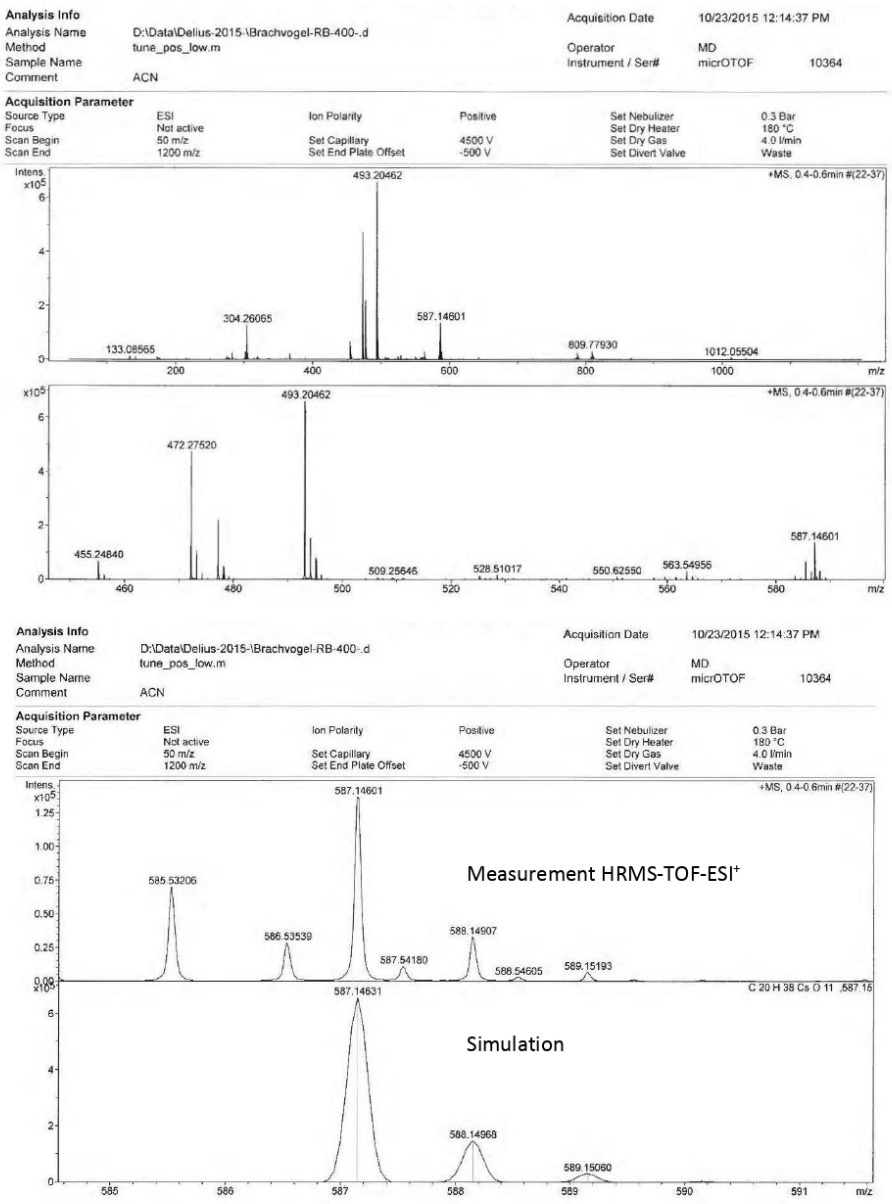

S16

3.2 Direct Synthesis

Synthesis of [K⁺⊂*o*-Me₂-2.1.1]TCPB⁻

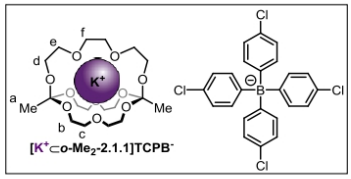

[K⁺⊂*o*-Me₂-2.1.1]TCPB⁻ was prepared according to general method A. To a schlenk-tube containing predried potassium tetrakis(4-chlorophenyl)borate (KTCPB, 147 μmol, 1 equiv., 73 mg) were added stock solutions of diethylenglycol (294 μmol, 2 equiv.), triethylenglycol (147 μmol, 1 equiv.), trimethyl orthoacetate (323 μmol, 2.2 equiv.) and PFPA (44 μmol, 5 mol%) under nitrogen atmosphere. The tube was tightly closed with a stopper, greased with PTFE grease, and the joint was additionally isolated with PTFE tape to prevent any leakage of moisture through it. The Schlenk tube was attached to a membrane pump and the reaction mixture was stirred under reduced pressure (20 mbar). Reaction progress was monitored using ^{1}H NMR spectroscopy (chloroform-d as a solvent). When all signals in 3.0-3.3 ppm region disappeared and only 1 signal left at 1.4-1.5 ppm, corresponding to cryptands methyl group, the solvent was removed under vacuum (10^{-2} mbar). Dry chloroform (ca. 300 μL) and triethylamine (147 μmol, 1 equiv., 19.8 μL) were added and the obtained mixture was passed through a plug of basic aluminum oxide (ca. 10mm) to remove non-reacted alcohols and products of hydrolysis. The plug was washed with ca. 2 mL of dry chloroform. Evaporation of $CHCl_3$ gave corresponding salts as a white solid (73.4 mg, 55% yield). In the case of KBArF the yield was 39%.

M. p.: 210 °C (for **[K⁺⊂*o*-Me₂-2.1.1]BArF⁻**).

^{1}H NMR (400 MHz, $CDCl_3$): δ = 7.24-7.20 (m, 8H), 7.01-6.99 (m, 8H), 3,71–3.69 (m, 4H, d), 3,70–3.64 (m, 8H, b), 3.59–3.54 (m, 4H, c), 3.52 (s, 4H, f), 3.50–3.48 (m, 4H, e), 3.47– 3.41 (m, 4H, c), 1.43 ppm (s, 6H, a).

^{13}C {^{1}H} NMR (100 MHz, $CDCl_3$): δ = 161.82, 161.33, 160.84, 147.10, 137.27, 128.05, 125.94, 113.99, 70.31, 69.78, 69.35, 62.77, 62.39, 17.07 ppm.

HRMS (ESI⁺): *m/z* = 449.1780 $[M+K]^+$ (calcd. 449.1784 for $C_{18}H_{34}O_{10}K$).

^{1}H NMR spectrum (400 MHz, $CDCl_3$, 298 K):

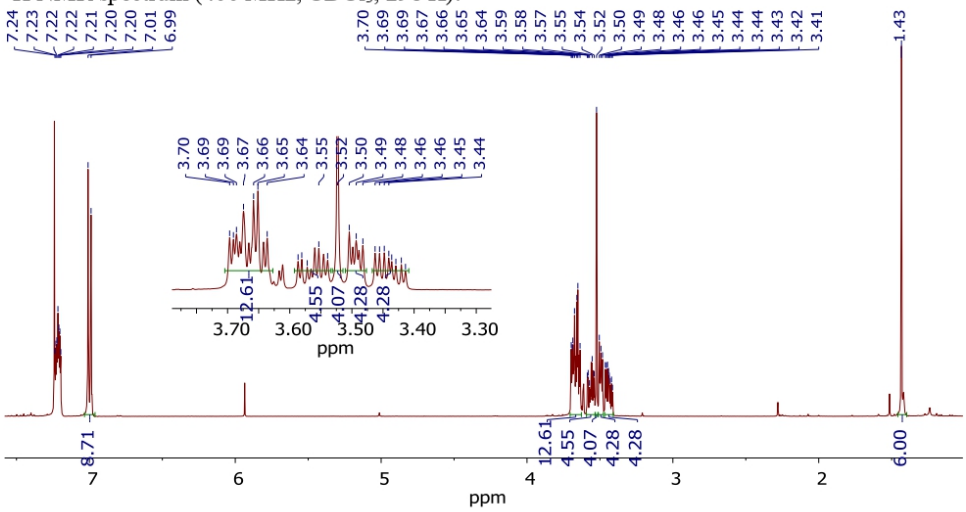

^{13}C NMR spectrum (100 MHz, $CDCl_3$, 298 K):

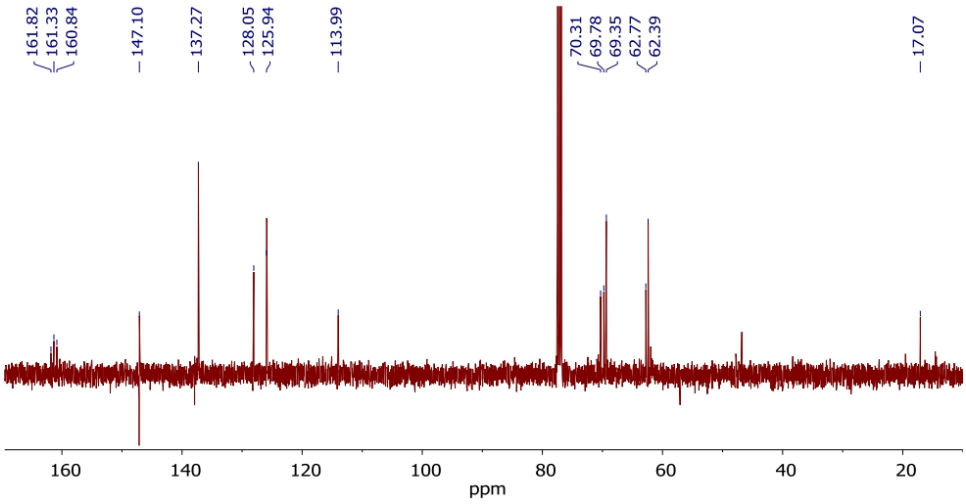

Synthesis of [Rb$^+$⊂*o*-Me$_2$-2.2.1]BArF$^-$

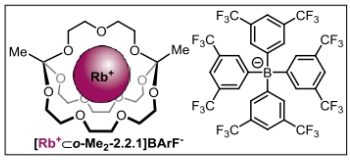

[Rb$^+$⊂*o*-Me$_2$-2.2.1]BArF$^-$ was prepared according to general method B. To a vial containing predried RbBArF (34.1 μmol, 1 equiv., 32.3 mg) were added stock solutions of diethylenglycol (34.1 μmol, 1 equiv.), triethylenglycol (68.2 μmol, 2 equiv.), trimethyl orthoacetate (71.6 μmol, 2.1 equiv.), $CDCl_3$ (1 mL), TFA (10.2 μmol, 5 mol%) and molecular sieves 5 Å (ca. 0.25 g) subsequently under an atmosphere of dry nitrogen. The reaction mixture was shaken and left to stand at room temperature. Every 24 h, 2.5 mol% of the TFA (5.1 μmol) from the acid stock solution were added to keep the exchange reaction active and the reaction progress was monitored regularly by ^{1}H NMR spectroscopy. Upon completion, the solution was transferred into a dry clean vial and the molecular sieves were washed with additional chloroform (1 mL). Triethylamine (34.1 μmol, 1 equiv., 4.6 μL) was added and the solvent was removed under vacuum. Dry chloroform (ca. 300 μL) was added to the residue and the obtained mixture was passed through a plug of basic aluminum oxide (10 mm) to remove nonreacted alcohols and products of hydrolyses. The plug was washed with ca. 2 mL of dry chloroform. Evaporation of $CHCl_3$ gave corresponding salts as a white solid (12.7 mg, 27%).

^{1}H NMR (400 MHz, $CDCl_3$): δ = 7.68 (t, *J* = 2.6 Hz, 8H), 7.51 (s, 4H) 3.69–3.59 (m, 15H), 3.53-3.49 (m, 17H), 1.47 ppm (s, 6H).

^{13}C {^{1}H} NMR (100 MHz, $CDCl_3$): δ = 162.55, 162.05, 161.56, 161.07, 134.93, 129.56, 129.25, 128.88, 128.75, 126.04, 123.33, 117.61, 114.19, 77.36, 70.04, 69.68, 63.02, 62.86, 17.22 ppm.

HRMS (ESI$^+$): *m*/*z* = 539.1538 [M+Rb]$^+$ (calcd. 539.1527 for $C_{20}H_{38}O_{11}Rb$).

^{1}H NMR spectrum (400 MHz, $CDCl_3$, 298 K):

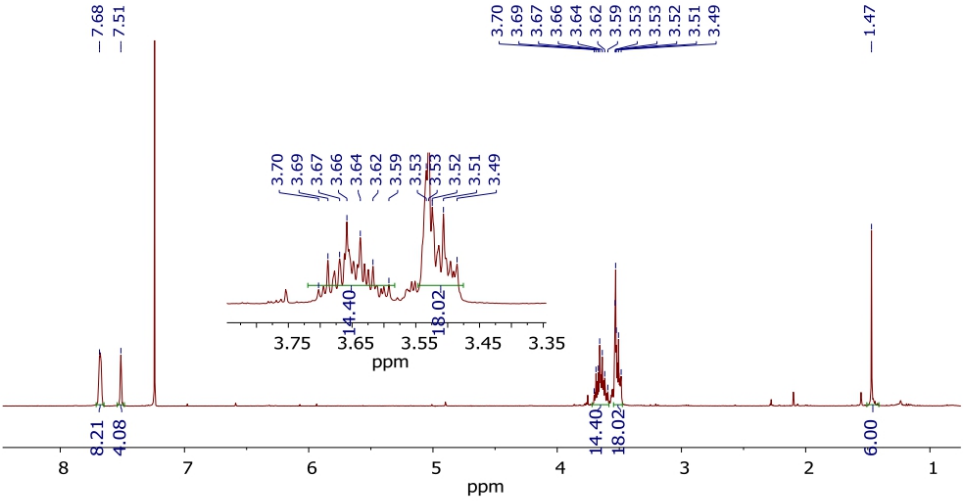

^{13}C NMR spectrum (100 MHz, $CDCl_3$, 298 K):

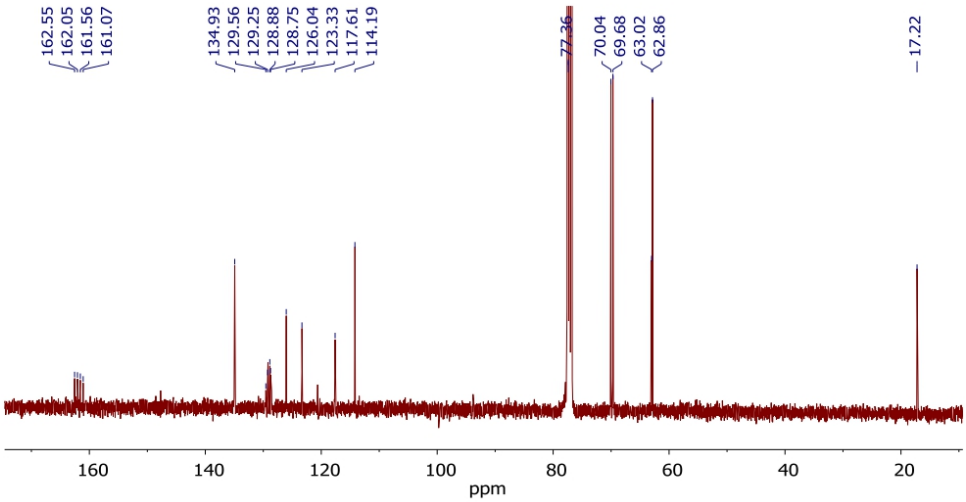

HighRes-MS-Spectrum (ESI^+):

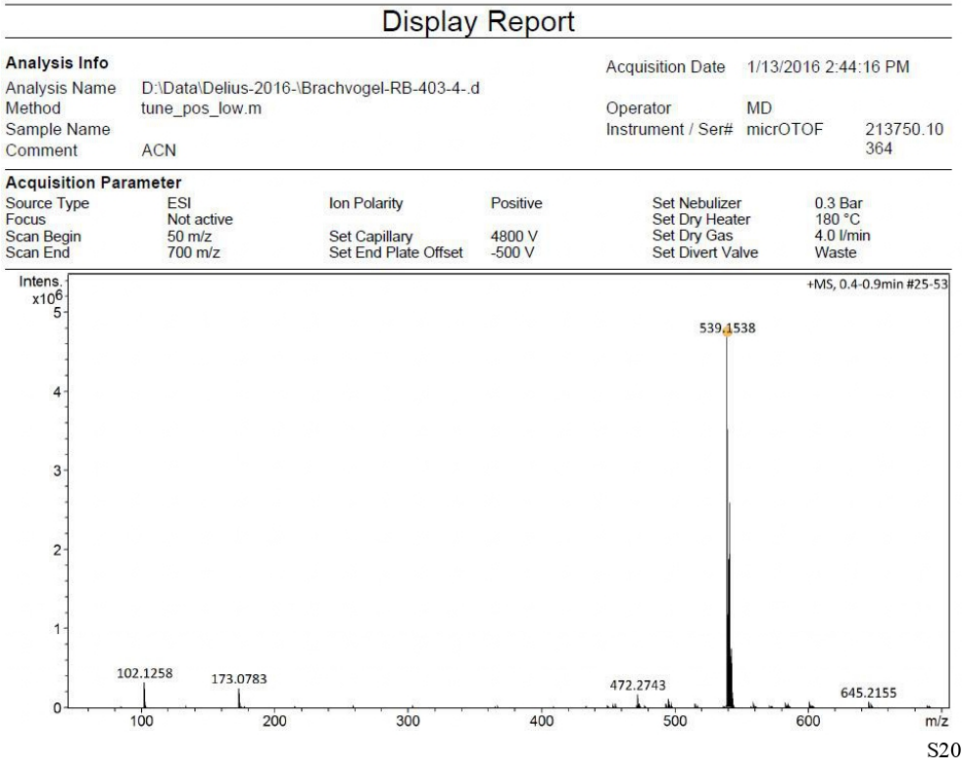

S20

HighRes-MS-Spectrum (ESI^+):

Display Report

Analysis Info

Analysis Name	D:\Data\Delius-2016-\Brachvogel-RB-403-4-.d	Acquisition Date	1/13/2016 2:44:16 PM
Method	tune_pos_low.m	Operator	MD
Sample Name		Instrument / Ser#	micrOTOF 213750.10364
Comment	ACN		

Acquisition Parameter

Source Type	ESI	Ion Polarity	Positive	Set Nebulizer	0.3 Bar
Focus	Not active			Set Dry Heater	180 °C
Scan Begin	50 m/z	Set Capillary	4800 V	Set Dry Gas	4.0 l/min
Scan End	700 m/z	Set End Plate Offset	-500 V	Set Divert Valve	Waste

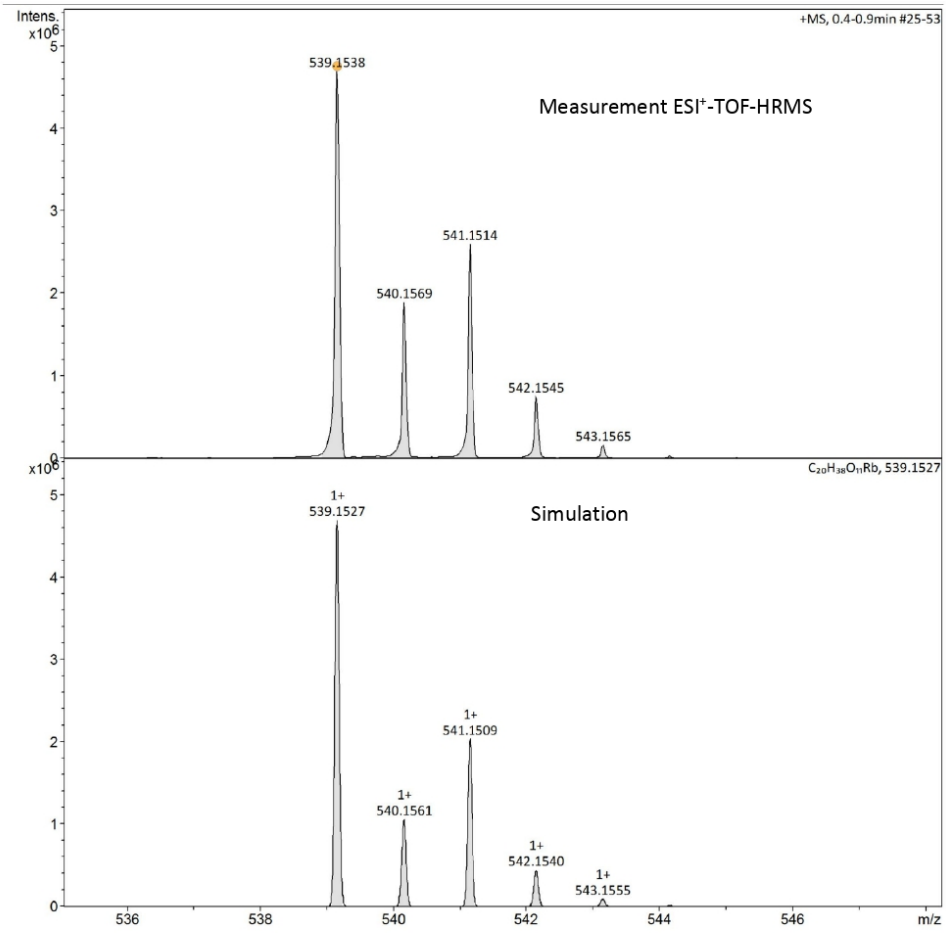

Bruker Compass DataAnalysis 4.2 printed: 9/26/2016 3:37:12 PM Page 1 of 1

S21

Synthesis of [Cs^+⊂*o*-Me_2-2.2.1]$BArF^-$

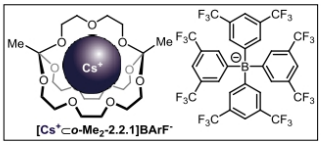

[Cs^+⊂*o*-Me_2-2.2.1]$BArF^-$ was prepared according to general method B. To a vial containing predried CsBArF (55.5 μmol, 1 equiv., 55.2 mg) were added stock solutions of diethylenglycol (55.2 μmol, 1 equiv.), triethylene glycol (111 μmol, 2 equiv.), trimethyl orthoacetate (117 μmol, 2.1 equiv.), $CDCl_3$ (1 mL), TFA (16.7 μmol, 5 mol%) and molecular sieves 5 Å (ca. 0.25 g) subsequently under an atmosphere of dry nitrogen. Reaction mixture was shaken and left to stand at room temperature. Every 24 h, 2.5 mol% of the TFA (8.35 μmol) from the acid stock solution were added to keep the exchange reaction active and the reaction progress was monitored regularly by ^{1}H NMR spectroscopy. Upon completion, solution was transferred into a dry clean vial, and the molecular sieves were washed with additional chloroform (1 mL). Triethylamine (34.1 μmol, 1 equiv., 4.6 μL) was added and solvent was removed under vacuum. To the residue was added dry chloroform (ca. 300 μL) and the obtained mixture was passed through a plug of basic aluminum oxide (10mm) to remove nonreacted alcohols and products of hydrolysis. Plug was washed with ca. 2 mL of dry chloroform. Evaporation of $CHCl_3$ gave corresponding salts as a white solid (39.4 mg, 49%).

Spectroscopical data was identical to those obtained via previous method (see above).

^{1}H NMR (400 MHz, $CDCl_3$): δ = 7.68 (t, *J* = 2.6 Hz, 8H), 7.51 (s, 4H), 3.68–3.60 (m, 12H), 3.56–3.51 (m, 20H), 1.45 ppm (s, 6H).

^{13}C {^{1}H} NMR (100 MHz, $CDCl_3$): δ = 162.6, 162.0, 161.6, 161.1, 134.9, 129.5, 129.2, 128.9, 128.8, 128.6, 126.0, 123.3, 120.6, 117.6, 114.3, 70.4, 70.1, 70.1, 63.1, 62.9, 17.3, 17.1 ppm.

HRMS (ESI$^+$): *m/z* = 587.1460 [M+Cs]$^+$ (calcd. 587.1463 for $C_{20}H_{38}O_{11}Cs$).

^{1}H NMR spectrum (400 MHz, $CDCl_3$, 298 K):

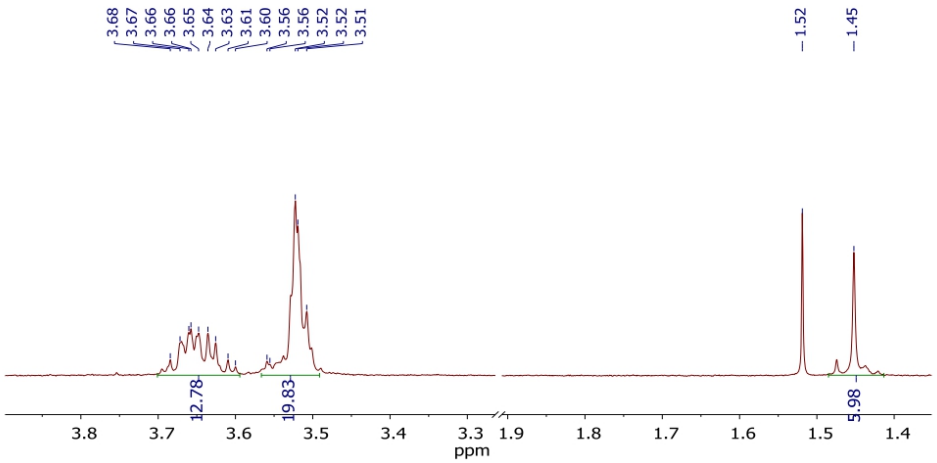

Synthesis of [Cs^+⊂*o*-Me_2-2.2.2]$BArF^-$

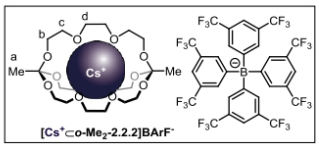

[Cs^+⊂*o*-Me_2-2.2.2]$BArF^-$ was prepared according to general method B. To a vial containing predried CsBArF (45.8 µmol, 1 equiv., 45.64 mg) were added stock triethylenglycol (137.4 µmol, 3 equiv.), trimethyl orthoacetate (96.2 µmol, 2.1 equiv.), $CDCl_3$ (1 mL), TFA (13.7 µmol, 5 mol%) and molecular sieves 5 Å (ca. 0.25 g) subsequently under an atmosphere of dry nitrogen. Reaction mixture was shaken and left to stand at room temperature. Every 24 h, 2.5 mol% of the TFA (6.85 µmol) from the acid stock solution were added to keep the exchange reaction active and the reaction progress was monitored regularly by ^{1}H NMR spectroscopy. Upon completion, the solution was transferred into a dry clean vial and the molecular sieves were washed with additional chloroform (1 mL). Triethylamine (45.8 µmol, 1 equiv., 6.2 µL) was added and solvent was removed under vacuum. To the residue was added dry chloroform (ca. 300 µL) and the obtained mixture was passed through a plug of basic aluminum oxide (10mm) to remove nonreacted alcohols and products of hydrolysis. The Plug was washed with ca. 2 mL of dry chloroform. Evaporation of $CHCl_3$ gave corresponding salts as a white solid (21.54 mg, 27%).

M. p.: 143-145 °C.

^{1}H NMR (400 MHz, $CDCl_3$): δ = 7.69 (t, *J* = 2.6 Hz, 8H), 7.51 (s, 4H), 3,64–3.62 (t, *J* = 8.44 Hz 12H, b), 3.55–3.53 (t, *J* = 8.44 Hz 12H, c), 3.51 (s, 12H, d), 1.46 ppm (s, 6H, a).

^{13}C {^{1}H} NMR (100 MHz, $CDCl_3$): δ = 162.56, 162.07, 161.57, 161.33, 161.07, 134.93, 129.19, 126.04, 123.34, 117.56, 114.67, 70.44, 70.29, 62.65, 18.05 ppm.

HRMS (ESI$^+$): *m*/*z* = 631.17099 [M+Cs]$^+$ (calcd. 631.17306 for $C_{22}H_{42}O_{12}Cs$).

^{1}H NMR spectrum (400 MHz, $CDCl_3$, 298 K):

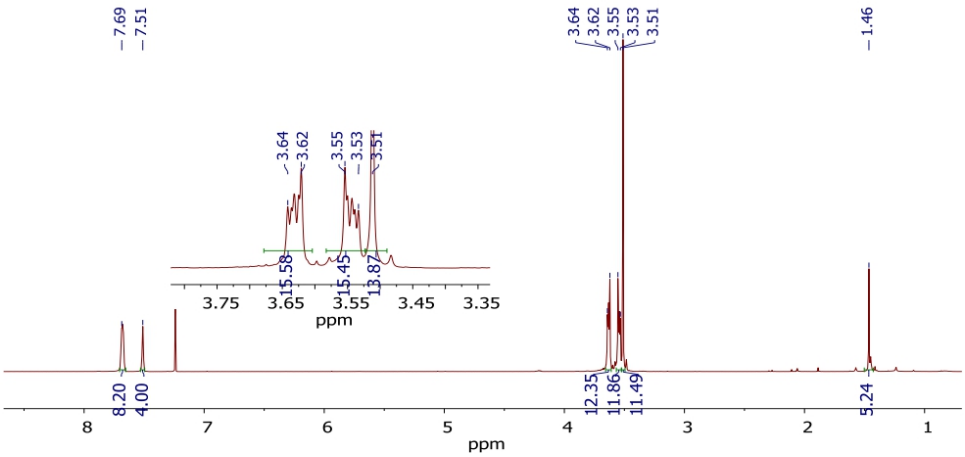

^{13}C {^{1}H} NMR spectrum (100 MHz, $CDCl_3$, 298 K):

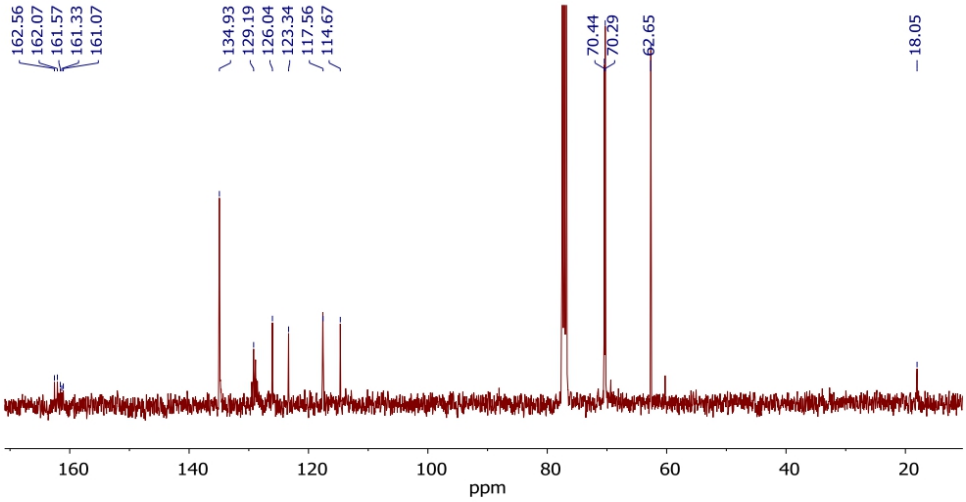

2D-^{1}H/^{13}C-HSQC-NMR spectrum ($CDCl_3$, 298 K):

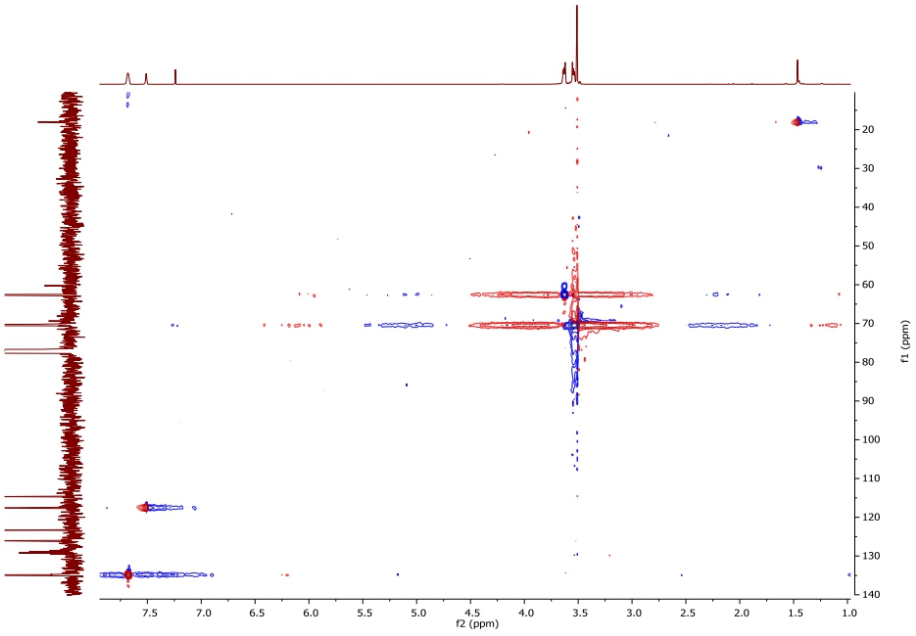

2D-$^{1}H/^{13}C$-HMBC-NMR spectrum ($CDCl_3$, 298 K):

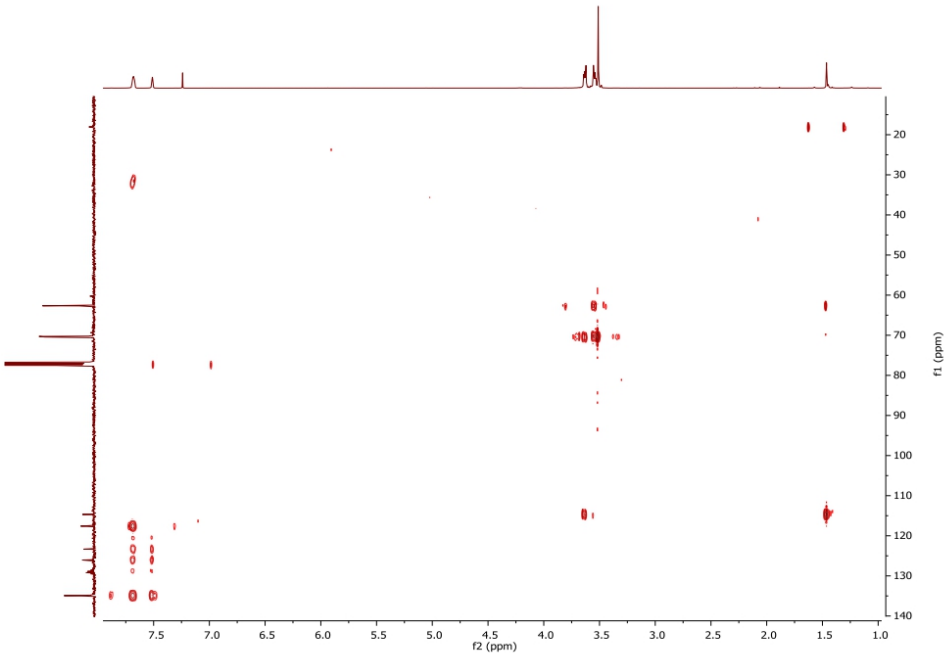

S25

HighRes-MS-Spectrum (ESI^+):

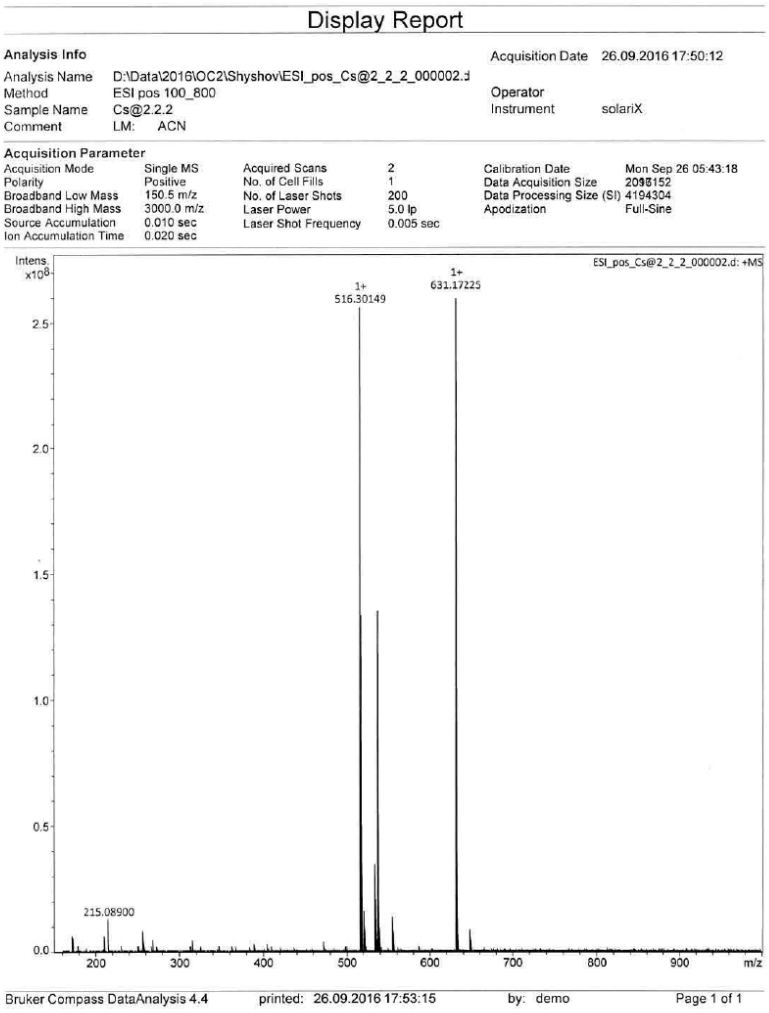

Display Report

Analysis Info

Analysis Name	D:\Data\2016\OC2\Shyshov\ESI_pos_Cs@2_2_2_000002.d	Acquisition Date	26.09.2016 17:50:12
Method	ESI pos 100_800	Operator	
Sample Name	Cs@2.2.2	Instrument	solariX
Comment	LM: ACN		

Acquisition Parameter

Acquisition Mode	Single MS	Acquired Scans	2	Calibration Date	Mon Sep 26 05:43:18
Polarity	Positive	No. of Cell Fills	1	Data Acquisition Size	2098152
Broadband Low Mass	150.5 m/z	No. of Laser Shots	200	Data Processing Size (SI)	4194304
Broadband High Mass	3000.0 m/z	Laser Power	5.0 lp	Apodization	Full-Sine
Source Accumulation	0.010 sec	Laser Shot Frequency	0.005 sec		
Ion Accumulation Time	0.020 sec				

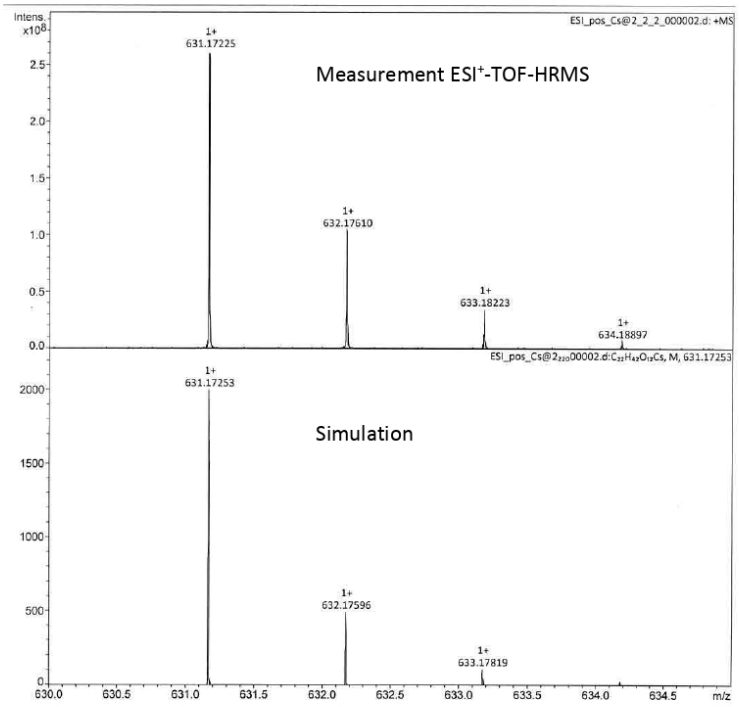

3.3 Synthesis of Cryptands

General experimental procedure

100 mg of a desired cryptate were dissolved in 5 mL $CDCl_3$ and 5 spatula (ca. 250 mg) Lewatit MP64 chloride anion exchange resins were added and stirred until the ^1H NMR showed just signals for the "empty" cryptand and signals of the **BArF**$^-$ anion disappeared. If the exchange is slow, solution can be filtered through a syringe filter and a new portion of Lewatit MP64 added. Usually two to three repetitions were sufficient to obtain cryptands reported below. Upon completion, the solution was filtered through a syringe filter, the resin was washed with an additional 1mL of $CDCl_3$ and filtered again. This solution was used directly for further experiments. Removal of the solvent under reduced pressure yielded the desired cryptands as colourless oily solids in quantitative yields.

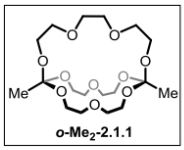

o-Me_2-2.1.1

^1H NMR (400 MHz, $CDCl_3$): δ = 3.77-3.60 (m, 29H) 1.42 ppm (s, 6H, a).

^{13}C {^1H} NMR (100 MHz, $CDCl_3$): δ = 114.0, 70.6, 70.6, 70.0, 62.4, 61.7, 20.3 ppm.

^1H NMR spectrum (400 MHz, $CDCl_3$, 298 K):

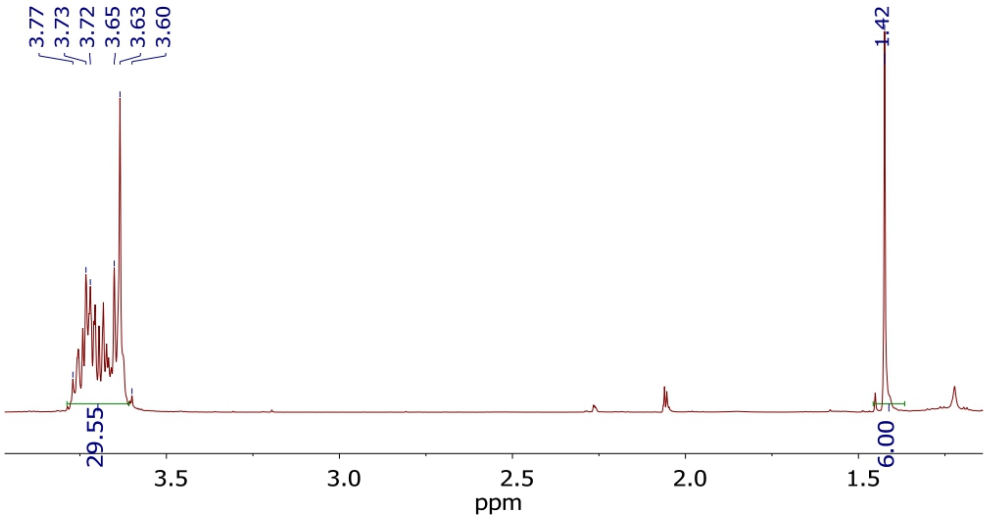

S28

^{13}C {^{1}H} NMR spectrum (100 MHz, $CDCl_3$, 298 K):

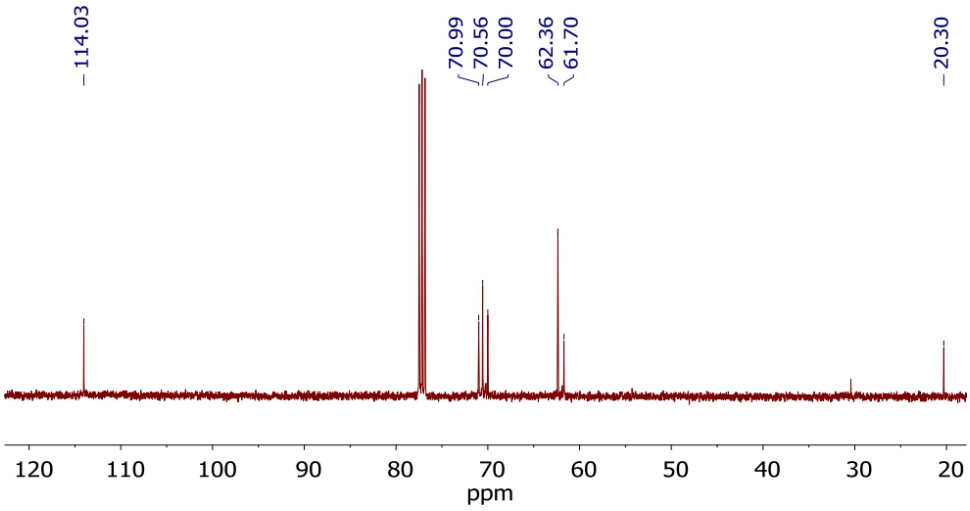

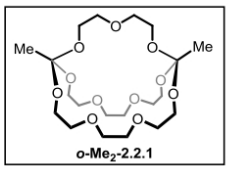

^{1}H NMR (400 MHz, $CDCl_3$): δ = 3.75-3.60 (m, 29H) 1.43 ppm (s, 6H, a).

^{13}C {^{1}H} NMR (100 MHz, $CDCl_3$): δ = 114.1, 70.9, 70.2, 70.2, 62.4, 61.8, 30.4 ppm.

^{1}H NMR spectrum (400 MHz, $CDCl_3$, 298 K):

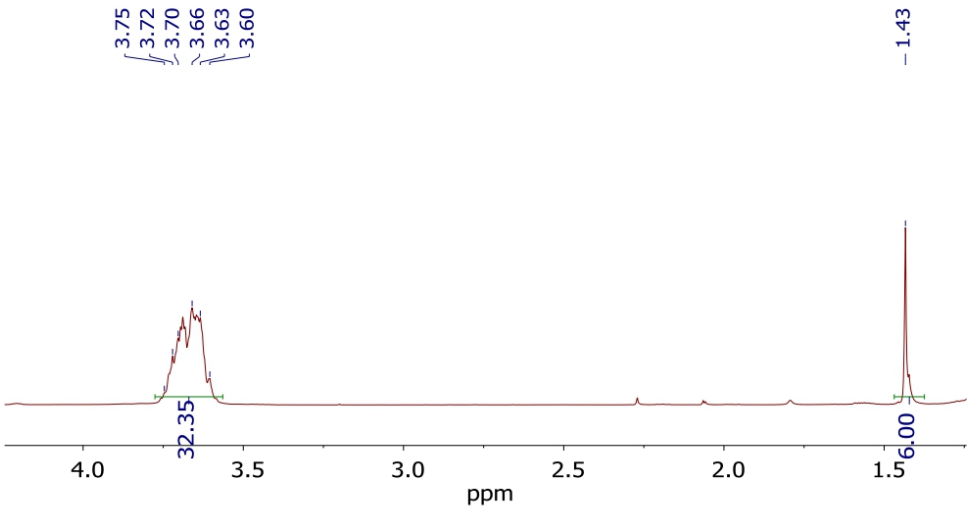

^{13}C {^{1}H} NMR spectrum (100 MHz, $CDCl_3$, 298 K):

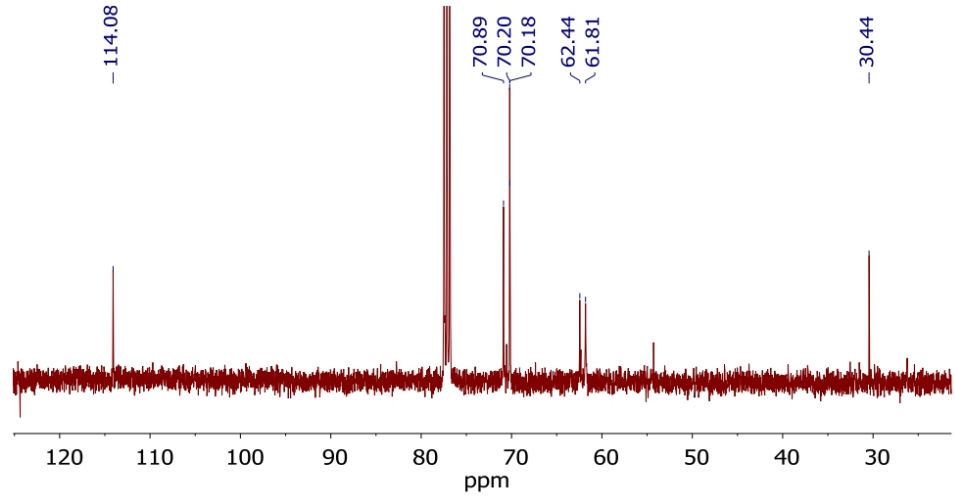

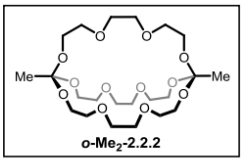

^{1}H NMR (400 MHz, $CDCl_3$): δ =3.69 (s, 24H), 3.65 (s, 12H), 1.46 ppm (s, 6H, a).

^{13}C {^{1}H} NMR (100 MHz, $CDCl_3$): δ = 114.1, 71,0, 70.3, 61.9, 30.5 ppm.

^{1}H NMR spectrum (400 MHz, $CDCl_3$, 298 K):

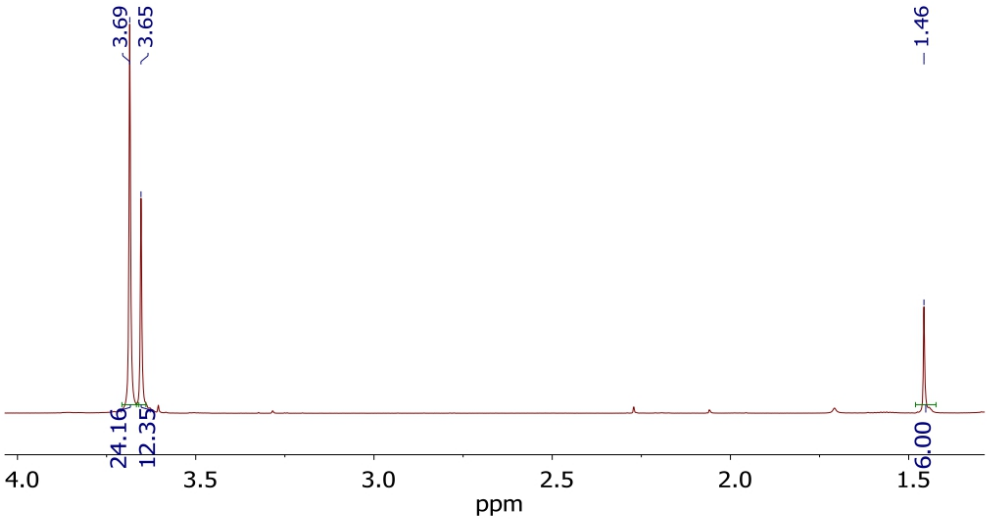

^{13}C {^{1}H} NMR spectrum (100 MHz, $CDCl_3$, 298 K):

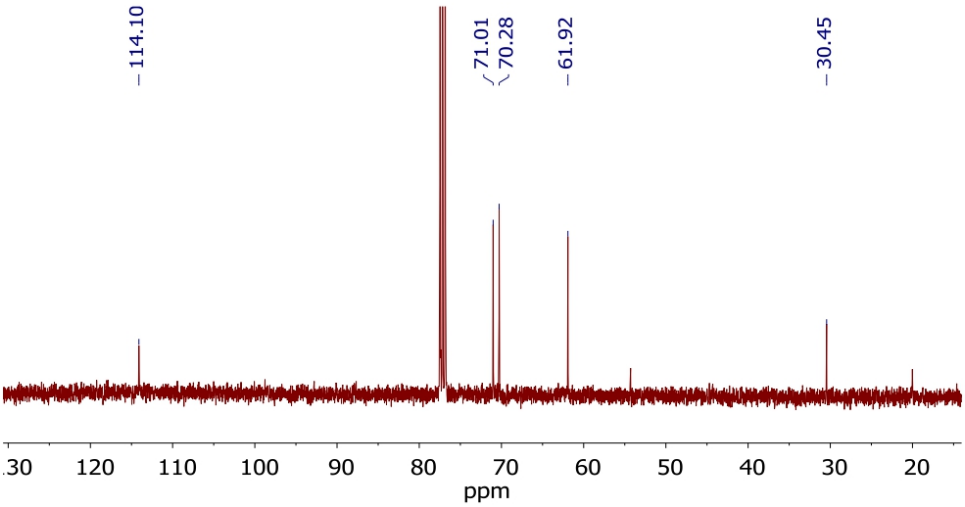
114.10
71.01
70.28
61.92
30.45
30
120
110
100
90
80
70
60
50
40
30
20
ppm

S31

4. Adaptive Behavior Experiments

General experimental procedure

Preparation of stock solutions

Stock solutions of every compound were prepared to achieve a high level of stoichiometric accuracy.

_o_-Me_2-1.1.1 stock solution

100 mg of **[Na^+⊂_o_-Me_2-1.1.1]BArF$^-$** were dissolved in 5 mL $CDCl_3$ and 5 spatula (ca. 250 mg) Lewatit MP64 chloride anion exchange resins were added and stirred for 6h. The solution was filtered over 50µm syringe filter and 5 spatula of Lewatit MP64 resins were added. This procedure was repeated until the proton NMR showed just signals for the empty cryptand. Usually two to three repetitions were sufficient to obtain **_o_-Me_2-1.1.1**. The precise amount of cryptand was determined with internal standard (NMR, 1,4-dinitrobenzene). The solution is slightly basic from the exchange resins, which guarantees that no cryptand hydrolysis occurs, at least for several days (in darkness). This solution was used directly for the further experiments.

Metal salt stock solution

Each metal salt was dissolved in CD_3CN and the metal salt quantity was determined with internal standard (^{1}H NMR, 1,4-dinitrobenzene).

Diol stock solution

To obtain the **diol stock solution**, 50.0 µmol of the required diol was topped up with $CDCl_3$ to obtain a total volume of 5.0 mL. The concentration of the stock solution was determined with internal standard (^{1}H NMR, 1,4-dinitrobenzene).

TFA acid stock solution

To obtain the **acid stock solution**, trifluoroacetic acid (TFA, 5.0 µmol, 3.83µL) was topped up with $CDCl_3$ to obtain a total volume of 1.0 mL.

General procedure for self-sorting reactions

A solution of 5 µmol **_o_-Me_2-1.1.1** (1 equiv.) with 5 µmol (1 equiv.) of the metal salt and 5-15 µmol (1-3 equiv.) of the diol was mixed from the stock solutions and dried under vacuum in a screw cap NMR tube. The solid residue was dissolved in 590 µL anhydrous $CDCl_3$ and 10 µL of the TFA acid stock solution (10 mol%, 0.5 µmol) was added to initiate orthoester exchange. To minimize orthoester hydrolysis, the experiment was performed under an atmosphere of nitrogen.

Before the other reagents were added, 1,4-dinitrobenzene was weighed accurately into the empty NMR tubes as internal standard. The reaction process was observed with ^{1}H-NMR and the yields of the formation of the cryptate were calculated relative to the internal standard.

Experiment of [*o*-Me$_2$-1.1.1] with LiTPFPB and EG

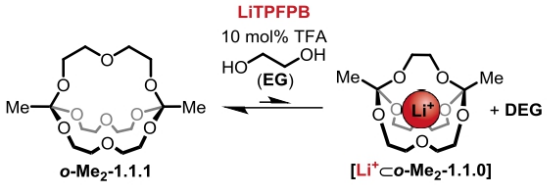

A solution of ***o*-Me$_2$-1.1.1** (5 µmol, 1 equiv.) with LiTPFPB (5 µmol, 1 equiv.) and ethylene glycol (EG, 5 µmol, 1 equiv.) was prepared accroding to the general procedure. The reaction progress was monitored by ^{1}H NMR spectroscopy.

Summary of results:

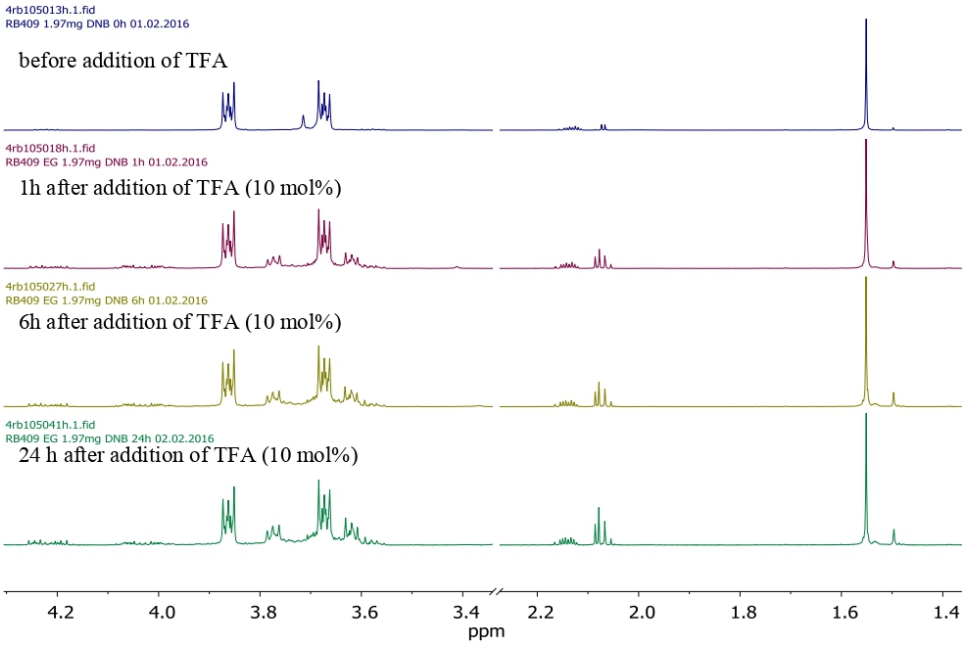

Stack plot of partial ^{1}H NMR spectra (400 MHz, $CDCl_3$, 298 K) before and after addition of TFA (10 mol%) to the solution.

Conclusion: the **[Li$^+$⊂*o*-Me$_2$-1.1.1]** complex appears to be more thermodynamically more stable compared to competing cryptand ***o*-Me$_2$-1.1.0**. The methyl peak for the **[Li$^+$⊂*o*-Me$_2$-1.1.1]** at 1.55 ppm was preserved. At the same time peaks indicative of orthoester hydrolysis occur (2.1 ppm, 3.62 and 3.77 ppm), demonstrating that a sufficient amount of acid was added to generate oxonium intermediates. Investigation of the reaction solution after 24h with ESI mass spectrometry showed no signals for formation of cryptand ***o*-Me$_2$-1.1.0**, only a strong signal for **[Na$^+$⊂*o*-Me$_2$-1.1.1]** (Note: Under ESI conditions Li$^+$ is replaced with ubiquitous Na$^+$). No signals for five-membered ring products are observed.

S33

Experiment of [*o*-Me$_2$-1.1.1] with LiTPFPB and PG

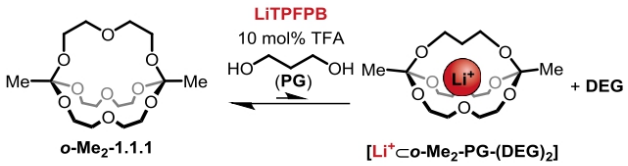

A solution of ***o*-Me$_2$-1.1.1** (5 µmol, 1 equiv.) with LiTPFPB (5 µmol, 1 equiv.) and 1,3-propanediol (PG, 5 µmol, 1 equiv.) was prepared according to the general procedure. The reaction progress was monitored by ^{1}H NMR.

Summary of results:

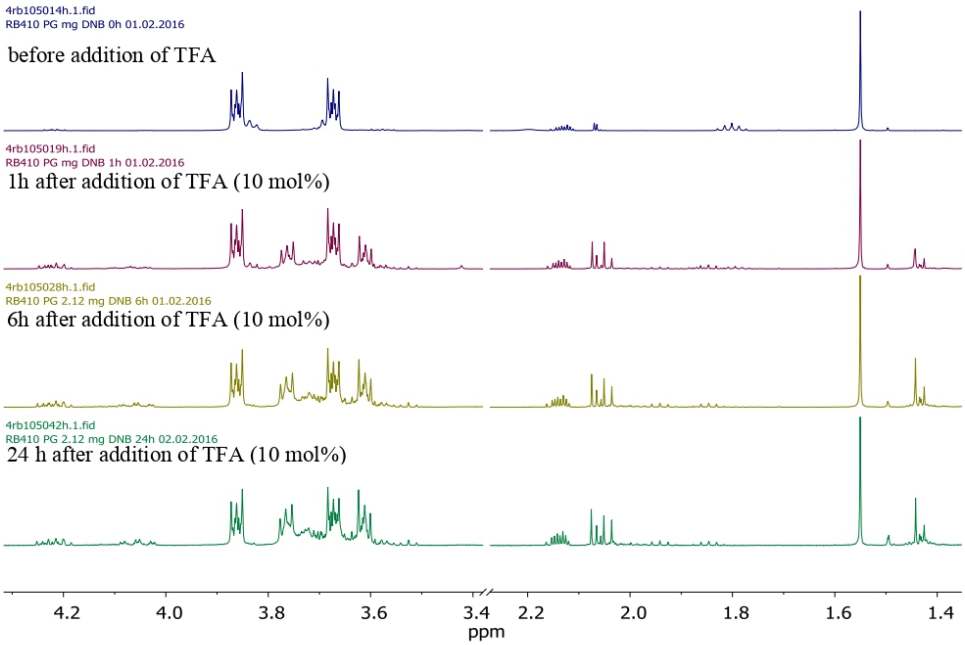

Stack plot of partial ^{1}H NMR spectra (400 MHz, $CDCl_3$, 298 K) before and after addition of TFA (10 mol%) to the solution.

Conclusion: even with longer diol propylene glycol, **[Li$^+$⊂*o*-Me$_2$-1.1.1]** appears to be the thermodynamic minimum in competition with a smaller cryptand (as evidenced by the methyl peak for the **[Li$^+$⊂*o*-Me$_2$-1.1.1]** complex at 1.55 ppm). Again, some hydrolysis occurs and a small number of unidentified orthoester side products formed. Investigation of the reaction solution after 24h with ESI$^+$ mass spectrometry showed no signals for formation of cryptand ***o*-Me$_2$-PG-(DEG)$_2$**, just a strong signal for **[Na$^+$⊂*o*-Me$_2$-1.1.1]** (Note: Under ESI conditions Li$^+$ is replaced with ubiquitous Na$^+$).

Experiment of [*o*-Me$_2$-1.1.1] with NaBArF and TEG

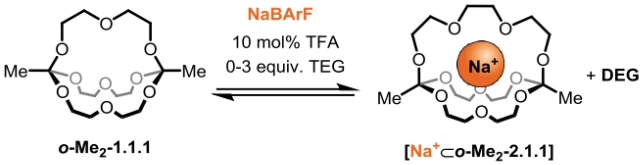

o-Me$_2$-1.1.1 [Na$^+$⊂*o*-Me$_2$-2.1.1]

Four solutions of ***o*-Me$_2$-1.1.1** (5 µmol, 1 equiv.) with NaBArF (5 µmol, 1 equiv.) and different amounts of triethylene glycol (TEG, 0-15 µmol, 0-3 equiv.) were prepared according to the general procedure. The yield was calculated with help of an internal standard (1,4-dinitrobenzene, estimated error: ±5%). The equilibration time was usually 3-6 hours.

Summary of results:

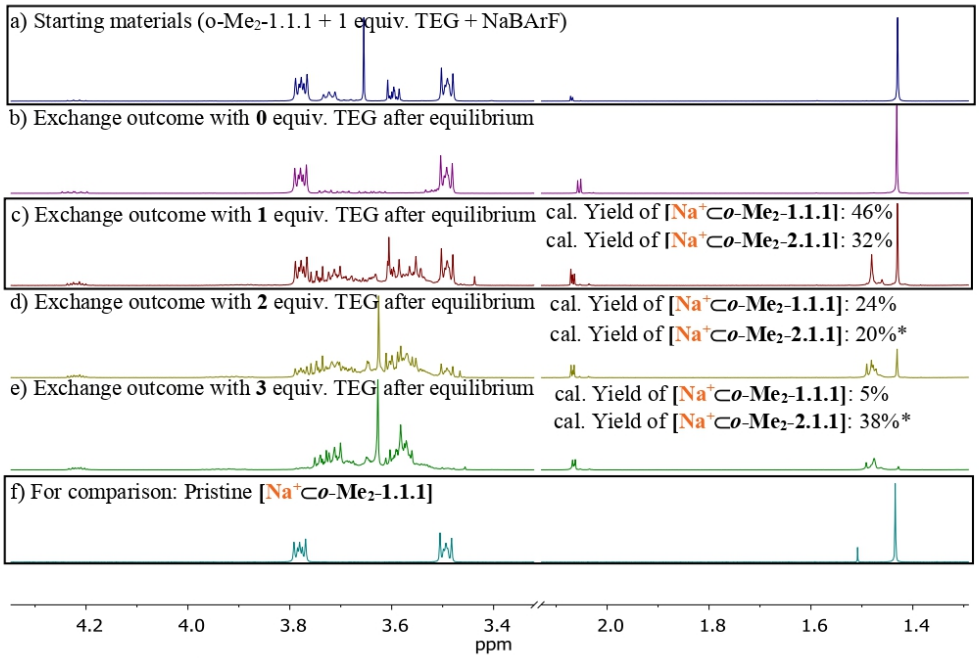

Stack plot of partial ^{1}H NMR spectra (400 MHz, $CDCl_3$, 298 K) before and after reaching the equilibrium with different amounts of TEG. (* Difficult integration due to peak overlap)

Conclusion: without any TEG in the mixture, the cryptate **[Na$^+$⊂*o*-Me$_2$-1.1.1]** remains the exclusive product, because Na$^+$ stabilizes the cage even while it is dynamic. With 1 equiv. TEG formation of **[Na$^+$⊂*o*-Me$_2$-2.1.1]** is observed, albeit as the minor product. When the amount of TEG is increased, the formation of **[Na$^+$⊂*o*-Me$_2$-2.1.1]** increases, but other, unidentified orthoester products are formed as well.

Experiment of [*o*-Me$_2$-1.1.1] with KBArF and TEG

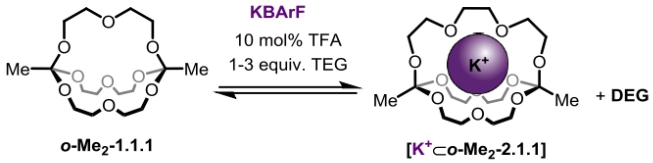

Four solutions of ***o*-Me$_2$-1.1.1** (5 µmol, 1 equiv.) with KBArF (5 µmol, 1 equiv.) and different amounts of triethylene glycol (TEG, 0-15 µmol, 0-3 equiv.) were prepared due to the general procedure. The yield was calculated with help of an internal standard (1,4-dinitrobenzene, estimated error: ±5%). The equilibration time was usually 3-6 hours.

Summary of results:

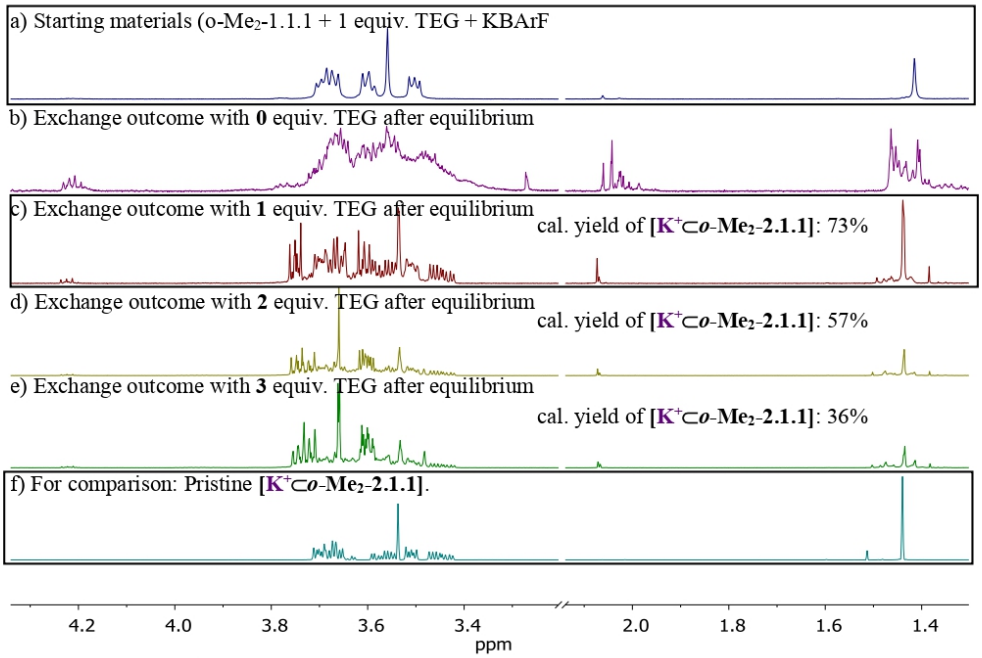

Stack plot of partial ^{1}H NMR spectra (400 MHz, $CDCl_3$, 298 K) before and after reaching the equilibrium with different amounts of TEG.

Conclusion: Without any TEG in the mixture, the cryptand ***o*-Me$_2$-1.1.1** falls apart, because K^+ is not a good template, and new (oligomeric) orthoester species (1.4-1.5 ppm), as well as different products of hydrolysis (around 2.05 ppm) are formed. With TEG, cryptand expansion to **[K$^+$⊂*o*-Me$_2$-2.1.1]** occurs. With one equivalent of TEG the best (NMR) yield was observed (73%).

Experiment of [*o*-Me$_2$-1.1.1] with RbBArF and TEG

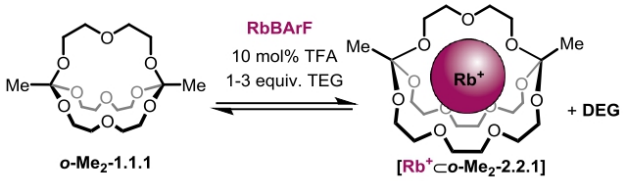

Four solutions of ***o*-Me$_2$-1.1.1** (5 µmol, 1 equiv.) with RbBArF (5 µmol, 1 equiv.) and different amounts of triethylene glycol (TEG, 0-15 µmol, 0-3 equiv.) were prepared according to the general procedure. The yield was calculated with help of an internal standard (NMR, 1,4-dinitrobenzene, estimated error: ±5%). The equilibration time was usually 3-6 hours.

Summary of results:

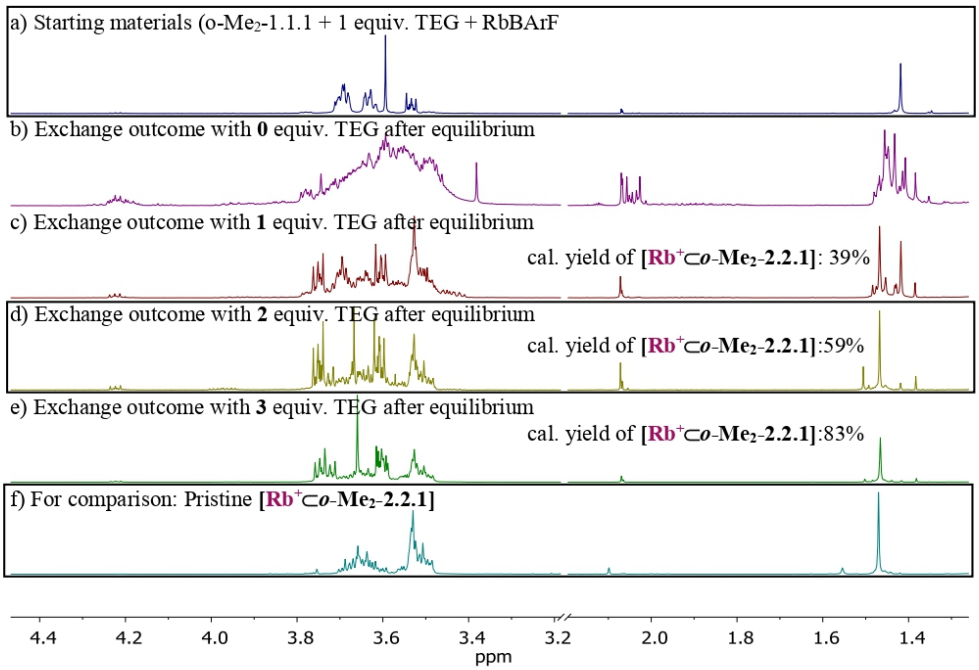

Stack plot of partial ^{1}H NMR spectra (400 MHz, $CDCl_3$, 298 K) before and after reaching the equilibrium with different amounts of TEG.

Conclusion: Without any TEG in the mixture, the cryptand ***o*-Me$_2$-1.1.1** falls apart and new (oligomeric) orthoester species (1.4-1.5 ppm), as well as different products of hydrolysis (around 2.05 ppm) are formed. With TEG, cryptand expansion to **[Rb$^+$⊂*o*-Me$_2$-2.2.1]** occurs due to the templating effect of the rubidium ion. With three equivalents of TEG a NMR yield of 83% was observed.

Experiment of [*o*-Me_2-1.1.1] with CsBArF and TEG

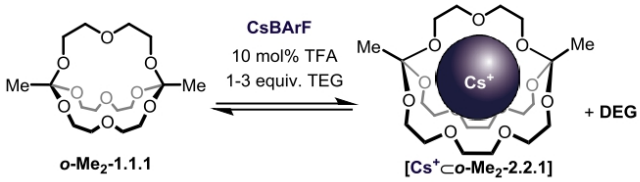

Four solutions of ***o*-Me_2-1.1.1** (5 µmol, 1 equiv.) with CsBArF (5 µmol, 1 equiv.) and different amounts of triethylene glycol (TEG, 0-15 µmol, 0-3 equiv.) were prepared according to the general procedure. The yield was calculated with help of an internal standard (1,4-dinitrobenzene, estimated error: ±5%). The equilibration time was usually 3-6 hours.

Summary of results:

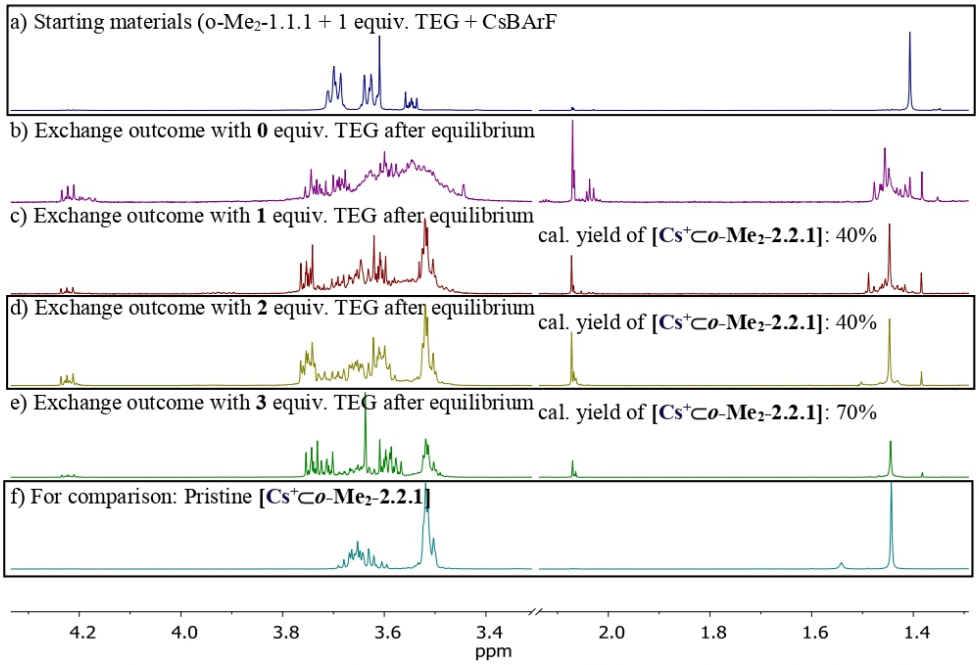

Stack plot of partial ^{1}H NMR spectra (400 MHz, $CDCl_3$, 298 K) before and after reaching the equilibrium with different amounts of TEG.

Conclusion: Without any TEG in the mixture, the cryptand ***o*-Me_2-1.1.1** falls apart and new (oligomeric) orthoester species (1.4-1.5 ppm), as well as different products of hydrolysis (around 2.05 ppm) are formed. With TEG, cryptand expansion to **[Cs^+⊂*o*-Me_2-2.2.1]** occurs due to the templating effect of the cesium ion. With three equivalents of TEG a NMR yield of 70% was observed.

Experiment of [*o*-Me$_2$-2.1.1] with CsBArF and TEG

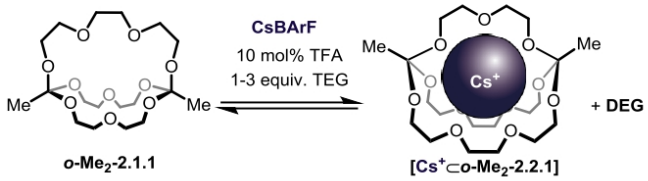

Three solutions of ***o*-Me$_2$-2.1.1** (5 µmol, 1 equiv.) with CsBArF (5 µmol, 1 equiv.) and different amounts of triethylene glycol (TEG, 0-15 µmol, 0-3 equiv.) were prepared according to the general procedure. The yield was calculated with help of an internal standard (1,4-dinitrobenzene, error: ±5%). The equilibration time was usually 3-6 hours.

Summary of results:

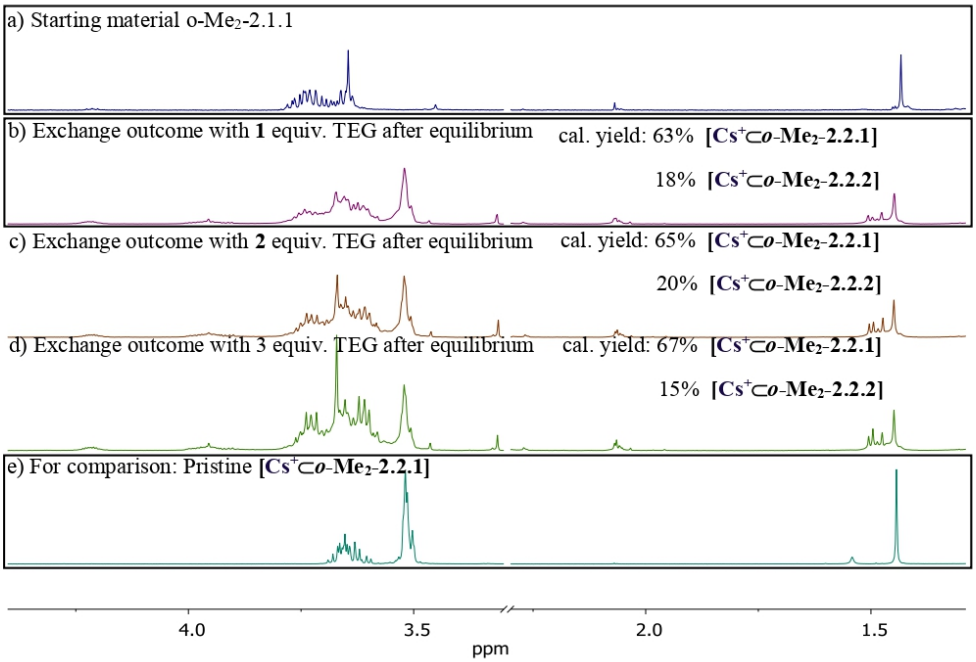

Stack plot of partial ^{1}H NMR spectra (400 MHz, $CDCl_3$, 298 K) after addition of TFA (10 mol%) to the solution.

Conclusion: with TEG unsymmetric cryptand ***o*-Me$_2$-2.1.1** further expands to form **[Cs$^+$⊂*o*-Me$_2$-2.2.1]** and **[Cs$^+$⊂*o*-Me$_2$-2.2.2]** in 63 and 18% yield upon addition of 1 equiv. TEG. This ratio does not significantly change upon addition of 2-3 equiv. TEG.

Experiment of [*o*-Me$_2$-2.2.2] with CsBArF and DEG

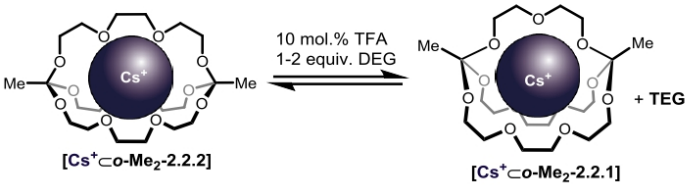

Two solutions of **[Cs$^+$⊂*o*-Me$_2$-2.2.2]** (5 µmol, 1 equiv.) with different amounts of triethylene glycol (TEG, 0-10 µmol, 0-2 equiv.) were prepared according to the general procedure. The yield was calculated with help of an internal standard (1,4-dinitrobenzene, error: ±5%). The equilibration time was usually 3-6 hours.

Summary of results:

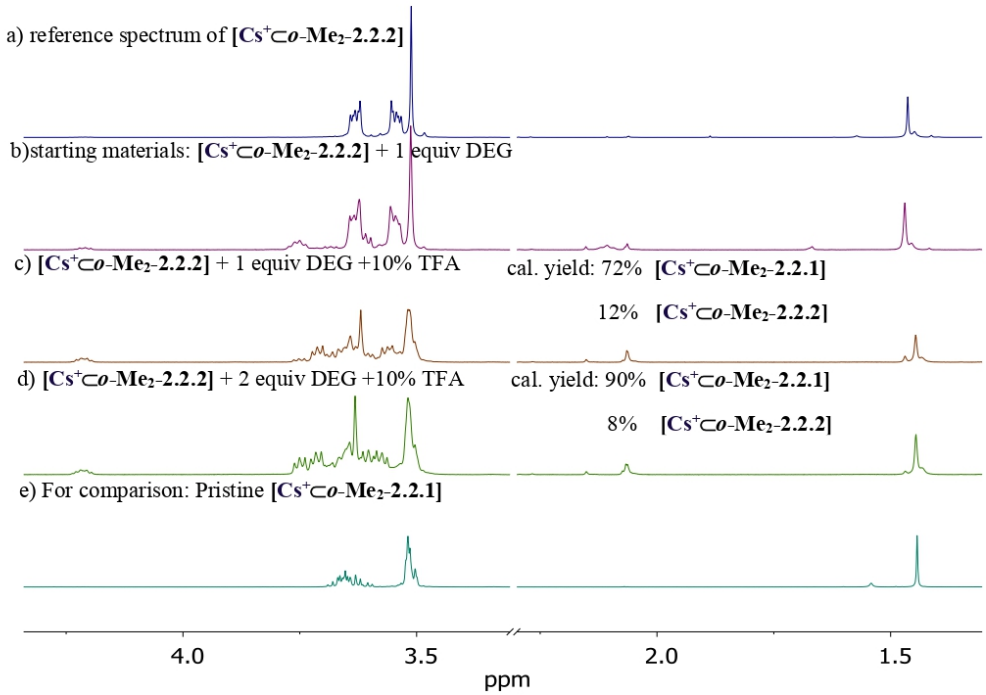

Stack plot of partial ^{1}H NMR spectra (400 MHz, $CDCl_3$, 298 K) before and after addition of TFA (10 mol%) to the solution.

Conclusion: upon addition of DEG to **[Cs$^+$⊂*o*-Me$_2$-2.2.2]** the mixture reconstitutes to form **[Cs$^+$⊂*o*-Me$_2$-2.2.1]** in 72% yield, which is evidently the preferred host for cesium, along with 12% of **[Cs$^+$⊂*o*-Me$_2$-2.2.2].** When the amount of DEG is increased to 2 equivalents, **[Cs$^+$⊂*o*-Me$_2$-2.2.1]** forms in ca. 90% yield.

Cryptate metathesis: *o*-Me_2-1.1.1 and *o*-Me_2-2.2.2 with KBArF and CsBArF

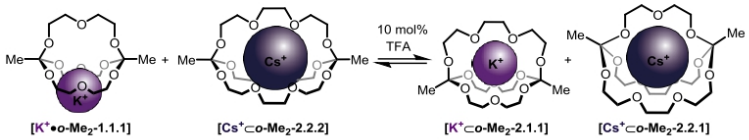

Solutions of ***o*-Me_2-1.1.1** (5 µmol, 1 equiv.) and ***o*-Me_2-2.2.2** (5 µmol, 1 equiv.) with KBArF (5 µmol, 1 equiv.) and CsBArF (5 µmol, 1 equiv.) were prepared according to the general procedure. The yield was calculated with help of an internal standard (1,4-dinitrobenzene, error: ±5%). The equilibration time was usually 3-6 hours.

Summary of results:

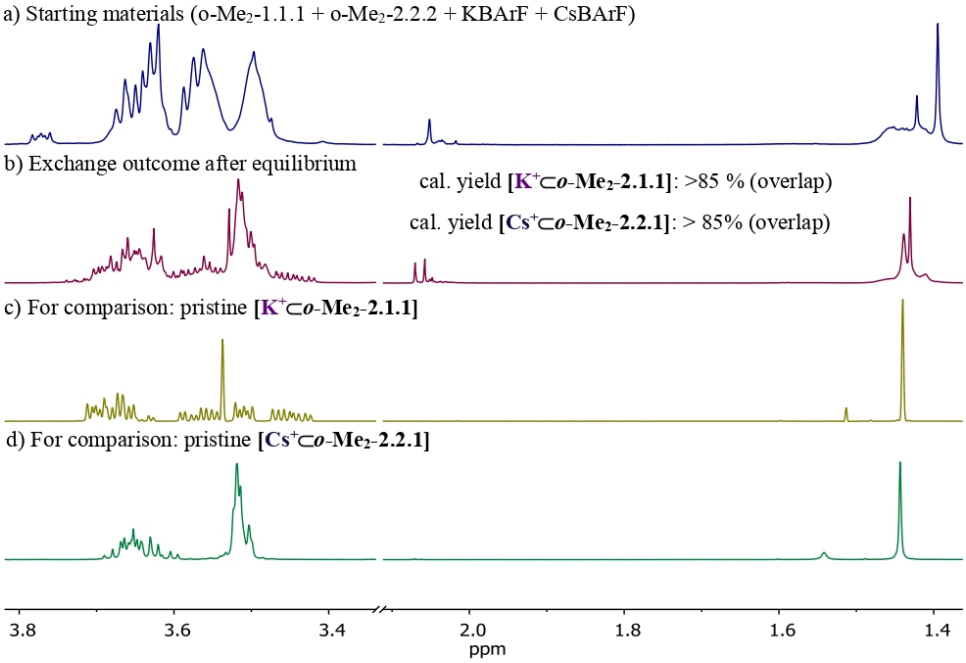

Conclusion: Symmetric cryptands ***o*-Me_2-1.1.1** and ***o*-Me_2-2.2.2** disassemble after addition of 10 mol% TFA. **[K^+⊂*o*-Me_2-2.1.1]** and **[Cs^+⊂*o*-Me_2-2.2.1]** are formed as nearly exclusive products of a reaction, in which 1 equiv. each of DEG and TEG is exchanged between the two starting materials (formally: a metathesis reaction). Comparison with the ^{1}H NMR spectra of pristine unsymmetric cryptands shows that the reaction is nearly quantitative (further corroborated by ESI^+-MS, see next page).

ESI$^+$-HRMS (after Et_3N quench) of mixed metal experiment

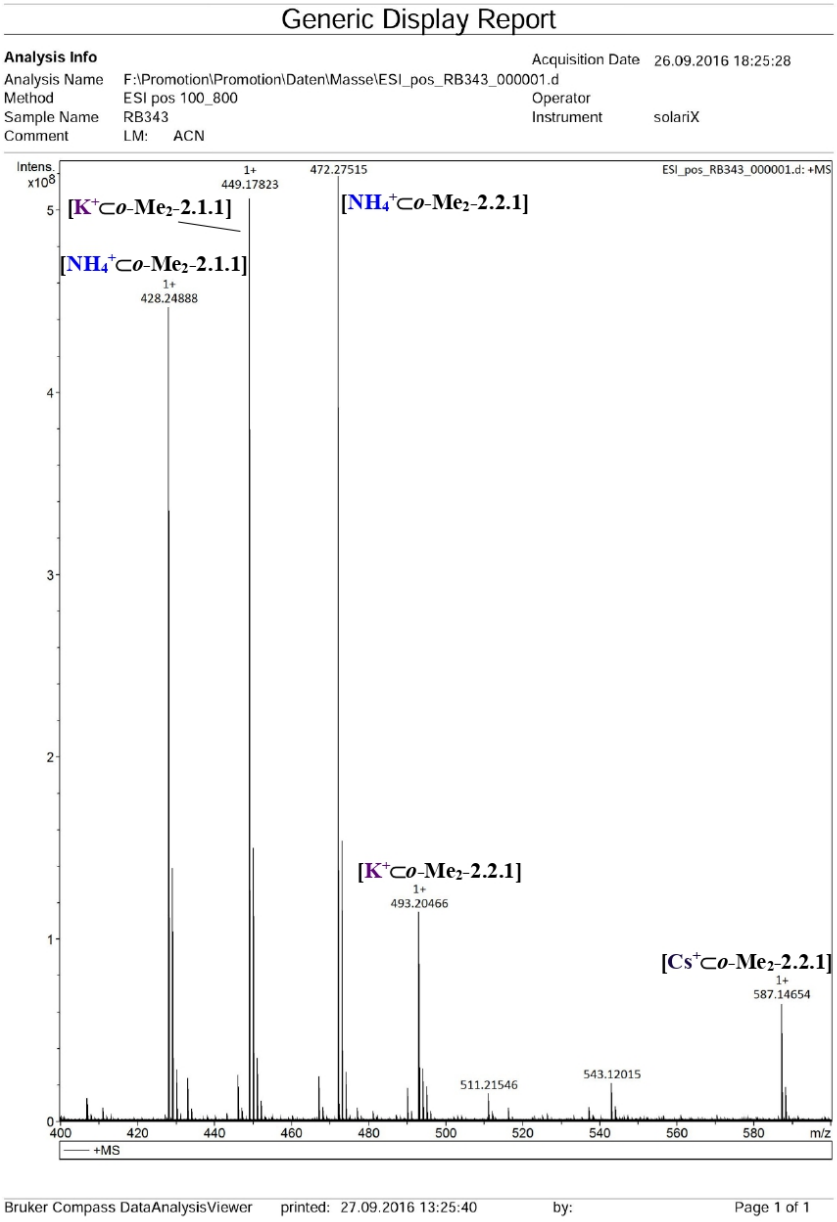

Note: ***o*-Me$_2$-1.1.1** or ***o*-Me$_2$-2.2.2** complexes were detected with 1 % intensity compared to the highest peak.

5. Synthesis of Chiral/Meso Diols and Cryptates

Synthesis of *S*,*S*-Dilactic acid diethyl ester (*S*,*S*-2)

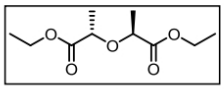

Ethyl (*L*)-lactate (5.36 mmol, 633 mg, 613 µL), ethyl (*R*)-lactate triflate (5.36 mmol, 1.342 g, 1.00 mL) and K_2CO_3 (23.58 mmol, 3.26 g) were stirred under N_2 in pentane: 1,2-dichloroethane 4:1 (10 mL) at room temperature. The reaction was monitored via TLC, and after 2 days, no starting material was present. The reaction mixture was filtered, the solvent removed and subsequently purified via column chromatography (silica, hexanes:EtOAc 7:3) to give the product as a colorless oil (0.76 g, 43%).

^{1}H NMR (400 MHz, $CDCl_3$, 293 K): δ = 4.25 – 4.11 (m, 4H), 4.06 (q, *J* = 6.9 Hz, 2H), 1.44 (d, *J* = 6.9 Hz, 6H), 1.26 (t, *J* = 7.1 Hz, 6H).

^{13}C {^{1}H} NMR (100 MHz, $CDCl_3$, 293 K): δ = 173.0, 74.1, 60.9, 18.7, 14.2.

R_f = 0.55 (hexanes:EtOAc 7:3).

LRMS (EI$^+$): m/z = 218 $[M]^+$, 145 $[M\text{-}CO_2Et]^+$.

^{1}H NMR spectrum (400 MHz, $CDCl_3$, 298 K):

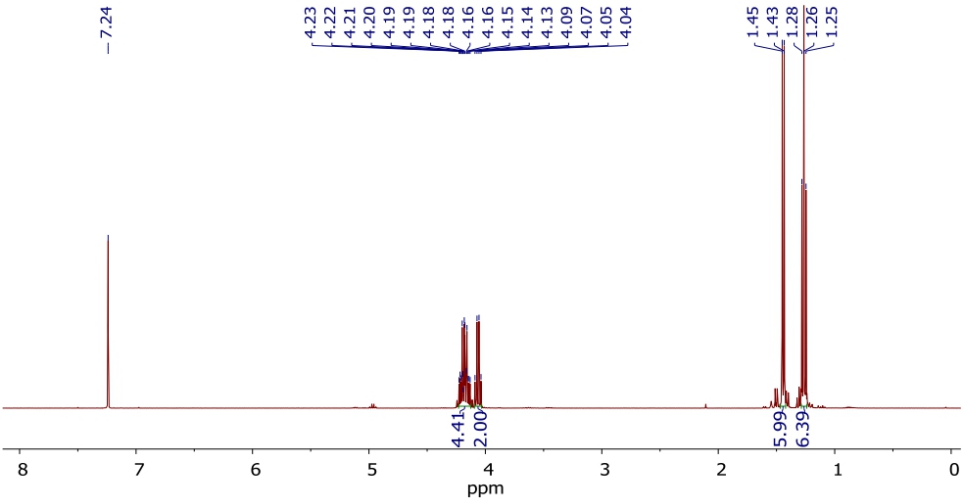

^{13}C {^{1}H} NMR spectrum (100 MHz, $CDCl_3$, 298 K):

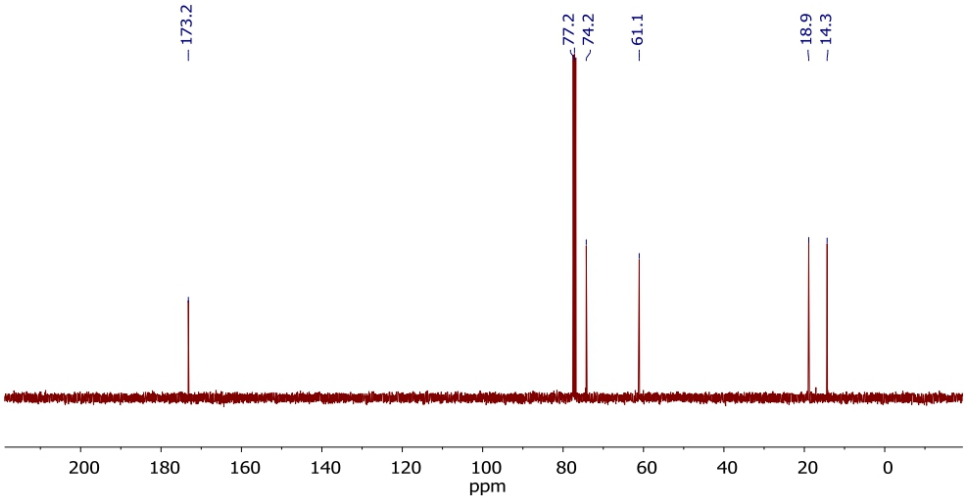

Synthesis of *S,S*-2,2'-Oxydi-1-propanol (*S,S*-1)

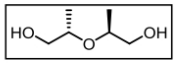

Lithium aluminium hydride (LAH, 0.82 mmol, 31.2 mg) was dissolved in Et_2O (20 mL) and stirred for 1 h at room temperature. *S,S'*-dilactic acid diethyl ester *S,S*-**1** (0.71 mmol, 156 mg), dissolved in Et_2O (5 mL) was added and stirred at room temperature for 20h.

Afterwards, the Fieser workup[3] was performed: per gram LAH, 1 mL water, 1.5 mL 10% NaOH, and 2.5 mL water were added carefully and stirred for 1h. $MgSO_4$ was added to remove excess water, and the mixture filtrated to remove the salts. The solvent was removed under reduced pressure to give the title compound without further purification as a slightly yellowish oil (66 mg, 69%).

^{1}H NMR (400 MHz, $CDCl_3$, 293 K): δ = 3.77 – 3.68 (m, 2H), 3.68 – 3.61 (m, 2H), 3.49 – 3.41 (m, 2H), 1.06 (d, *J* = 6.3 Hz, 6H).

^{13}C {^{1}H} NMR (100 MHz, $CDCl_3$, 293 K): δ = 73.4, 66.6, 16.3.

HRMS (ESI$^+$): m/z = 157.0837 $[M+Na]^+$ (calc. 157.0835).

$[\alpha]_D^{20} = 24.2°$ (c $8.05 \cdot 10^{-3}$, $CDCl_3$)

^{1}H NMR spectrum (400 MHz, $CDCl_3$, 298 K):

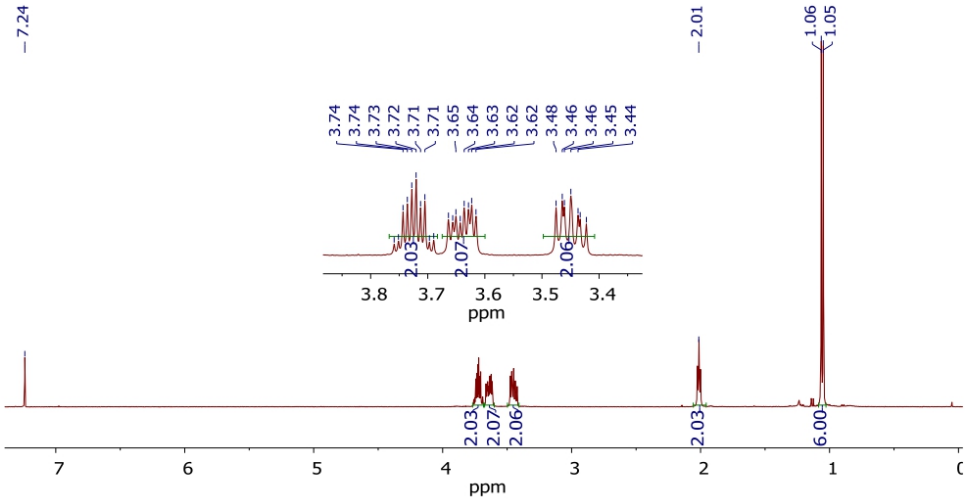

^{13}C {^{1}H} NMR spectrum (100 MHz, $CDCl_3$, 298 K):

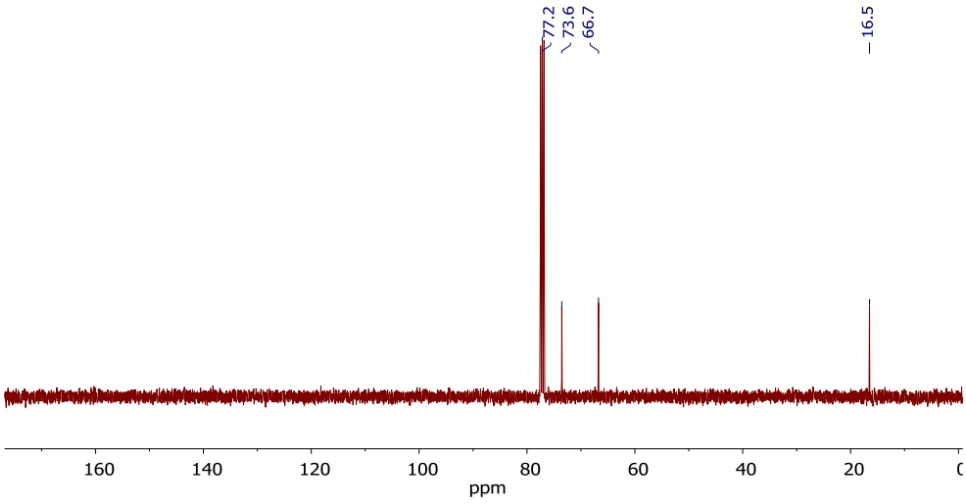

Synthesis of Ethyl (L)-lactate triflate (*S*-3)

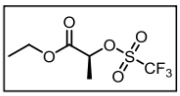

Ethyl (L)-lactate (10.62 mmol, 1.25 g, 1.21 mL) and 2,6-lutidine (11.70 mmol, 1.254 g, 1.36 mL) were dissolved in CH_2Cl_2 and cooled to 0 °C. Triflic anhydride (10.62 mmol, 3.00 g, 1.79 mL) was slowly added by means of a syringe over 30 min and the solution stirred over night at 0 °C→ rt. Afterwards, the amount of solvent was narrowed to approx. 5 mL and puri-fied via a short column (silica, CH_2Cl_2) to give the product as a slightly yellow liquid (2.60 g, 98%), that turns brown over time.

^{1}H NMR (400 MHz, $CDCl_3$, 293 K): δ = 5.20 (q, J = 7.0 Hz, 1H), 4.28 (qd, J = 7.1, 1.9 Hz, 2H), 1.69 (d, J = 7.0 Hz, 3H), 1.31 (t, J = 7.1 Hz, 3H).

^{13}C {^{1}H} NMR (100 MHz, CDCl3, 293 K): δ = 167.5, 118.6 (q, 1J = 319.4 Hz), 80.2, 62.9, 18.2, 14.0.

R_f = 0.80 (CH_2Cl_2).

^{1}H NMR spectrum (400 MHz, $CDCl_3$, 298 K):

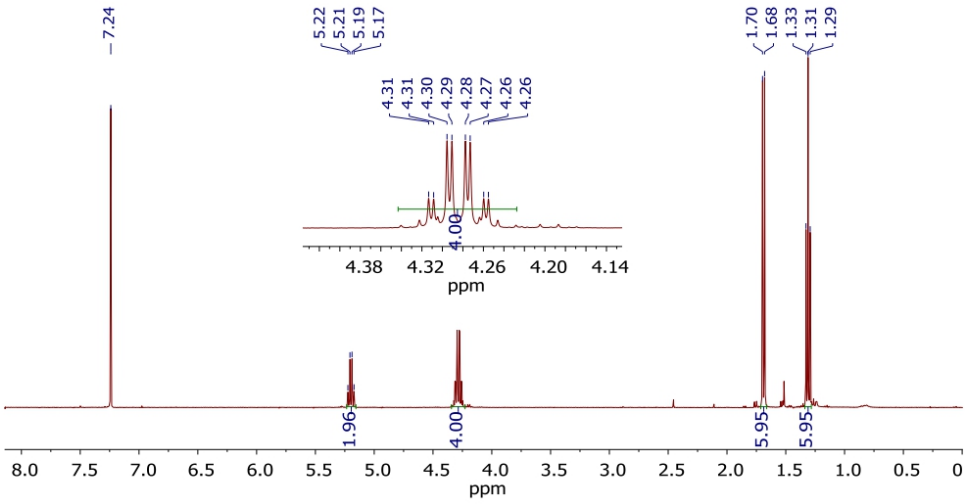

^{13}C {^{1}H} NMR spectrum (100 MHz, $CDCl_3$, 298 K):

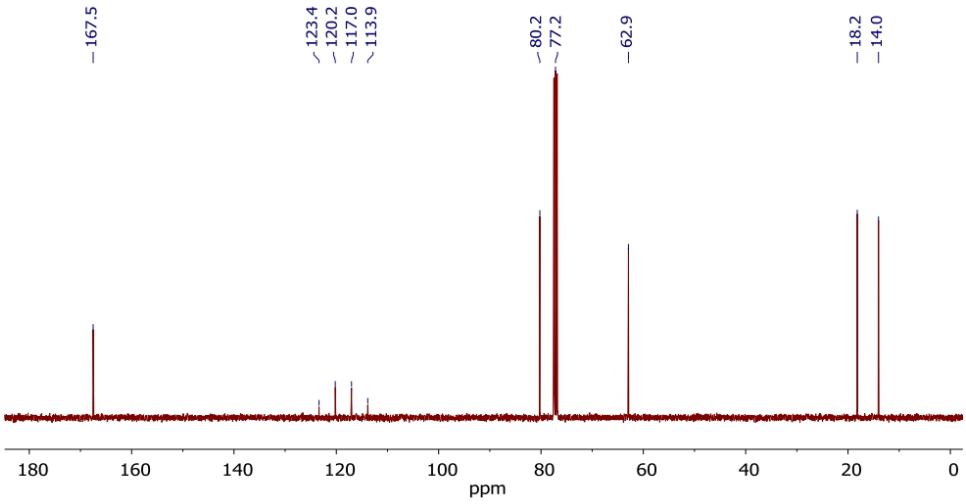

Synthesis of *R,S*-Dilactic acid diethyl ester (*R,S*-2)

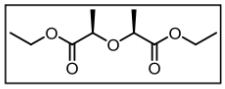

Ethyl (L)-lactate (5.36 mmol, 633 mg, 613 µL), ethyl (L)-lactate triflate (*S*-**3**) (5.36 mmol, 1.342 g, 1.00 mL) and K_2CO_3 (23.58 mmol, 3.26 g) were stirred under N_2 in pentane:1,2-dichloroethane 4:1 (10 mL) at room temperature. The reaction was monitored via TLC, and after 2 days, no starting material was present. K_2CO_3 was filtered off and washed with diethyl ether. The solvent was removed under reduced pressure, and the resulting colorless liquid was purified via column chromatography (silica, hexanes:EtOAc 7:3) to give the product as a colorless oil (0.46 g, 39%).

^{1}H NMR (400 MHz, $CDCl_3$, 293 K): δ = 4.17 (q, J = 7.1 Hz, 4H), 4.08 (q, J = 6.8 Hz, 2H), 1.41 (d, J = 6.8 Hz, 6H), 1.25 (t, J = 7.1 Hz, 6H).

^{13}C {^{1}H} NMR (100 MHz, $CDCl_3$, 293 K): δ = 172.6, 74.4, 61.1, 18.5, 14.3.

R_f = 0.39 (Hexanes:EtOAc 7:3).

HRMS (ESI+): m/z = 219.1222 (calc. 219.1227).

^{1}H NMR spectrum (400 MHz, $CDCl_3$, 298 K):

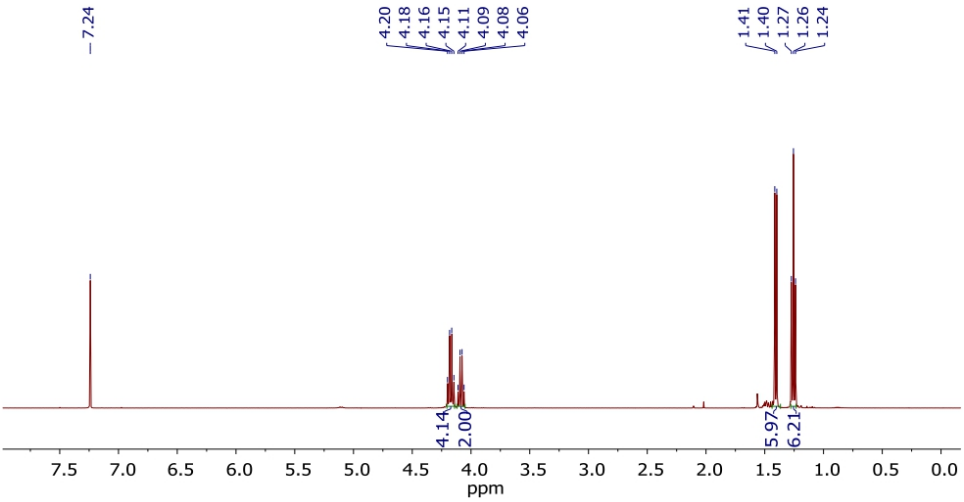

^{13}C {^{1}H} NMR spectrum (100 MHz, $CDCl_3$, 298 K):

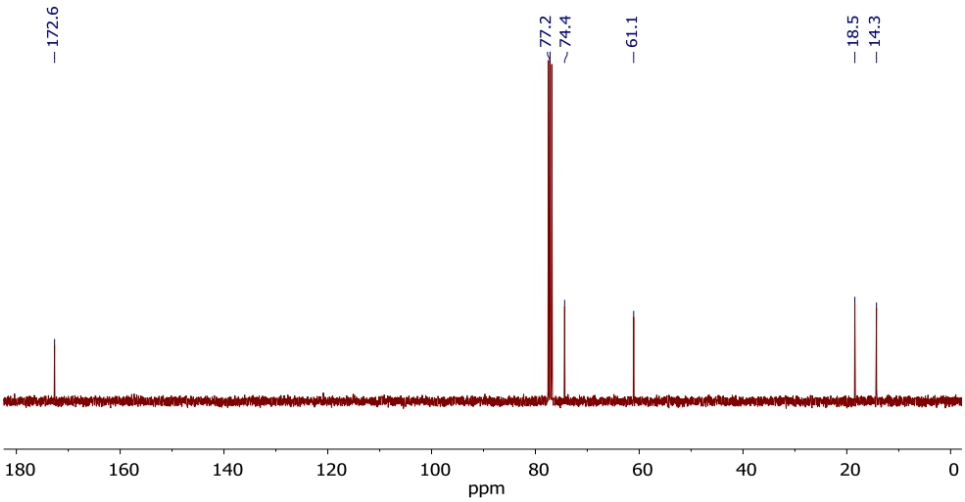

Synthesis of *R,S*-2,2'-Oxydi-1-propanol (*R,S*-1)

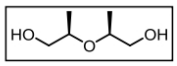

Lithium aluminium hydride (LAH, 14.9 mmol, 565 mg) was dissolved in Et_2O (20 mL) and stirred for 1h at room temperature. *R,S*-Dilactic acid diethyl ester (*R,S*-2) (1.15 mmol, 250 mg) dissolved in Et_2O (5 mL) was added and stirred at room temperature for 20h.

Afterwards, the Fieser workup[3] was performed: per gram LAH, 1 mL water, 1.5 mL 10% NaOH, and 2.5 mL water were added carefully and stirred for 1h. $MgSO_4$ was added to remove excess water, and the mixture filtrated to remove the salts. The solvent was removed under reduced pressure to give the title compound without further purification as a slightly yellowish oil (118 mg, 77%).

^{1}H NMR (400 MHz, $CDCl_3$, 298 K): δ = 3.73 – 3.63 (m, 2H), 3.60 (dd, *J* = 11.4, 2.9 Hz, 2H), 3.45 (dd, *J* = 11.4, 8.0 Hz, 2H), 1.10 (d, J = 6.4 Hz, 6H).

^{13}C {^{1}H} NMR (100 MHz, $CDCl_3$, 298 K): δ = 76.3, 66.9, 17.8.

HRMS (ESI$^+$): m/z = 157.0837 $[M+Na]^+$ (calc. 157.0835 $C_6H_{14}O_3Na$).

^{1}H NMR spectrum (400 MHz, $CDCl_3$, 298 K):

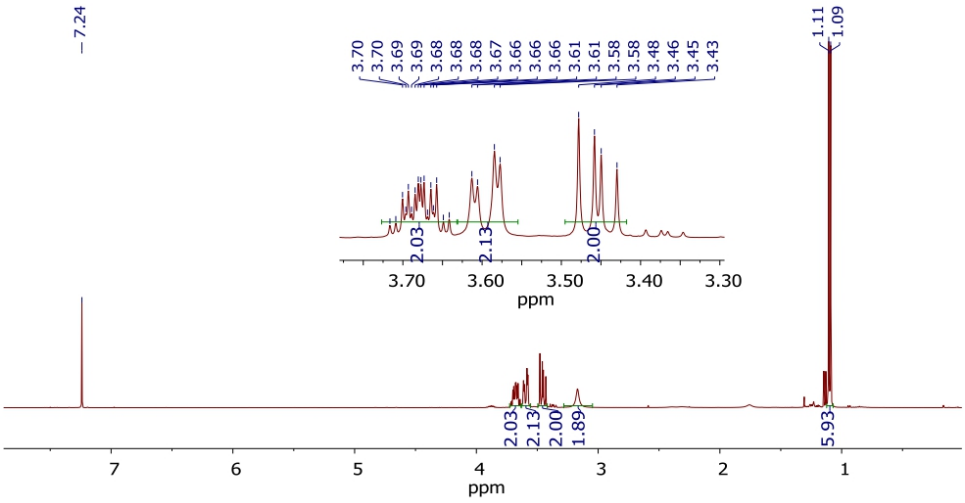

^{13}C {^{1}H} NMR spectrum (100 MHz, $CDCl_3$, 298 K):

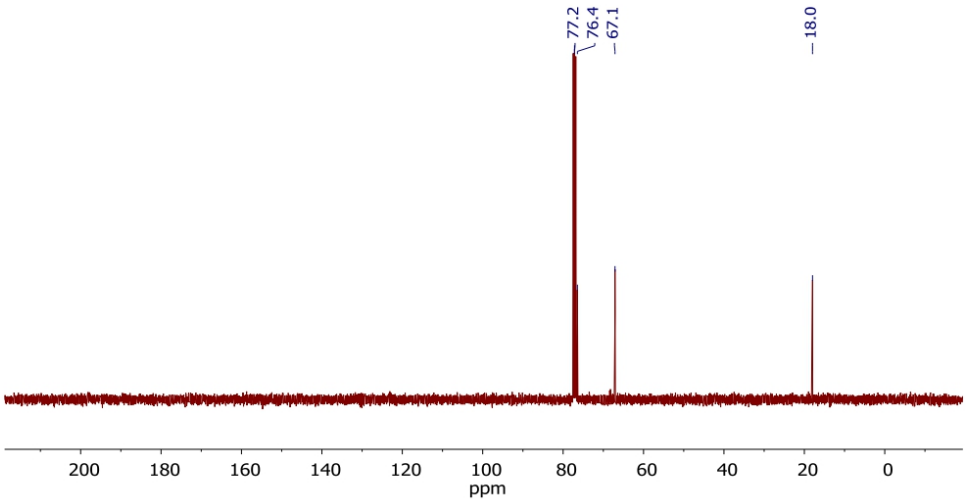

Synthesis of *R*,*R*-Dilactic acid diethyl ester (*R*,*R*-2)

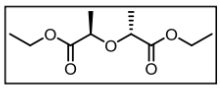

Ethyl (D)-lactate (5.36 mmol, 633 mg, 613 µL), Ethyl (*S*)-lactate triflate (5.36 mmol, 1.342 g, 1.00 mL) and K_2CO_3 (23.58 mmol, 3.26 g) were stirred under N_2 in pentane: 1,2-dichloroethane 4:1 (10 mL) at room temperature. The reaction was monitored via TLC, and after 2 days, no starting material was present. The reaction mixture was filtered, the solvent removed and subsequently purified via column chromatography (silica, hexanes:EtOAc 7:3) to give the product as a colorless oil (0.23 g, 20%).

^{1}H NMR (400 MHz, $CDCl_3$, 298 K): δ = 4.22 – 4.14 (m, 4H), 4.06 (q, *J* = 7.0 Hz, 2H), 1.44 (d, *J* = 7.0 Hz, 6H), 1.27 (t, *J* = 7.2 Hz, 6H).

^{13}C {^{1}H} NMR (100 MHz, $CDCl_3$, 298 K): δ = 173.2, 74.3, 61.1, 18.9, 14.3.

HRMS (ESI^+): m/z = 241.1051 $[M+Na]^+$ (calc. 241.1046 $C_{10}H_{18}O_5Na$).

^{1}H NMR spectrum (400 MHz, $CDCl_3$, 298 K):

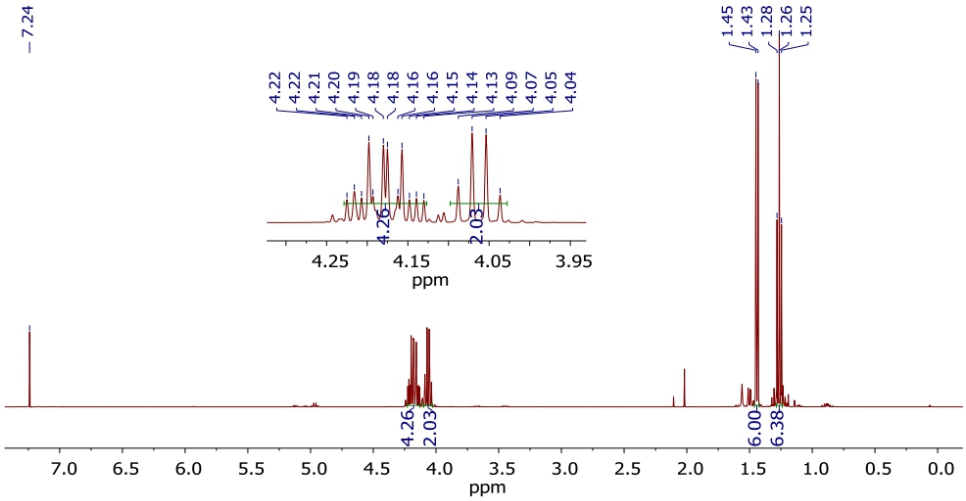

^{13}C {^{1}H} NMR spectrum (100 MHz, $CDCl_3$, 298 K):

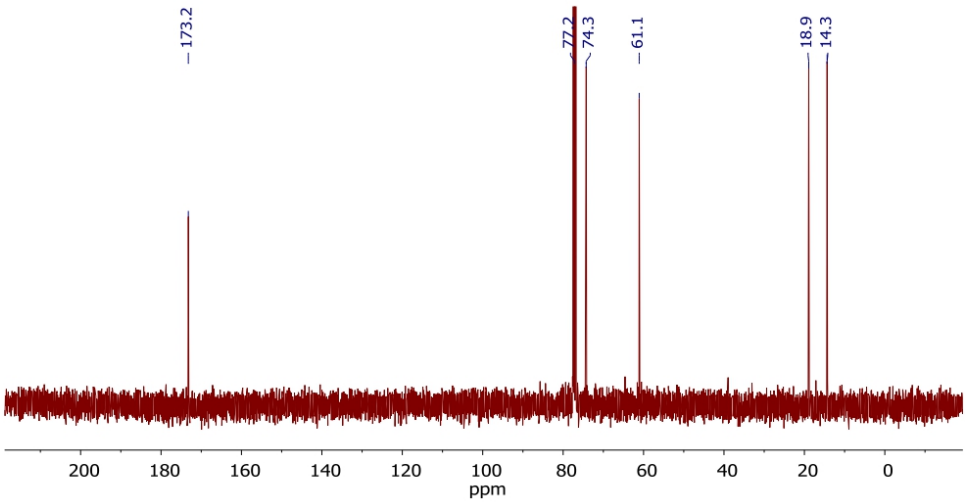

Synthesis of d$_4$-*R,R*-2,2'-Oxydi-1-propanol (d$_4$-*RR*-1)

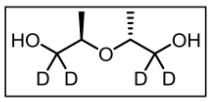

Lithium aluminium deuteride (LAD, 1.46 mmol, 62.4 mg) was dissolved in Et_2O (10 mL) and stirred for 10min at room temperature. *R,R*-dilactic acid diethyl ester *R,R*-**2** (0.97 mmol, 212 mg), dissolved in Et_2O (10 mL) was added and stirred at room temperature for 20h.

Afterwards, the Fieser workup[3] was performed: per gram LAD, 1 mL water, 1.5 mL 10% NaOH, and 2.5 mL water were added carefully and stirred for 1h. $MgSO_4$ was added to remove excess water, and the mixture filtrated to remove the salts. The solvent was removed under reduced pressure to give the title compound without further purification as a slightly yellowish oil (110 mg, 82%).

^{1}H NMR (400 MHz, $CDCl_3$, 293 K): δ =3.69-3.65 (q, *J* = 7.0 Hz, 2H), 2.08 (s, 2H), 31.11-1.09 (d, *J* = 7.0 Hz, 6H).

^{13}C {^{1}H} NMR (100 MHz, $CDCl_3$, 293 K): δ = 73.6, 66.7, 16.5.

HRMS (ESI$^+$): m/z = 161.1094 $[M+Na]^+$ (calc. 161.1086 $C_6H_8D_4O_2Na$).

^{1}H NMR spectrum (400 MHz, $CDCl_3$, 298 K):

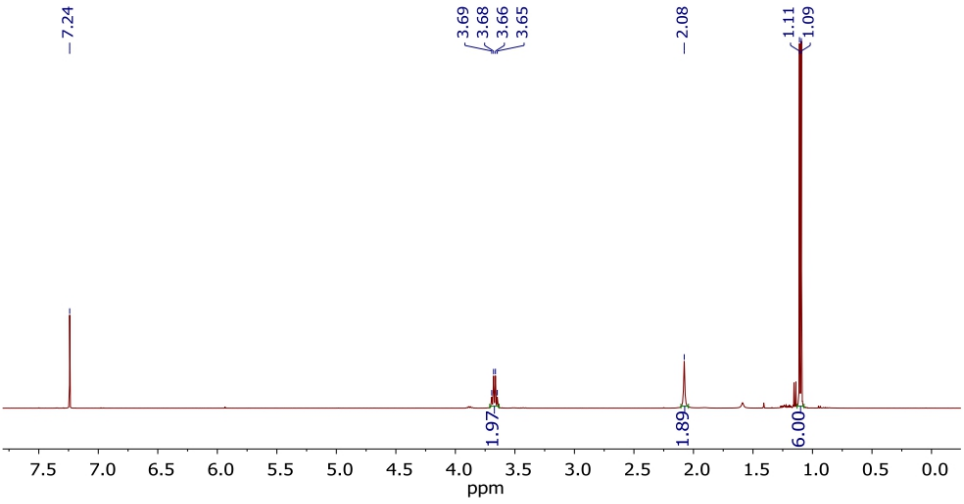

^{13}C {^{1}H} NMR spectrum (100 MHz, $CDCl_3$, 298 K):

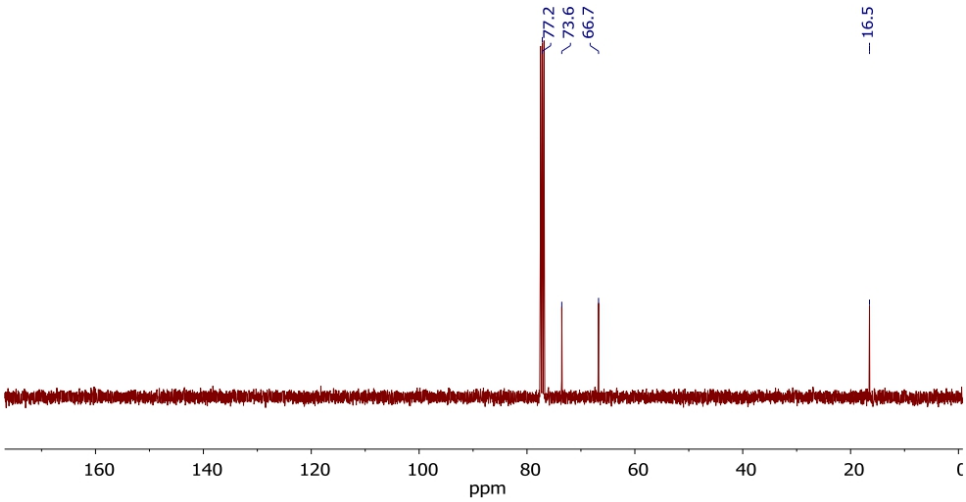

General procedure for chiral cryptate synthesis

Preparation of stock solutions

To achieve a high level of stoichiometric accuracy and adequate exclusion of moisture, metal salts and diethylene glycol were added from stock solutions that were dried over molecular sieves prior to addition of orthoester and acid catalyst.

In a typical example for the **salt stock solution**, sodium tetrakis[3,5-bis(trifluoromethyl)phenyl]borate (NaBArF, 0.14 mmol, 127.8 mg) and the corresponding diol (0.42 mmol, 3 eq.) were dissolved in $CDCl_3$ (14 mL) and dried over 4Å molecular sieves (ca. 1 g) for 3 days.

To obtain the **acid stock solution**, trifluoroacetic acid (TFA, 240 µmol, 18.4 µL) was topped up with $CDCl_3$ to obtain a total volume of 2 mL.

General procedure for cryptate synthesis

Molecular sieves 5Å (1 g) were added to 6.0 mL of the **salt stock solution** and the reaction mixture was left to stand at room temperature for 16 h. The orthoester (0.12 mmol, 2 eq.) and 10 µL of the **acid stock solution** (1 mol%) was added and the reaction mixture was shaken. Every 24 h, 10 µL of the **acid stock solution** (1 mol%) was added to keep the exchange reaction active (molecular sieves slowly transform the acid catalyst into inactive anhydride and/or esters) and the reaction progress was monitored regularly by ^{1}H NMR spectroscopy.

Synthesis of [Na$^+$⊂*o*-Me$_2$-*SS*,*SS*,*SS*]BArF$^-$

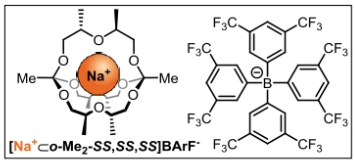

[Na$^+$⊂*o*-Me$_2$-*SS*,*SS*,*SS*]BArF$^-$ was prepared according to the standard procedure from NaBArF, trimethyl orthoacetate and *S,S*-2,2-oxydi-1-propanol (*SS*-**1**).

After 14 days, the mixture was passed through a short plug of silica gel (about 1cm in a glass pipette, each plug about 1 mL reaction mixture, and further 1.5 mL of $CDCl_3$ to purge the plug). The solvent was removed under reduced pressure to give the title compound as a white solid (12.11 mg, 15%).

M. p.: 275 °C.

^{1}H NMR (400 MHz, $CDCl_3$): δ = 7.68 (s, 8H), 7.51 (s, 4H), 3.89–3.86 (dd *J* = 9.4, 3.0 Hz, 6H), 3.76–3.69 (m, *J* = 9.4, 6.3, 3.1 Hz, 6H), 3.46–3.43 (dd, *J* = 9.4, 3.1 Hz, 6H), 1.39 (s, 6H), 1.13 (d, *J* = 6.3 Hz, 18H).

^{13}C {^{1}H} NMR (100 MHz, $CDCl_3$): δ = 162.6, 162.1, 161.6, 161.1, 134.9, 129.5, 129.2, 128.9, 128.8, 128.6, 126.1, 123.4, 120.6, 117.6, 113.2, 69.9, 66.7, 15.7 ppm.

HRMS (ESI$^+$): *m*/*z* = 473.27276 [M+Na]$^+$ (calcd. 473.27210 for $C_{22}H_{42}O_9Na$).

^{1}H NMR spectrum (400 MHz, $CDCl_3$, 298 K):

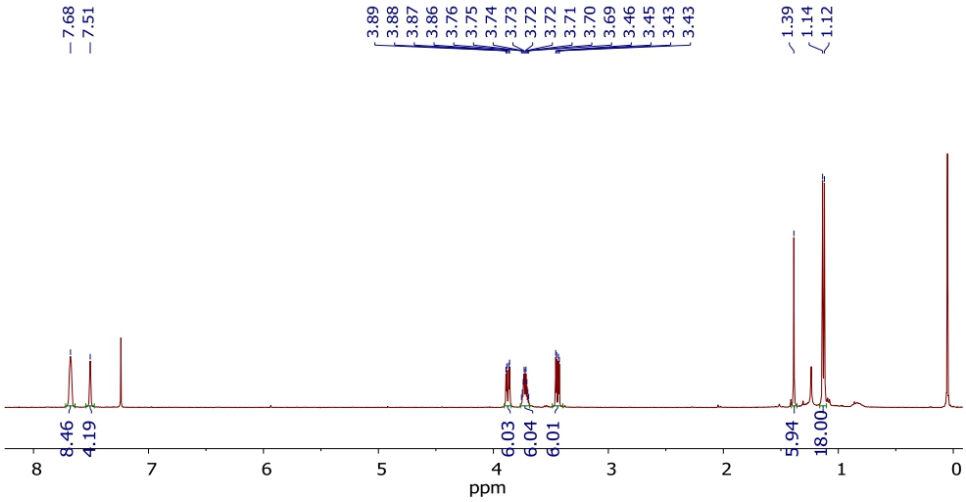

^{13}C {^{1}H} NMR spectrum (100 MHz, $CDCl_3$, 298 K):

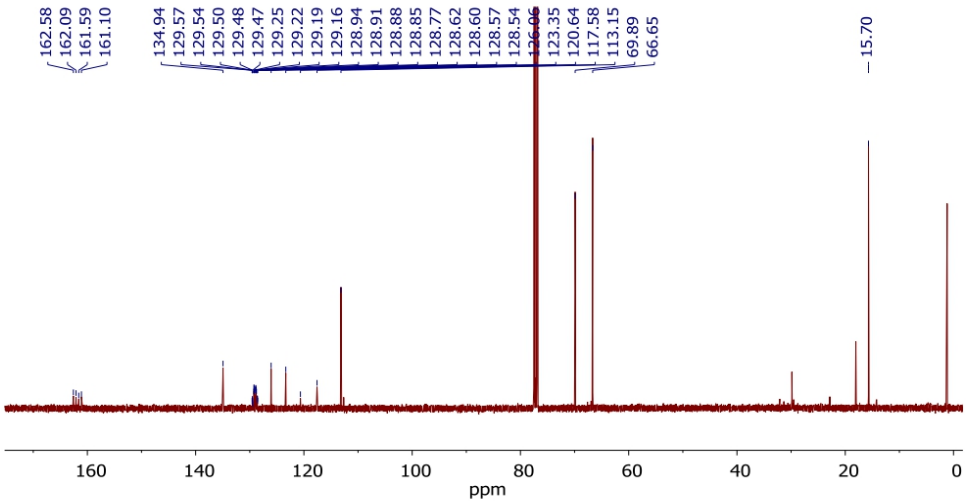

Synthesis of d_{12}-[Na^+⊂*o*-Me_2-*RR*,*RR*,*RR*]BArF$^-$

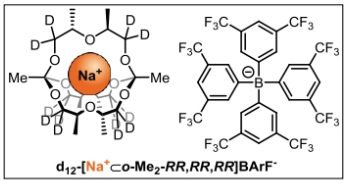

d_{12}-[Na^+⊂*o*-Me_2-*RR*,*RR*,*RR*]BArF$^-$ was prepared according to the standard procedure from NaBArF, trimethyl orthoacetate and d_4-*R*,*R*-2,2'-oxydi-1-propanol (d_4-*RR*-**1**).

After 12 days, the mixture was passed through a short plug of silica gel (about 1cm in a glass pipette, each plug about 1 mL reaction mixture, and further 1.5 mL of $CDCl_3$ to purge the plug). The solvent was removed under reduced pressure to give the title compound as a white solid (9.7 mg, 12%).

^{1}H NMR (400 MHz, $CDCl_3$): δ = 7.68 (s, 8H), 7.51 (s, 4H), 3,74–3.69 (q, *J* = 6.3 Hz 6H), 1.38 (s, 6H), 1.12 ppm (d, *J* = 6.3 Hz 18H).

^{13}C NMR: The measurement was omitted due to extensive coupling of the ^{13}C atom with the ^{2}H atoms. Proton NMR and HRMS provide unambiguous evidence for the formation of the cryptate (see also overview).

HRMS (ESI$^+$): *m*/*z* = 485.3465 [M+Na]$^+$ (calcd. 485.3474 for $C_{22}H_{30}D_{12}O_9Na$).

^{1}H NMR spectrum (400 MHz, $CDCl_3$, 298 K):

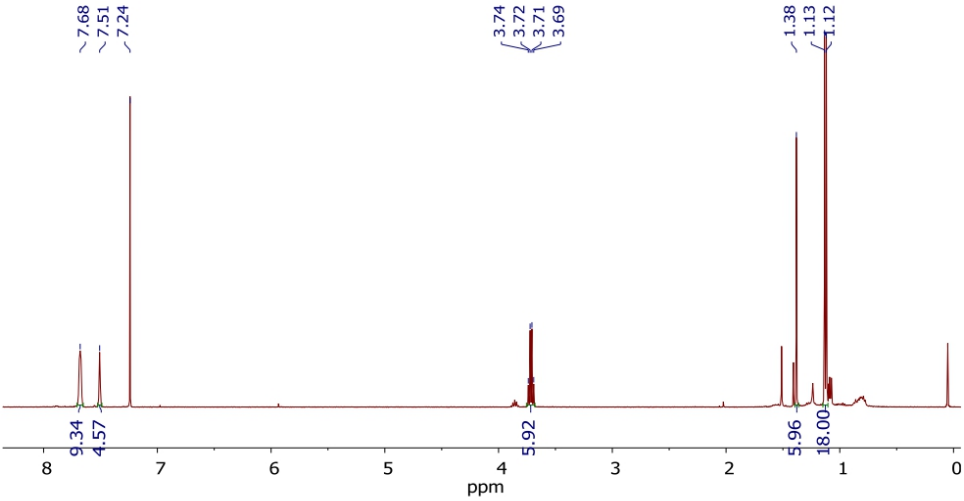

ESI$^+$-TOF-HRMS (Acetonitrile) of pristine **d_{12}-[Na$^+$⊂o-Me$_2$-*RR,RR,RR*]BArF$^-$**

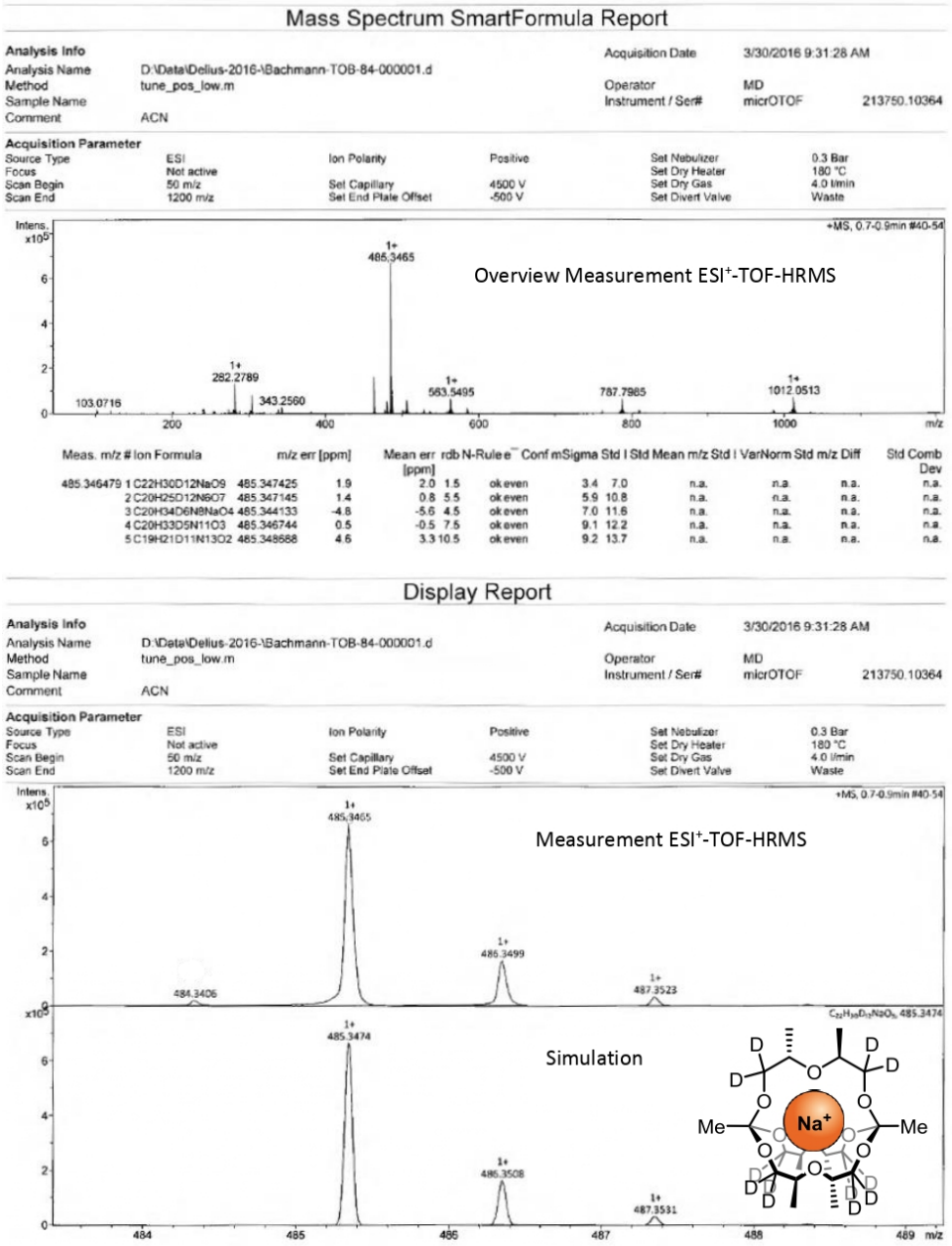

Overview of self-sorting experiments with chiral Diols (*SS*-1, *RS*-1 and d$_4$-*RR*-1)

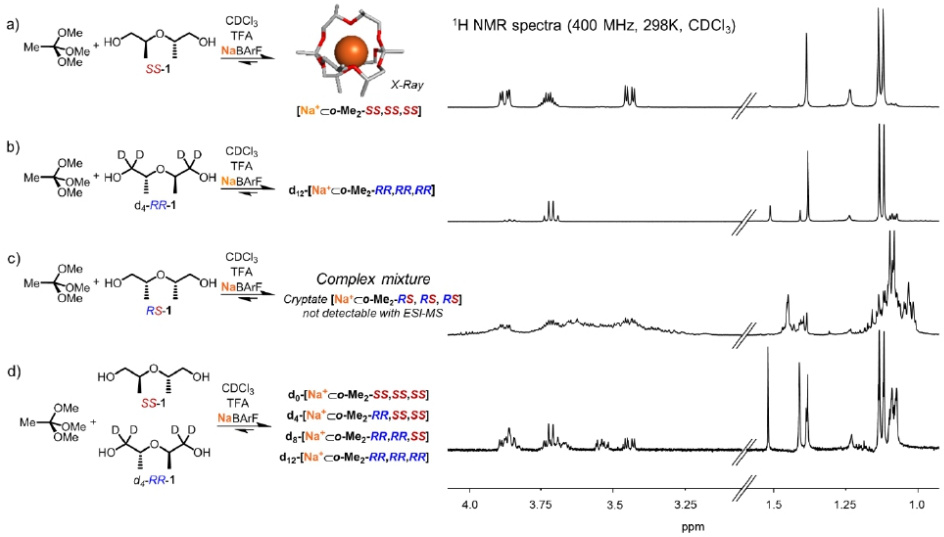

Reaction conditions:

For a): see synthesis of. **[Na$^+$⊂*o*-Me$_2$-*SS*,*SS*,*SS*]BArF$^-$.**

For b): see synthesis of **d$_{12}$-[Na$^+$⊂*o*-Me$_2$-*RR*,*RR*,*RR*]BArF$^-$.**

For c): same conditions like for the synthesis of **[Na$^+$⊂*o*-Me$_2$-*SS*,*SS*,*SS*]BArF$^-$** just with diol *RS*-**1** instead of *SS*-**1**. No detectable cryptate in the crude mixture with mass spectrometry and also no cryptate found after silica plug in the ^{1}H NMR spectrum.

For d): same conditions like for the synthesis of **[Na$^+$⊂*o*-Me$_2$-*SS*,*SS*,*SS*]BArF$^-$** just with both diols *SS*-**1** and d$_4$-*RR*-**1** in the stock solution (0.42 mmol from each diols in the stock solution). After a plug of silica all four cryptates was analyzed by mass spectrometry and ^{1}H-NMR. Separation of different cryptates was not possible on a silica plug.

6. Crystallographic Data

Compound [K^+⊂*o*-Me_2-2.1.1]$BArF^-$:

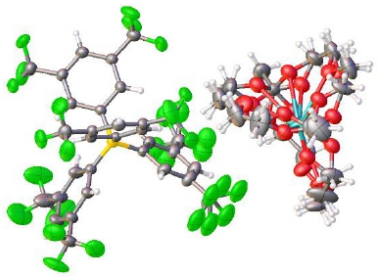

Notes on structure solution and refinement for [K^+⊂*o*-Me_2-2.1.1]$BArF^-$:

Goniometer type:	Agilent SuperNova with Atlas detector
Structure solution :	SHELXS-2014
Structure refinement :	SHELXL-2014
Hydrogen treatment:	riding model
Disorder:	O1/O1a, O2/O2a, O3/O3a,O4/O4a, O5/O5a, O6/O6a, O7/O7a, O9/O9a = 60:40%
Comments:	Highest rest-electron density close at CF_3; not assignable because of disorder
	1 $CHCl_3$ molecule not sufficient assignable => masked during refinement

Crystal data for [K^+⊂*o*-Me_2-2.1.1]$BArF^-$:

Identification code	RB02
Empirical formula	$C_{50}H_{46}BF_{24}KO_{10}$
Formula weight	1312.78

Temperature/K	173.00(10)
Crystal system	monoclinic
Space group	P2/c
a/Å	19.9298(3)
b/Å	16.6196(2)
c/Å	18.6004(2)
α/°	90
β/°	108.5239(15)
γ/°	90
Volume/Å^3	5841.75(14)
Z	4
ρ_{calc}g/cm^3	1.493
μ/mm^{-1}	1.983
F(000)	2664.0
Crystal size/mm^3	0.2522 × 0.1208 × 0.0951
2Θ range for data collection	7.08 to 123.2°
Index ranges	-22 ≤ h ≤ 22, -18 ≤ k ≤ 18, -13 ≤ l ≤ 21
Reflections collected	31738
Independent reflections	9009[$R_{(int)}$ = 0.0382]
Data/restraints/parameters	9009/63/771
Goodness-of-fit on F^2	1.111
Final R indexes [I>=2σ (I)]	R1 = 0.0874, wR2 = 0.2463
Final R indexes [all data]	R1 = 0.1013, wR2 = 0.2617
Largest diff. peak/hole / e Å^{-3}	1.31/-1.07

[K$^+$⊂*o*-Me$_2$-2.1.1]BArF$^-$ was crystallized by slow diffusion of cyclopentane into a solution of **[K$^+$⊂*o*-Me$_2$-2.1.1]BArF$^-$** in chlorofrom. The cif-file was deposited in the Cambridge structural database under identifier CCDC 1505902.

Compound [Rb^+⊂*o*-Me_2-2.2.1]$BArF^-$:

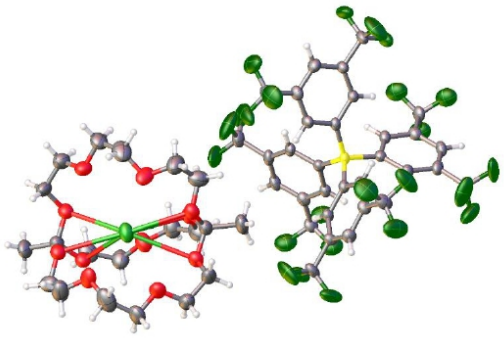

Notes on structure solution and refinement for [Rb^+⊂*o*-Me_2-2.2.1]$BArF^-$:

Goniometer type:	Agilent SuperNova with Atlas detector
Structure solution :	SHELXS-2014
Structure refinement :	SHELXL-2014
Hydrogen treatment:	riding model
Disorder:	F31/32/33 : F31a/32a/33a = 76:24% O11/12/13 : O11a/12a/13a = 18 : 82% O6:O6a = 64:36% C15:C15a = 41:59%
Comments:	Absolute structure determined

Crystal data for [Rb^+⊂*o*-Me_2-2.2.1]$BArF^-$:

Identification code	16Del_OS05
Empirical formula	$C_{52}H_{50}BF_{24}O_{11}Rb$
Formula weight	1403.20
Temperature/K	173.00(14)
Crystal system	monoclinic

Space group	C2
a/Å	25.062(4)
b/Å	8.9025(4)
c/Å	18.963(3)
α/°	90
β/°	136.52(3)
γ/°	90
Volume/Å^3	2911.5(11)
Z	2
ρ_{calc}g/cm^3	1.601
μ/mm^{-1}	2.394
F(000)	1416.0
Crystal size/mm^3	0.130 × 0.054 × 0.038
2Θ range for data collection	7.086 to 123.13°
Index ranges	$-22 \leq h \leq 28$, $-9 \leq k \leq 9$, $-21 \leq l \leq 20$
Reflections collected	6283
Independent reflections	4305 [R_{int} = 0.0288, R_{sigma} = 0.0437]
Data/restraints/parameters	4305/54/408
Goodness-of-fit on F^2	1.049
Final R indexes [I>=2σ (I)]	R_1 = 0.0654, wR_2 = 0.1721
Final R indexes [all data]	R_1 = 0.0679, wR_2 = 0.1766
Largest diff. peak/hole / e Å^{-3}	0.75/-0.60

[Rb$^+$⊂*o*-Me$_2$-2.2.1]BArF$^-$ was crystallized by solvent layering of heptane over solution of **[Rb$^+$⊂*o*-Me$_2$-2.2.1]BArF$^-$** in chloroform. The cif-file was deposited in the Cambridge structural database under identifier CCDC 1505906.

Compound [$Cs^+ \subset o$-Me_2-2.2.2]$BArF^-$:

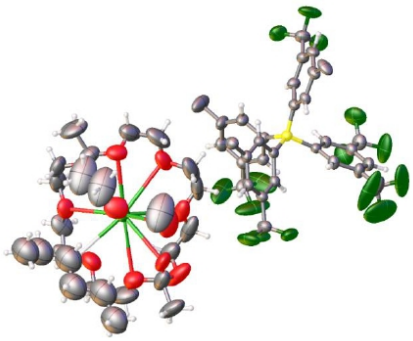

Notes on structure solution and refinement for [$Cs^+ \subset o$-Me_2-2.2.2]$BArF^-$:

Goniometer type:	Agilent SuperNova with Atlas detector
Structure solution :	SHELXS-2014
Structure refinement :	SHELXL-2014
Hydrogen treatment:	riding model
Disorder:	C35 : C35b = 45:55% C38,C39 : C38c,C39c = 88:12% C12a,C13a : C12c,C13c = 60:40% F13,14,15 : F13d,14d,15d = 58:42% F7,8,9 : F7d,8d,9d = 63:37% F22,23,24 : F22d,23d,24d = 54:46% F4a,5a,6a : F4b,5b,6b = 64:36%
Comments:	All disorders were very hard to model and refine – Alert A's in checkcif are caused by this, but not avoidable
	2 molecules in asymmetric unit 1 hexane in asymmetric unit

Crystal data for [Cs^+⊂*o*-Me_2-2.2.2]$BArF^-$:

Identification code	16Del-OS03
Empirical formula	$C_{57}H_{61}BCsF_{24}O_{12}$
Formula weight	1537.77
Temperature/K	172.95(10)
Crystal system	monoclinic
Space group	I2/a
a/Å	37.6811(9)
b/Å	12.7437(2)
c/Å	57.3975(12)
α/°	90
β/°	103.874(2)
γ/°	90
Volume/Å^3	26758.1(10)
Z	16
ρ_{calc}g/cm^3	1.527
μ/mm^{-1}	5.430
F(000)	12400.0
Crystal size/mm^3	0.186 × 0.170 × 0.116
2Θ range for data collection	7.116 to 123.486°
Index ranges	$-41 \leq h \leq 42$, $-14 \leq k \leq 14$, $-63 \leq l \leq 54$
Reflections collected	60202
Independent reflections	20307 [R_{int} = 0.0379, R_{sigma} = 0.0314]
Data/restraints/parameters	20307/78/1656
Goodness-of-fit on F^2	1.052
Final R indexes [I>=2σ (I)]	R_1 = 0.0804, wR_2 = 0.2236

Final R indexes [all data]	$R_1 = 0.0895$, $wR_2 = 0.2354$
Largest diff. peak/hole / e Å^{-3}	1.73/-1.21

[Cs$^+$⊂*o*-Me$_2$-2.2.2]BArF$^-$ was crystallized by solvent layering of heptane over solution of **[Cs$^+$⊂*o*-Me$_2$-2.2.2]BArF$^-$** in chlorofrom. The cif-file was deposited in the Cambridge structural database under identifier CCDC 1505904.

Compound [$Cs^+ \subset o$-Me_2-2.2.1]$BArF^-$:

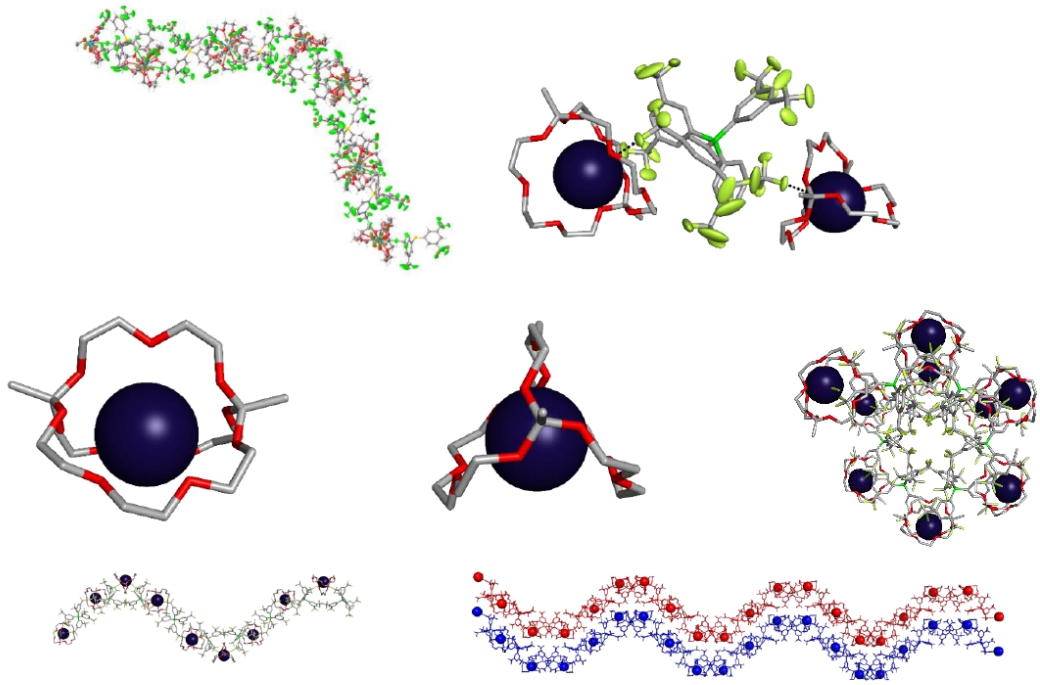

1.5 repeat units of helix,

view along crystallographic **a** axis.

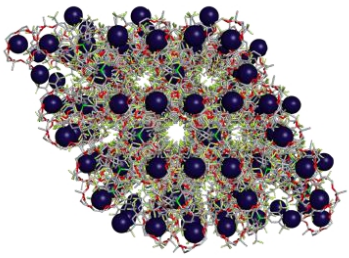

Crystal packing, view along crystallographic **c** axis

S66

Additional Data for Xray Analysis of [$Cs^+ \subset o$-Me_2-2.2.1]$BArF^-$:

Goniometer type:	Agilent SuperNova with Atlas detector
Structure solution :	SHELXS-2014
Structure refinement :	SHELXL-2014
Hydrogen treatment:	riding model
Disorder:	F4-6 : F4a-6a = 75:25% F10-12 : F10a – 12a = 78:23%
Comments:	Absolute structure determined: Flack=-0.010(3)

Crystal data for [$Cs^+ \subset o$-Me_2-2.2.1]$BArF^-$:

Identification code	16Del_OS04
Empirical formula	$C_{52}H_{50}BCsF_{24}O_{11}$
Formula weight	1450.64
Temperature/K	173.00(10)
Crystal system	hexagonal
Space group	$P6_122$
a/Å	13.03037(18)
b/Å	13.03037(18)
c/Å	61.8289(13)
α/°	90
β/°	90
γ/°	120
Volume/Å^3	9091.5(3)
Z	6

ρ_{calc}g/cm^3	1.590
μ/mm^{-1}	5.943
F(000)	4356.0
Crystal size/mm^3	0.157 × 0.136 × 0.116
2Θ range for data collection	7.834 to 123.138°
Index ranges	$-14 \leq h \leq 14$, $-14 \leq k \leq 14$, $-68 \leq l \leq 68$
Reflections collected	29439
Independent reflections	4703 [R_{int} = 0.0514, R_{sigma} = 0.0276]
Data/restraints/parameters	4703/30/424
Goodness-of-fit on F^2	1.082
Final R indexes [I>=2σ (I)]	R_1 = 0.0420, wR_2 = 0.1045
Final R indexes [all data]	R_1 = 0.0445, wR_2 = 0.1068
Largest diff. peak/hole / e Å^{-3}	0.59/-0.44

[Cs$^+$⊂*o*-Me$_2$-2.2.1]BArF$^-$ was crystallized by solvent layering of heptane over a solution of **[Cs$^+$⊂*o*-Me$_2$-2.2.2]BArF$^-$** in chlorofrom. The cif-file was deposited in the Cambridge structural database under identifier CCDC 1505905.

Compound [Na^+⊂*o*-Me_2-*SS*, *SS*, *SS*]$BArF^-$:

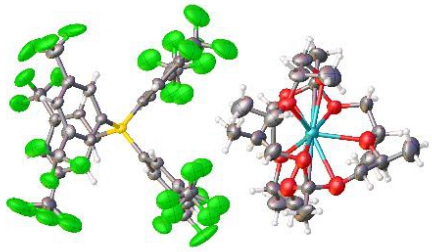

Notes on structure solution and refinement for [Na^+⊂*o*-Me_2-*SS*, *SS*, *SS*]$BArF^-$:

Goniometer type:	Agilent SuperNova with Atlas detector
Structure solution :	SHELXS-2014
Structure refinement :	SHELXL-2014
Hydrogen treatment:	riding model
Disorder:	-CF_3 groups: F4/5/6 : F4a/5a/6a = 72:28% F10/11/12 : F10a/11a/12a = 59:415 F16/17/18 : F16a/17a/18a = 65:35%
Comments:	Absolute structure determined

Crystal data for [Na^+⊂*o*-Me_2-*SS*, *SS*, *SS*]$BArF^-$:

Identification code	TOB01
Empirical formula	$C_{54}H_{54}BF_{24}NaO_9$
Formula weight	1336.77
Temperature/K	173.00(10)
Crystal system	tetragonal
Space group	$P4_1$

a/Å	12.97888(17)
b/Å	12.97888(17)
c/Å	35.6158(8)
α/°	90
β/°	90
γ/°	90
Volume/Å^3	5999.5(2)
Z	4
ρ_{calc}g/cm^3	1.480
μ/mm^{-1}	1.384
F(000)	2728.0
Crystal size/mm^3	0.2038 × 0.1381 × 0.096
2Θ range for data collection	6.81 to 123.296°
Index ranges	-14 ≤ h ≤ 12, -14 ≤ k ≤ 8, -38 ≤ l ≤ 39
Reflections collected	14520
Independent reflections	8995[R_{int} = 0.0306]
Data/restraints/parameters	8995/44/774
Goodness-of-fit on F^2	1.024
Final R indexes [I>=2σ (I)]	R_1 = 0.0822, wR_2 = 0.2177
Final R indexes [all data]	R_1 = 0.0898, wR_2 = 0.2291
Largest diff. peak/hole / e Å^{-3}	0.81/-0.60

[Na$^+$⊂*o*-Me$_2$-*SS*, *SS*, *SS*]BArF$^-$ was crystallized by slow diffusion of cyclopentane into a solution of **[Na$^+$⊂*o*-Me$_2$-*SS*, *SS*, *SS*]BArF$^-$** in chlorofrom. The cif-file was deposited in the Cambridge structural database under identifier CCDC 1505903.

7. Computational Chemistry

Methods:

We performed hybrid density functional calculations using the B3LYP functional[4] and the LANL2DZ basis set with effective core potentials,[5] augmented with polarization functions on non-hydrogen atoms.[6] The performance of this level (denoted as B3LYP/LANL2DZp) has been documented by us and others.[7] Structures were characterized as minima, transition structures, or higher-order saddle points by computation of vibrational frequencies. Relative energies were corrected for zero-point vibrational energy. The GAUSSIAN suite of programs was used.[8]

Discussion:

To get additional information on the ion selectivity of the investigated orthoester cryptands from a theoretical point of view, we performed DFT calculations (B3LYP/LANL2DZp) and derived complexation energies based on the model equation (1)

$$[M(H_2O)_6]^+ + \text{Cryptand} \rightarrow [M\subset\text{Cryptand}]^+ + 6H_2O \quad (1)$$

For consistency, all alkali metal cations were calculated in a six-fold coordination environment. For the lithium[9] cation, the well-known four-fold coordinated structures were found. It shows the additional two water molecules, which do not interact directly with the metal ion, located in the second coordination sphere via hydrogen bonds. However, the gas phase species $[Li(H_2O)_6]^+$ exists as a local minimum.

The complexation energies computed in this way are summarized in Table S1 and are plotted against the metal ions in the manuscript (Figure 1c).

metal ion	***o*-Me$_2$-1.1.0**	***o*-Me$_2$-1.1.1**	***o*-Me$_2$-2.1.1**	***o*-Me$_2$-2.2.1**	***o*-Me$_2$-2.2.2**
Li^+	27.1	18.7	15.9	25.2	20.9
Na^+	27.1	7.8	6.1	11.2	5.2
K^+	29.8	14.4	-1.9	-5.3	-5.5
Rb^+	31.1	32.5	3.4	-7.8	-9.4
Cs^+	29.4	60.9	14.4	-8.9	-13.6

Table S1: Comparison of the complexation energies (B3LYP/LANL2DZp) (kcal/mol) for [$M^+\subset$*o*Me$_2$-cryptands].

We are well aware that for experimental studies water is not a viable solvent, but this common approach[10] allows comparing the encapsulated alkali cations in the host and the free nearly unrestrained cations in solutions. The plots show that ***o*-Me$_2$-1.1.0** is not a favourable host for any alkali ion, while ***o*-Me$_2$-1.1.1** best complexes Na^+, as corroborated by our experiments. The larger hosts ***o*-Me$_2$-2.2.1** and ***o*-Me$_2$-2.2.2** have cavities suitable for binding of the largest alkali metal ions.

The approach of equation 1 can be inverted to compare complexation properties between different cryptands. These model equations (see general equation 2 and specific equations in Table S2) represent a second approach for rationalizing our experimental findings. It is important to note that these equations are biased by two effects: i) the binding situation of the metal ion can be different in the two hosts that are correlated by the model equation. For example, Li^+ is clearly too small to bind to the donor atoms in host ***o*-Me-2.2.2**, and Cs^+ is much too large to fit into host ***o*-Me-1.1.0**. ii) the equations are hardly isodesmic and not homodesmotic. These two effects can lead to over- or underestimated energy values and have to be considered while interpreting our calculated data. Finally, the calculations do not consider solvent effects, the presence of the counteranion and the presence of free diols.

[M⊂Cryptand 1]$^+$ + Cryptand 2 → Cryptand 1 + [M⊂Cryptand 2]$^+$ (2)

metal ion	**[M$^+$⊂*o*-Me$_2$-1.1.0] + *o*-Me$_2$-1.1.1 → *o*-Me$_2$-1.1.0 + [M$^+$⊂*o*-Me$_2$-1.1.1]**	**[M$^+$⊂*o*-Me$_2$-1.1.1] + *o*-Me$_2$-2.1.1 → *o*-Me$_2$-1.1.1 + [M$^+$⊂*o*-Me$_2$-2.1.1]**
Li^+	-5.3	-6.0
Na^+	-19.6	-1.7
K^+	-15.4	-16.6
Rb^+	3.0	-30.3
Cs^+	35.6	-49.0
metal ion	**[M$^+$⊂*o*-Me$_2$-2.1.1] + *o*-Me$_2$-2.2.1 → *o*-Me$_2$-2.1.1 + [M$^+$⊂*o*-Me$_2$-2.2.1]**	**[M$^+$⊂*o*-Me$_2$-2.2.1] + *o*-Me$_2$-2.2.2 → *o*-Me$_2$-2.2.1 + [M$^+$⊂*o*-Me$_2$-2.2.2]**
Li^+	9.0	-3.1
Na^+	4.1	-5.6
K^+	-5.0	0.3
Rb^+	-13.3	-1.5
Cs^+	-26.2	-4.9

Table S2: Comparison of the complexation energies (B3LYP/LANL2DZp) (kcal/mol)

In the manuscript, the four energy differences for one metal ion are transformed into energy levels by arbitrarily assigning an energy of 0 kcal/mol to the host-guest pair with the lowest energy. As a result, meaningful comparisons can only be drawn within host-guest pairs for one metal ion (as indicated graphically by the energy level diagram presented in Figure 1c (bottom)).

Illustrations of calculated structures

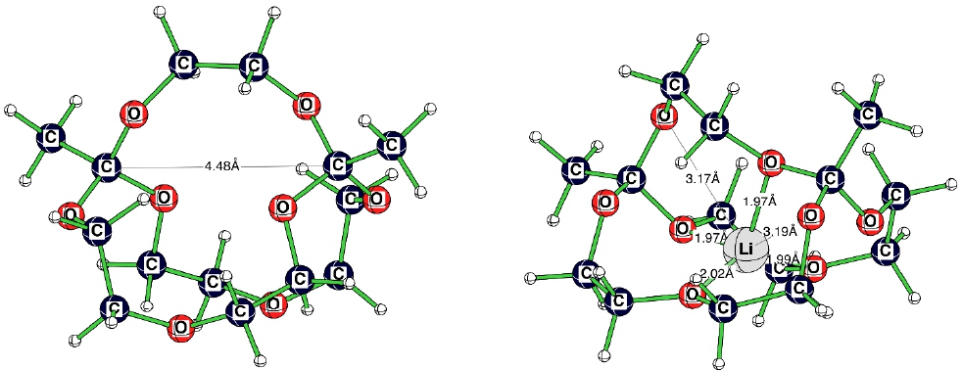

Calculated (B3LYP/LANL2DZp) structure for *o*-Me$_2$-1.1.0 (left) and [Li$^+$⊂*o*-Me$_2$-1.1.0] (right).

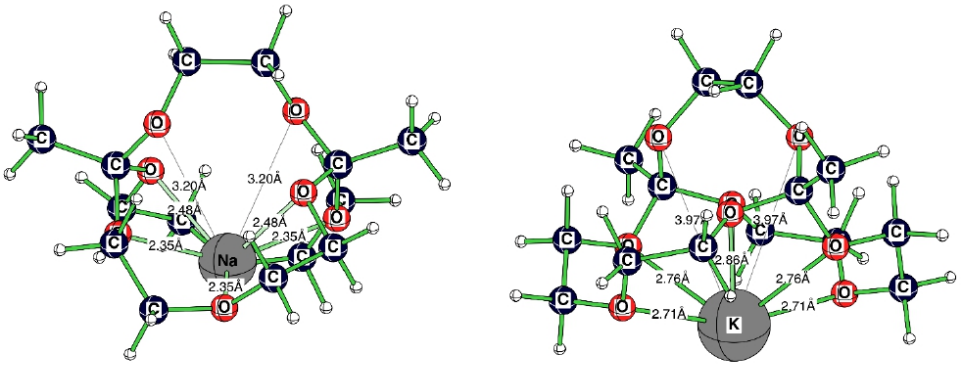

Calculated (B3LYP/LANL2DZp) structure for [Na$^+$⊂*o*-Me$_2$-1.1.0] (left) and [K$^+$⊂*o*-Me$_2$-1.1.0] (right).

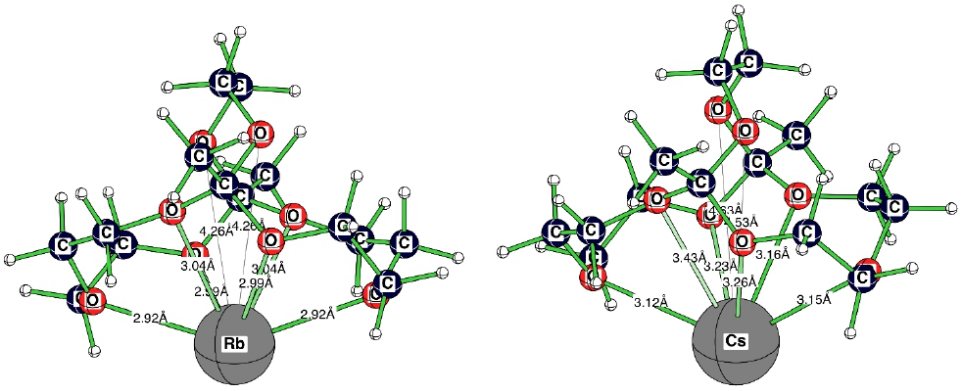

Calculated (B3LYP/LANL2DZp) structure for [Rb$^+$⊂*o*-Me$_2$-1.1.0] and [Cs$^+$⊂*o*-Me$_2$-1.1.0].

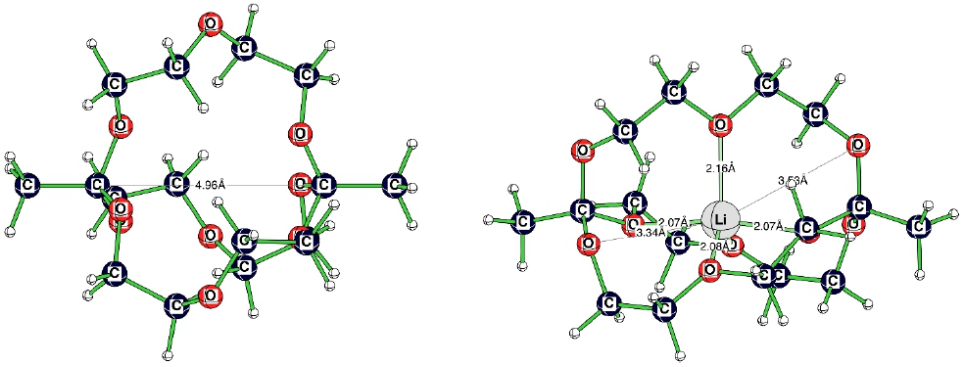

Calculated (B3LYP/LANL2DZp) structure for *o*-Me$_2$-1.1.1 (left) and [Li$^+$⊂*o*-Me$_2$-1.1.1] (right).

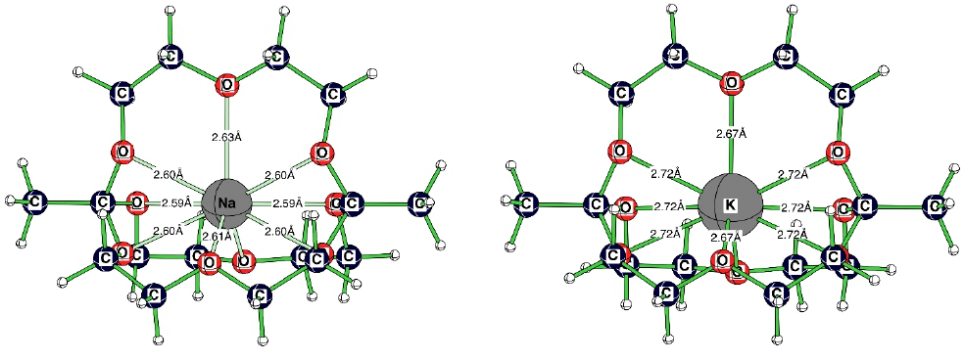

Calculated (B3LYP/LANL2DZp) structure for [Na$^+$⊂*o*-Me$_2$-1.1.1] (left) and [K$^+$⊂*o*-Me$_2$-1.1.1] (right).

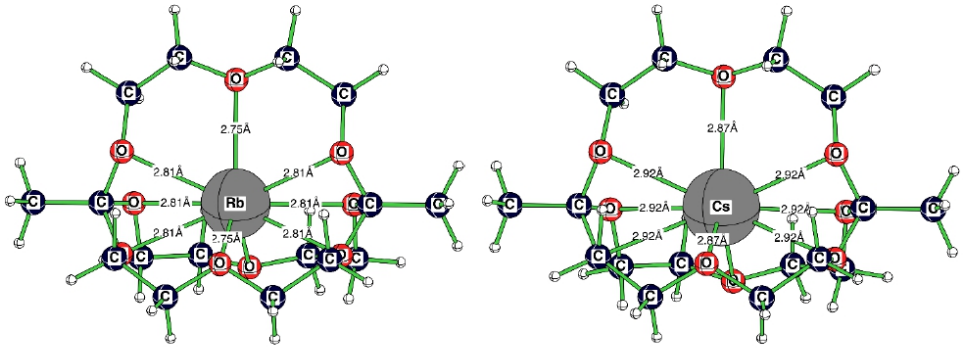

Calculated (B3LYP/LANL2DZp) structure for [Rb$^+$⊂*o*-Me$_2$-1.1.1] (left) and [Cs$^+$⊂*o*-Me$_2$-1.1.1] (right).

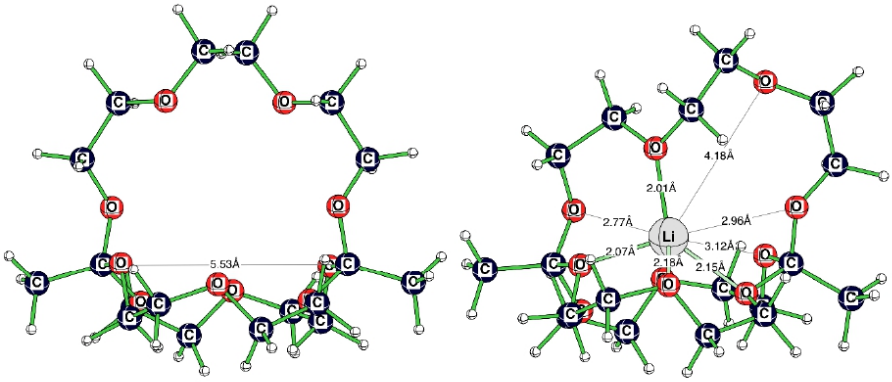

Calculated (B3LYP/LANL2DZp) structure for *o*-Me$_2$-2.1.1 (left) and [Li$^+$⊂*o*-Me$_2$-2.1.1] (right).

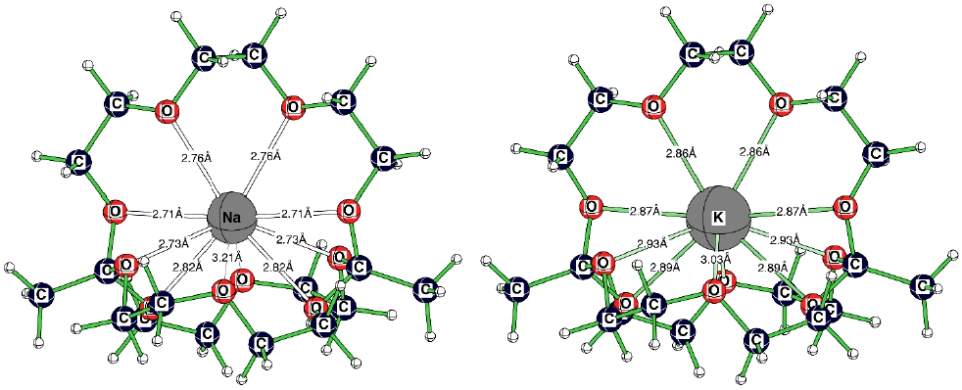

Calculated (B3LYP/LANL2DZp) structure for [Na$^+$⊂*o*-Me$_2$-2.1.1] (left) and [K$^+$⊂*o*-Me$_2$-2.1.1] (right).

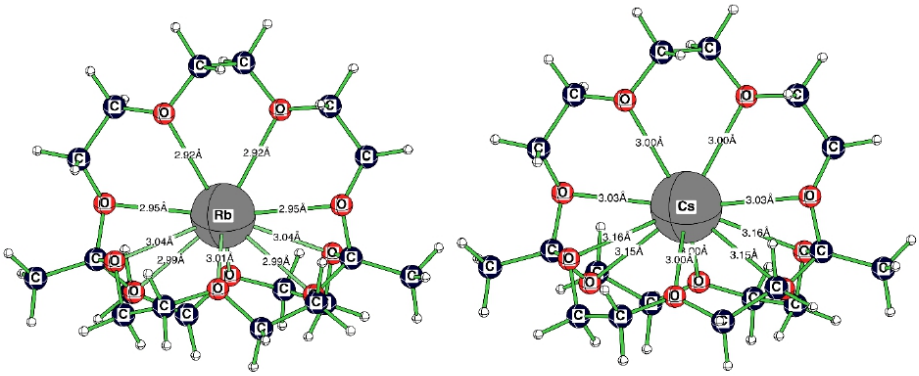

Calculated (B3LYP/LANL2DZp) structure for [Rb$^+$⊂*o*-Me$_2$-2.1.1] (left) and [Cs$^+$⊂*o*-Me$_2$-2.1.1] (right).

S75

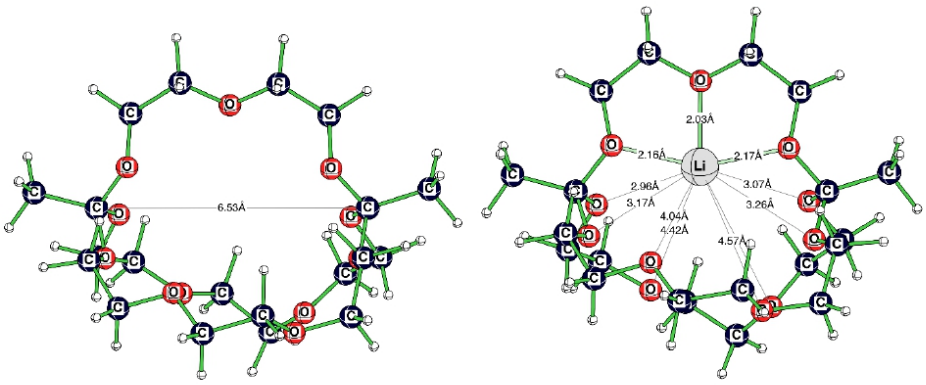

Calculated (B3LYP/LANL2DZp) structure for *o*-Me$_2$-2.2.1 (left) and [Li$^+$⊂*o*-Me$_2$-2.2.1] (right).

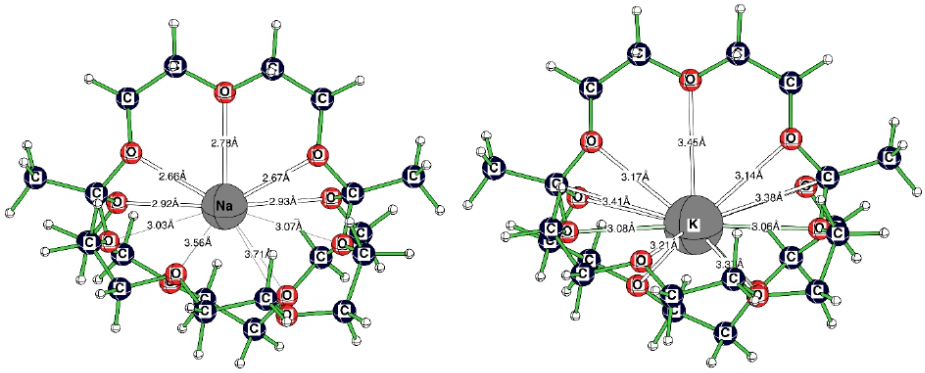

Calculated (B3LYP/LANL2DZp) structure for [Na$^+$⊂*o*-Me$_2$-2.2.1] (left) and [K$^+$⊂*o*-Me$_2$-2.2.1] (right).

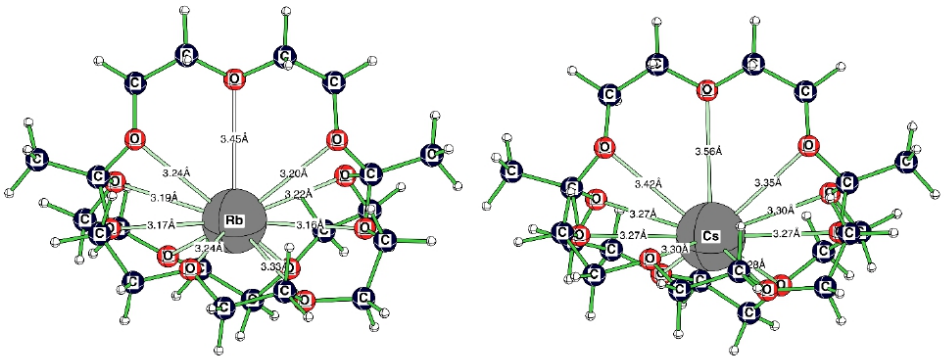

Calculated (B3LYP/LANL2DZp) structure for [Rb$^+$⊂*o*-Me$_2$-2.2.1] (left) and [Cs$^+$⊂*o*-Me$_2$-2.2.1] (right).

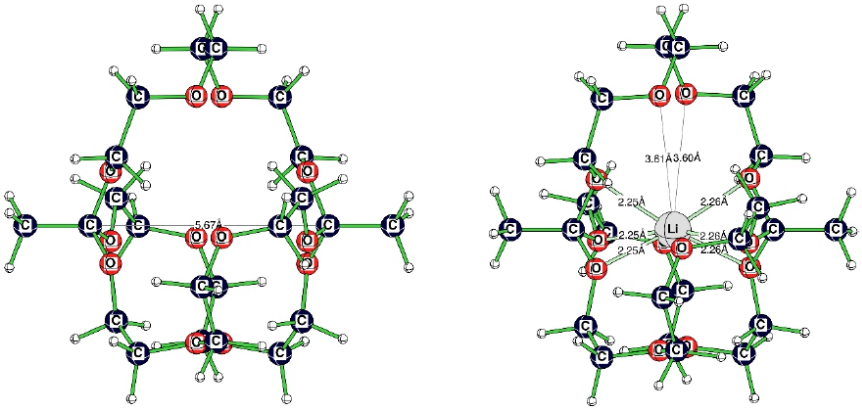

Calculated (B3LYP/LANL2DZp) structure for *o*-Me$_2$-2.2.2 (left) and [Li$^+$⊂*o*-Me$_2$-2.2.2] (right).

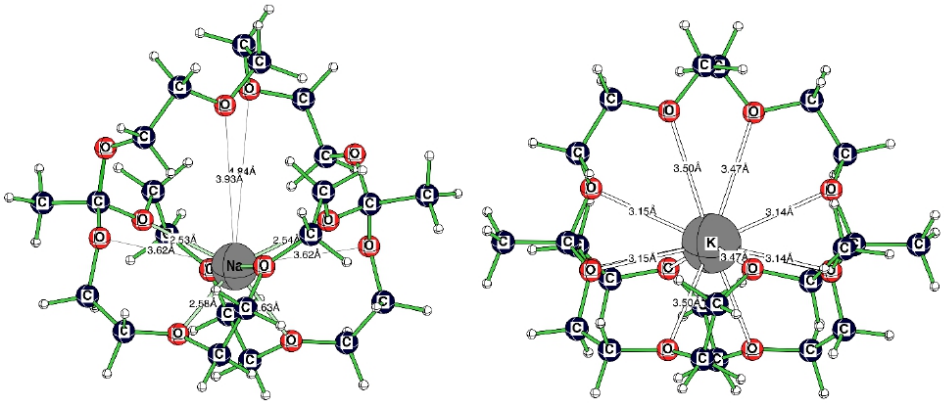

Calculated (B3LYP/LANL2DZp) structure for [Na$^+$⊂*o*-Me$_2$-2.2.2] (left) and [K$^+$⊂*o*-Me$_2$-2.2.2] (right).

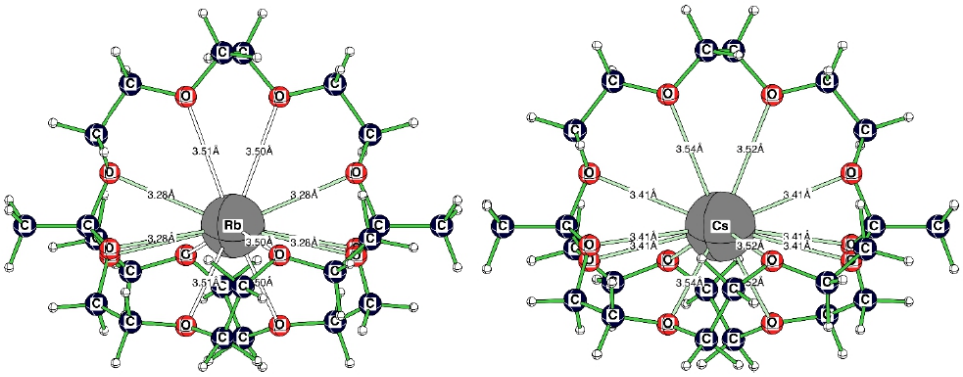

Calculated (B3LYP/LANL2DZp) structure for [Rb$^+$⊂*o*-Me$_2$-2.2.2] (left) and [Cs$^+$⊂*o*-Me$_2$-2.2.2] (right).

S77

8. Experimental Binding Studies

8.1 Results of Experimental Binding Studies

Measured binding constants and calculated ΔG

	LiBArF	NaBArF	KBArF	RbBArF	CsBArF
***o*-Me$_2$-1.1.1**	K_A: 2750 K_2: 10* ΔG_1: -4.685	K_A: 1600 ΔG_1: -4.365	K_A: 35 ΔG_1: -2.103	K_A: 700 ΔG_1: -3.876	K_A: 5 ΔG_1: -0.952
***o*-Me$_2$-2.1.1**	K_A: 60 ΔG_1: -2.422	K_A: 450 ΔG_1: -3.614	K_A: 2500 ΔG_1: -4.629	K_A: 300 ΔG_1: -3.375	K_A: 250 ΔG_1: -3.266
***o*-Me$_2$-2.2.1**	K_A: 45 ΔG_1: -2.252	K_A: 125 ΔG_1: -2.856	K_A: 4365 ΔG_1: -4.959	K_A: 14800 ΔG_1: -5.681	K_A: 19950 ΔG_1: -5.858
***o*-Me$_2$-2.2.2**	K_A: 25 ΔG_1: -1.905	K_A: 30 ΔG_1: -2.012	K_A: 180 ΔG_1: -3.072	K_A: 900 ΔG_1: -4.024	K_A: 1000 ΔG_1: -4.087

K_A=Measured binding constants for 1:1 complexes (M^{-1})

ΔG_1=Calculated Gibbs Free Energy (kcal/mol)

$\Delta G_1 = -RT\ln K_A$ (R= general gas constant = 8.314 J/mol•K; T=Temperature = 298 K)

ΔG_1 were calculated into kcal/mol by multiplicate the value with 0.0002388.

*The fit for the binding constant of Li^+ in o-Me$_2$-1.1.1 was significantly better when the 1:2 complex (one ion:two hosts) was taking into account.

Binding constants for Li^+, Na^+, and K^+ for cryptand o-Me$_2$-1.1.1 was previously published.[11]

8.2 Determination of Binding Constants by NMR Titrations

General procedure for ^{1}H NMR titrations

Molecular sieves were dried by heating for 3 days at 150 °C under reduced pressure (10^{-2} mbar). NMR solvents $CDCl_3$, and CD_3CN were stored over molecular sieves. NMR spectra were recorded on Bruker Avance 400 (^{1}H: 400 MHz) spectrometer at 298 K and referenced to the residual solvent peak (^{1}H: $CDCl_3$, 7.24 ppm; CD_3CN, 1.94 ppm). The cryptands were always freshly prepared as described above (Chapter Synthesis of Cryptands). The precise quantity of cryptand in $CDCl_3$ solution was determined with 1,4-dinitrobenzene as internal standard. For titration experiments a 5 mM cryptand solution was prepared via dilution. $CDCl_3$ was removed under reduced pressure and subsequently replaced by CD_3CN, for titrations in CD_3CN. The concentrations of the titrated salt solutions (LiBArF, NaBArF, KBArF, RbBArF and CsBArF) were 75 mM with 5 mM cryptand added to keep the concentration of the cryptand constant throughout the titration. Binding constants were fitted with HypNMR.

NMR Titration of *o*-Me$_2$-1.1.1 with LiBArF

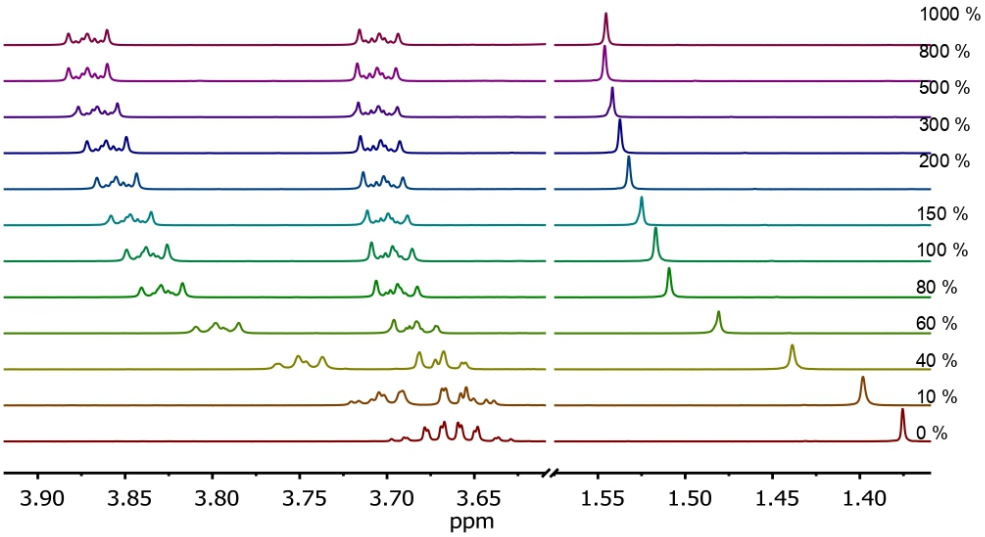

Partial ^{1}H NMR (400 MHz, 298 K, CD_3CN) stack plot of ***o*-Me$_2$-1.1.1** (5 mM) titration with **LiBArF** from 0% - 1000%

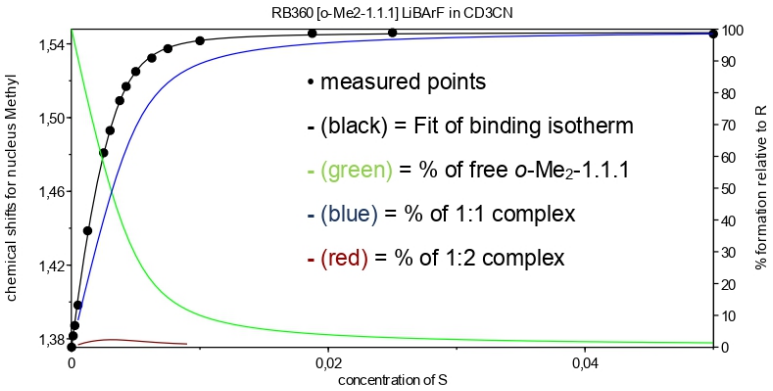

Binding isotherm with plot of different species for titration of ***o*-Me$_2$-1.1.1** (5mM) with **LiBArF** from 0% - 1000% in CD_3CN (below 1% HypNMR does not plot species).

Note: The data on Li^+/***o*-Me$_2$-1.1.1** represents an outlier, because the binding constant is higher than expected (by theory) and observed in chloroform. Also, a 1:2 complex (one ion:two hosts) had to be taken into account for data fitting. An explanation for this behavior is offered in ref. 11.

NMR Titration of *o*-Me$_2$-1.1.1 with NaBArF

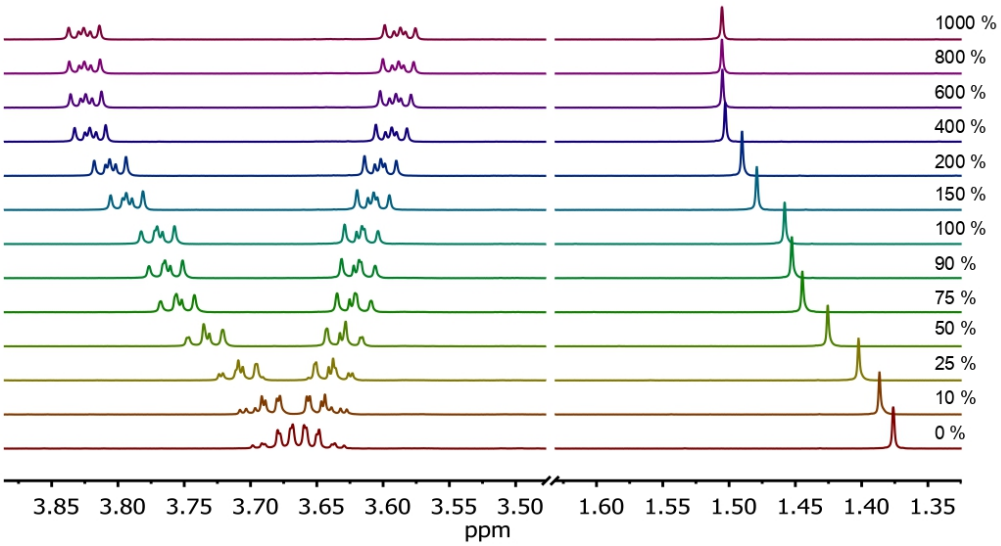

Partial ^{1}H NMR (400 MHz, 298 K, CD_3CN) stack plot of ***o*-Me$_2$-1.1.1** (5 mM) titration with **NaBArF** from 0% - 1000%

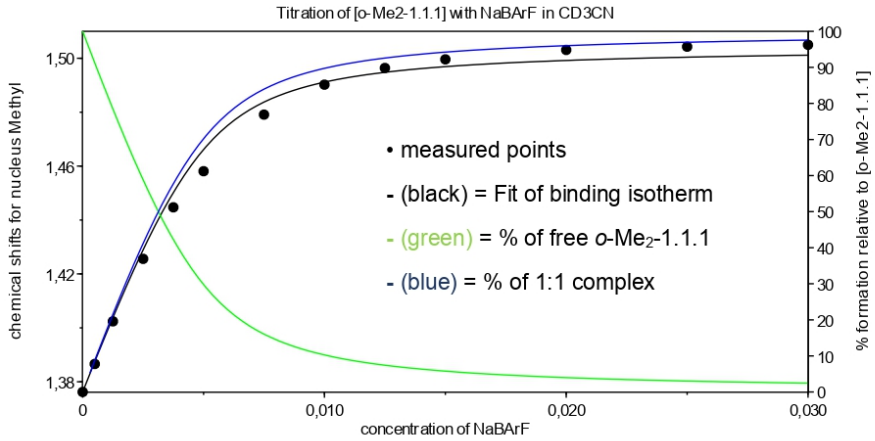

Binding isotherm with plot of different species for titration of ***o*-Me$_2$-1.1.1** (5mM) with **NaBArF** from 0% - 600% in CD_3CN (below 1% HypNMR does not plot species)

NMR Titration of *o*-Me_2-1.1.1 with KBArF

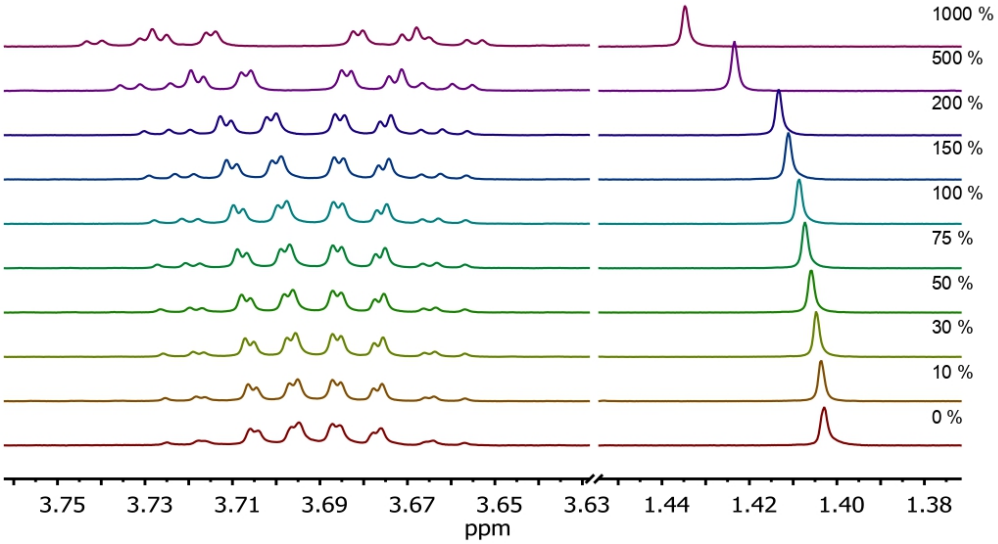

Partial ^{1}H NMR (400 MHz, 298 K, CD_3CN) stack plot of ***o*-Me_2-1.1.1** (5 mM) titration with **KBArF** from 0% - 1000%

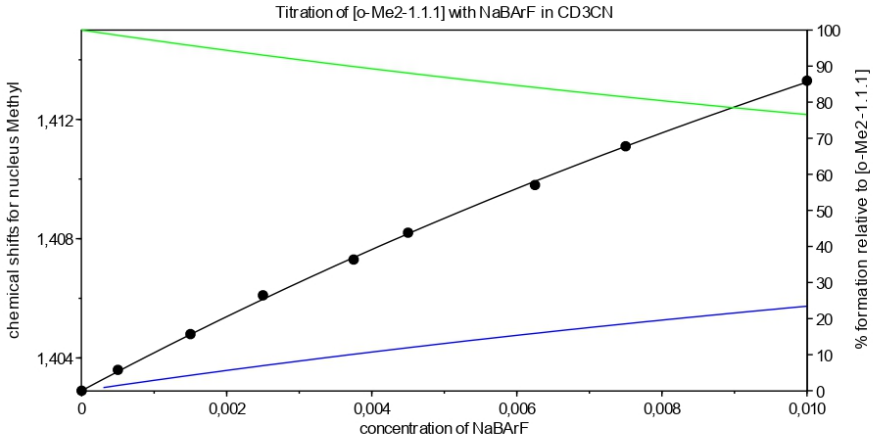

- measured points
- (black) = Fit of binding isotherm
- (green) = % of free *o*-Me_2-1.1.1
- (blue) = % of 1:1 complex

Binding isotherm with plot of different species for titration of ***o*-Me_2-1.1.1** (5mM) with **KBArF** from 0% - 200% in CD_3CN (below 1% HypNMR does not plot species, which is why there is no red line shown)

S81

NMR Titration of *o*-Me_2-1.1.1 with RbBArF

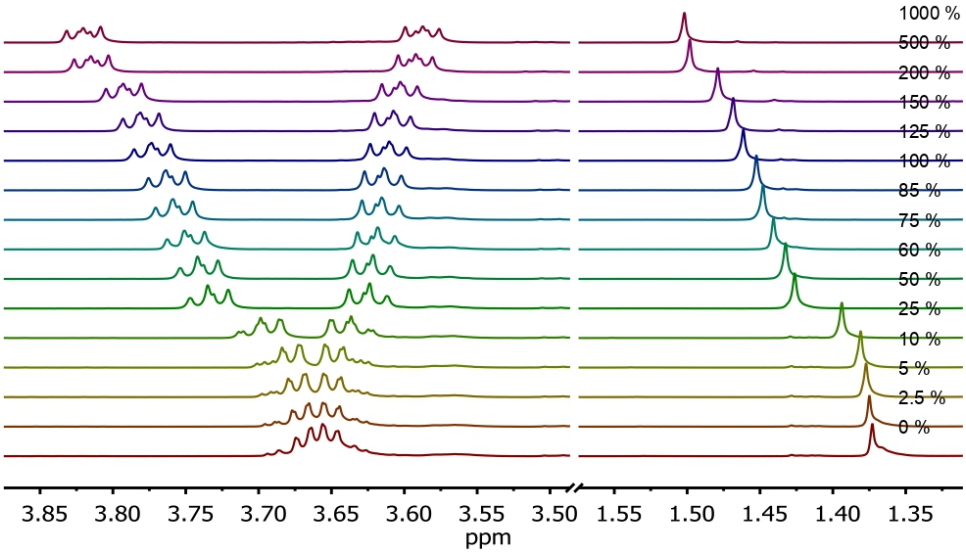

Partial ^{1}H NMR (400 MHz, 298 K, CD_3CN) stack plot of ***o*-Me_2-1.1.1** (5 mM) titration with **RbBArF** from 0% - 1000%

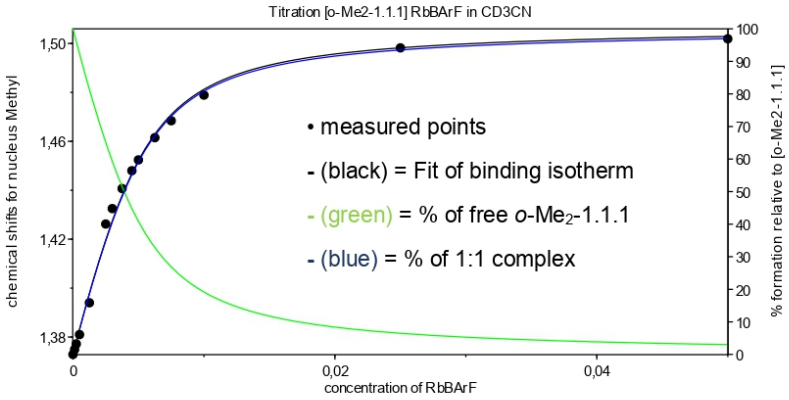

Binding isotherm with plot of different species for titration of ***o*-Me_2-1.1.1** (5mM) with **RbBArF** from 0% - 1000% in CD_3CN (below 1% HypNMR does not plot species).

Note: The NMR titration shows a rigidification of the CH_2 groups of the diethylene glycol chain. This is likely due to "crown ether"-type binding of Rb^+ to ***o*-Me_2-1.1.1**, which would also explain the "outlier" binding constant of 700 M^{-1} (larger than K_A for both K^+ (ion too small for crown ether binding) and Cs^+ (ion too big for crown ether binding).

NMR Titration of *o*-Me$_2$-1.1.1 with CsBArF

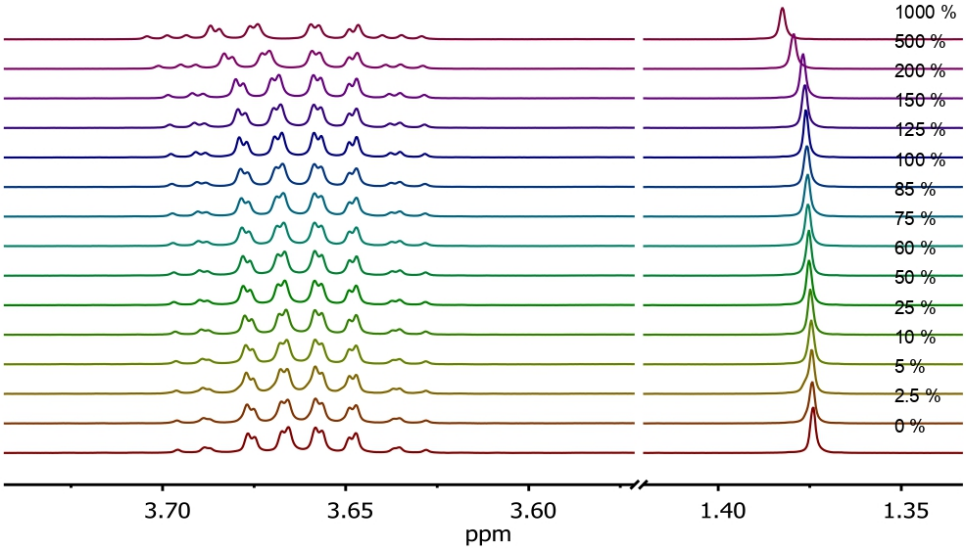

Partial ^{1}H NMR (400 MHz, 298 K, CD_3CN) stack plot of ***o*-Me$_2$-1.1.1** (5 mM) titration with **CsBArF** from 0% - 1000%

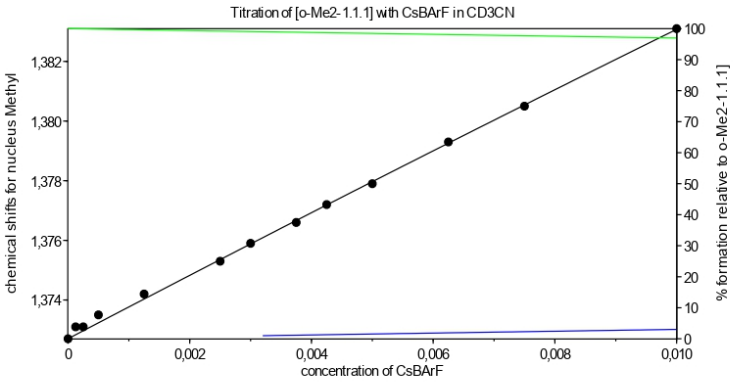

- measured points
- (black) = Fit of binding isotherm
- (green) = % of free *o*-Me$_2$-1.1.1
- (blue) = % of 1:1 complex

Binding isotherm with plot of different species for titration of ***o*-Me$_2$-1.1.1** (5mM) with **CsBArF** from 0% - 200% in CD_3CN (below 1% HypNMR does not plot species)

S83

NMR Titration of *o*-Me$_2$-2.1.1 with LiBArF

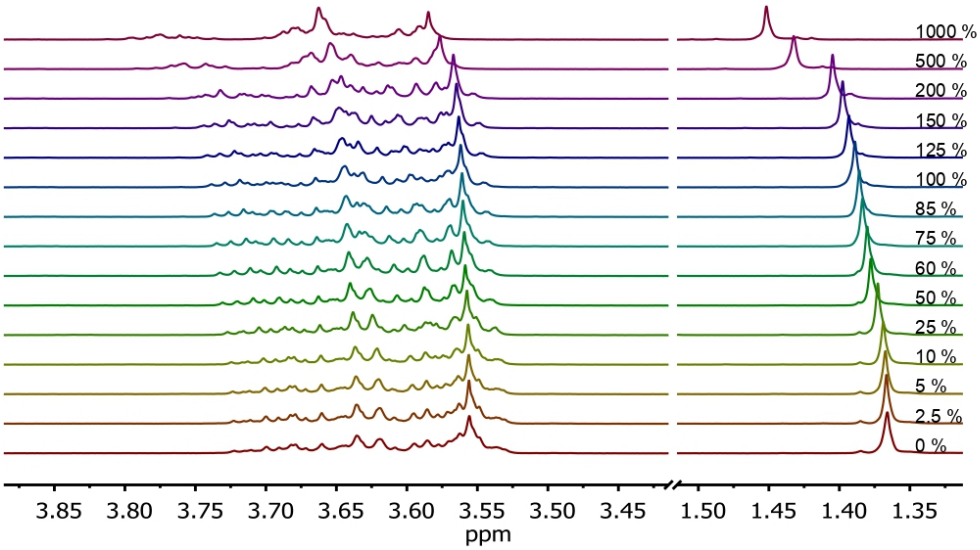

Partial ^{1}H NMR (400 MHz, 298 K, CD_3CN) stack plot of ***o*-Me$_2$-2.1.1** (5 mM) titration with **LiBArF** from 0% - 1000%

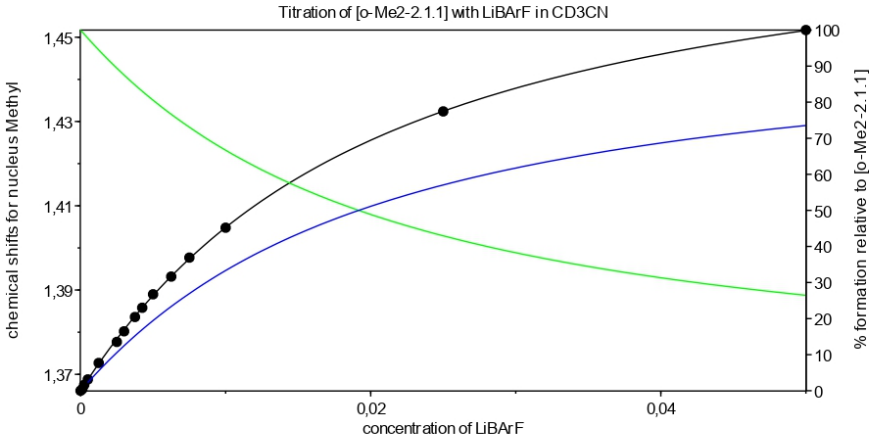

- measured points
- (black) = Fit of binding isotherm
- (green) = % of free *o*-Me$_2$-1.1.1
- (blue) = % of 1:1 complex

Binding isotherm with plot of different species for titration of ***o*-Me$_2$-2.1.1** (5mM) with **LiBArF** from 0% - 1000% in CD_3CN (below 1% HypNMR does not plot species which is why there is no red line shown)

S84

NMR Titration of *o*-Me$_2$-2.1.1 with NaBArF

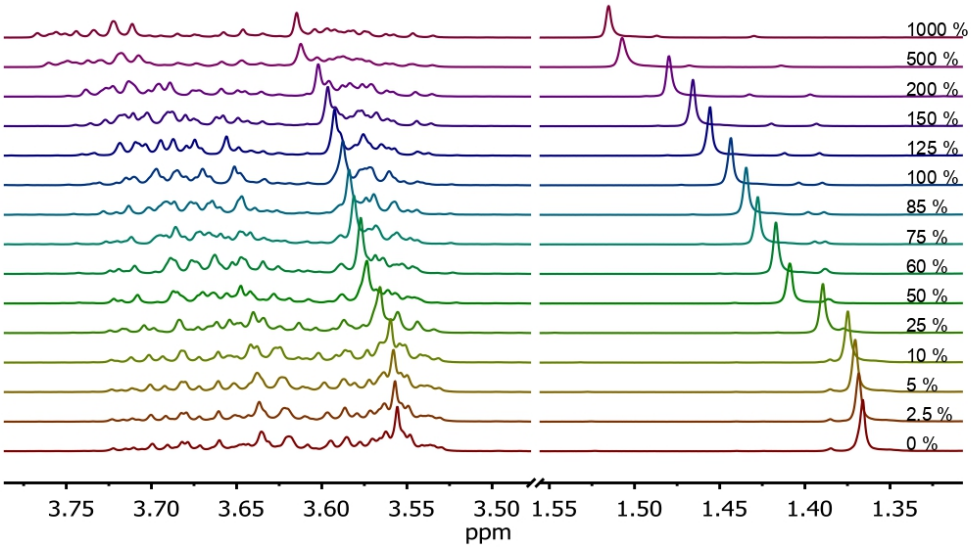

Partial ^{1}H NMR (400 MHz, 298 K, CD_3CN) stack plot of ***o*-Me$_2$-2.1.1** (5 mM) titration with **NaBArF** from 0% - 1000%

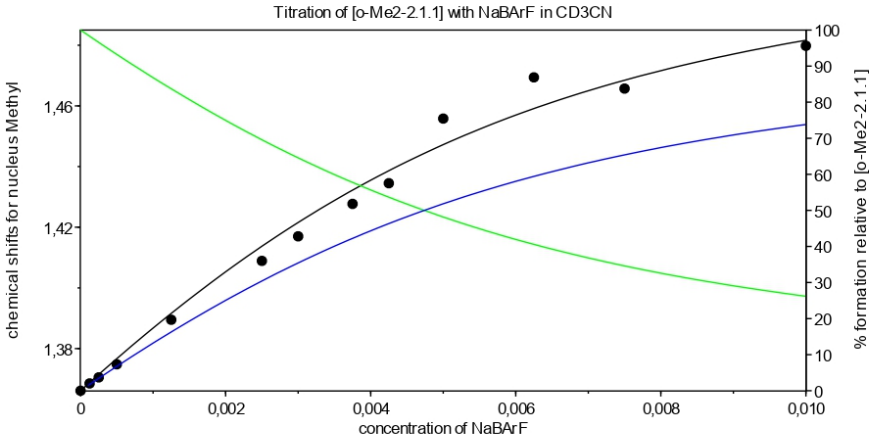

- measured points
- (black) = Fit of binding isotherm
- (green) = % of free *o*-Me$_2$-1.1.1
- (blue) = % of 1:1 complex

Binding isotherm with plot of different species for titration of ***o*-Me$_2$-2.1.1** (5mM) with **NaBArF** from 0% - 200% in CD_3CN.

S85

NMR Titration of *o*-Me$_2$-2.1.1 with KBArF

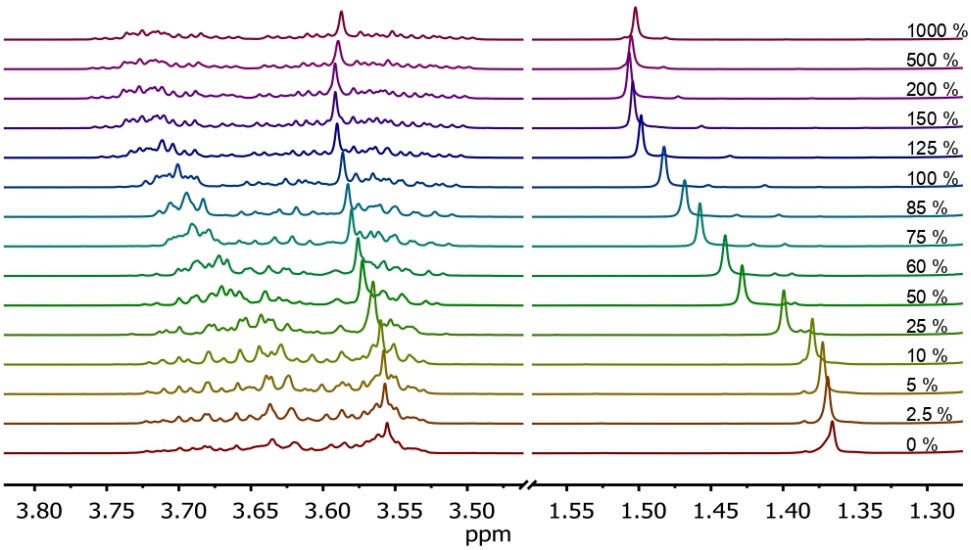

Partial ^{1}H NMR (400 MHz, 298 K, CD_3CN) stack plot of ***o*-Me$_2$-2.1.1** (5 mM) titration with **KBArF** from 0% - 1000%

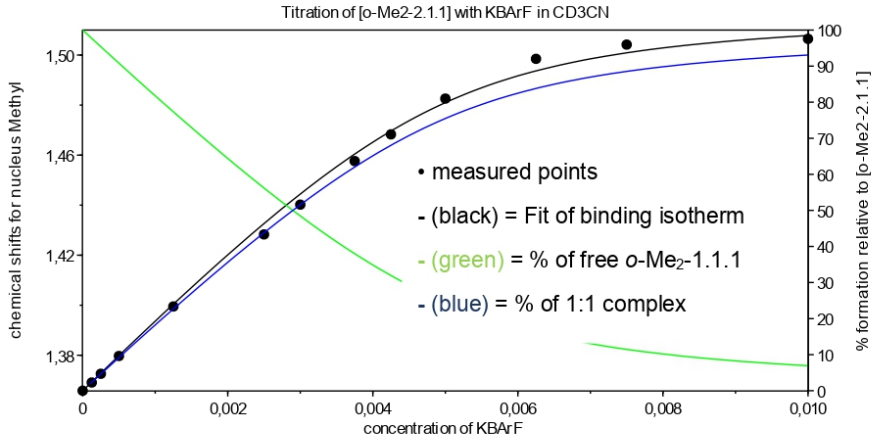

Binding isotherm with plot of different species for titration of ***o*-Me$_2$-2.1.1** (5mM) with **KBArF** from 0% - 1000% in CD_3CN.

S86

NMR Titration of *o*-Me$_2$-2.1.1 with RbBArF

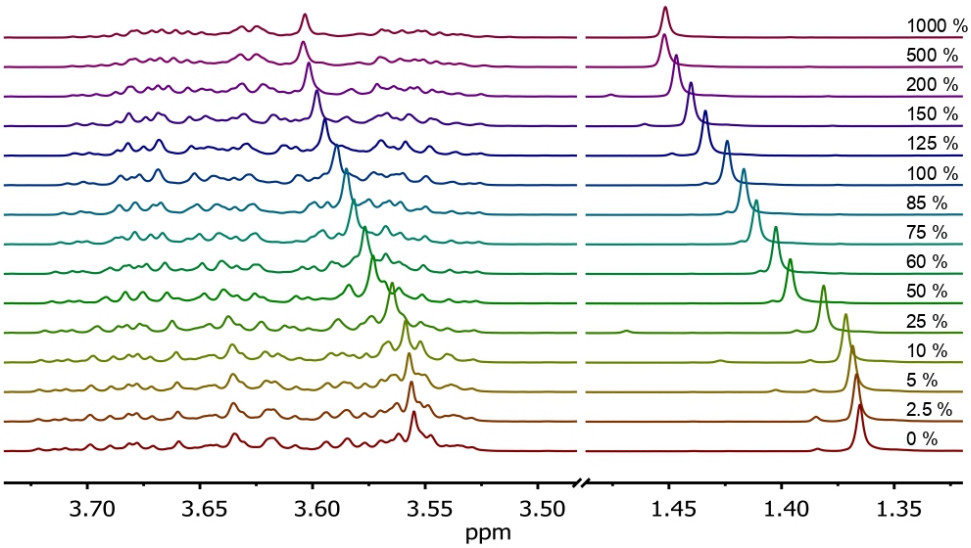

Partial ^{1}H NMR (400 MHz, 298 K, CD_3CN) stack plot of ***o*-Me$_2$-2.1.1** (5 mM) titration with **RbBArF** from 0% - 1000%

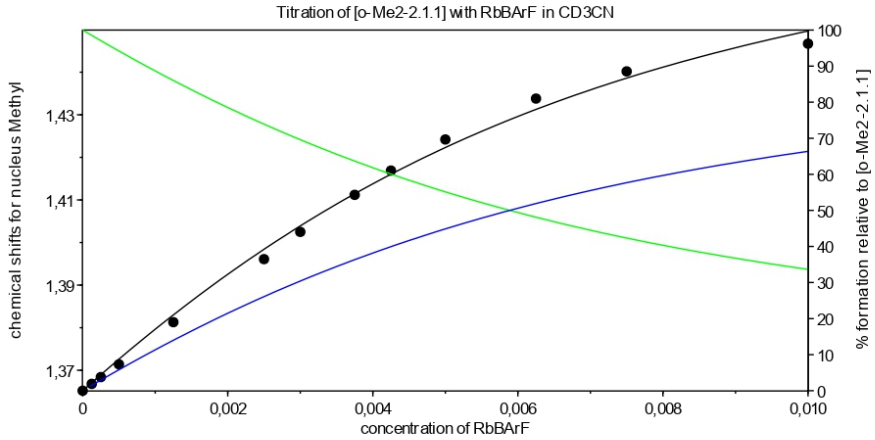

- measured points
- (black) = Fit of binding isotherm
- (green) = % of free *o*-Me$_2$-1.1.1
- (blue) = % of 1:1 complex

Binding isotherm with plot of different species for titration of ***o*-Me$_2$-2.1.1** (5mM) with **RbBArF** from 0% - 200% in CD_3CN.

S87

NMR Titration of *o*-Me$_2$-2.1.1 with CsBArF

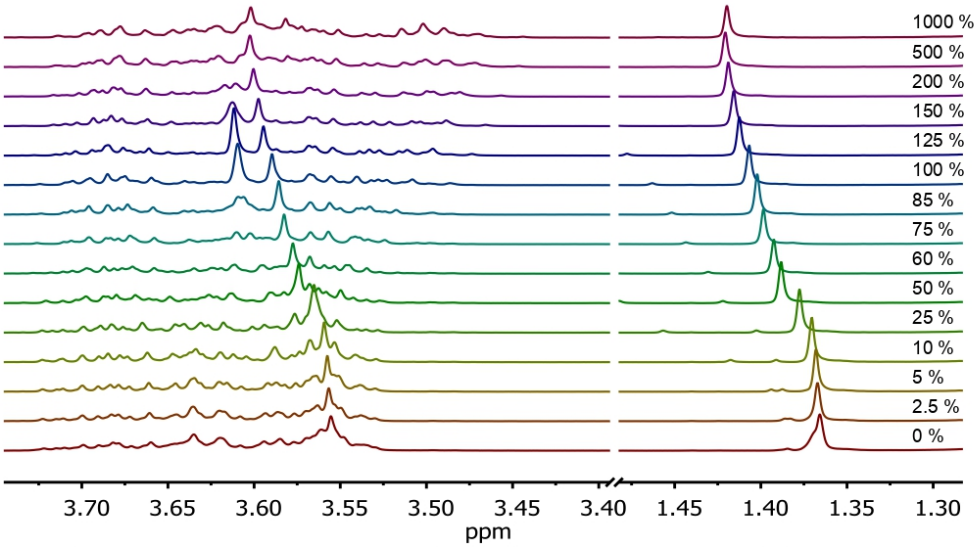

Partial ^{1}H NMR (400 MHz, 298 K, CD_3CN) stack plot of ***o*-Me$_2$-2.1.1** (5 mM) titration with **CsBArF** from 0% - 1000%

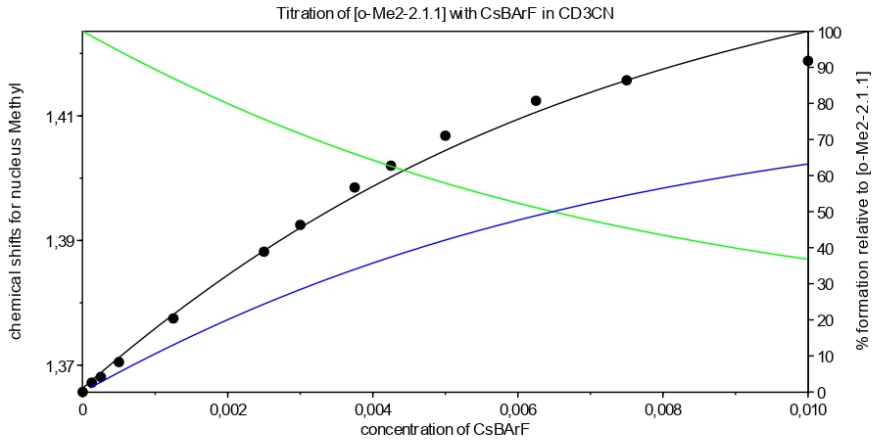

• measured points

- (black) = Fit of binding isotherm

- (green) = % of free *o*-Me$_2$-1.1.1

- (blue) = % of 1:1 complex

Binding isotherm with plot of different species for titration of ***o*-Me$_2$-2.1.1** (5mM) with **CsBArF** from 0% - 200% in CD_3CN.

S88

NMR Titration of *o*-Me$_2$-2.2.1 with LiBArF

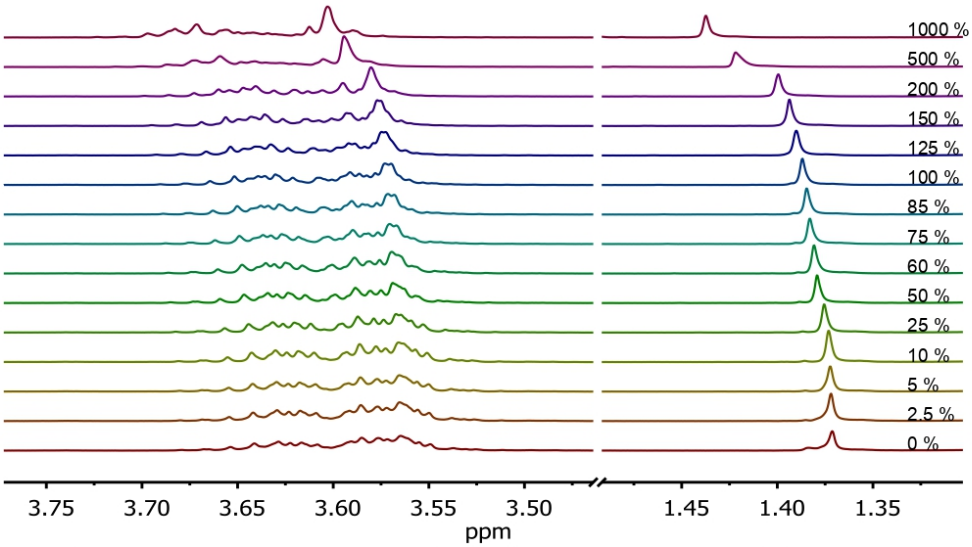

Partial ^{1}H NMR (400 MHz, 298 K, CD_3CN) stack plot of ***o*-Me$_2$-2.2.1** (5 mM) titration with **LiBArF** from 0% - 1000%

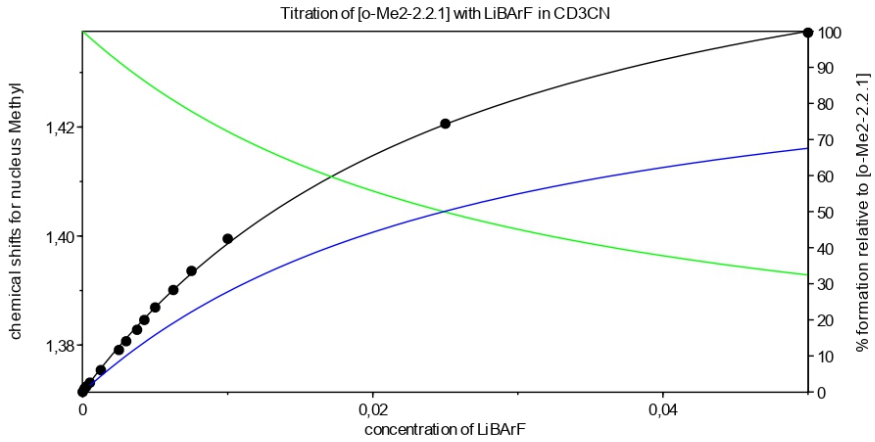

• measured points

- (black) = Fit of binding isotherm

- (green) = % of free *o*-Me$_2$-1.1.1

- (blue) = % of 1:1 complex

Binding isotherm with plot of different species for titration of ***o*-Me$_2$-2.2.1** (5mM) with **LiBArF** from 0% - 1000% in CD_3CN.

S89

NMR Titration of *o*-Me$_2$-2.2.1 with NaBArF

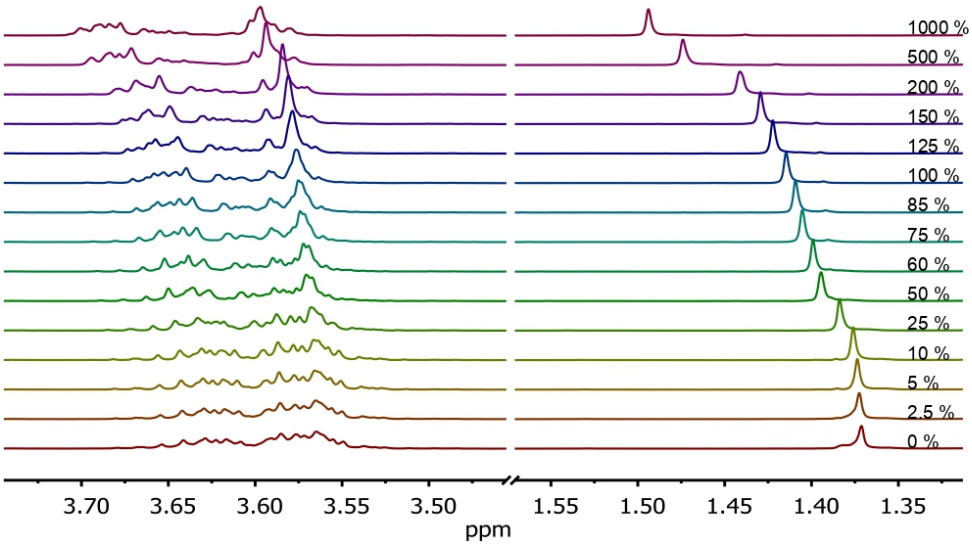

Partial ^{1}H NMR (400 MHz, 298 K, CD_3CN) stack plot of ***o*-Me$_2$-2.2.1** (5 mM) titration with **NaBArF** from 0% - 1000%

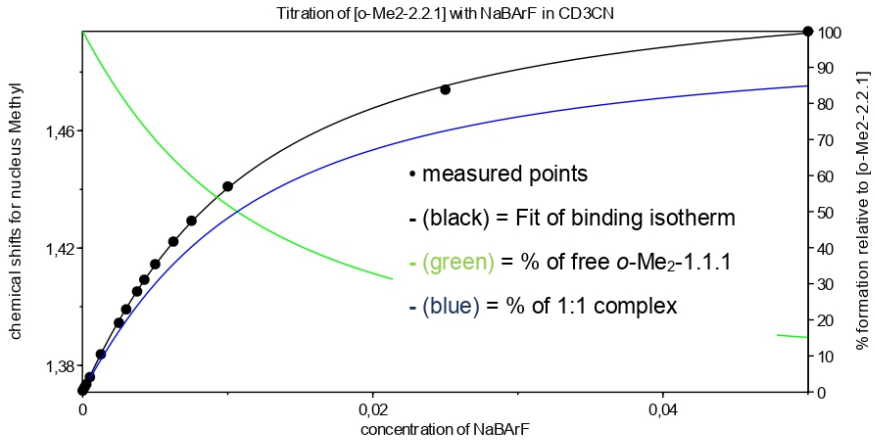

Binding isotherm with plot of different species for titration of ***o*-Me$_2$-2.2.1** (5mM) with **NaBArF** from 0% - 1000% in CD_3CN.

NMR Titration of *o*-Me$_2$-2.2.1 with KBArF

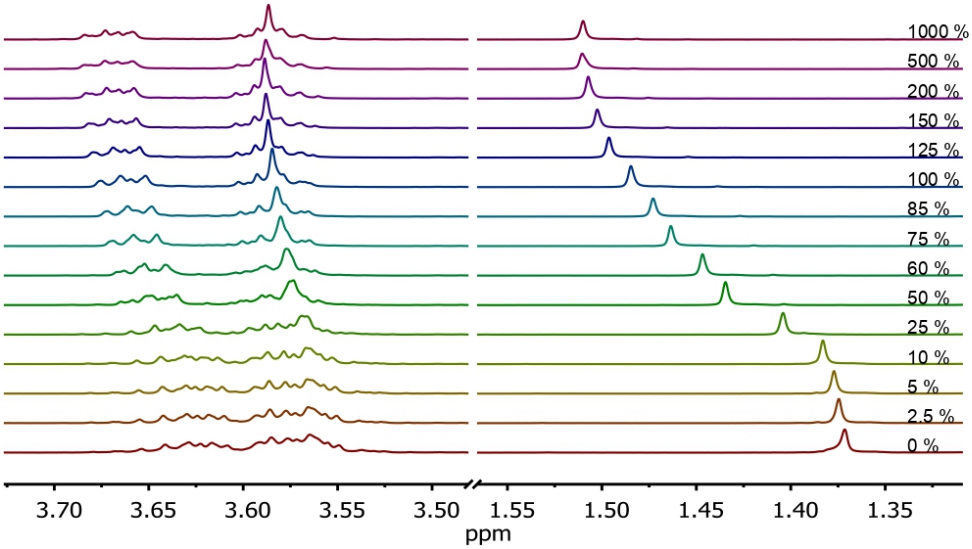

Partial ^{1}H NMR (400 MHz, 298 K, CD_3CN) stack plot of ***o*-Me$_2$-2.2.1** (5 mM) titration with **KBArF** from 0% - 1000%

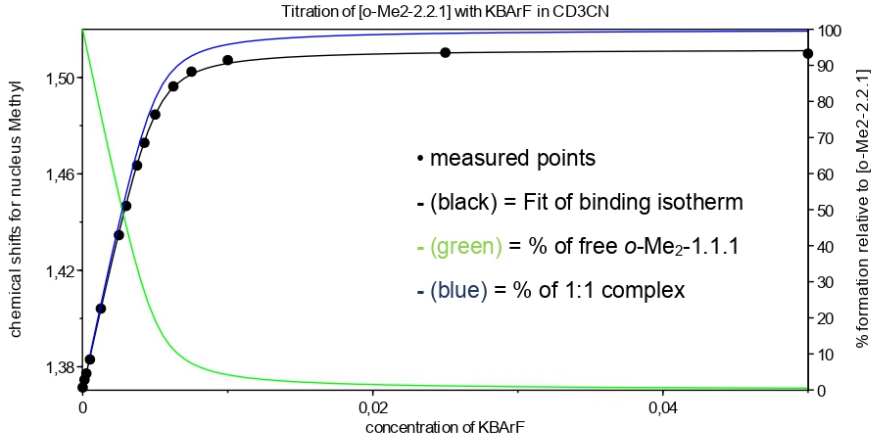

Binding isotherm with plot of different species for titration of ***o*-Me$_2$-2.2.1** (5mM) with **KBArF** from 0% - 1000% in CD_3CN.

S91

NMR Titration of *o*-Me$_2$-2.2.1 with RbBArF

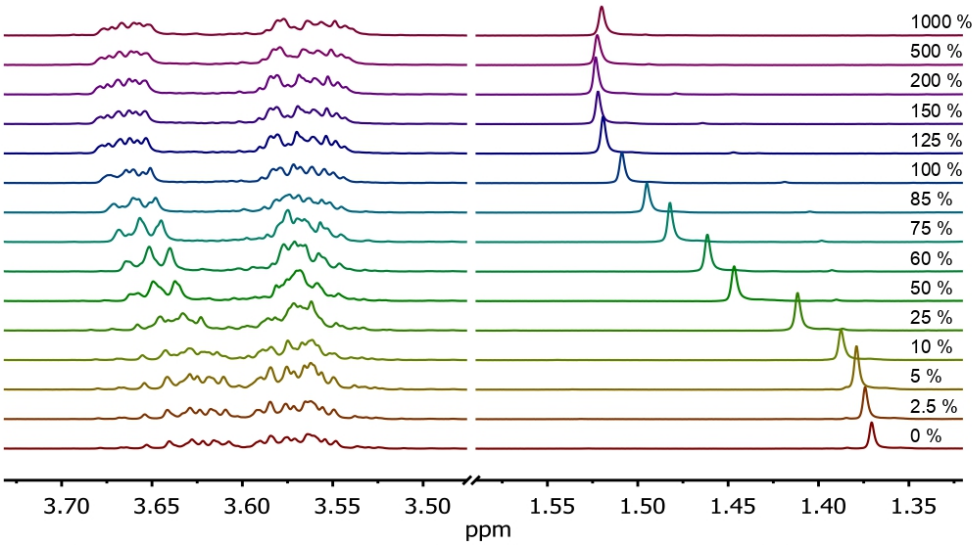

Partial ^{1}H NMR (400 MHz, 298 K, CD_3CN) stack plot of ***o*-Me$_2$-2.2.1** (5 mM) titration with **RbBArF** from 0% - 1000%

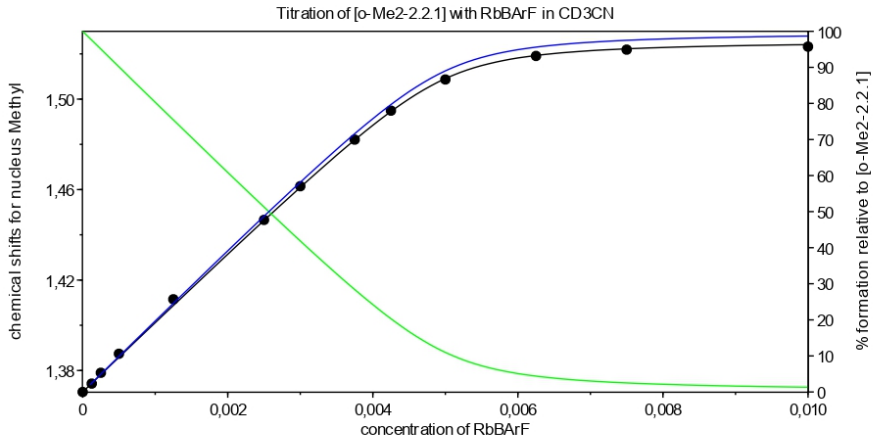

• measured points

- (black) = Fit of binding isotherm

- (green) = % of free *o*-Me$_2$-1.1.1

- (blue) = % of 1:1 complex

Binding isotherm with plot of different species for titration of ***o*-Me$_2$-2.2.1** (5mM) with **RbBArF** from 0% - 200% in CD_3CN.

S92

NMR Titration of *o*-Me$_2$-2.2.1 with CsBArF

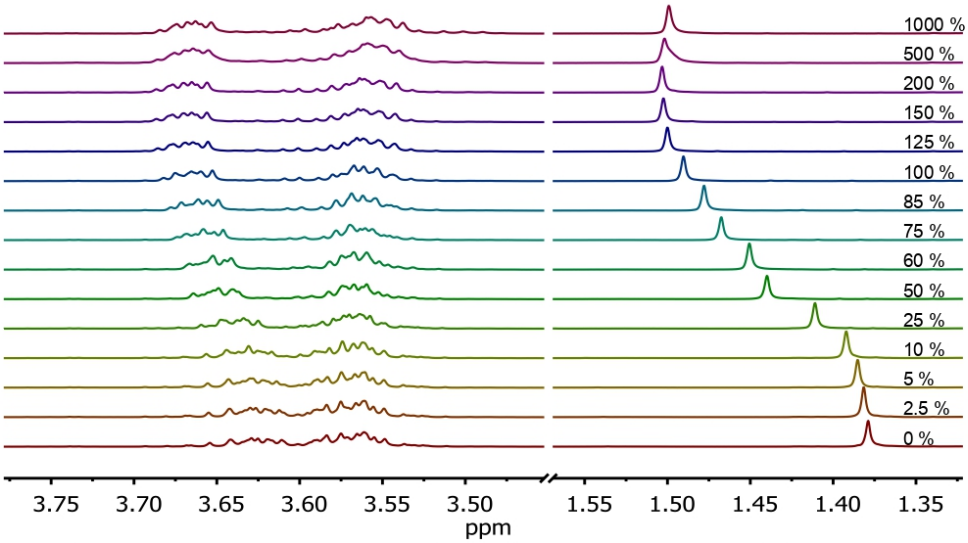

Partial ^{1}H NMR (400 MHz, 298 K, CD_3CN) stack plot of ***o*-Me$_2$-2.2.1** (5 mM) titration with **CsBArF** from 0% - 1000%

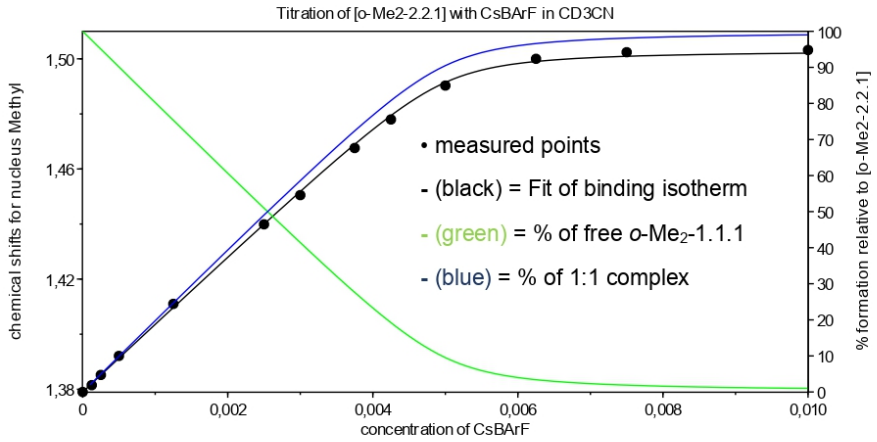

Binding isotherm with plot of different species for titration of ***o*-Me$_2$-2.2.1** (5mM) with **CsBArF** from 0% - 200% in CD_3CN.

S93

NMR Titration of *o*-Me$_2$-2.2.2 with LiBArF

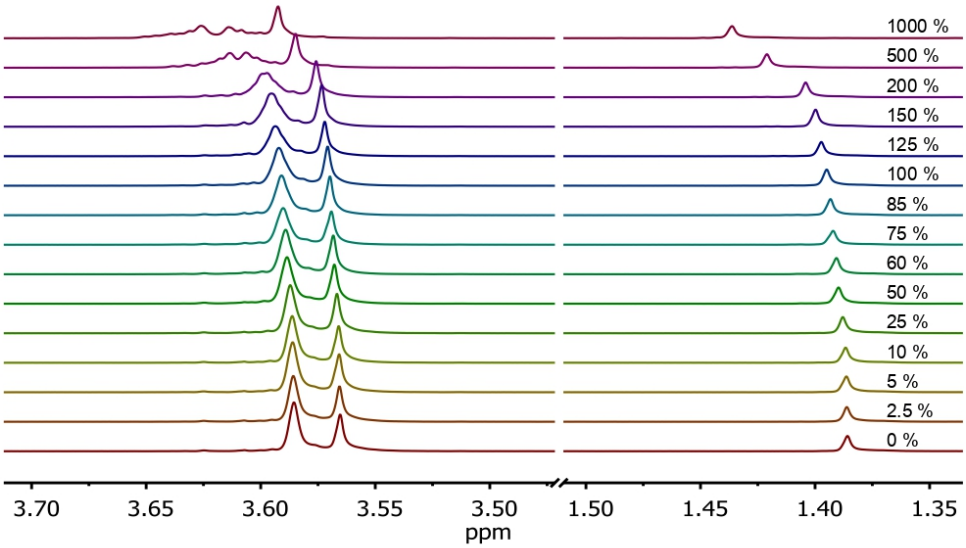

Partial ^{1}H NMR (400 MHz, 298 K, CD_3CN) stack plot of ***o*-Me$_2$-2.2.2** (5 mM) titration with **LiBArF** from 0% - 1000%

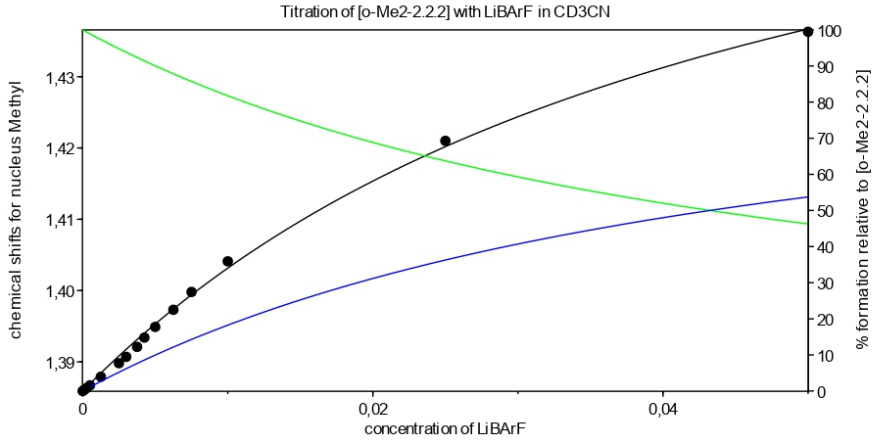

- measured points
- (black) = Fit of binding isotherm
- (green) = % of free *o*-Me$_2$-1.1.1
- (blue) = % of 1:1 complex

Binding isotherm with plot of different species for titration of ***o*-Me$_2$-2.2.2** (5mM) with **NaBArF** from 0% - 1000% in CD_3CN.

S94

NMR Titration of *o*-Me$_2$-2.2.2 with NaBArF

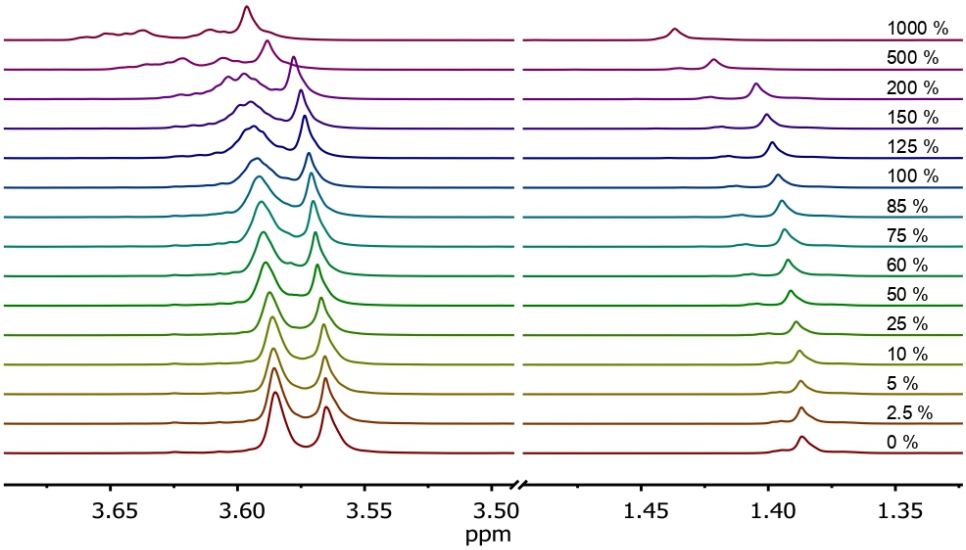

Partial ^{1}H NMR (400 MHz, 298 K, CD_3CN) stack plot of ***o*-Me$_2$-2.2.2** (5 mM) titration with **NaBArF** from 0% - 1000%

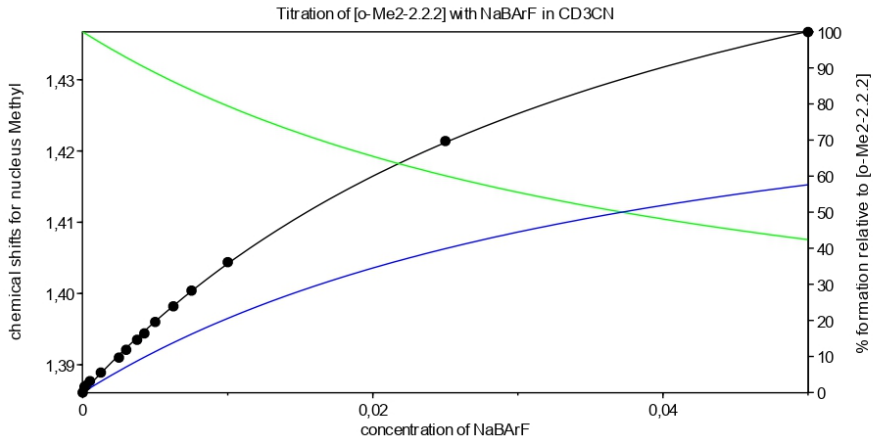

- measured points
- (black) = Fit of binding isotherm
- (green) = % of free *o*-Me$_2$-1.1.1
- (blue) = % of 1:1 complex

Binding isotherm with plot of different species for titration of ***o*-Me$_2$-2.2.2** (5mM) with **NaBArF** from 0% - 1000% in CD_3CN.

S95

NMR Titration of *o*-Me_2-2.2.2 with KBArF

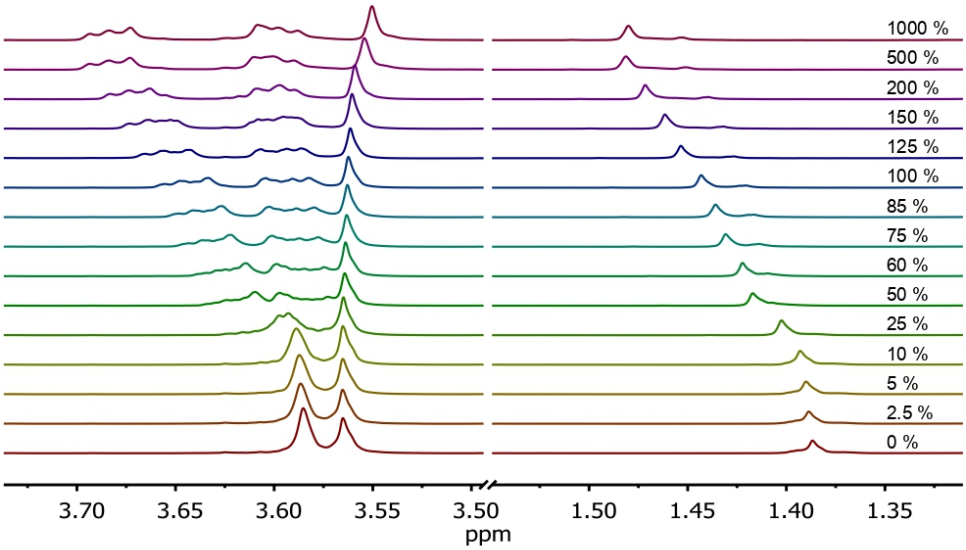

Partial ^{1}H NMR (400 MHz, 298 K, CD_3CN) stack plot of ***o*-Me_2-2.2.2** (5 mM) titration with **KBArF** from 0% - 1000%

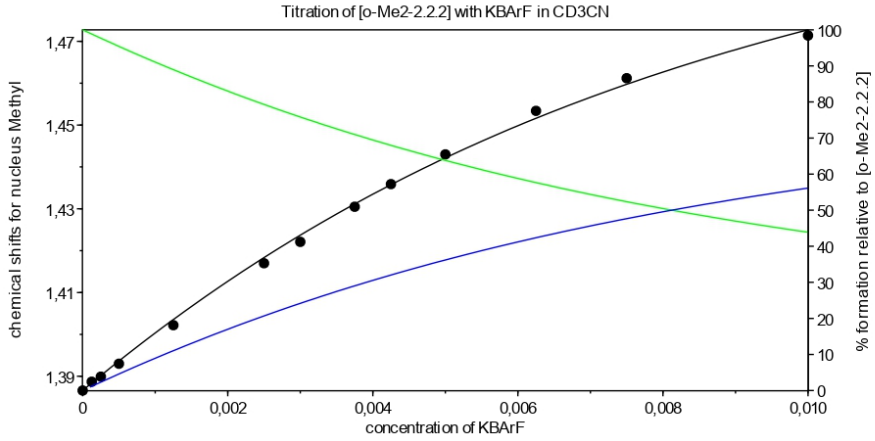

- measured points
- (black) = Fit of binding isotherm
- (green) = % of free *o*-Me_2-1.1.1
- (blue) = % of 1:1 complex

Binding isotherm with plot of different species for titration of ***o*-Me_2-2.2.2** (5mM) with **KBArF** from 0% - 200% in CD_3CN.

S96

NMR Titration of *o*-Me$_2$-2.2.2 with RbBArF

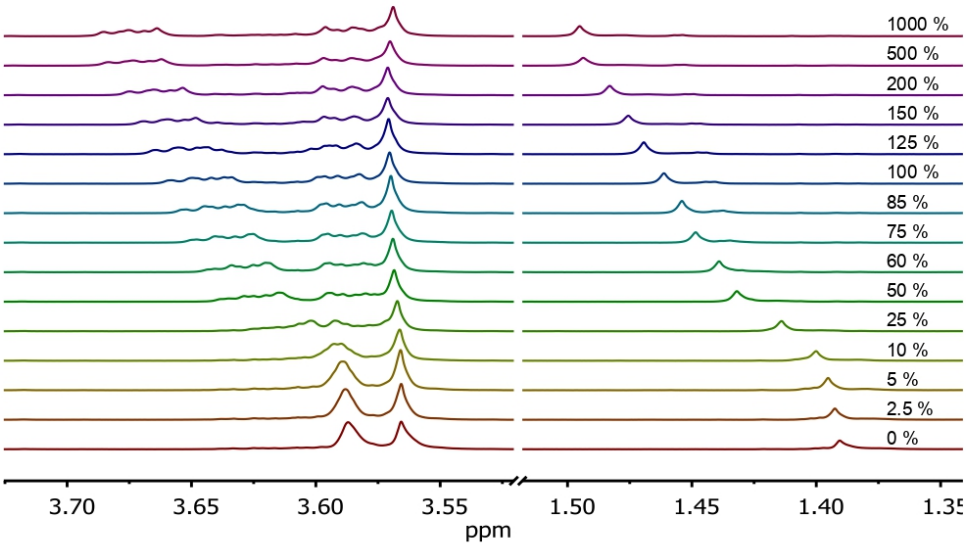

Partial ^{1}H NMR (400 MHz, 298 K, CD_3CN) stack plot of ***o*-Me$_2$-2.2.2** (5 mM) titration with **RbBArF** from 0% - 1000%

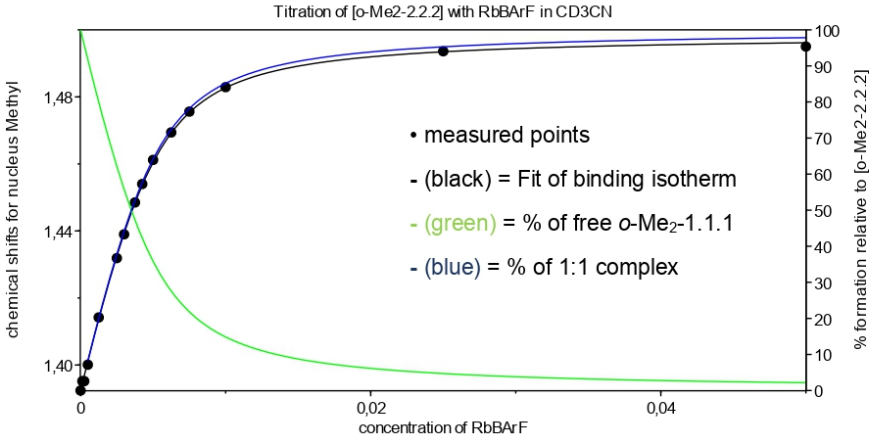

Binding isotherm with plot of different species for titration of ***o*-Me$_2$-2.2.2** (5mM) with **RbBArF** from 0% - 1000% in CD_3CN.

S97

NMR Titration of *o*-Me$_2$-2.2.2 with CsBArF

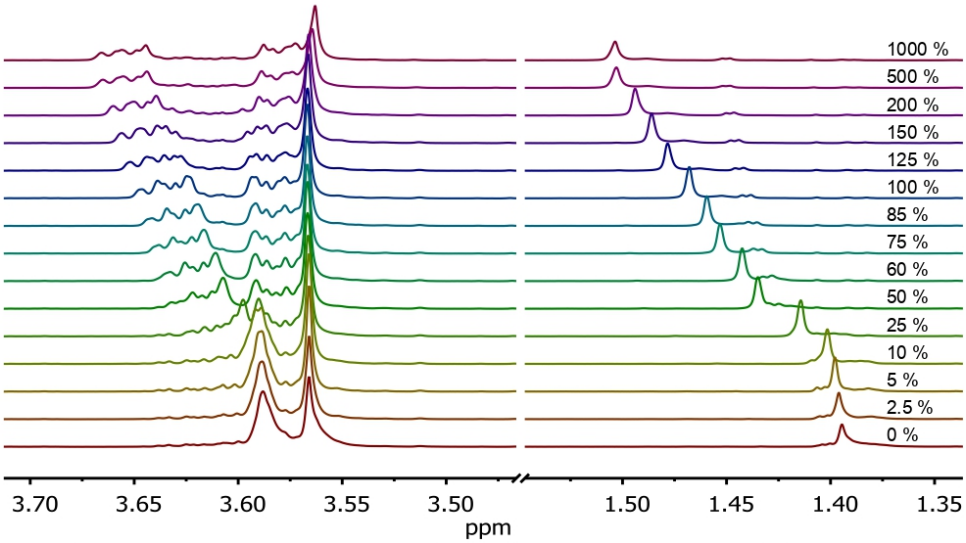

Partial ^{1}H NMR (400 MHz, 298 K, CD_3CN) stack plot of ***o*-Me$_2$-2.2.2** (5 mM) titration with **CsBArF** from 0% - 1000%

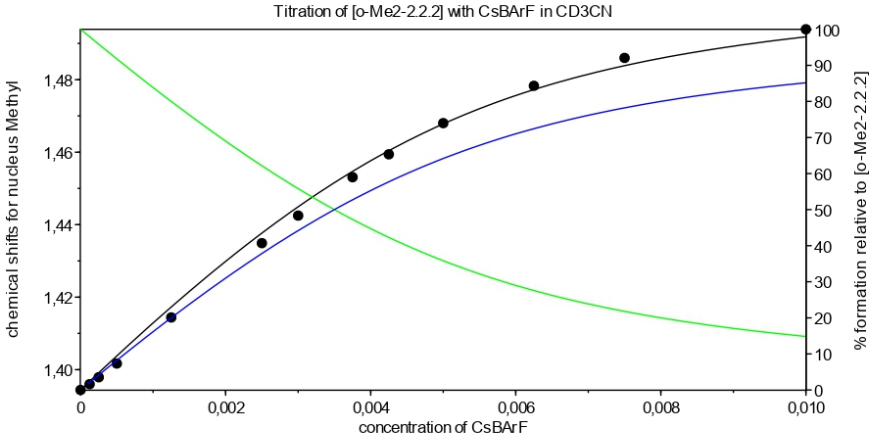

• measured points

- (black) = Fit of binding isotherm

- (green) = % of free *o*-Me$_2$-1.1.1

- (blue) = % of 1:1 complex

Binding isotherm with plot of different species for titration of ***o*-Me$_2$-2.2.2** (5mM) with **NaBArF** from 0% - 1000% in CD_3CN.

S98

8.2 ITC Titration

Heat flow measurements were performed at 25 °C using a TAM III thermostat (TA Instruments) that is equipped with a nanocalorimeter (TA Instruments) as a highly sensitive calorimetric system. For all investigations, 4 mL titration and reference vials made of stainless steel were used. All investigations were done in acetonitrile (HPLC grade). For the measurement, 24 aliquots with a volume of 20 µL 30 mM NaBArF solution were injected from a 500 µL Hamilton glass syringe into a solution of 5 mM o-Me2-1.1.1 of 700 µL starting volume. The interval time between consecutive injections was set in each experiment to 60 min in order to reach an equilibrium state after every titration step. The titration vial was stirred continuously at 100 rpm, and measurements were started when background fluctuations were below the limit of 300 ± 50 nW h^{-1}. Contributions from dilution effects were subtracted through analogous control experiments. Throughout all experiments, the reference vial was filled with 940 µL of acetonitrile to address for the heat capacity of the sample. The measurements were analyzed with NanoAnalyze Data Analysis from TA Instruments.

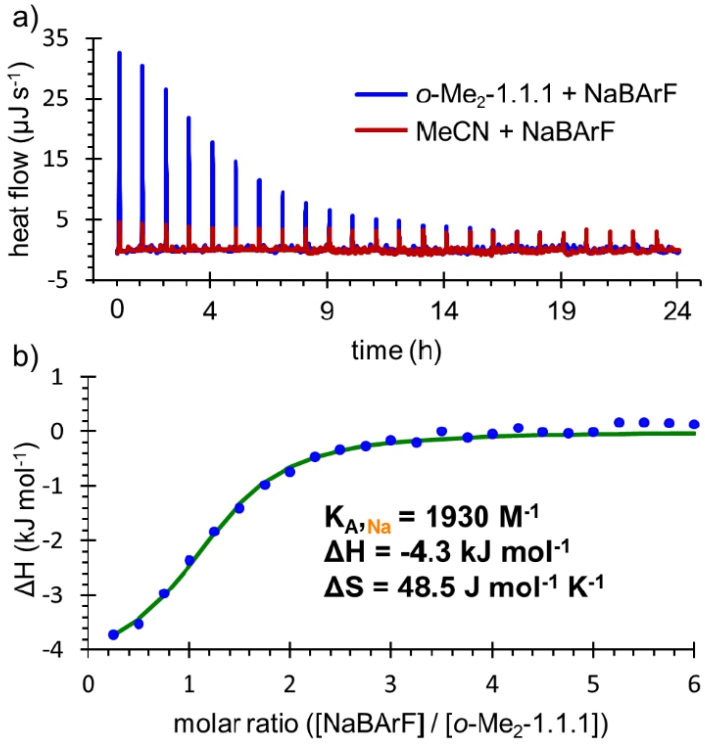

(a) Heat flow of ITC measurement. Titration of NaBArF into *o*-Me_2-1.1.1 solution (blue line) and reference experiment titration of NaBArF into pure MeCN (red line). (b) ITC results after the stepwise addition of NaBArF to a solution of *o*-Me_2-1.1.1 in MeCN at 298 K (green line shows fitting to a 1:1 binding model.

S99

9. References

[1] Y. Hayashi, J. J. Rohde, E. J. Corey *J. Am. Chem. Soc.* **1996**, *118*, 5502-5503.
[2] R. Brachvogel, F. Hampel, M. von Delius *Nat. Comm.*, **2015**, *6*, 7129.
[3] L. Fieser, M. Fieser *Reagents for Organic Synthesis Vol. 1*, Wiley, New York, **1967**, pp. 581-595.
[4] (a) A. D. Becke. *J. Phys. Chem*., **1993**, *97*, 5648. (b) C. Lee, W. Yang, R. G. Parr. *Phys. Rev. B: Condens. Matter*, **1988**, *37*, 785. (c) P. J. Stephens, F. J. Devlin, C. F. Chabalowski, M. J. Frisch. *J. Phys. Chem*., **1994**, *98*, 11623.
[5] (a) T.H. Dunning Jr, P.J. Hay. In *Modern Theoretical Chemistry: Methods of Electronic Structure Theory*, H.F. Schaefer III (Ed.), Chap. 1, Vol. 3, Plenum, New York, **1977**; (b) P.J. Hay, W.R. Wadt. *J. Chem. Phys*., **1985**, *82*, 270; (c) P.J. Hay, W.R. Wadt. *J. Chem. Phys*., **1985**, *82*, 284; (d) P.J. Hay, W.R. Wadt. *J. Chem.Phys*., **1985**, *82*, 299.
[6] S. Huzinaga (Ed.), Gaussian Basis Sets for Molecular, Elsevier, Amsterdam, **1984**.
[7] See e.g.: (a) S. Klaus, H. Neumann, H. Jiao, A. Jacobi von Wangelin, D. Gördes, D. Strübing, S. Hübner, M. Hately, C. Weckbecker, K. Huthmacher, T. Riermeier, M. Beller. J. Organomet. Chem., **2004**, *689*, 3685; (b) R. W. Saalfrank, C. Deutscher, H. Maid, A. M. Ako, S. Sperner, T. Nakajima, W. Bauer, F. Hampel, B. A. Heß, N. J. R. van Eikema Hommes, R. Puchta, F. W. Heinemann. Chem. Eur. J., **2004**, *10*, 1899; (c) P. Illner, A. Zahl, R. Puchta, N. J. R. van Eikema Hommes, P. Wasserscheid, R. van Eldik. J. Organomet. Chem., **2005**, *690*, 3567; (d) A. Scheurer, H. Maid, F. Hampel, R. W. Saalfrank, L. Toupet, P. Mosset, R. Puchta, N. J. R. van Eikema Hommes. Eur. J. Org. Chem., **2005**, 2566; (e) A. Scheurer, R. Puchta, F. Hampel. J. Coord. Chem., **2010**, *63*, 2868. (f) M. Walther, B. M. Alzubi, R. Puchta, G. Linti, R. Meier, R. van Eldik. J. Coord. Chem., **2011**, *64*, 18 and references cited therein.
[8] Gaussian 09, Revision C.01, M. J. Frisch, G. W. Trucks, H. B. Schlegel, G. E. Scuseria, M. A. Robb, J. R. Cheeseman, G. Scalmani, V. Barone, B. Mennucci, G. A. Petersson, H. Nakatsuji, M. Caricato, X. Li, H. P. Hratchian, A. F. Izmaylov, J. Bloino, G. Zheng, J. L. Sonnenberg, M. Hada, M. Ehara, K. Toyota, R. Fukuda, J. Hasegawa, M. Ishida, T. Nakajima, Y. Honda, O. Kitao, H. Nakai, T. Vreven, J. A. Montgomery, Jr., J. E. Peralta, F. Ogliaro, M. Bearpark, J. J. Heyd, E. Brothers, K. N. Kudin, V. N. Staroverov, T. Keith, R. Kobayashi, J. Normand, K. Raghavachari, A. Rendell, J. C. Burant, S. S. Iyengar, J. Tomasi, M. Cossi, N. Rega, J. M. Millam, M. Klene, J. E. Knox, J. B. Cross, V. Bakken, C. Adamo, J. Jaramillo, R. Gomperts, R. E. Stratmann, O. Yazyev, A. J. Austin, R. Cammi, C. Pomelli, J. W. Ochterski, R. L. Martin, K. Morokuma, V. G. Zakrzewski, G. A. Voth, P. Salvador, J. J. Dannenberg, S. Dapprich, A. D. Daniels, O. Farkas, J. B. Foresman, J. V. Ortiz, J. Cioslowski, and D. J. Fox, Gaussian, Inc., Wallingford CT, **2010**.
[9] R. Puchta, M. Galle, N. van Eikema Hommes, E. Pasgreta, R. van Eldik, *Inorg. Chem*. **2004**, *43*, 8227 and references cited therein.
[10] (a) S. Begel, A. Scheurer, R. Puchta, *J. Coord. Chem*. **2015**, *68*, 3374. (b) S. Begel, A. Scheurer, R. Puchta, R. van Eldik *Z. Anorg. Allg. Chem*. **2016**, *642*, 395 and references cited therein.
[11] R.-C. Brachvogel, H. Maid, M. von Delius, Int. J. Mol. Sci. **2015**, *16*, 20641-20656.

4.2 Ammonium Complexes of Orthoester Cryptands are Inherently Dynamic and Adaptive

Xiang Wang, Oleksandr Shyshov, Marko Hanževački, Christof M. Jäger, and Max von Delius

Journal of the American Chemical Society **2019** *141* (22), 8868-8876
DOI: 10.1021/jacs.9b01350

Reprinted with permission from Journal of the American Chemical Society. Copyright 2021 American Chemical Society.

Abstract:

Fluxional chemical species such as bullvalene have been a valuable source of inspiration and fundamental insight into the nature of chemical bonds. A supramolecular analogue of bullvalene, i.e., a "fluxional host-guest system", in which the ensemble of a well-defined host and guest is engaged in continuous, degenerate constitutional rearrangements, is still elusive, however. Here, we report experimental and computational evidence for guest-induced dynamic covalent rearrangements in the ammonium complexes of self-assembled orthoester cryptands. This unique behaviour is made possible by the ammonium guest playing a dual role: it is sufficiently acidic to initiate dynamic covalent exchange reactions at the orthoester bridgeheads, and as a hydrogen bond donor it acts as a supramolecular template, governing the outcome of a multitude of possible intra- and intermolecular rearrangement reactions. One particularly striking example of inherent dynamic behaviour was observed in host-guest complex [**NH_4^+⊂*o*-Me_2-2.1.1**], which spontaneously rearranged into the larger and thermodynamically more stable complex [**NH_4^+⊂*o*-Me_2-2.2.1**], even though this process led to the formation of poor host ***o*-Me_2-1.1.1** as a consequence of the excess of one subcomponent (diethylene glycol; "1" in our nomenclature). These inherently adaptive host-guest networks represent a unique platform for exploring the interrelationship between kinetic and thermodynamic stability. For instance, as a result of optimal NH_4^+ binding, complex [**NH_4^+⊂*o*-Me_2-2.2.1**] was found to be thermodynamically stable (negligible *inter*molecular rearrangements over weeks), whereas computational studies indicate that the compound is far from kinetically stable (*intra*molecular rearrangements).

Comments on own contributions:

Prof. Max von Delius had the original idea. Dr. Wang performed all experiments on fluxional behaviour and titrations studies. I performed experiments on the fluxional behaviour of ammonium cryptates using “silver-free” ammonium salts, and during the early stage of the project, I provided some starting cryptands. I participated in all discussions, including some valuable experimental suggestions, manuscript preparation, and writing of the supporting information.

JACS
JOURNAL OF THE AMERICAN CHEMICAL SOCIETY
Article
Cite This: J. Am. Chem. Soc. 2019, 141, 8868−8876
pubs.acs.org/JACS

Ammonium Complexes of Orthoester Cryptands Are Inherently Dynamic and Adaptive

Xiang Wang,[†] Oleksandr Shyshov,[†] Marko Hanževački,[‡,§] Christof M. Jäger,*[,‡] and Max von Delius*[,†]

[†]Institute of Organic Chemistry and Advanced Materials, University of Ulm, Albert-Einstein-Allee 11, 89081 Ulm, Germany
[‡]Department of Chemical and Environmental Engineering, University of Nottingham, University Park, Nottingham NG7 2RD, United Kingdom
[§]Rudjer Boskovic Institute, Bijenicka 54, 10000 Zagreb, Croatia

Supporting Information

ABSTRACT: Fluxional chemical species such as bullvalene have been a valuable source of inspiration and fundamental insight into the nature of chemical bonds. A supramolecular analogue of bullvalene, i.e., a "fluxional host−guest system", in which the ensemble of a well-defined host and guest is engaged in continuous, degenerate constitutional rearrangements, is still elusive, however. Here, we report experimental and computational evidence for guest-induced dynamic covalent rearrangements in the ammonium complexes of self-assembled orthoester cryptands. This unique behavior is made possible by the ammonium guest playing a dual role: it is sufficiently acidic to initiate dynamic covalent exchange reactions at the orthoester bridgeheads, and as a hydrogen bond donor it acts as a supramolecular template, governing the outcome of a multitude of possible intra- and intermolecular rearrangement reactions. One particularly striking example of inherent dynamic behavior was observed in host−guest complex [NH_4^+⊂***o*-Me$_2$-2.1.1**], which spontaneously rearranged into the larger and thermodynamically more stable complex [NH_4^+⊂***o*-Me$_2$-2.2.1**], even though this process led to the formation of poor host ***o*-Me$_2$-1.1.1** as a consequence of the excess of one subcomponent (diethylene glycol; "1" in our nomenclature). These inherently adaptive host−guest networks represent a unique platform for exploring the interrelationship between kinetic and thermodynamic stability. For instance, as a result of optimal NH_4^+ binding, complex [NH_4^+⊂***o*-Me$_2$-2.2.1**] was found to be thermodynamically stable (negligible *inter*molecular rearrangements over weeks), whereas computational studies indicate that the compound is far from kinetically stable (*intra*molecular rearrangements).

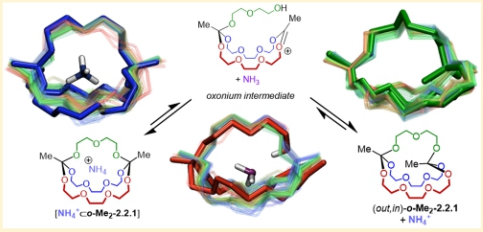

INTRODUCTION

Fluxional chemical species, defined as entities undergoing rapid degenerate rearrangements (IUPAC),[1] have inspired much research and controversy over the past half-century.[2−6] Bullvalene is perhaps the most widely known example of an organic molecule that, above a certain temperature, exists as a mixture of numerous, rapidly interconverting degenerate constitutional isomers (Scheme 1a; left).[7,8] Examples of more recent work include the fascinating case of quasi-rotation of a cyclic B_3 fragment in the B_{13}^+ cluster (Scheme 1a; right), degenerate 1,2,6-hydride shifts in the nonclassical 2-norbornyl cation ($C_7H_{11}^+$),[9] as well as (partially) degenerate positional dynamics in cyclic[10] and linear "walking" systems.[10−15] While fluxional systems are often considered scientific curiosities, of no use beyond revealing fundamental insights, Bode has recently demonstrated that the room-temperature fluxionality of "shape-shifting"[16−18] bullvalone derivatives provides a unique approach for establishing analytic fingerprint readouts for components of complex food products such as carbohydrates, flavanols, and sialic acids.[19,20]

Dynamic combinatorial chemistry[21−25] makes use of reversible chemical bonds for generating complex mixtures that are typically subject to global thermodynamic control. This implies that all members of a dynamic combinatorial library (DCL) are connected through a network of, more or less, rapid equilibria. As a consequence, even in a DCL that is at equilibrium, exchange of subcomponents occurs continuously and in a degenerate fashion. However, because this exchange is generally not an intramolecular process (rearrangement), it does not represent fluxionality according to the IUPAC definition.[1] Dynamic covalent bonds, e.g., imines, disulfides, and hydrazones, also typically require the addition of a chemical species (e.g., acid catalyst) for inducing the transition from kinetically stable to dynamic, which is in

Received: February 19, 2019
Published: May 22, 2019

ACS Publications © 2019 American Chemical Society

DOI: 10.1021/jacs.9b01350
J. Am. Chem. Soc. 2019, 141, 8868−8876

Downloaded via UNIV ULM on May 21, 2020 at 15:36:33 (UTC).
See https://pubs.acs.org/sharingguidelines for options on how to legitimately share published articles.

Scheme 1. (a) Prototypical Fluxional Systems. (b) Schematic Illustration of Fluxional Behavior of Orthoester Cryptate [NH_4^+⊂*o*-Me_2-2.2.1] via NH_4^+-Catalyzed Ring-Opened Oxonium Intermediate

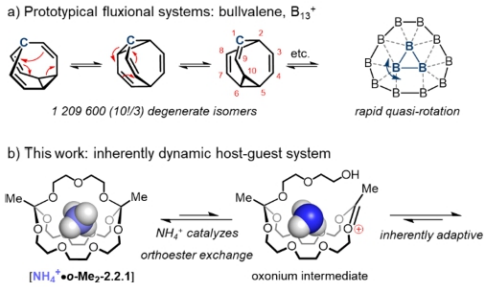

contrast to fluxional species that must be inherently dynamic, at least above a certain temperature.

Herein, we report a dynamic covalent host–guest system that is inherently dynamic at room temperature, i.e., shows evidence for adaptive constitutional dynamic rearrangements that do not require the addition of external agents.[26] The platform giving rise to this behavior is the dynamic covalent reaction between orthoesters and diols,[27] which we have recently utilized to self-assemble monometallic cryptates.[28−31] We have also demonstrated that such cryptands exhibit adaptive behavior upon addition of acid catalysts and metal ion templates.[29] We now report that the ammonium cation is sufficiently acidic to act both as a catalyst for orthoester exchange and as a template that governs the outcome of constitutional rearrangements (Scheme 1b). Experimental studies are accompanied by computational simulations designed to shed light on the transfer of H^+ from guest to host and to answer the question whether ammonium complexes of orthoester cryptands can be considered "fluxional host–guest complexes".

■ RESULTS AND DISCUSSION

Inherent Adaptive Behavior of Orthoester Cryptands. Following investigations on the adaptive behavior of orthoester cryptands in the presence of trifluoroacetic acid and alkali cations,[29] we envisaged that the ammonium cation (NH_4^+) could also be a suitable template for the self-assembly of orthoester cryptates. Under typical conditions for self-assembly,[28] we indeed observed ^{1}H NMR spectroscopic and ESI mass spectrometric evidence for ammonium cryptate formation. However, despite numerous attempts, we were not able to isolate the corresponding products, which we thought could be due to the acidity of the NH_4^+ guest that would render the cryptate complexes constitutionally dynamic and exceptionally fragile to hydrolysis during workup procedures.[31] To verify this hypothesis, we tested NH_4BArF (ammonium tetrakis[3,5-bis(trifluoromethyl)phenyl]borate)[32] as a catalyst for orthoester exchange between trimethyl orthoacetate and ethanol. The experiment revealed that the addition of 4 mol % of NH_4BArF was sufficient to reach equilibrium in this exchange reaction within only 10 min (Figure 1a and Figure S6).

Having established that NH_4^+ indeed catalyzes orthoester exchange under conditions typically used for cryptate self-

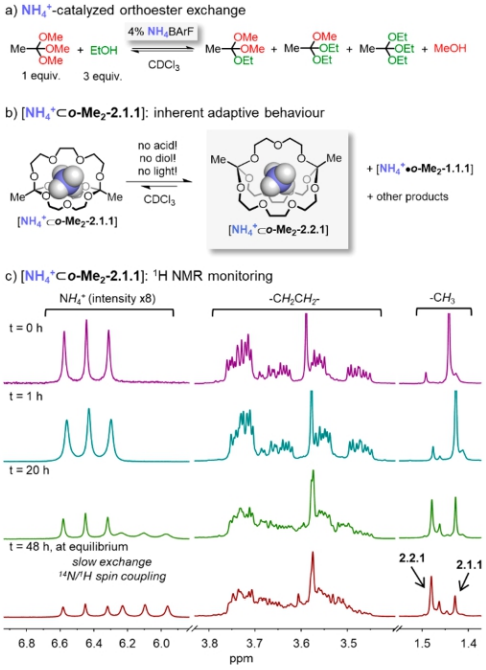

Figure 1. (a) NH_4BArF-catalyzed orthoester exchange (orthoester concentration: 80 mM). (b) Schematic representation of a key experiment on the inherent adaptive behavior of orthoester cryptate [**NH_4^+⊂*o*-Me_2-2.1.1**]BArF$^-$ (cryptate concentration: 80 mM). (c) Partial ^{1}H NMR spectra of [**NH_4^+⊂*o*-Me_2-2.1.1**]BArF$^-$ over time, showing the evolution from [**NH_4^+⊂*o*-Me_2-2.1.1**] to thermodynamically favored [**NH_4^+⊂*o*-Me_2-2.2.1**].

assembly, we monitored ammonium complexes of orthoester cryptands under careful exclusion of acid as well as light (possible formation of HCl from chloroform) and under the best-possible exclusion of water[33] by means of ^{1}H NMR spectroscopy and ESI$^+$ mass spectrometry (Supporting Information). Symmetric cryptands ***o*-Me_2-1.1.1** and ***o*-Me_2-2.2.2** based on either DEG (diethylene glycol) or TEG (triethylene glycol) building blocks were investigated first. Five hours after we added 1 equiv of NH_4BArF to cryptands ***o*-Me_2-1.1.1** or the larger cryptand ***o*-Me_2-2.2.2**, which we had prepared by means of metal-templated self-assembly (Supporting Information), we observed clear evidence for orthoester exchange, i.e., formation of hydrolysis products (due to residual water) and higher orthoester oligomers (e.g., crown ethers) along with ca. 35% and 55% of the two respective starting materials.

We next turned our attention to the more interesting unsymmetric cryptands ***o*-Me_2-2.1.1** and ***o*-Me_2-2.2.1**, whose NH_4^+-catalyzed constitutional dynamics can give rise to the formation of all four possible cryptates (of type **1.1.1**, **2.1.1**, **2.2.1**, and **2.2.2**) along with oligomers. As shown in Figure 1c, [**NH_4^+⊂*o*-Me_2-2.1.1**] slowly converted over 48 h to a mixture containing larger cryptate [**NH_4^+⊂*o*-Me_2-2.2.1**] as main product, suggesting that [**NH_4^+⊂*o*-Me_2-2.2.1**] is thermody-

DOI: 10.1021/jacs.9b01350
J. Am. Chem. Soc. 2019, 141, 8868−8876

namically more stable than [NH_4^+⊂*o*-Me_2-**2.1.1**]. ^{1}H NMR integration shows that the ratio between these two compounds at equilibrium is ca. 2.5:1, which would indicate a free energy difference of ca. 0.5 kcal mol^{-1} if mass balance effects[34,35] were not taken into account. Even though the observation of some hydrolysis complicates the picture even further (Figure S13), it stands to reason that the mass balance in fact provides a bias toward smaller cryptate [NH_4^+⊂*o*-Me_2-**2.1.1**] in this experiment because, simply speaking, there is not enough TEG available to form [NH_4^+⊂*o*-Me_2-**2.2.1**] exclusively, which forces the reaction in the opposite direction. As such, the thermodynamic preference for [NH_4^+⊂*o*-Me_2-**2.2.1**] may well be larger than 0.5 kcal mol^{-1}. Interestingly, the dynamic network seems to respond to the deficiency in TEG by forming the smallest cryptate [NH_4^+•*o*-Me_2-**1.1.1**] as a major side product (ESI$^+$-MS).

If [NH_4^+⊂*o*-Me_2-**2.2.1**] is the thermodynamically most stable within the four possible cryptates, it is an intriguing question if and how this host−guest complex rearranges over time. A ^{1}H NMR monitoring study over 50 days showed that [NH_4^+⊂*o*-Me_2-**2.2.1**] remains the dominant library member over the entire period (Figure S18). It should be noted that we can be rather certain that the library is in fact dynamic because we observe a slow increase of hydrolysis products DEG (diethylene glycol), TEG (triethylene glycol), and esters that require the formation of the same oxonium intermediates that are involved in orthoester exchange. The observation of esters can thus be considered as "trapping" of oxonium ions (see the Supporting Information, Scheme S1 and Figure S19, for further trapping experiments). A noteworthy NMR spectroscopic phenomenon in the unsymmetric cryptates is that heteronuclear spin−spin coupling between ^{1}H and ^{14}N in NH_4^+ was observed. We suggest that this phenomenon is due to slow exchange kinetics of the acidic NH_4^+ protons, which only seems to be the case in the two more strongly binding cryptates [NH_4^+⊂*o*-Me_2-**2.1.1**] and [NH_4^+⊂*o*-Me_2-**2.2.2**] (Figure 2b).

The extent of hydrolysis in the rearrangement of [NH_4^+⊂*o*-Me_2-**2.1.1**] to [NH_4^+⊂*o*-Me_2-**2.2.1**] gave us a valuable clue regarding the mechanism of such cage-to-cage transformations because we noticed that the rearrangement proceeds significantly faster in experiments where more than the typically observed 10−20% of hydrolysis had occurred due to inadequately dried reagents.[33] The mechanistic implication of this finding is that free diols generated by hydrolysis are most likely the species that do attack oxonium ions and thus lead to the rearrangement of one cryptate into another.[26,36] An alternative, less likely mechanistic scenario would involve diol scrambling via compounds, in which a diol forms a bridge between two cages (Scheme S2).

To provide further support for our hypothesis that [NH_4^+⊂*o*-Me_2-**2.2.1**] is the thermodynamically most stable complex within the series of ammonium cryptates, we carried out experiments in which **TEG** or **DEG** was added to freshly prepared cryptates [NH_4^+•*o*-Me_2-**1.1.1**], [NH_4^+⊂*o*-Me_2-**2.1.1**], and [NH_4^+⊂*o*-Me_2-**2.2.2**] (Figure 2). In all three experiments, relatively fast orthoester exchange kinetics were observed, e.g., equilibration in 4 h instead of 48 h, further supporting our mechanistic hypothesis. More importantly, [NH_4^+⊂*o*-Me_2-**2.2.1**] was found to be the major product at equilibrium in these experiments (Figure 2b), which we conducted in such a way that there is no mass balance bias between pairs of cryptates (e.g., between *o*-Me_2-**2.1.1** and *o*-Me_2-**2.2.1** in Figure 2a, top). It is also worth noting that particularly low extents of hydrolysis were observed in these fast reactions, e.g., only 6%, suggesting that higher extents of hydrolysis in experiments that required significantly longer equilibration times were likely due to water influx.

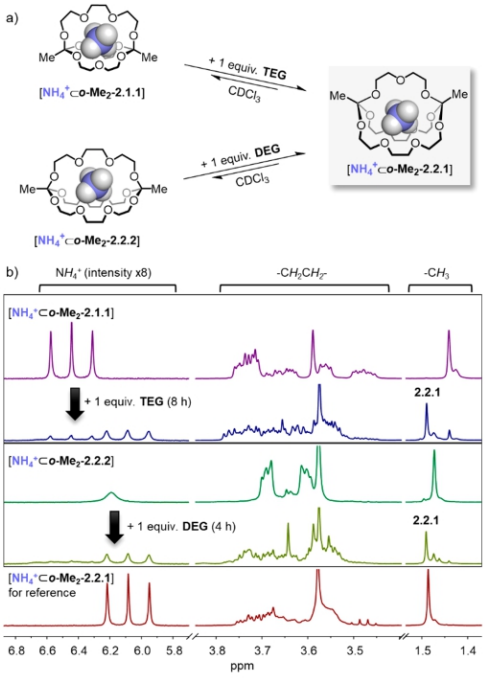

Figure 2. (a) Schematic representation and (b) partial ^{1}H NMR spectra corresponding to the adaptive behavior of [NH_4^+⊂*o*-Me_2-**2.1.1**] and [NH_4^+⊂*o*-Me_2-**2.2.2**] in the presence of 1 equiv of TEG or DEG, respectively (cryptate concentrations: 80 mM).

Thermodynamics of Ammonium Binding and Solid-State Structure of [NH_4^+⊂*o*-Me_2-2.2.1]BArF$^-$. In order to better understand the thermodynamic origins of the observed adaptive behavior that is inherent to these host−guest systems, we determined the binding constants between all four cryptands and NH_4^+ in anhydrous MeCN-d_3 by ^{1}H NMR spectroscopy (Figure 3 and Table 1). To minimize hydrolysis and competing intermolecular dynamic exchange processes, NMR spectra were recorded as fast as possible in J-Young tubes and the experiments were carried out at lower concentrations compared to the experiments on adaptive behavior. As shown in Figure 3b, after addition of NH_4BArF to cryptand *o*-Me_2-**2.2.1** in MeCN-d_3, the ^{1}H NMR signal of the methyl bridgehead shifted to low field, indicating the formation of cryptate [NH_4^+⊂*o*-Me_2-**2.2.1**], as well as fast exchange kinetics in this solvent. Interestingly, with more than 1 equiv of NH_4BArF, the triplet of the NH_4^+ protons converge to a broad peak, further confirming that the observation of ^{1}H/^{14}N spin−spin coupling is somewhat correlated with guest inclusion. Data fitting using supramolecular.org according to 1:1 stoichiometry gave a binding constant (K_a) of ca. 6000 M^{-1} for this host−guest complex.

DOI: 10.1021/jacs.9b01350
J. Am. Chem. Soc. 2019, 141, 8868−8876

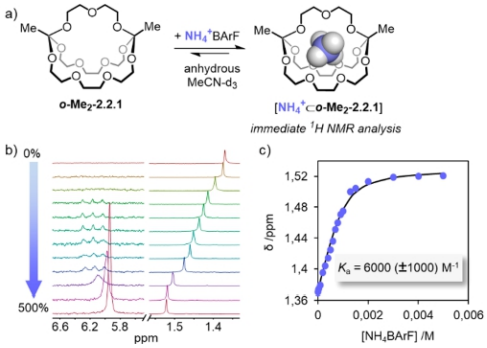

Figure 3. (a) Schematic representation of titration of ***o*-Me$_2$-2.2.1** with NH_4BArF. (b) Partial ^1H NMR (400 MHz, 298 K, CD_3CN) stack plot for titration of ***o*-Me$_2$-2.2.1** (1.0 mM) with NH_4BArF. (c) Binding isotherm for titration of ***o*-Me$_2$-2.2.1** with NH_4BArF. Blue spheres: experimental points. Black line: fit according to 1:1 model.

Table 1. Binding Constants (K_a) for Three Representative Nitrogen-Based Cations[a]

K_a (M^{-1})	NH_4^+	$CH_3NH_3^+$	$C(NH_2)_3^+$
***o*-Me$_2$-1.1.1**	540 ± 40	290 ± 10	nd
***o*-Me$_2$-2.1.1**	1100 ± 100	750 ± 30	nd
***o*-Me$_2$-2.2.1**	**6000 ± 1000**	1700 ± 20	nd
***o*-Me$_2$-2.2.2**	400 ± 30	120 ± 10	70 ± 10

[a] ^1H NMR titrations carried out in separate J-Young tubes (solvent: MeCN-d_3; counteranions: tetrakis[3,5-bis(trifluoromethyl)phenyl]-borate). In the spirit of open science,[37] the raw data is available on supramolecular.org (see Supporting Information for hyperlinks). Errors reflect goodness of fit.

The binding constants of ***o*-Me$_2$-1.1.1**, ***o*-Me$_2$-2.1.1**, and ***o*-Me$_2$-2.2.2** with NH_4BArF were determined in the same manner (Supporting Information), and the results are summarized in Table 1. Even though experiments on adaptive behavior were carried out in less polar solvent chloroform, these results in acetonitrile corroborate that ***o*-Me$_2$-2.2.1** possesses the highest affinity toward NH_4^+. We also investigated the complexation of methylammonium, which binds significantly weaker to all four cryptands, while unsymmetric cryptands ***o*-Me$_2$-2.2.1**, and ***o*-Me$_2$-2.1.1** are also the preferred hosts for this larger cation. Finally, we tested whether the larger, D_3h-symmetric and less acidic guanidinium ion would potentially be an ideal guest for the ***o*-Me$_2$-2.2.2** cryptand. Based on the observed binding constant of ca. 70 M^{-1}, we suggest that this complex does either not fit the cavity of this cryptand or that there is simply no strain-free conformation available that would allow effective hydrogen bonding between host oxygen atoms and the six guanidinium hydrogen atoms.

The high thermodynamic stability of cryptand [**NH_4^+⊂*o*-Me$_2$-2.2.1**]$BArF^-$ and thus relatively low propensity of this compound to undergo intermolecular rearrangements allowed us to obtain crystallographic data on this host–guest architecture. Suitable single crystals were obtained by slow vapor diffusion of anhydrous *n*-pentane into a solution of [**NH_4^+⊂*o*-Me$_2$-2.2.1**]$BArF^-$ in $CDCl_3$ in a well-sealed vial devoid of moisture. As shown in Figure 4, the solid-state

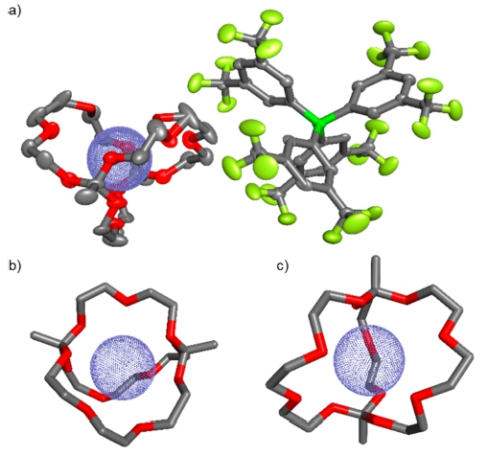

Figure 4. (a) Solid-state structure of [**NH_4^+⊂*o*-Me$_2$-2.2.1**]$BArF^-$. (b) Side view and (c) top view of cryptate complex [**NH_4^+⊂*o*-Me$_2$-2.2.1**]. Hydrogen atoms, solvent, and disorder (where applicable) are omitted for clarity. Carbon: gray. Nitrogen: purple. Oxygen: red. Fluorine: lime. Boron: green.

structure unambiguously confirms the inclusion of NH_4^+ into the cavity of cryptand ***o*-Me$_2$-2.2.1**. The nitrogen atom is located at the center of the cavity, as becomes evident from N–O distances in the relatively narrow range of 2.69–3.55 Å. The cryptand framework is somewhat less symmetric compared to previously reported crystal structures of alkali metal complexes of orthoester cryptands,[28,29,31] which is also observed in simulations (vide infra) but could in principle also be due to packing effects. X-ray crystallography does unfortunately not provide information on the location of the ammonium hydrogen atoms, which is one of the reasons why we decided to investigate the structural and dynamic behavior of the cryptates in more detail by computational methods.

Computational Studies of Ammonium Binding. The intrinsic flexibility and reactivity of the described ammonium orthoester cryptates results in a complex dynamic picture of their behavior. Hence, we chose classical molecular-dynamics (MD), hybrid quantum mechanics / molecular mechanics (QM/MM) simulations, (QM/MM) simulations, and static DFT calculations to investigate the structure.

From classical atomistic MD simulations of the cryptates in chloroform (detailed methods described in section 5.1 of the Supporting Information), we were able to retrieve a dynamic picture of the cryptates' structural flexibility and their hydrogen bonding with NH_4^+. Not surprisingly, the flexibility of the systems increases with increasing size of the cryptand framework from ***o*-Me$_2$-1.1.1** over ***o*-Me$_2$-2.1.1** to ***o*-Me$_2$-2.2.2**, as demonstrated by higher atomic root-mean-square fluctuation (rmsf) values extracted from 200 ns simulations (Figure 5a,b and Table S11). The differences in flexibility seem to be driven by how well the ion fits into and forms favorable interactions within the cavity. When compared with flexibility patterns of monometallic cryptates (Figure S43 and Table S11, Supporting Information), the ammonium cryptates resemble most closely the Rb^+ cryptates, which also preferentially self-assembles into the [**Rb^+⊂*o*-Me$_2$-2.2.1**] cage.[29]

DOI: 10.1021/jacs.9b01350
J. Am. Chem. Soc. 2019, 141, 8868–8876

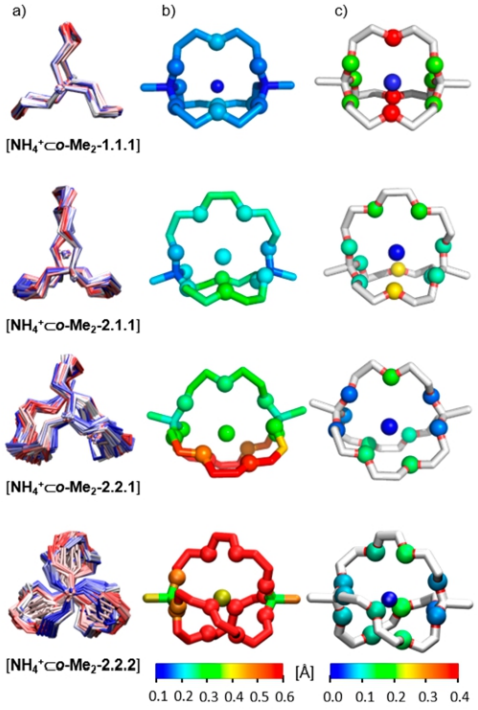

Figure 5. (a) Flexibility of cryptands illustrated by superimposed and smoothed snapshots from 200 ns MD simulations color coded by simulation time, (b) RMSF fluctuations (in Å), and (c) hydrogen-bonding occupancy derived from 200 ns MD simulations mapped on averaged cryptate structures. Oxygen and nitrogen atoms shown as spheres; hydrogen atoms omitted for clarity.

The trends in flexibility are also reflected in the hydrogen-bonding features of the encapsulated ammonium ions (Figure 5b, Table S12) with average hydrogen bonding numbers of 1.3, 1.1, 1.7, and 3.3 following decreasing cryptand size. More importantly, hydrogen bonds between NH_4^+ and ether oxygens (O_e) are preferred over orthoester oxygens (O_o), and hydrogen bonds to DEG oxygens are preferred over TEG oxygens. The average occupancy of hydrogen bonds to O_o drops from 0.25 for [NH_4^+•***o*-Me$_2$-1.1.1**] to the minimum of 0.04 for [NH_4^+⊂***o*-Me$_2$-2.2.1**] with the latter additionally having the highest O_e:O_o hydrogen bond ratio (3.6:1) in the series. In other words, hydrogen bonding to orthoester oxygens is very limited in this cryptate, which might influence its thermodynamic and kinetic stability (tendency to form an oxonium ion intermediate).

Additionally, it becomes apparent from these simulations that ***o*-Me$_2$-1.1.1** is essentially too small to accommodate the NH_4^+ ion, resulting in an *exo* mode of binding, whereas ***o*-Me$_2$-2.2.2** is too large and leads to a highly dynamic *endo* mode of binding.

More detailed umbrella sampling simulations to pull the ammonium ion out of the cavity into the solvent (Supporting Information, section 5.3, and Figure S46) support these observations, in which a distinct barrier between *exo* and *endo* binding is observable for [NH_4^+•***o*-Me$_2$-1.1.1**]. Regarding the two unsymmetric cryptates, the simulations suggest that within the series of cryptands the *exo* association is most favorable for [NH_4^+⊂***o*-Me$_2$-2.2.1**] by 3.8 kcal mol^{-1} over [NH_4^+•***o*-Me$_2$-1.1.1**] and 4.5 kcal mol^{-1} over [NH_4^+⊂***o*-Me$_2$-2.1.1**], while *endo* binding is significantly more stable than *exo* binding in both unsymmetric cryptands (e.g., [NH_4^+⊂***o*-Me$_2$-2.1.1**] favored by 2.5 kcal mol^{-1}). Thus, the simulations are in good qualitative agreement with the experimental association constants (Table 1), while the subtle difference in affinity between ***o*-Me$_2$-2.1.1** and ***o*-Me$_2$-2.2.1** is beyond the limitations of this computational method. Additional density functional theory (DFT) calculations starting from selected snapshots of these simulations (Supporting Information, section 5.8) and carried out with implicit solvation additionally indicate that [NH_4^+⊂***o*-Me$_2$-2.2.1**] is thermodynamically the most stable cryptate. Calculating the reaction energies (zero point corrected free energies) of the cryptate formation also shows that the Gibbs free energies in chloroform is always exergonic with the formation of [NH_4^+⊂***o*-Me$_2$-2.2.1**] being the most favorable.

Computational Studies of Proton Transfer and Cage Opening. The formation of oxonium ions as key intermediates for orthoester exchange reactions, as shown in Scheme 1, was investigated by means of combined quantum mechanical and molecular mechanics (QM/MM) simulations. Here, the cryptand and the ammonium ion were treated by the density functional based tight binding method (DFTB),[38] while the solvent was treated by classical molecular mechanics (Supporting Information, sections 5.4–5.6). On the basis of these simulations, the cryptand opening was first simulated using umbrella sampling. To investigate if the mechanism is stepwise or concerted we carried out two-dimensional umbrella sampling scans investigating the energy profile for the C–O_o bond breakage and the H–O_o bond formation simultaneously (Figure 6). The ring-opening transition state indeed represents a concerted mechanism with simultaneous proton transfer and C–O bond dissociation. The barrier of 16.2 kcal mol^{-1} and the strongly endergonic character remain comparable with the 1D scan for [NH_4^+⊂***o*-Me$_2$-2.2.1**]. Therefore, these results confirm that the formation of the oxonium ion is very slow due to a high barrier and that the concentration of free oxonium ions must be very small. Another observation was that in all simulations the formed NH_3 tends to leave the open cryptand cage after oxonium ion formation, which is in agreement with the results of trapping experiments (Figure S19).

In summary, our simulations show that oxonium ion formation by proton transfer from an encapsulated ammonium ion is plausible but subject to a significant kinetic barrier, which is very similar for [NH_4^+⊂***o*-Me$_2$-2.2.1**] and [NH_4^+⊂***o*-Me$_2$-2.1.1**]. One of the reasons for the high barrier for ring-opening seems to lie in the fact that the strong hydrogen-bonding network of the ammonium ion decreases its reactivity (acidity) significantly, which is a well-established effect often referred to as "complexation-induced pK_a shift".[39−41] DFT calculations based on the QM/MM simulations (Supporting Information, section 5.9) show that the protonation and ring opening barriers are predominately influenced by the number of hydrogen bonds formed with the cage.

Based on these considerations, ammonium ions approaching from the outside of the cage should demonstrate higher acidity and reactivity. However, this attack competes with the high

DOI: 10.1021/jacs.9b01350
J. Am. Chem. Soc. 2019, 141, 8868−8876

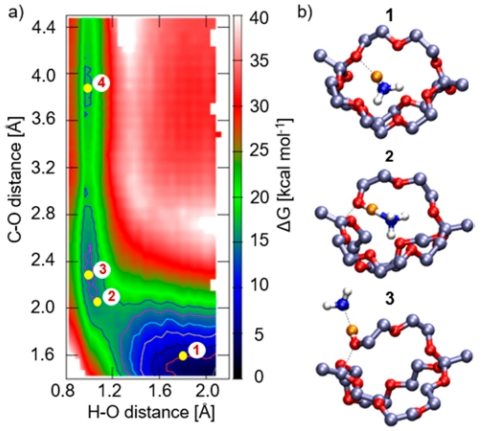

Figure 6. (a) Free energy representation of a two-dimensional QM/MM umbrella sampling trajectory of oxonium ion formation of [NH_4^+⊂**o-Me$_2$-2.2.1**]. Bond formation between the orthoester oxygen and the hydrogen from NH_4^+ ion and the carbon oxygen bond breakage have been used as sampling coordinates. Energies given in kcal mol^{-1}; contour lines shown represent steps of 2.5 kcal mol^{-1} between 2.5 and 20.0 kcal mol^{-1}. (b) Representative structures at characteristic points from this simulation. All cryptand hydrogens omitted for clarity. Hydrogen involved in reaction shown in orange.

driving force to enter the cavity, and all QM/MM umbrella sampling approaches for this reaction step with ***o*-Me$_2$-2.2.1** resulted in the highly stable encapsulated configuration and no ring-opening attack. Moreover, the free energy difference associated with NH_4^+ dissociation is more endergonic than the kinetic barrier for ring opening (in case of **NH_4^+⊂*o*-Me$_2$-2.2.1** and **NH_4^+⊂*o*-Me$_2$-2.1.1**). We therefore consider it highly unlikely that adaptive behavior would be based on the dissociation of the ammonium ion.

Are These Host–guest Complexes Fluxional? Finally, we attempted to answer the question whether the ammonium cryptates are undergoing intramolecular rearrangements in a manner that would meet the definition of fluxionality according to IUPAC.[1]

As shown in Figure 7a, the first step for such a rearrangement would be oxonium ion formation (vide supra), leading to release of NH_3 into the solvent. Oxonium ion I is essentially a lariate crown ether[42−44] whose alcohol group can attack the electrophilic carbon atom from the opposite side from where it left and therefore invert the absolute configuration at this bridgehead (Figure 7a,b). The possible formation of this (*out,in*) intermediate structure was confirmed for ***o*-Me$_2$-2.2.1** by umbrella sampling simulations. Unsurprisingly, the (*out,in*) cage is not able to accommodate an ammonium ion within its cavity (Supporting Information, sections 5.7−5.8). Thus, the reactivity of this species will not be decreased by strong hydrogen-bonding networks and attack by external ammonium ions should be fast, which is confirmed by DFT calculations presented in section 5.9 of the Supporting Information. Also, the fact that (*out,in*) cryptands cannot accommodate the NH_4^+ ion helps to explain why such species are not observed in significant quantities during our experiments (thermodynamic control provides a strong driving force for effective hosts).

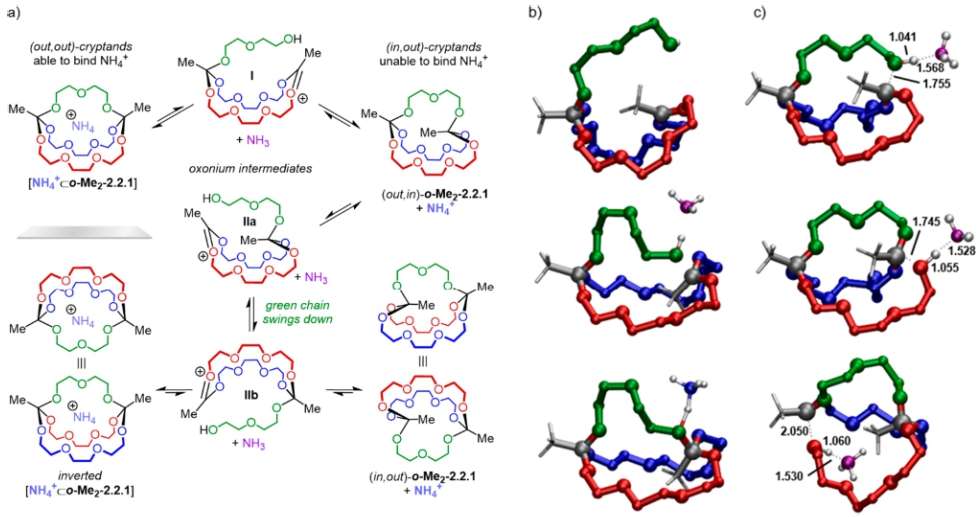

Figure 7. (a) Reaction sequence of a "fluxional" intramolecular rearrangement leading to exchange of the two triethylene glycol chains via several ring-opening and -closing reactions. (b) Snapshots extracted from QM/MM umbrella sampling simulations for the backside attack of the oxonium ion to form the inverted ***o*-Me$_2$-2.2.1** (*out,in*) intermediate. All CH_2 hydrogens omitted for clarity. Orthoester atoms of different side chains highlighted in different colors in analogy to part a of this figure. (c) DFT-optimized transition-state structures for the ring-opening of the ***o*-Me$_2$-2.2.1** (*out,in*) intermediate. Selected interatomic distances given in Å.

DOI: 10.1021/jacs.9b01350
J. Am. Chem. Soc. 2019, 141, 8868−8876

DFT transition-state calculations (Figure 7c and section 5.9 of the Supporting Information) at the PBE0/def2TZVP(D3) level of theory provided barriers for ring-opening by proton transfer between 1.3 and 26.3 kcal mol^{-1} for either side of the ***o*-Me$_2$-2.2.1** (*out,in*) intermediate. As indicated in the previous section, the large difference between the activation barriers is related to the nature of noncovalent interactions of NH_4^+ with the host in the optimized precursor structures. For cases where NH_4^+ is engaged in strong hydrogen bonding, the barrier is high, whereas the barrier is minimal, if the cation is only associated with one orthoester oxygen atom. In general, the reactivity of NH_4^+ decreases with effective encapsulation, and NH_4^+ should be most reactive in conjunction with hosts ***o*-Me$_2$-1.1.1** and (*out,in*)-***o*-Me$_2$-2.2.1** and least reactive for ***o*-Me$_2$-2.2.1** and ***o*-Me$_2$-2.1.1**.

To complete the fluxional rearrangement sequence, the second orthoester oxygen of the diethylene glycol chain (green in Figure 7) needs to be involved in a second ring-opening step, so that the cryptand can subsequently undergo inversion of the second bridgehead (via backside attack) to form an inverted (*out,out*) configuration with encapsulated ammonium ion (Figure 7a). From the structures displayed on the left-hand side of Figure 7, it is evident that the two triethylene glycol chains (red and blue) have now changed position and that their stereochemical relationship is enantiotopic (mirror plane in Figure 7).

The described inversion pathway based on the formation of an (*in,out*) cryptand and reactive oxonium ions **I** and **II** is plausible for three reasons. First, the formed NH_3 dissociates after ring opening, which allows the flexible side chains to adopt conformations suitable for back-side attack and ring closure as a key process leading to stereochemical inversion. Second, the (*out,in*) cryptand as a key intermediate has a calculated ground-state energy that is 7.2 kcal mol^{-1} more stable than the corresponding empty ***o*-Me$_2$-2.1.1** cryptand (5.2 kcal mol^{-1} in case of ***o*-Me$_2$-2.2.1**), which suggests that its formation is possible, even though it cannot encapsulate the NH_4^+ ion. Third, for that same reason, the formed reactive (*out,in*) cryptand is equally prone to NH_4^+ attack on both sides of the molecule (if no additional hydrogen bonds are formed) leading to a stochastic chance for ring opening on both sides including the described pathway. We therefore conclude that there is a plausible pathway for "fluxional" intramolecular degenerate rearrangements in the [**NH$_4^+$⊂*o*-Me$_2$-2.2.1**] host–guest complex with each elementary step of the corresponding reaction sequence supported by computational evidence (DFT, QM/MM, and MD simulations).

CONCLUSION

In this study, we demonstrated experimentally that the ammonium complexes of orthoester cryptands are highly unusual chemical species. The ammonium guest is sufficiently acidic to initiate orthoester exchange and thus imparts constitutional dynamics onto the covalent framework of the host. The inherently dynamic nature of these host–guest complexes became evident in experiments, in which the unsymmetric cryptate [**NH$_4^+$⊂*o*-Me$_2$-2.1.1**] spontaneously rearranged into the thermodynamically more stable cryptate [**NH$_4^+$⊂*o*-Me$_2$-2.2.1**] by means of intermolecular subcomponent exchange. In the context of decades of work on supramolecular hosts acting as "artificial enzymes",[45−50] this study therefore represents a rare complement because in this case the modulation of reactivity occurs from the guest to the host,[51−54] and not in the other direction.

Comprehensive computational studies confirmed that the crucial step for constitutional cryptate rearrangement, i.e., the formation of oxonium ion intermediates is significantly hindered by the ammonium ion's ability to strongly bind to the cryptands through multiple hydrogen bonds and the associated complexation-induced pK_a shift. This finding also explains the rather slow kinetics of the intermolecular rearrangement processes and the failure to trap oxonium ion intermediates experimentally. QM/MM simulations and DFT calculations further indicated that the host-guest system [**NH$_4^+$⊂*o*-Me$_2$-2.2.1**] is indeed fluxional, i.e., that the experimentally proven *inter*molecular rearrangements are accompanied by *intra*molecular degenerate rearrangements.

ASSOCIATED CONTENT

Supporting Information

The Supporting Information is available free of charge on the ACS Publications website at DOI: 10.1021/jacs.9b01350.

Experimental procedures, characterization and spectral data. Detailed description of the simulations (MD and QM/MM) and DFT setups, Cartesian coordinates, details into the 2D umbrella sampling strategies, and more detailed DFT results and analysis and force field parameters used (PDF)

X-ray data for compound [**NH$_4^+$⊂*o*-Me$_2$-2.2.1**]BArF$^-$ (CIF)

AUTHOR INFORMATION

Corresponding Authors

*max.vondelius@uni-ulm.de

*christof.jaeger@nottingham.ac.uk

ORCID

Christof M. Jäger: 0000-0002-1802-1892

Max von Delius: 0000-0003-1852-2969

Notes

The authors declare no competing financial interest.

ACKNOWLEDGMENTS

This work was supported by the Deutsche Forschungsgemeinschaft (Emmy-Noether grant DE1830/2-1), an Experiment! grant of the VolkswagenStiftung, and the DAAD (PhD fellowship to O.S.). We thank Dr. Elena Mena-Osteritz for crystal structure refinement, Mrs. Margit Lang for ICP-AES analyses, and Dr. René-Chris Brachvogel for laying early foundations of this study. C.M.J. gratefully acknowledges access to the University of Nottingham's Augusta HPC service. The Croatian Science Foundation (Project No. IP11-2013-8238) and the British Scholarship Trust are acknowledged for the additional financial support.

REFERENCES

(1) A chemical species is said to be fluxional if it undergoes rapid degenerate rearrangements (generally detectable by methods which allow the observation of the behavior of individual nuclei in a rearranged chemical species, e.g., NMR, X-ray). The term is also used to designate positional change among ligands of complex compounds and organometallics. In these cases, the change is not necessarily degenerate. *IUPAC Compendium of Chemical Terminology*; IUPAC: Research Triangle Park, NC, 2006.

DOI: 10.1021/jacs.9b01350
J. Am. Chem. Soc. 2019, 141, 8868−8876

(2) Cotton, F. A. Fluxional organometallic molecules. *Acc. Chem. Res.* **1968**, *1*, 257−265.
(3) Cotton, F. A. A Half-Century of Nonclassical Organometallic Chemistry: A Personal Perspective. *Inorg. Chem.* **2002**, *41*, 643−658.
(4) Schreiner, P. R. Does CH_5^+ Have (a) "Structure?" A Tough Test for Experiment and Theory. *Angew. Chem., Int. Ed.* **2000**, *39*, 3239−3241.
(5) King, R. B. *Fluxional Organometallic and Coordination Compounds*; Wiley & Sons: Chichester, UK, 2005; pp 1−39.
(6) McKee, M. L. Fluctional molecules. *Interdiscip. Rev. Comput. Mol. Sci.* **2011**, *1*, 943−951.
(7) von E. Doering, W.; Roth, W. R. Thermal Rearrangements. *Angew. Chem., Int. Ed. Engl.* **1963**, *2*, 115−122.
(8) Ault, A. The Bullvalene Story. The Concept of Bullvalene, a Molecule That Has No Permanent Structure. *J. Chem. Educ.* **2001**, *78*, 924.
(9) Scholz, F.; Himmel, D.; Heinemann, F. W.; Schleyer, P. v. R.; Meyer, K.; Krossing, I. Crystal Structure Determination of the Nonclassical 2-Norbornyl Cation. *Science* **2013**, *341*, 62−64.
(10) Weimann, D. P.; Winkler, H. D. F.; Falenski, J. A.; Koksch, B.; Schalley, C. A. Highly dynamic motion of crown ethers along oligolysine peptide chains. *Nat. Chem.* **2009**, *1*, 573−577.
(11) Kovaříček, P.; Lehn, J.-M. Merging Constitutional and Motional Covalent Dynamics in Reversible Imine Formation and Exchange Reaction. *J. Am. Chem. Soc.* **2012**, *134*, 9446−9455.
(12) Kovaříček, P.; Lehn, J.-M. Directional Dynamic Covalent Motion of a Carbonyl Walker on a Polyamine Track. *Chem. - Eur. J.* **2015**, *21*, 9380−9384.
(13) Campaña, A. G.; Carlone, A.; Chen, K.; Dryden, D. T. F.; Leigh, D. A.; Lewandowska, U.; Mullen, K. M. A Small Molecule that Walks Non-Directionally Along a Track without External Intervention. *Angew. Chem., Int. Ed.* **2012**, *51*, 5480−5483.
(14) Campaña, A. G.; Leigh, D. A.; Lewandowska, U. One Dimensional Random Walk of a Synthetic Small Molecule Toward a Thermodynamic Sink. *J. Am. Chem. Soc.* **2013**, *135*, 8639−8645.
(15) von Delius, M.; Leigh, D. A. Walking molecules. *Chem. Soc. Rev.* **2011**, *40*, 3656−3676.
(16) He, M.; Bode, J. W. Racemization as a stereochemical measure of dynamics and robustness in shape-shifting organic molecules. *Proc. Natl. Acad. Sci. U. S. A.* **2011**, *108*, 14752−14756.
(17) Lippert, A. R.; Kaeobamrung, J.; Bode, J. W. Synthesis of Oligosubstituted Bullvalones: Shapeshifting Molecules Under Basic Conditions. *J. Am. Chem. Soc.* **2006**, *128*, 14738−14739.
(18) Bismillah, A. N.; Sturala, J.; Chapin, B. M.; Yufit, D. S.; Hodgkinson, P.; McGonigal, P. R. Shape-selective crystallization of fluxional carbon cages. *Chem. Sci.* **2018**, *9*, 8631−8636.
(19) Teichert, J. F.; Mazunin, D.; Bode, J. W. Chemical Sensing of Polyols with Shapeshifting Boronic Acids As a Self-Contained Sensor Array. *J. Am. Chem. Soc.* **2013**, *135*, 11314−11321.
(20) Larson, K. K.; He, M.; Teichert, J. F.; Naganawa, A.; Bode, J. W. Chemical sensing with shapeshifting organic molecules. *Chem. Sci.* **2012**, *3*, 1825−1828.
(21) Corbett, P. T.; Leclaire, J.; Vial, L.; West, K. R.; Wietor, J.-L.; Sanders, J. K. M.; Otto, S. Dynamic Combinatorial Chemistry. *Chem. Rev.* **2006**, *106*, 3652−3711.
(22) Jin, Y.; Yu, C.; Denman, R. J.; Zhang, W. Recent advances in dynamic covalent chemistry. *Chem. Soc. Rev.* **2013**, *42*, 6634.
(23) Herrmann, A. Dynamic combinatorial/covalent chemistry: a tool to read, generate and modulate the bioactivity of compounds and compound mixtures. *Chem. Soc. Rev.* **2014**, *43*, 1899−1933.
(24) Li, J.; Nowak, P.; Otto, S. Dynamic Combinatorial Libraries: From Exploring Molecular Recognition to Systems Chemistry. *J. Am. Chem. Soc.* **2013**, *135*, 9222−9239.
(25) Lehn, J.-M. Perspective in Chemistry − Aspects of Adaptive Chemistry and Materials. *Angew. Chem., Int. Ed.* **2015**, *54*, 3276−3289.
(26) Lehn, J.-M. From supramolecular chemistry towards constitutional dynamic chemistry and adaptive chemistry. *Chem. Soc. Rev.* **2007**, *36*, 151−160.
(27) Brachvogel, R.-C.; von Delius, M. Orthoester exchange: a tripodal tool for dynamic covalent and systems chemistry. *Chem. Sci.* **2015**, *6*, 1399−1403.
(28) Brachvogel, R.-C.; Hampel, F.; von Delius, M. Self-assembly of dynamic orthoester cryptates. *Nat. Commun.* **2015**, *6*, 7129.
(29) Shyshov, O.; Brachvogel, R.-C.; Bachmann, T.; Srikantharajah, R.; Segets, D.; Hampel, F.; Puchta, R.; von Delius, M. Adaptive Behavior of Dynamic Orthoester Cryptands. *Angew. Chem., Int. Ed.* **2017**, *56*, 776−781.
(30) von Delius, M. Small Is (also) Beautiful: Dynamic Covalent Self-Assembly of Cryptates. *Synlett* **2016**, *27*, 177−180.
(31) Löw, H.; Mena-Osteritz, E.; von Delius, M. Self-assembled orthoester cryptands: orthoester scope, post-functionalization, kinetick locking and tunable degradation kinetics. *Chem. Sci.* **2018**, *9*, 4785−4793.
(32) A reviewer of this article raised the justified concern that residual silver ions in our NH_4BArF synthesized from AgBArF could be responsible for the observed reactivity. To address this concern, we carried out a number of experiments, which indicate very clearly that Ag^+ is not the catalyst for dynamic covalent exchange. For instance, NH_4BArF synthesized from NaBArF gives rise to the same dynamic behaviour as that synthesized from AgBArF. For further details, see section 1 in the SI.
(33) Stock solutions of cryptands and diols were dried over 3 Å molecular sieves. NH_4BArF powder was dried overnight under high vacuum in a desiccator equipped with P_2O_5.
(34) Severin, K. The Advantage of Being Virtual − Target Induced Adaptation and Selection in Dynamic Combinatorial Libraries. *Chem. - Eur. J.* **2004**, *10*, 2565−2580.
(35) Corbett, P. T.; Sanders, J. K. M.; Otto, S. Exploring the Relation between Amplification and Binding in Dynamic Combinatorial Libraries of Macrocyclic Synthetic Receptors in Water. *Chem. - Eur. J.* **2008**, *14*, 2153−2166.
(36) Ciaccia, M.; Pilati, S.; Cacciapaglia, R.; Mandolini, L.; Di Stefano, S. Effective catalysis of imine metathesis by means of fast transiminations between aromatic-aromatic or aromatic-aliphatic amines. *Org. Biomol. Chem.* **2014**, *12*, 3282−3287.
(37) Hibbert, D. B.; Thordarson, P. The death of the Job plot, transparency, open science and online tools, uncertainty estimation methods and other developments in supramolecular chemistry data analyses. *Chem. Commun.* **2016**, *52*, 12792−12805.
(38) Elstner, M.; Porezag, D.; Jungnickel, G.; Elsner, J.; Haugk, M.; Frauenheim, T.; Suhai, S.; Seifert, G. Self-consistent-charge density-functional tight-binding method for simulations of complex materials properties. *Phys. Rev. B: Condens. Matter Mater. Phys.* **1998**, *58*, 7260−7268.
(39) Späth, A.; König, B. Molecular recognition of organic ammonium ions in solution using synthetic receptors. *Beilstein J. Org. Chem.* **2010**, *6*, 32.
(40) Graf, E.; Kintzinger, J. P.; Lehn, J.-M.; LeMoigne, J. Molecular recognition. Selective ammonium cryptates of synthetic receptor molecules possessing a tetrahedral recognition site. *J. Am. Chem. Soc.* **1982**, *104* (6), 1672−1678.
(41) Lazar, A. I.; Rohacova, J.; Nau, W. M. Comparison of Complexation-Induced pK_a Shifts in the Ground and Excited States of Dyes as Well as Different Macrocyclic Hosts and Their Manifestation in Host-Retarded Excited−Dye Deprotonation. *J. Phys. Chem. B* **2017**, *121* (50), 11390−11398.
(42) Gokel, G. W.; Dishong, D. M.; Diamond, C. J. Lariat ethers. Synthesis and cation binding of macrocyclic polyethers possessing axially disposed secondary donor groups. *J. Chem. Soc., Chem. Commun.* **1980**, *1053*.1053
(43) Abbas, A. A.; Elwahy, A. H. M. Synthesis of C-Pivot Lariat Ethers. *J. Heterocycl. Chem.* **2009**, *46*, 1035−1079.
(44) Cragg, P. J.; Vahora, R. *Supramolecular Chemistry*; John Wiley & Sons, Chichester, UK, 2012.
(45) Cram, D. J. The Design of Molecular Hosts, Guests, and Their Complexis (Nobel Lecture). *Angew. Chem., Int. Ed. Engl.* **1988**, *27*, 1009−1020.

DOI: 10.1021/jacs.9b01350
J. Am. Chem. Soc. 2019, 141, 8868−8876

(46) Raynal, M.; Ballester, P.; Vidal-Ferran, A.; van Leeuwen, P. W. N. M. Supramolecular catalyses. Part 2: artificial enzyme mimics. *Chem. Soc. Rev.* **2014**, *43*, 1734−1787.
(47) Brown, C. J.; Toste, F. D.; Bergman, R. G.; Raymond, K. N. Supramolecular Catalysis in Metal-Ligand Cluster Hosts. *Chem. Rev.* **2015**, *115*, 3012−3035.
(48) Leenders, S. H. A. M.; Gramage-Doria, R.; de Bruin, B.; Reek, J. N. H. Transition metal catalysis in confined spaces. *Chem. Soc. Rev.* **2015**, *44*, 433−448.
(49) Zarra, S.; Wood, D. M.; Roberts, D. A.; Nitschke, J. R. Molecular containers in complex chemical systems. *Chem. Soc. Rev.* **2015**, *44*, 419−432.
(50) Catti, L.; Zhang, Q.; Tiefenbacher, K. Self-Assembled Supramolecular Structures as Catalysts for Reactions Involving Cationic Transition States. *Synthesis* **2016**, *48*, 313−328.
(51) He, Q.-T.; Li, X.-P.; Chen, L.-F.; Zhang, L.; Wang, W.; Su, C.-Y. Nanosized Coordination Cages Incorporating Multiple Cu(I) Reactive Sites: Host-Guest Modulated Catalytic Activity. *ACS Catal.* **2013**, *3*, 1−9.
(52) He, Q.-T.; Li, X.-P.; Liu, Y.; Yu, Z.-Q.; Wang, W.; Su, C.-Y. Copper(I) Cubooctahedral Coordination Cages: Host-Guest Dependent Redox Activity. *Angew. Chem., Int. Ed.* **2009**, *48*, 6156−6159.
(53) Jones, F. J.; Kilner, C. A.; Halcrow, M. A. A Cobalt Metallacrown Anion Host with Guest-Dependent Redox Activity. *Chem. - Eur. J.* **2009**, *15*, 4667−4675.
(54) Ratjen, L.; Vantomme, G.; Lehn, J.-M. Strain-Induced Reactivity in the Dynamic Covalent Chemistry of Macrocyclic Imines. *Chem. - Eur. J.* **2015**, *21*, 10070−10081.

DOI: 10.1021/jacs.9b01350
J. Am. Chem. Soc. 2019, 141, 8868−8876

Supporting Information

Ammonium Complexes of Orthoester Cryptands are Inherently Dynamic and Adaptive

Xiang Wang,[a] Oleksandr Shyshov,[a] Marko Hanževački,[b,c] Christof M. Jäger[b*] and Max von Delius[a*]

a) Institute of Organic Chemistry and Advanced Materials, University of Ulm, Albert-Einstein-Allee 11, 89081 Ulm, Germany. E-Mail: max.vondelius@uni-ulm.de.

b) Department of Chemical and Environmental Engineering, University of Nottingham, University Park, Nottingham, NG7 2RD, United Kingdom. E-Mail: christof.jaeger@nottingham.ac.uk

c) Rudjer Boskovic Institute, Bijenicka 54, 10000 Zagreb, Croatia.

Contents

Contents ... **1**

1. General Experimental Section ... **3**

NH_4^+ catalyzed orthoester exchange ... 7

Comparison of NH_4BArF obtained from AgBArF and directly from NaBArF ... 8

2. Characterization and Inherent Dynamics of Orthoester Cryptand-NH_4^+ Complexes ... **10**

Inherent dynamics of $[NH_4^+ \bullet o\text{-}Me_2\text{-}1.1.1]BArF^-$ ... 10

Inherent dynamics of $[NH_4^+ \subset o\text{-}Me_2\text{-}2.2.2]BArF^-$ ... 12

Inherent dynamics of $[NH_4^+ \subset o\text{-}Me_2\text{-}2.1.1]BArF^-$ ... 14

Characterization of $[NH_4^+ \subset o\text{-}Me_2\text{-}2.2.1]BArF^-$ ... 16

Inherent dynamics of $[NH_4^+ \subset o\text{-}Me_2\text{-}2.2.1]BArF^-$ ... 18

Attempts to trap orthoamide intermediate by hydrolysis of $[NH_4^+ \subset o\text{-}Me_2\text{-}2.2.1]BArF^-$ ... 18

Proposed mechanism for the inherent adaptive behavior of orthoester cryptate $[NH_4^+ \subset o\text{-}Me_2\text{-}2.1.1]BArF^-$ ... 19

3. Inherently Adaptive Behavior of Cryptand-NH_4^+ Complexes: Reaction with Diols ... **20**

Adaptive behavior of $[NH_4^+ \bullet o\text{-}Me_2\text{-}1.1.1]BArF^-$: addition of 2 equivalents of TEG ... 20

Adaptive behavior of $[NH_4^+ \subset o\text{-}Me_2\text{-}2.1.1]BArF^-$: addition of 1 equivalent of TEG ... 22

Adaptive behavior of $[NH_4^+ \subset o\text{-}Me_2\text{-}2.2.2]BArF^-$: addition of 1 equivalent of DEG ... 24

4. Binding Constants Determination ... **26**

General procedure for ^{1}H NMR titrations 26
^{1}H NMR Titration of *o*-Me_2-1.1.1 with NH_4BArF 26
^{1}H NMR Titration of *o*-Me_2-2.1.1 with NH_4BArF 28
^{1}H NMR Titration of *o*-Me_2-2.2.1 with NH_4BArF 29
^{1}H NMR Titration of *o*-Me_2-2.2.2 with NH_4BArF 30
^{1}H NMR Titration of *o*-Me_2-1.1.1 with CH_3NH_3BArF 32
^{1}H NMR Titration of *o*-Me_2-2.1.1 with CH_3NH_3BArF 33
^{1}H NMR Titration of *o*-Me_2-2.2.1 with CH_3NH_3BArF 35
^{1}H NMR Titration of *o*-Me_2-2.2.2 with CH_3NH_3BArF 36
^{1}H NMR Titration of *o*-Me_2-2.2.2 with $C(NH_2)_3BArF$ 38
5. Computational Chemistry 40
5.1 Molecular-dynamics simulations setup 40
5.2 Molecular-dynamics simulations analysis 47
5.3 Umbrella sampling setup 50
5.4 QM/MM simulation setup 51
5.5 QM/MM umbrella sampling setup 52
5.6 QM/MM umbrella sampling results 52
5.7 QM and QM/MM sampling of inversion and fluxional behaviour 54
5.8 DFT calculations of cryptand and cryptate formation 55
5.9 DFT calculations of cryptate ring opening barriers 60
6. Crystallographic Data 63
7. References 70

1. General Experimental Section

Reagents and instruments

All commercially available reagents were purchased from Sigma Aldrich, Alfa Aesar, Acros Organics or TCI and were used without further purification. Molecular sieves and aluminum oxide were dried for 3 days at 150 °C under reduced pressure (10^{-2} mbar) before use. $CDCl_3$ was dried for at least 3 days and stored over molecular sieves. All solvents were dried over molecular sieves for at least 24 hours. All orthoester exchange reactions were carried out under nitrogen in MBraun Glovebox (< 0.5 ppm H_2O). NMR spectra were recorded on Bruker Avance 400 (^{1}H: 400 MHz) spectrometers at 298 K and referenced to the residual solvent peak (^{1}H: $CDCl_3$, 7.26 ppm; ^{13}C: $CDCl_3$, 77.0 ppm). Coupling constants (*J*) are denoted in Hz and chemical shifts (δ) in ppm. High resolution mass spectra were obtained on Bruker SolariX instrument. Direct ESI-MS spectra were obtained on a Shimadzu LCMS 2020 instrument. Residual silver content was determined using Jobin Yvon Horiba – Ultima 2 ICP-AES spectrometer.

Cryptands ***o*-Me$_2$-1.1.1**, ***o*-Me$_2$-2.1.1**, ***o*-Me$_2$-2.2.1**, and ***o*-Me$_2$-2.2.2** were synthesized according to procedure reported previously. [S1,S2] Stock solutions of freshly prepared cryptands in $CDCl_3$ were dried over 3Å molecular sieves and Na_2CO_3 for 48 hours before use. Stock solutions of DEG (diethylene glycol) and TEG (triethylene glycol) in $CDCl_3$ were dried with 3Å molecular sieves for 48 hours before use. The concentration of cryptands, DEG, and TEG were determined using 1,4-dinitrobenzene as an internal standard.

Preparation of NH_4BArF

Method A: From NaBArF

NaBArF (100 mg, 1 equiv., 0.113 mmol) was placed in a 15 mL Teflon-coated screw cap vial. 9 mL of ether was added and the organic phase was washed 4 times was concentrated aqueous solution of NH_4Cl. The organic layer was separated, dried over sodium sulfate and evaporated to afford NH_4BArF (90 mg, 91% yield) as a white crystalline solid.

Residual NaBArF content was estimated to be ≤ 10% (based on integration of ^{1}H NMR signals)

Method B: from AgBArF

NaBArF (886 mg, 1 equiv., 1 mmol) was dissolved in diethyl ether (80 mL) and vigorously shaken for 5 min in a separatory funnel wrapped in aluminum foil with silver nitrate (340 mg, 2 equiv., 2 mmol) dissolved in 20 mL of water. The organic layer was separated and evaporated to give AgBArF as white solid, which was dissolved in 10 mL of acetonitrile. Ammonium chloride (160 mg, 3 equiv.) was added and the reaction mixture was stirred overnight under exclusion of light. The precipitate was filtered off and the solvent was removed under reduced pressure to give a white solid, which was purified by precipitation form a mixture of CH_2Cl_2 and n-hexane to afford NH_4BArF (500 mg, 56% yield) as a white crystalline solid.

Residual content of Ag in NH_4BArF was determined using ICP-AES. Due to extremely low solubility of BArF salts in water, the sample had to be digested. For this, 30.07 mg of NH_4BArF was stirred with 200 µL of 65% HNO_3 (trace metal analyses quality) in a Teflon-coated screw cap vial at 110 °C for 15 h. The sample was dissolved in deionized water, transferred into a 10 mL volumetric flask and filled to meniscus with deionized water. Residual Ag content was determined to be 117.39 µg(Ag)/g (0.0117%).

$MeNH_3$BArF, $C(NH_2)_3$BArF, and ^{15}N labeled $^{15}NH_4$BArF were synthesized following a similar procedure.

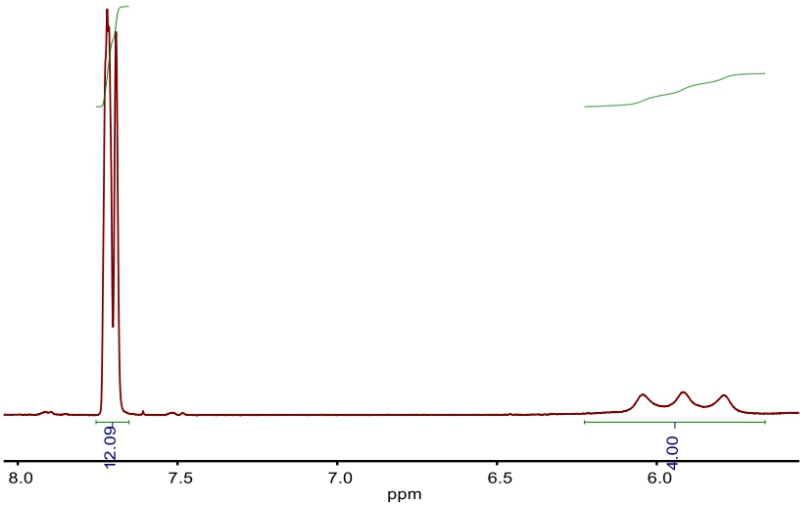

Figure S1. ^{1}H NMR spectrum (400 MHz, CD_3CN, 298 K) of NH_4BArF used in this study.

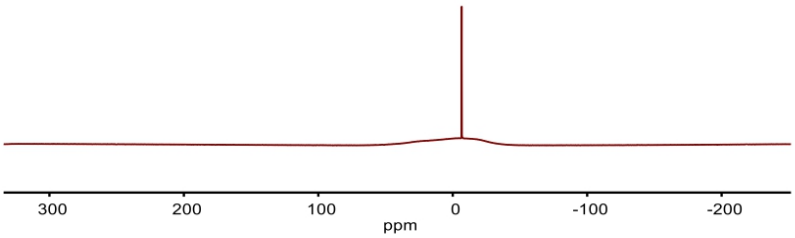

Figure S2. ^{11}B NMR spectrum (128.4 MHz, CD_3CN, 298 K) of NH_4BArF used in this study.

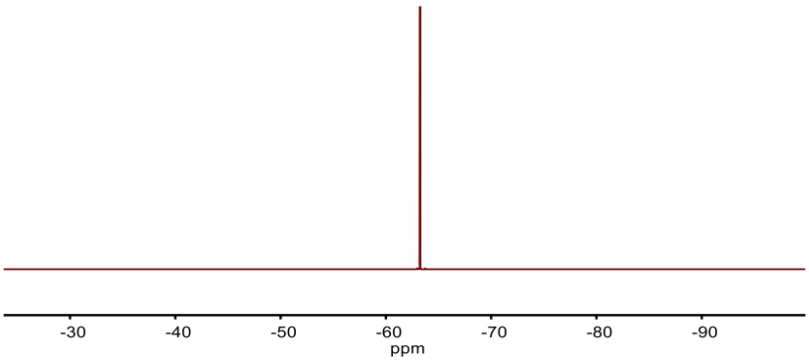

Figure S3. ^{19}F NMR spectrum (377 MHz, CD_3CN, 298 K) of NH_4BarF used in this study.

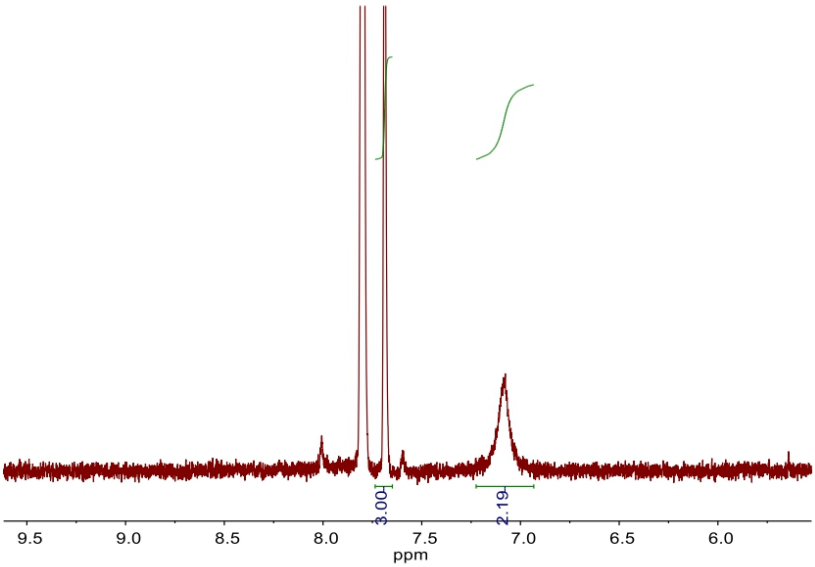

Figure S4. ^{1}H NMR spectrum (400 MHz, acetone-d_6, 298 K) of $C(NH_2)_3BArF$ used in this study.

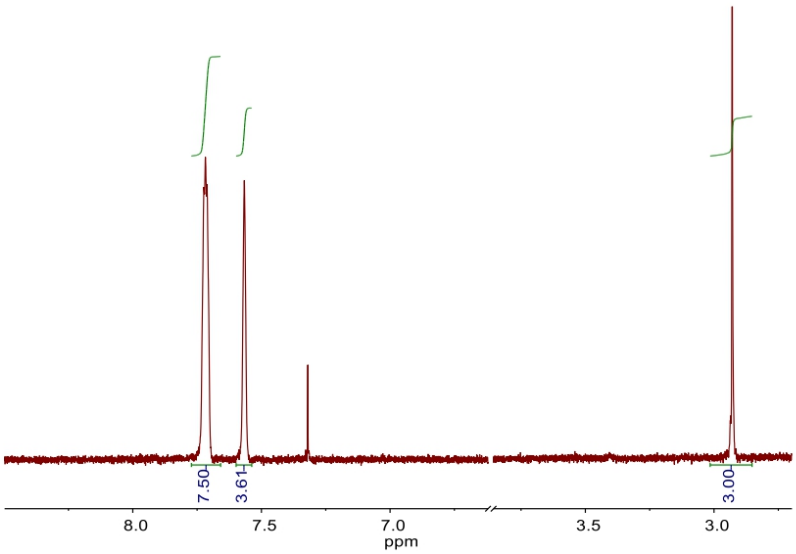

Figure S5. ^{1}H NMR spectrum (400 MHz, DCM-d_2, 298 K) of $MeNH_3BArF$ used in this study.

NH_4^+ catalyzed orthoester exchange

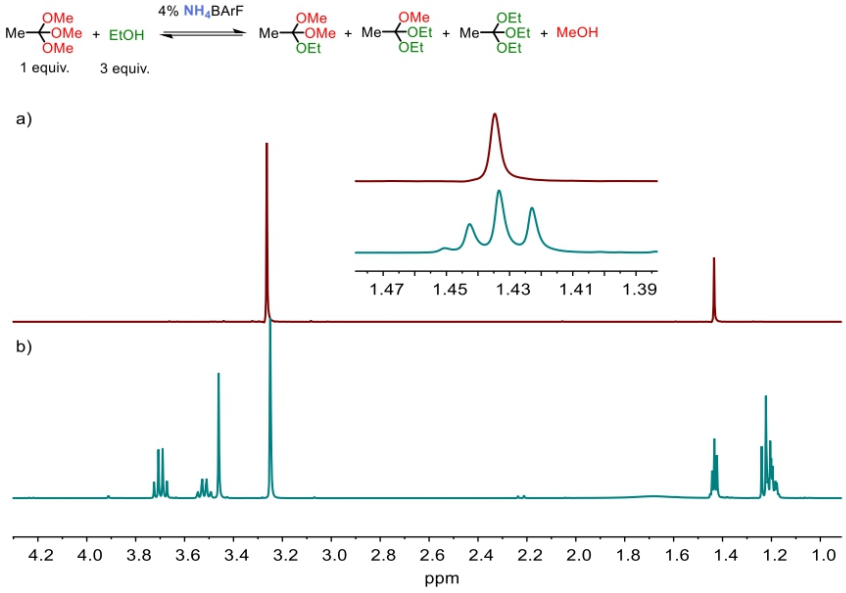

Figure S6. Partial ^{1}H NMR spectrum (400 MHz, 298 K, $CDCl_3$) of a) trimethyl orthoacetate (80 mM); b) orthoester exchange reaction after addition of 3 equivalents of ethanol at equilibrium (after 10 minutes).

Comparison of NH_4BArF prepared from AgBArF and directly from NaBArF

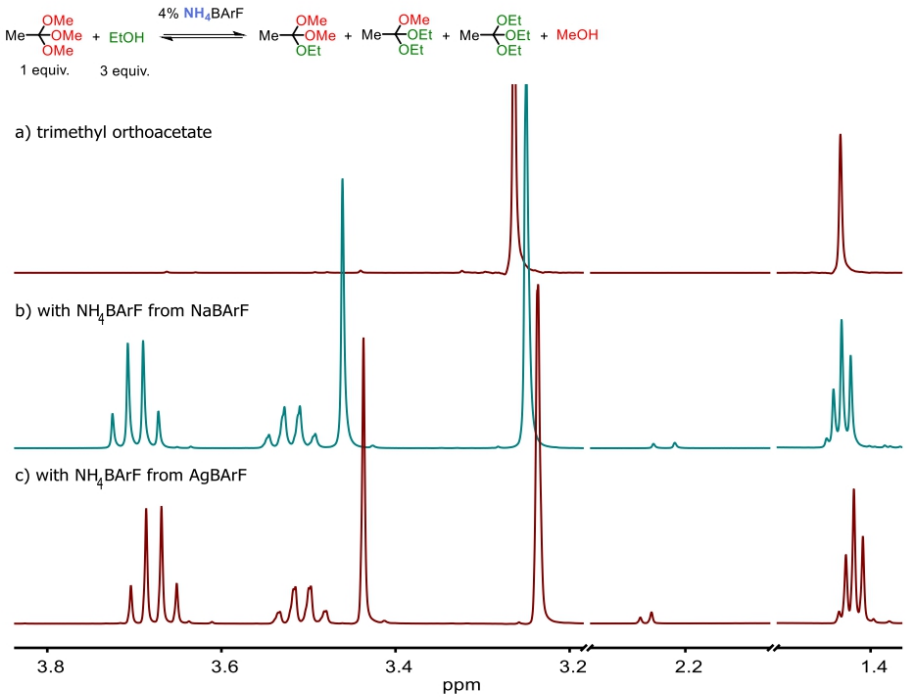

Figure S7. Partial ^1H NMR spectrum (400 MHz, 298 K, $CDCl_3$) of a) trimethyl orthoacetate (80 mM); b) orthoester exchange reaction after addition of 3 equivalents of ethanol at equilibrium (after 10 minutes) using NH_4BArF synthesized according to Method A; c) orthoester exchange reaction after addition of 3 equivalents of ethanol at equilibrium using NH_4BArF synthesized according to Method B (after 10 minutes).

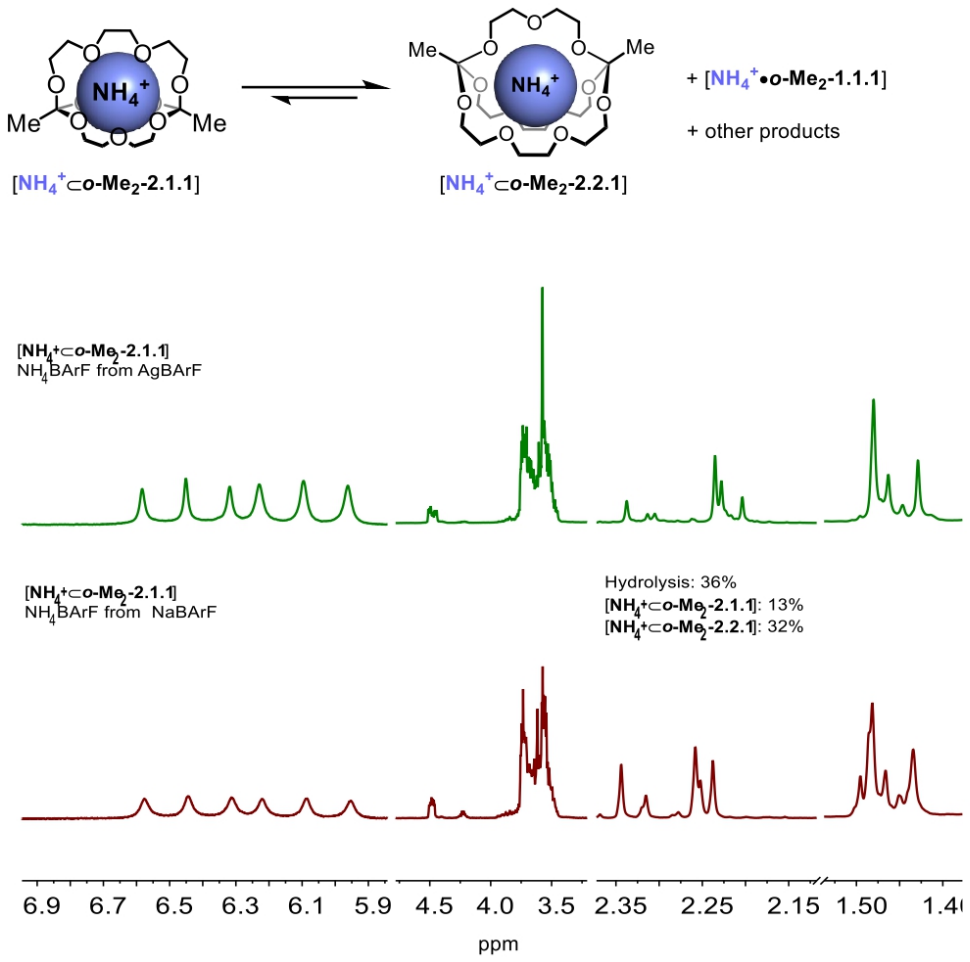

Figure S8. Partial ^{1}H NMR (400 MHz, 298 K, $CDCl_3$) of [**NH_4^+⊂*o*-Me$_2$-2.1.1**]$BArF^-$ (80 mM) at equilibrium (2-3 days) with NH_4BArF obtained from AgBArF (top spectrum) and from NaBArF (bottom spectrum). The solution was sealed in a J-Young NMR tube and stored under N_2 during the interval of NMR measurements. Proton resonances of NH_4^+ are enlarged by a factor of 8 for clarity.

2. Characterization and Inherent Dynamics of Orthoester Cryptand-NH_4^+ Complexes

Inherent dynamics of [NH_4^+•*o*-Me_2-1.1.1]BArF$^-$

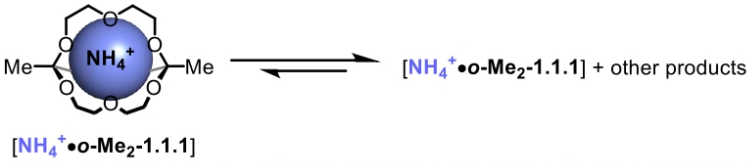

[NH_4^+•*o*-Me_2-1.1.1]

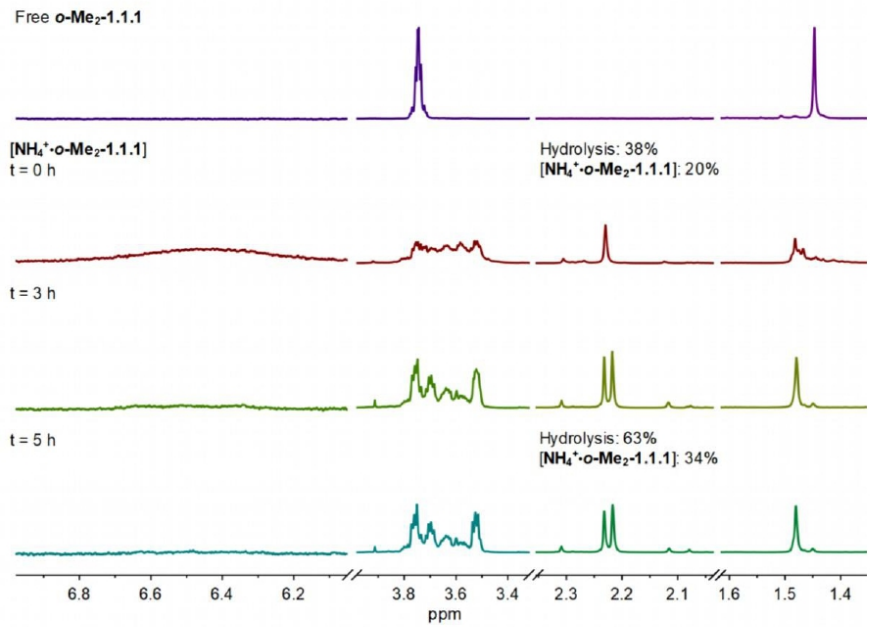

Figure S9. Partial ^{1}H NMR (400 MHz, 298 K, $CDCl_3$) of [**NH_4^+•*o*-Me_2-1.1.1**]BArF$^-$ (80 mM) at different time. The solution was sealed in a J-Young NMR tube and stored under N_2 during the interval of NMR measurements. Proton resonances of NH_4^+ are enlarged by a factor of 32 for clarity.

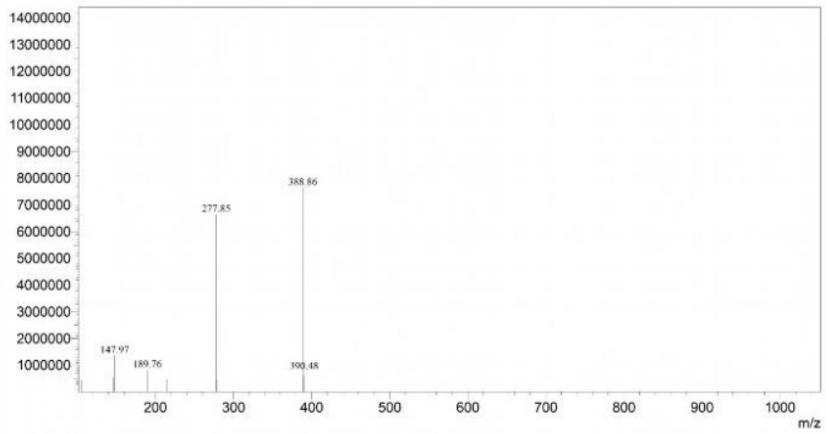

Figure S10. ESI-MS spectrum of [NH_4^+•***o***-Me_2-**1.1.1**]$BArF^-$ (80 mM) after 5 hours. Cryptate [Na^+•***o***-Me_2-**1.1.1**] (m/z = 388.86) was detected.

Inherent dynamics of [NH_4^+⊂*o*-Me_2-2.2.2]BArF$^-$

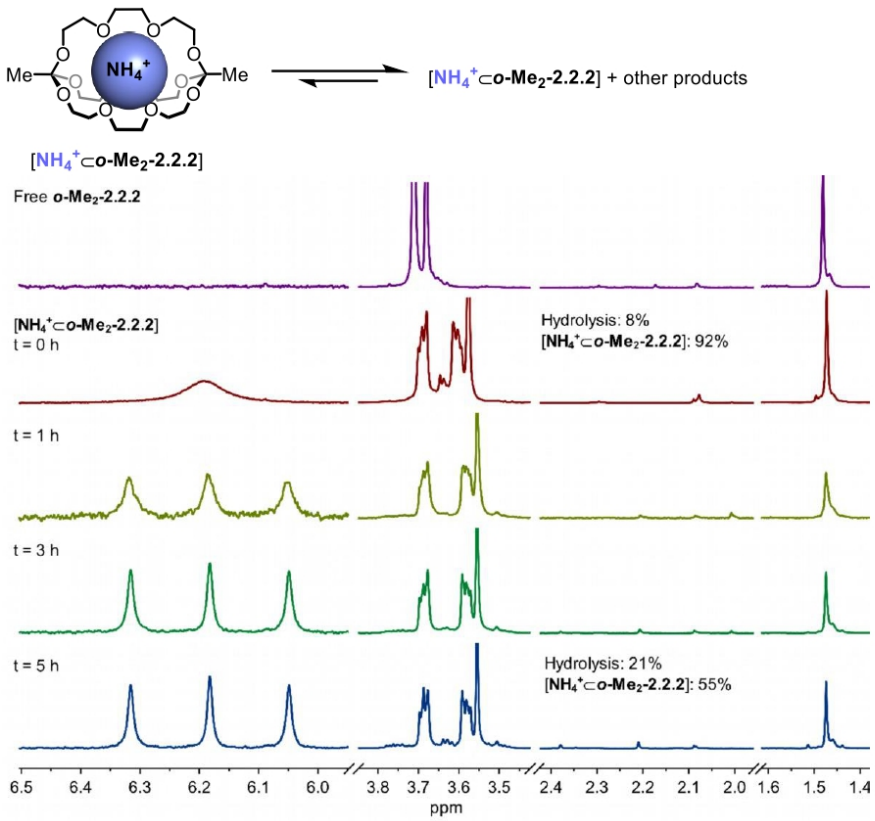

Figure S11. Partial ^{1}H NMR (400 MHz, 298 K, $CDCl_3$) of [**NH_4^+⊂*o*-Me_2-2.2.2**]BArF$^-$ (80 mM) at different time. The solution was sealed in a J-Young NMR tube and stored under N_2 during the interval of NMR measurements. Proton resonances of NH_4^+ are enlarged by a factor of 8 for clarity.

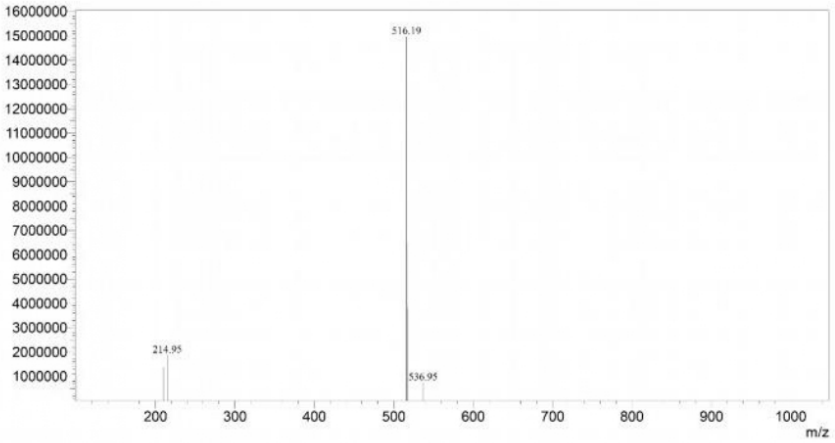

Figure S12. ESI-MS spectrum of [$\mathbf{NH_4^+}$⊂***o*-$\mathbf{Me_2}$-**2.2.2**]$BArF^-$ (80 mM) after 5 hours. Cryptate [$\mathbf{NH_4^+}$⊂***o*-$\mathbf{Me_2}$-**2.2.2**] (m/z = 516.19) was detected.

Inherent dynamics of [NH_4^+⊂*o*-Me_2-2.1.1]BArF$^-$

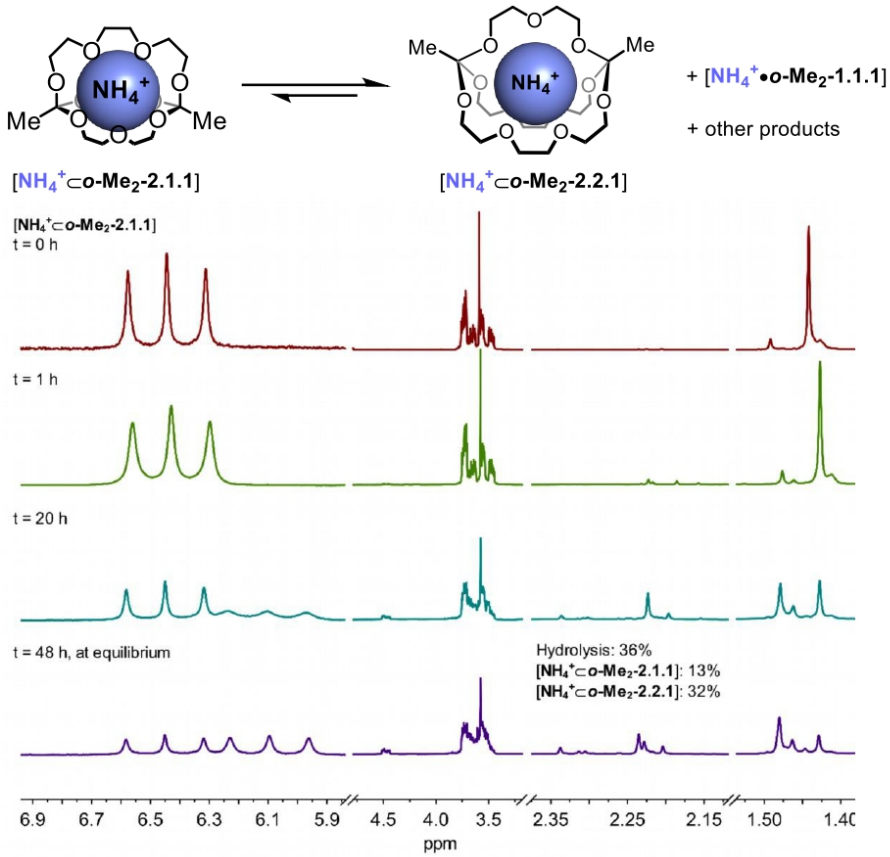

Figure S13. Partial ^{1}H NMR (400 MHz, 298 K, $CDCl_3$) of [**NH_4^+⊂*o*-Me_2-2.1.1**]BArF$^-$ (80 mM) at different time. The solution was sealed in a J-Young NMR tube and stored under N_2 during the interval of NMR measurements. Proton resonances of NH_4^+ are enlarged by a factor of 8 for clarity.

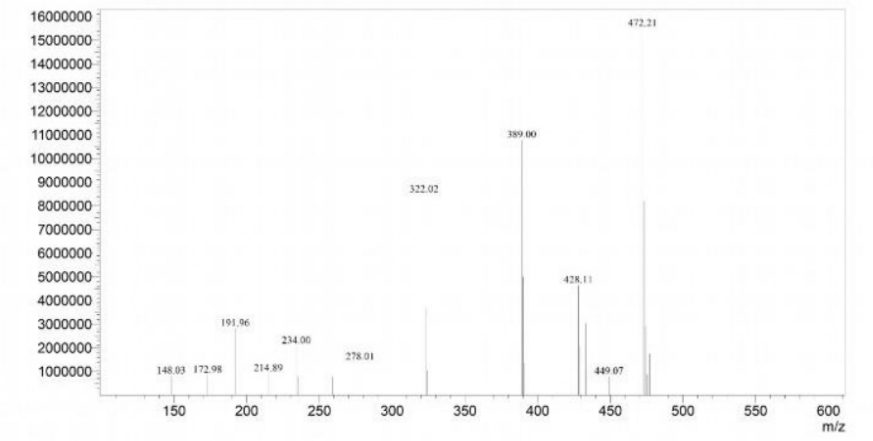

Figure S14. ESI-MS spectrum of [NH_4^+⊂***o***-Me_2-**2.2.2**]$BArF^-$ (80 mM) after 5 hours. Cryptates [Na^+•***o***-Me_2-**1.1.1**] (m/z = 389.00), [NH_4^+⊂***o***-Me_2-**2.1.1**] (m/z = 428.11), and [NH_4^+⊂***o***-Me_2-**2.2.1**] (m/z = 472.21) were detected.

Characterization of [NH_4^+⊂*o*-Me_2-2.2.1]$BArF^-$

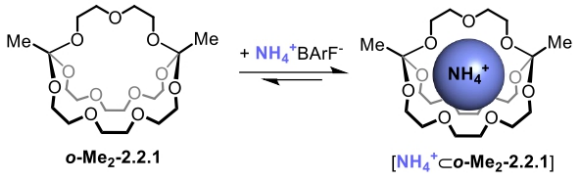

o-Me_2-2.2.1 [NH_4^+⊂*o*-Me_2-2.2.1]

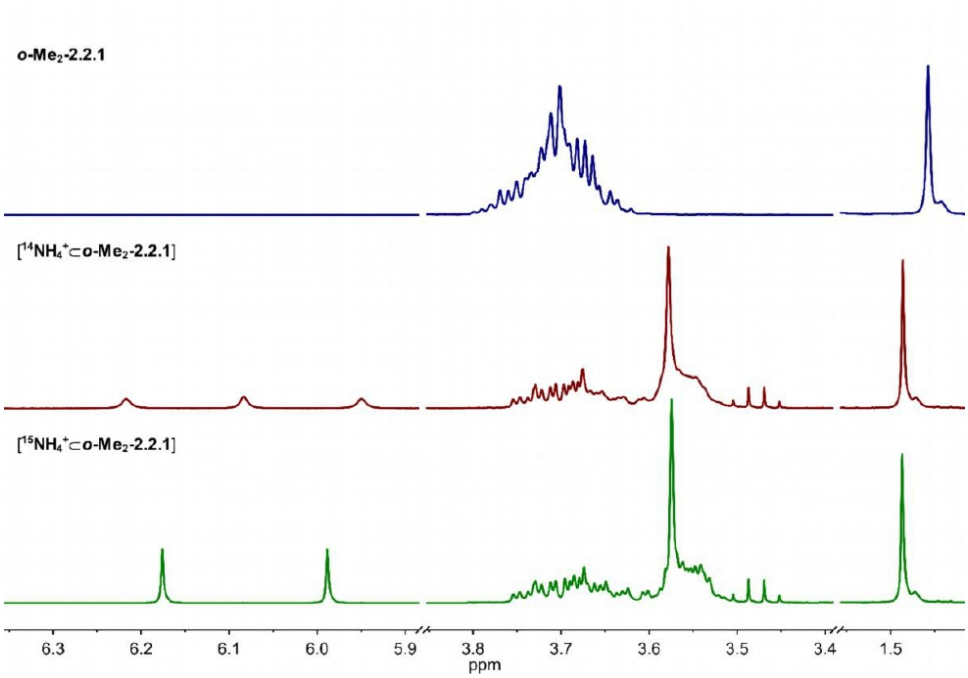

Figure S15. ^1H NMR spectra (400 MHz, 298 K, $CDCl_3$) of free ***o*-Me$_2$-2.2.1** (10 mM) and cryptates [**NH_4^+⊂*o*-Me$_2$-2.2.1**]$BArF^-$ with nitrogen isotopes ^{14}N and ^{15}N, respectively. Coupling of ^1H to ^{14}N or ^{15}N gives triplet or doublet, respectively.

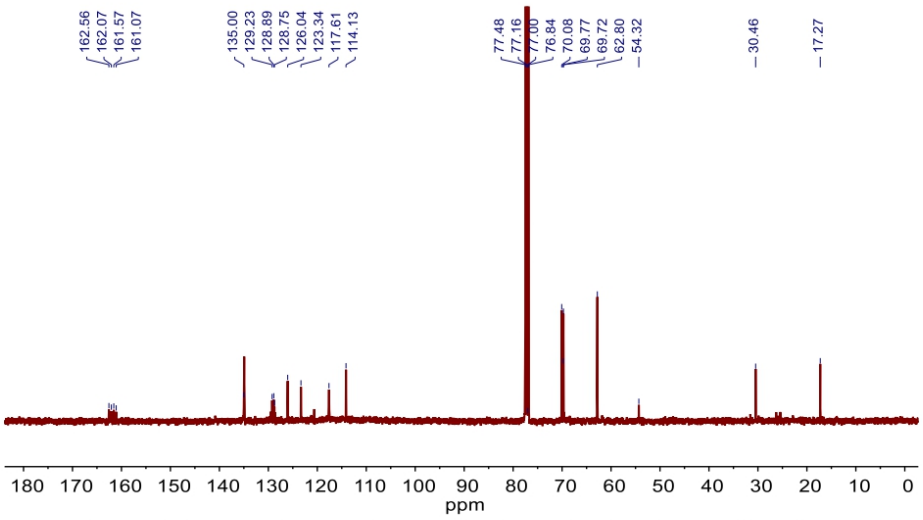

Figure S16. ^{13}C NMR spectrum (100 MHz, $CDCl_3$, 298 K) of cryptate **[NH_4^+⊂*o*-Me_2-2.2.1]**$BArF^-$.

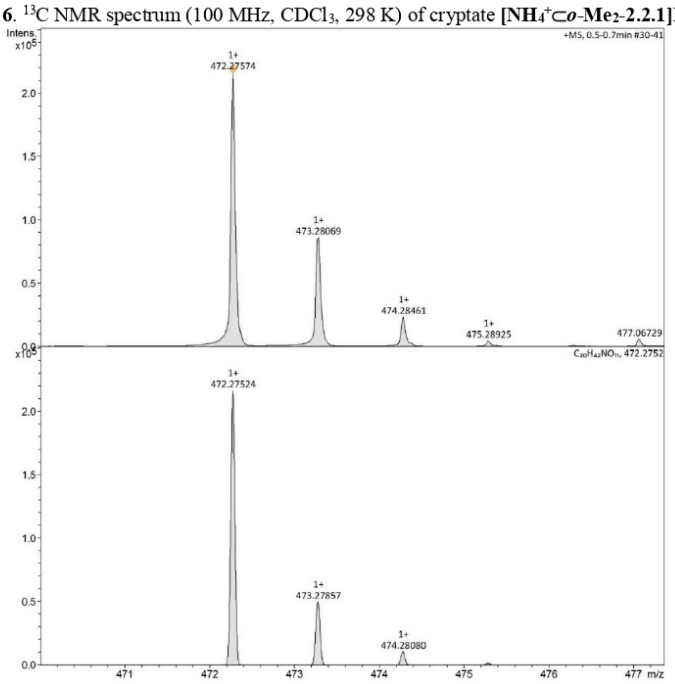

Figure S17. ESI-HRMS (top) and simulated (bottom) spectrum of cryptate **[NH_4^+⊂*o*-Me_2-2.2.1]**.

Inherent dynamics of [NH_4^+⊂*o*-Me_2-2.2.1]BArF$^-$

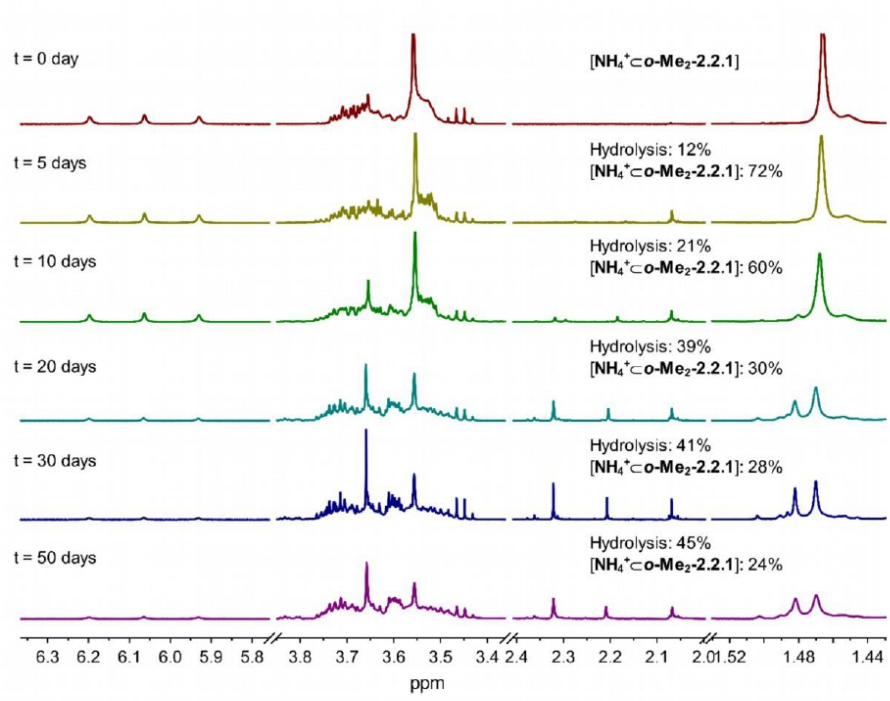

Figure S18. Partial ^{1}H NMR (400 MHz, 298 K, $CDCl_3$) of **[NH_4^+⊂*o*-Me_2-2.2.1]**BArF$^-$ (10 mM) over time. The solution was sealed in a J-Young NMR tube and stored under N_2 during the interval of NMR measurements.

Attempts to trap orthoamide intermediate by hydrolysis of [NH_4^+⊂*o*-Me_2-2.2.1]BArF$^-$

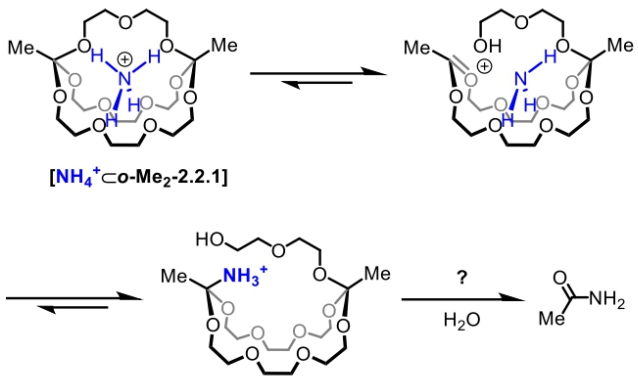

Scheme S1. Mechanism of acetamide formation through *N*,*O*,*O*-orthoamide intermediate.

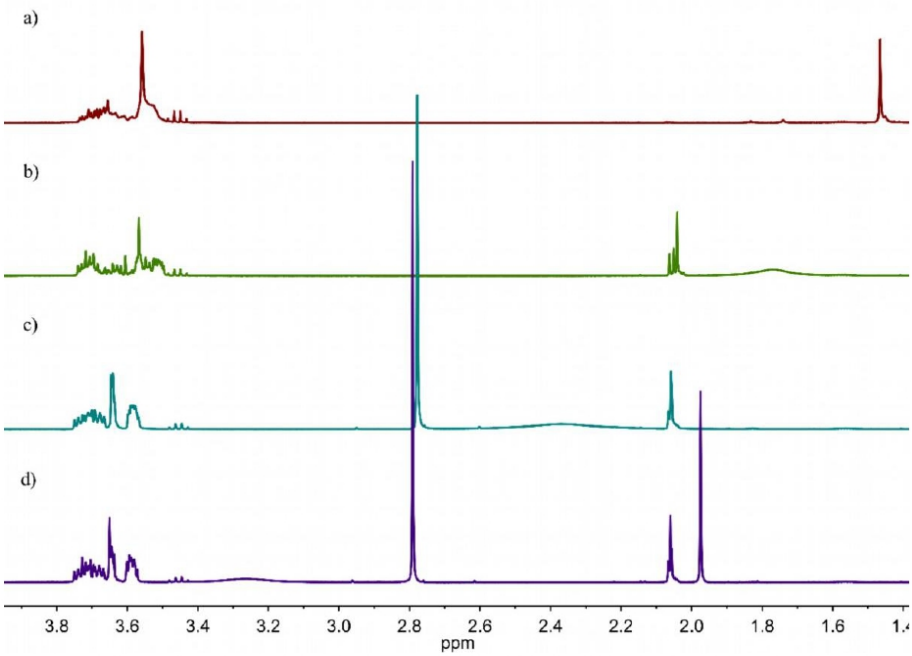

Figure S19. Partial ^{1}H NMR (400 MHz, 298 K, $CDCl_3$) of a) [**NH_4^+⊂*o*-Me_2-2.2.1**]$BArF^-$ (10 mM); b) after hydrolysis with H_2O (5 equiv.); c) after addition of 1,1,3,3-tetramethylguanidine (1.5 equiv.); and d) after addition of acetamide (1 equiv.).

Proposed mechanism for the inherent adaptive behavior of orthoester cryptate [NH_4^+⊂*o*-Me_2-2.1.1]$BArF^-$

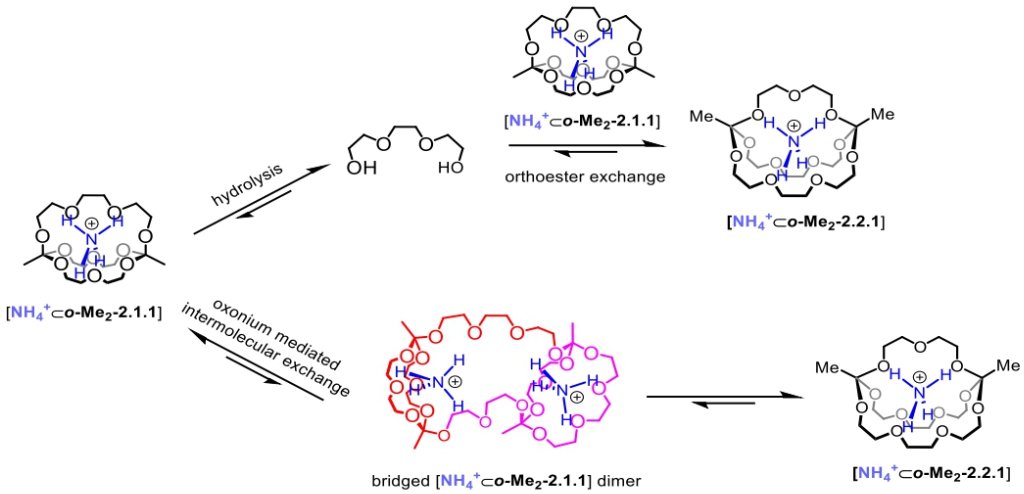

Scheme S2. Proposed mechanisms for the inherent adaptive behavior of orthoester cryptate [**NH_4^+⊂*o*-Me_2-2.1.1**]$BArF^-$. Top pathway: partial hydrolysis of [**NH_4^+⊂*o*-Me_2-2.1.1**] releases free TEG; Bottom: two [**NH_4^+⊂*o*-Me_2-2.1.1**] form bridged dimer via oxonium mediated intermolecular exchange.

3. Inherently Adaptive Behavior of Cryptand-NH_4^+ Complexes: Reaction with Diols

General Procedure:

In a nitrogen-filled glovebox, to a suspension of NH_4BArF in anhydrous $CDCl_3$ were added the corresponding amounts of the diol and the cryptands from their stock solution consequently. The mixture was transferred to a J-Young NMR tube for ^1H NMR investigation and was stored in the glovebox between the measurements.

Adaptive behavior of [NH_4^+•*o*-Me_2-1.1.1]$BArF^-$: addition of 2 equivalents of TEG

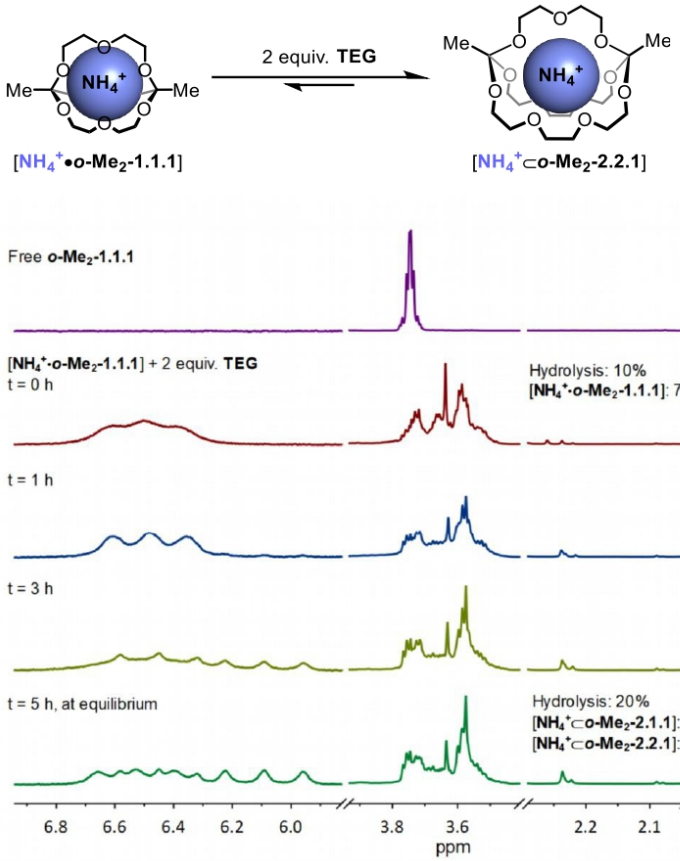

Figure S20. Partial ^1H NMR (400 MHz, 298 K, $CDCl_3$) of [NH_4^+•*o*-Me_2-1.1.1]$BArF^-$ (80 mM) with 2 equivalents of DEG after different time. Proton resonances of NH_4^+ are enlarged by a factor of 8 for clarity.

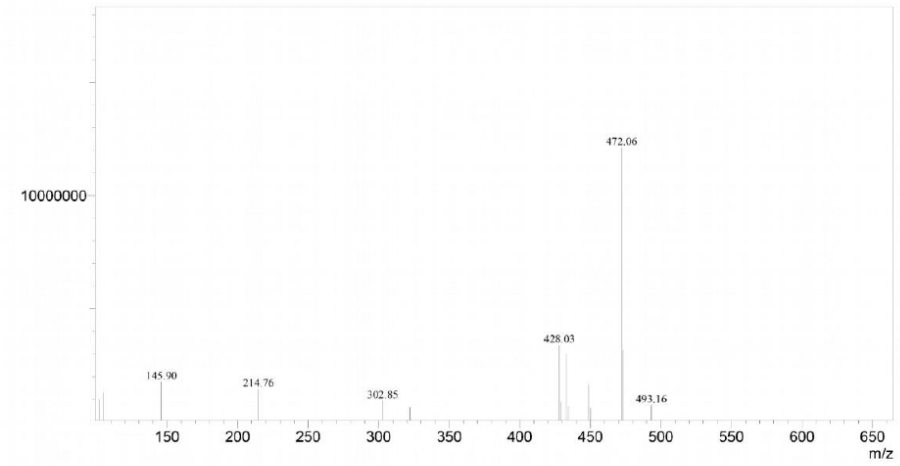

Figure S21. ESI-MS spectrum of [NH_4^+•***o*-Me_2-**1.1.1**]$BArF^-$ (80 mM) with 2 equivalents of DEG at equilibrium. Cryptates [NH_4^+⊂***o*-Me_2-**2.1.1**] (m/z = 428.03) and [NH_4^+⊂***o*-Me_2-**2.2.1**] (m/z = 472.06) were detected.

Adaptive behavior of [NH_4^+⊂*o*-Me_2-2.1.1]BArF$^-$: addition of 1 equivalent of TEG

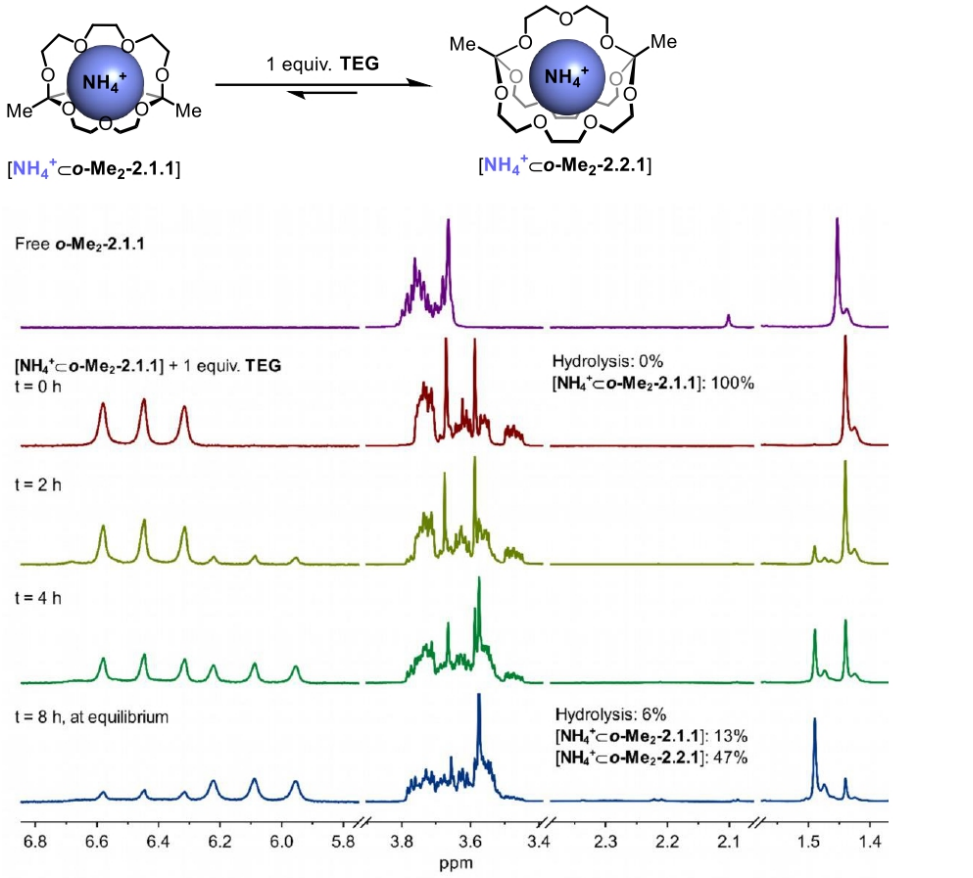

Figure S22. Partial ^{1}H NMR (400 MHz, 298 K, $CDCl_3$) of [**NH_4^+⊂*o*-Me_2-2.1.1**]BArF$^-$ (80 mM) with 1 equivalent of TEG after different time. Proton resonances of NH_4^+ are enlarged by a factor of 8 for clarity.

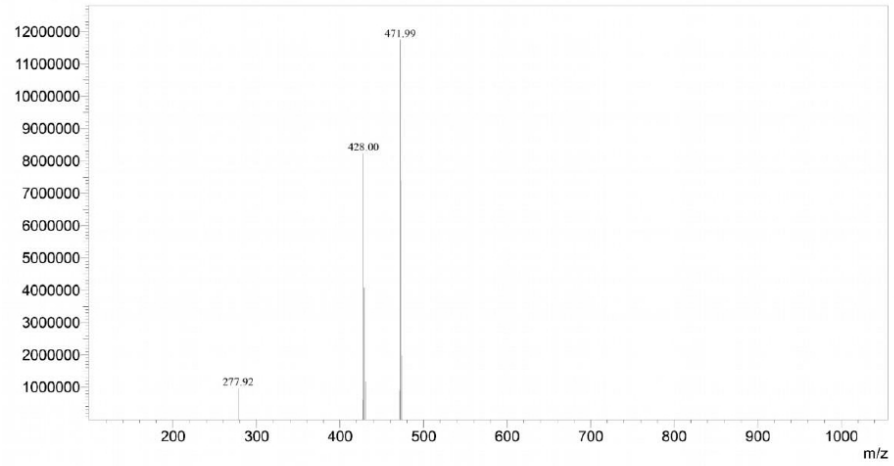

Figure S23. ESI-MS spectrum of [NH_4^+⊂***o***-Me_2-**2.1.1**]$BArF^-$ (80 mM) with 1 equivalent of TEG at equilibrium. Cryptates [NH_4^+⊂***o***-Me_2-**2.1.1**] (m/z = 428.00) and [NH_4^+⊂***o***-Me_2-**2.2.1**] (m/z = 471.99) were detected.

Adaptive behavior of [NH_4^+⊂*o*-Me_2-2.2.2]BArF$^-$: addition of 1 equivalent of DEG

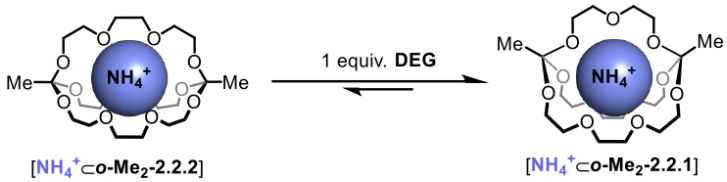

[NH_4^+⊂*o*-Me_2-2.2.2] [NH_4^+⊂*o*-Me_2-2.2.1]

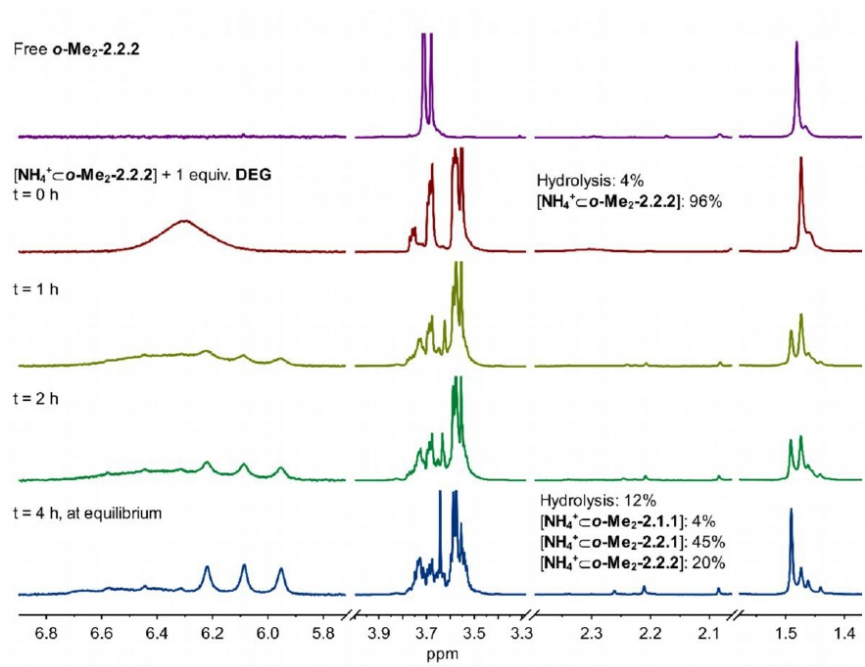

Figure S24. Partial ^{1}H NMR (400 MHz, 298 K, $CDCl_3$) of [**NH_4^+⊂*o*-Me_2-2.2.2**]BArF$^-$ (80 mM) with 1 equivalent of DEG after different time. Proton resonances of NH_4^+ are enlarged by a factor of 8 for clarity.

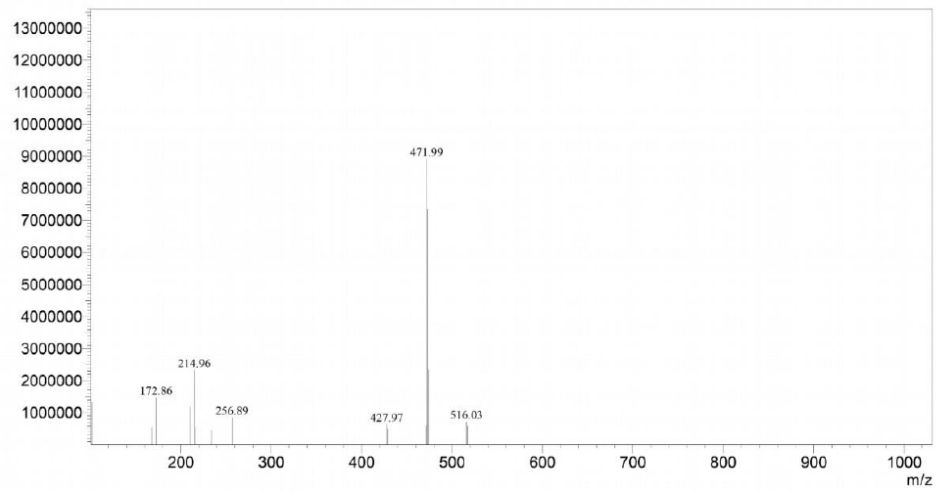

Figure S25. ESI-MS spectrum of [NH_4^+⊂***o***-Me_2-**2.2.2**]$BArF^-$ (80 mM) with 1 equivalents of DEG at equilibrium. Cryptates [NH_4^+⊂***o***-Me_2-**2.1.1**] (m/z =427.97), [NH_4^+⊂***o***-Me_2-**2.2.1**] (m/z = 471.99), and [NH_4^+⊂***o***-Me_2-**2.2.2**] (m/z = 516.03) were detected.

4. Binding Constants Determination

General procedure for ^{1}H NMR titrations

A stock solution of freshly prepared cryptand (20 mM) in CD_3CN was dried with 3 Å molecular sieves for 24 hours and stored under N_2. A stock solution of NH_4BArF (20 mM) in CD_3CN was dried with 5 Å molecular sieves for 24 hours and stored under N_2. For ^{1}H NMR titration experiments, 50 uL of cryptand stock solution and different volume of NH_4BArF stock solution was mixed and diluted to 500 uL. Binding constants were obtained by fitting the titration data using supramolecular.org.

^{1}H NMR Titration of *o*-Me_2-1.1.1 with NH_4BArF

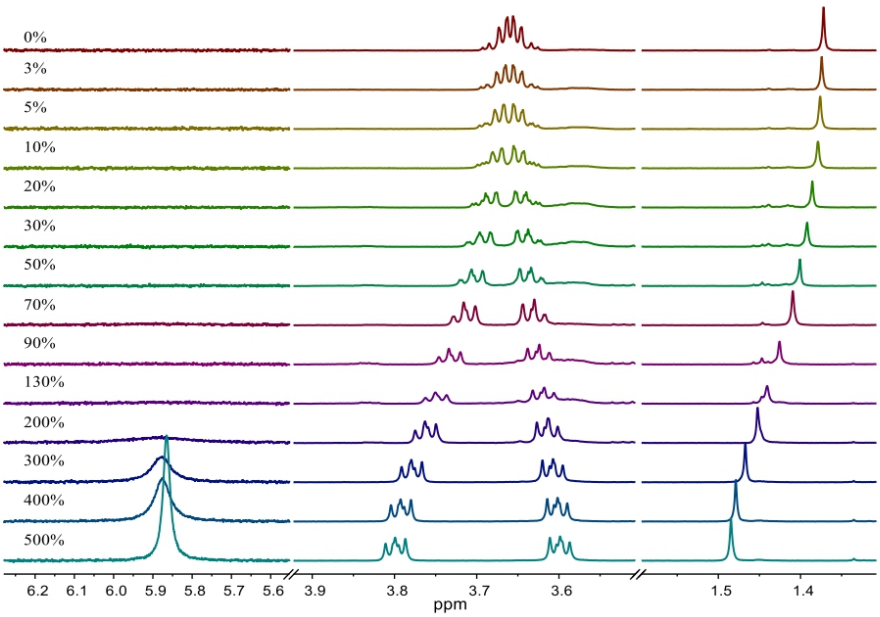

Figure S26. Partial ^{1}H NMR (400 MHz, 298 K, CD_3CN) stack plot of ***o*-Me$_2$-1.1.1** (2 mM) titration with NH_4BArF from 0% - 500%.

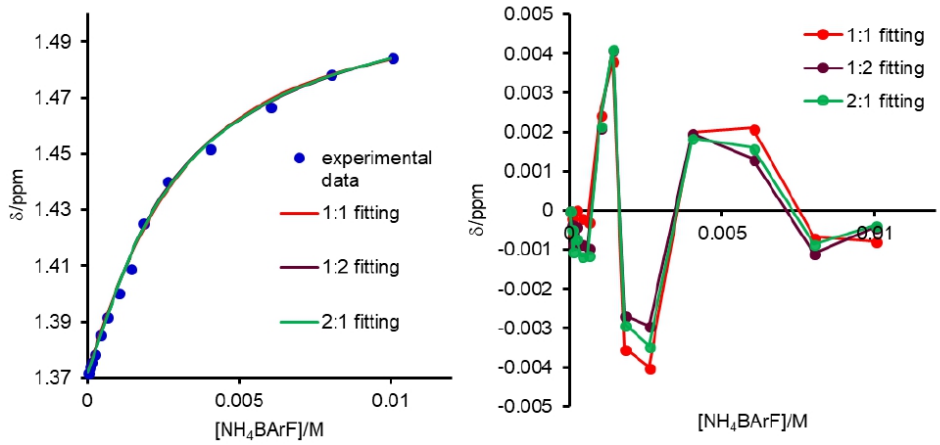

Figure S27. Left column: experimental and calculated chemical shifts for titration of ***o*-Me$_2$-1.1.1** (2 mM) with **NH$_4$BArF** from 0 - 500% in CD_3CN. Blue circles correspond to experimental values. Red line, purple line and green line correspond to fitted binding isotherms using 1:1 model, 1:2 model, and 2:1 model respectively. Right column: residual plots. The data fitting details for 1:1 binding model is available at http://app.supramolecular.org/bindfit/view/2b79a138-45c0-424f-a7e6-e470203ac492. The data fitting details for 1:2 binding model is available at http://app.supramolecular.org/bindfit/view/6f48d153-2e1a-40b3-905b-7c42b66d7167. The data fitting details for 2:1 binding model is available at http://app.supramolecular.org/bindfit/view/5cb42010-343f-4265-bfb0-24480ef53bcd.

Table S1. Binding constants of ***o*-Me$_2$-1.1.1** toward NH_4BArF.

1:1 fitting	1:2 fitting	2:1 fitting
540±40 M^{-1}	K_{11} = 4 000±1 000 M^{-1}	K_{11} = 1 000±1 000 M^{-1}
	K_{12} = 170±30 M^{-1}	K_{21} = 600±1 000 M^{-1}

^{1}H NMR Titration of *o*-Me$_2$-2.1.1 with NH$_4$BArF

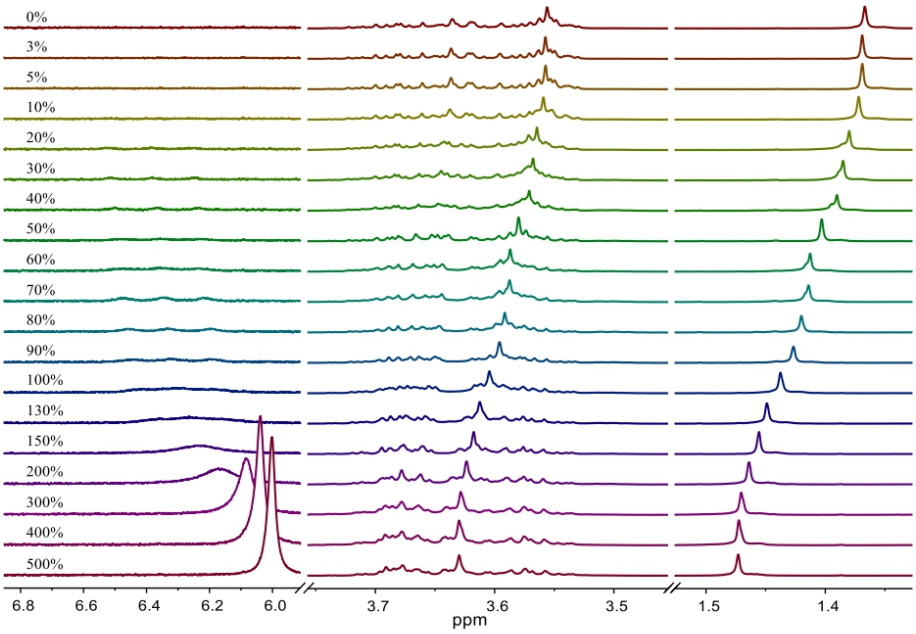

Figure S28. Partial ^{1}H NMR (400 MHz, 298 K, CD_3CN) stack plot of ***o*-Me$_2$-2.1.1** (2 mM) titration with NH_4BArF from 0 - 500%.

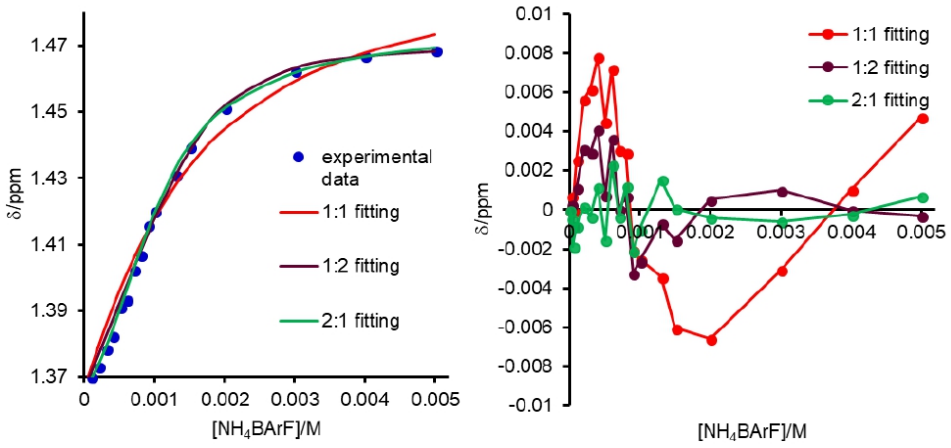

Figure S29. Left column: experimental and calculated chemical shifts for titration of ***o*-Me$_2$-2.1.1** (1 mM) with NH_4BArF from 0 - 500% in CD_3CN. Blue circles correspond to experimental values. Red line, purple line and green

line correspond to fitted binding isotherm using 1:1 model, 1:2 model and 2:1 model respectively. Right column: residual plots. The data fitting details for 1:1 binding model is available at http://app.supramolecular.org/bindfit/view/daa0b8c0-301b-408c-9f9b-1dba2be84daf. The data fitting details for 1:2 binding model is available at http://app.supramolecular.org/bindfit/view/cc522ca3-f2eb-4152-9acd-e158e19d8a9b. The data fitting details for 2:1 binding model is available at http://app.supramolecular.org/bindfit/view/a99c2a24-e8df-4634-836e-f961c712daea.

Table S2. Binding constants of ***o*-Me$_2$-2.1.1** toward NH_4BArF.

1:1 fitting	1:2 fitting	2:1 fitting
	K_{11} = 2 000 000±3 000 000 M^{-1}	
1 000±100 M^{-1}		K_{11} = 4 800±400 M^{-1}
	K_{12} = 5 000±2 000 M^{-1}	K_{21} = 8.6(±0.7) ×10^{-7} M^{-1}

^{1}H NMR Titration of *o*-Me$_2$-2.2.1 with NH_4BArF

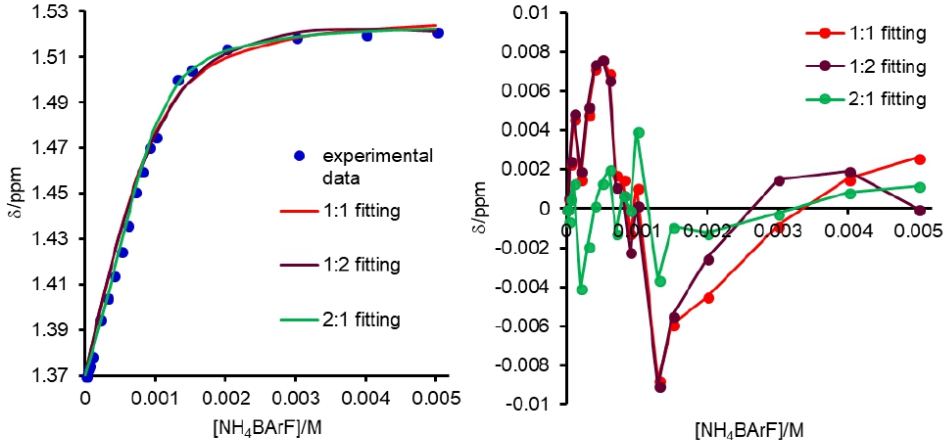

Figure S30. Left column: experimental and calculated chemical shifts for titration of ***o*-Me$_2$-2.2.1** (1 mM) with NH_4BArF from 0 - 500% in CD_3CN. Blue circles correspond to experimental values. Red line, purple line and green line correspond to fitted binding isotherms using 1:1 model, 1:2 model and 2:1 model respectively. Right column: residual plots. The data fitting details for 1:1 binding model is available at http://app.supramolecular.org/bindfit/view/d9e9e5a5-b287-4c94-ae0e-7c44174c6dcc. The data fitting details for 1:2 binding model is available at http://app.supramolecular.org/bindfit/view/c2668d68-3184-45be-ab01-db1dba02eb3b. The data fitting details for 2:1 binding model is available at http://app.supramolecular.org/bindfit/view/ba8165c9-fb1e-482a-b34e-f82b72605a6b.

Table S3. Binding constants of ***o*-Me$_2$-2.2.1** toward **NH$_4$BArF**

1:1 fitting	1:2 fitting	2:1 fitting
6 000±1 000 M^{-1}	K_{11} = 3 500±500 M^{-1}	K_{11} = 13 000±2 000 M^{-1}
	K_{12} = 6(±3) ×10^{-10} M^{-1}	K_{21} = 1.3(±0.3) ×10^{-8} M^{-1}

^{1}H NMR Titration of *o*-Me$_2$-2.2.2 with NH$_4$BArF

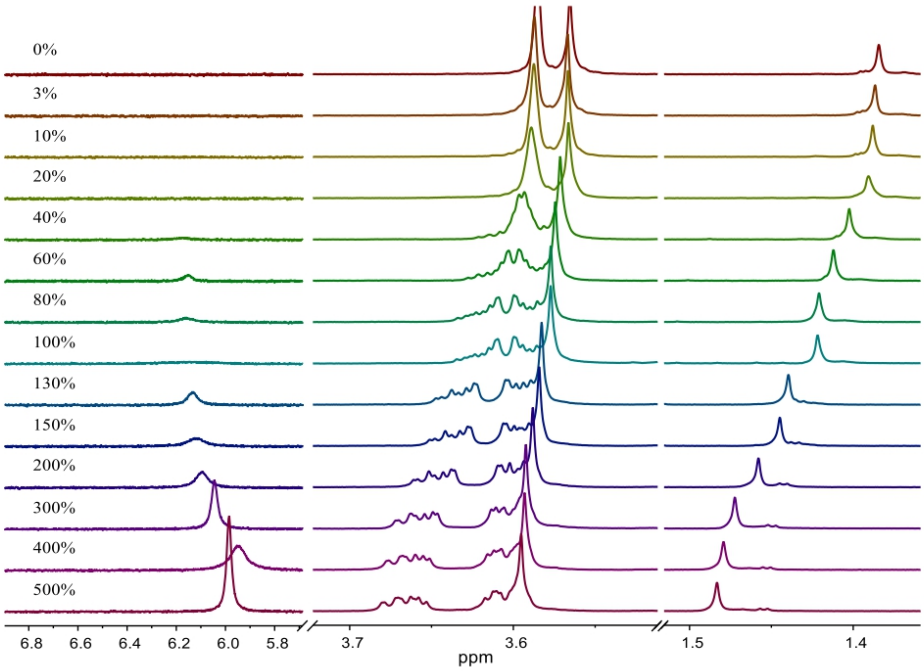

Figure S31. Partial ^{1}H NMR (400 MHz, 298 K, CD_3CN) stack plot of ***o*-Me$_2$-2.2.2** (2 mM) titration with NH_4BArF from 0 - 500 %.

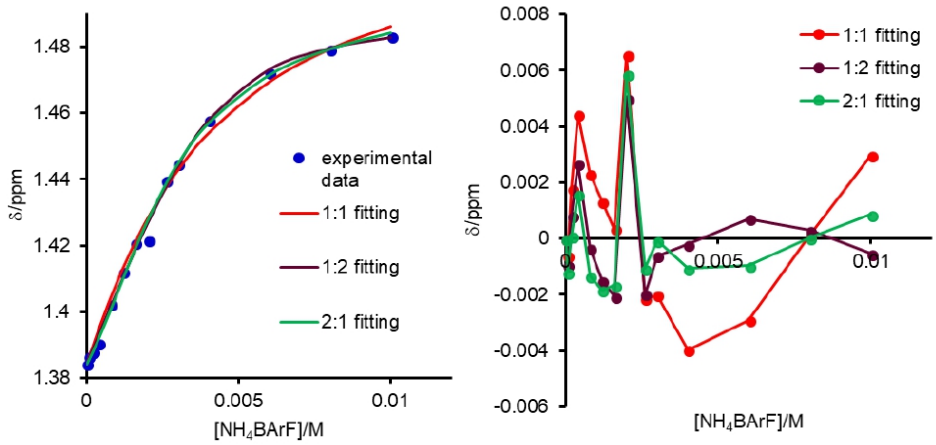

Figure S32. Left column: experimental and calculated chemical shift for titration of ***o*-Me$_2$-2.2.2** (2 mM) with **NH$_4$BArF** from 0 - 500% in CD_3CN. Blue circles correspond to experimental values. Red line, purple line and green line correspond to fitted binding isotherms using 1:1 model, 1:2 model and 2:1 model respectively. Right column: residual plots. The data fitting details using 1:1 binding model is available at http://app.supramolecular.org/bindfit/view/b7b20e05-cd8a-4ccb-9b1d-4748f7144fc3. The data fitting details using 1:2 binding model is available at http://app.supramolecular.org/bindfit/view/870ce343-a587-47c3-95af-dfc0bf76fdd9. The data fitting details using 2:1 binding model is available at http://app.supramolecular.org/bindfit/view/7b99241f-dc45-4d83-81d3-db389087048c.

Table S4. Binding constants of ***o*-Me$_2$-2.2.2** toward NH_4BArF.

1:1 fitting	1:2 fitting	2:1 fitting
350±30 M^{-1}	K_{11} = 3 000±2 000 M^{-1}	K_{11} = 1 000±200 M^{-1}
	K_{12} = 1 000±400M^{-1}	K_{21} = 3(±1) ×10^{-8} M^{-1}

^{1}H NMR Titration of *o*-Me$_2$-1.1.1 with CH_3NH_3BArF

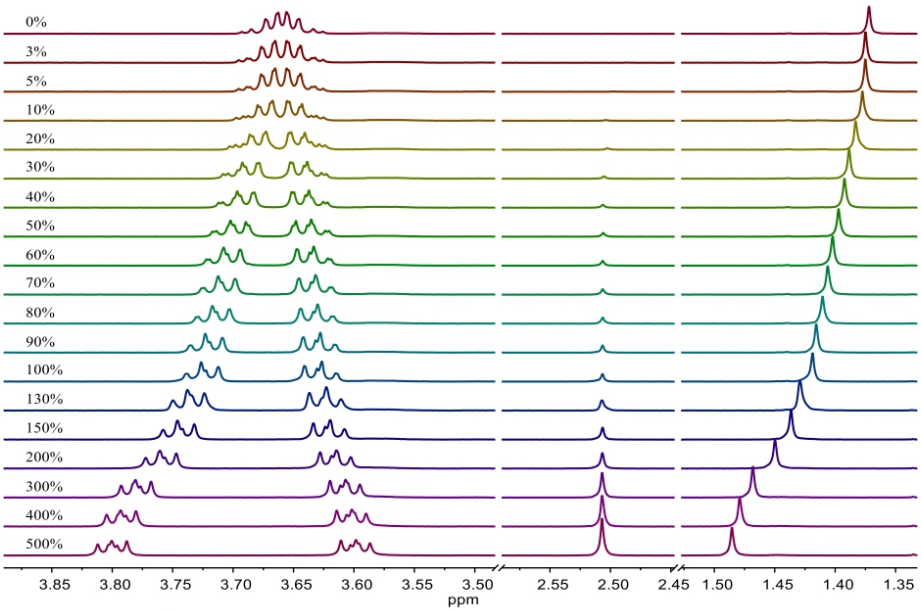

Figure S33. Partial ^{1}H NMR (400 MHz, 298 K, CD_3CN) stack plot of ***o*-Me$_2$-1.1.1** (2 mM) titration with CH_3NH_3BArF from 0% - 500%.

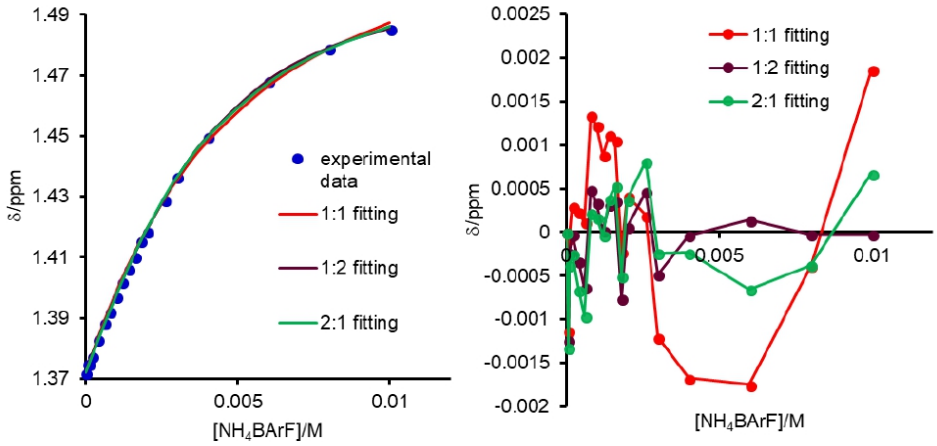

Figure S34. Left column: experimental and calculated chemical shifts for titration of ***o*-Me$_2$-1.1.1** (2 mM) with CH_3NH_3BArF from 0 - 500% in CD_3CN. Blue circles correspond to experimental values. Red line, purple line and green line correspond to fitted binding isotherm using 1:1 model, 1:2 model, and 2:1 model respectively. Right column: residual plots. The data fitting details using 1:1 binding model is available at http://app.supramolecular.org/bindfit/view/32bdcabf-3410-4645-83d7-5263bbd6a26e. The data fitting details using

1:2 binding model is available at http://app.supramolecular.org/bindfit/view/5dd15099-54b4-4720-bf3b-ef4f20ebe691. The data fitting details using 2:1 binding model is available at http://app.supramolecular.org/bindfit/view/65b2e111-a169-49df-b43c-088eb44d6ee3.

Table S5. Binding constants of ***o*-Me$_2$-1.1.1** toward CH_3NH_3BArF.

1:1 fitting	1:2 fitting	2:1 fitting
290±6 M^{-1}	K_{11} = 790±30 M^{-1}	K_{11} = 520±30 M^{-1}
	K_{12} = 330±20M^{-1}	K_{21} = 1.5(±0.2) ×10^{-4} M^{-1}

^{1}H NMR Titration of *o*-Me$_2$-2.1.1 with CH_3NH_3BArF

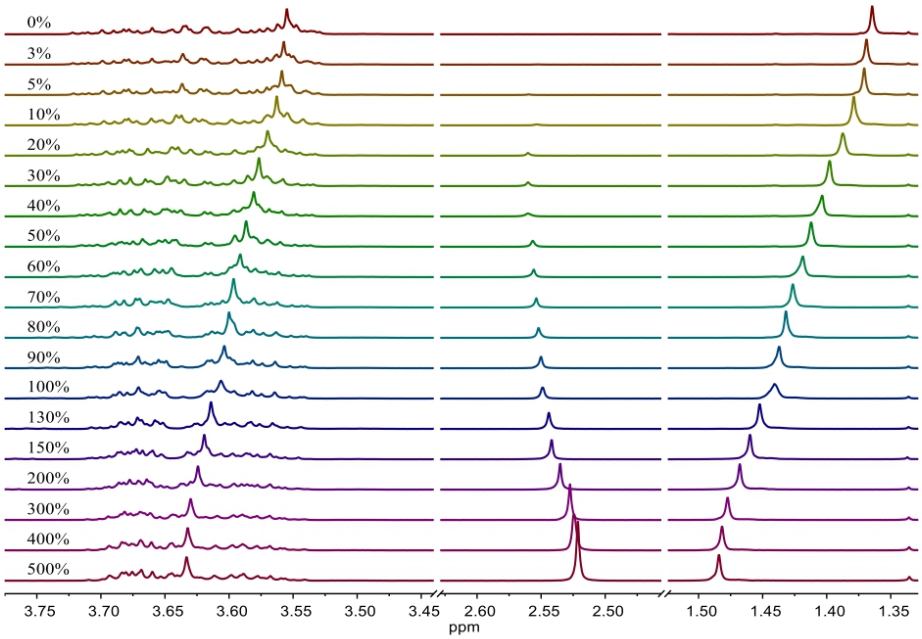

Figure S35. Partial ^{1}H NMR (400 MHz, 298 K, CD_3CN) stack plot of ***o*-Me$_2$-2.1.1** (2 mM) titration with CH_3NH_3BArF from 0 - 500 %.

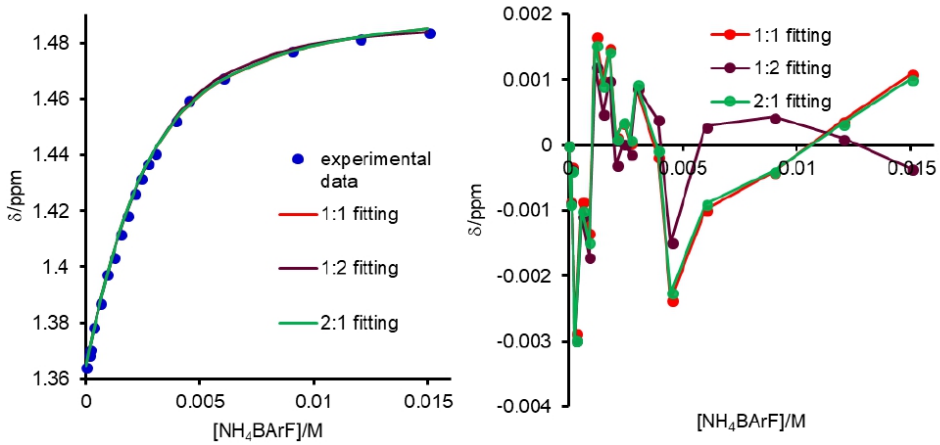

Figure S36. Left column: experimental and calculated chemical shifts for titration of ***o*-Me$_2$-2.1.1** (2 mM) with CH_3NH_3BArF from 0 - 500% in CD_3CN. Blue circles denote to experimental values. Red line, purple line and green line denotes to fitted binding isotherm using 1:1 model, 1:2 model and 2:1 model, respectively. Right column: residual plots. The data fitting details using 1:1 binding model is available at http://app.supramolecular.org/bindfit/view/844b9f05-3c1e-4b5a-80a3-9c784e01b4a4. The data fitting details using 1:2 binding model is available at http://app.supramolecular.org/bindfit/view/4a20363e-2cb6-48ea-b2b1-0f9b9775220d. The data fitting details using 2:1 binding model is available at http://app.supramolecular.org/bindfit/view/6f3259b6-2d9f-4b97-97fc-8d2a929cf225.

Table S6. Binding constants of ***o*-Me$_2$-2.1.1** toward CH_3NH_3BArF.

1:1 fitting	1:2 fitting	2:1 fitting
750±30 M^{-1}	K_{11} = 770±30 M^{-1}	K_{11} = 800±200 M^{-1}
	K_{12} = 100±100M^{-1}	K_{21} = 1 (±6) ×10^{-8} M^{-1}

^{1}H NMR Titration of *o*-Me$_2$-2.2.1 with CH_3NH_3BArF

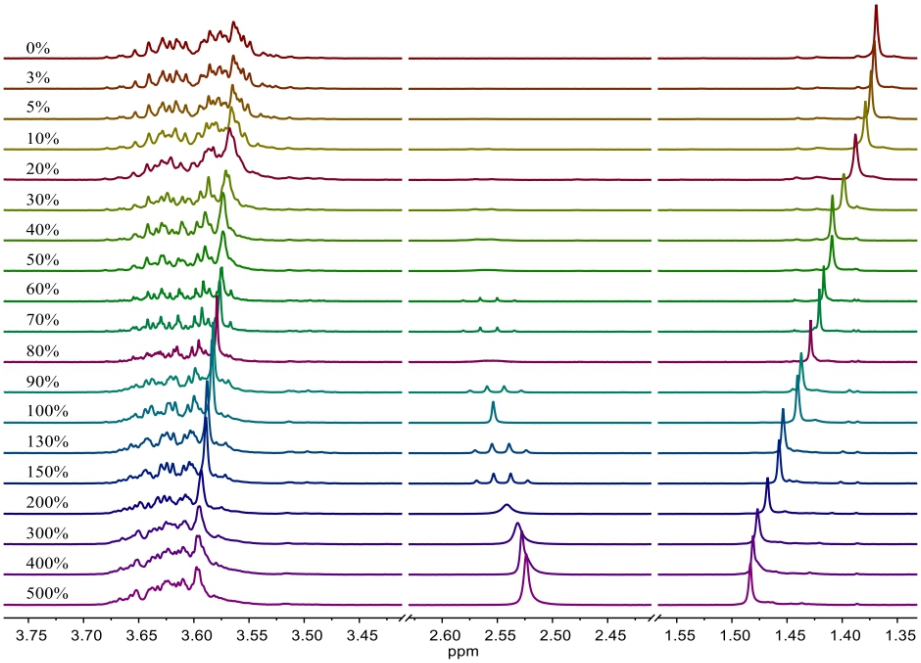

Figure S37. Partial ^{1}H NMR (400 MHz, 298 K, CD_3CN) stack plot of ***o*-Me$_2$-2.2.1** (2 mM) titration with CH_3NH_3BArF from 0 - 500%.

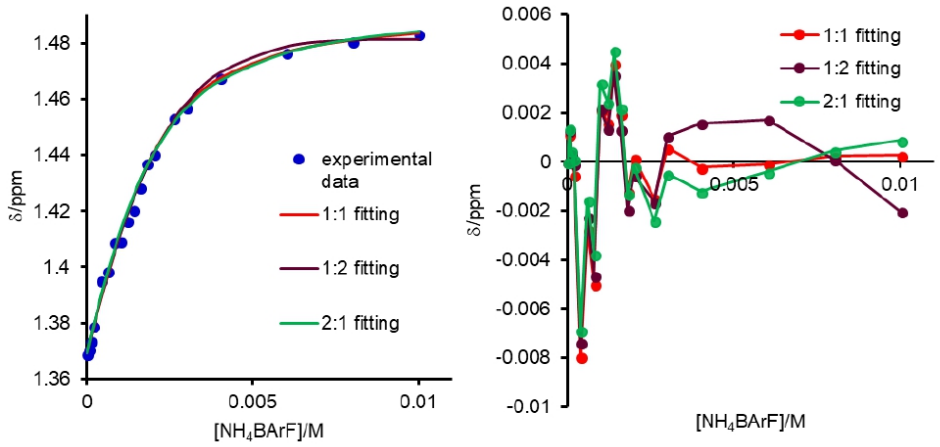

Figure S38. Left column: experimental and calculated chemical shifts for titration of ***o*-Me$_2$-2.2.1** (2 mM) with CH_3NH_3BArF from 0 - 500% in CD_3CN. Blue circles correspond to experimental values. Red line, purple line and green line correspond to fitted binding isotherm using 1:1 model, 1:2 model, and 2:1 model respectively. Right column: residual plots. The data fitting details using 1:1 binding model is available at

http://app.supramolecular.org/bindfit/view/74ce079b-254f-4d43-b119-f51ee909e242. The data fitting details using 1:2 binding model is available at http://app.supramolecular.org/bindfit/view/075665ab-656a-4edd-bfd1-1ffa173db58c. The data fitting detaisl using 2:1 binding model is available at http://app.supramolecular.org/bindfit/view/c8a66031-c8f3-4b15-aa39-f4321050d1aa.

Table S7. Binding constants of ***o*-Me$_2$-2.2.1** toward CH_3NH_3BArF.

1:1 fitting	1:2 fitting	2:1 fitting
1 700±200 M^{-1}	K_{11} = 1 300±300 M^{-1}	K_{11} = 1 200±400 M^{-1}
	K_{12} = 400±500M^{-1}	K_{21} = 20±40 M^{-1}

^{1}H NMR Titration of *o*-Me$_2$-2.2.2 with CH_3NH_3BArF

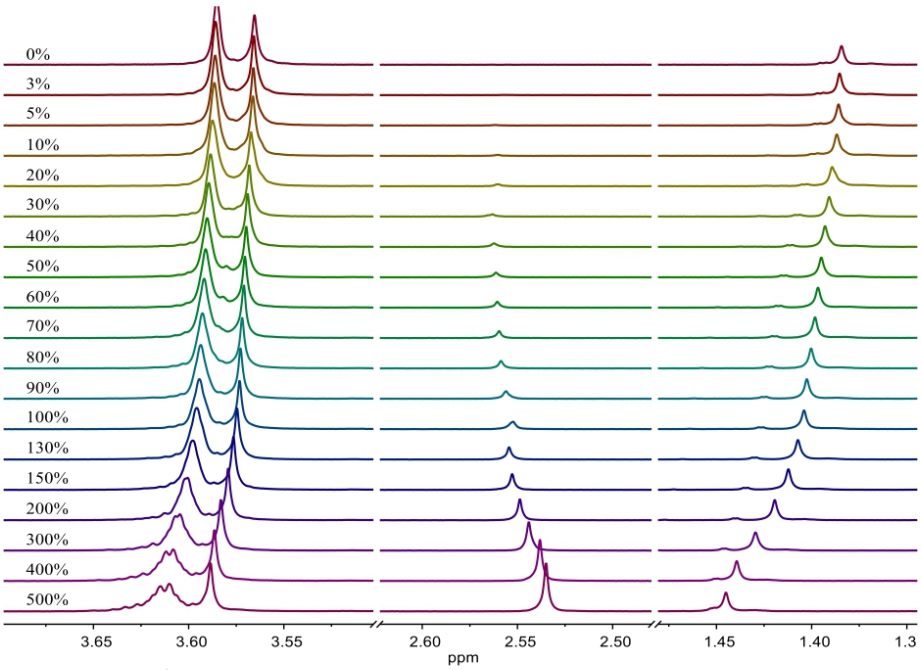

Figure S39. Partial ^{1}H NMR (400 MHz, 298 K, CD_3CN) stack plot of ***o*-Me$_2$-2.2.2** (2 mM) titration with CH_3NH_3BArF from 0 - 500%.

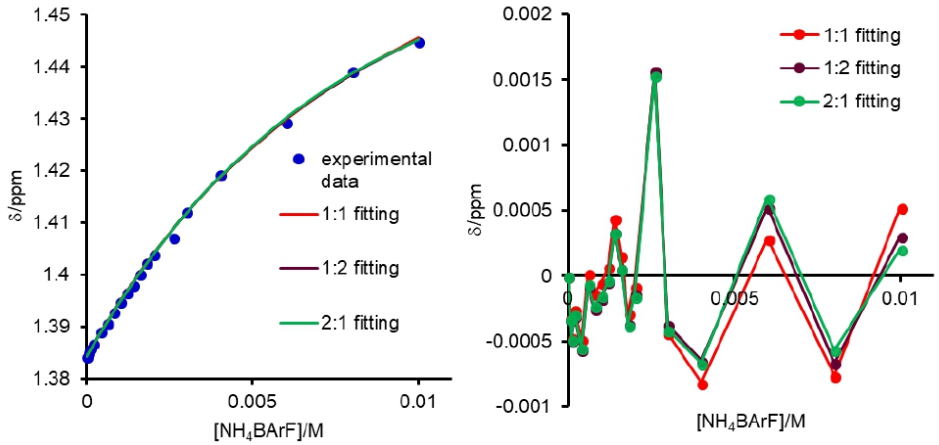

Figure S40. Left column: experimental and calculated chemical shifts for titration of ***o*-Me$_2$-2.2.2** (2 mM) with CH_3NH_3BArF from 0 - 500% in CD_3CN. Blue circles correspond to experimental values. Red line, purple line and green line correspond to fitted binding isotherms using 1:1 model, 1:2 model and 2:1 model respectively. Right column: residual. The data fitting details using 1:1 binding model is available at http://app.supramolecular.org/bindfit/view/28a9c2a4-d721-4fa4-bb1c-fcf5d67cf67e. The data fitting details using 1:2 binding model is available at http://app.supramolecular.org/bindfit/view/9541d22c-0958-4553-a64b-e0e996253487. The data fitting details using 2:1 binding model is available at http://app.supramolecular.org/bindfit/view/bca8d833-10e3-4e0c-a327-bab14e7b3122.

Table S8. Binding constants of ***o*-Me$_2$-2.2.2** toward CH_3NH_3BArF.

1:1 fitting	1:2 fitting	2:1 fitting
118±3 M^{-1}	K_{11} = 360±20 M^{-1}	K_{11} = 0.21±0.01 M^{-1}
	K_{12} = 88±8 M^{-1}	K_{21} = 25 300±400 M^{-1}

^{1}H NMR Titration of *o*-Me$_2$-2.2.2 with C(NH$_2$)$_3$BArF

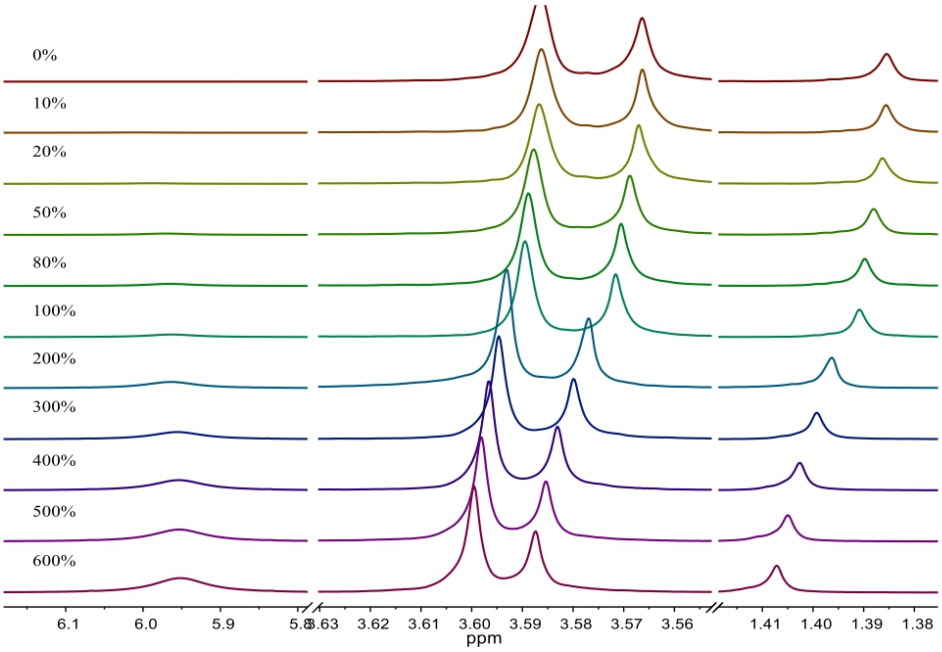

Figure S41. Partial ^{1}H NMR (400 MHz, 298 K, CD_3CN) stack plot of ***o*-Me$_2$-2.2.2** (2 mM) titration with C(NH$_2$)$_3$BArF from 0 - 600%.

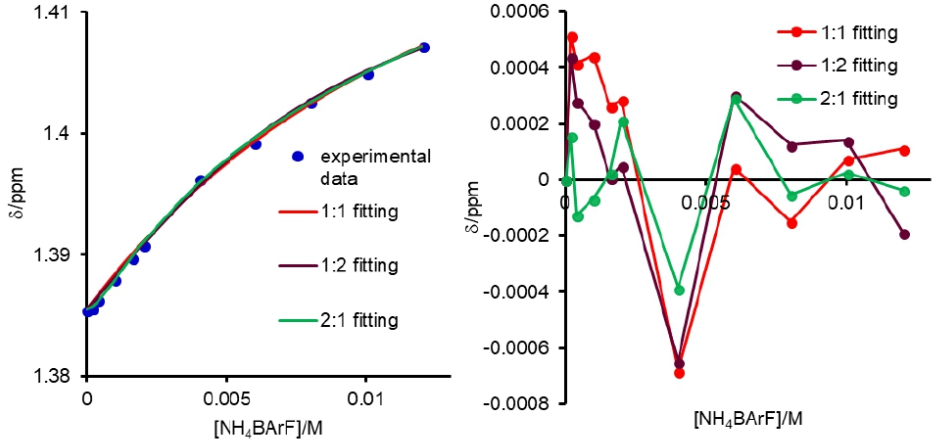

Figure S42. Left column: experimental and calculated chemical shift for titration of ***o*-Me$_2$-2.2.2** (2 mM) with C(NH$_2$)$_3$BArF from 0 - 500% in CD_3CN. Blue circles correspond to experimental values. Red line, purple line and green line correspond to fitted binding isotherms using 1:1 model, 1:2 model and 2:1 model respectively. Right column:

residual plots. The data fitting details using 1:1 binding model is available at http://app.supramolecular.org/bindfit/view/bde5698f-faf2-42ea-af70-a092622729c3. The data fitting details using 1:2 binding model is available at http://app.supramolecular.org/bindfit/view/e8d270fa-a628-45fc-ba25-33a9fb38417d. The data fitting details using 2:1 binding model is available at http://app.supramolecular.org/bindfit/view/9efcb3c2-d4fc-41c5-93b7-8640d6288136.

Table S9. Binding constants of ***o*-Me$_2$-2.2.2** toward $C(NH_2)_3BArF$.

1:1 fitting	1:2 fitting	2:1 fitting
73±3 M^{-1}	K_{11} = 250±50 M^{-1}	K_{11} = 220±50 M^{-1}
	K_{12} = 150±30 M^{-1}	K_{21} = 2 500±700 M^{-1}

5. Computational Chemistry

All simulation coordinates (and truncated simulation trajectories) and simulation input files necessary to reproduce the computational outcomes, analysis files and scripts (e.g. umbrella sampling analysis) are also available online on the figshare repository.[S3] Analysis and simulation setup scripts designed and used for this project are also presented there free for download and usage.

5.1 Molecular-dynamics simulations setup

Classical atomistic molecular dynamics simulations have been performed with the AMBER 16 suit of programs[S4] including the GPU accelerated CUDA implementation.[S5-S7] The force field parameters for the ammonium ion and the the cryptand are based on the general Amber force field (GAFF).[S8] The atomistic point charges have been derived by the standard restrained electrostatic potential (RESP)[S9] charge fitting procedure for GAFF. This is based on gas phase geometry optimizations at the B3LYP[S10-S12]/6-31G(d)[S13, S14] level of theory, followed by ESP charge generation from single point calculations at the HF[S15]/6-31G(d) level of theory and RESP fitting using antechamber program from the Amber tools. All cryptand structures have been solvated in a periodic truncated octahedral box of chloroform based on the Amber ff14SB force field.[S16] The ion parameters used for simulations with encapsulated monovalent ions are based on the paremeterisations by Joung and Cheatham.[S17]

Following a combined steepest descent and conjugate gradient minimisation for 6000 steps, all simulations were carried out for at least 200 ns using integration time step intervals of 1 fs and applying constant pressure (NPT) molecular dynamics at one atmosphere and 300 K using a Langevin dynamics[S18] for pressure control. All bonds including hydrogens were treated constrained, applying Amber's shake algorithm. Electrostatic long range interactions were treated with the Particle Mesh Ewald (PME)[S19] method and a 12 Å cut-off for nonbonding interactions. For all simulations the cryptates have been placed in a chloroform box with a minimum distance between the box boundary and the cryptates of 20 Å.

Table S10. Initial atomic coordinates, General Amber Force Field atom types, and atomic charges for all cryptands:

***o*-Me$_2$-1.1.1:**

1	C1	-4.2770	0.0000	0.0010	c3	-0.09751
2	C2	-2.7400	0.0000	0.0000	c3	0.12517
3	O1	-2.2230	1.2490	-0.3830	os	-0.20277
4	O2	-2.2220	-0.2910	1.2730	os	-0.20277
5	O3	-2.2220	-0.9560	-0.8890	os	-0.20277
6	C3	-2.3380	2.3530	0.5120	c3	0.03048
7	C4	-2.3380	-1.6190	1.7810	c3	0.03048
8	C5	-2.3370	-0.7320	-2.2930	c3	0.03048
9	C6	2.7400	0.0000	0.0000	c3	0.12517
10	O4	0.0000	-2.0300	2.0260	os	-0.30140
11	O5	0.0000	2.7720	0.7450	os	-0.30140
12	O6	2.2220	-0.2910	1.2730	os	-0.20277
13	O7	2.2230	1.2490	-0.3840	os	-0.20277
14	O8	2.2220	-0.9560	-0.8890	os	-0.20277
15	O9	0.0000	-0.7410	-2.7740	os	-0.30140
16	C7	-1.1960	3.3130	0.2230	c3	0.02357
17	C8	-1.1960	-1.8510	2.7570	c3	0.02357
18	C9	-1.1970	-1.4650	-2.9800	c3	0.02357
19	C10	4.2770	0.0000	0.0010	c3	-0.09751
20	C11	1.1960	3.3130	0.2220	c3	0.02357
21	C12	1.1960	-1.8510	2.7570	c3	0.02357
22	C13	2.3380	2.3530	0.5110	c3	0.03048
23	C14	2.3380	-1.6190	1.7810	c3	0.03048
24	C15	2.3370	-0.7330	-2.2930	c3	0.03048
25	C16	1.1970	-1.4650	-2.9800	c3	0.02357
26	H1	-4.6590	0.2630	-0.9910	hc	0.04441
27	H2	-4.6580	0.7260	0.7250	hc	0.04441
28	H3	-4.6580	-0.9910	0.2690	hc	0.04441
29	H4	-2.2790	2.0150	1.5500	h1	0.06622
30	H5	-3.2970	2.8720	0.3510	h1	0.06622
31	H6	-2.2780	-2.3480	0.9680	h1	0.06622
32	H7	-3.2960	-1.7400	2.3100	h1	0.06622
33	H8	-2.2750	0.3360	-2.5180	h1	0.06622
34	H9	-3.2960	-1.1290	-2.6620	h1	0.06622
35	H10	-1.4180	4.2910	0.6860	h1	0.05667
36	H11	-1.1110	3.4600	-0.8650	h1	0.05667
37	H12	-1.4180	-2.7440	3.3690	h1	0.05667
38	H13	-1.1110	-0.9850	3.4320	h1	0.05667
39	H14	-1.4200	-1.5540	-4.0580	h1	0.05667
40	H15	-1.1110	-2.4800	-2.5620	h1	0.05667

41	H16	4.6580	-0.9910	0.2690	hc	0.04441
42	H17	4.6580	0.7270	0.7250	hc	0.04441
43	H18	4.6590	0.2630	-0.9910	hc	0.04441
44	H19	1.4180	4.2910	0.6850	h1	0.05667
45	H20	1.1110	3.4600	-0.8660	h1	0.05667
46	H21	1.4190	-2.7430	3.3690	h1	0.05667
47	H22	1.1110	-0.9850	3.4320	h1	0.05667
48	H23	3.2970	2.8720	0.3500	h1	0.06622
49	H24	2.2790	2.0150	1.5500	h1	0.06622
50	H25	3.2960	-1.7400	2.3110	h1	0.06622
51	H26	2.2780	-2.3480	0.9680	h1	0.06622
52	H27	3.2960	-1.1290	-2.6620	h1	0.06622
53	H28	2.2750	0.3360	-2.5180	h1	0.06622
54	H29	1.4200	-1.5540	-4.0580	h1	0.05667
55	H30	1.1110	-2.4800	-2.5620	h1	0.05667

***o*-Me$_2$-2.1.1**

1	C1	4.6560	-0.4690	-0.2020	c3	-0.325277
2	C2	3.1600	-0.1900	-0.3740	c3	0.055786
3	O1	2.3760	-0.7900	0.6440	os	-0.216916
4	O2	2.8190	-0.6420	-1.6520	os	-0.216916
5	O3	2.8890	1.1870	-0.3330	os	-0.168761
6	C3	2.3320	-2.2210	0.6640	c3	0.012843
7	C4	1.6200	-0.1230	-2.2480	c3	0.012843
8	C5	2.9130	1.8720	0.9140	c3	0.003097
9	C6	-3.0240	-0.8950	0.4570	c3	0.055786
10	O4	0.3580	-2.4990	2.1460	os	-0.314309
11	O5	-2.1900	-1.1990	1.5260	os	-0.216916
12	O6	0.1130	-1.9040	-1.7390	os	-0.314309
13	O7	-2.4730	-1.2830	-0.7910	os	-0.216916
14	O8	0.8290	3.0120	0.6070	os	-0.298505
15	O9	-1.7740	2.8170	-0.5740	os	-0.298505
16	O10	-3.1640	0.5060	0.4260	os	-0.168761
17	C7	1.7500	-2.6950	1.9900	c3	0.041043
18	C8	0.7650	-1.2440	-2.8070	c3	0.041043
19	C9	2.2270	3.2090	0.7030	c3	0.036401
20	C10	-4.3650	-1.5770	0.7260	c3	-0.325277
21	C11	-0.0540	-1.2020	2.5770	c3	0.041043
22	C12	-0.9240	-0.5110	1.5470	c3	0.012843
23	C13	-1.0370	-2.6560	-2.0790	c3	0.041043
24	C14	-1.9970	-2.6220	-0.9030	c3	0.012843
25	C15	0.1590	4.1110	0.0190	c3	0.054072

26	C16	-3.1810	2.6440	-0.5670	c3	0.036401
27	C17	-1.3420	3.9450	0.1560	c3	0.054072
28	C18	-3.5020	1.1760	-0.7810	c3	0.003097
29	H1	4.8930	-1.5150	-0.4090	hc	0.116050
30	H2	4.9720	-0.2300	0.8180	hc	0.116050
31	H3	5.2120	0.1520	-0.9090	hc	0.116050
32	H4	3.3450	-2.6390	0.5760	h1	0.086302
33	H5	1.7240	-2.5820	-0.1690	h1	0.086302
34	H6	1.9170	0.5440	-3.0680	h1	0.086302
35	H7	1.0420	0.4580	-1.5270	h1	0.086302
36	H8	3.9500	2.0450	1.2420	h1	0.087620
37	H9	2.3910	1.3000	1.6860	h1	0.087620
38	H10	2.3070	-2.2320	2.8210	h1	0.056193
39	H11	1.9060	-3.7800	2.0480	h1	0.056193
40	H12	1.3820	-1.9440	-3.3940	h1	0.056193
41	H13	0.0210	-0.7990	-3.4880	h1	0.056193
42	H14	2.6230	3.6670	-0.2170	h1	0.043962
43	H15	2.4650	3.8840	1.5440	h1	0.043962
44	H16	-4.7840	-1.1940	1.6590	hc	0.116050
45	H17	-4.2410	-2.6600	0.8180	hc	0.116050
46	H18	-5.0580	-1.3690	-0.0950	hc	0.116050
47	H19	0.8160	-0.5690	2.7860	h1	0.056193
48	H20	-0.6250	-1.3240	3.5080	h1	0.056193
49	H21	-1.0770	0.5380	1.8220	h1	0.086302
50	H22	-0.4510	-0.5470	0.5630	h1	0.086302
51	H23	-0.7740	-3.7000	-2.3160	h1	0.056193
52	H24	-1.5320	-2.2230	-2.9620	h1	0.056193
53	H25	-2.8280	-3.3200	-1.0930	h1	0.086302
54	H26	-1.4820	-2.9240	0.0150	h1	0.086302
55	H27	0.4300	4.1990	-1.0450	h1	0.051131
56	H28	0.4420	5.0550	0.5180	h1	0.051131
57	H29	-3.6480	3.2500	-1.3620	h1	0.043962
58	H30	-3.6080	2.9620	0.3960	h1	0.043962
59	H31	-1.6070	3.8390	1.2210	h1	0.051131
60	H32	-1.8200	4.8690	-0.2170	h1	0.051131
61	H33	-4.5750	1.0650	-1.0070	h1	0.087620
62	H34	-2.9250	0.7850	-1.6220	h1	0.087620

***o*-Me$_2$-2.2.1**

1	O1	3.67397	15.25660	14.91068	os	-0.349769
2	O2	4.32410	13.77750	12.61292	os	-0.337136
3	O3	6.61881	12.11294	12.46302	os	-0.337136

4	O4	7.37355	11.13864	14.99249	os	-0.349769
5	O5	4.76038	16.08702	16.76330	os	-0.306893
6	O6	5.33303	13.47937	17.76255	os	-0.317352
7	O7	7.81366	12.22809	16.99664	os	-0.306893
8	O8	5.14988	17.01209	14.67929	os	-0.349769
9	O9	7.97322	17.37526	15.34879	os	-0.337136
10	O10	9.75405	15.09735	15.91570	os	-0.337136
11	O11	9.34755	12.30586	15.28128	os	-0.349769
12	C1	4.14086	16.45522	15.53103	c3	0.473912
13	C2	2.94408	17.43147	15.78781	c3	-0.228478
14	H1	2.53878	17.83090	14.83573	hc	0.062208
15	H2	3.22389	18.28742	16.43749	hc	0.062208
16	C3	8.39855	11.46736	15.93580	c3	0.473912
17	C4	9.06803	10.16990	16.47355	c3	-0.228478
18	H3	9.80459	10.40316	17.27339	hc	0.062208
19	H4	9.61210	9.63942	15.66258	hc	0.062208
20	H5	8.31556	9.46919	16.88699	hc	0.062208
21	C5	3.00701	15.47075	13.67456	c3	0.199382
22	H6	3.50245	16.24416	13.05310	h1	0.018572
23	H7	1.95276	15.76515	13.86395	h1	0.018572
24	C6	2.99600	14.16175	12.89052	c3	0.026135
25	H8	2.42628	14.33845	11.94728	h1	0.047029
26	H9	2.47953	13.38180	13.49437	h1	0.047029
27	C7	4.33105	12.61074	11.80883	c3	0.157630
28	C8	5.76210	12.32577	11.35508	c3	0.157630
29	H10	5.74818	11.47294	10.63443	h1	0.012091
30	H11	6.13455	13.20324	10.79010	h1	0.012091
31	C9	6.84915	10.73608	12.67573	c3	0.026135
32	C10	7.87227	10.55687	13.79344	c3	0.199382
33	H12	8.04031	9.47121	13.94139	h1	0.018572
34	H13	8.82189	11.02046	13.43800	h1	0.018572
35	C11	3.89834	15.40868	17.66771	c3	0.054256
36	H14	3.11180	14.79464	17.16656	h1	0.055089
37	H15	3.39569	16.15978	18.31859	h1	0.055089
38	C12	4.71899	14.47378	18.55923	c3	0.107158
39	H16	4.03269	14.01263	19.29889	h1	0.029334
40	H17	5.48860	15.07741	19.09445	h1	0.029334
41	C13	6.02481	12.55534	18.58064	c3	0.107158
42	H18	5.29649	11.98601	19.19575	h1	0.029334
43	H19	6.74955	13.06993	19.25096	h1	0.029334
44	C14	6.79502	11.55566	17.70955	c3	0.054256
45	H20	7.25569	10.81360	18.39923	h1	0.055089
46	H21	6.07361	11.03886	17.04330	h1	0.055089
47	C15	5.72073	18.24992	15.07878	c3	0.199382

48	H22	4.99882	18.94392	15.54760	h1	0.018572
49	H23	6.05479	18.77311	14.15554	h1	0.018572
50	C16	6.94934	18.11342	15.99183	c3	0.026135
51	H24	7.30035	19.14452	16.21991	h1	0.047029
52	H25	6.65759	17.62551	16.94734	h1	0.047029
53	C17	9.16281	17.44652	16.11754	c3	0.157630
54	H26	8.97698	17.27463	17.20341	h1	0.012091
55	H27	9.60729	18.45468	15.98368	h1	0.012091
56	C18	0.19257	16.41232	15.64297	c3	0.157630
57	H28	0.37756	16.54971	14.55262	h1	0.012091
58	H29	1.13495	16.63253	16.19936	h1	0.012091
59	C19	0.81123	14.17806	15.68843	c3	0.026135
60	H30	1.70372	14.45155	16.30010	h1	0.047029
61	H31	1.09554	14.16342	14.61284	h1	0.047029
62	C20	0.39341	12.77100	16.11861	c3	0.199382
63	H32	1.26530	12.09079	15.99461	h1	0.018572
64	H33	0.12755	12.80313	17.19527	h1	0.018572
65	H34	5.90267	10.22400	12.96396	h1	0.047029
66	H35	3.94164	11.73987	12.37863	h1	0.012091
67	H36	2.12501	16.90941	16.31481	hc	0.062208
68	H37	3.71581	12.75841	10.89300	h1	0.012091
69	H38	7.26801	10.25268	11.75952	h1	0.047029

***o*-Me$_2$-2.2.2**

1	C1	-4.2770	0.0000	0.0010	c3	-0.097508
2	C2	-2.7400	0.0000	0.0000	c3	0.125172
3	O1	-2.2230	1.2490	-0.3830	os	-0.20277
4	O2	-2.2220	-0.2910	1.2730	os	-0.20277
5	O3	-2.2220	-0.9560	-0.8890	os	-0.20277
6	C3	-2.3380	2.3530	0.5120	c3	0.030482
7	C4	-2.3380	-1.6190	1.7810	c3	0.030482
8	C5	-2.3370	-0.7320	-2.2930	c3	0.030482
9	C6	2.7400	0.0000	0.0000	c3	0.125172
10	O4	0.0000	-2.0300	2.0260	os	-0.301403
11	O5	0.0000	2.7720	0.7450	os	-0.301403
12	O6	2.2220	-0.2910	1.2730	os	-0.20277
13	O7	2.2230	1.2490	-0.3840	os	-0.20277
14	O8	2.2220	-0.9560	-0.8890	os	-0.20277
15	O9	0.0000	-0.7410	-2.7740	os	-0.301403
16	C7	-1.1960	3.3130	0.2230	c3	0.023574
17	C8	-1.1960	-1.8510	2.7570	c3	0.023574

18	C9	-1.1970	-1.4650	-2.9800	c3	0.023574
19	C10	4.2770	0.0000	0.0010	c3	-0.097508
20	C11	1.1960	3.3130	0.2220	c3	0.023574
21	C12	1.1960	-1.8510	2.7570	c3	0.023574
22	C13	2.3380	2.3530	0.5110	c3	0.030482
23	C14	2.3380	-1.6190	1.7810	c3	0.030482
24	C15	2.3370	-0.7330	-2.2930	c3	0.030482
25	C16	1.1970	-1.4650	-2.9800	c3	0.023574
26	H1	-4.6590	0.2630	-0.9910	hc	0.044408
27	H2	-4.6580	0.7260	0.7250	hc	0.044408
28	H3	-4.6580	-0.9910	0.2690	hc	0.044408
29	H4	-2.2790	2.0150	1.5500	h1	0.066224
30	H5	-3.2970	2.8720	0.3510	h1	0.066224
31	H6	-2.2780	-2.3480	0.9680	h1	0.066224
32	H7	-3.2960	-1.7400	2.3100	h1	0.066224
33	H8	-2.2750	0.3360	-2.5180	h1	0.066224
34	H9	-3.2960	-1.1290	-2.6620	h1	0.066224
35	H10	-1.4180	4.2910	0.6860	h1	0.05667
36	H11	-1.1110	3.4600	-0.8650	h1	0.05667
37	H12	-1.4180	-2.7440	3.3690	h1	0.05667
38	H13	-1.1110	-0.9850	3.4320	h1	0.05667
39	H14	-1.4200	-1.5540	-4.0580	h1	0.05667
40	H15	-1.1110	-2.4800	-2.5620	h1	0.05667
41	H16	4.6580	-0.9910	0.2690	hc	0.044408
42	H17	4.6580	0.7270	0.7250	hc	0.044408
43	H18	4.6590	0.2630	-0.9910	hc	0.044408
44	H19	1.4180	4.2910	0.6850	h1	0.05667
45	H20	1.1110	3.4600	-0.8660	h1	0.05667
46	H21	1.4190	-2.7430	3.3690	h1	0.05667
47	H22	1.1110	-0.9850	3.4320	h1	0.05667
48	H23	3.2970	2.8720	0.3500	h1	0.066224
49	H24	2.2790	2.0150	1.5500	h1	0.066224
50	H25	3.2960	-1.7400	2.3110	h1	0.066224
51	H26	2.2780	-2.3480	0.9680	h1	0.066224
52	H27	3.2960	-1.1290	-2.6620	h1	0.066224
53	H28	2.2750	0.3360	-2.5180	h1	0.066224
54	H29	1.4200	-1.5540	-4.0580	h1	0.05667
55	H30	1.1110	-2.4800	-2.5620	h1	0.05667

5.2 Molecular-dynamics simulations analysis

Table S11. Root mean square deviations (rmsd), mean atomic root mean square fluctuations (rmsf) for all cryptate atoms excluding hydrogens, electrostatic interaction (EELEC) and van der Waals (VDW) interaction energies between the cryptands and their encapsulated ions, from 200 ns MD simulations of the cryptates in explicit chloroform.

	rmsd [Å]	sd	Mean atomic RMSF [Å]	sd	EELEC [kcal mol^{-1}]	sd	VDW [kcal mol^{-1}]	sd
[NH_4^+•***o***-Me_2-**1.1.1**]	0.6626	0.0919	0.1648	0.0238	-79.1377	2.9856	13.2217	2.6525
[NH_4^+⊂***o***-Me_2-**2.1.1**]	0.7009	0.1109	0.2614	0.0565	-88.907	3.6772	-0.4079	1.4049
[NH_4^+⊂***o***-Me_2-**2.2.1**]	1.2053	0.1986	0.4778	0.1777	-81.0107	4.6537	-2.7794	1.3519
[NH_4^+⊂***o***-Me_2-**2.2.2**]	2.8815	0.1318	0.7179	0.1652	-92.7049	7.9993	-2.1317	1.6569
[Li^+⊂***o***-Me_2-**1.1.1**]	1.3896	0.1713	0.5947	0.1359	-106.701	5.2427	-0.3937	1.6935
[Li^+⊂***o***-Me_2-**2.1.1**]	2.1515	0.1194	0.6293	0.1671	-128.442	4.8799	0.0519	1.4483
[Li^+⊂***o***-Me_2-**2.2.1**]	2.3775	0.3233	1.1195	0.2898	-112.923	5.4049	0.4215	1.5943
[Na^+⊂***o***-Me_2-**1.1.1**]	0.6512	0.1862	0.2706	0.0553	-90.9584	3.1285	-1.5533	1.1421
[Na^+⊂***o***-Me_2-**2.1.1**]	1.3776	0.3657	0.7125	0.2182	-104.34	7.7661	-1.575	1.5576
[Na^+⊂***o***-Me_2-**2.2.1**]	1.999	0.1644	0.921	0.2284	-106.718	5.5169	-1.0017	1.676
[K^+⊂***o***-Me_2-**1.1.1**]	0.5542	0.1086	0.1723	0.0233	-82.353	2.7838	6.2234	2.0268
[K^+⊂***o***-Me_2-**2.1.1**]	0.7177	0.2163	0.3395	0.084	-90.4259	4.1054	-2.8719	0.1582
[K^+⊂***o***-Me_2-**2.2.1**]	1.6282	0.2068	0.6288	0.1779	-83.2886	5.5761	-3.903	1.3468
[Rb^+⊂***o***-Me_2-**1.1.1**]	0.5365	0.1136	0.1646	0.0233	-77.2658	2.805	11.7177	2.6003
[Rb^+⊂***o***-Me_2-**2.1.1**]	0.6202	0.1355	0.2686	0.0602	-87.0813	3.6065	-1.9427	1.3815
[Rb^+⊂***o***-Me_2-**2.2.1**]	1.3053	0.1817	0.5176	0.1687	-79.8436	4.6624	-4.4734	1.1807
[Cs^+⊂***o***-Me_2-**1.1.1**]	0.5656	0.1052	0.162	0.0229	-74.4101	2.8438	21.3234	2.9334

[Cs^+⊂*o*-Me_2-**2.1.1**]	0.6247	0.1356	0.2449	0.053	-85.1607	3.5054	4.3662	1.516
[Cs^+⊂*o*-Me_2-**2.2.1**]	1.0014	0.1644	0.4109	0.1487	-78.7331	4.2934	-0.1419	1.254

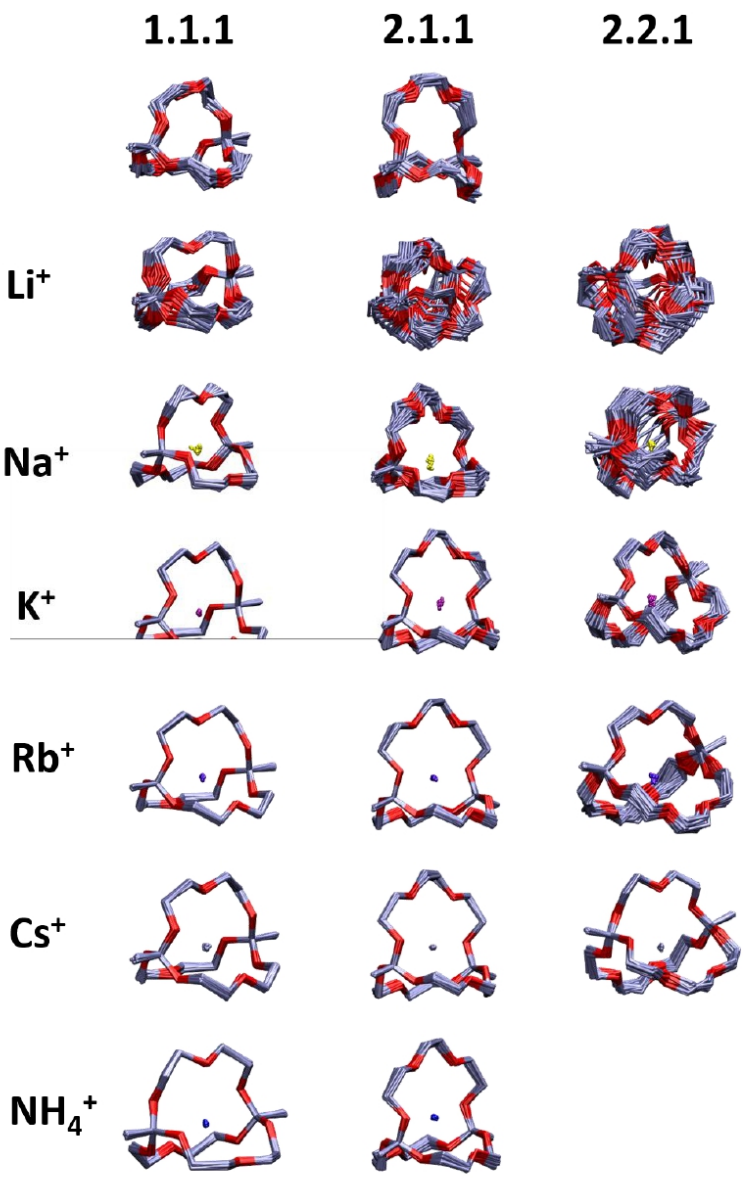

Figure S43. Superimposed and smoothed structures of different cryptands with incorporated ions demonstrating the differences in their flexibility. Data extracted from 200 ns long simulations in explicit chloroform.

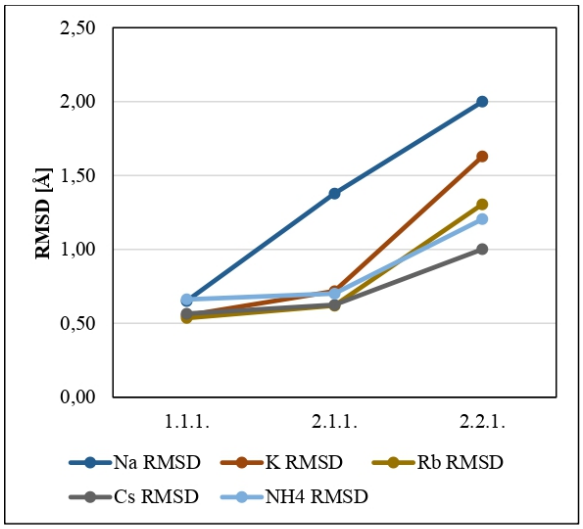

Figure S44. Root means square deviation for different cryptand sizes and included ions extracted from 200 ns MD simulations in chloroform.

Table S12. Hydrogen bonding occupancies between cryptands and ammonium ions from 200 ns MD simulations of different cryptates in explicit chloroform. Orthoester (O_O) oxygen atoms are highlighted in yellow. Kc represents the equilibrium constant between configurations with O_O hydrogen bonds and all other configurations calculated by taking the mean O_O hydrogen bond occupancy multiplied by the average number of hydrogen bonds as approximation for the concentration of O_O hydrogen bonded ring opening precursor. dG describes the associated free energy difference.

	[NH_4^+•*o*-Me_2-1.1.1]	**[NH_4^+⊂*o*-Me_2-2.1.1]**	**[NH_4^+⊂*o*-Me_2-2.2.1]**	**[NH_4^+⊂*o*-Me_2-2.2.2]**
O1	**0.2512**	**0.1316**	**0.0348**	**0.0870**
O2	**0.2498**	**0.1174**	0.1340	0.1188
O3	**0.2492**	**0.1270**	0.1464	0.1465
O4	0.6124	0.3110	**0.0506**	**0.0689**
O5	0.6009	**0.1169**	**0.0412**	**0.0920**
O6	**0.2520**	0.3101	0.1758	0.1243
O7	**0.2517**	**0.1316**	**0.0392**	0.1575
O8	**0.2509**	0.1754	**0.0475**	**0.0784**
O9	0.6131	0.1716	0.1498	**0.1016**
O10		**0.1268**	0.1309	0.1203
O11			**0.0331**	0.1689
O1				**0.0621**

O_e mean	0.61	0.24	0.15	0.14
O_o mean	0.25	0.13	0.04	0.08
O_e/O_o	2.43	1.93	3.59	1.71
Mean number of h-bonds	3.34	1.72	1.06	1.33
K_c [s^{-1}]	5.16	0.28	0.05	0.12
dG [kcal mol^{-1}]	-0.98	0.77	1.84	1.26

5.3 Umbrella sampling setup

Umbrella sampling has been carried out to calculate the binding affinity of ammonium ions to the differently sized cryptand structures. The central ammonium ion has been pulled out of the cavity along a sampling coordinate that has been defined as the distance between the ammonium ion nitrogen and the centre of mass of all orthoester oxygen atoms of the cryptands. To follow this coordinate a harmonic umbrella potential has been applied in form of a specific restraint to the simulation. The coordinate was scanned in 0.1 Å steps between 0.0 and 14.0 Å to give a total of 141 sampling windows. To ensure proper sampling each window has been sampled for at least 0.5 ns. To test convergence a sampling

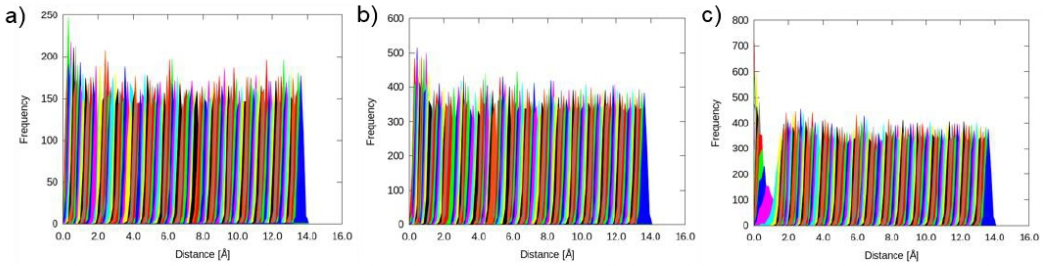

Figure S45. Histogram representation of the umbrella coordinate sampled in all 141 umbrella windows for a) ***o*-Me$_2$-2.2.1** (0.5 ns sampling per window), b) ***o*-Me$_2$-2.1.1** (1 ns sampling per window), c) ***o*-Me$_2$-1.1.1** (1 ns sampling per window).

duration of 1 ns per window was also applied and resulted in similar results. The spring constant for the umbrella potential has been tested for a range between 5 and 400 kcal mol^{-1}. Sampling with a 20 kcal mol^{-1} force constant resulted in the most reliable results and is presented in this work. It has been ensured that the sampling windows present sufficient overlap before the weighted histogram analysis method (WHAM)[S20] to retrieve free energy difference along the given reaction coordinate. Input and output files of the WHAM analysis can also be found on the Figshare repository.[S3] For each umbrella sampling run the tolerance threshold for the WHAM analysis has been tested for convergence of the results and a tolerance value of 0.0001 (that showed convergence for all simulations) has been applied for all reported analysis.

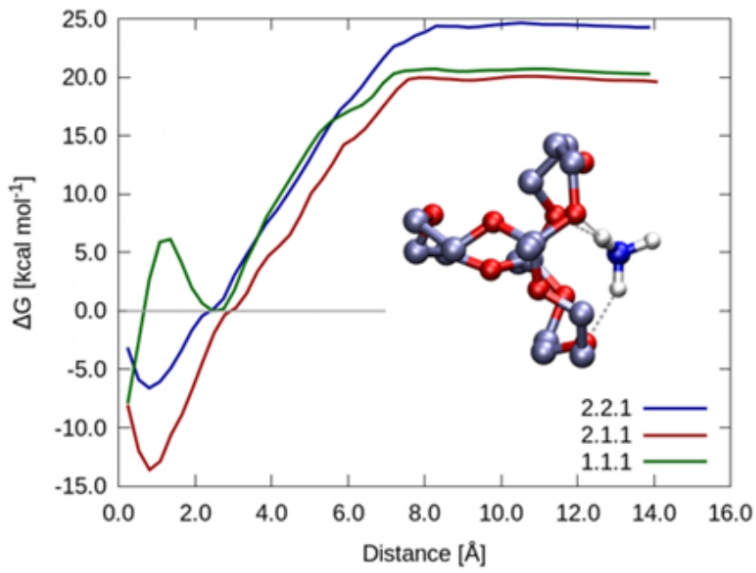

Figure S46. Free energy profile from umbrella sampling simulations of ammonium ion inclusion. The sampling coordinate describes the distance between the ammonium nitrogen and the centre of mass of all orthoester oxygen atoms. The structure depicts the hydrogen bonded external binding of ammonium to [$\mathbf{NH_4^+}$•***o***-$\mathbf{Me_2}$-**1.1.1**].

5.4 QM/MM simulation setup

Hybrid QM/MM simulations have been either performed with the built-in SCC-DFTB QM/MM support in AMBER16[S21], or linked to an external QM programme,[S22] in this study Gaussian09.[S23] Based on the MD simulation setup described before the cryptand and the ammonium ion have been defined as the QM region of the simulation. For the results presented in the main manuscript the QM region has been treated with the density functional based tight binding method (DFTB) [S24, S25] and the results have been tested against QMMM simulations using the BLYP/6-31G(d) level of theory for the QM region.

The solvent chloroform was treated classically and was embedded electrostatically. Differently to the MD simulations the cut-off for all nonbonding interactions were set to 8 Å retaining the use of Particle Mesh Ewald (PME) to calculate all QM-QM and QM-MM long range electrostatic interactions. No shake algorithm was applied on any atoms in the system and the integration time steps were decreased to 0.5 fs. For better stability of the QM/MM simulations a NVT ensemble has been used applying a Berendsen type weak coupling[S26] for temperature control.

5.5 QM/MM umbrella sampling setup

To investigate the ring opining of the cryptates and the formation of the oxonium ion intermediate QM/MM umbrella sampling simulations were performed starting from equilibrated QM/MM simulations described above. Analysis have been performed analogue to the MD umbrella sampling runs described before. Based on tests of various sampling setups and convergence tests of the results all presented umbrella sampling trajectories used a force constant of 400 kcal mol^{-1} and 10,000 integration time steps (5 ps) per umbrella window in case of runs using DFTB and 2,500 integration time steps (and an integration time step size of 1 fs) in case of simulations applying BLYP/6-31G(d) DFT. A side outcome of this study was, that for these systems QM/MM setups using semiempirical Hamiltonians for the QM region resulted in unstable simulations and unreliable outcomes.

Either one- or two-dimensional umbrella sampling runs have been performed. The first reaction coordinate represents the ring opening distance between one of orthoester oxygen of a DEG unit and the quaternary carbon connected. The second coordinate represents the protonation necessary between the same orthoester oxygen and one hydrogen of the ammonium ion.

5.6 QM/MM umbrella sampling results

One-dimensional umbrella sampling scans have been compared with two-dimensional runs in order to evaluate if the opening follows a stepwise or concerted mechanism. The one-dimensional scans already showed that the hydrogen transfer is necessary for the ring opening. Runs in that this transfer did not occur resulted in extremely high barriers and unreasonable thermodynamics of the ring opening. In order to test the quality of the DFTB method it has been compared to a BLYP/6-31G(d)/MM umbrella sampling run. The resulting ring opening barrier for **[NH_4^+⊂*o*-Me_2-2.2.1]** show very good agreement as shown in Figure S47.

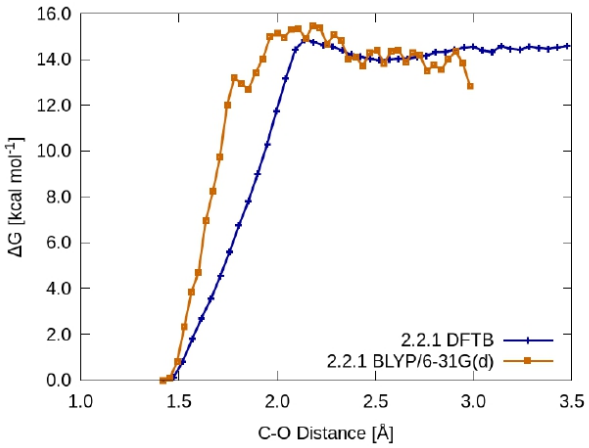

Figure S47. Comparison of DFTB and BLYP one-dimensional QM/MM umbrella sampling scans for ring opening to oxonium ion intermediate of **[NH_4^+⊂o-Me_2-2.2.1]**.

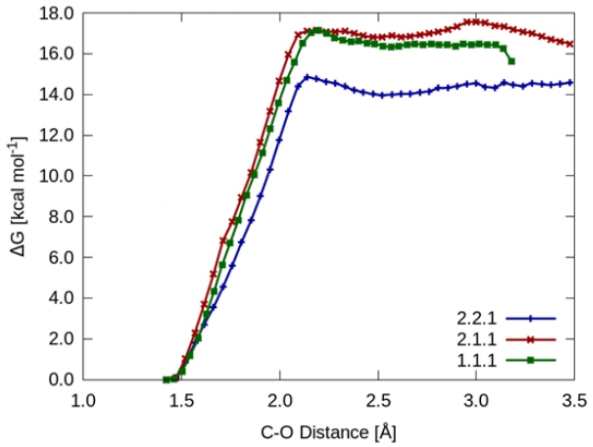

Figure S48. Free energy profile of oxonium ion formation from one-dimensional umbrella sampling for [NH_4^+⊂*o*-Me_2-**2.2.1**], [NH_4^+⊂*o*-Me_2-**2.1.1**], and [NH_4^+⊂*o*-Me_2-**1.1.1**].

Subsequent two-dimensional scans showed to be significantly influenced by the choice of the sampling direction. All umbrella sampling scans were performed in sequence, meaning that the last frame of the previous step was taken as input conformation for the next step. For the two-dimensional scans several options are possible. The different setups either started from the ground state with the ammonium ion bound inside the cryptand, or from the ring opening state retrieved from a previous one-dimensional san. The options tested are represented in Figure S49 and lead to significantly different results. A closer examination for the reasons reveals that the high flexibility of the system and the presence of more than one acidic proton is the source of this effect. Since only one proton of the ammonium ion is part of the sampling coordinates, the others remain reactive in the QM/MM simulation and so do other oxygen atoms as acceptors. The only sampling option giving reliable and reproducible results for the formation of the oxonium ions

as option c which is starting from the protonation of one orthoester oxygen.

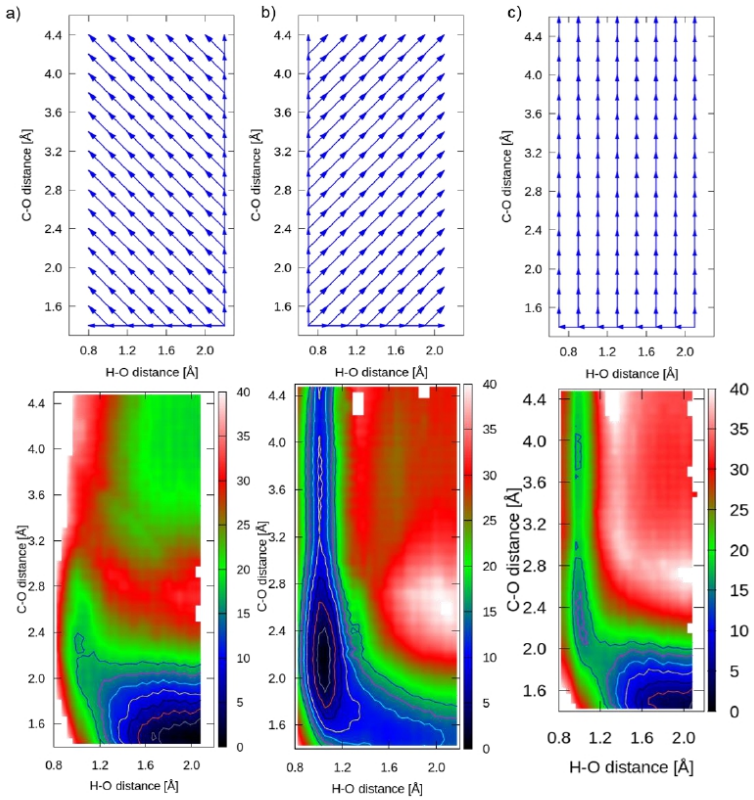

Figure S49. Sampling directions for two-dimensional umbrella sampling scans represented as vector plots (top). Free energy surface resulting for the sampling options above. Energies given in kcal mol^{-1}, contour lines shown represent steps of 2.5 kcal mol^{-1} between 2.5 and 20.0 kcal mol^{-1}.

5.7 QM and QM/MM sampling of inversion and fluxional behaviour

Additional DFT calculations and hybrid QM/MM simulations have been performed with the built-in SCC-DFTB QM/MM to investigate ring closure and fluxional behaviour of the cryptates. Starting from the DEG ring opened structure of ***o*-Me$_2$-2.2.1** further 500 ps of free SCC-DFTB QM/MM MD have been carried out. During this simulation the structure opened up the unbound DEG moiety completely. Without biasing these simulation the methyl substituted oxonium ion flips to point to the inside of the cryptand. Subsequently, steered umbrella sampling simulations were used to pull the DEG hydroxyl to the oxonium ion carbon and the ammonium ion towards the hydroxyl group. Small force constants of 10 kcal mol^{-1} have been applied for both coordinates and a ring closing event could be detected.

Starting from this inverted *(out,in)* geometry several PBE0/def2TZP(D3) DFT gas phase PES scans have been performed to identify ring opening transition states. Transition states were subsequently optimized and characterised by frequency calculations.

5.8 DFT calculations of cryptand and cryptate formation

The reported geometry optimizations have been conducted at the PBE0/def2TZP(D3) level of theory. All stationary points were confirmed by calculating their normal vibrations at the same level of theory. All relative energies were corrected with unscaled zero point vibration energies. Reported relative energies also incorporate thermal corrections to enthalpy (ΔH) and Gibbs free energies (ΔG).

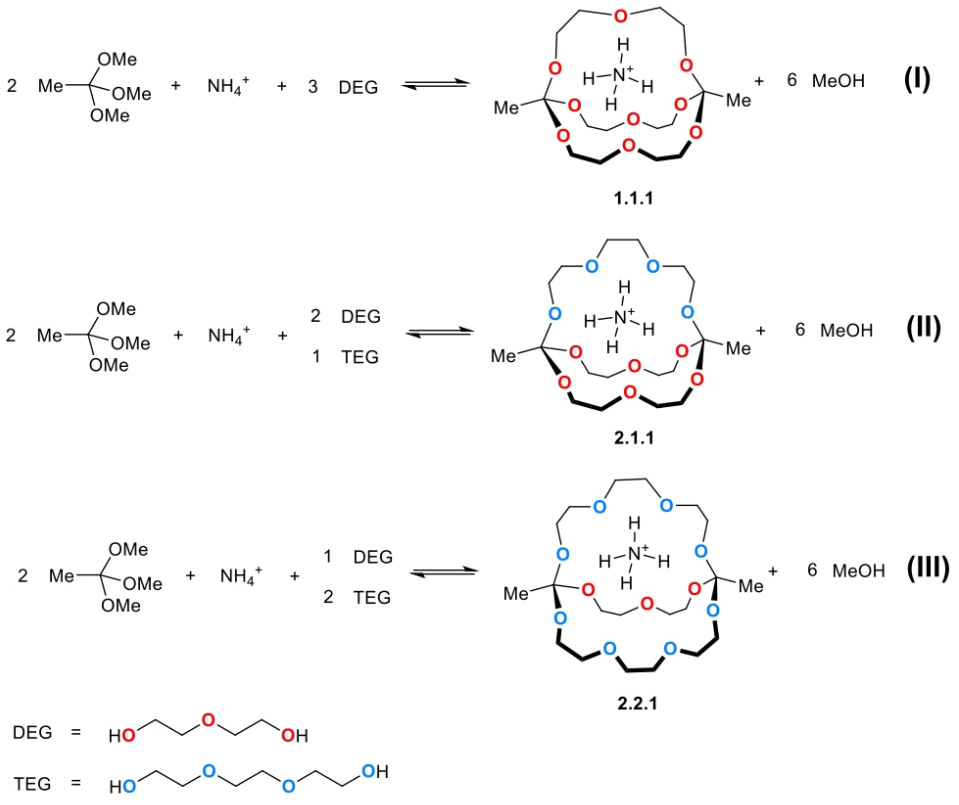

Table S13. Sum of E_0 (E_{ele} + ZPVE) and thermal correction to the internal energy (ΔE) and Gibbs free energy (ΔG) for the complexation at 298.15 K. All energies are reported in kcal mol^{-1}.

	ΔE_{ele}			ΔE			ΔG		
	Vacuum	H_2O	$CHCl_3$	Vacuum	H_2O	$CHCl_3$	Vacuum	H_2O	$CHCl_3$
(I)	**-47.47**	**-3.60**	**-13.13**	**-49.51**	**-5.75**	**-16.28**	**-44.88**	**1.71**	**-10.12**
(II)	**-73.56**	**-28.15**	**-37.94**	**-75.19**	**-29.25**	**-39.63**	**-70.12**	**-23.08**	**-32.20**
(III)	**-77.56**	**-31.05**	**-40.95**	**-78.96**	**-31.34**	**-42.39**	**-74.26**	**-27.82**	**-34.44**

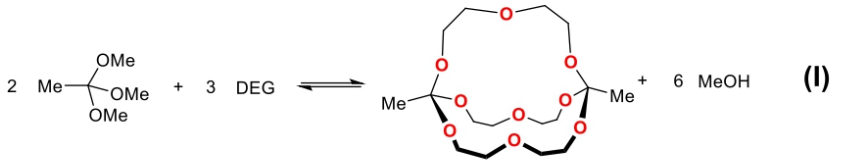

1.1.1

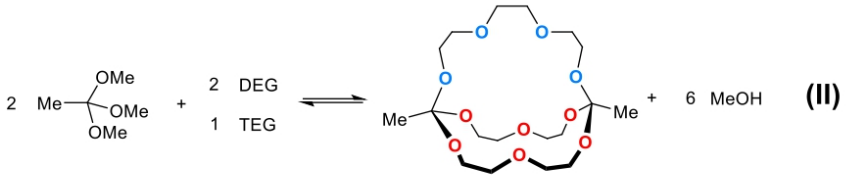

2.1.1

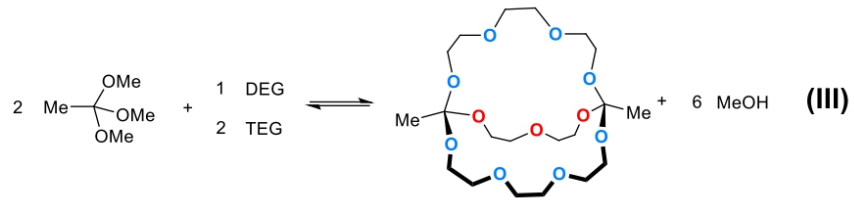

2.2.1

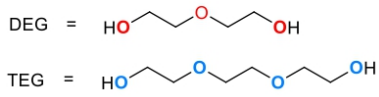

Table S14. Sum of E_0 (E_{ele} + ZPVE) and thermal correction to the internal energy (ΔE) and Gibbs free energy (ΔG) for the cryptate formation at 298.15 K. All energies are reported in kcal mol^{-1}.

	ΔE_{ele}			ΔE			ΔG		
	Vacuum	H_2O	$CHCl_3$	Vacuum	H_2O	$CHCl_3$	Vacuum	H_2O	$CHCl_3$
(I)	**14.86**	**4.76**	**11.11**	**10.17**	**0.93**	**6.97**	**0.75**	**-5.31**	**0.15**
(II)	**14.41**	**1.01**	**9.34**	**9.76**	**-1.99**	**5.36**	**1.57**	**-8.74**	**0.78**
(III)	**12.35**	**0.26**	**7.50**	**7.69**	**-2.87**	**2.15**	**0.19**	**-10.53**	**0.64**

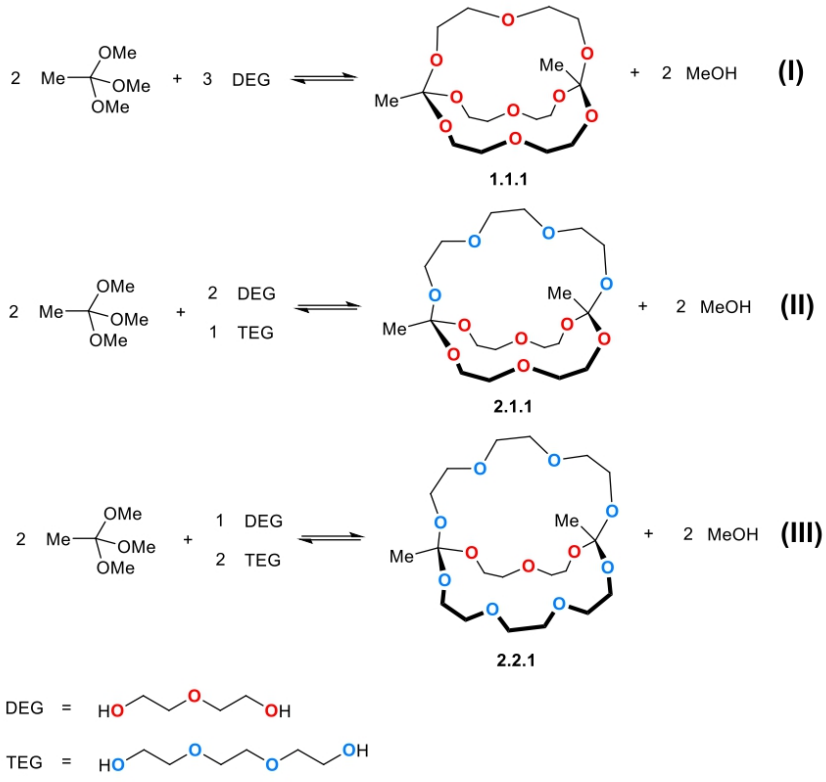

Table S15. Sum of E_0 (E_{ele} + ZPVE) and thermal correction to the internal energy (ΔE) and Gibbs free energy (ΔG) for the inverted cryptate formation at 298.15 K. All energies are reported in kcal mol^{-1}.

	ΔE_{ele}			ΔE			ΔG		
	Vacuum	H_2O	$CHCl_3$	Vacuum	H_2O	$CHCl_3$	Vacuum	H_2O	$CHCl_3$
(I)	**17.99**	**15.77**	**16.39**	**14.41**	**12.54**	**13.08**	**7.14**	**8.33**	**7.28**
(II)	**7.19**	**2.63**	**4.60**	**3.23**	**-0.24**	**0.95**	**-3.85**	**-6.12**	**-4.74**
(III)	**7.13**	**3.51**	**4.84**	**3.04**	**1.01**	**1.08**	**-3.67**	**-7.58**	**-2.47**

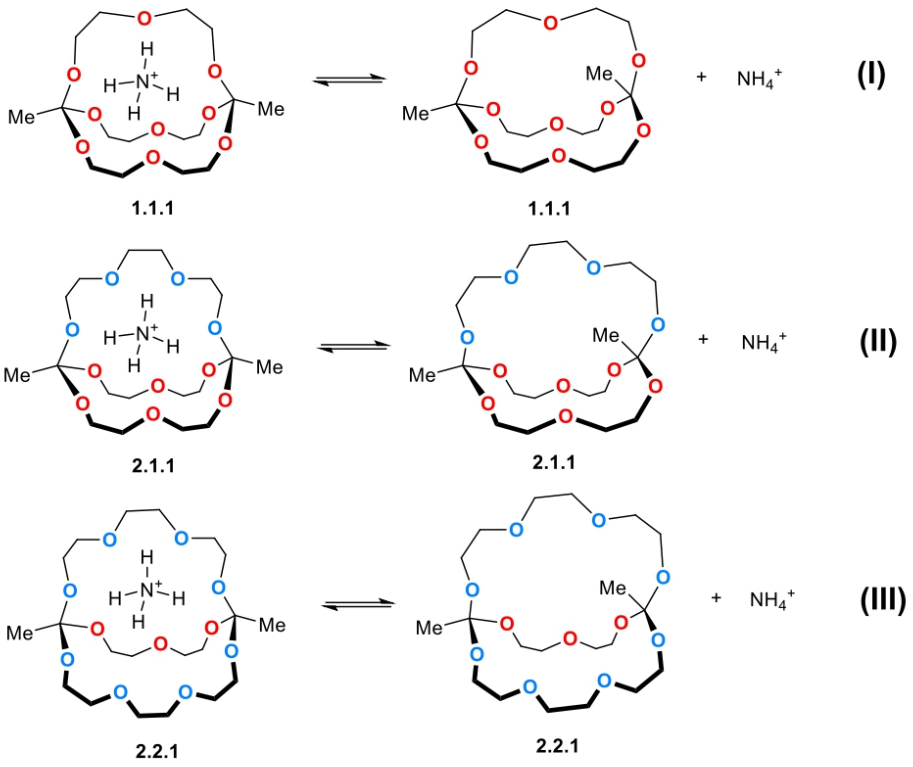

Table S16. Sum of E_0 (E_{ele} + ZPVE) and thermal correction to the internal energy (ΔE) and Gibbs free energy (ΔG) for the complex inversion at 298.15 K. All energies reported in kcal mol^{-1}.

	ΔE_{ele}			ΔE			ΔG		
	Vacuum	H_2O	$CHCl_3$	Vacuum	H_2O	$CHCl_3$	Vacuum	H_2O	$CHCl_3$
(I)	**65.45**	**19.37**	**29.52**	**63.92**	**18.29**	**29.36**	**52.02**	**6.62**	**17.39**
(II)	**80.75**	**30.79**	**42.54**	**78.42**	**29.01**	**40.58**	**66.27**	**16.96**	**27.46**
(III)	**84.69**	**34.57**	**45.79**	**82.00**	**32.36**	**43.47**	**70.59**	**20.24**	**31.97**

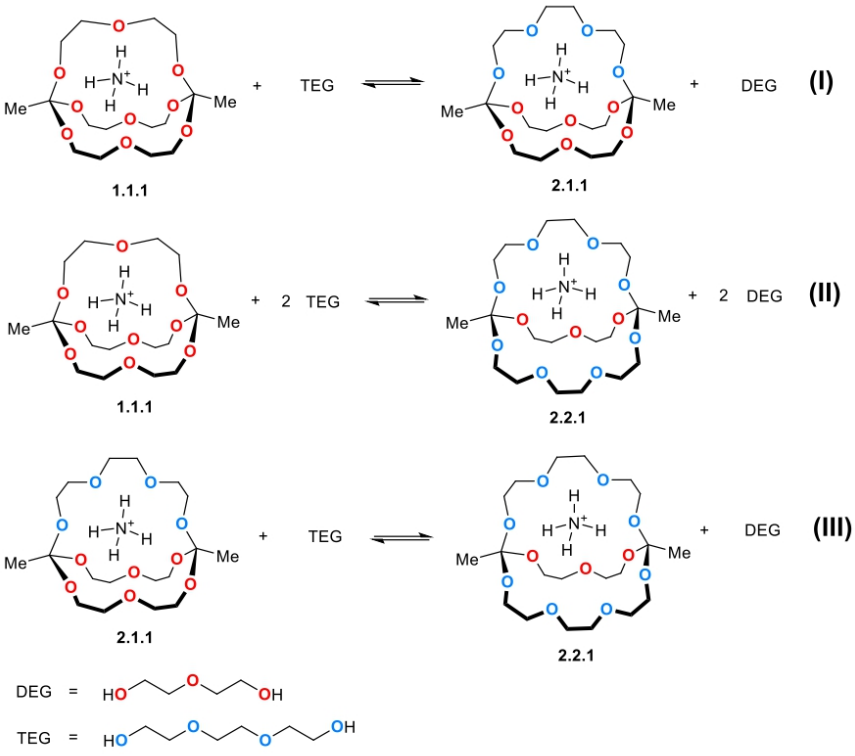

Table S17. Sum of E_0 (E_{ele} + ZPVE) and thermal correction to the internal energy (ΔE) and Gibbs free energy (ΔG) for the rearrangement at 298.15 K. All energies reported in kcal mol^{-1}.

	ΔE_{ele}			ΔE			ΔG		
	Vacuum	H_2O	$CHCl_3$	Vacuum	H_2O	$CHCl_3$	Vacuum	H_2O	$CHCl_3$
(I)	**-26.09**	**-24.56**	**-24.81**	**-25.68**	**-25.59**	**-26.11**	**-25.24**	**-29.53**	**-24.33**
(II)	**-30.09**	**-27.46**	**-27.82**	**-29.45**	**-23.50**	**-23.35**	**-29.39**	**-24.79**	**-22.09**
(III)	**-4.00**	**-2.90**	**-3.01**	**-3.77**	**-2.10**	**-2.76**	**-4.15**	**-4.73**	**-2.24**

5.9 DFT calculations of cryptate ring opening barriers

The reported geometry and transition state optimizations have been conducted at the PBE0/def2TZP(D3) level of theory. All stationary points were confirmed by calculating their normal vibrations at the same level of theory. All relative energies were corrected with unscaled zero point vibration energies. Reported relative energies referring to total electronic energies and presented in kcal mol^{-1}.

***o*-Me$_2$-1.1.1**

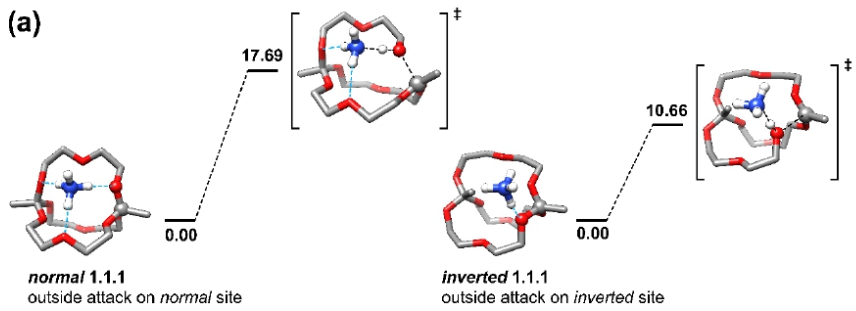

o-Me_2-2.1.1

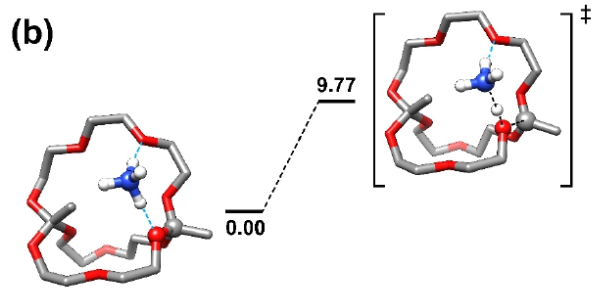

***inverted* 2.1.1**
outside attack on *normal* site

o-Me_2-2.2.1

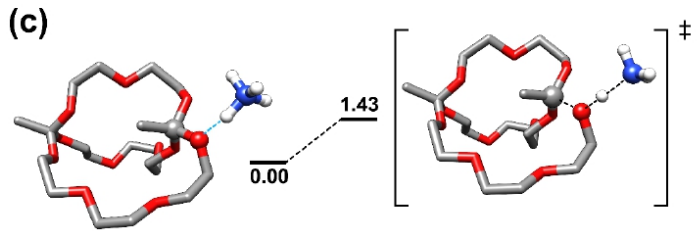

***inverted* 2.2.1**
outisde attack on *inverted* site

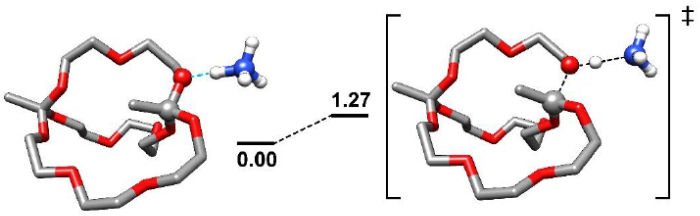

***inverted* 2.2.1**
outisde attack on *inverted* site

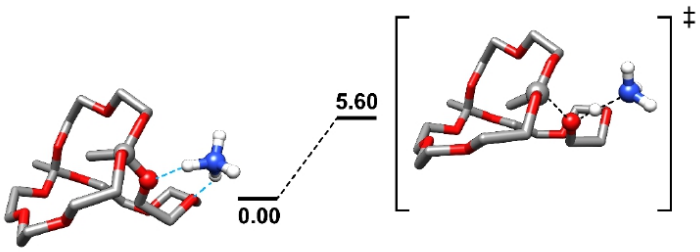

***inverted* 2.2.1**
outisde attack on *inverted* site

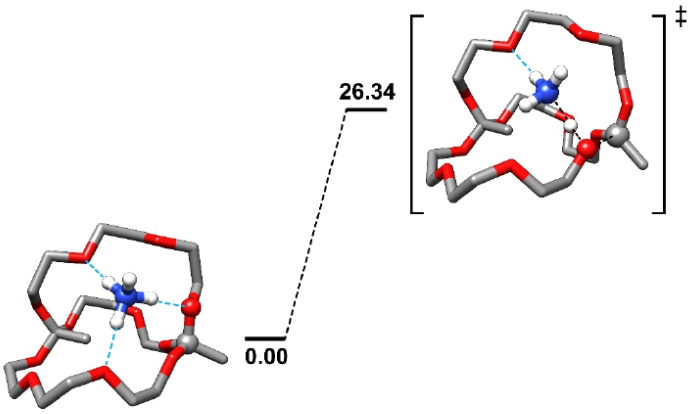

***inverted* 2.2.1**
outisde attack on *normal* site

Figure S50. DFT calculated cryptate ring opening barriers.

6. Crystallographic Data

Suitable single crystals were obtained by slow vapor diffusion of anhydrous n-pentane into a solution of [**NH_4^+⊂*o*-Me$_2$-2.2.1**]$BArF^-$ in $CDCl_3$ in a well-sealed vial devoid of moisture.

The cif-file was deposited in the Cambridge Structural Database under identifier CCDC 1875533.

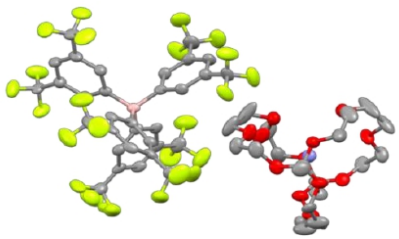

Figure S51. Solid state structure of [**NH_4^+⊂*o*-Me$_2$-2.2.1**]$BArF^-$. Thermal ellipsoids are shown at the 50% probability level.

Table S18. Crystal data and structure refinement for XW17084_04.95 Iso.[S27-S29]

Identification code	XW17084_04.95 Iso
Empirical formula	$C_{26}H_{26.5}B_{0.5}F_{12}N_{0.5}O_{5.5}$
Formula weight	667.38
Temperature/K	293.15
Crystal system	monoclinic
Space group	C2
a/Å	24.92(2)
b/Å	8.848(8)
c/Å	19.069(16)
α/°	90
β/°	137.02(3)
γ/°	90
Volume/Å^3	2866(5)
Z	4
ρ_{calc}g/cm^3	1.547
μ/mm^{-1}	0.157
F(000)	1362.0
Crystal size/mm^3	0.312 × 0.155 × 0.072
Radiation	MoKα (λ = 0.71073)
2Θ range for data collection/°	4.278 to 46.778
Index ranges	-24 ≤ h ≤ 24, -8 ≤ k ≤ 8, -17 ≤ l ≤ 16
Reflections collected	6961

Independent reflections	2981 [R_{int} = 0.0430, R_{sigma} = 0.0565]
Data/restraints/parameters	2981/343/452
Goodness-of-fit on F^2	1.045
Final R indexes [I>=2σ (I)]	R_1 = 0.0495, wR_2 = 0.1168
Final R indexes [all data]	R_1 = 0.0617, wR_2 = 0.1254
Largest diff. peak/hole / e $Å^{-3}$	0.24/-0.23
Flack parameter	-0.1(5)

Table S19. Fractional Atomic Coordinates (×10^4) and Equivalent Isotropic Displacement Parameters ($Å^2$×10^3) for XW17084_04.95 Iso. U_{eq} is defined as 1/3 of the trace of the orthogonalised U_{IJ} tensor.

Atom	*x*	*y*	*z*	U(eq)
O	3439(3)	2667(6)	-1687(5)	50.1(16)
F1	6887(3)	5522(6)	4547(4)	68.9(18)
O4AA	3832(3)	1241(7)	-2294(4)	50.4(17)
F	6372(3)	6679(8)	3140(5)	76.9(18)
F4AA	6968(3)	7897(7)	4544(5)	92(2)
F2	4434(3)	10729(7)	2928(5)	81.4(19)
F0AA	2207(3)	3097(9)	751(4)	99(2)
F1AA	4259(3)	9654(7)	1673(5)	79.0(19)
F8AA	2737(4)	407(12)	3647(8)	108(4)
F9AA	3636(3)	9057(7)	2088(5)	95(2)
F3	3693(5)	749(8)	5145(5)	75(3)
O2AA	3709(3)	259(6)	-1216(5)	56.1(17)
C1	5190(4)	6210(8)	4428(5)	31.1(19)
O1AA	5321(3)	3610(7)	2055(4)	56.4(18)
C2	3309(4)	3309(9)	2398(6)	42(2)
F2AA	2841(4)	4943(7)	1017(4)	97(2)
C3	5778(4)	6078(9)	4509(6)	37(2)
F3AA	3094(3)	2719(8)	878(4)	89(2)
F4	3652(5)	-686(7)	4125(7)	84(3)
C4	6528(5)	6771(10)	4050(8)	46(2)
C5	3888(4)	4257(9)	3084(6)	36(2)
C6	5881(4)	6951(9)	3929(7)	40(2)
C7	3162(4)	2147(9)	2762(7)	43(2)
C8	4288(6)	9397(12)	2466(8)	58(3)
C9	4164(4)	2841(9)	4483(6)	38(2)
C10	4809(4)	8210(9)	3166(6)	43(2)
C11	3389(4)	1215(9)	-2064(6)	50(2)
B3BA	5000	5148(15)	5000	35(3)
C12	3580(4)	1888(9)	3814(6)	40(2)
C13	4718(4)	7352(9)	3750(6)	39(2)
C14	2634(4)	768(11)	-2976(7)	68(3)
C15	4335(4)	4049(8)	4159(6)	36(2)
C16	4721(5)	4177(14)	1902(8)	81(4)
C17	2872(5)	3567(13)	1279(7)	60(3)

C18	5395(4)	8028(9)	3251(6)	43(2)
C19	4265(5)	2660(12)	-2934(7)	56(3)
C20	3442(4)	670(10)	4206(7)	51(2)
C21	3620(5)	2244(12)	-3120(7)	60(3)
C22	3027(6)	2958(12)	-1403(8)	69(3)
O0AA	5000	-1292(9)	0	56(3)
O1A	4161(12)	4840(30)	21(17)	58(11)
C23	3310(5)	4353(14)	-782(7)	80(4)
N1	5000	2312(15)	0	51(3)
F8AB	2970(30)	1040(80)	4320(40)	64(19)
F3A	4010(20)	-50(80)	5130(40)	70(20)
F4A	2950(40)	-330(60)	3440(40)	70(20)
C24	3763(8)	-1270(13)	-1475(19)	48(5)
C25	4341(8)	-1953(17)	-581(17)	84(10)
C26	3800(20)	-1330(20)	-1070(30)	38(12)
C27	4516(14)	-1750(30)	-915(16)	22(9)
O1B	3950(5)	3845(11)	138(6)	63(5)
C28	4294(6)	5072(16)	947(8)	109(6)

Table S20. Anisotropic Displacement Parameters ($Å^2 \times 10^3$) for XW17084_04.95 Iso. The Anisotropic displacement factor exponent takes the form: $-2\pi^2[h^2a^{*2}U_{11}+2hka^*b^*U_{12}+\ldots]$.

Atom	U_{11}	U_{22}	U_{33}	U_{23}	U_{13}	U_{12}
O	42(3)	43(4)	67(4)	2(3)	40(3)	1(3)
F1	31(3)	70(4)	95(4)	43(3)	43(3)	26(3)
O4AA	16(3)	63(4)	45(4)	-10(3)	14(3)	-9(3)
F	51(3)	110(5)	79(4)	41(4)	51(3)	33(3)
F4AA	37(3)	57(4)	145(6)	-1(4)	55(4)	-3(3)
F2	59(4)	56(4)	97(5)	23(4)	47(4)	31(3)
F0AA	25(3)	138(6)	44(4)	-2(4)	-4(3)	-1(3)
F1AA	62(4)	92(4)	64(4)	45(3)	40(3)	43(3)
F8AA	32(4)	123(9)	98(7)	9(7)	25(4)	-25(4)
F9AA	26(3)	101(5)	96(5)	58(4)	25(3)	31(3)
F3	83(6)	68(5)	62(4)	-27(4)	50(5)	-48(5)
O2AA	31(3)	37(4)	75(4)	3(3)	31(3)	1(3)
C1	17(4)	29(5)	24(5)	-4(3)	7(4)	-2(3)
O1AA	23(3)	81(4)	41(4)	10(3)	16(3)	23(3)
C2	19(4)	39(5)	36(5)	-6(4)	10(4)	14(4)
F2AA	80(4)	65(4)	35(3)	9(3)	8(3)	7(3)
C3	19(4)	36(5)	33(5)	7(4)	12(4)	6(3)
F3AA	57(3)	121(5)	38(3)	-5(3)	18(3)	32(4)
F4	104(7)	45(4)	130(8)	-4(4)	94(7)	-2(4)
C4	34(5)	46(6)	53(6)	29(5)	30(5)	22(5)
C5	18(4)	32(4)	36(4)	1(4)	14(4)	10(3)
C6	24(4)	41(5)	44(5)	5(4)	21(4)	5(4)
C7	12(4)	39(5)	39(5)	-8(4)	6(4)	3(3)

C8	43(6)	45(7)	64(7)	25(5) 31(5)	23(5)
C9	20(4)	37(5)	34(5)	-3(4) 13(4)	3(3)
C10	30(4)	40(5)	33(5)	5(4) 15(4)	12(4)
C11	25(4)	43(6)	60(6)	-3(5) 24(4)	-8(4)
B3BA	27(6)	28(7)	28(7)	0 13(6)	0
C12	19(4)	36(5)	42(5)	-14(4) 15(4)	2(3)
C13	22(4)	42(5)	36(5)	4(4) 16(4)	7(4)
C14	23(4)	66(6)	75(6)	2(5) 23(5)	-8(4)
C15	13(3)	34(5)	29(4)	-2(4) 6(3)	6(3)
C16	33(5)	117(10)	51(7)	-21(7) 18(5)	26(6)
C17	32(6)	71(8)	38(5)	4(5) 13(5)	19(5)
C18	33(4)	36(5)	51(5)	14(4) 28(4)	11(4)
C19	25(4)	85(7)	35(6)	-4(5) 15(4)	-10(5)
C20	29(4)	50(6)	55(5)	-14(4) 25(4)	-10(4)
C21	21(4)	87(8)	38(6)	-14(5) 11(4)	-12(4)
C22	62(6)	67(7)	87(8)	26(7) 58(6)	24(6)
O0AA	26(5)	38(5)	75(7)	0 28(5)	0
C23	44(6)	104(9)	43(6)	15(7) 16(5)	39(6)
N1	42(7)	52(9)	42(10)	0 25(7)	0
F8AB	0(30)	110(50)	40(40)	10(30) 0(30)	10(20)
F3A	30(20)	80(50)	73(19)	10(20) 28(17)	0(20)
F4A	70(40)	40(30)	60(20)	0(20) 30(20)	-10(30)
C24	40(8)	31(8)	67(12)	-1(6) 37(8)	-11(5)
C25	41(9)	48(9)	71(12)	-3(8) 12(8)	-4(8)
O1B	32(5)	74(8)	34(6)	10(5) 8(4)	33(5)
C28	55(7)	152(12)	38(7)	-17(8) 8(6)	60(8)

Table S21. Bond Lengths for XW17084_04.95 Iso.

Atom	Atom	Length/Å	Atom	Atom	Length/Å
O	C11	1.432(9)	C4	C6	1.461(12)
O	C22	1.494(10)	C5	C15	1.462(12)
F1	C4	1.296(9)	C6	C18	1.324(11)
O4AA	C11	1.454(10)	C7	C12	1.451(12)
O4AA	C21	1.527(11)	C8	C10	1.427(12)
F	C4	1.476(11)	C9	C12	1.318(11)
F4AA	C4	1.253(11)	C9	C15	1.447(11)
F2	C8	1.352(11)	C10	C13	1.496(12)
F0AA	C17	1.222(11)	C10	C18	1.354(11)
F1AA	C8	1.478(12)	C11	C14	1.391(10)
F8AA	C20	1.240(9)	B3BA	C15	1.541(11)
F9AA	C8	1.241(11)	B3BA	C15^2	1.541(11)
F3	C20	1.401(10)	C12	C20	1.488(11)
O2AA	C11	1.442(10)	C16	C28	1.496(16)

O2AA	C24	1.480(14)	C19	C21	1.417(12)
O2AA	C26	1.42(2)	C20	F8AB	1.38(2)
C1	C3	1.360(11)	C20	F3A	1.36(2)
C1	B3BA	1.749(11)	C20	F4A	1.34(2)
C1	C13	1.360(10)	C22	C23	1.484(13)
O1AA	C16	1.391(11)	O0AA	C27[1]	1.26(2)
O1AA	C19[1]	1.431(11)	O0AA	C27	1.26(2)
C2	C5	1.318(11)	O1A	C23	1.51(2)
C2	C7	1.430(12)	O1A	C28	1.55(3)
C2	C17	1.546(14)	C23	O1B	1.315(11)
F2AA	C17	1.297(12)	C24	C25	1.32(3)
C3	C6	1.517(12)	C26	C27	1.61(6)
F3AA	C17	1.440(11)	O1B	C28	1.537(14)
F4	C20	1.362(10)			

[1]1-X,+Y,-Z; [2]1-X,+Y,1-Z

Table S22. Bond Angles for XW17084_04.95 Iso.

Atom	Atom	Atom	Angle/°	Atom	Atom	Atom	Angle/°
C11	O	C22	120.4(7)	C15[2]	B3BA	C1	114.4(4)
C11	O4AA	C21	123.7(6)	C15	B3BA	C15[2]	101.8(9)
C11	O2AA	C24	105.8(12)	C7	C12	C20	127.8(7)
C26	O2AA	C11	133(2)	C9	C12	C7	113.9(8)
C3	C1	B3BA	130.1(6)	C9	C12	C20	118.3(8)
C3	C1	C13	106.5(7)	C1	C13	C10	125.9(7)
C13	C1	B3BA	123.3(7)	C5	C15	B3BA	121.1(7)
C16	O1AA	C19[1]	101.6(7)	C9	C15	C5	122.1(7)
C5	C2	C7	117.4(8)	C9	C15	B3BA	116.8(7)
C5	C2	C17	115.5(9)	O1AA	C16	C28	98.4(9)
C7	C2	C17	127.2(8)	F0AA	C17	C2	104.3(9)
C1	C3	C6	128.0(7)	F0AA	C17	F2AA	109.9(8)
F1	C4	F	105.1(8)	F0AA	C17	F3AA	101.7(8)
F1	C4	C6	107.5(7)	F2AA	C17	C2	117.0(9)
F4AA	C4	F1	111.8(7)	F2AA	C17	F3AA	102.8(9)
F4AA	C4	F	105.1(8)	F3AA	C17	C2	120.0(7)
F4AA	C4	C6	106.8(8)	C6	C18	C10	109.8(8)
C6	C4	F	120.6(7)	C21	C19	O1AA[1]	99.2(7)
C2	C5	C15	118.0(8)	F8AA	C20	F3	97.8(8)
C4	C6	C3	125.8(7)	F8AA	C20	F4	99.1(8)
C18	C6	C3	123.7(7)	F8AA	C20	C12	114.1(8)
C18	C6	C4	110.5(8)	F3	C20	C12	123.6(7)
C2	C7	C12	127.2(7)	F4	C20	F3	109.8(8)
F2	C8	F1AA	108.7(8)	F4	C20	C12	109.4(7)
F2	C8	C10	113.9(8)	F8AB	C20	C12	116(3)
F9AA	C8	F2	101.7(9)	F3A	C20	C12	126(2)

F9AA	C8	F1AA	112.5(9)	F3A	C20	F8AB	96(3)
F9AA	C8	C10	105.8(9)	F4A	C20	C12	107(3)
C10	C8	F1AA	113.6(8)	F4A	C20	F8AB	97(3)
C12	C9	C15	121.4(8)	F4A	C20	F3A	111(4)
C8	C10	C13	122.7(8)	C19	C21	O4AA	114.8(7)
C18	C10	C8	111.2(8)	C23	C22	O	112.4(9)
C18	C10	C13	126.0(7)	C27[1]	O0AA	C27	143(3)
O	C11	O4AA	109.2(6)	C23	O1A	C28	99.5(16)
O	C11	O2AA	101.0(6)	C22	C23	O1A	122.9(13)
O2AA	C11	O4AA	115.4(6)	O1B	C23	C22	100.7(9)
C14	C11	O	115.1(7)	C25	C24	O2AA	105(2)
C14	C11	O4AA	105.0(8)	O0AA	C25	C24	114(2)
C14	C11	O2AA	111.6(7)	O2AA	C26	C27	105(3)
C1	B3BA	C1[2]	115.0(9)	O0AA	C27	C26	89(3)
C15	B3BA	C1[2]	114.4(4)	C23	O1B	C28	109.8(8)
C15[2]	B3BA	C1[2]	105.4(4)	C16	C28	O1A	133.1(14)
C15	B3BA	C1	105.4(4)	C16	C28	O1B	103.0(10)

[1]1-X,+Y,-Z; [2]1-X,+Y,1-Z

Table S23. Hydrogen Atom Coordinates (Å×10^4) and Isotropic Displacement Parameters (Å^2×10^3) for XW17084_04.95 Iso.

Atom	*x*	*y*	*z*	U(eq)
H3	6163.99	5364.45	4977.43	44
H5	4009.39	5035.33	2889.76	43
H7	2751.78	1485.2	2269.03	52
H9	4471.69	2733.57	5177.5	45
H13	4300.19	7623.61	3640.16	47
H14A	2333.4	551.17	-2848.77	102
H14B	2662.85	-120.59	-3235.6	102
H14C	2383.05	1566.64	-3473.52	102
H16A	4921.32	4810.99	2467.57	98
H16B	4396.18	3379.37	1786.11	98
H18	5447.2	8577.16	2888.66	52
H19A	4096.47	3209.41	-3508.43	67
H19B	4575.78	1790.46	-2775.36	67
H21A	3236	1717.69	-3773.62	72
H21B	3372.24	3156.84	-3181.98	72
H22A	2465.92	3047.29	-2026.06	83
H22B	3107.68	2103.5	-1015.58	83
H23A	3159.86	4271.41	-436.46	96
H23B	3007.79	5183.12	-1265.71	96
H23C	3429.38	5142.4	-1004.67	96
H23D	2931.24	4728.07	-805.88	96
H24A	3272.42	-1814.23	-1884.65	58

H24B	3881.89	-1208.1	-1858.84	58
H25A	4199.21	-2025.78	-225.42	100
H25B	4395.02	-2974.09	-709.23	100
H26A	3325.58	-1846.9	-1663.74	46
H26B	3935.35	-1611.39	-466.79	46
H27A	4557.62	-2818.8	-977.15	26
H27B	4518.65	-1156.61	-1341.34	26
H28A	4526.86	6070.66	1201.81	131
H28B	3766.55	5176.88	631.35	131
H28C	4651.87	5726.35	1034.53	131
H28D	3880.48	5680.63	759.72	131
H1A	5000	1100(400)	0	200(120)
H1B	5130(60)	2530(110)	510(70)	50(40)

Table S24. Atomic Occupancy for XW17084_04.95 Iso.

Atom	***Occupancy***	**Atom**	***Occupancy***	**Atom**	***Occupancy***
F8AA	0.905(16)	F3	0.905(16)	F4	0.905(16)
O1A	0.26(2)	H23A	0.26(2)	H23B	0.26(2)
H23C	0.74(2)	H23D	0.74(2)	F8AB	0.095(16)
F3A	0.095(16)	F4A	0.095(16)	C24	0.68(4)
H24A	0.68(4)	H24B	0.68(4)	C25	0.68(4)
H25A	0.68(4)	H25B	0.68(4)	C26	0.32(4)
H26A	0.32(4)	H26B	0.32(4)	C27	0.32(4)
H27A	0.32(4)	H27B	0.32(4)	O1B	0.74(2)
H28A	0.26(2)	H28B	0.26(2)	H28C	0.74(2)
H28D	0.74(2)				

7. References

S1 O. Shyshov, R.-C. Brachvogel, T. Bachmann, R. Srikantharajah, D. Segets, F. Hampel, R. Puchta and M. von Delius, *Angew. Chem., Int. Ed.,* **2017**, 56, 776-781.

S2 R.-C. Brachvogel, F. Hampel and M. von Delius, *Nat. Commun.,* **2015**, *6*, 7129.

S3 https://doi.org/10.6084/m9.figshare.c.4096289.v1

S4 R. M. B. D. A. Case, W. Botello-Smith, D. S. Cerutti, T. E. Cheatham, III, T. A. Darden, R. E. Duke, T. J. Giese, H. Gohlke, A. W. Goetz, N. Homeyer, S. Izadi, P. Janowski, J. Kaus, A. Kovalenko, T. S. Lee, S. LeGrand, P. Li, C. Lin, T. Luchko, R. Luo, B. Madej, D. Mermelstein, K. M. Merz, G. Monard, H. Nguyen, H. T. Nguyen, I. Omelyan, A. Onufriev, D. R. Roe, A. Roitberg, C. Sagui, C. L. Simmerling, J. Swails, R. C. Walker, J. Wang, R. M. Wolf, X. Wu, L. Xiao, D. M. York and P. A. Kollman (2016), AMBER 2016, University of California, San Francisco.

S5 R. Salomon-Ferrer, A. W. Götz, D. Poole, S. Le Grand and R. C. Walker, *J. Chem. Theor. Comput.*, **2013**, 9, 3878-3888.

S6 S. Le Grand, A. W. Götz and R. C. Walker, *Comput. Phys. Commun.*, **2013**, 184, 374-380.

S7 A. W. Götz, M. J. Williamson, D. Xu, D. Poole, S. Le Grand and R. C. Walker, *J. Chem. Theor. Comput.*, **2012**, 8, 1542-1555.

S8 Z. X. Wang and Y. Duan, *J. Comput. Chem.*, **2004**, 25, 1699-1716.

S9 C. I. Bayly, P. Cieplak, W. D. Cornell and P. A. Kollman, *J. Phys. Chem.*, **1993**, 97, 10269-10280.

S10 A. D. Becke, *J. Chem. Phys.*, **1993**, 98, 5648.

S11 C. Lee, W. Yang and R. G. Parr, *Phys. Rev. B: Condens. Matter Mater. Phys.*, **1988**, 37, 785.

S12 P. J. Stephens, F. J. Devlin, C. F. Chabalowski and M. J. Frisch, *J. Phys. Chem.*, **1994**, 98, 11623.

S13 B. G. Johnson, C. A. Gonzales, P. M. W. Gill and J. A. Pople, *Chem. Phys. Lett.*, **1994**, 221, 100-108.

S14 T. H. Dunning, *J. Chem. Phys.*, **1989**, 90, 1007-1023.

S15 C. C. J. Roothaan, *Rev. Mod. Phys.*, **1951**, 23, 69-89.

S16 J. A. Maier, C. Martinez, K. Kasavajhala, L. Wickstrom, K. E. Hauser and C. Simmerling, *J. Chem. Theor. Comput.*, **2015**, 11, 3696-3713.

S17 I. S. Joung and T. E. Cheatham, *J. Phys. Chem. B*, **2008**, 112, 9020-9041.

S18 R. Zwanzig, *J. Stat. Phys.*, **1973**, 9, 215-220.

S19 T. Darden, D. York and L. Pedersen, *J. Chem. Phys.*, **1993**, 98, 10089-10092.

S20 A. Grossfield, "*WHAM: an implementation of the weighted histogram analysis method*", http://membrane.urmc.rochester.edu/content/wham/, version 2.0.9.1.

S21 R. C. Walker, M. F. Crowley and D. A. Case, *J. Comput. Chem.*, **2008**, 29, 1019-1031.

S22 A. W. Gotz, M. A. Clark and R. C. Walker, *J. Comput. Chem.*, **2014**, 35, 95-108.

S23 M. J. Frisch, G. W. Trucks, H. B. Schlegel, G. E. Scuseria, M. A. Robb, J. R. Cheeseman, G. Scalmani, V. Barone, B. Mennucci, G. A. Petersson, H. Nakatsuji, M. Caricato, X. Li, H. P. Hratchian, A. F. Izmaylov, J. Bloino, G. Zheng, J. L. Sonnenberg, M. Hada, M. Ehara, K. Toyota, R. Fukuda, J. Hasegawa, M. Ishida, T. Nakajima, Y. Honda, O. Kitao, H. Nakai, T. Vreven, J. A. Montgomery, J. E. Peralta, F. Ogliaro, M. Bearpark, J. J. Heyd, E. Brothers, K. N. Kudin, V. N. Staroverov, R. Kobayashi, J. Normand, K. Raghavachari, A. Rendell, J. C. Burant, n. Iyengar, J. Tomasi, M. Cossi, N. Rega, N. J. Millam, M. Klene, J. E. Knox, J. B. Cross, V. Bakken, C. Adamo, J. Jaramillo, R. Gomperts, R. E. Stratmann, O. Yazyev, A. J. Austin, R. Cammi, C. Pomelli, J. W. Ochterski, R. L. Martin, K. Morokuma, V. G. Zakrzewski, G. A. Voth, P. Salvador, J. J. Dannenberg, S. Dapprich, A. D. Daniels, Ö. Farkas, J. B. Foresman, J. V. Ortiz, J. Cioslowski and D. J. Fox, *Gaussian 09*, **2009**.

S24 M. Elstner, D. Porezag, G. Jungnickel, J. Elsner, M. Haugk, T. Frauenheim, S. Suhai and G. Seifert, *Phys. Rev. B*, **1998**, 58, 7260-7268.

S25 G. d. M. Seabra, R. C. Walker, M. Elstner, D. A. Case and A. E. Roitberg, *J. Phys. Chem. A*, **2007**, 111, 5655-5664.

S26 A. Mudi and C. Chakravarty, *Mol. Phys.*, 2004, **102**, 681-685.

S27 V. Dolomanov, L. J. Bourhis, R. J. Gildea, J. A. K. Howard and H. Puschmann, *J. Appl. Cryst.,* **2009**, 42, 339-341.

S28 G. M. Sheldrick, *Acta Cryst.* **2015**, A71, 3-8.

S29 G. M. Sheldrick, *Acta Cryst.* **2015**, C71, 3-8.

4.3 Long-Chain Polyorthoesters as Degradable Polyethylene Mimics

Tobias Haider, Oleksandr Shyshov, Oksana Suraeva, Ingo Lieberwirth, Max von Delius, and Frederik R. Wurm *Macromolecules* **2019** *52* (6), 2411-2420
DOI: 10.1021/acs.macromol.9b00180

This is an open access article published under a Creative Commons Attribution (CC-BY) License, which permits unrestricted use, distribution and reproduction in any medium, provided the author and source are cited.

Abstract:

The persistence of commodity polymers makes the research for degradable alternatives with similar properties necessary. Degradable polyethylene mimics containing orthoester groups were synthesized by olefin metathesis polymerization for the first time. Ring-opening metathesis copolymerization (ROMP) of 1,5-cyclooctadiene with four different cyclic orthoester monomers gave linear copolymers with molecular weights up to 38000 g mol^{-1}. Hydrogenation of such copolymers produced semicrystalline polyethylene-like materials, which were only soluble in hot organic solvents. The crystallinity and melting points of the materials were controlled by the orthoester content of the copolymers. The polymers crystallized similar to polyethylene, but the relatively bulky orthoester groups were expelled from the crystal lattice. The lamellar thickness of the crystals was dependent on the amount of the orthoester groups. In addition, the orthoester substituents influenced the hydrolysis rate of the polymers in solution. Additionally, we were able to prove that non-hydrogenated copolymers with a high orthoester content were biodegraded by microorganisms from activated sludge from a local sewage plant. In general, all copolymers hydrolyzed under ambient conditions over a period of several months. This study represents the first report of hydrolysis-labile and potentially biodegradable PE mimics based on orthoester linkages. These materials may find use in applications that require the relatively rapid release of cargo, e.g., in biomedicine or nanomaterials.

Comments on own contributions:

Prof. Max von Delius and Prof. Frederik R. Wurm had the original idea. I performed the synthesis of orthoester monomers, carried out some preliminary attempts on polymerization using ADMET, shared my experience on orthoester handling, and participated in the writing of the supplementary information. Polymer synthesis, characterization, and studies on degradability were performed at MPIP Mainz.

This is an open access article published under a Creative Commons Attribution (CC-BY) License, which permits unrestricted use, distribution and reproduction in any medium, provided the author and source are cited.

Macromolecules
Cite This: Macromolecules 2019, 52, 2411−2420
Article
pubs.acs.org/Macromolecules

Long-Chain Polyorthoesters as Degradable Polyethylene Mimics

Tobias Haider,[†] Oleksandr Shyshov,[‡] Oksana Suraeva,[†] Ingo Lieberwirth,[†] Max von Delius,[‡] and Frederik R. Wurm*[,†]

[†]Max Planck Institute for Polymer Research, Ackermannweg 10, 55128 Mainz, Germany
[‡]Institute of Organic Chemistry and Advanced Materials, University of Ulm, Albert-Einstein-Allee 11, 89081 Ulm, Germany

Supporting Information

ABSTRACT: The persistence of commodity polymers makes the research for degradable alternatives with similar properties necessary. Degradable polyethylene mimics containing orthoester groups were synthesized by olefin metathesis polymerization for the first time. Ring-opening metathesis copolymerization (ROMP) of 1,5-cyclooctadiene with four different cyclic orthoester monomers gave linear copolymers with molecular weights up to 38000 g mol^{-1}. Hydrogenation of such copolymers produced semicrystalline polyethylene-like materials, which were only soluble in hot organic solvents. The crystallinity and melting points of the materials were controlled by the orthoester content of the copolymers. The polymers crystallized similar to polyethylene, but the relatively bulky orthoester groups were expelled from the crystal lattice. The lamellar thickness of the crystals was dependent on the amount of the orthoester groups. In addition, the orthoester substituents influenced the hydrolysis rate of the polymers in solution. Additionally, we were able to prove that non-hydrogenated copolymers with a high orthoester content were biodegraded by microorganisms from activated sludge from a local sewage plant. In general, all copolymers hydrolyzed under ambient conditions over a period of several months. This study represents the first report of hydrolysis-labile and potentially biodegradable PE mimics based on orthoester linkages. These materials may find use in applications that require the relatively rapid release of cargo, e.g., in biomedicine or nanomaterials.

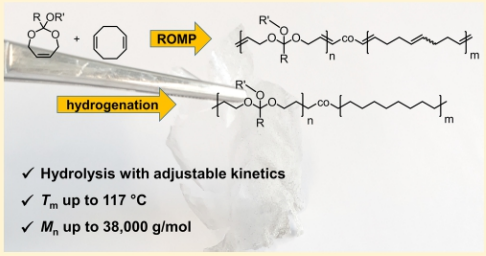

1. INTRODUCTION

Today polyethylene (PE) is the most used commodity polymer in the world.[1] Because of its excellent mechanical properties, PE is used for a variety of applications.[2] However, there are environmental issues related to the low degradability of PE in the environment. Increasing plastic pollution in natural environments amplifies the need for degradable alternatives.[3]

To mimic the properties of polyethylene while potentially enabling degradation at the same time, one approach lies in the incorporation of functional groups in long aliphatic polymer chains.[4] Among others, long-chain polyesters,[5] polyamides,[6] polyketones,[7] or polyphosphoesters[8] have been reported. There, the functional groups act as "defects" in the polymer chains of the semicrystalline materials. Depending on their size, the defects are either part of the lamellar PE crystals (small defect size) or forced into the amorphous phase (bulky defects).[9] An increasing number of methylene units between the functional groups enhances van der Waals interactions between the polymer chains, leading to a higher degree of crystallinity.[4] As a result, hydrophobicity, melting temperature, and stiffness of the material increase.[4] Yet, concerning degradability, long-chain polyesters, for example, did not show relevant enzymatic or hydrolytic degradation as water is hindered from penetrating into the materials due to the high crystallinity and hydrophobicity.[4] Also, long chain polyacetals revealed only minor degradation in acidic media.[10] Thus, the use of functional groups, which are more prone to hydrolysis, is advisable. Similar to acetals in molecular structure, but with a higher hydrolysis rate[11] and steric bulk, orthoesters can be a suitable alternative to synthesize acid-sensitive polymers.

Acid-degradable polymers are also attractive for drug delivery;[12] polyorthoesters were developed in the 1970s by the group of Jorge Heller for biomedical applications.[13−16] The hydrolysis of polyorthoesters in acidic media yields alcohols and esters (Scheme 1), while the degradation of the bulk material was shown to proceed via surface erosion.[15]

While polyacetals were synthesized by acyclic diene metathesis (ADMET) polymerization,[17,18] ring-opening metathesis copolymerization (ROMP),[19] or polycondensation,[20] polyorthoesters are mainly prepared either through transesterification of orthoesters with diols or through polyaddition between a diol and a diketene acetal (Scheme 2).[21]

Received: January 24, 2019
Revised: February 27, 2019
Published: March 13, 2019

ACS Publications © 2019 American Chemical Society

DOI: 10.1021/acs.macromol.9b00180
Macromolecules 2019, 52, 2411−2420

Downloaded via UNIV ULM on October 24, 2019 at 15:48:41 (UTC).
See https://pubs.acs.org/sharingguidelines for options on how to legitimately share published articles.

Scheme 1. Hydrolysis of Polyorthoesters to Alcohols and Esters

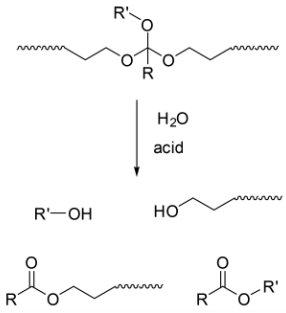

Scheme 2. Synthesis Methods for Polyorthoesters

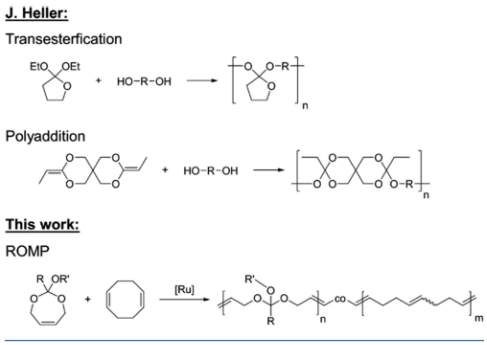

Dove et al. reported the synthesis of different polyorthoesters by polyaddition using bifunctional, air- and moisture-stable vinyl acetal precursors.[22] In general, the mechanical and thermal properties of polyorthoesters can be adjusted by varying the structure of the monomers (mainly the diols). By changing the hydrophobicity of the polymer, the degradability of the material can be tuned. However, this requires the use of new, different monomers if the polymerization is conducted by transesterification or polyaddition. Recently, von Delius and co-workers explored the use of orthoesters for the self-assembly of novel supramolecular hosts[23−25] and in this context demonstrated that the degradation rate of orthoesters strongly depends on the orthoester substituent (R group in Scheme 1): electron-rich orthoesters (R = $-CH_3$) hydrolyze even at neutral pH, while more electron-deficient orthoesters (R = $-CCl_3$) are remarkably stable.[26] For drug delivery applications, von Delius recommend the use of orthoformates (R = −H) and chloromethyl-substituted orthoesters (R = $-CH_2Cl$) based on observed hydrolysis half-lives of 20 and 120 min at pH 5, respectively.

In this work, we present a straightforward approach to long-chain polyorthoesters by performing for the first time a ring-opening metathesis copolymerization of cyclic orthoesters with 1,5-cyclooctadiene followed by exhaustive hydrogenation. By the variation of the comonomer ratio, the number of methylene groups between two orthoester units can be controlled. Monomers featuring three different orthoester substituents were studied based on the hypothesis that the corresponding polymers would differ in hydrolysis rate. The thermal and mechanical properties of the polyethylene-like polymers were studied as well as the degradation in an organic solvent and in aqueous media.

2. RESULTS AND DISCUSSION

Monomer Synthesis. Starting from the corresponding orthoesters trimethyl orthoacetate, trimethyl orthoformate, triisopropyl orthoformate, and 2-chloro-1,1,1-trimethoxyethane, we synthesized four different cyclic orthoester monomers (**1**−**4**) by reacting the respective starting compounds with *cis*-2-butene-1,4-diol under acidic catalysis (Scheme 3A). Moisture had to be strictly excluded during these procedures, as it would lead to hydrolysis of the orthoester. The monomers were purified by (repeated) distillation to yield colorless oils.

Ring-Opening Metathesis Polymerization. The cyclic orthoester monomers are seven-membered and substituted 4,7-dihydro-1,3-dioxepins (Scheme 3) with a substitution at the C2. In previous works, Kilbinger and co-workers synthesized polyacetals as sacrificial blocks to prepare telechelic polynorbornenes using dioxepins.[27] Grubbs et al. reported the ROMP of 4,7-dihydro-1,3-dioxepine and phenyl-substituted 4,7-dihydro-2-phenyl-1,3-dioxepin to polyacetals.[19] However, they were able to prove that only the unsubstituted dioxepin underwent successful homopolymerization. In contrast, we were able in previous work to produce homopolymers of phosphorus-containing seven-membered rings, namely 2-phenoxy-4,7-dihydro-1,3,2-dioxaphosphepine 2-oxide[28] and 2-methyl-4,7-dihydro-1,3,2-dioxaphosphepine 2-oxide.[8]

To date, no polyorthoesters have been reported by metathesis polymerization. In accordance with previous studies, the attempted homopolymerization of the orthoester monomers **1** and **2** did not yield any polymers, even if catalyst type and conditions were varied (cf. Table S1).

During ROMP, the release of ring strain of the cyclic olefin is the driving force of the polymerization.[29] The unsubstituted dioxepin, however, already exhibits relatively low ring strain. Further substituents hinder the ROMP due to the Thorpe−Ingold effect: substituents on a ring stabilize the ring-closed form relative to the linear counterpart. With ROMP being an equilibrium process, the Thorpe−Ingold effect results in a higher critical monomer concentration. This leads to a lower yield of the linear polymer—or to no polymer at all.[30−32] However, monomers with low ring strain can be activated by a more active comonomer: the copolymerization of 1,5-cyclooctadiene (COD) with an unsubstituted or a methyl-substituted 4,7-dihydro-1,3-dioxepins gave statistical COD/dioxepin copolymers.[19] Thus, we followed this approach to copolymerize our four cyclic orthoester monomers with COD using a first-generation Hoveyda−Grubbs catalyst as the initiator (0.4 mol % relative to the total amount of comonomers). The polymerizations were conducted in bulk at room temperature overnight, yielding polymers with apparent molecular weights up to 38000 g mol^{-1} (by SEC vs polystyrene standard). Monomers **1**−**4** were transformed successfully into copolymers with different amounts of orthoesters incorporated into the polymer chain, which controls the chain length of the degradation products (Table 1).

In comparison to the monomers, the corresponding ^1H NMR spectra show a shift of both the orthoester double bond

DOI: 10.1021/acs.macromol.9b00180
Macromolecules 2019, 52, 2411−2420

Scheme 3. (A) Synthesis of Cyclic Orthoester Monomers for ROMP (1−4), (B) ROMP Homopolymerization and (C) Copolymerization of Cyclic Orthoesters with 1,5-Cyclooctadiene and Subsequent Hydrogenation to Orthoester-Containing PE Mimics

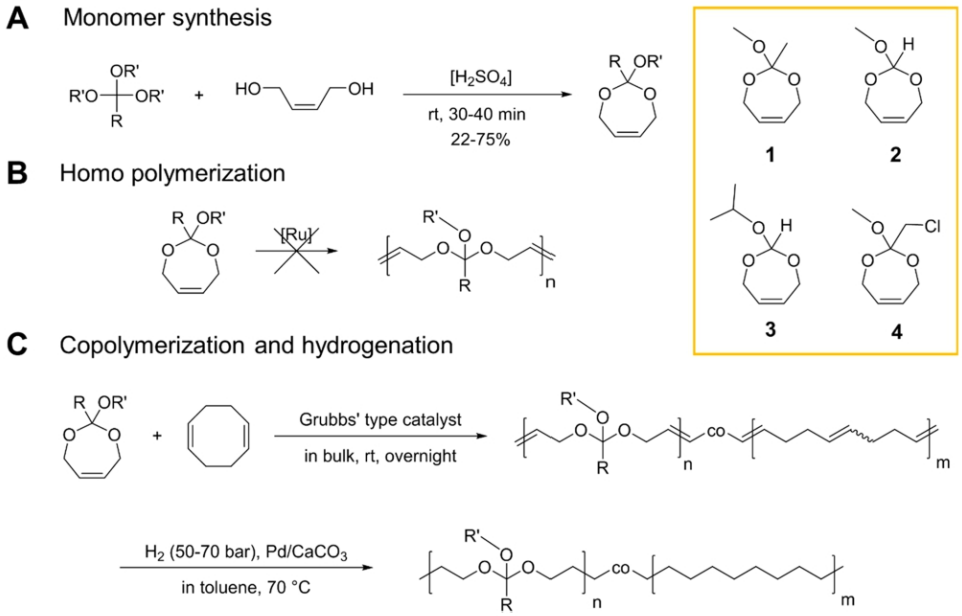

Table 1. Copolymerization of Orthoester Monomers 1−4 with Cyclooctadiene Using First-Generation Grubbs−Hoveyda Catalyst[a]

monomer	ortho:COD feed	ortho:COD NMR[d]	M_n[e] [g mol^{-1}]	M_w[e] [g mol^{-1}]	M_n/M_w[e]	yield [%]
1[b]	1:1	1:2	900	1200	1.43	n.d.
1[b]	1:2	1:3.5	1300	2000	1.61	n.d.
1[b]	1:4	1:6.5	1700	3100	1.79	n.d.
2	1:1	1:2	10500	22500	2.14	60
2	1:2	1:4	11000	32200	2.95	83
2	1:4	1:6	15000	31000	2.60	n.d.
2[c]	1:4	1:9	11600	30800	2.66	n.d.
3	1:1	1:2	5600	15000	2.75	47
3	1:2	1:3	8400	16600	1.99	65
3	1:4	1:5	11000	24000	2.20	77
3[c]	1:4	1:9	10700	27300	2.54	75
4	1:1	1:2.5	6300	15300	2.42	n.d.
4	1:2	1:3.5	8900	24700	2.79	75
4	1:4	1:7	12700	38100	3.01	82

[a]All polymerizations were performed overnight at room temperature with first-generation Grubbs−Hoveyda catalyst (0.4 mol %) in bulk. [b]48 h polymerization time. [c]Large-scale polymerization (>10 g). [d]Determined by ^{1}H NMR. [e]Determined by SEC.

and the −O−CH_2 group of the orthoester monomers to lower field (Figure 1). Overlapping poly-COD signals with slightly different chemical shifts elucidate the copolymer sequence as for poly(**1**)-*co*-COD, where the signal at 2.12 ppm corresponds to the −CH_2 group of a COD unit next to another COD unit, while the signal at 2.06 ppm indicates a neighboring orthoester unit. Additional information about the copolymer sequence is given by the signals corresponding to the polyorthoester double bonds: the signal at 5.72 ppm corresponds to an orthoester−COD dyad. The small signal at 5.90 ppm, however, is giving a hint on an orthoester−orthoester dyad, even though the homopolymerization of **1** previously was not achieved.

By integration of the resonances of COD at 2.09 ppm and comparison to the orthoester resonances at 3.23 ppm, the relative ratio of orthoester to COD in the polymer was determined (indicated in the text by indices as in poly($\mathbf{1}$)$_1$-*co*-COD_2). The experimentally determined ratio is lower than the feed ratio since COD is the more reactive monomer during ROMP. The incorporation of orthoester units into the polymer chain was dependent on several factors: First, a lower amount

DOI: 10.1021/acs.macromol.9b00180
Macromolecules 2019, 52, 2411−2420

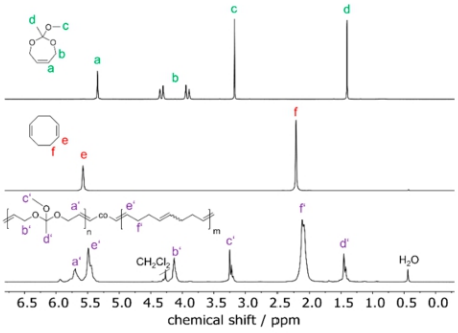

Figure 1. ^{1}H NMR (300 MHz at 298 K, in C_6D_6) of monomer **1** (top), cyclooctadiene (COD, middle), and the corresponding copolymer poly(**1**)$_1$-*co*-COD$_2$ (bottom).

of initiator to monomers resulted in lower incorporation of the orthoester monomer (Table S1). Performing the polymerization in diluted conditions using THF as a solvent decreased the orthoester content in the copolymer in comparison to the polymerization in bulk. In terms of the initiator, the first-generation Grubbs–Hoveyda catalyst revealed the highest conversion of the orthoester monomers. The more active second-generation Grubbs–Hoveyda catalyst and third-generation Grubbs catalyst led to rapid consumption of COD, and no incorporation of **1**–**4** was detected. Increasing the amount of **1**–**4** in the monomer feed resulted in increased incorporations, however, always lower than the monomer feed ratio (20–65% lower than feed). When the copolymerizations of **2** and **3** with COD were performed at a larger scale (ca. 10 g), lower incorporations were obtained compared to the small scale reactions (200–400 mg).

Polymerizations were terminated by the addition of ethyl vinyl ether and isolated by precipitation into basic methanol (ca. 1 wt % of triethylamine were added to prevent hydrolysis). The polymers were recovered as brown viscous oils, indicating that the initiator could not be removed completely by simple precipitation. As the ROMP of COD produces linear poly(1,4-butadiene) with a mixture of *cis*- and *trans*-configurated double bonds, crystallization of the polymer chains is hindered,[33] and all copolymers exhibited melting temperatures below room temperature (T_m maximum −9 °C).

To produce PE-like materials, we performed hydrogenation of the polymers with Pd on $CaCO_3$ in toluene at temperatures above 70 °C. Because of the high sensitivity of orthoesters toward hydrolysis in solution, the hydrogenation proved to be challenging. Despite using of anhydrous conditions and the addition of DIPEA (a soluble and relatively high-boiling amine base) certain hydrolysis of the orthoester functionality could not be prevented. Presumably, the remaining Grubbs' type catalyst could have caused the hydrolysis since HCl can be abstracted during the decomposition of the catalyst.[34] Especially the most sensitive poly(**1**)-*co*-COD (R = methyl) hydrolyzed rapidly. Furthermore, the solubility of the copolymers reduced drastically with ongoing hydrogenation, resulting in the copolymers being insoluble in toluene at room temperature. Thus, for purification the copolymers were dissolved in boiling toluene, the catalyst was filtered off while the solution was still hot, and the copolymers were immediately precipitated into methanol containing DIPEA. The obtained off-white, solid materials were hard and partly brittle. The ^{1}H NMR spectrum of poly(**3**)-*co*-COD in toluene-d_8 (at 90 °C) proves the successful hydrogenation, as the resonances of the double bonds had disappeared completely, while an intense alkyl signal at 1.4 ppm indicates the presence of only methylene groups in the saturated polymer (Figure 2).

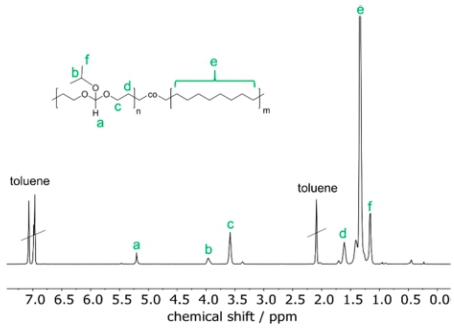

Figure 2. ^{1}H NMR (500 MHz at 353 K, in toluene-d_8) of hydrogenated copolymer poly(**3**)$_1$-*co*-COD$_2$.

Solid-State Characterization. The non-hydrogenated poly(orthoester)-*co*-COD copolymers are honey-like, viscous oils, while the hydrogenated polymers are hard, solid materials. Yet, the hydrogenated copolymers were brittle, so we were unable to make a specimen for tensile strength tests. Possibly the molecular weights of the synthesized polymers were too low, as Gross and co-workers reported a brittle-to-ductile transformation for long-chain polyesters for an M_w between 53 × 10^3 and 78 × 10^3 g mol^{-1}.[35] The thermal stabilities of the copolymers were examined with thermal gravimetric analysis (TGA). The first derivative shows two main points of degradation (Figure S36), indicating that the orthoester and COD units degrade at different temperatures. For instance, hydrogenated poly(**3**)$_1$-*co*-COD$_3$ has one main point of degradation at 343 °C and one at 475 °C (compared to 483 °C of HDPE). Furthermore, the weight loss after the first degradation process is dependent on the orthoester content in the copolymer (Figure 3A). For instance, the thermogram of hydrogenated poly(**3**)$_1$-*co*-COD$_2$ reveals a weight loss of about 40% after the first degradation process, which matches the mol % of the orthoester monomers in the polymer. In general, the hydrogenated polymers are remarkably stable at elevated temperatures with an onset temperature (T_{on}) after 5% degradation for e.g. poly(**3**)$_1$-*co*-COD$_5$ at 338 °C, which is about 100 °C below the measured T_{on} of HDPE. The non-hydrogenated copolymers decompose at lower temperatures in comparison to the related hydrogenated polymers (Figure 3 B). As an example, T_{on} after 5% degradation for non-hydrogenated poly(**3**)$_1$-*co*-COD$_5$ is 265 °C.

By differential scanning calorimetry (DSC), the melting points (T_m) and the crystallinity were determined. In most cases, a glass transition point was either not detectable or outside the measured range (minimum −100 °C). While the non-hydrogenated polymers are either amorphous or show a T_m below room temperature, the hydrogenated polymers have T_m up to 117 °C for poly(**2**)$_1$-*co*-COD$_9$, which is similar to

DOI: 10.1021/acs.macromol.9b00180
Macromolecules 2019, 52, 2411–2420

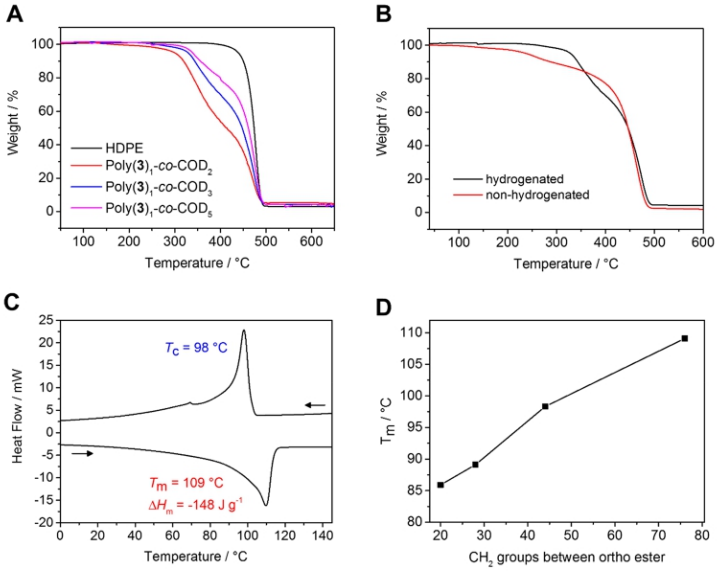

Figure 3. (A) TGA thermogram of hydrogenated poly(**3**)$_1$-*co*-COD$_2$, poly(**3**)$_1$-*co*-COD$_3$, poly(**3**)$_1$-*co*-COD$_5$, and HDPE. (B) TGA thermogram of hydrogenated (black) and non-hydrogenated (red) poly(**3**)$_1$-*co*-COD$_3$. (C) DSC thermogram of poly(**3**)$_1$-*co*-COD$_9$ (exo up, heating and cooling rate 10 K min^{-1} (second run)). (D) Correlation of melting point T_m (from DSC) and the number of CH_2 groups between orthoester (by ^{1}H NMR) for poly(**3**)-*co*-COD.

completely linear PE with 134 °C[6] (cf. Figure 3C shows the DSC thermogram of poly(**3**)$_1$-*co*-COD$_9$ with T_m = 109 °C). The melting enthalpies ΔH_m were between −84 and −162 J g^{-1} and was compared to ΔH of 100% crystalline polyethylene (ΔH_m = 293 J g^{-1})[36] to calculate the crystallinity of the hydrogenated polymers. Both crystallinity and melting temperatures increased with increasing number of methylene groups between the orthoester groups, as the material becomes more similar to PE (cf. Table 2 and Figure 3D). The melting temperatures of our PE mimics start at ca. 86 °C for poly(**3**)$_1$-*co*-COD$_2$, which on average has 20 CH_2 groups between the orthoester groups (determined by ^{1}H NMR), and increase to 109 °C for poly(**3**)$_1$-*co*-COD$_9$ with on average 76 CH_2 groups as spacer (Figure 3D). Thus, with increasing COD amount in the copolymer, the melting point of the hydrogenated polymers converges toward the value for PE.

Table 2. Thermal Properties of Hydrogenated Copolymers

polymer	ortho:COD[a]	T_m[b] [°C]	ΔH[b] [J g^{-1}]	crystallinity[c] [%]
poly(**1**)-*co*-COD	1:2	102	−156	53
poly(**1**)-*co*-COD	1:3.5	109	−167	57
poly(**2**)-*co*-COD	1:4.5	92	−116	39
poly(**2**)-*co*-COD	1:9	117	−163	55
poly(**3**)-*co*-COD	1:2	86	−84	29
poly(**3**)-*co*-COD	1:3	89	−93	32
poly(**3**)-*co*-COD	1:5	98	−95	33
poly(**3**)-*co*-COD	1:9	109	−148	51
poly(**4**)-*co*-COD	1:3.5	93	−86	29
poly(**4**)-*co*-COD	1:7	104	−116	40

[a]Determined by ^{1}H NMR. [b]Determined by DSC. [c]Relative to 100% crystalline PE (ΔH_m = −293 J g^{-1}).

The crystal structures of the three hydrogenated copolymers poly(**2**)$_1$-*co*-COD$_9$, poly(**3**)$_1$-*co*-COD$_9$, and poly(**4**)$_1$-*co*-COD$_9$ were compared to HDPE by XRD (Figure 4). A similar peak

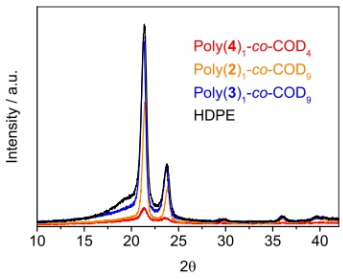

Figure 4. XRD diffractograms of hydrogenated poly(**2**)$_1$-*co*-COD$_9$, poly(**3**)$_1$-*co*-COD$_4$, and poly(**4**)$_1$-*co*-COD$_9$ and HDPE.

pattern in the X-ray diffractogram indicates an orthorhombic structure like HDPE in all three copolymer samples. The intensity of the peaks correlates with the degree of crystallinity.

The crystallization behavior of the orthoester−PE mimics was studied by drop-cast TEM measurements of solution grown crystals. Figure 5 shows a TEM micrograph of solution-grown crystals of hydrogenated poly(**2**)$_1$-*co*-COD$_9$, prepared from cooling a 0.05% solution of the polymer in *n*-octane to room temperature. The solution was heated to 70 °C in a temperature-controlled oil bath for 1 h and slowly cooled to

DOI: 10.1021/acs.macromol.9b00180
Macromolecules 2019, 52, 2411−2420

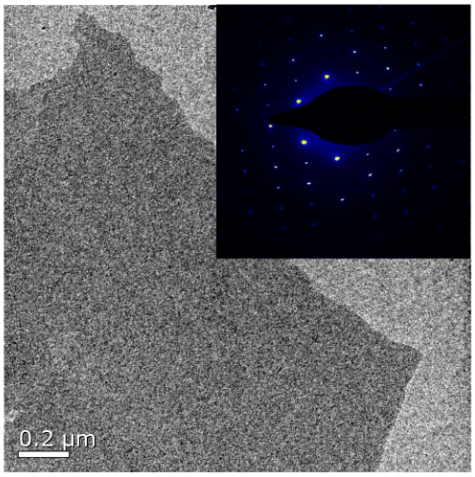

Figure 5. TEM bright-field micrograph and corresponding diffraction pattern (inset) of hydrogenated poly(**2**)$_1$-*co*-COD$_9$.

room temperature. One drop of this dispersion was applied to a carbon-coated TEM grid, excess liquid was blotted off with a filter paper, and the specimen was allowed to dry under ambient conditions. This preparation led to the formation of anisotropic polymer platelets with a thickness of only a few nanometers and much higher lateral dimensions (Figure 5). Electron diffraction correlated to XRD data and reveals the single crystal pattern of flat-on orthorhombic PE crystals. All these polymers have similar crystal structure as common PE, and the introduction of orthoester defects into the PE main chain does not alter the crystal structure.

Moreover, the influence of defect frequency on lamellar thickness was studied using energy-filtered transmission electron microscopy (EFTEM) thickness mapping. Measurement of the crystals of hydrogenated poly(**3**)$_1$-*co*-COD$_2$ and poly(**3**)$_1$-*co*-COD$_5$ with an average number of CH_2 groups between ortho esters of 20 and 44, respectively, was carried out. This experiment revealed that the mean total lamellar thickness is ~3.7 nm for poly(**3**)$_1$-*co*-COD$_2$ and 9.8 nm for poly(**3**)$_1$-*co*-COD$_5$, demonstrating that randomly distributed orthoester groups along the polymer chain control the averaged thickness of PE−platelets; i.e., a decreased amount of orthoester groups resulted in an increased thickness of the polymer platelets. Furthermore, the mean total lamellar thickness for poly(**3**)$_1$-*co*-COD$_2$ was higher compared to the value for polyethylene with precise butyl branches at every 21st carbon (2.9 nm).[9]

Polymer Degradation. The degradation of polyorthoesters in acidic media occurs by hydrolysis to the corresponding alcohols and esters (Scheme 1). We varied the R′ group to change the molecular structure of the degradation products. While the hydrolysis of poly(**1**)-*co*-COD, poly(**2**)-*co*-COD, and poly(**4**)-*co*-COD yields methanol, poly(**3**)-*co*-COD produces less toxic isopropanol. Furthermore, the substituent at the orthoester group has an influence on the hydrolysis rate:

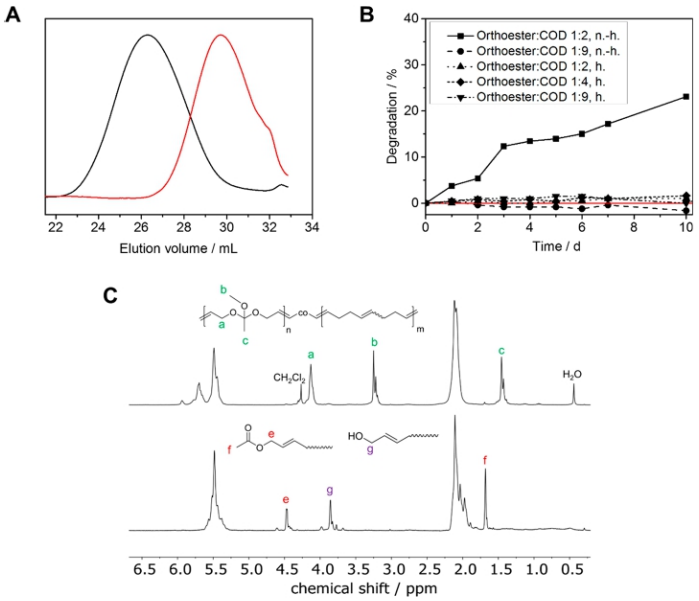

Figure 6. (A) SEC elugram (in THF) of poly(**3**)-*co*-COD before (black) and after degradation by hydrolysis (red). (B) Manometric respirometry biodegradation test of hydrogenated (h.) and non-hydrogenated (n.h.) poly(**2**)-*co*-COD using activated sludge from a local sewage plant. (C) ^{1}H NMR (300 MHz at 298 K, in C_6D_6) of poly(**1**)-*co*-COD (top) and after hydrolysis (bottom) with peak assignments.

DOI: 10.1021/acs.macromol.9b00180
Macromolecules 2019, 52, 2411−2420

von Delius and co-workers proved that relative to the electron density induced by the R-group hydrolysis the rate increases from CH_2Cl < H < Me.[26] Thus, our PE mimics were expected to exhibit an adjustable hydrolysis rate. In general, the unsaturated polymers exhibited shelf lives of below 6 months of storage (at room temperature under air), indicating hydrolysis of the honey-like materials from atmospheric moisture; the M_n of poly(**3**)-*co*-COD decreased from 8400 to 900 g mol^{-1} after storing the sample for 6 months without any precautions (Figure 6A). Comparing the ^{1}H NMR spectrum of poly(**1**)-*co*-COD directly after the synthesis with the spectrum after 6 months of storage, all corresponding orthoester signals had vanished completely (Figure 6C). Instead, peaks corresponding to the hydrolysis products (methyl ester and alcohol) were detected. We proceeded to examine the influence of the orthoester substituent on the hydrolytic degradation in a solution of the non-hydrogenated copolymers poly(**1**)-*co*-COD (R = −Me), poly(**2**)-*co*-COD (R = −H), and poly(**4**)-*co*-COD (R = $-CH_2Cl$). We performed these hydrolysis tests in *d*-THF and added 10 vol % of a solution of trifluoroacetic acid (TFA) in D_2O (i.e., 0.4 mol % TFA in relation to the orthoester). The reactions were monitored by ^{1}H NMR spectroscopy to determine the kinetic rate k and the half-life $t_{1/2}$ of hydrolysis. Our results were in agreement with the earlier findings of von Delius et al.[26] More electron-deficient orthoesters (R = $-CH_2Cl$, $t_{1/2}$ = 111 h) were found to be more stable than orthoformates (R = H, $t_{1/2}$ = 10 h), which in turn were found to be more stable than electron-rich orthoacetates (R = Me, $t_{1/2}$ = 3 min) (Table 3).

Table 3. k and $t_{1/2}$ Values for Hydrolysis in *d*-THF with TFA in D_2O Observed by ^{1}H NMR at 298 K

polymer	substituent	k [s^{-1}]	$t_{1/2}$ [min]
poly(**1**)$_1$-*co*-COD_2	−Me	3.8×10^{-3}	3
poly(**2**)$_1$-*co*-COD_2	−H	1.9×10^{-5}	583
poly(**4**)$_1$-*co*-$COD_{2.5}$	$-CH_2Cl$	1.7×10^{-6}	6651

Polymer biodegradation studies in aerobic aqueous medium were performed according to the OECD 301F guideline for ready biodegradability using activated sludge from the local sewage treatment plant in Mainz, Germany, as the inoculum.[37] During this manometric respirometry test, the microorganism of the activated sludge converted the polymer to CO_2 under aerobic conditions. The CO_2 is trapped by KOH leading to a pressure decrease in the system. This pressure decrease can be measured and allows the calculation of the amount of biodegradation. For this test, we used an Oxitop setup and starch as the positive control. We tested three different copolymers: non-hydrogenated poly(**3**)$_1$-*co*-COD_2 and poly(**3**)$_1$-*co*-COD_9, the hydrogenated copolymers poly(**3**)$_1$-*co*-COD_2, poly(**3**)$_1$-*co*-COD_3 and poly(**3**)$_1$-*co*-COD_9 (Figure 6B). We followed literature procedures for biodegradation tests of hydrophobic compounds and doubled the amount of inoculum in comparison to the OECD guideline.[38] The surface of the polymers was increased prior to the test by emulsification (by ultrasound) of the oily non-hydrogenated polymers and by grinding of the solid hydrogenated polymer. The test was performed at a constant temperature of 20 °C. For the non-hydrogenated polymers, almost 25% of poly(**3**)$_1$-*co*-COD_2 was degraded after 10 days while no significant degradation of poly(**3**)$_1$-*co*-COD_9 was observed. Because of the aqueous media, we assume that first hydrolysis of the copolymers occurs followed by the mineralization of the hydrolysis products (alcohols and esters) to CO_2 and H_2O by the microorganism. For fatty acid esters, the biodegradation rates decrease with increasing chain length.[39,40] Because the hydrolysis products of poly(**3**)-*co*-COD are similar to them, this can explain the different biodegradability of poly(**3**)$_1$-*co*-COD_2 in comparison to poly(**3**)$_1$-*co*-COD_9. None of the hydrogenated polymers showed any biodegradability after 20 days. This can be explained by the increased hydrophobicity of the saturated polymers in comparison to the unsaturated polymers. However, the OECD 301F test aims to survey ready biodegradation (90% biodegradation within 30 days) and is optimized for water-soluble compounds. Thus, different long-term biodegradation tests for the long run have to be performed in the future to test the biodegradability of the synthesized orthoester copolymers. The fact that the ^{1}H NMR spectrum for the hydrogenated copolymers (e.g., poly(**3**)$_1$-*co*-COD_2, Figure S31) reveals hydrolysis after 6 months storage (at room temperature under air) suggests that further biodegradation is possible after this time.

3. EXPERIMENTAL SECTION

Materials. All commercially available reagents were purchased from Sigma-Aldrich, Alfa Aesar, Acros Organics, or TCI and were used without further purification unless otherwise stated. *cis*-2-Butene-1,4-diol was stored over dried 3 Å molecular sieves. Deuterated solvents were purchased from Sigma-Aldrich. All solvents were dried over molecular sieves for at least 24 h; chloroform-*d* was stored over anhydrous sodium carbonate, to quench residual acid, and activated 3 Å molecular sieves. Benzene-d_6 and toluene-d_8 were stored over activated 3 Å molecular sieves.

Instrumentation and Characterization Techniques. Size exclusion chromatography (SEC) measurements were performed in THF on an Agilent Technologies 1260 instrument consisting of an autosampler, a pump, and a column oven. The column set consists of three columns—SDV 10^6 Å, SDV 10^4 Å, and SDV 500 Å (PSS Standards Service GmbH, Mainz, Germany), all of 300 × 8 mm^2 and 10 μm average particle size—which were used at a flow rate of 1.0 mL/min and a column temperature of 30 °C. The injection volume was 100 μL. Detection was accomplished with an RI detector (Agilent Technologies). The data acquisition and evaluation were performed using PSS WINGPC UniChrom (PSS Polymer Standards Service GmbH, Mainz, Germany). Calibration was performed by using polystyrene provided by PSS Polymer Standards Service GmbH (Mainz, Germany). For nuclear magnetic resonance (NMR) analysis ^{1}H and ^{13}C NMR spectra of the monomers were recorded on a Bruker AVANCE III 300, 400, 500, or 700 MHz spectrometer. All spectra were measured in either $CDCl_3$, C_6D_6, toluene-d_8, or THF-d_8 at 298 K or in toluene-d_8 at 353 K. The spectra were calibrated against the solvent signal and analyzed using a MestReNova 12 from Mestrelab Research S.L. The thermal properties of the synthesized polymers have been measured by differential scanning calorimetry (DSC) on a Mettler Toledo DSC 823 calorimeter. Three scanning cycles of heating/cooling were performed in a nitrogen atmosphere (30 mL/min) with a heating and cooling rate of 10 °C/min. TGA was measured on a Mettler Toledo ThermoSTAR TGA/SDTA 851-Thermowaage in a nitrogen atmosphere. The heating rate was 10 °C/min in a range of temperature between 35 and 600–900 °C. Dynamic mechanical analysis (DMA) was performed using an Advanced Rheometric Expansion System (ARES) equipped with a force-rebalanced transducer. Plate/plate geometry was used with plate diameters of 6 mm. The gap between plates was around 1 mm. Experiments were performed under dry nitrogen atmosphere. The isochronal temperature dependencies of G' and G'' were determined for ω = 10 rad/s. For wide-angle X-ray scattering (WAXS) experiments were performed using a Philips PW1820 powder diffractometer with Cu radiation (wavelength 1.5418 Å). The crystal

DOI: 10.1021/acs.macromol.9b00180
Macromolecules 2019, 52, 2411−2420

morphology, thickness, and crystal structure were determined using an FEI Tecnai F20 transmission electron microscope operated at an acceleration voltage of 200 kV. Bright-field (BF) and energy-filtered transmission electron microscopy (EFTEM) techniques were used for measurements. As solution-grown crystals lie flat-on on the supporting carbon film, their thickness was measured by EFTEM. The thickness estimation obtained from EFTEM was determined by

$$\frac{I_0}{I_t} = \exp\left(-\frac{t}{\lambda}\right)$$

where I_t is the total intensity of the inelastic spectrum energy, I_0 is the zeroth loss intensity of elastic spectrum energy, λ is the mean free path, and t is the thickness of the specimen. The relative thickness of the specimen t/λ can be directly determined by thickness mapping from EFTEM. The value of the mean free path λ depends on the composition of the specimen and on the convergence and collection semiangles of the TEM. Actually, the mean free paths of the carbon support, poly(**3**)$_1$-*co*-COD$_2$, and poly(**3**)$_1$-*co*-COD$_5$ were determined to λ_C = 241 nm, $\lambda_{\text{poly(3)-co-COD}_2}$ = 291 nm, and $\lambda_{\text{poly(3)}_1\text{-co-COD}_5}$ = 294 nm, respectively. The information contained in a thickness map image is the relative thickness t/λ and contains the superposition of the crystal lamellae and the supporting carbon film underneath. Accordingly, it is necessary to deconvolve these two in terms of thickness. It is easy to measure the thickness t_C of the carbon support alone. From the measured relative thickness t/λ of support and crystal it is then straightforward to calculate the crystal thickness $t_{crystal}$. For hydrolysis tests, 11−13 mg of each copolymer was dissolved in 550 μL of *d*-THF, and 50 μL of a 8.7 × 10^{-3} M TFA in D_2O solution was added directly before the start of the measurements. The hydrolysis reaction was monitored by ^{1}H NMR spectroscopy using a Bruker AVANCE III 500 spectrometer over a period of 2 h to 5 days. Biodegradation tests were performed using a WTW OxiTop IS 6 device. All bottles were equipped with a stirring bar, a rubber tubular charged with two pellets of KOH (to bind CO_2) and a measuring head. Activated sludge from the local sewage treatment plant in Mainz, Germany, was used as the inoculum. The activated sludge was aerated for 2 days prior to the biodegradation tests to minimize the residual organic content inside. All mineral media were prepared according to OECD guideline 301.[37] The inoculum was added without filtration to give an overall solid content of the inoculum of ca. 60 mg mL^{-1}. Between 27 and 34 mg of the test substances were added to each bottle to achieve a theoretical oxygen demand of about 80 mg L^{-1}. The oily, non-hydrogenated polymers were dispersed in the mineral medium and further ultrasonificated for 5 min prior to the addition to the bottles. Solid, hydrogenated polymers were grinded to minimize the particle size. Biodegradation tests were performed, in duplicate, over 30 days at a constant temperature of 20 °C. Starch was used as a positive control, and two bottles contained solely the inoculum and the mineral media to determine the blank value.

Synthetic Procedures. *Synthesis of 2-Chloro-1,1,1-trimethoxyethane.* 2-Chloro-1,1,1-trimethoxyethane was prepared according to the procedure reported by Moos et al.[41]

General Experimental Procedure for the Synthesis of Cyclic Orthoester Monomers.[42] An oven-dried round-bottom flask equipped with a stirring bar was charged with orthoester (1.2 equiv) and *cis*-2-butene-1,4-diol (1 equiv). One drop of concentrated sulfuric acid was added to the reaction mixture under vigorous stirring. The reaction mixture was stirred at room temperature until all starting material was consumed (^{1}H NMR control) which took approximately 30−40 min. Anhydrous sodium carbonate (300 mg) was added to quench the acid. We noticed that too long reaction times can lead to the decomposition of the target compound. The reaction mixture was decanted and immediately distilled under reduced pressure (10^{-2} bar) with a short Vigreux column to yield the desired monomers as colorless liquids. If necessary to obtain high purities, distillation was repeated several times.

*2-Methoxy-2-methyl-4,7-dihydro-1,3-dioxepine (**1**).* Yield: 22%. ^{1}H NMR (400 MHz, $CDCl_3$): δ 5.65 (t, J = 1.7 Hz, 2H), 4.38−4.45 (m, 2H), 4.16−4.10 (m, 2H), 3.34 (s, 1H), 1.51 (s, 3H). ^{13}C NMR (101 MHz, $CDCl_3$): δ 128.79, 116.32, 61.39, 50.89, 18.26.

*2-Methoxy-4,7-dihydro-1,3-dioxepine (**2**).* Yield: 39%. ^{1}H NMR (400 MHz, $CDCl_3$): δ 5.71 (t, J = 1.7 Hz, 2H), 5.39 (s, 1H), 4.51−4.43 (m, 2H), 4.17−4.09 (m, 2H), 3.40 (s, 3 H). ^{13}C NMR (101 MHz, $CDCl_3$): δ 129.15, 113.71, 61.51, 53.52.

*2-Isopropoxy-4,7-dihydro-1,3-dioxepine (**3**).* Yield: 66%. ^{1}H NMR (400 MHz, $CDCl_3$): δ 5.68 (t, J = 1.8 Hz, 1H), 5.55 (s, 1H), 4.50−4.43 (m, 2H), 4.13−4.07 (m, 2H), 3.96 (hept, J = 8.3, 6.2 Hz, 1H), 1.21 (d, J = 6.3 Hz, 6H). ^{13}C NMR (101 MHz, $CDCl_3$): δ 129.20, 111.67, 68.45, 61.39, 22.57.

*2-(Chloromethyl)-2-methoxy-4,7-dihydro-1,3-dioxepine (**4**).* Yield: 75%. ^{1}H NMR (400 MHz, $CDCl_3$): δ 5.61 (t, J = 1.8 Hz, 2H), 4.46−4.39 (m, 2H), 4.19−4.12 (m, 2H), 3.66 (s, 2H), 3.34 (s, 3H). ^{13}C NMR (101 MHz, $CDCl_3$): δ 128.30, 114.21, 61.94, 50.93, 39.98.

Representative Procedure for the Ring-Opening Metathesis Polymerization. The first-generation Grubbs−Hoveyda catalyst (5 mg) was charged in a 2 mL screw-top vial equipped with a stirring bar and flushed with argon before the vial was closed with a lid containing a septum. The respective orthoester monomer **2** (144 mg, 1.1 mmol) and 1,5-cyclooctadiene (239 mg, 2.2 mmol) were degassed by bubbling argon through the solution prior to the addition to the initiator via a syringe. The initiator quickly dissolved in the monomer mixture. The polymerization was conducted at room temperature and vigorous stirring. An increase in viscosity indicated the ongoing polymerization process. After 17 h, 1 mL of dichloromethane was added to dissolve the polymer, then 100 μL of ethyl vinyl ether to quench the polymerization, and 100 μL of trimethylamine to prevent hydrolysis. The mixture was further diluted with dichloromethane before precipitating from methanol containing a few droplets of trimethylamine. After centrifugation, the product was isolated and dried under reduced pressure to yield a brown, honey-like polymer. The ROMP polymers were obtained in 40−83% yield.

*Poly(**1**)-co-COD.* ^{1}H NMR (300 MHz, benzene-d_6): δ 5.72 (m, −O−CH_2−C**H**=), 5.48 (m, −CH_2−C**H**= (COD)), 4.13 (m, −O−C**H**$_2$−CH=), 3.23 (s, −O−C**H**$_3$), 2.09 (m, −C**H**$_2$−CH= (COD)), 1.44 (s, −C−C**H**$_3$). ^{13}C NMR (75 MHz, benzene-d_6): δ 132.11, 129.73, 63.21, 49.71, 34.69−31.16 (m), 27.49, 20.19.

*Poly(**2**)-co-COD.* ^{1}H NMR (300 MHz, benzene-d_6): δ 5.65 (m, −O−CH_2−C**H**=), 5.57−5.35 (m, −CH_2−C**H**= (COD)), 5.27−5.17 (s, −C**H**), 4.20−4.00 (m, −O−C**H**$_2$−CH=), 3.23 (s, −O−C**H**$_3$), 2.09 (m, −C**H**$_2$−CH= (COD)). ^{13}C NMR (75 MHz, benzene-d_6): δ 133.09, 130.04, 64.89, 50.74, 33.77−31.37 (m), 27.45.

*Poly(**3**)-co-COD.* ^{1}H NMR (300 MHz, benzene-d_6): δ 5.76−5.59 (m, −O−CH_2−C**H**=), 5.58−5.40 (m, −CH_2−C**H**= (COD)), 5.40−5.30 (s, −C**H**), 4.17 (m, −O−C**H**$_2$−CH=), 4.00 (m, −O−C**H**−(CH_3)$_2$), 2.10 (m, −C**H**$_2$−CH= (COD)), 1.16 (m, −O−CH−(C**H**$_3$)$_2$). ^{13}C NMR (75 MHz, benzene-d_6): δ 130.36, 127.26, 67.18, 58.36, 38.40, 25.30, 23.76.

*Poly(**4**)-co-COD.* ^{1}H NMR (300 MHz, benzene-d_6): δ 5.65 (m, −O−CH_2−C**H**=), 5.58−5.34 (m, −CH_2−C**H**= (COD)), 4.20−3.96 (m, −O−C**H**$_2$−CH=), 3.50 (s, −C**H**$_2$−Cl), 3.18 (s, −O−C**H**$_3$), 2.09 (m, −C**H**$_2$−CH= (COD)). ^{13}C NMR (75 MHz, benzene-d_6): δ 133.11, 130.45, 63.89, 50.24, 43.51, 33.25, 27.32.

Representative Procedure for Hydrogenation. The polymer (300 mg) was dissolved in 10 mL of dry toluene in a glass vessel, and the solution was degassed by bubbling argon through the solution for 15 min. 50 mg of 10 wt % Pd/$CaCO_3$ was added, and the glass vessel was charged into a 250 mL ROTH autoclave. Hydrogenation was performed at 70 °C and 70 bar of H_2. After completion of the reaction, hot toluene was added, and the hot reaction mixture was filtered and directly precipitated from cold methanol (containing NEt_3 to prevent hydrolysis). After centrifugation, the product was isolated and dried at reduced pressure to yield the polymer as an off-white powder. Yields were between 60% to quantitative yield.

*Poly(**1**)-co-COD, Hydrogenated.* ^{1}H NMR (500 MHz, toluene-d_8): δ 3.55 (m, −O−C**H**$_2$−CH_2−), 3.20 (s, −O−C**H**$_3$), 1.61 (m, −O−CH_2−C**H**$_2$−), 1.33 (b, alkyl backbone).

DOI: 10.1021/acs.macromol.9b00180
Macromolecules 2019, 52, 2411−2420

Poly(2)-co-COD, Hydrogenated. ^{1}H NMR (700 MHz, toluene-d_8): δ 5.05 (s, −C<u>H</u>), 3.36 (m, −O−C<u>H</u>$_2$−CH$_2$−), 3.21 (s, −O−C<u>H</u>$_3$), 1.59 (m, −O−CH$_2$−C<u>H</u>$_2$−), 1.52−1.09 (b, alkyl backbone).

Poly(3)-co-COD, Hydrogenated. ^{1}H NMR (500 MHz, toluene-d_8): δ 5.21 (s, −C<u>H</u>), 3.97 (m, −O−C<u>H</u>−(CH$_3$)$_2$), 3.75−3.46 (m, −O−C<u>H</u>$_2$−CH$_2$−), 1.76−1.52 (m, −O−CH$_2$−C<u>H</u>$_2$−), 1.34 (b, alkyl backbone), 1.18 (d, −O−CH−(C<u>H</u>$_3$)$_2$).

Poly(4)-co-COD, Hydrogenated. ^{1}H NMR (500 MHz, toluene-d_8): δ 3.73−3.55 (m, −O−C<u>H</u>$_2$−CH$_2$−), 3.53 (s, −C<u>H</u>$_2$−Cl), 3.24 (s, −O−C<u>H</u>$_3$), 1.68−1.52 (m, −O−CH$_2$−C<u>H</u>$_2$−), 1.36 (b, alkyl backbone).

4. SUMMARY

In this work, we report the synthesis of polyorthoesters by ring-opening metathesis polymerization (ROMP). Four different orthoester monomers were copolymerized with 1,5-cyclooctadiene (COD) in different ratios to yield unsaturated polymers with molecular weights up to 38000 g mol^{-1}. Postpolymerization hydrogenation gave hard, solid materials with thermal properties similar to polyethylene. The number of orthoester units in the polymer chain influenced thermal properties such as melting point or onset temperature of decomposition. Because of the brittle nature of the material, future work will focus on increasing the molecular weight of the long-chain polyorthoesters to better mimic the mechanical properties of polyethylene. Nevertheless, the biodegradability of the unsaturated orthoester copolymers represents a potential advantage when compared to polyethylene. All copolymers, hydrogenated and non-hydrogenated, hydrolyze slowly when exposed to atmospheric moisture. The hydrolysis rate in solution was found to be dependent on the orthoester substituent. In conclusion, long-chain polyorthoester copolymers are promising materials with the potential of replacing polyethylene for applications where a degradation over time is advantageous.

■ ASSOCIATED CONTENT

Supporting Information

The Supporting Information is available free of charge on the ACS Publications website at DOI: 10.1021/acs.macromol.9b00180.

Analytical and spectral characterization data as well as evaluation of biodegradation test (PDF)

■ AUTHOR INFORMATION

Corresponding Author

*E-mail wurm@mpip-mainz.mpg.de, Ph 0049 6131 379581, Fax 0049 6131 370 330 (F.R.W.).

ORCID

Ingo Lieberwirth: 0000-0003-1323-524X

Max von Delius: 0000-0003-1852-2969

Frederik R. Wurm: 0000-0002-6955-8489

Notes

The authors declare no competing financial interest.

■ ACKNOWLEDGMENTS

The authors thank the German Federal Ministry for Education and Research (BMBF) for their support of the program "Research for sustainable development (FONA)", "PlastX − Plastics as a systemic risk for social-ecological supply systems" (grant 01UU1603A). O.Sh. and M.v.D. thank the University of Ulm and the German Research Foundation (DFG, Emmy-Noether grant DE 1830/2-1) for financial support. O.Sh. is grateful for a doctoral scholarship by the German Academic Exchange Service (DAAD). We thank Michael Steiert (MPIP) for XRD measurements.

■ REFERENCES

(1) Bioplastics market data 2017; https://www.european-bioplastics.org/market/ (accessed 21.06.2018).

(2) Malpass, D. B. *Introduction to Industrial Polyethylene: Properties, Catalysts, and Processes*; Wiley: 2010.

(3) Haider, T. P.; Völker, C.; Kramm, J.; Landfester, K.; Wurm, F. R. Plastics of the Future? The Impact of Biodegradable Polymers on the Environment and on Society. *Angew. Chem., Int. Ed.* **2019**, *58* (1), 50−62.

(4) Stempfle, F.; Ortmann, P.; Mecking, S. Long-Chain Aliphatic Polymers To Bridge the Gap between Semicrystalline Polyolefins and Traditional Polycondensates. *Chem. Rev.* **2016**, *116* (7), 4597−4641.

(5) Trzaskowski, J.; Quinzler, D.; Bährle, C.; Mecking, S. Aliphatic Long-Chain C20 Polyesters from Olefin Metathesis. *Macromol. Rapid Commun.* **2011**, *32* (17), 1352−1356.

(6) Ortmann, P.; Lemke, T. A.; Mecking, S. Long-Spaced Polyamides: Elucidating the Gap between Polyethylene Crystallinity and Hydrogen Bonding. *Macromolecules* **2015**, *48* (5), 1463−1472.

(7) Ortmann, P.; Wimmer, F. P.; Mecking, S. Long-Spaced Polyketones from ADMET Copolymerizations as Ideal Models for Ethylene/CO Copolymers. *ACS Macro Lett.* **2015**, *4* (7), 704−707.

(8) Steinbach, T.; Alexandrino, E. M.; Wahlen, C.; Landfester, K.; Wurm, F. R. Poly(phosphonate)s via Olefin Metathesis: Adjusting Hydrophobicity and Morphology. *Macromolecules* **2014**, *47* (15), 4884−4893.

(9) Zheng, Y.-R.; Tee, H. T.; Wei, Y.; Wu, X.-L.; Mezger, M.; Yan, S.; Landfester, K.; Wagener, K.; Wurm, F. R.; Lieberwirth, I. Morphology and Thermal Properties of Precision Polymers: The Crystallization of Butyl Branched Polyethylene and Polyphosphoesters. *Macromolecules* **2016**, *49* (4), 1321−1330.

(10) Ortmann, P.; Heckler, I.; Mecking, S. Physical properties and hydrolytic degradability of polyethylene-like polyacetals and polycarbonates. *Green Chem.* **2014**, *16* (4), 1816−1827.

(11) Cordes, E. H. Mechanism and Catalysis for the Hydrolysis of Acetals, Ketals, and Ortho Esters. *Prog. Phys. Org. Chem.* **2007**, *4*, 1−44.

(12) Binauld, S.; Stenzel, M. H. Acid-degradable polymers for drug delivery: a decade of innovation. *Chem. Commun.* **2013**, *49* (21), 2082−2102.

(13) Heller, J. Synthesis of Biodegradable Polymers for Biomedical Utilization. *ACS Symp. Ser.* **1983**, *212*, 373−392.

(14) Heller, J. In *Poly(ortho esters)*; Springer: Berlin, 1993; pp 41−92.

(15) Heller, J.; Barr, J. Poly(ortho esters)From Concept to Reality. *Biomacromolecules* **2004**, *5* (5), 1625−1632.

(16) Ng, S. Y.; Shen, H. R.; Lopez, E.; Zherebin, Y.; Barr, J.; Schacht, E.; Heller, J. Development of a poly(ortho ester) prototype with a latent acid in the polymer backbone for 5-fluorouracil delivery. *J. Controlled Release* **2000**, *65* (3), 367−374.

(17) Wolfe, P. S.; Wagener, K. B. An ADMET route to unsaturated polyacetals. *Macromol. Rapid Commun.* **1998**, *19* (6), 305−308.

(18) Khaja, S. D.; Lee, S.; Murthy, N. Acid-Degradable Protein Delivery Vehicles Based on Metathesis Chemistry. *Biomacromolecules* **2007**, *8* (5), 1391−1395.

(19) Fraser, C.; Hillmyer, M. A.; Gutierrez, E.; Grubbs, R. H. Degradable Cyclooctadiene/Acetal Copolymers: Versatile Precursors to 1,4-Hydroxytelechelic Polybutadiene and Hydroxytelechelic Polyethylene. *Macromolecules* **1995**, *28* (21), 7256−7261.

(20) Chikkali, S.; Stempfle, F.; Mecking, S. Long-Chain Polyacetals From Plant Oils. *Macromol. Rapid Commun.* **2012**, *33* (13), 1126−1129.

DOI: 10.1021/acs.macromol.9b00180
Macromolecules 2019, 52, 2411−2420

(21) Heller, J.; Barr, J.; Ng, S. Y.; Abdellauoi, K. S.; Gurny, R. Poly(ortho esters): synthesis, characterization, properties and uses. *Adv. Drug Delivery Rev.* **2002**, *54* (7), 1015−1039.
(22) Tschan, M. J.-L.; Ieong, N. S.; Todd, R.; Everson, J.; Dove, A. P. Unlocking the Potential of Poly(Ortho Ester)s: A General Catalytic Approach to the Synthesis of Surface-Erodible Materials. *Angew. Chem., Int. Ed.* **2017**, *56* (52), 16664−16668.
(23) Shyshov, O.; Brachvogel, R.-C.; Bachmann, T.; Srikantharajah, R.; Segets, D.; Hampel, F.; Puchta, R.; von Delius, M. Adaptive Behavior of Dynamic Orthoester Cryptands. *Angew. Chem., Int. Ed.* **2017**, *56* (3), 776−781.
(24) Brachvogel, R.-C.; Hampel, F.; von Delius, M. Self-assembly of dynamic orthoester cryptates. *Nat. Commun.* **2015**, *6*, 7129.
(25) Brachvogel, R.-C.; von Delius, M. Orthoester exchange: a tripodal tool for dynamic covalent and systems chemistry. *Chem. Sci.* **2015**, *6* (2), 1399−1403.
(26) Low, H.; Mena-Osteritz, E.; von Delius, M. Self-assembled orthoester cryptands: orthoester scope, post-functionalization, kinetic locking and tunable degradation kinetics. *Chem. Sci.* **2018**, *9*, 4785.
(27) Hilf, S.; Berger-Nicoletti, E.; Grubbs, R. H.; Kilbinger, A. F. M. Monofunctional Metathesis Polymers via Sacrificial Diblock Copolymers. *Angew. Chem., Int. Ed.* **2006**, *45* (47), 8045−8048.
(28) Steinbach, T.; Alexandrino, E. M.; Wurm, F. R. Unsaturated poly(phosphoester)s via ring-opening metathesis polymerization. *Polym. Chem.* **2013**, *4* (13), 3800−3806.
(29) Sutthasupa, S.; Shiotsuki, M.; Sanda, F. Recent advances in ring-opening metathesis polymerization, and application to synthesis of functional materials. *Polym. J.* **2010**, *42*, 905.
(30) Hejl, A.; Scherman, O. A.; Grubbs, R. H. Ring-Opening Metathesis Polymerization of Functionalized Low-Strain Monomers with Ruthenium-Based Catalysts. *Macromolecules* **2005**, *38* (17), 7214−7218.
(31) Jung, M. E.; Piizzi, G. gem-Disubstituent Effect: Theoretical Basis and Synthetic Applications. *Chem. Rev.* **2005**, *105* (5), 1735−1766.
(32) Neary, W. J.; Kennemur, J. G. A Precision Ethylene-Styrene Copolymer with High Styrene Content from Ring-Opening Metathesis Polymerization of 4-Phenylcyclopentene. *Macromol. Rapid Commun.* **2016**, *37* (12), 975−979.
(33) Wagener, K. B.; Boncella, J. M.; Nel, J. G. Acyclic diene metathesis (ADMET) polymerization. *Macromolecules* **1991**, *24* (10), 2649−2657.
(34) Nelson, D. J.; Manzini, S.; Urbina-Blanco, C. A.; Nolan, S. P. Key processes in ruthenium-catalysed olefin metathesis. *Chem. Commun.* **2014**, *50* (72), 10355−10375.
(35) Liu, C.; Liu, F.; Cai, J.; Xie, W.; Long, T. E.; Turner, S. R.; Lyons, A.; Gross, R. A. Polymers from Fatty Acids: Poly(ω-hydroxyl tetradecanoic acid) Synthesis and Physico-Mechanical Studies. *Biomacromolecules* **2011**, *12* (9), 3291−3298.
(36) Busch, H.; Schiebel, E.; Sickinger, A.; Mecking, S. Ultralong-Chain-Spaced Crystalline Poly(H-phosphonate)s and Poly(phenylphosphonate)s. *Macromolecules* **2017**, *50* (20), 7901−7910.
(37) OECD Test No. 301: Ready Biodegradability, 1992.
(38) de Morsier, A.; Blok, J.; Gerike, P.; Reynolds, L.; Wellens, H.; Bontinck, W. J. Biodegradation tests for poorly-soluble compounds. *Chemosphere* **1987**, *16* (4), 833−847.
(39) Kleeberg, I.; Welzel, K.; VandenHeuvel, J.; Müller, R. J.; Deckwer, W. D. Characterization of a New Extracellular Hydrolase from Thermobifida fusca Degrading Aliphatic−Aromatic Copolyesters. *Biomacromolecules* **2005**, *6* (1), 262−270.
(40) Gerike, P. The biodegradability testing of poorly water soluble compounds. *Chemosphere* **1984**, *13* (1), 169−190.
(41) Moos, W. H.; Gless, R. D.; Rapoport, H. Codeine analogs. Synthesis of spiro[benzofuran-3(2H)4′-piperidines] and octahydro-1H-benzofuro[3,2-e]isoquinolines. *J. Org. Chem.* **1981**, *46* (25), 5064−5074.
(42) Pawlowski, C. Substituted 1,3-dioxepins. US3966768A, June 29, 1976.

DOI: 10.1021/acs.macromol.9b00180
Macromolecules 2019, 52, 2411−2420

Supporting Information for

Long-chain polyorthoesters as degradable polyethylene-mimics

Tobias Haider[1], Oleksandr Shyshov[2], Oksana Suraeva[1], Ingo Lieberwirth[1], Max von Delius[2], Frederik R. Wurm[1*]

[1]Max Planck Institute for Polymer Research, Ackermannweg 10, 55128 Mainz, Germany, wurm@mpip-mainz.mpg.de

[2]University of Ulm, Institute of Organic Chemistry and Advanced Materials, Albert-Einstein-Allee 11, 89081 Ulm, Germany

Tables

Table S1. Synthetic results for ring-opening metathesis (co)polymerizations of monomers **1** and **2** using different initiators, monomer to initiator ratios and solvent or in bulk conditions.

Monomer	Initiator	solvent	Feed ratio ([COD]:[ortho ester]:[Ru])	Incorporation (COD:ortho ester)[a]	M_n[b] / g mol^{-1}]	M_w[b] / g mol^{-1}]	M_n/M_w[b]	yield / %
1	Grubbs 1	THF	0:500:1		-	-	-	no reaction
1	Grubbs 3	in bulk	0:200:1		-	-	-	no reaction
1	Grubbs 1	THF	800:200:1	35:1	3,200	8,700	2.35	20
1	Grubbs 3	THF	800:200:1	150:1	21,900	39,000	1.78	48
2	Grubbs 3	THF	1000:1		-	-	-	no reaction

2	Grubbs 3	THF	800:200:1	30:1	15,800	33,000	2.10	66
2	Grubbs 1	in bulk	800:200:1	15:1	17,200	39,500	2.30	93
2	Grubbs 2	in bulk	800:200:1	18:1	25,400	47,400	1.87	75
2	Hoveyda 1	in bulk	800:200:1	13:1	18,800	37,300	1.99	86
2	Hoveyda 2	in bulk	800:200:1	30:1	27,600	55,100	1.99	85
2	Hoveyda 1	in bulk	80:20:1	8:1	6,700	16,800	2.49	87
2	Hoveyda 1	in bulk	200:200:1	2.5:1	6,800	23,700	3.47	n.d.

[a]Determined by ^{1}H NMR. [b]Determined by SEC with PS standard.

^{1}H, ^{13}C NMR spectra

Monomer NMR spectra

2-Methoxy-2-methyl-4,7-dihydro-1,3-dioxepine (1)

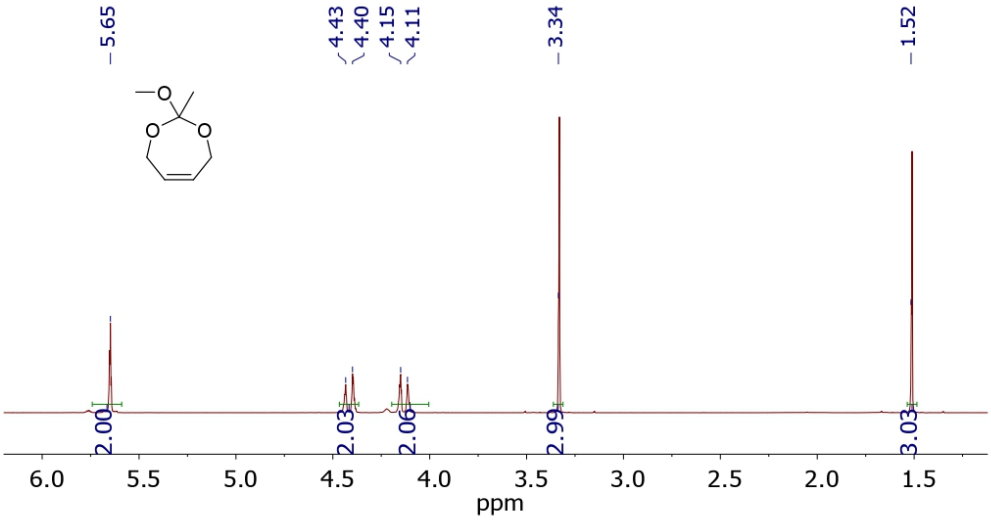

Figure S1: ^{1}H NMR spectra of monomer **1** in $CDCl_3$ at 400 MHz at 298 K.

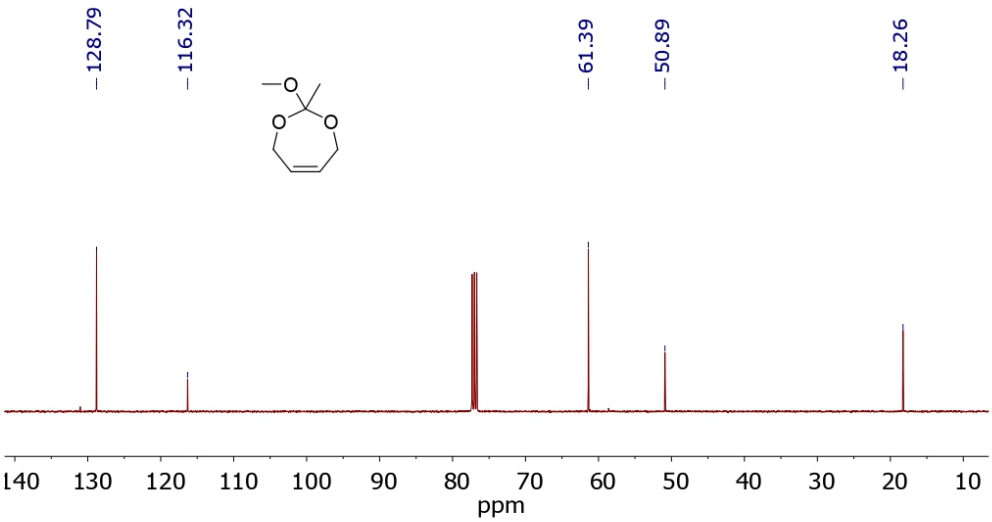

Figure S2: ^{13}C NMR spectra of monomer **1** in $CDCl_3$ at 101 MHz at 298 K.

2-Methoxy-4,7-dihydro-1,3-dioxepine (2)

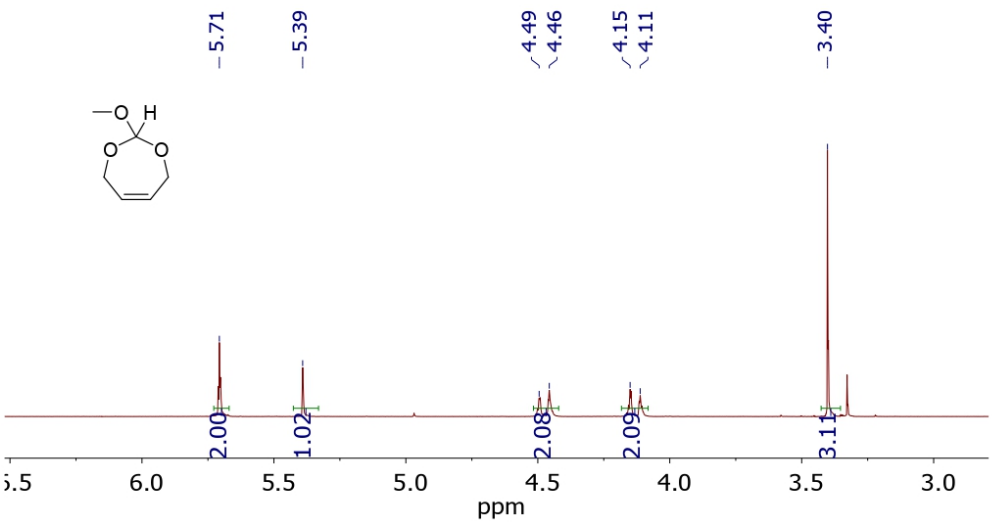

Figure S3: ^{1}H NMR spectra of monomer **2** in $CDCl_3$ at 400 MHz at 298 K.

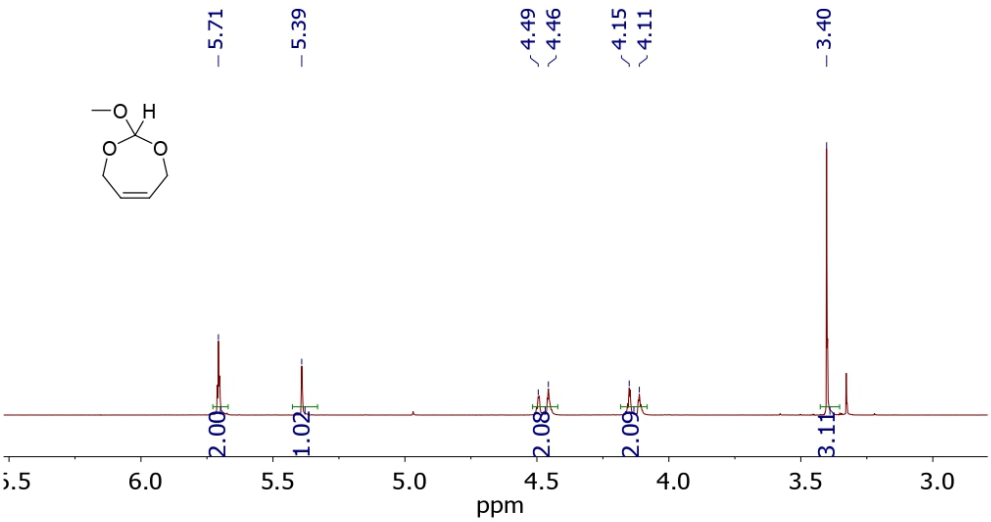

Figure S4: ^{13}C NMR spectra of monomer **2** in $CDCl_3$ at 101 MHz at 298 K.

2-Isopropoxy-4,7-dihydro-1,3-dioxepine (3)

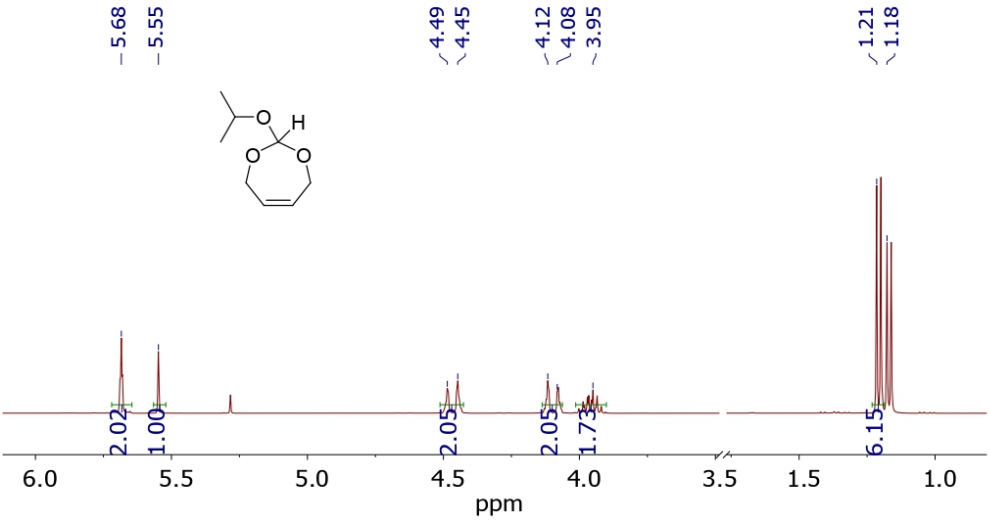

Figure S5: ^{1}H NMR spectra of monomer **3** in $CDCl_3$ at 400 MHz at 298 K.

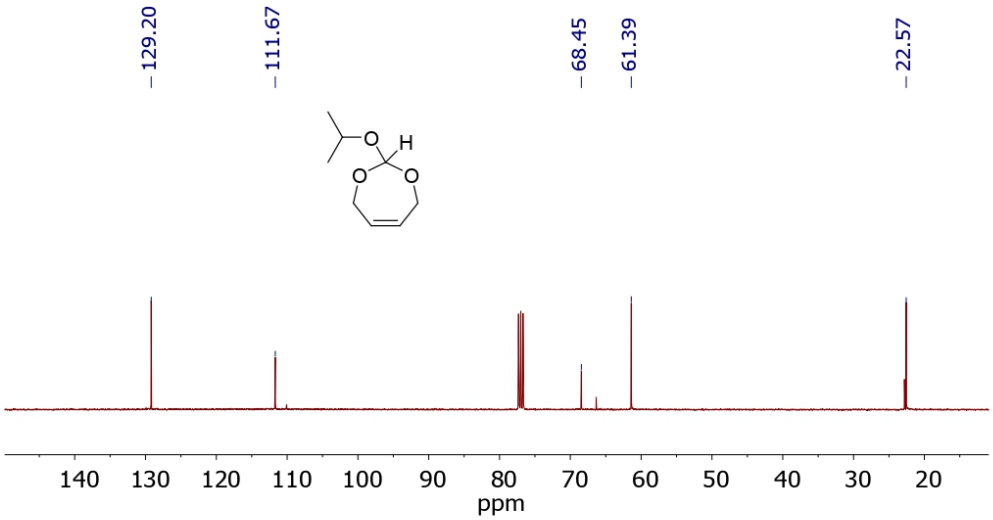

Figure S6: ^{13}C NMR spectra of monomer **3** in $CDCl_3$ at 101 MHz at 298 K.

2-(Chloromethyl)-2-methoxy-4,7-dihydro-1,3-dioxepine (4)

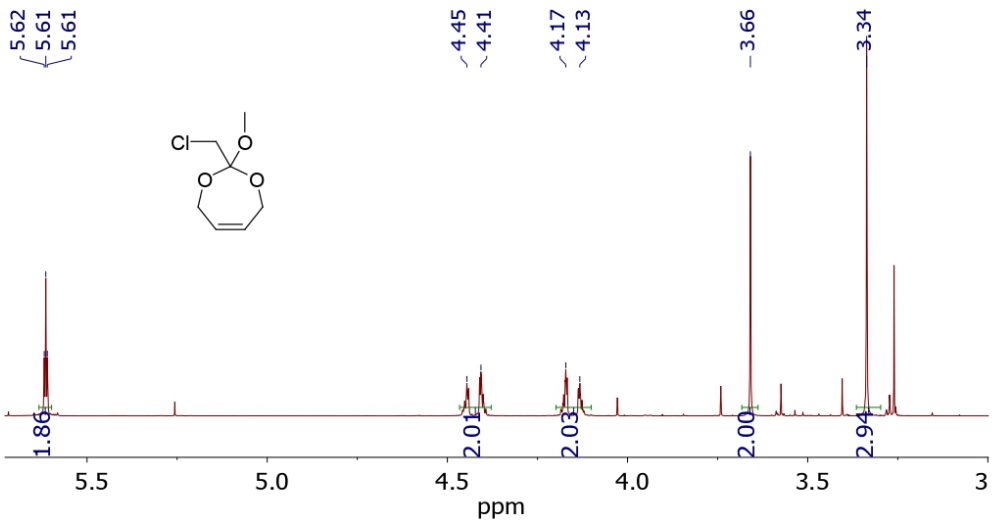

Figure S7: ^{1}H NMR spectra of monomer **4** in $CDCl_3$ at 400 MHz at 298 K.

5

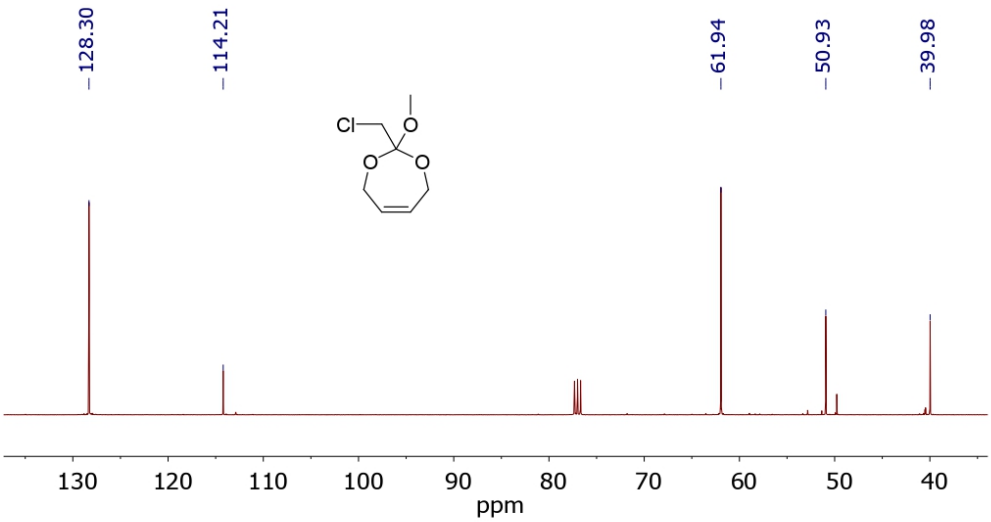

Figure S8: ^{13}C NMR spectra of monomer **4** in $CDCl_3$ at 101 MHz at 298 K.

Polymer NMR spectra – non-hydrogenated polymers

Poly(**1**)-*co*-COD

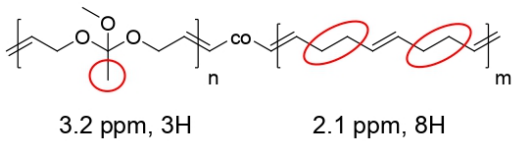

Scheme S1: Determination of orthoester/COD ratio for poly(**1**)-*co*-COD by ^{1}H NMR.

6

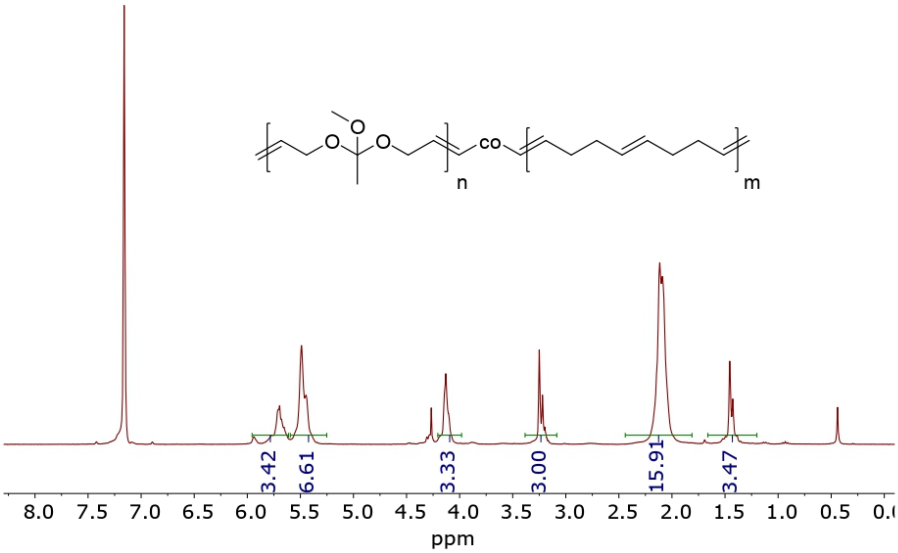

Figure S9: ^{1}H NMR spectra of poly(**1**)$_1$-*co*-COD$_2$ in C_6D_6 at 300 MHz at 298 K.

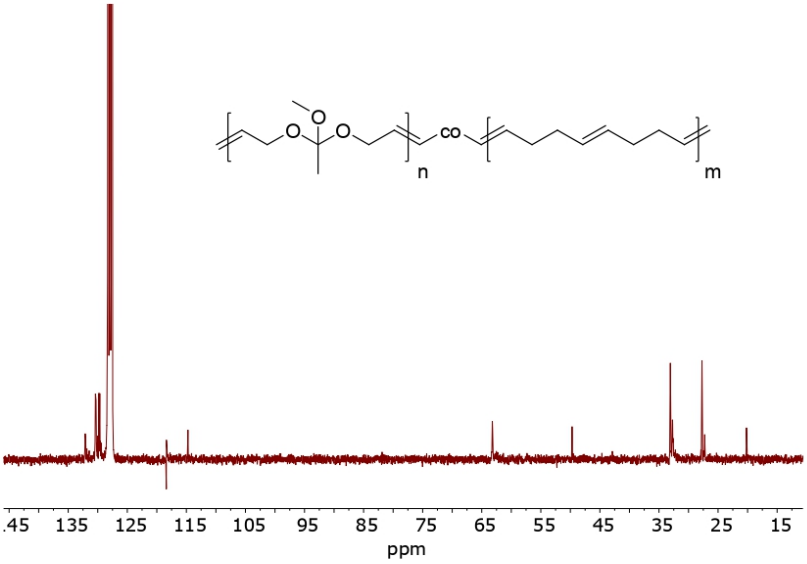

Figure S10: ^{13}C NMR spectra of poly(**1**)$_1$-co-COD$_2$ in C_6D_6 at 75 MHz at 298 K.

7

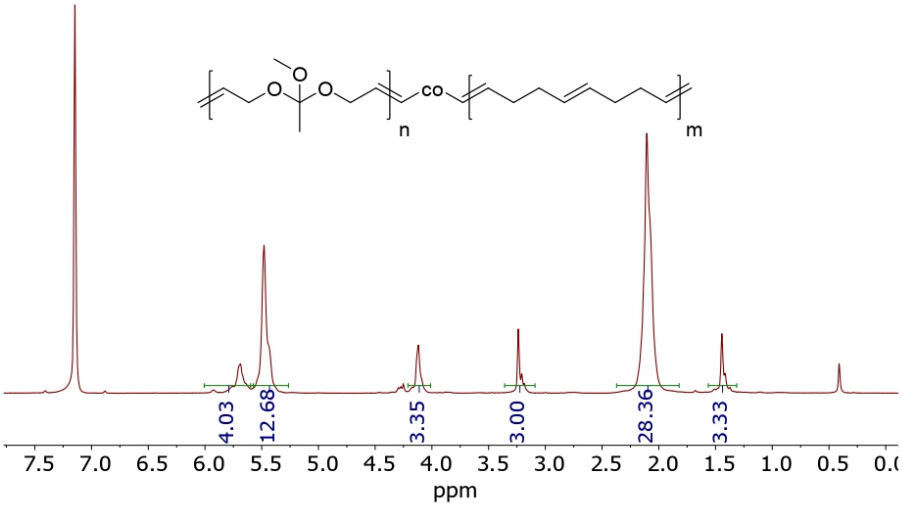

Figure S11: ^{1}H NMR spectra of poly(**1**)$_{1}$-*co*-COD$_{3.5}$ in C_6D_6 at 300 MHz at 298 K.

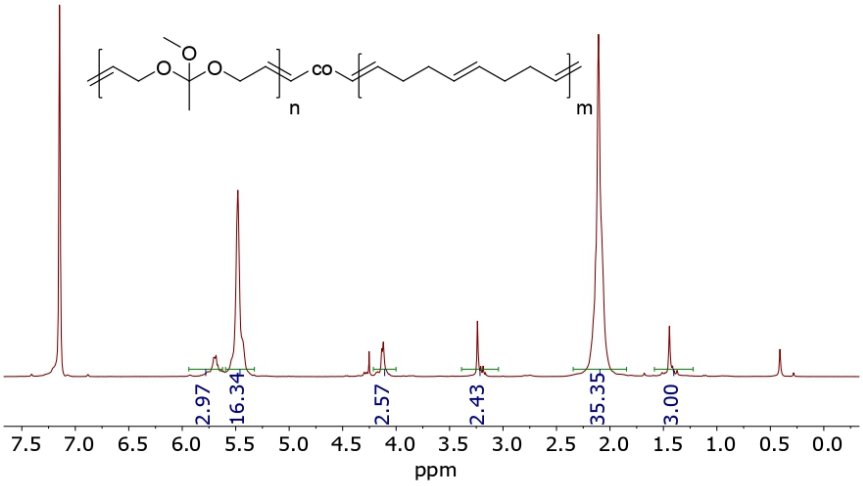

Figure S12: ^{1}H NMR spectra of poly(**1**)$_{1}$-*co*-COD$_{6.5}$ in C_6D_6 at 300 MHz at 298 K.

8

Poly(**2**)-*co*-COD

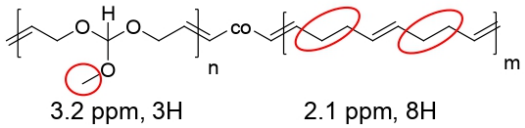

Scheme S2: Determination of orthoester/COD ratio for poly(**2**)-*co*-COD by ^{1}H NMR.

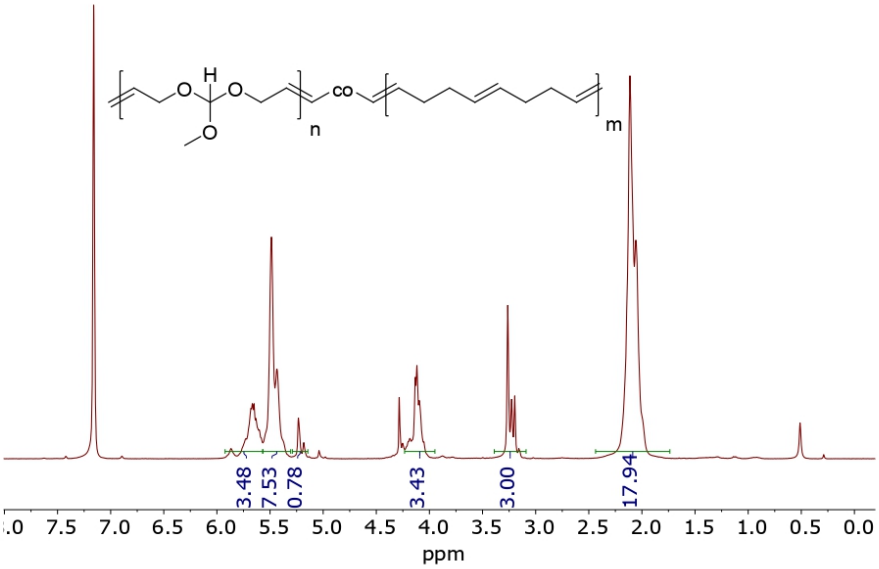

Figure S13: ^{1}H NMR spectra of poly(**2**)$_1$-*co*-COD$_2$ in C_6D_6 at 300 MHz at 298 K.

9

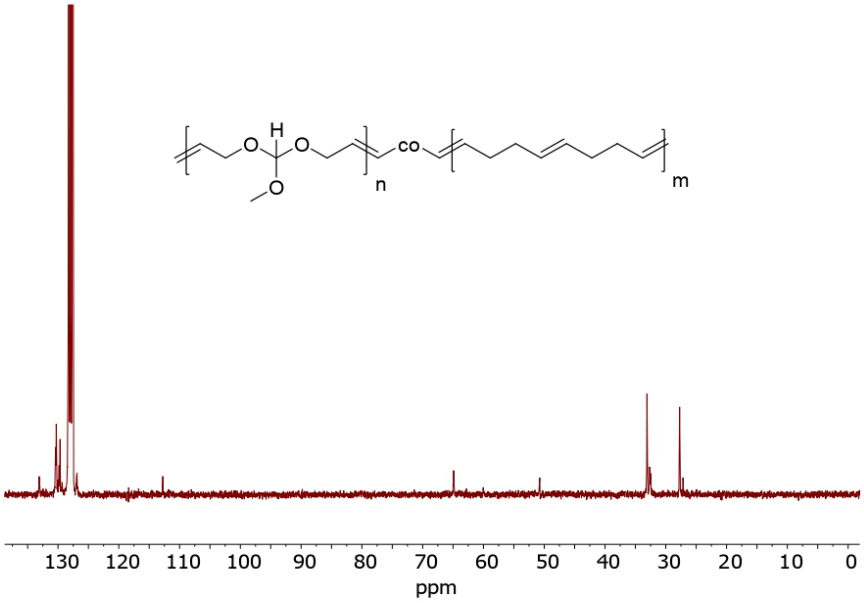

Figure S14: ^{13}C NMR spectra of poly(**2**)$_1$-co-COD$_2$ in C_6D_6 at 75 MHz at 298 K.

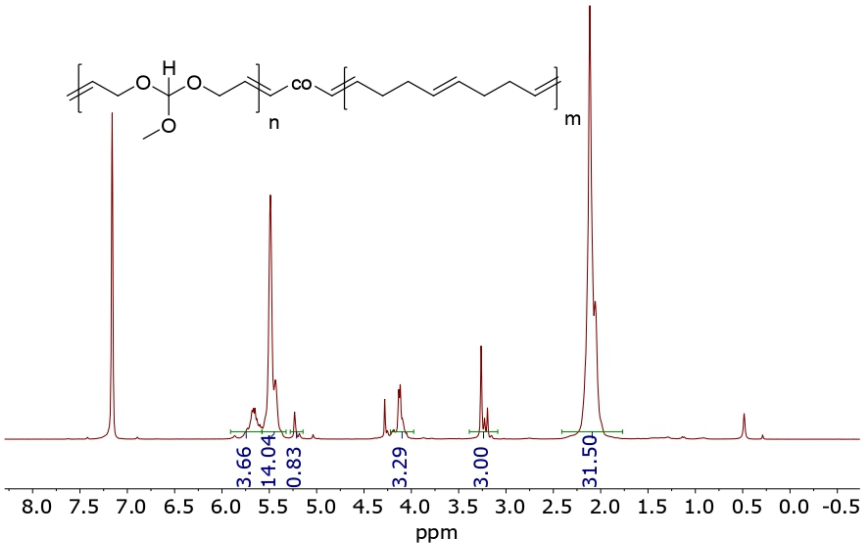

Figure S14: ^{1}H NMR spectra of poly(**2**)$_1$-*co*-COD$_4$ in C_6D_6 at 300 MHz at 298 K.

10

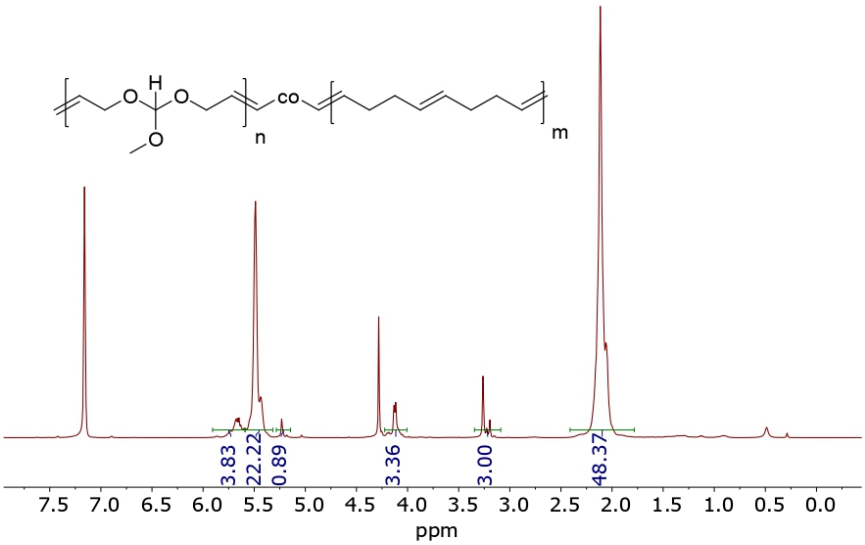

Figure S15: ^{1}H NMR spectra of poly(**2**)$_1$-co-COD$_6$ in C_6D_6 at 300 MHz at 298 K.

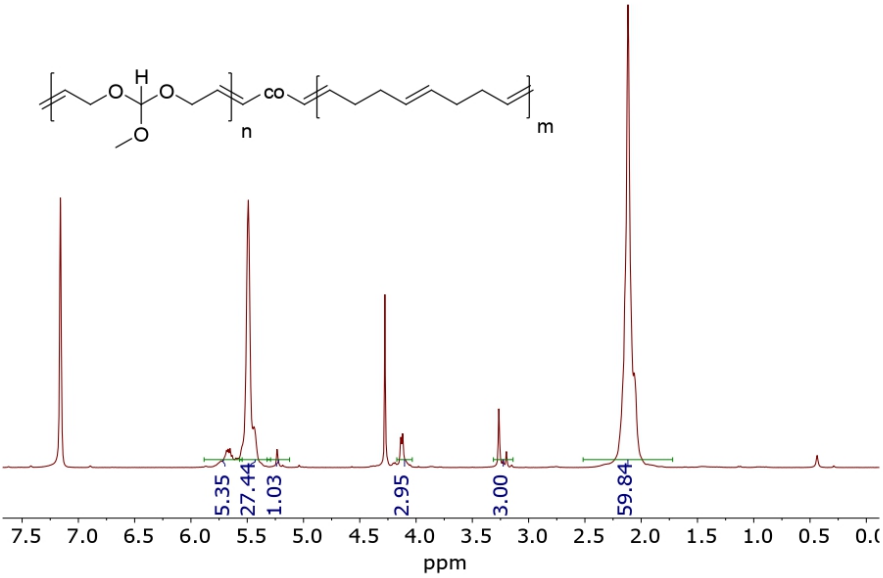

Figure S16: ^{1}H NMR spectra of poly(**2**)$_1$-co-COD$_9$ in C_6D_6 at 300 MHz at 298 K.

11

Poly(**3**)-*co*-COD

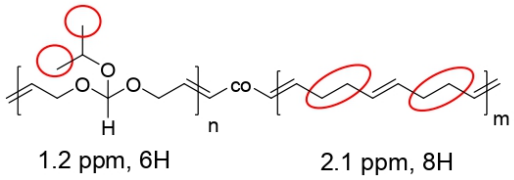

Scheme S3: Determination of orthoester/COD ratio for poly(**3**)-*co*-COD by ^{1}H NMR.

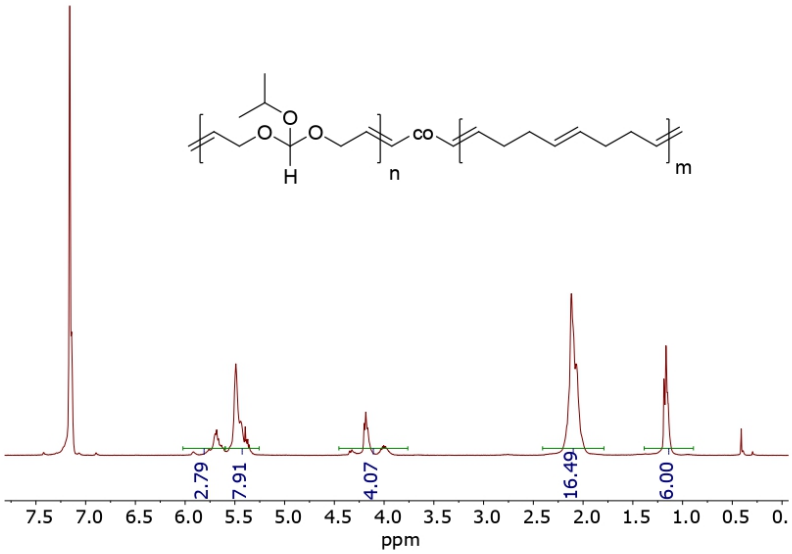

Figure S17: ^{1}H NMR spectra of poly(**3**)$_1$-*co*-COD$_2$ in C_6D_6 at 300 MHz at 298 K.

12

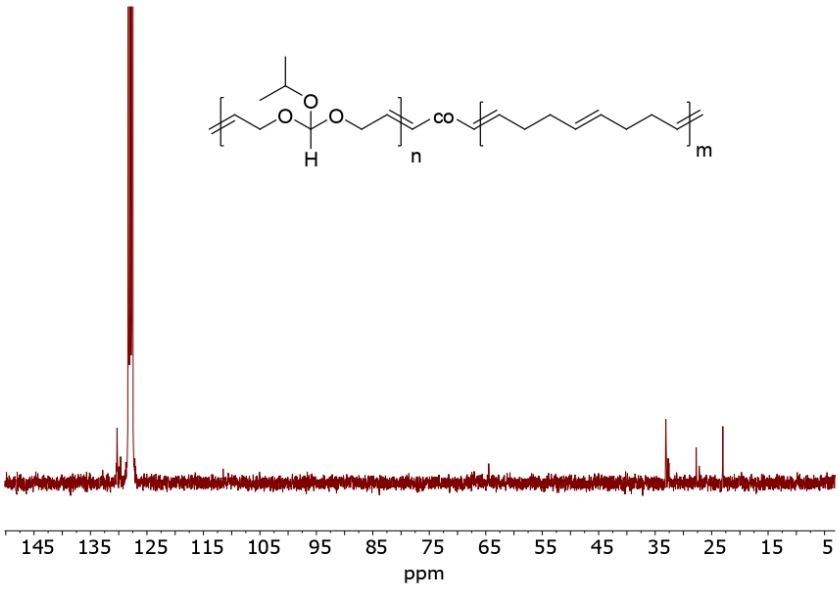

Figure S18: ^{13}C NMR spectra of poly(**3**)$_1$-co-COD_2 in C_6D_6 at 75 MHz at 298 K.

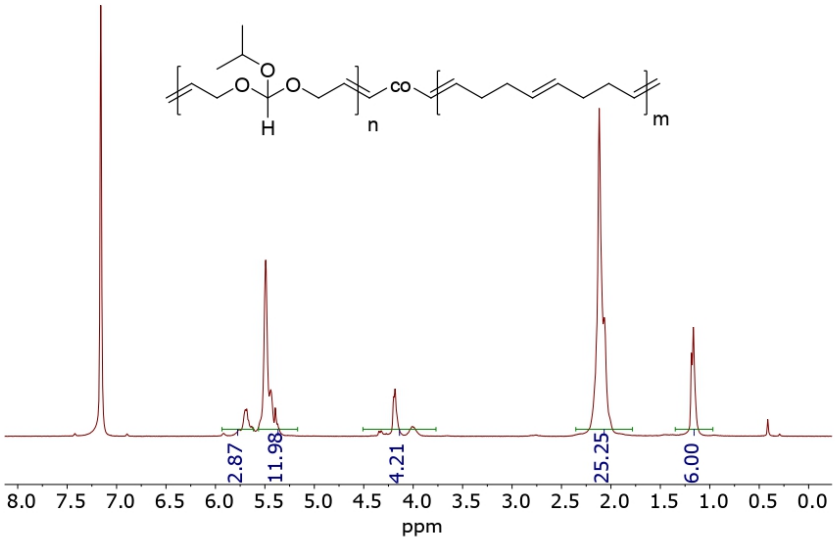

Figure S19: ^{1}H NMR spectra of poly(**3**)$_1$-*co*-COD_3 in C_6D_6 at 300 MHz at 298 K.

13

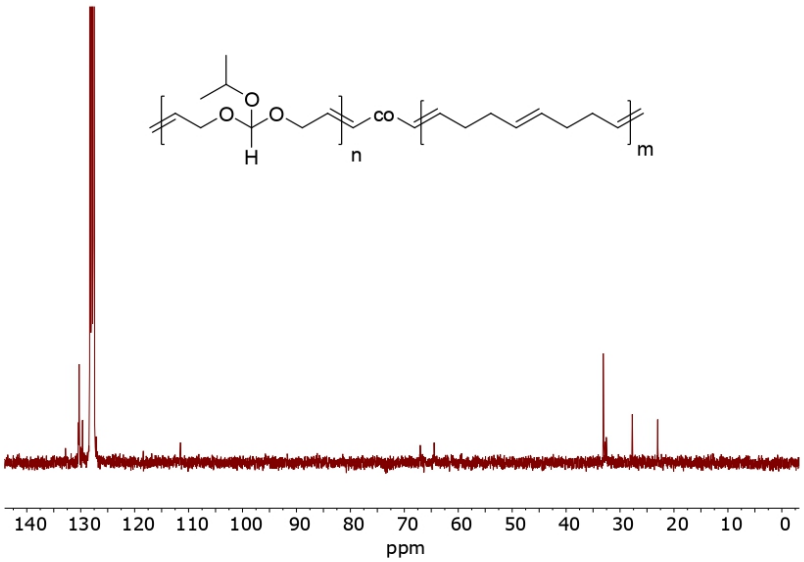

Figure S20: ^{13}C NMR spectra of poly(**3**)$_1$-co-COD$_3$ in C_6D_6 at 75 MHz at 298 K.

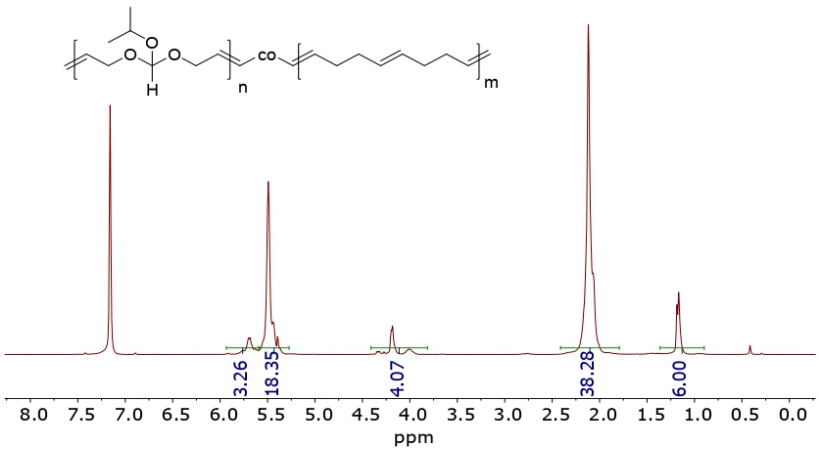

Figure S21: ^{1}H NMR spectra of poly(**3**)$_1$-*co*-COD$_5$ in C_6D_6 at 300 MHz at 298 K.

14

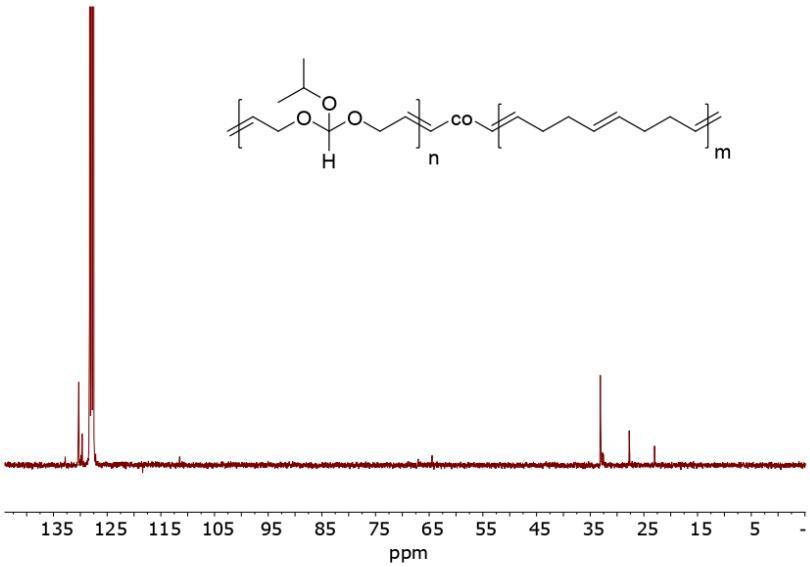

Figure S22: ^{13}C NMR spectra of poly(**3**)$_1$-co-COD$_5$ in C_6D_6 at 75 MHz at 298 K.

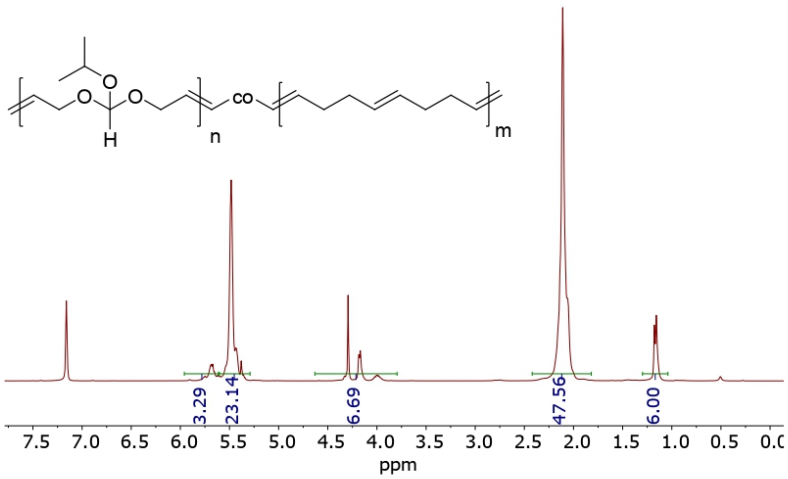

Figure S23: ^{1}H NMR spectra of poly(**3**)$_1$-*co*-COD$_9$ in C_6D_6 at 300 MHz at 298 K.

15

Poly(**4**)-*co*-COD

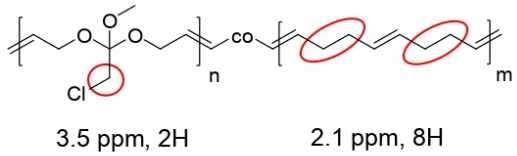

Scheme S4: Determination of orthoester/COD ratio for poly(**4**)-*co*-COD by ^{1}H NMR.

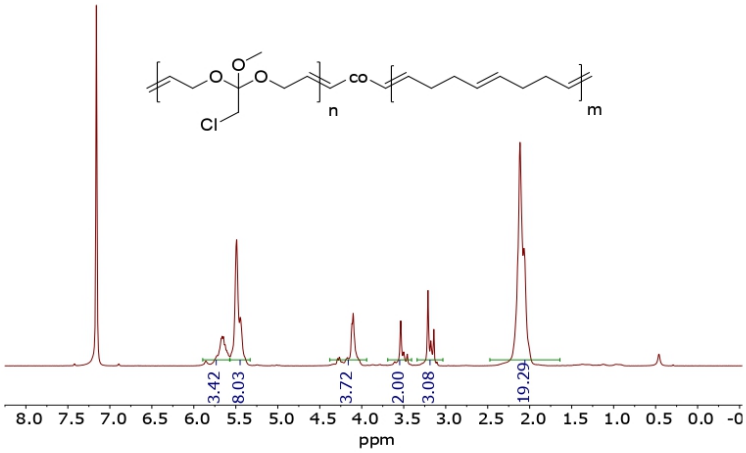

Figure S24: ^{1}H NMR spectra of poly(**4**)$_{1}$-*co*-COD$_{2.5}$ in C_6D_6 at 300 MHz at 298 K.

16

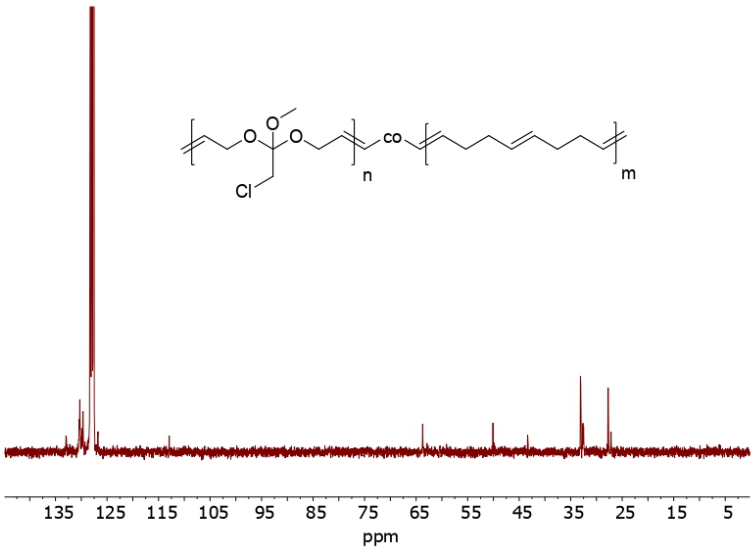

Figure S25: ^{13}C NMR spectra of poly(**4**)$_1$-co-COD$_{2.5}$ in C_6D_6 at 75 MHz at 298 K.

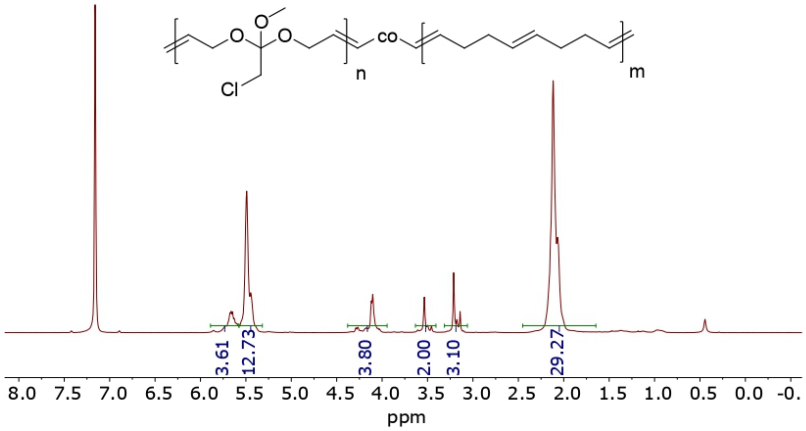

Figure S26: ^{1}H NMR spectra of poly(**4**)$_1$-*co*-COD$_{3.5}$ in C_6D_6 at 300 MHz at 298 K.

17

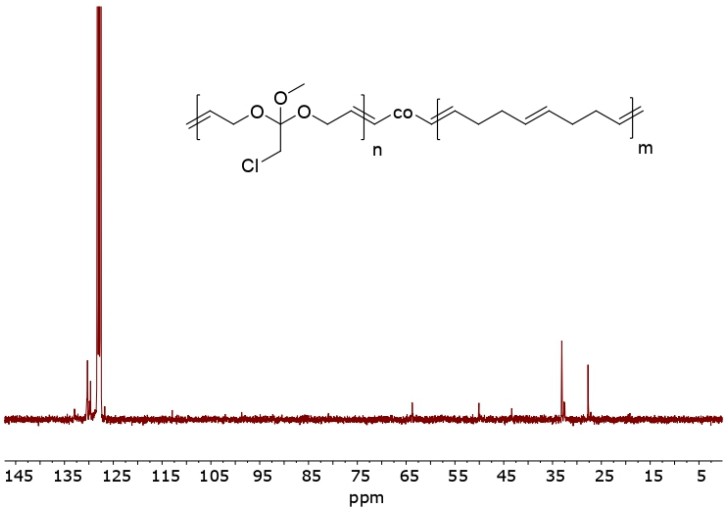

Figure S27: ^{13}C NMR spectra of poly(**4**)$_1$-co-COD$_{3.5}$ in C_6D_6 at 75 MHz at 298 K.

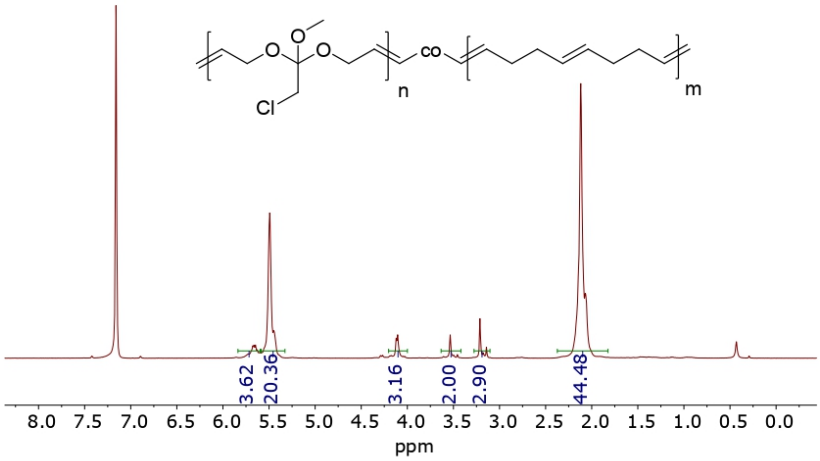

Figure S28: ^{1}H NMR spectra of poly(**4**)$_1$-*co*-COD$_7$ in C_6D_6 at 300 MHz at 298 K.

18

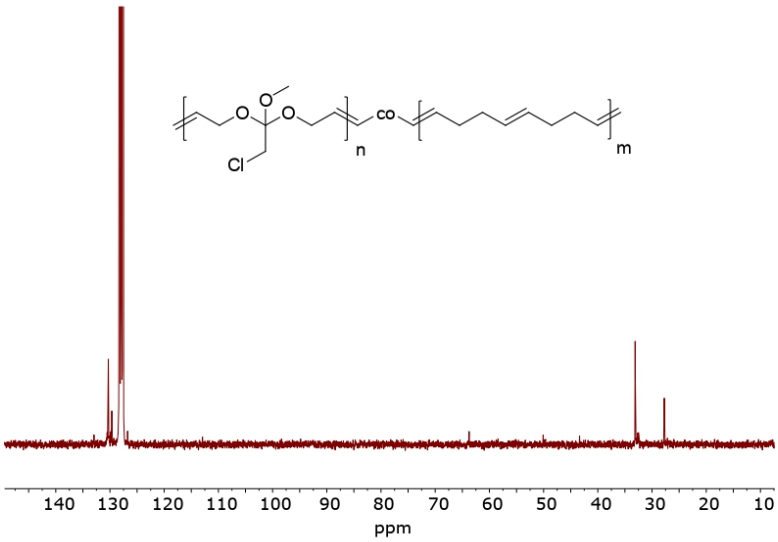

Figure S29: ^{13}C NMR spectra of poly(**4**)$_1$-co-COD$_7$ in C_6D_6 at 75 MHz at 298 K.

Polymer NMR spectra –hydrogenated polymers

Poly(**1**)-*co*-COD

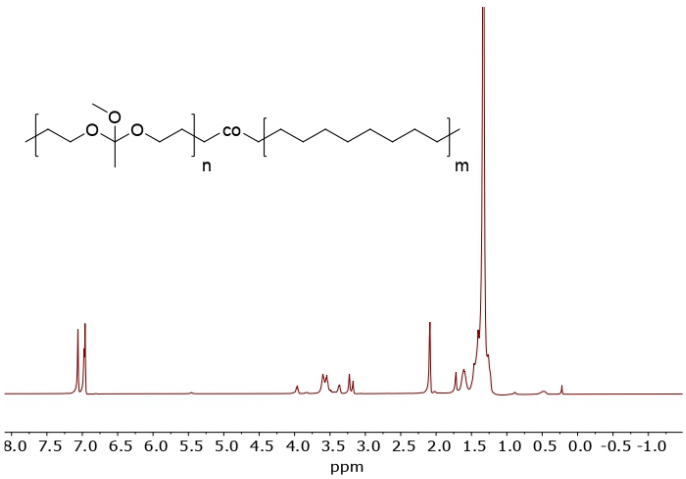

Figure S30: ^{1}H NMR spectra of poly(**1**)$_1$-*co*-COD$_2$ in toluene-d_8 at 500 MHz at 353 K.

19

Poly(**2**)-*co*-COD

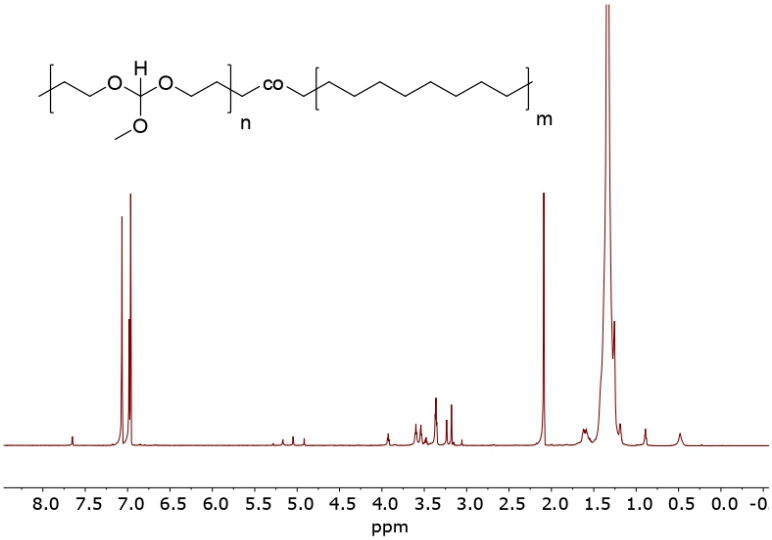

Figure S30: ^{1}H NMR spectra of poly(**2**)$_{1}$-*co*-COD$_{9}$ in toluene-d_8 at 500 MHz at 353 K.

20

Poly(**3**)-*co*-COD

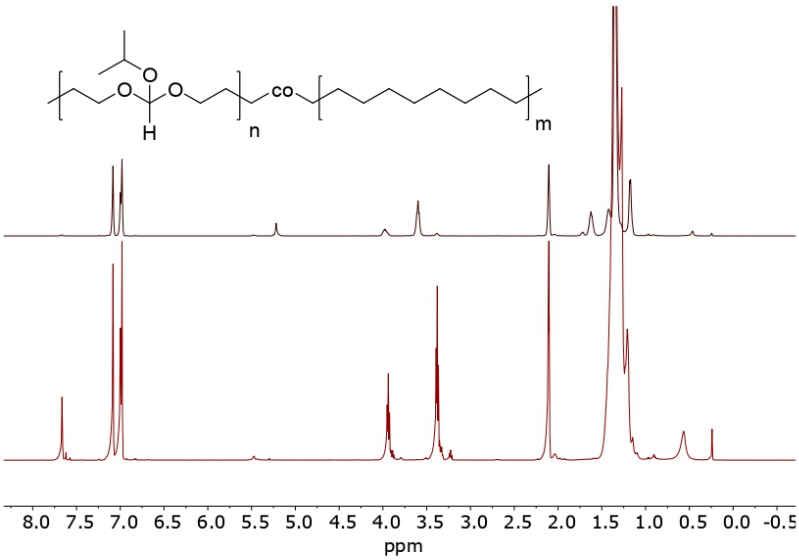

Figure S31: ^{1}H NMR spectra of poly(**3**)$_1$-*co*-COD$_2$ in toluene-d_8 at 500 MHz at 353 K before (top) and after storage upon air at room temperature for 6 months (bottom).

Poly(**4**)-*co*-COD

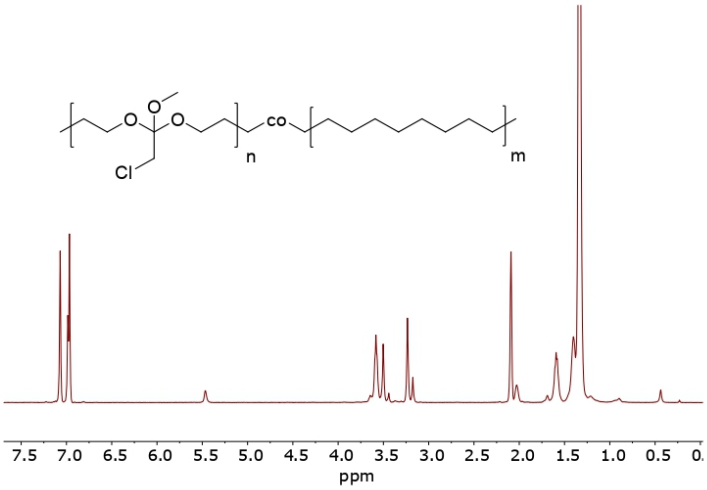

Figure S32: ^{1}H NMR spectra of poly(**4**)$_1$-*co*-COD$_{3.5}$ in toluene-d_8 at 500 MHz at 353 K.

21

Size exclusion chromatography (SEC)

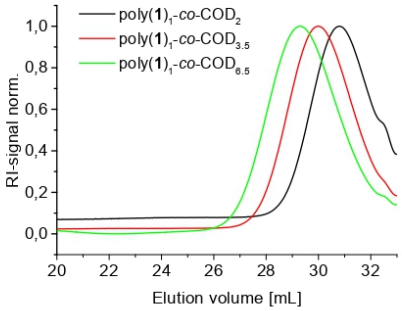

Figure S33: SEC elugrams of poly(**1**)-*co*-COD prepared by ROMP.

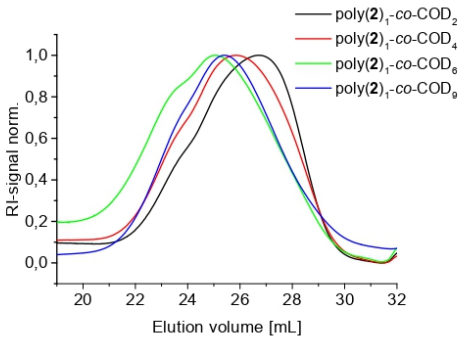

Figure S34: SEC elugrams of poly(**2**)-*co*-COD prepared by ROMP.

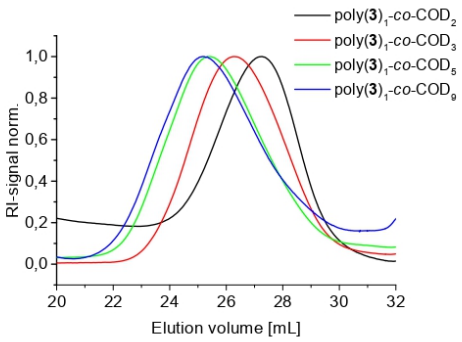

Figure S35: SEC elugrams of poly(**3**)-*co*-COD prepared by ROMP.

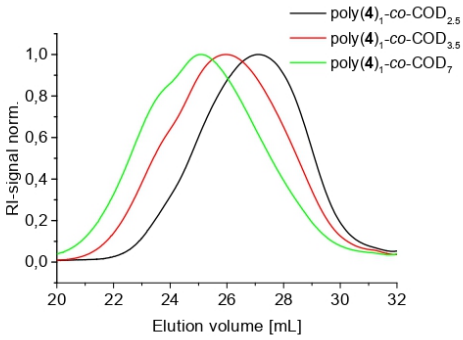

Figure S35: SEC elugrams of poly(**4**)-*co*-COD prepared by ROMP.

Thermal gravimetric analysis (TGA), Differential Scanning Calorimetry (DSC)

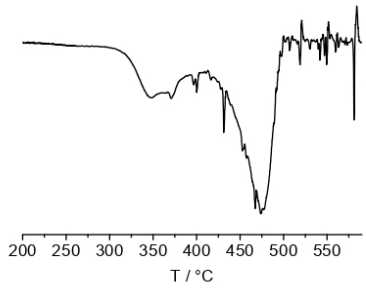

Figure S36: First derivative of TGA thermogram of hydrogenated poly(**3**)$_1$-*co*-COD$_3$.

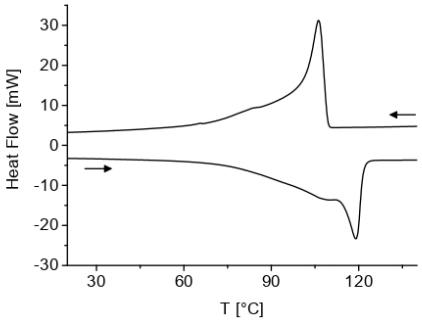

Figure S37: DSC thermogram of hydrogenated poly(**2**)$_1$-*co*-COD$_9$.

24

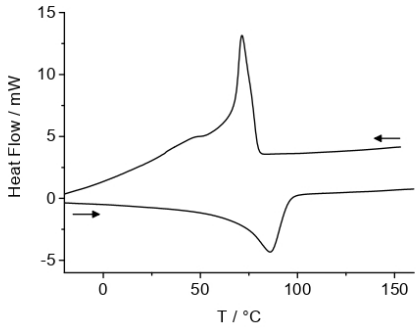

Figure S38: DSC thermogram of hydrogenated poly(**3**)$_1$-*co*-COD$_2$.

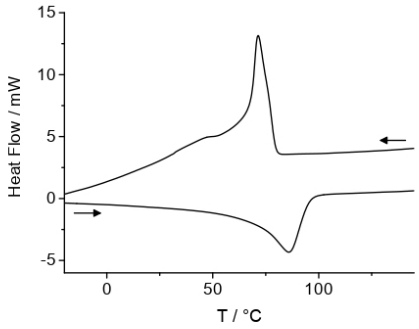

Figure S39: DSC thermogram of hydrogenated poly(**3**)$_1$-*co*-COD$_3$.

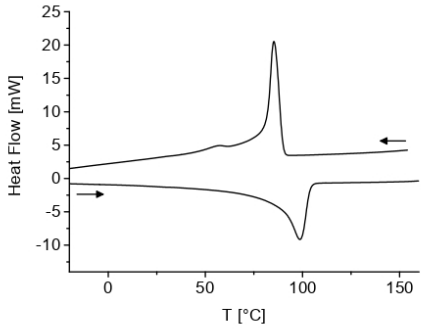

Figure S39: DSC thermogram of hydrogenated poly(**3**)$_1$-*co*-COD$_5$.

25

Transition Electron Microscopy (TEM), Electron Diffraction

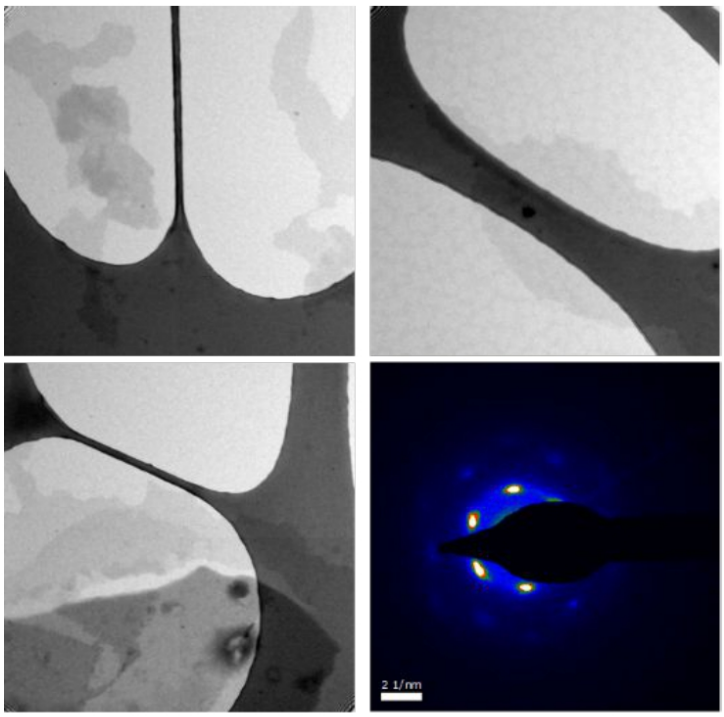

Figure S40: TEM bright-field micrograph and corresponding diffraction pattern of hydrogenated poly(**3**)$_1$-*co*-COD$_2$.

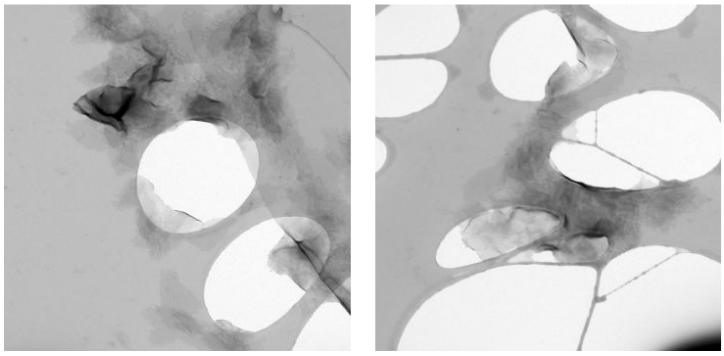

Figure S41: TEM bright-field micrograph and corresponding diffraction pattern of hydrogenated poly(**3**)$_1$-*co*-COD$_5$.

Biodegradation Test

The sample preparation is described in the experimental part.

For the manometric respirometry biodegradation test, we used a WTW OxiTop® IS 6 device, which gives automatically the biological oxygen demand (BOD) of the measured samples. To get the value for BOD for each polymer sample, the blank value was subtracted. All values were determined in duplicate. To calculate the amount of biodegradation, at first the molecular weight (MW) of one theoretical repeating unit for each copolymer was determined. With this value, the theoretical oxygen demand (ThOD) for a compound $C_cH_hCl_{cl}N_nNa_{na}O_oP_pS_s$ was calculated according to following equation:

$$ThOD = \frac{16\left[2c + \frac{1}{2}(h - cl - 3n) + 3s + \frac{5}{2}p + \frac{1}{2}na - o\right] mg/mg}{MW}$$

The amount of biodegradation was given by:

$$\%\ degradation = \frac{BOD}{ThOD\ \times\ mg\ test\ substance\ added} \times 100$$

4.4 Evidence for Anion-Binding of all-*cis* Hexafluorocyclohexane in Solution and Solid State

Shyshov, O., Siewert, K. A., von Delius, M., *Chem. Commun*. **2018**, 54, 4353-4355.

https://doi.org/10.1039/C8CC01797B

Reprinted with permission from the Royal Society of Chemistry.

Abstract:

We report a solution NMR and X-ray crystallographic study on the anion affinity of all-*cis* 1,2,3,4,5,6-hexafluorocyclohexane, which has only recently become synthetically accessible. Our results suggest that the interaction exhibits preferential 1 : 1 stoichiometry, while its strength is only moderate (*e.g.* K_a = 400 M^{-1} in acetone for Cl^-) and depends mainly on the size of the anion and the dielectric constant of the solvent.

Comments on own contributions:

I had the original idea. I performed the synthesis of all compounds, all titration experiments, X-ray crystallographic studies, wrote supporting information, and the first draft of the manuscript. Kevin Siewerth helped to optimize the synthesis of the catalyst and to establish the hydrogenation procedure.

ChemComm

COMMUNICATION

View Article Online
View Journal | View Issue

Check for updates

Cite this: *Chem. Commun.*, 2018, **54**, 4353

Received 5th March 2018,
Accepted 5th April 2018

DOI: 10.1039/c8cc01797b

rsc.li/chemcomm

Published on 05 April 2018. Downloaded by Universitat Ulm on 5/21/2020 5:09:19 PM.

Evidence for anion-binding of all-*cis* hexafluorocyclohexane in solution and solid state†

Oleksandr Shyshov, Kevin Andre Siewerth and Max von Delius *

We report a solution NMR and X-ray crystallographic study on the anion affinity of all-*cis* 1,2,3,4,5,6-hexafluorocyclohexane, which has only recently become synthetically accessible. Our results suggest that the interaction exhibits preferential 1 : 1 stoichiometry, while its strength is only moderate (*e.g.* K_a = 400 M^{-1} in acetone for Cl^-) and depends mainly on the size of the anion and the dielectric constant of the solvent.

Receptors for inorganic anions such as chloride, fluoride, sulfate or nitrate have recently received considerable attention,[1] because their vast potential for applications in sensing,[2] catalysis[3] and medicinal chemistry[4] has been recognized. For instance, compounds that promote the transport of chloride across the cell membrane are potential therapeutics for diseases such as cystic fibrosis[5] and cancer.[6] Selective nitrate sensors could help minimize fertilizer use in agriculture[7] and next-generation battery technology requires electrolytes that stabilize both cations and anions.[8] Well-known motifs for anion binding include (thio)ureas,[9] triazoles,[10] pyrroles,[11] and fluoroarenes[12] (Fig. 1a), which typically only give rise to strong anion binding as part of multidentate tripodal or macrocyclic architectures.

We wondered whether the unusual compound all-*cis* 1,2,3,4,5,6-hexafluorocyclohexane (**1**; Fig. 1b) with its rigid array of three highly polarized axial hydrogen atoms could be a useful addition to the known repertoire of anion-binding motifs. The first synthesis of **1** (12 linear steps) was described in 2015 by Keddie *et al.*, and a remarkable dipole moment of μ = 6.2 D was determined, which makes **1** the most polar aliphatic compound ever reported.[13] In the past two years, several theoretical and gas-phase studies were reported on the physicochemical properties of **1**,[14] yet studies in solution or the solid state remained elusive, presumably due to the labour-intensive synthesis. A robust one-step synthesis of **1** and simple monosubstituted derivatives was reported last year by Wiesenfeldt *et al.*[15] thus providing an opportunity to investigate the supramolecular properties of this compound class. Herein we report that the association of **1** and its methoxy derivative **2** with simple anions such as chloride is mainly based on electrostatics, is moderate in strength and occurs with preferential 1 : 1 stoichiometry. Moreover, we disclose a solid state structure, in which all-*cis* 1,2,3,4,5,6-hexafluorocyclohexane interacts with a $(Cl^-)_2(H_2O)_2$ cluster.

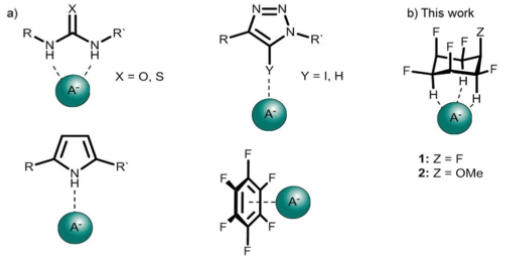

Fig. 1 Schematic illustration of commonly used anion-binding motifs (a) and all-*cis* $C_6F_5ZH_6$ as a new anion-binding motif (b).

Our first objective was to probe the anion binding affinity of **1** in solution by ^{19}F NMR titrations. Due to the large dipole moment of all-*cis* $C_6H_6F_6$, a question we wanted to answer qualitatively is whether the strength of the hydrogen bonds between **1** and the anion (Fig. 1b) correlates with relevant solvent parameters.[16] Therefore, we performed titrations in three different solvents that differ significantly in dielectric constant (ε), H bond donating (α scale) and accepting (β scale) ability: acetone (ε = 20.7; α = 0.08; β = 0.48), acetonitrile (ε = 36.6; α = 0.19; β = 0.31), and dimethyl sulfoxide (ε = 47.2; α = 0.00; β = 0.76).[17] Titrations were carried out in triplicate with all halide ions, in order to investigate the influence of size and polarizability, with nitrate (NO_3^-) as a representative example of an oxoanion and with hexafluorophosphate (PF_6^-) as an anion traditionally considered "weakly coordinating".[18] Dilution experiments

Institute of Organic Chemistry and Advanced Materials, University of Ulm, Albert-Einstein-Allee 11, Ulm 89081, Germany. E-mail: max.vondelius@uni-ulm.de

† Electronic supplementary information (ESI) available: General experimental procedures, binding isotherms and crystallographic data. CCDC 1826208. For ESI and crystallographic data in CIF or other electronic format see DOI: 10.1039/c8cc01797b

Published on 05 April 2018. Downloaded by Universitat Ulm on 5/21/2020 5:09:19 PM.

Table 1 Association constants[a] for the interaction of **1** with simple anions

Anion[b]	Acetone-d_6 K_a (1 : 1 fit)	CD_3CN K_a (1 : 1 fit)	DMSO-d_6 K_a (1 : 1 fit)
F^-	600 ± 400 M^{-1}[c]	HF elimination[c]	
Cl^-	400 ± 40 M^{-1}	19 ± 8 M^{-1}	—[e]
Br^-	150 ± 40 M^{-1}	13 ± 5 M^{-1}	—[e]
I^-	38 ± 7 M^{-1}[d,f]	<10 M^{-1}	—[e]
NO_3^-	37 ± 7 M^{-1}[f]	<10 M^{-1}	—[e]
PF_6^-	—[e]	—[e]	—[e]

[a] Determined by ^{19}F NMR titration and fitting of the isotherms on supramolecular.org.[19] Estimates of uncertainty reflect 95% confidence intervals (triplicate titrations). [b] As tetrabutylammonium (TBA) salt.§ [c] The high basicity of anhydrous TBAF causes an HF elimination reaction that, depending on the solvent, either precludes K_a determination or leads to high uncertainty. [d] Acetone-d_6/DCM-d_2 mixture (88/12 w/w) had to be used as solvent due to the low solubility of this particular salt. [e] Differences in chemical shift were too small to determine K_a. [f] Quadruplicate titrations.

ascertained that **1** does not aggregate at the concentrations chosen for the titrations (2 mM, 5 mM and in some cases 10 mM; see the ESI†). The resulting binding isotherms were fitted according to 1 : 1 and 2 : 1 models on the website supramolecular.org,[19] where in the spirit of "open science"[20] our original data is available for download.‡ The quality of the data was evaluated based on the three-fold repetition of titrations (95% confidence interval) and the goodness of individual fits (statistical error, as well as inspection of residuals).[21]

Table 1 summarizes the association constants and uncertainties that were derived from the triplicate titration experiments.§ All-*cis* $C_6H_6F_6$ exhibits moderate binding affinity for F^-, Cl^- and Br^- in acetone with association constants in the range of roughly 100 to 500 M^{-1}. When comparing solvents, binding affinities are *ca.* one order of magnitude lower in acetonitrile and below the level required for determination by NMR in DMSO. In all cases where K_a determination was possible, both methods for evaluating uncertainties strongly suggested that the stoichiometry is 1 : 1 (**1**·Cl^-) rather than 2 : 1 (**1**·Cl^-·**1**; see Table S1, ESI†).[20] Importantly, this does not mean that the formation of a 2 : 1 complex is impossible – rather the second binding constant appears to be too low to allow its determination with reasonable confidence.[20] This interpretation of the data is also plausible in light of McMahon's gas-phase study on **1**·Cl^-, which concluded that the second binding event is significantly weaker than the first, even in the absence of solvent.[14a]

When comparing the series of halide ions, a notable trend is that the binding affinity increases from I^- to Br^- and Cl^-, while competing HF elimination unfortunately precludes an accurate determination of K_a for F^-.[15] We propose that the halide and solvent trends, as well as the preference for 1 : 1 stoichiometry point towards the predominant electrostatic nature of the interaction between **1** and anions and that the degree of covalency is likely negligible.[22] Our findings thus qualitatively agree with Flood's recent demonstration that the strength of H bonding between a triazolophane macrocycle and chloride is inversely proportional to solvent ε.[16] Smaller anions have a larger charge surface density, which explains the K_a trend for Cl^-, Br^- and I^- in acetone, which due to its low ε only poorly "screens out" electrostatics. Within the electrostatic regime,[16] one would also expect that the second binding event is less favorable than the first, which is indeed what we observed.

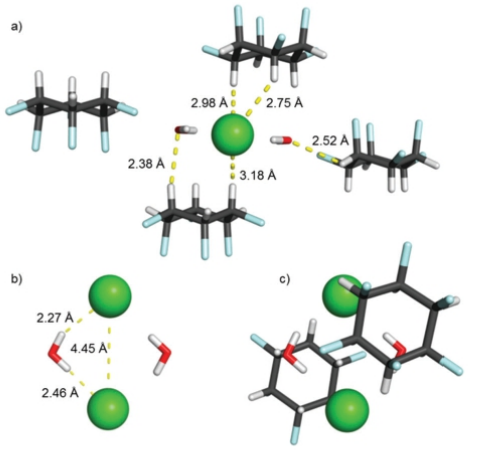

Fig. 2 Solid state structure of the co-crystal of **1** with tetraphenylphosphonium chloride (cations omitted for clarity). (a) $(Cl^-)_2$·$(H_2O)_2$ coordinated to four molecules **1**; (b) structure of the $(Cl^-)_2$·$(H_2O)_2$ cluster; (c) $(Cl^-)_2$·$(H_2O)_2$ cluster stacked between two molecules of **1**. Single crystals were obtained by the layering method (*n*-hexane/acetone + chloroform). Green: Cl; turquoise: F; red: O; grey: C; white: H.‖

To gain deeper structural insights, we co-crystallized $C_6H_6F_6$ with tetraphenylphosphonium chloride. X-ray crystallography of suitable single crystals (see the ESI†) showed that the ratio of all-*cis* $C_6H_6F_6$ to Cl^- was 1 : 1 and that water had co-crystallized, presumably due to the presence of atmospheric moisture.¶ As becomes evident from Fig. 2a, the solid state structure provides unambiguous evidence for attractive interactions between axial hydrogen atoms in **1** and the chloride ion. However, to our surprise we observed the formation of a $(Cl^-)_2(H_2O)_2$ cluster (Fig. 2b),[23] in which two chloride ions are held together by hydrogen bonds with two bridging water molecules with O–H···Cl bond distances of 2.46 and 2.27 Å and a Cl–Cl distance of 4.45 Å (for comparison: sum of Cl–Cl r_w = 3.5 Å).[24] Each cluster is surrounded by four molecules of **1** (Fig. 2a) that stabilize the cluster by means of C–H···Cl and C–H···O interactions with bond distances of 3.18, 2.98, 2.75 Å and 2.52, 2.38 Å, respectively. Compared to the previously reported gas-phase calculations,[14a] our X-ray crystallographic data attests to longer bond lengths between **1** and Cl^-, which is not surprising however, in light of two water molecules essentially competing with **1** for hydrogen bonding¶ and gas phase H bonds generally being shorter due to the lack of dielectric screening.

To investigate how the substitution of fluorine atoms in **1** would affect anion binding, we decided to prepare its methoxy derivative **2** (Fig. 3a) and test whether its affinity for chloride would significantly deviate from the parent compound. It is worth noting in this context that **2** can be transformed into the corresponding alcohol, which opens up the prospect of generating multidentate or macrocyclic architectures with potentially increased

 This journal is © The Royal Society of Chemistry 2018

Published on 05 April 2018. Downloaded by Universitat Ulm on 5/21/2020 5:09:19 PM.

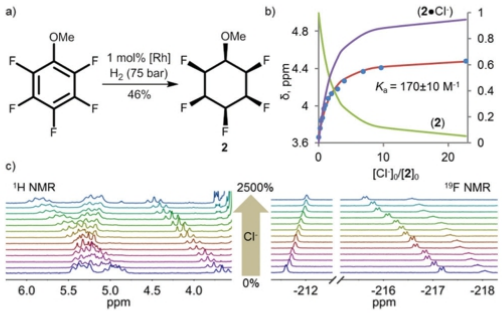

Fig. 3 (a) Synthesis of **2** according to method reported by Wiesenfeldt *et al.*;[15] (b) binding isotherm and species concentration plot for titration of **2** with TBACl. Blue spheres: experimental points, red line: fit according to 1 : 1 model,[19] purple and green: mole fractions of corresponding species; (c) partial ^{1}H and ^{19}F NMR (acetone-d_6, 400 MHz, 293 K) stacked plots for titration of **2** with TBACl.§

binding affinities and size-dependent anion selectivities. Fig. 3c shows the ^{19}F NMR titration of **2** with TBACl in acetone. All three sets of peaks shift significantly upon binding of Cl^- and a well-behaved binding isotherm is obtained that could be fitted very well according to a 1 : 1 model (Fig. 3b). The resulting binding constant is only about a factor of two lower than the one obtained for **1**, indicating that monoalkoxy-substituted derivatives of **1** could indeed give rise to more potent anion receptors.

In conclusion, this study suggests that all-*cis* perfluorocyclohexanes constitute a promising new type of anion binding motif. We demonstrated that 1 : 1 complexes are formed with moderate binding constants that mainly depend on the size of the anion and the dielectric constant of the medium, and we disclosed the first solid state structure featuring the interaction of all-*cis* $C_6H_6F_6$ with an anion. These findings could be useful for the rational design of future, structurally more complex architectures that may feature a combination of all-*cis* perfluorocyclohexanes with traditional H bonding motifs.

This work was supported by the Deutsche Forschungsgemeinschaft (Emmy-Noether grant DE1830/2-1) and the DAAD (PhD fellowship to O. S.). We thank Dr Elena-Mena Osteritz for crystal structure refinement.

Conflicts of interest

There are no conflicts to declare.

Notes and references

‡ URLs to the raw data, calculated fits and statistical information for titrations can be found in the ESI† (Tables S3–S5).
§ Our experimental data does not correct for the ion pairing interaction of anions with tetrabutylammonium. As such, the reported binding affinities should be seen as relative, rather than absolute values.
¶ So far, we were unable to obtain water-free single crystals.
‖ The cif file was deposited in the Cambridge Structural Database under identifier CCDC 1826208.

1 (*a*) P. A. Gale, E. N. W. Howe and X. Wu, *Chem*, 2016, **1**, 352–422; (*b*) N. Busschaert, C. Caltagirone, W. V. Rossom and P. A. Gale, *Chem. Rev.*, 2015, **115**, 8038–8155.
2 (*a*) G. Nie, Y. Sun, F. Zhang, M. Song, D. Tian, L. Jiang and H. Li, *Chem. Sci.*, 2015, **6**, 5859–5865; (*b*) L. Qin, A. Hartley, P. Turner, R. B. P. Elmes and K. A. Jolliffe, *Chem. Sci.*, 2016, **7**, 4563–4572; (*c*) C. F. Chow, P. Y. Ho, W. L. Wong, Y. J. Lu, Q. Tang and C. B. Gong, *Chem. Sci.*, 2017, **8**, 3812–3820.
3 M. Zurro, S. Asmus, S. Beckendorf, C. Mück-Lichtenfeld and O. G. Mancheño, *J. Am. Chem. Soc.*, 2014, **136**, 13999–14002.
4 (*a*) P. A. Gale, J. T. Davis and R. Quesada, *Chem. Soc. Rev.*, 2017, **46**, 2497–2519; (*b*) A. J. Plaunt, K. M. Harmatys, W. R. Wolter, M. A. Suckow and B. D. Smith, *Bioconjugate Chem.*, 2014, **25**, 724–737.
5 J. Y. Choi, D. Muallem, K. Kiselyov, M. G. Lee, P. J. Thomas and S. Muallem, *Nature*, 2001, **410**, 94–97.
6 N. Busschaert, S.-H. Park, K.-H. Baek, Y. P. Choi, J. Park, E. N. W. Howe, J. R. Hiscock, L. E. Karagiannidis, I. Marques, V. Félix, W. Namkung, J. L. Sessler, P. A. Gale and I. Shin, *Nat. Chem.*, 2017, **9**, 667–675.
7 (*a*) M. M. Watt, L. N. Zakharov, M. N. Haley and D. W. Johnson, *Angew. Chem., Int. Ed.*, 2013, **52**, 10275–10280; (*b*) T. A. Barendt, A. Docker, I. Marques, V. Félix and P. D. Beer, *Angew. Chem., Int. Ed.*, 2016, **55**, 11069–11076.
8 (*a*) C. Brissot, M. Rosso, J.-N. Chazalviel and S. Lascaud, *J. Power Sources*, 1999, **81–82**, 925–929; (*b*) T. Husch and M. Korth, *Phys. Chem. Chem. Phys.*, 2015, **17**, 22596–22603.
9 M. C. Etter, Z. Urbañ-Lipkowska, M. Zia-Ebrahimi and T. W. Panunto, *J. Am. Chem. Soc.*, 1990, **112**, 8415–8426.
10 (*a*) R. O. Ramabhadran, Y. Liu, Y. Hua, M. Ciardi, A. H. Flood and K. Raghavachari, *J. Am. Chem. Soc.*, 2014, **136**, 5078–5089; (*b*) G. Cavallo, P. Metrangolo, R. Milani, T. Pilati, A. Priimagi, G. Resnati and G. Terraneo, *Chem. Rev.*, 2016, **116**, 2478–2601.
11 (*a*) P. A. Gale, J. L. Sessler, V. Král and V. Lynch, *J. Am. Chem. Soc.*, 1996, **118**, 5140–5141; (*b*) J. L. Sessler, M. J. Cyr, E. McGhee, J. A. Ibers and V. Lynch, *J. Am. Chem. Soc.*, 1990, **112**, 2810–2813.
12 L. Adriaenssens, G. Gil-Ramírez, A. Frontera, D. Quiñonero, E. C. Escudero-Adán and P. Ballester, *J. Am. Chem. Soc.*, 2014, **136**, 3208–3218.
13 N. S. Keddie, A. M. Z. Slawin, T. Lebl, D. Philp and D. O'Hagan, *Nat. Chem.*, 2015, **7**, 483–488.
14 (*a*) B. E. Ziegler, M. Lecours, R. A. Marta, J. Featherstone, E. Fillion, W. S. Hopkins, V. Steinmetz, N. S. Keddie, D. O'Hagan and T. B. McMahon, *J. Am. Chem. Soc.*, 2016, **138**, 7460–7463; (*b*) S. Md Pratik, A. Nijamudheen and A. Datta, *ChemPhysChem*, 2016, **17**, 2373–2381; (*c*) W.-M. Sun, B.-L. Ni, D. Wu, J.-M. Lan, C.-Y. Li, Y. Li and Z.-R. Li, *Organometallics*, 2017, **35**, 3352–3359; (*d*) R. A. Carmanich, N. S. Keddie, R. Rittner, D. O'Hagan and M. Bühl, *Phys. Chem. Chem. Phys.*, 2017, **17**, 29475–29478; (*e*) M. J. Lecours, R. A. Marta, V. Steinmetz, N. Keddie, E. Fillion, D. O'Hagan, T. B. McMahon and W. S. Hopkins, *J. Phys. Chem. Lett.*, 2017, **8**, 109–113; (*f*) S. Md Pratik, A. Nijamudheen and A. Datta, *J. Phys. Chem. C*, 2017, **121**, 1752–1762.
15 M. P. Wiesenfeldt, Z. Nairoukh, W. Li and F. Glorius, *Science*, 2017, **357**, 908–912.
16 Y. Liu, A. Sengupta, K. Raghavachari and A. H. Flood, *Chem*, 2017, **3**, 411–427.
17 M. J. Kamlet, J.-L. M. Abboud, M. H. Abraham and R. W. Taft, *J. Org. Chem.*, 1983, **48**, 2877–2887.
18 (*a*) S. Lee, C.-H. Chen and A. H. Flood, *Nat. Chem.*, 2013, **5**, 704–710; (*b*) D. Zhang, T. K. Ronson, J. Mosquera, A. Martinez, L. Guy and J. R. Nitschke, *J. Am. Chem. Soc.*, 2017, **139**, 6574–6577; (*c*) D. A. McMorran and P. J. Steel, *Angew. Chem., Int. Ed.*, 1998, **37**, 3295–3297; (*d*) M. R. Rosenthal, *J. Chem. Educ.*, 1973, **50**, 331–335.
19 http://supramolecular.org/.
20 D. B. Hibbert and P. Thordarson, *Chem. Commun.*, 2016, **52**, 12792–12805.
21 (*a*) F. Ulatowski, K. Dąbrowa, T. Bałakier and J. Jurczak, *J. Org. Chem.*, 2016, **81**, 1746–1756; (*b*) P. Thordarson, *Chem. Rev.*, 2011, **40**, 1305–1323.
22 (*a*) S. J. Grabowski, *Chem. Rev.*, 2011, **111**, 2597–2625; (*b*) V. L. Deringer, U. Englert and R. Dronskowski, *Chem. Commun.*, 2014, **50**, 11547–11549; (*c*) H. Elgabarty, R. Z. Khaliullin and T. D. Kühne, *Nat. Commun.*, 2015, **6**, 8318; (*d*) S. W. Robinson, C. L. Mustoe, N. G. White, A. Brown, A. L. Thompson, P. Kennepohl and P. D. Beer, *J. Am. Chem. Soc.*, 2015, **137**, 499–507.
23 (*a*) M. N. Hoque and G. Das, *J. Mol. Struct.*, 2016, **1108**, 298–306; (*b*) Q. He, P. Tu and J. L. Sessler, *Chem*, 2018, **4**, 46–93.
24 A. Bondi, *J. Phys. Chem.*, 1964, **68**, 441–451.

Electronic Supplementary Material (ESI) for ChemComm.
This journal is © The Royal Society of Chemistry 2018

Supporting information

Evidence for anion-binding of all-cis hexafluorocyclohexane in solution and solid state

Oleksandr Shyshov, Kevin Andre Siewerth, Max von Delius*

Institute of Organic Chemistry and Advanced Materials, University of Ulm, Albert-Einstein-Allee 11, 89081 Ulm, Germany.

Email: max.vondelius@uni-ulm.de

Contents

General Experimental Section S2
Synthesis of the Catalyst S2
Synthesis of all-cis 1,2,3,4,5,6-hexafluorocyclohexane (1) S2
Synthesis of all-cis 1-methoxy-2,3,4,5,6-pentafluorocyclohexane (2) S2
NMR Titration Data S3
URLs to NMR Titrations S13
Crystallographic Data S15
References S21

General Experimental Section

All commercially available reagents were purchased from Sigma Aldrich, Alfa Aesar, Acros Organics or TCI and were used without further purification unless otherwise stated. Hydrogenation reactions were carried out in a 150mL Roth High Pressure Autoclave. Deuterated solvents were purchased from Sigma Aldrich. All solvents except acetone were dried over molecular sieves for at least 24 hours. For titrations with TBAF acetone-d_6 was distilled from Drierite™ and immediately used. NMR spectra were recorded on Bruker Avance 400 (^{1}H: 400 MHz) spectrometers at 293 K and referenced to the residual solvent peak (^{1}H: acetone-d_6, 2.05 ppm; ^{13}C: acetone-d_6, 206.68, 29.92 ppm) ^{19}F NMR spectra were referenced to hexafluorobenzene as internal standard (^{19}F: C_6F_6, -164.9 ppm). Coupling constants (J) are denoted in Hz and chemical shifts (δ) in ppm. Mass spectra were obtained on a Bruker SolariX (HRMS-ESI$^+$, solvent: acetonitrile) instrument.

Synthesis of the Catalyst

[Rh(CAAC)(COD)Cl] was prepared according to the procedure reported by Wiesenfeldt et al. and references therein.[S1]

Synthesis of all-cis 1,2,3,4,5,6-hexafluorocyclohexane (1)

All-cis 1,2,3,4,5,6-hexafluorocyclohexane was prepared according to the procedure reported by Wiesenfeldt et al.[S1]

Synthesis of all-cis 1-methoxy-2,3,4,5,6-pentafluorocyclohexane (2)



In a dry 22 mL screw-cap vial containing a stirring bar, were placed Rh(CAAC)(COD)Cl catalyst (6.23 mg, 11 µmol, 0.01 equiv.) and dry silica gel (605 mg). The vial was closed with a septum containing a needle and the vial was placed in a Schlenk tube. High vacuum (<0.1 mbar) was applied for at least 20 minutes. 2,3,4,5,6-Pentafluoroanisol (216.12 mg, 0.135 mL, 1.09 mmol, 1 equiv.) and anhydrous hexane (17 mL) were added subsequently under argon. The reaction mixture was subjected to 5 quick vacuum/argon cycles to remove residual air and the vial was transferred to the 150 mL autoclave under argon which was carefully evacuated again after transferring. The autoclave was pressurized and depressurized 3 times to 30 bars with hydrogen gas and then the pressure was finally set to 75 bars. The reaction mixture was stirred at this pressure for 14 h at room temperature after which the autoclave was carefully depressurized, silica gel was filtered off and thoroughly washed with acetone. The solvent was removed under reduced pressure and the crude product was purified via flash column chromatography (DCM/acetone, 95/5 v/v) to give 99.7 mg (46%) of the desired compound as a colorless solid.

^{1}H NMR (400 MHz, acetone-d_6): δ 5.46 - 5.26 (m, 3H), 5.07 - 4.84 (m, 2H), 3.67 (t, J = 29.2 Hz, 1H), 3.51 (s, 1H). ^{19}F NMR (377 MHz, acetone-d_6): δ -211.6 (s, 2F), -217.18 (d, J = 25 Hz, 2F), -218.06 (tt, J = 24.6, 9.9 Hz, 1F). ^{13}C NMR (101 MHz, acetone-d_6): δ 88.27 (d, J = 18.6 Hz), 87.24, 86.32 (d, J = 18.4 Hz), 85.29 (m), 74.58 (m), 57.23.

HRMS (ESI$^+$): m/z = 431.1041 [2M+Na]$^+$ (calculated 431.1039 for $C_{14}H_{18}F_{10}O_2Na^+$).

NMR Titration Data

All salts and hosts were dried under high vacuum (10^{-3} bar) over phosphorus pentoxide overnight prior to titrations. As a source of fluoride, we used a 1.0 M anhydrous solution of tetrabutylammonium fluoride in THF. ^{19}F NMR titrations were performed via addition of aliquots of the guest anion in the tetrabutylammonium form dissolved in a stock solution of the host, to the solution of the host, containing hexafluorobenzene as an internal standard. Spectra were recorded using a Bruker Avance 400 spectrometer and spectra were referenced to the peak of hexafluorobenzene (^{19}F: C_6F_6, -164.9 ppm). All titrations were repeated 3 times. Titration data was fitted using supramolecular.org. All raw data, calculated fits and related data can be accessed via supramolecular.org.[S2]

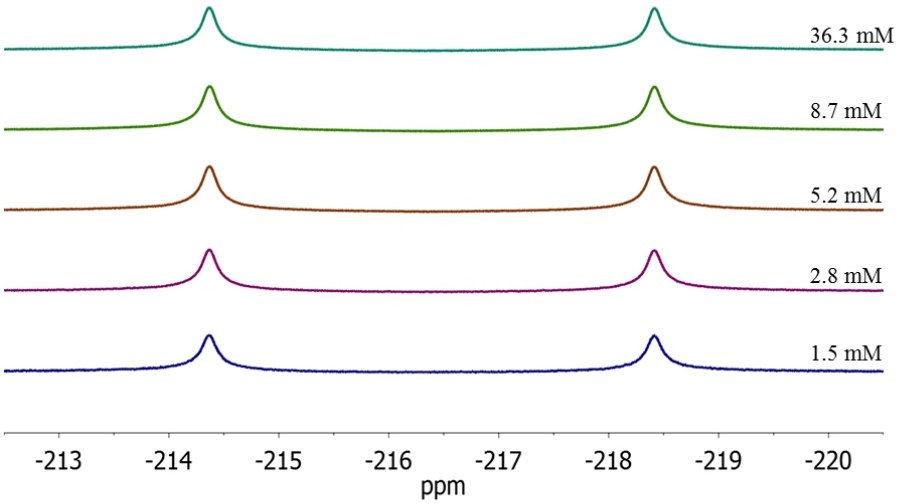

Figure S1. Investigation of possible aggregation: ^{19}F NMR stacked plot of **1** at different concentrations (acetone-d_6, 293 K).

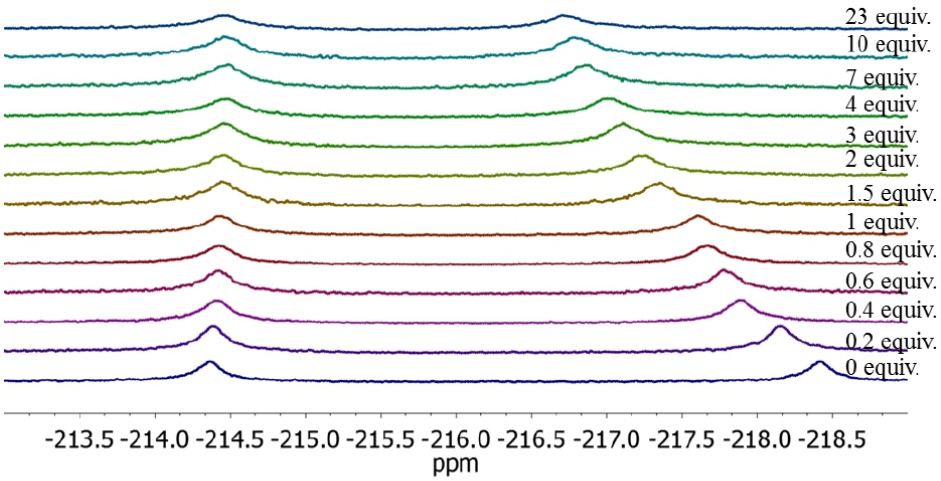

Figure S2. ^{19}F NMR stack plot for titration of **1** (5 mM) with TBACl in acetone-d_6 at 293 K. The signal at -218.4 ppm was used to obtain binding isotherms.

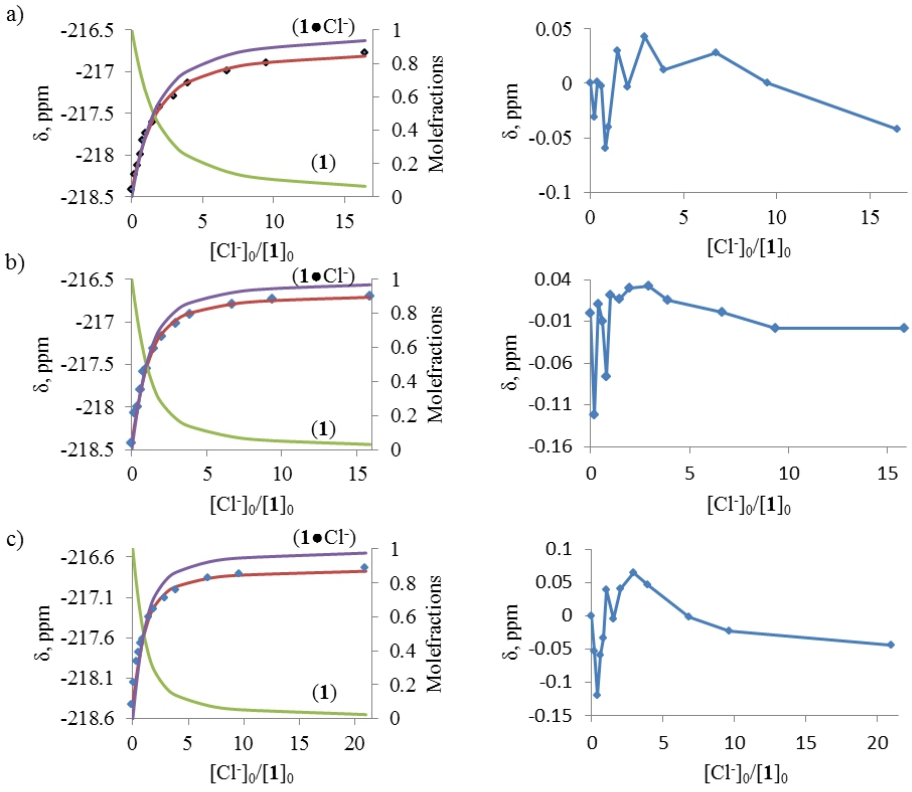

Figure S3. Left column: binding isotherms and species concentration plots for titration of **1** ($[\mathbf{1}]_0$: a) 2 mM, b) and c) 5 mM) with TBACl in acetone-d_6 at 293 K. Blue diamonds: experimental points, red line: fit according to 1:1 model, purple and green: mole fractions of corresponding species. Right column: residual plots.

Table S1. Association constants obtained for the titration of **1** with TBACl in acetone-d_6 at 293 K and fitted with 2:1 (Nelder-Mead) and 1:1 models.

	H_2G + HG model					HG model	
	C, mM	K_1, M^{-1}	Fit error, $\pm$ M^{-1}	K_2, M^{-1}	Fit error, $\pm$ M^{-1}	K_a, M^{-1}	Fit error, $\pm$ M^{-1}
TBACl	2	700	400	600	700	400	40
	5	90	40	100	40	390	60
	5	20	5	1000	200	420	70
K_a (mean)		300 M^{-1}		600 M^{-1}		400 M^{-1}	
$s/\sqrt{n}$		400 M^{-1}		300 M^{-1}		10 M^{-1}	
$\pm t_{(0.05,\,2)}\, s/\sqrt{n}$		2000 M^{-1}		1000 M^{-1}		40 M^{-1}	

To estimate a confidence interval at 95% probability for $n = 3$ repeat measurements standard uncertainty $u = s/\sqrt{n}$, where s is the sample standard deviation, was multiplied by the Student t-value for the degrees of freedom $(n - 1)$.[S3]

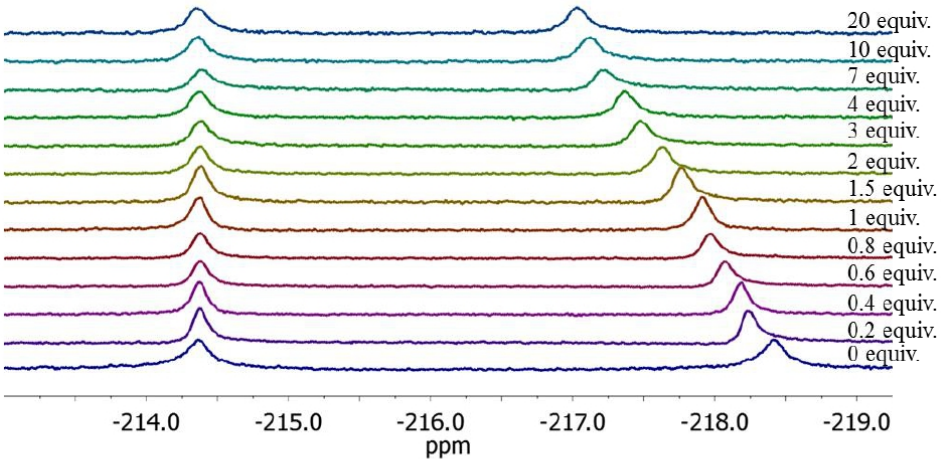

Figure S4. ^{19}F NMR stack plot for titration of **1** (5 mM) with TBABr in acetone-d_6 at 293 K. Signal at -218.4 ppm was used to obtain binding isotherms.

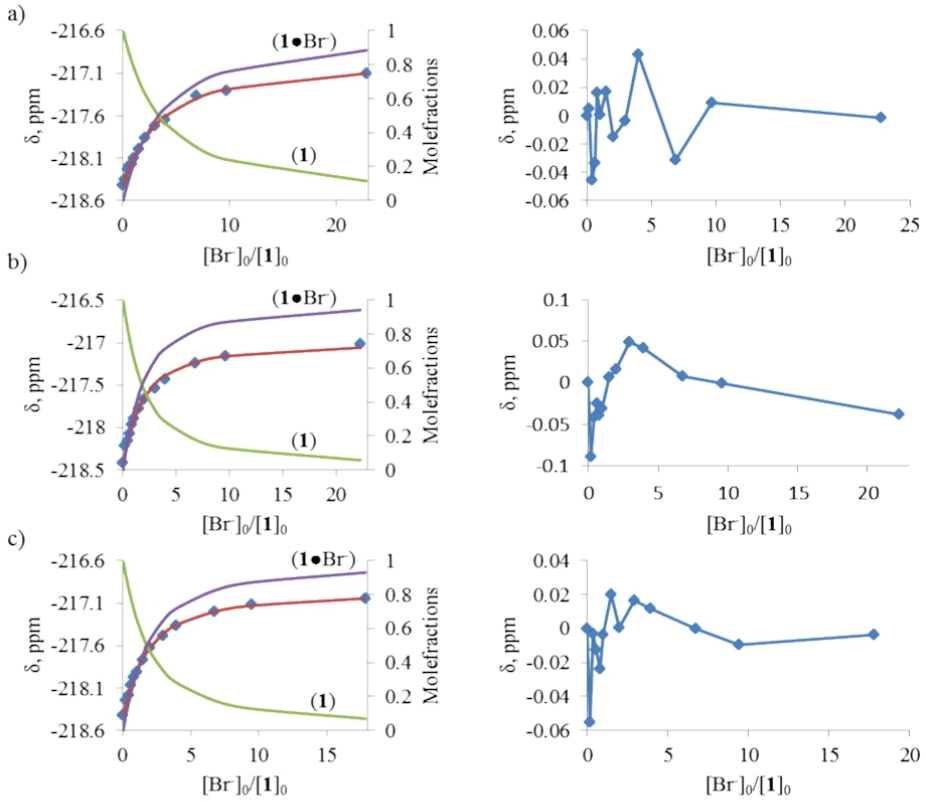

Figure S5. Left column: binding isotherms and species concentration plots for titration of **1** ([**1**]$_0$: a) 2 mM, b) and c) 5 mM) with TBABr in acetone-d_6 at 293 K. Blue diamonds: experimental points, red

line: fit according to 1:1 model, purple and green: mole fractions of corresponding species. Right column: residual plots.

Table S2. Association constants obtained for the titration of **1** with TBABr in acetone-d_6 at 293 K and fitted with 2:1 (Nelder-Mead) and 1:1 models.

	H_2G + HG model					HG model	
	C, mM	K_1, M^{-1}	Fit error, $\pm M^{-1}$	K_2, M^{-1}	Fit error, $\pm M^{-1}$	K_a, M^{-1}	Fit error, $\pm M^{-1}$
TBABr	2	3	1	5000	500	160	10
	5	17	2	350	30	160	10
	5	1	0.3	8000	2000	140	20
K_a (mean)		7 M^{-1}		4600 M^{-1}		150 M^{-1}	
$s/\sqrt{n}$		5 M^{-1}		2300 M^{-1}		10 M^{-1}	
$\pm t_{(0.05,\,2)}\, s/\sqrt{n}$		20 M^{-1}		10000 M^{-1}		40 M^{-1}	

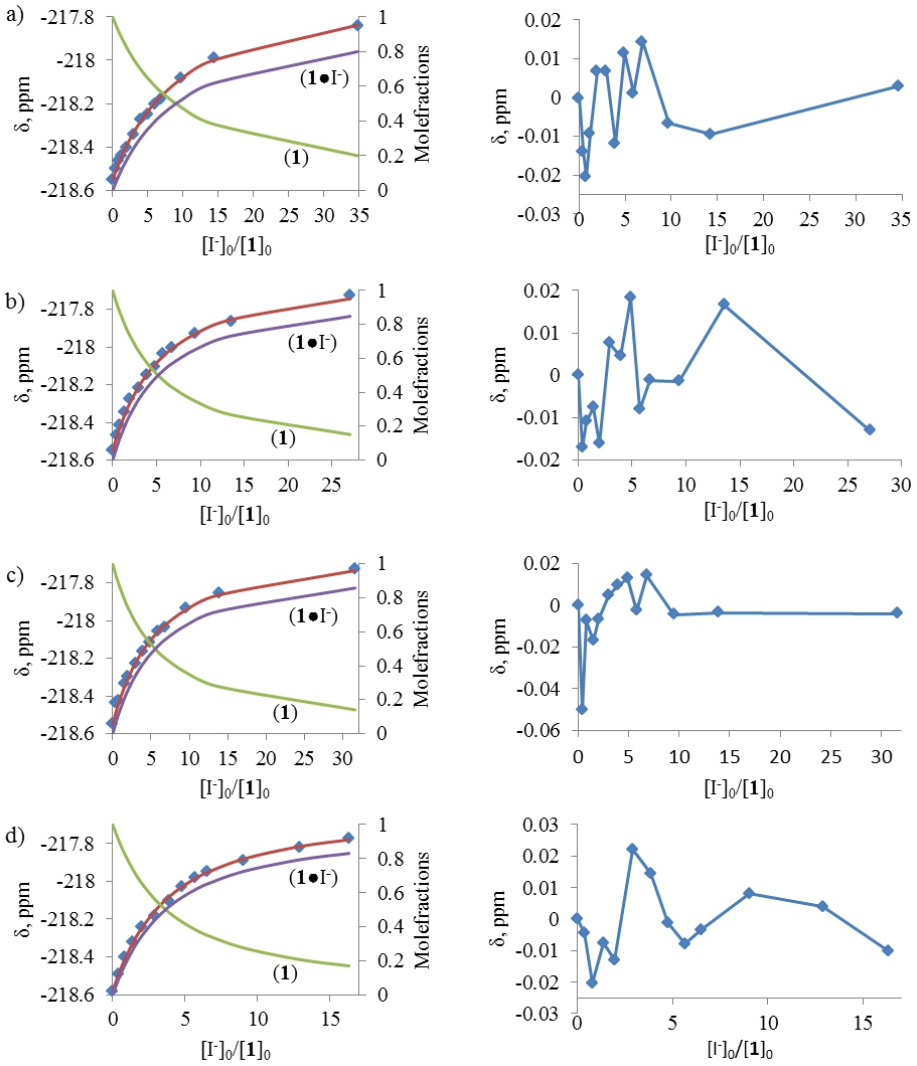

Figure S6. Left column: binding isotherms and species concentration plots for titration of **1** ([**1**]$_0$: a) 2 mM, b) and c) 5 mM, d) – 10 mM) with TBAI in acetone-d_6/DCM-d_2 (88/12 w/w) at 293 K. Blue diamonds: experimental points, red line: fit according to 1:1 model, purple and green: mole fractions of corresponding species. Right column: residual plots.

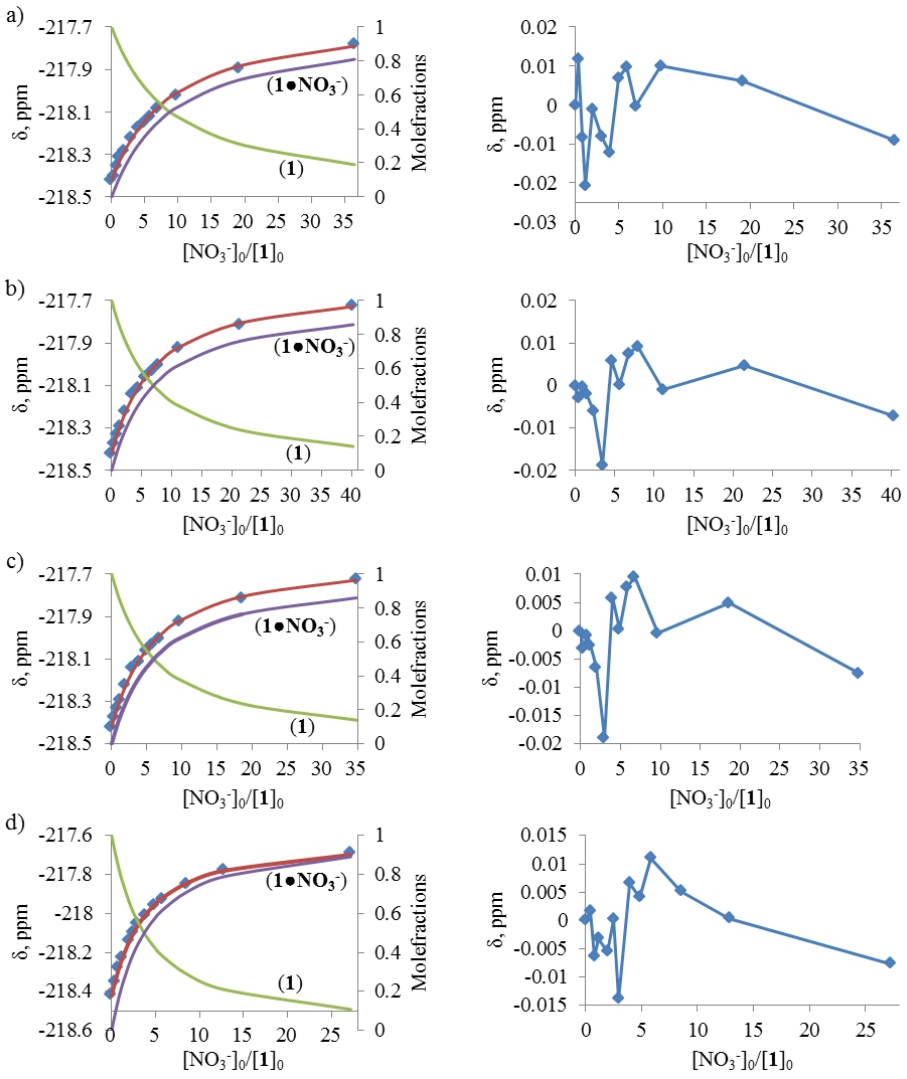

Figure S7. Left column: binding isotherms and species concentration plots for titration of **1** ($[\mathbf{1}]_0$: a) 2 mM, b) and c) 5 mM, d) – 10 mM) with $TBANO_3$ in acetone-d_6 at 293 K. Blue diamonds: experimental points, red line: fit according to 1:1 model, purple and green: mole fractions of corresponding species. Right column: residual plots.

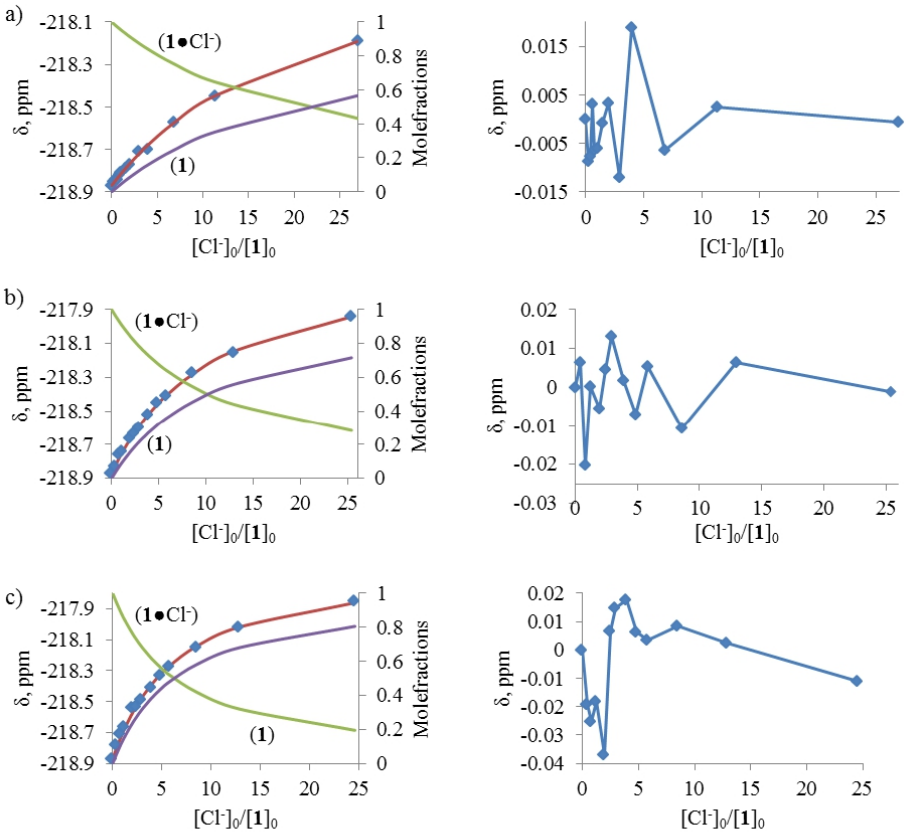

Figure S8. Left column: binding isotherms and species concentration plots for titration of **1** ($[\mathbf{1}]_0$: a) 2 mM, b) 5 mM, c) 10 mM) with TBACl in acetonitrile-d_3 at 293 K. Blue diamonds: experimental points, red line: fit according to 1:1 model, purple and green: mole fractions of corresponding species. Right column: residual plots.

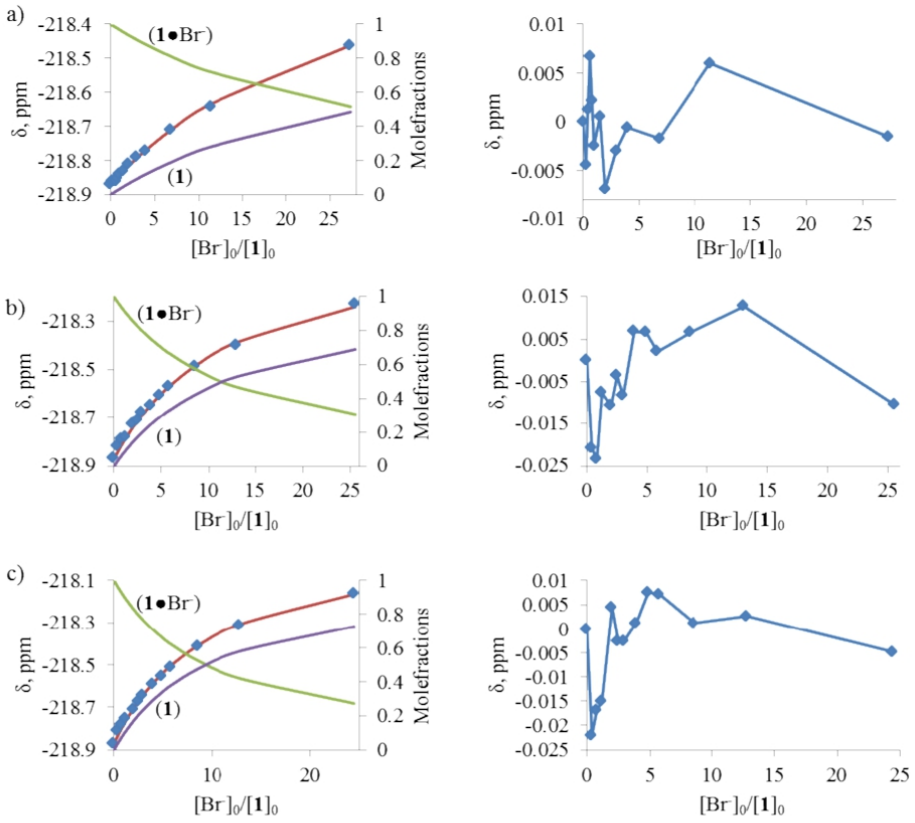

Figure S9. Left column: binding isotherms and species concentration plots for titration of **1** ($[\mathbf{1}]_0$: a) 2 mM, b) 5 mM, c) 10 mM) with TBABr in acetonitrile-d_3 at 293 K. Blue diamonds: experimental points, red line: fit according to 1:1 model, purple and green: mole fractions of corresponding species. Right column: residual plots.

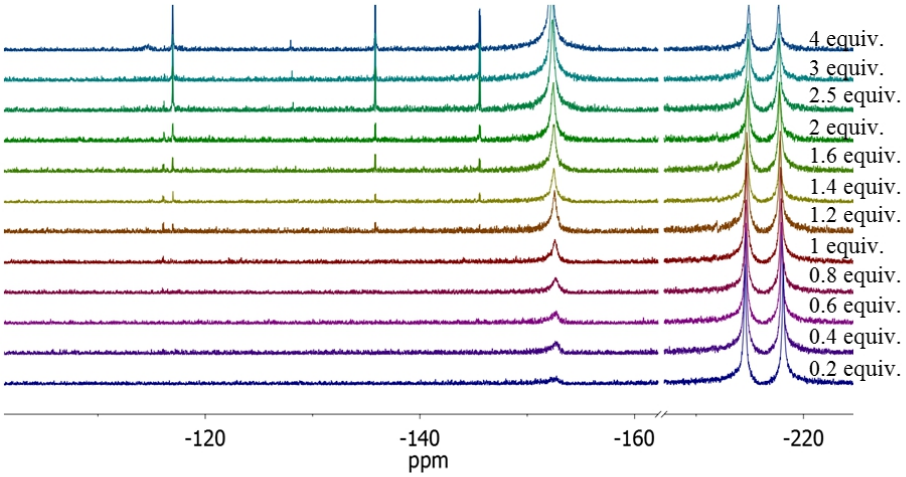

Figure S10. ^{19}F NMR stack plot for titration of **1** (5 mM) with TBAF in acetone-d_6 at 293 K. Signal at -218.4 ppm was used to obtain binding isotherms.

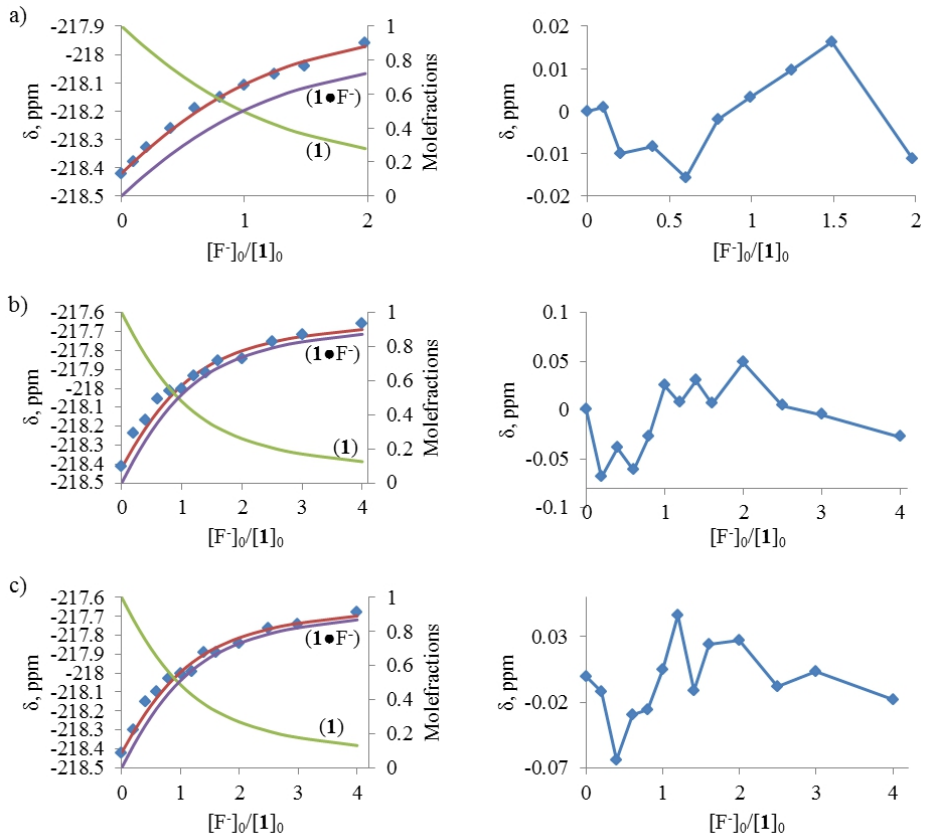

Figure S11. Left column: binding isotherms and species concentration plots for titration of **1** ($[\mathbf{1}]_0$: a) 2 mM, b) and c) 5 mM) with TBAF in acetone-d_6 at 293 K. Blue diamonds: experimental points, red line: fit according to 1:1 model, purple and green: mole fractions of corresponding species. Right column: residual plots.

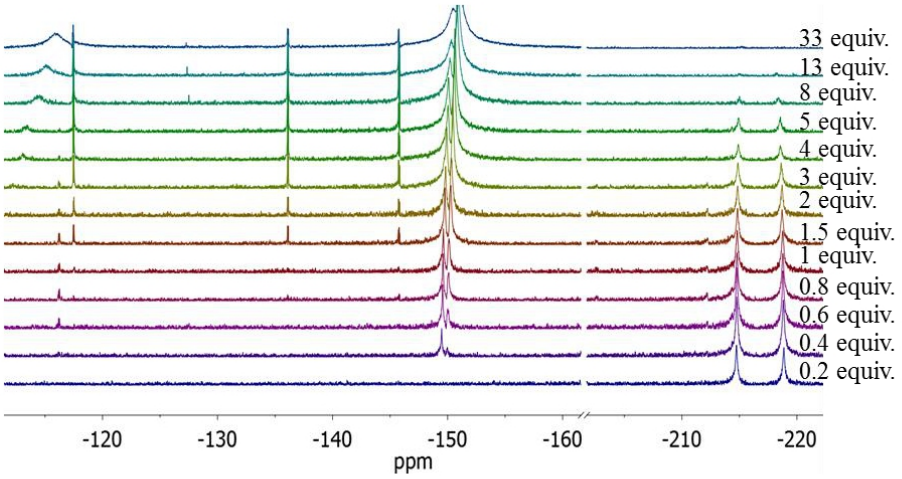

Figure S12. Decomposition of **1** (2 mM) during titration with TBAF in acetonitrile-d_3 at 293 K.

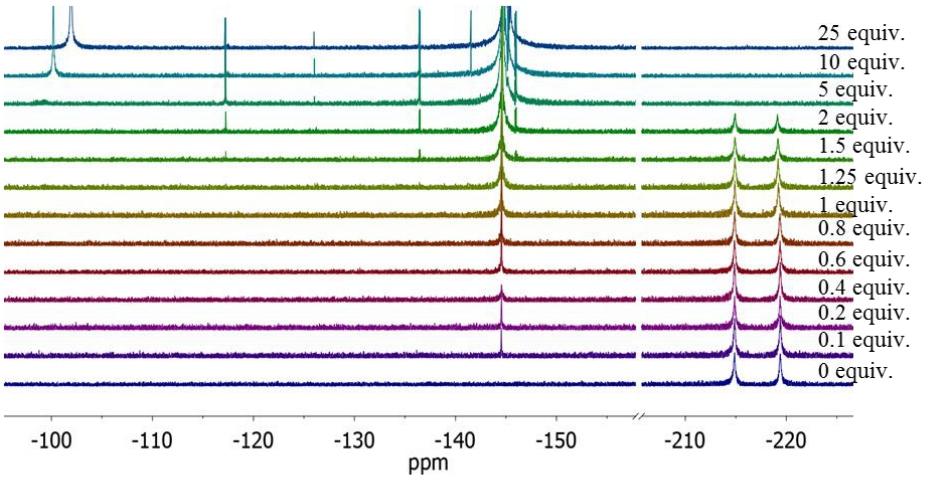

Figure S13. Decomposition of **1** (2 mM) during titration with TBAF in DMSO-d_6 at 293 K.

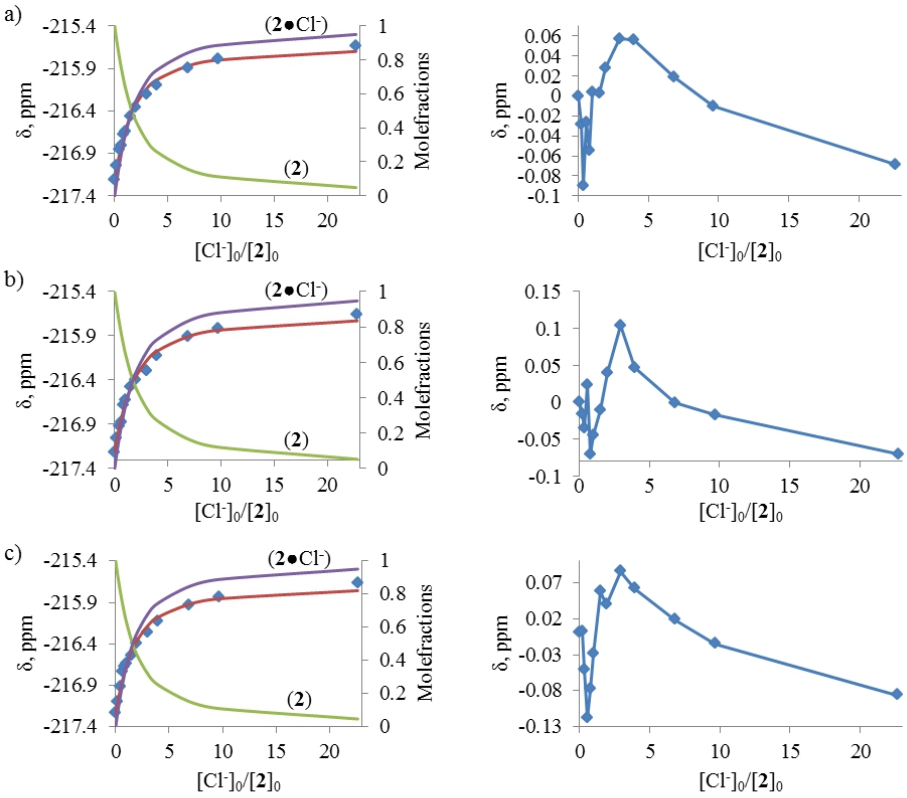

Figure S14. Left column: binding isotherms and species concentration plots for titration of **2** ([**2**]$_0$: 5 mM) with TBACl in acetone-d_6 at 293 K. Blue diamonds: experimental points, red line: fit according to 1:1 model, purple and green: mole fractions of corresponding species. Right column: residual plots. Chemical shift of only one fluorine was shown for clarity.

URLs to NMR Titrations

Table S3. URLs to the raw data, calculated fit and statistical information for the titration of **1** in acetone-d_6 at 293 K.

Salt	URL
TBAF	http://app.supramolecular.org/bindfit/view/7ea20f6e-20b4-4f03-abbd-573be2dbc4d2
	http://app.supramolecular.org/bindfit/view/a6144c0b-61d7-4a06-b524-fdd0c67561aa
	http://app.supramolecular.org/bindfit/view/853c7d7c-6e1d-4127-9ffc-0c7aba46ba38
TBACl	http://app.supramolecular.org/bindfit/view/ba5c0152-1b63-44bc-9fd6-d72b9c260660
	http://app.supramolecular.org/bindfit/view/f3127579-8411-4b61-94c5-df9914684a2d
	http://app.supramolecular.org/bindfit/view/f5f3822e-7224-433a-8218-f519cccc641a
TBABr	http://app.supramolecular.org/bindfit/view/ba9aab15-cc2a-4531-ba1e-dd5cfe07f653
	http://app.supramolecular.org/bindfit/view/f6147ca7-265b-4293-ae03-3045ed195d68

	http://app.supramolecular.org/bindfit/view/20591e77-a2ae-4326-abc1-4b692f3d9c74
TBAI	http://app.supramolecular.org/bindfit/view/4c42aede-b764-40d4-8ded-1e8cb188aaf0
	http://app.supramolecular.org/bindfit/view/987f6e84-497d-46d2-8f74-b90722895c3a
	http://app.supramolecular.org/bindfit/view/d3d769e8-333a-4a99-9e53-3f4e4189effe
	http://app.supramolecular.org/bindfit/view/b941fef1-1c8e-4813-8552-1bcd0c6bdf56
$TBANO_3$	http://app.supramolecular.org/bindfit/view/c22a80b8-4d48-4278-877c-4801dc4f6b32
	http://app.supramolecular.org/bindfit/view/1d19502b-057e-4349-8a86-69317d22c016
	http://app.supramolecular.org/bindfit/view/790f7df9-7a06-4ac8-8e3b-e639fdc174a2
	http://app.supramolecular.org/bindfit/view/dc963425-d231-4e92-a785-e1f4394201cd

Table S4. URLs to the raw data, calculated fit and statistical information for the titration of **1** in acetonitrile-d_3 at 293 K.

Salt	URL
TBACl	http://app.supramolecular.org/bindfit/view/fb0dd0cc-d8e9-43cd-9622-e42e42ca9fd2
	http://app.supramolecular.org/bindfit/view/05e6e248-8e8f-4477-b02e-e5df9b53dc99
	http://app.supramolecular.org/bindfit/view/503f5dca-a32f-4edb-ba80-8a4dd37af7b2
TBABr	http://app.supramolecular.org/bindfit/view/0a288146-6926-4708-b3d5-a22a39d0691d
	http://app.supramolecular.org/bindfit/view/62f19df1-1ff7-4bbe-964b-039a349a37b3
	http://app.supramolecular.org/bindfit/view/2b732ce3-1b2c-495e-b32f-768ffc68d996

Table S5. URLs to the raw data, calculated fit and statistical information for the titration of **2** in acetone-d_6 at 293 K.

Salt	URL
TBACl	http://app.supramolecular.org/bindfit/view/dd46e7f8-4c5b-4f8c-af30-ace29d420d7d
	http://app.supramolecular.org/bindfit/view/578ecf57-cc44-4de0-96c6-73b235571ede
	http://app.supramolecular.org/bindfit/view/d82fdca8-82c7-435c-b718-25baa95cbc9b

Crystallographic Data

All-cis 1,2,3,4,5,6-hexafluorocyclohexane (**1**) (5.2 mg, 0.027 mmol, 2 equiv.) and tetraphenylphosphonium chloride (5.1 mg, 0.0136 mmol, 1 equiv.) was dissolved in 1 mL of anhydrous acetone. To dissolve all tetraphenylphosphonium chloride, a small amount of chloroform was added. The obtained clear solution was filtered through a syringe filter and transferred into 1 mL clear vials (c.a. 0.1 mL in each). Solutions were frozen down in liquid nitrogen and anhydrous n-hexane was layered on top.

The cif-file was deposited in the Cambridge Structural Database under identifier CCDC 1826208.

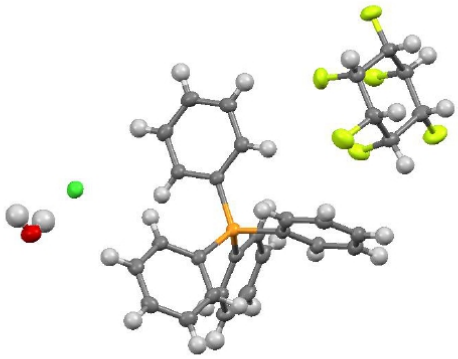

Figure S15. Co-crystal of **1** with tetraphenylphosphonium chloride. Thermal ellipsoids are shown at the 50% probability level.

Table S6. Crystal data and structure refinement for shy17098.[S4-S6]

Identification code	shy17098
Empirical formula	$C_{30}H_{28}ClF_6OP$
Formula weight	584.94
Temperature/K	150(2)
Crystal system	triclinic
Space group	P-1
a/Å	7.1352(3)
b/Å	13.5280(7)
c/Å	14.6245(8)
α/°	70.019(5)
β/°	86.507(4)
γ/°	89.808(4)
Volume/Å^3	1323.96(12)
Z	2
ρ_{calc}g/cm^3	1.467
μ/mm^{-1}	0.271
F(000)	604.0
Crystal size/mm^3	0.220 × 0.170 × 0.100
Radiation	MoKα (λ = 0.71073)
2Θ range for data collection/°	5.704 to 59.04
Index ranges	-8 ≤ h ≤ 9, -18 ≤ k ≤ 18, -20 ≤ l ≤ 20
Reflections collected	14548
Independent reflections	6333 [R_{int} = 0.0391, R_{sigma} = 0.0495]
Data/restraints/parameters	6333/0/355
Goodness-of-fit on F^2	1.044
Final R indexes [I>=2σ (I)]	R_1 = 0.0493, wR_2 = 0.1211

Table S7. Fractional atomic coordinates ($\times 10^4$) and equivalent isotropic displacement parameters ($Å^2 \times 10^3$) for shy17098. U_{eq} is defined as 1/3 of of the trace of the orthogonalised U_{IJ} tensor.

Atom	*x*	*y*	*z*	U(eq)
P001	909.1(7)	8252.5(3)	7791.6(3)	23.74(13)
Cl02	-1162.1(7)	6335.4(4)	5398.6(4)	34.62(14)
F003	-4670.7(17)	6943.6(10)	12329.2(9)	41.7(3)
F004	-1589.9(18)	7958.7(10)	11117.4(9)	44.1(3)
F005	-3898.1(19)	4894.9(9)	13375.7(10)	46.4(3)
F006	-2776.2(19)	8527.0(9)	12687.4(11)	49.3(4)
F007	-2242(2)	5772.1(11)	11553.2(10)	50.0(4)
F008	1275.3(19)	6599.3(11)	11277.5(10)	50.9(4)
O00	2445(2)	6089.1(12)	4183.1(12)	42.0(4)
C00A	2627(3)	8195.8(14)	6867.6(14)	25.7(4)
C00B	2171(3)	8355.0(13)	8784.1(14)	25.0(4)
C00C	-493(3)	9405.1(13)	7330.8(14)	24.6(4)
C00D	-652(3)	7131.6(13)	8194.9(14)	25.0(4)
C00E	2589(3)	7462.1(14)	6394.7(14)	28.7(4)
C00F	4105(3)	8943.6(15)	6631.1(15)	29.6(4)
C00G	-1760(3)	6950.7(14)	7507.0(14)	27.8(4)
C00H	2(3)	10202.7(14)	6454.9(15)	30.0(4)
C00I	1824(3)	9157.5(14)	9163.3(15)	28.3(4)
C00J	-854(3)	6486.5(14)	9172.4(14)	28.7(4)
C00K	-2068(3)	9502.7(14)	7906.5(15)	28.4(4)
C00L	5490(3)	8953.5(15)	5928.1(16)	32.2(4)
C00M	-3020(3)	6112.1(15)	7790.8(16)	32.2(4)
C00N	3996(3)	7479.1(14)	5694.2(15)	31.6(4)
C00O	-2143(3)	5648.6(15)	9448.6(15)	32.4(4)
C00P	5438(3)	8220.8(15)	5459.7(15)	32.0(4)
C00Q	4604(3)	7701.8(15)	9896.9(15)	31.9(4)
C00R	4254(3)	8501.6(15)	10277.2(15)	32.1(4)
C00S	-2514(3)	5667.0(14)	13215.9(15)	31.3(4)
C00T	3580(3)	7632.7(14)	9149.3(14)	28.8(4)
C00U	-3455(3)	6707.3(15)	13083.5(15)	31.0(4)
C00V	-3110(3)	10414.5(15)	7606.4(16)	32.3(4)
C00W	-1939(3)	7549.7(14)	12847.8(16)	32.5(4)
C00X	-3212(3)	5469.1(15)	8758.1(16)	32.9(4)
C00Y	2873(3)	9223.6(15)	9910.1(16)	33.7(5)
C00Z	-1214(3)	5663.5(15)	12362.8(16)	34.9(5)
C010	-632(3)	7622.4(15)	11972.5(15)	32.0(4)
C011	-1057(3)	11111.2(15)	6158.3(16)	35.9(5)
C012	-2596(3)	11213.3(15)	6740.4(17)	35.8(5)
C013	212(3)	6553.8(16)	12122.0(16)	33.6(4)

Table S8. Anisotropic displacement parameters ($Å^2 \times 10^3$) for shy17098. The anisotropic displacement factor exponent takes the form: $-2\pi^2[h^2a^{*2}U_{11}+2hka^*b^*U_{12}+\ldots]$.

Atom	U_{11}	U_{22}	U_{33}	U_{23}	U_{13}	U_{12}
P001	25.0(3)	20.2(2)	26.9(3)	-9.11(19)	-2.63(19)	1.69(17)
Cl02	37.1(3)	32.2(3)	37.7(3)	-16.8(2)	2.4(2)	0.8(2)
F003	30.8(7)	43.4(7)	43.2(7)	-3.8(6)	-8.7(5)	-0.2(5)
F004	41.7(7)	43.6(7)	34.8(7)	3.0(6)	-5.7(6)	0.2(6)
F005	51.6(8)	30.8(6)	53.3(8)	-10.7(6)	2.1(6)	-13.5(6)
F006	50.4(8)	25.3(6)	71.8(10)	-17.1(6)	1.0(7)	7.5(5)
F007	60.4(9)	58.8(8)	38.3(7)	-26.2(7)	-3.3(7)	-9.8(7)
F008	45.6(8)	56.0(8)	48.1(8)	-16.9(7)	13.9(6)	3.1(6)
O00	42.0(9)	34.4(8)	49.2(10)	-16.0(7)	9.3(7)	-2.2(7)
C00A	26.0(9)	23.1(8)	28.9(10)	-9.5(7)	-3.9(8)	3.9(7)
C00B	24.8(9)	23.8(8)	27.5(10)	-10.4(7)	-1.5(7)	-0.1(7)
C00C	25.0(9)	19.8(8)	30.8(10)	-10.2(7)	-5.8(8)	1.9(7)
C00D	25.5(9)	20.5(8)	30.4(10)	-10.9(7)	0.8(7)	1.5(7)
C00E	32.1(10)	22.9(9)	31.4(10)	-9.5(8)	-1.9(8)	0.4(7)
C00F	27.6(10)	28.4(9)	35.4(11)	-14.2(8)	-4.1(8)	-1.1(7)
C00G	29.7(10)	25.2(9)	29.2(10)	-10.1(8)	-3.1(8)	1.2(7)
C00H	28.3(10)	26.3(9)	33.8(11)	-8.0(8)	-2.7(8)	-0.7(7)
C00I	28.6(10)	25.1(9)	32.3(10)	-10.7(8)	-5.5(8)	4.1(7)
C00J	29.6(10)	28.0(9)	29.3(10)	-10.8(8)	-2.5(8)	2.8(7)
C00K	28.1(10)	25.8(9)	32.3(10)	-11.2(8)	-2.8(8)	0.3(7)
C00L	24.9(10)	31.7(10)	37.8(11)	-9.1(9)	-3.3(8)	1.0(8)
C00M	28.1(10)	31.7(10)	41.7(12)	-18.9(9)	-2.8(9)	-0.4(8)
C00N	38.7(11)	25.0(9)	32.5(11)	-11.7(8)	-2.2(9)	6.4(8)
C00O	36.4(11)	25.0(9)	32.7(11)	-6.8(8)	2.4(9)	1.1(8)
C00P	27.9(10)	33.5(10)	31.4(10)	-7.7(8)	2.0(8)	6.8(8)
C00Q	27.1(10)	29.6(10)	35.3(11)	-6.4(8)	-2.1(8)	3.1(8)
C00R	31.4(11)	34.1(10)	29.9(10)	-9.3(8)	-4.8(8)	-3.9(8)
C00S	33.4(11)	24.4(9)	34.7(11)	-8.3(8)	-2.7(9)	-4.0(8)
C00T	28.9(10)	26.4(9)	31.7(10)	-11.2(8)	-0.8(8)	3.3(7)
C00U	29.8(10)	30(1)	30.8(10)	-7.4(8)	-1.8(8)	2.0(8)
C00V	28.9(10)	32.3(10)	43.1(12)	-21.6(9)	-7.3(9)	6.1(8)
C00W	33.6(11)	21.8(9)	41.6(12)	-10.2(8)	-3.7(9)	4.9(8)
C00X	29.7(11)	26.3(9)	43.9(12)	-14.7(9)	4.5(9)	-1.4(8)
C00Y	38.4(12)	29.4(10)	36.6(11)	-15.2(9)	-3.1(9)	0.8(8)
C00Z	42.8(12)	27.9(10)	35.4(11)	-12.5(9)	-2.3(9)	3.0(8)
C010	29.9(10)	28.0(9)	34.3(11)	-5.3(8)	-5.0(8)	-2.0(8)
C011	39.3(12)	24.7(9)	39.4(12)	-4.3(8)	-10.2(10)	-0.1(8)
C012	36.3(11)	25.4(9)	48.9(13)	-15.3(9)	-13.1(10)	6.1(8)
C013	29.3(11)	36.6(11)	33.2(11)	-10.6(9)	1.6(8)	3.1(8)

Table S9. Bond lengths for shy17098.

Atom	Atom	Length/Å	Atom	Atom	Length/Å
P001	C00A	1.789(2)	C00G	C00M	1.381(3)
P001	C00D	1.7909(18)	C00H	C011	1.392(3)
P001	C00B	1.7983(19)	C00I	C00Y	1.389(3)
P001	C00C	1.8000(18)	C00J	C00O	1.394(3)
F003	C00U	1.395(2)	C00K	C00V	1.390(3)
F004	C010	1.397(2)	C00L	C00P	1.386(3)
F005	C00S	1.390(2)	C00M	C00X	1.383(3)
F006	C00W	1.400(2)	C00N	C00P	1.383(3)
F007	C00Z	1.396(2)	C00O	C00X	1.387(3)
F008	C013	1.392(2)	C00Q	C00T	1.380(3)
C00A	C00E	1.391(3)	C00Q	C00R	1.391(3)
C00A	C00F	1.407(3)	C00R	C00Y	1.383(3)
C00B	C00I	1.393(3)	C00S	C00Z	1.510(3)
C00B	C00T	1.398(3)	C00S	C00U	1.514(3)
C00C	C00H	1.390(3)	C00U	C00W	1.511(3)
C00C	C00K	1.396(3)	C00V	C012	1.384(3)
C00D	C00J	1.396(3)	C00W	C010	1.512(3)
C00D	C00G	1.401(3)	C00Z	C013	1.512(3)
C00E	C00N	1.384(3)	C010	C013	1.515(3)
C00F	C00L	1.379(3)	C011	C012	1.384(3)

Table S10. Bond angles for shy17098.

Atom	Atom	Atom	Angle/°	Atom	Atom	Atom	Angle/°
C00A	P001	C00D	112.60(8)	C00X	C00O	C00J	120.05(19)
C00A	P001	C00B	106.91(9)	C00N	C00P	C00L	120.15(19)
C00D	P001	C00B	110.95(9)	C00T	C00Q	C00R	120.00(18)
C00A	P001	C00C	109.95(9)	C00Y	C00R	C00Q	119.98(18)
C00D	P001	C00C	107.60(8)	F005	C00S	C00Z	108.69(16)
C00B	P001	C00C	108.78(8)	F005	C00S	C00U	108.58(16)
C00E	C00A	C00F	119.46(18)	C00Z	C00S	C00U	114.35(17)
C00E	C00A	P001	124.22(15)	C00Q	C00T	C00B	120.11(17)
C00F	C00A	P001	116.31(14)	F003	C00U	C00W	109.92(16)
C00I	C00B	C00T	119.87(17)	F003	C00U	C00S	110.65(16)
C00I	C00B	P001	121.52(14)	C00W	C00U	C00S	108.02(16)
C00T	C00B	P001	118.56(14)	C012	C00V	C00K	120.16(19)
C00H	C00C	C00K	120.29(17)	F006	C00W	C00U	109.15(16)
C00H	C00C	P001	121.91(15)	F006	C00W	C010	108.61(16)
C00K	C00C	P001	117.74(14)	C00U	C00W	C010	114.62(17)
C00J	C00D	C00G	120.32(17)	C00M	C00X	C00O	120.92(18)
C00J	C00D	P001	121.66(14)	C00R	C00Y	C00I	120.57(18)
C00G	C00D	P001	117.92(14)	F007	C00Z	C00S	110.13(17)
C00N	C00E	C00A	119.78(18)	F007	C00Z	C013	109.89(17)
C00L	C00F	C00A	120.04(18)	C00S	C00Z	C013	109.74(16)
C00M	C00G	C00D	119.92(19)	F004	C010	C00W	110.84(16)
C00C	C00H	C011	119.90(19)	F004	C010	C013	110.52(17)
C00Y	C00I	C00B	119.46(18)	C00W	C010	C013	108.85(16)
C00O	C00J	C00D	119.05(18)	C012	C011	C00H	119.6(2)
C00V	C00K	C00C	119.36(18)	C011	C012	C00V	120.66(19)
C00F	C00L	C00P	120.06(18)	F008	C013	C00Z	108.73(16)
C00G	C00M	C00X	119.73(19)	F008	C013	C010	108.63(17)
C00P	C00N	C00E	120.51(18)	C00Z	C013	C010	114.32(17)

Table S11. Hydrogen atom coordinates (Å×10^4) and isotropic displacement parameters (Å^2×10^3) for shy17098.

Atom	*x*	*y*	*z*	U(eq)
H00A	1473.2	6132.61	4532.67	63
H00B	2466.79	5446.92	4225.46	63
H00E	1600.97	6951.09	6552.07	34
H00F	4148.73	9442.21	6955.9	35
H00G	-1644.21	7404.27	6846.26	33
H00H	1061.55	10127.92	6059.25	36
H00I	877.9	9655.64	8912.94	34
H00J	-123.57	6616.71	9642.59	34
H00K	-2423.9	8951.01	8497.68	34
H00L	6481.24	9463	5764.66	39
H00M	-3752.67	5977.53	7323.53	39
H00N	3969.99	6977.46	5372.05	38
H00O	-2289.61	5200.15	10110.36	39
H00P	6395.04	8228.15	4976.4	38
H00Q	5547.02	7203.15	10151.74	38
H00R	4964.16	8551.86	10789.05	39
H00S	-1770.72	5484.59	13807.64	38
H00T	3834.51	7093.41	8882.48	35
H00U	-4177.09	6668.74	13702.87	37
H00V	-4178.35	10489.94	7996.29	39
H00W	-1167.94	7398.33	13427.33	39
H00X	-4087.4	4896.48	8952.12	39
H00Y	2640.67	9769.38	10171.09	40
H00Z	-541.36	4980.5	12541.73	42
H010	401.51	8140.42	11918.54	38
H011	-724.3	11657.76	5559.93	43
H012	-3307.18	11837.74	6543.83	43
H013	1069.05	6395.2	12668.36	40

References

S1 M. P. Wiesenfeldt, Z. Nairoukh, W. Li and F. Glorius, *Science*, 2017, **357**, 908-912.

S2 http://supramolecular.org/

S3 D. B. Hibbert and P. Thordarson, *Chem. Commun.*, 2016, **52**, 12792-12805.

S4 V. Dolomanov, L. J. Bourhis, R. J. Gildea, J. A. K. Howard and H. Puschmann, *J. Appl. Cryst.,* 2009, **42**, 339-341.

S5 G. M. Sheldrick, *Acta Cryst.* 2015, **A71**, 3-8.

S6 G. M. Sheldrick, *Acta Cryst*. 2015, **C71**, 3-8.

4.5 Living Supramolecular Polymerization of Fluorinated Cyclohexanes

Shyshov, O., Haridas, S. V., Pesce, L. *et. al.* Living supramolecular polymerization of fluorinated cyclohexanes. *Nat Commun* **12**, 3134 (2021). https://doi.org/10.1038/s41467-021-23370-y

The article is licensed under a Creative Commons Attribution 4.0, https://creativecommons.org/licenses/by/4.0/

Abstract:

The development of powerful methods for living polymerization (LP) has enabled the precise synthesis of covalent block copolymers and has been a key driver of progress in organic materials science. While there have been remarkable reports on living supramolecular polymerization (LSP) recently, the scope of monomers is still narrow and a simple and general solution to the problem is elusive. Here we describe a minimalistic molecular platform for living supramolecular polymerization that is based on the unique structure of all-*cis* 1,2,3,4,5,6-hexafluorocyclohexane, the most polar aliphatic compound reported to date (6.2 Debye). We use this extraordinary dipole moment not only to thermodynamically drive the self-assembly of supramolecular polymers, but also to generate kinetically trapped monomeric states, in which $C_6H_6F_5OR$ derivatives fold onto a tethered amide motif. Upon addition of well-defined seeds, we observe that the dormant monomers engage in a kinetically controlled supramolecular polymerization that is primarily driven by intermolecular dipole-dipole interactions. The obtained polymeric fibers have narrow polydispersity and their length can be controlled by the ratio between seeds and monomers. Atomistic resolution molecular simulations indicate that the fibers have a unique helical structure, in which two molecular stacks combine in such a way that solvophobic interactions are minimized and the two macrodipole moments cancel out. We were able to demonstrate the versatility of our LSP approach by synthesizing supramolecular block copolymers based on different side chains decorating the core structure of our monomers. The all-*cis*-fluorinated cyclohexane motif therefore may become a privileged building block for the synthesis of functional supramolecular materials.

Comments on own contributions:

I had the initial idea to arrange dipole of all-*cis* $C_6H_6F_6$ around a rigid polymer core. Prof. von Delius suggested using instead of covalent core a supramolecular core (e. g. BTA) however gradually I abandoned both approaches and decided to study supramolecular polymerization of all-*cis* $C_6H_6F_6$ derivatives by itself. I discovered folding and conceived the idea to use it for LSP. I designed and supervised all experiments, performed most of the synthetic work (90%) and experimental studies on supramolecular polymerization. I wrote the supporting information, the first draft of the manuscript, and continuously worked on the manuscript refinement during the finalization. V. H. Shyamkumar synthesized $\mathbf{M_5}$ and carried out studies on block copolymers. Dr. Pesce, Dr. Bochicchio and Prof. Pavan carried out computational studies. Dr. Qi and Prof. Kaiser performed TEM studies. Prof. von Delius supervised the project.

nature COMMUNICATIONS

ARTICLE

https://doi.org/10.1038/s41467-021-23370-y OPEN

Living supramolecular polymerization of fluorinated cyclohexanes

Oleksandr Shyshov[1], Shyamkumar Vadakket Haridas[1], Luca Pesce[2], Haoyuan Qi[3,4], Andrea Gardin[5], Davide Bochicchio[2,6], Ute Kaiser[3], Giovanni M. Pavan[2,5✉] & Max von Delius[1✉]

The development of powerful methods for living covalent polymerization has been a key driver of progress in organic materials science. While there have been remarkable reports on living supramolecular polymerization recently, the scope of monomers is still narrow and a simple solution to the problem is elusive. Here we report a minimalistic molecular platform for living supramolecular polymerization that is based on the unique structure of all-cis 1,2,3,4,5,6-hexafluorocyclohexane, the most polar aliphatic compound reported to date. We use this large dipole moment (6.2 Debye) not only to thermodynamically drive the self-assembly of supramolecular polymers, but also to generate kinetically trapped monomeric states. Upon addition of well-defined seeds, we observed that the dormant monomers engage in a kinetically controlled supramolecular polymerization. The obtained nanofibers have an unusual double helical structure and their length can be controlled by the ratio between seeds and monomers. The successful preparation of supramolecular block copolymers demonstrates the versatility of the approach.

[1] Institute of Organic Chemistry, University of Ulm, Ulm, Germany. [2] Department of Innovative Technologies, University of Applied Sciences and Arts of Southern Switzerland, Lugano-Viganello, Switzerland. [3] Central Facility of Electron Microscopy, Electron Microscopy Group of Materials Science, University of Ulm, Ulm, Germany. [4] Center for Advancing Electronics Dresden (cfaed) and Faculty of Chemistry and Food Chemistry, Technical University of Dresden, Dresden, Germany. [5] Department of Applied Science and Technology, Politecnico di Torino, Torino, Italy. [6] Department of Physics, Università degli studi di Genova, Genova, Italy. ✉email: giovanni.pavan@polito.it; max.vondelius@uni-ulm.de

Controlled polymerization methods such as atom transfer radical polymerization[1] have revolutionized polymer chemistry by endowing artificial macromolecules with a degree of structural precision that is only surpassed by biopolymers[2]. By providing facile access to homo- and block copolymers of various composition and topology, living polymerization (LP)[3] has paved the way toward diverse applications in solar cell manufacturing[4], nanophotonics[5] and biomedicine[6]. A similar transformation toward precision materials is currently underway in supramolecular polymer chemistry, a field that is only three decades old[7–9] and increasingly finds applications[10–12]. In 2014, Takeuchi and Sugiyasu reported the first example of living supramolecular polymerization (LSP) based on the aggregation of a porphyrin derivative into metastable nanoparticles that could be converted into thermodynamically more stable nanofibers of relatively precise length by the addition of nanofiber seeds and subsequent kinetically controlled chain-growth[13]. Many recent examples of LSP are based on a similar use of off-pathway aggregates[14], which can be self-assembled from diverse building blocks such as rylene dyes[15–21], (aza)-BODIPY dyes[22,23], N-heteroangulenes[24] and amphiphilic Pt^{II} complexes[25]. Further examples make use of the counter-anion modulated aggregation of Pt^{II} and Pd^{II} pincer-type complexes[26], the coupling of SP with a chemical fuel or light[27–30], the trapping of an active monomer using "dummy" monomers incapable of 1D supramolecular polymerization[31] and the amplification of macrocycles from dynamic combinatorial libraries[32]. Moreover, supramolecular precision materials with remarkable complexity have been obtained via living epitaxial growth[33–44].

However, for LSP to become a general and versatile synthetic method, a simple and minimalistic molecular platform should be developed that is easily functionalized and allows a predictable fine-tuning of LSP characteristics. Arguably, the most important step in this direction would be to avoid off-pathway aggregates and use instead the predictable folding of a monomeric core fragment into a metastable state[45–49]. A breakthrough to this end was recently reported by Aida et al. who have designed a sophisticated C_5-symmetric corannulene derivative that is prevented from spontaneous polymerization by the formation of a network of intramolecular hydrogen bonds within the amide groups of the five side chains[50]. By addition of a molecularly dissolved, *N*-methylated corannulene derivative, the authors were able to initiate LSP and demonstrate control over the length of the formed fibers[51]. When analyzing the design aspects behind this groundbreaking study, one cannot help but notice that the crucial role of the concave corannulene motif, namely to impart directionality to the growing fibers, could perhaps be realized based on a simpler molecular platform. Specifically, it occurred to us that all-cis 1,2,3,4,5,6-hexafluorocyclohexane ($C_6H_6F_6$) with its enormous dipole moment[52], straightforward synthesis[53] and emerging potential as a supramolecular host[54] would be an excellent candidate. Furthermore, theoretical studies predict a large and cooperative enhancement of the dipole moment during aggregation of all-cis $C_6H_6F_6$ into one-dimensional stacks[55]. We wondered whether this cooperativity could be used to drive the formation of thermodynamically stable supramolecular polymers, while the large dipole moment of all-cis $C_6H_6F_6$ (6.2 Debye) could lead to folded, metastable states that would allow us to perform LSP.

In this work we demonstrate that simple derivatives of all-cis 1,2,3,4,5,6-hexafluorocyclohexane (Fig. 1) indeed give rise to LSP and that supramolecular block copolymers can be prepared using this approach. We show that the key monomer is kinetically trapped due to folding and that well-defined seeds initiate the growth of fibers, whose average length can be controlled by the ratio of seeds to monomer (Fig. 1).

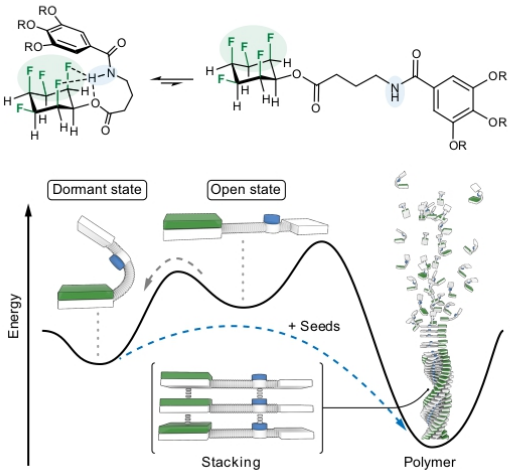

Fig. 1 General structure of monomers and energy landscape of supramolecular polymerization. Top: general molecular design of the key monomer in a representative folded and the unfolded state. Bottom: schematic illustration of the partial energy profile of LSP. Folding of a monomer into dormant states inhibits spontaneous aggregation, whereas seeds can initiate LSP.

Results and discussion

Molecular design and synthesis. Our monomer design is based on all-cis 2,3,4,5,6-pentafluorocyclohexan-1-ol, which is linked via an ester bond, a short alkyl chain and an amide bond to an alkylated derivative of gallic acid that imparts solubility (Fig. 2). Monomer $\mathbf{M_1}$ is achiral, whereas monomers $\mathbf{M_2}$–$\mathbf{M_5}$ bear stereogenic centers (for their synthesis and characterization, see Supplementary Methods), allowing the use of circular dichroism (CD) spectroscopy to study the kinetics of self-assembly.

The synthesis of monomers starts from commercially available pentafluoroanisol, which was hydrogenated according to a procedure reported by Glorius[53] and deprotected to furnish all-cis 2,3,4,5,6-pentafluorocyclohexan-1-ol (Fig. 2). Esterification furnished compounds **2**–**4** quantitatively by reaction with pentafluorophenol-based active esters. The single-crystal X-ray structure of all-cis 2,3,4,5,6-pentafluorocyclohexyl acetate ($\mathbf{Ref_1}$) confirms the equatorial position of the ester group and the all-cis arrangement of the fluorine atoms in compounds of this general structure. Straightforward deprotection and coupling steps gave the desired monomers in good to excellent yields. All reactions were found to be scalable and reproducible, allowing gram-scale syntheses of all monomers reported herein.

During column chromatography of $\mathbf{M_1}$, we observed the formation of thick crystalline fibers on the liquid/air interface (Supplementary Figs. 5–7) inside a test tube. Propagation from the interface into the bulk solution led to complete gelation within 10–15 min (Supplementary Figs. 5, 8), while fiber formation appeared to be initially absent in the bulk solution. This unusual gelation behavior of achiral monomer $\mathbf{M_1}$ was a promising lead result that convinced us to prepare its more soluble, chiral analogue $\mathbf{M_3}$ to study its self-assembly in greater detail.

Monomer folding inhibits spontaneous supramolecular polymerization. Our initial studies on supramolecular polymerization were carried out in a mixture of cyclohexane and chloroform

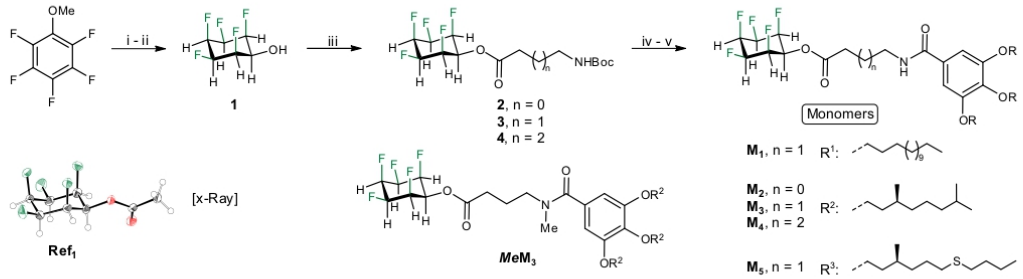

Fig. 2 Synthesis of compounds used in this study. Conditions: (i) Rh(CAAC)(COD)Cl, SiO_2, H_2 (80 atm.), n-hexane, r.t., 24 h;[53] (ii) n-BuSH, $AlCl_3$, CH_2Cl_2, r.t., 12 h, 83%; (iii) **S1**–**S3**, DMF, Et_3N, 120 °C, 2 h, 92–100%; (iv) TFA, CH_2Cl_2, r.t., 2 h; (v) **2**–**4**, DMF, Et_3N, room temperature, 12 h, 23–87%. Color code: green: F; red: O; gray: C.

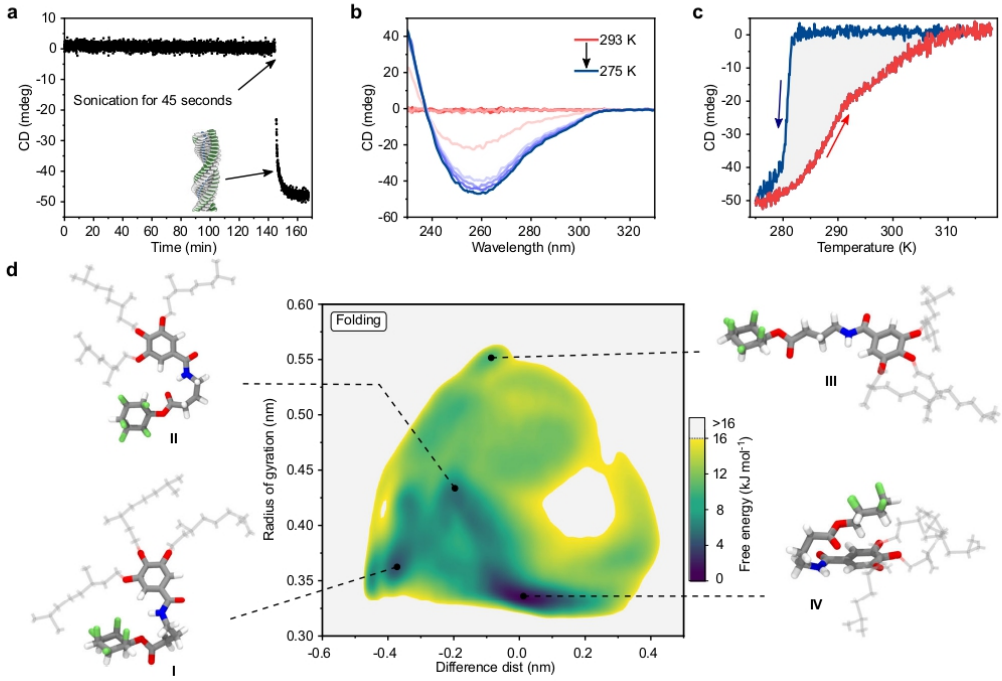

Fig. 3 Studies on monomer folding. a CD monitoring (260 nm) of $\mathbf{M_3}$ (1.2 mM) in cyclohexane/chloroform (84:16 v/v) at 293 K, indicating remarkable kinetic stability. **b** Temperature-dependent CD spectra of $\mathbf{M_3}$ (1.2 mM) in cyclohexane/chloroform (84:16 v/v) upon cooling from 293 K to 275 K (0.5 K min^{-1}). **c** CD monitoring (260 nm) of cooling (blue) and heating (red) of a 1.2 mM solution of $\mathbf{M_3}$ in cyclohexane/chloroform (84:16 v/v) at a rate of 0.5 K min^{-1}. Once nucleation starts in a concentrated solution at temperatures for which ΔG is already negative, polymerization proceeds very rapidly since the concentration of free monomer in solution is high, leading to a very sharp transition during cooling (blue line). **d** Free energy surface (FES) estimated from WT-MetaD simulations, showing monomer conformations and their relative free energies as a function of collective variables CV1 (*x*-axis: difference between the distance between pentafluorocyclohexyl-Hs and the amide oxygen and the distance between the pentafluorocyclohexyl-Fs and the amide nitrogen) and CV2 (*y*-axis: radius of gyration of $\mathbf{M_3}$ monomer core). Blue colored areas represent the low free energy domains while the gray colored background is high in free energy or not accessible. Four representative monomer conformations (I, II, III, IV) taken from the FES are reported (alkyl chains are shown in transparency for clarity). Color code: green: F; red: O; blue: N; gray: C.

(84:16 v/v, standard solvent) because time-dependent CD measurements of a 1.2 mM solution of $\mathbf{M_3}$ at 293K, revealed that in this medium, $\mathbf{M_3}$ is remarkably kinetically persistent and remains molecularly dissolved for hours. However, ultrasonication for 45 s induces polymerization (Fig. 3a), forming a clear viscous solution. Slow cooling (0.5 K min^{-1}) of a 1.2 mM solution of $\mathbf{M_3}$ resulted in a pronounced negative Cotton effect with an absorption maximum at 260 nm, indicating the formation of chiral supramolecular aggregates (Fig. 3b). The transition from the dissolved to the polymerized state occurs abruptly with an elongation

temperate (T_e) of 282K. The AFM height image of a cooled (275K) solution of $\mathbf{M_3}$ spin-coated on a silicon wafer reveals a dense fibrous network (Supplementary Fig. 7). No evidence for supramolecular aggregates was observed when an analogous study was carried out with reference compounds $\mathbf{Ref_2}$ (conventional cyclohexane) and $\boldsymbol{Me}\mathbf{M_3}$ (methylated amide), indicating that both the all-cis $C_6H_6F_5$ motif and the amide bond are crucial for supramolecular polymerization (Supplementary Fig. 9).

Variable temperature CD measurements of $\mathbf{M_3}$ at slow cooling and heating rates (0.5 K min^{-1}) revealed pronounced hysteresis (Fig. 3c). For monomer $\mathbf{M_2}$, in which only two methylene groups separate all-cis $C_6H_6F_5$ and the amide bond, hysteresis was also observed but the T_e during cooling was 11 K higher (Supplementary Fig. 10), while for monomer $\mathbf{M_4}$ hysteresis was negligible and oligomeric species were observed already at 328 K (Supplementary Fig. 10). The observation of hysteresis and the distinct differences observed for $\mathbf{M_2}$, $\mathbf{M_3}$, and $\mathbf{M_4}$ can be explained by the varying ability of these monomers to form intramolecular interactions such as hydrogen bonds[56], whose strength should heavily depend on the length of the spacer.

We therefore proceeded to gather experimental and computational evidence for monomer folding. First, we investigated whether the kinetic stability of $\mathbf{M_3}$ (Fig. 3a) may be a result of intramolecular interactions by studying the kinetics of the polymerization at different concentrations at a constant temperature of 293 K. At all concentrations studied, we observed sigmoidal kinetic curves with lag times decreasing upon increasing concentration of $\mathbf{M_3}$ (Supplementary Fig. 11). DLS analyses performed on 1.2 mM solution of $\mathbf{M_3}$ in the solvent mixture used for kinetic studies (cyclohexane/chloroform 84:16 v/v) displayed a unimodal scattering peak with a hydrodynamic diameter of ~ 1.1 nm (Supplementary Fig. 12). The diffusion-ordered spectroscopy (DOSY) of $\mathbf{M_3}$ (1.2 mM in $C_6D_{12}/CDCl_3$ 84:16 v/v at 295 K) provided a diffusion coefficient similar to non-assembling and non-folding reference compound $\mathbf{Ref_2}$ (Supplementary Figs. 13, 14). While these results clearly indicate that no off-pathway aggregates are involved, we also attempted to study folding more directly by variable temperature ^{1}H NMR spectroscopy. To this end, a 1.2 mM solution of $\mathbf{M_3}$ in $C_6D_{12}/CDCl_3$ (84:16 v/v) was cooled from 333 to 283 K, revealing a strong temperature-dependence of the chemical shift of the amide and aromatic protons, which is in agreement with the expected temperature-dependence of the equilibrium between unfolded and folded states (Supplementary Figs. 15, 16). In a ^{19}F/^{1}H-HOESY NMR experiment on $\mathbf{M_1}$ in 30 mM solution ($CDCl_3$), we observed weak ^{19}F/^{1}H NOE of two fluorine atoms in all-cis $C_6H_6F_5$ with both amide and aromatic protons (Supplementary Fig. 18). Fourier-transform infrared spectral measurement (FT-IR) performed with 1.2 mM solution of $\mathbf{M_3}$ $C_6H_{12}/CHCl_3$ (84:16 v/v) revealed no presence of stretching frequency corresponding to hydrogen-bonded amide hydrogens but small shifts of amide I band which could be attributed to the formation of CH···π interactions between all-cis $C_6H_6F_5$ and aromatic ring (Supplementary Figs. 23, 24). Combined HOESY and FTIR results confirm that folding is indeed present but likely not limited to a single structure and conventional C=O···H–N intramolecular hydrogen bond.

To gain a deeper understanding of monomer folding, we carried out all-atom well-tempered metadynamics (WT-MetaD)[57] simulations of $\mathbf{M_3}$ in explicit solvent molecules ($C_6H_{12}/CHCl_3$ in the ratio of 84:16 v/v; see Supplementary Methods for more details). These simulations allowed us to compute the free energy surface (FES) of the monomer folding/unfolding (Fig. 3d). The conformations accessible to the monomer are identified in the FES as a function of the two collective variables (CV1 and CV2) used during the WT-MetaD: CV1 represents the orientation of pentafluorocyclohexyl with respect to the amide-carbonyl group (Supplementary Fig. 25c), and CV2 is indicative of the opening of the monomer "core" (Supplementary Fig. 25b). The FES shows that the monomer $\mathbf{M_3}$ tends to assume a folded conformation (Fig. 3d: dark blue region characterized by low CV2 values), in which the hydrogen atoms of pentafluorocyclohexyl are close to the benzene moiety (Fig. 3d: IV conformer)[58]. Other (less) energetically accessible conformations (within ~5 kJ/mol from the global free energy minimum) are favored either by the interaction of the fluorine atoms with the amide-H (Fig. 3d: I conformer) or by the formation of a hydrogen bond with the carbonyl group (II conformer). Similar analyses were performed on $\mathbf{M_2}$, $\mathbf{M_4}$ and $\boldsymbol{Me}\mathbf{M_3}$ (Supplementary Fig. 26), showing that for $\mathbf{M_2}$ and $\boldsymbol{Me}\mathbf{M_3}$ the opening of the monomer is much more likely than for $\mathbf{M_3}$ and $\mathbf{M_4}$.

Living supramolecular polymerization. Having gained an understanding of the folding of monomer $\mathbf{M_3}$ into kinetically trapped states, we proceeded to test whether we could use this molecular property to facilitate LSP. Initially, we attempted to use the *N*-methylated analogue $\boldsymbol{Me}\mathbf{M_3}$ as a molecular initiator based on the assumption that it is less prone to folding, but could interact with $\mathbf{M_3}$ in a way that triggers unidirectional polymerization[51]. While this initiation mode was not successful, we were able to develop a protocol that makes use of well-defined seeds to trigger LSP. $\mathbf{M_3^{Seed}}$ was prepared by sonication of a mixture of $\mathbf{M_3}$ and $\boldsymbol{Me}\mathbf{M_3}$ ($c_{tot} = 1.2$ mM, $\mathbf{M_3}/\boldsymbol{Me}\mathbf{M_3} = 3{:}1$ mol/mol) in standard solvent at 273 K for 20 min (Fig. 4b). In the absence of $\boldsymbol{Me}\mathbf{M_3}$, we obtained longer, non-uniform fibers (Supplementary Fig. 27) that have a higher tendency to bundle and which induce polymerization with decreased reproducibility and higher polydispersity (Supplementary Fig. 30). Based on the effect that the $\mathbf{M_3}/\boldsymbol{Me}\mathbf{M_3}$ ratio has on the size of seeds (Supplementary Figs. 27, 28) we propose that $\boldsymbol{Me}\mathbf{M_3}$ acts as a sequestrator[59] that competitively interacts with $\mathbf{M_3}$ and therefore reduces the available amount of $\mathbf{M_3}$ that can be incorporated into polymer chains. The sequestrator $\boldsymbol{Me}\mathbf{M_3}$ thus lowers the degree of polymerization, which results in a more effective size control during seed formation (Supplementary Discussion). This optimized procedure allowed us to prepare $\mathbf{M_3^{Seed}}$ fibers with a weight-averaged length (L_w) of 83 nm and a polydispersity index (PDI) of ca. 1.2 (Fig. 4b, c). When we added different volumes of the $\mathbf{M_3^{Seed}}$ solution ($[\mathbf{M_3}]/[\mathbf{M_3^{Seed}}]$: 50:1, 100:1, 150:1 and 200:1 volume ratios) to a solution of $\mathbf{M_3}$ (1.2 mM, 293 K), polymerization started without lag time and was complete within 2–15 min (Fig. 4d). The crucial plot shown in Fig. 4e confirms that the logarithm of the apparent polymerization rate ($\log(-d\theta/dt)$) is directly proportional to the logarithmic amount of $\mathbf{M_3^{Seed}}$ initiator, which is expected for a well-behaved chain-growth polymerization.

The size distributions of supramolecular polymers prepared by seeded LSP were determined by atomic force microscopy (AFM) under carefully optimized conditions (Fig. 4f). The obtained AFM images revealed individual, uniform, separate fibers, alongside bundles, which could however clearly be distinguished based on image contrast and AFM height profile (Fig. 3g). Weight-averaged lengths (L_w) of 955, 665, 499, and 317 nm, could be determined for individual fibers prepared from $[\mathbf{M_3}]/[\mathbf{M_3^{Seed}}]$ ratios of 3:1, 5:1, 7:1 and 10:1 (v/v), respectively (Fig. 4g, h and Supplementary Fig. 33). The linearity of the plot of fiber length versus $[\mathbf{M_3}]/[\mathbf{M_3^{Seed}}]$ (Fig. 4f) provides further evidence for the living nature of the observed polymerization. When using a $[\mathbf{M_3}]/[\mathbf{M_3^{Seed}}]$ ratio of 20:1 we observed polymers with a length of ca. 1–3 µm, whose bundling precluded reliable statistical AFM analyses (Supplementary Fig. 34). Further increase of $\mathbf{M_3}/\mathbf{M_3^{Seed}}$

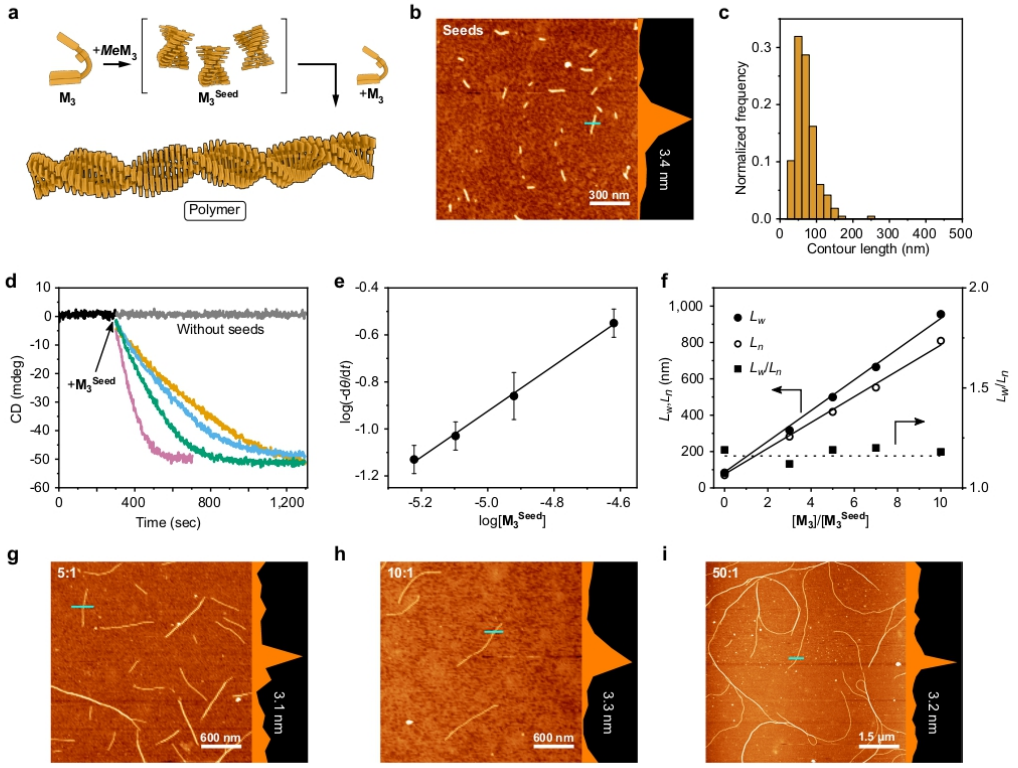

Fig. 4 Living supramolecular polymerization. a Schematic illustration of seeded living supramolecular polymerization. **b** AFM height image of $\mathbf{M_3^{Seed}}$ spin-coated on a silicon wafer. Cross-section was measured along the blue line. **c** Histogram of the length distribution of $\mathbf{M_3^{Seed}}$. **d** Time course of supramolecular polymerization of $\mathbf{M_3}$ initiated by addition of different amounts of $\mathbf{M_3^{Seed}}$ ($[\mathbf{M_3}]/[\mathbf{M_3^{Seed}}] = 50{:}1$ (pink curve), 100:1 (green curve), 150:1 (blue curve), 200:1 (yellow curve) v/v). **e** Log-log plot of the rate of polymerization as a function of $\mathbf{M_3^{Seed}}$ concentration. Error bars correspond to one standard deviation of a triplicate measurement. Solid line – linear fit with slope 0.97 (correlation coefficient 0.998). **f** Weight-average length (L_w), number-average length (L_n) and PDI (L_w/L_n) obtained by measuring AFM length of supramolecular polymers obtained with different $[\mathbf{M_3}]/[\mathbf{M_3^{Seed}}]$ ratios (3:1, 5:1, 7:1, 10:1 v/v) plotted against $[\mathbf{M_3}]/[\mathbf{M_3^{Seed}}]$ v/v. Solid lines represent linear fit (correlation coefficients 0.995) indicating linear dependence of the size of supramolecular polymers on the amount of $\mathbf{M_3^{Seed}}$ added. Dashed line serves as guide for the eye. **g–i** Representative AFM height images of supramolecular polymers obtained with different $[\mathbf{M_3}]/[\mathbf{M_3^{Seed}}]$ ratios ((**g**) 5:1, (**h**) 10:1, (**i**) 50:1 v/v) spin-coated on silicon wafer.

to 50:1 led to the formation of even longer fibers (Fig. 4i). In all cases that allowed reliable statistical analyses, the PDI was below 1.2 (Supplementary Fig. 35 and Supplementary Table 1). Polymer chains remain active and continue to elongate upon addition of $\mathbf{M_3}$, as was demonstrated in multicycle dilution CD experiments.

Supramolecular block copolymers. We wondered whether it would be possible to carry out kinetically controlled LSP of monomers with different side chains. This approach would be reminiscent of the living chain-growth polymerization of acrylates, where a molecule of interest is attached to an acrylate or acrylamide that undergoes living covalent polymerization. Instead of acrylates we would rely on all-cis 2,3,4,5,6-pentafluorocyclohexyl 4-amidobutanoates, which represent the core structure facilitating LSP, as was demonstrated above.

While there has been remarkable progress recently with preparing supramolecular block copolymers under thermodynamic control[60–62] or by slow cooling of monomer mixtures[63–65], a growing number of such precision polymers has been prepared by LSP, which can provide superior structural and sequence control. However to date, these LSP approaches either rely on the modification of the polymerizable core, e.g., substituents are attached to the core of rylene dyes[16,66] or the complexation of different metal ions to identical ligands[67,68]. A modular approach based on the variation of the side chain, as pioneered by Otto, Faul, Manners and Sugiyasu[19,32,69], would be complementary to these methods and could offer distinct advantages for applications in organic materials science. For obtaining a proof of principle, we decided to introduce a structural change to the aliphatic side chains in $\mathbf{M_3}$. Keeping the crucial design elements for LSP as well as the aromatic core and the stereogenic centres in place should allow us to use the same analytical techniques and correlate the observed data with $\mathbf{M_3^{Polymer}}$. Based on this reasoning, we prepared monomer $\mathbf{M_5}$, which contains three thiobutyl group instead of isopropyl groups (Fig. 2). When performing LSP with this monomer, we were delighted to find that this considerable structural change (insertion of a heteroatom, side chain elongation and removal of a branching point) did not significantly affect the polymerization behavior. In general,

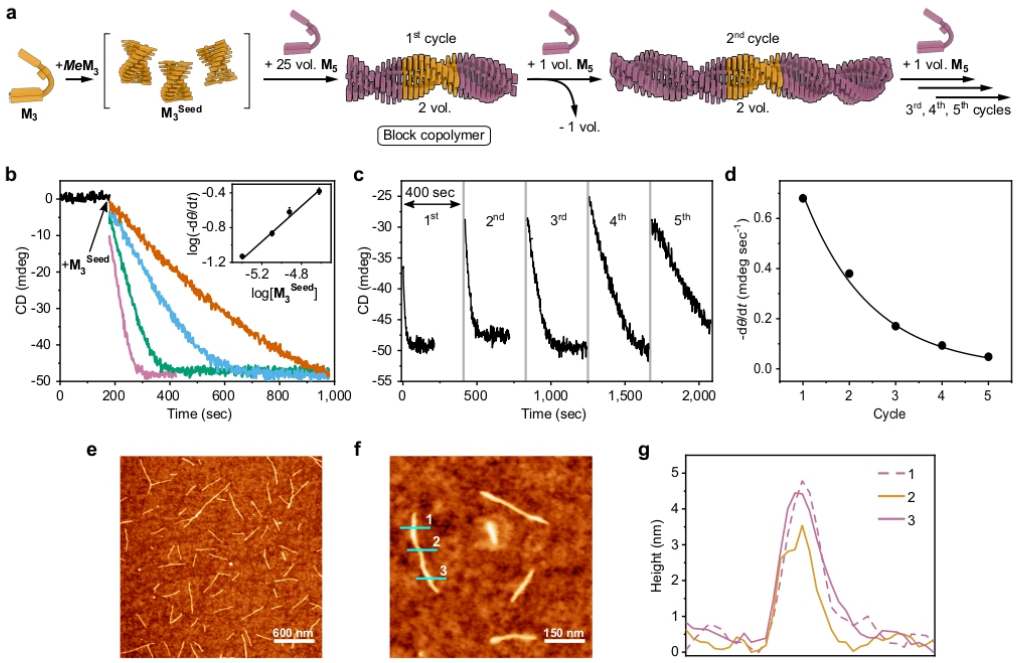

Fig. 5 Supramolecular block copolymers. a Schematic illustration of the synthesis of block copolymers by seeded LSP in a multicycle kinetic experiment. **b** Time course of supramolecular polymerization of $\mathbf{M_5}$ initiated by addition of different amounts of $\mathbf{M_3^{Seed}}$. $[\mathbf{M_5}]/[\mathbf{M_3^{Seed}}] = 50{:}1$ (pink curve), 100:1 (green curve), 150/1 (blue curve), 300:1 (orange curve) v/v. Inset shows log-log plot of the rate of polymerization as a function of $\mathbf{M_3^{Seed}}$ concentration. Error bars correspond to one standard deviation of a triplicate measurement. Solid line corresponds to linear fit with slope 1.02 (correlation coefficient 0.987). **c** Time course of change of the CD signal at 260 nm, while $\mathbf{M_5}$-$\mathbf{M_3}$-$\mathbf{M_5}$ supramolecular block copolymer obtained using $[\mathbf{M_5}]/[\mathbf{M_3^{Seed}}] = 25{:}1$ ratio (1st cycle), was diluted with $\mathbf{M_5}$ over five cycles. Polymerization continues upon each addition of $\mathbf{M_5}$ but at increasingly slower rate. **d** Plot of initial slopes (sec^{-1}) as a function of the cycle number. Solid line corresponds to exponential fit, demonstrating bisection of the slope during each cycle. **e** Representative AFM height image of $\mathbf{M_5}$-$\mathbf{M_3}$-$\mathbf{M_5}$ supramolecular block copolymers obtained using $[\mathbf{M_5}]/[\mathbf{M_3^{Seed}}] = 3{:}1$ ratio, spin-coated on silicon wafer. **f**, **g** AFM height image and cross-section analyses along the blue lines demonstrating the presence of thicker termini, corresponding to $\mathbf{M_5}$ block, and thinner middle part, corresponding to $\mathbf{M_3}$ block.

$\mathbf{M_5}$ behaved similarly to $\mathbf{M_3}$, while it is kinetically more stable, such that a solution of $\mathbf{M_5}$ (1.2 mM, $C_6H_{12}/CHCl_3$ 84:16 v/v) starts to polymerize only after prolonged ultrasonication (>7 min at RT). Therefore, we decided to decrease the polarity of our solvent mixture for the following block copolymer syntheses by increasing the volume fraction of cyclohexane to 93% (Supplementary Fig. 37).

To prepare an ABA type block copolymer we used $\mathbf{M_3^{Seed}}$ polymer (golden, Fig. 5a) to initiate the supramolecular polymerization of the sulfur-containing monomer $\mathbf{M_5}$ (pink, Fig. 5a). CD spectroscopy revealed polymerization kinetics similar to those observed for LSP of $\mathbf{M_3}$ (Fig. 5b). Polymerization of $\mathbf{M_5}$ starts without lag time with rates proportional to the amount of $\mathbf{M_3^{Seed}}$ added (Fig. 5b, inset), indicating that the chain-growth mechanism is preserved. The average length of fibers observed by AFM and the calculated PDI of $\mathbf{M_5}$-$\mathbf{M_3}$-$\mathbf{M_5}$ supramolecular polymers obtained with 3:1 and 5:1 $[\mathbf{M_5}]/[\mathbf{M_3^{Seed}}]$ ratios perfectly matched the results observed for the corresponding $\mathbf{M_3}$ homopolymer (Supplementary Fig. 35).

To demonstrate that chain fragmentation does not occur during copolymerization, which is a prerequisite for sequence control in the block copolymer, we performed a multicycle kinetic experiment (Fig. 5c)[70]. First, we prepared an $\mathbf{M_5}$-$\mathbf{M_3}$-$\mathbf{M_5}$ block copolymer using a $[\mathbf{M_5}]/[\mathbf{M_3^{Seed}}]$ ratio of 25:1 and followed the time-course of polymerization by CD spectroscopy. We then took half of the obtained solution and added an identical volume of $\mathbf{M_5}$ (1.2 mM, $C_6H_{12}/CHCl_3$ 93:7 v/v) (Fig. 5a). As expected, the "living" supramolecular block copolymer resumed elongation after the addition of fresh monomer. To be able to draw conclusions from the reaction kinetics, we repeated this combined monomer addition and dilution experiment for three more cycles. We found that after each dilution cycle the rate of polymerization was reduced by half, which is consistent with the fact that the initial concentration of active termini $\mathbf{M_3^{Seed}}$ was decreased by a factor of two after each dilution cycle. The initial slopes of the polymerization kinetics could be fitted according to the equation $y = 0.7(1/2)^{n-1}$, where n is the number of cycles (Fig. 4d), providing a solid confirmation for the absence of fragmentation during LSP. Importantly, AFM analyses revealed elongation of $\mathbf{M_5}$-$\mathbf{M_3}$-$\mathbf{M_5}$ block copolymer upon addition of fresh feed of $\mathbf{M_3}$ further corroborating the "living" nature of supramolecular polymerization (Supplementary Figs. 40, 41). Finally, we were able to directly visualize supramolecular block copolymers by AFM. Height profiles along the fibers of $\mathbf{M_5}$-$\mathbf{M_3}$-$\mathbf{M_5}$ supramolecular copolymers revealed the presence of thinner middle parts with z-displacement of ca. 3.0–3.4 nm (Fig. 5f, g), which is in excellent agreement for the observed fiber width observed for the $\mathbf{M_3}$ homopolymer. The thicker termini, on the other hand,

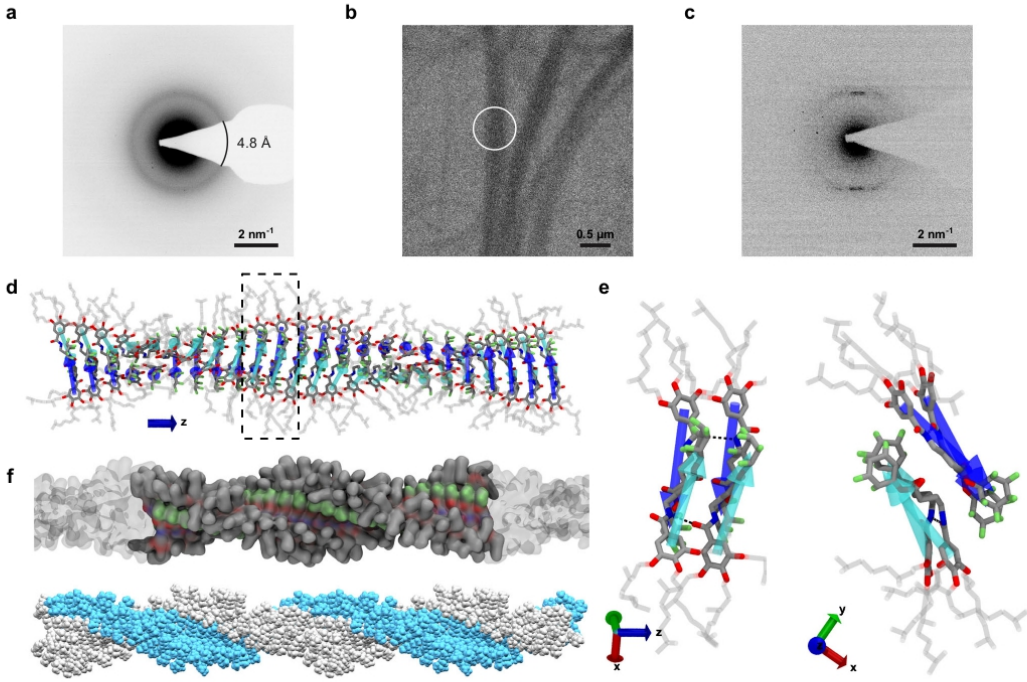

Fig. 6 Structure of the fibers. a Electron diffraction pattern of the organic fibers under low-dose conditions (electron dose: 0.45 $e^-/Å^2$). The diameter of the illuminated area was c.a. 5 µm. The diffraction ring is located at 2.1 nm^{-1}, corresponding to a lattice spacing of 4.8 Å. **b** Bright-field TEM image showing several bundles of the organic fibers. The circle indicates the position of the selected-area aperture with a diameter of 0.7 µm. **c** Selected-area electron diffraction pattern acquired from the circular region in (**b**) with an electron dose of 0.12 $e^-/Å^2$. **d** Atomistic detail of the monomer arrangement in the helix structure—blue and cyan arrows connecting the benzene (tail) to the pentafluorocyclohexyl groups (head). Color code: green: F; red: O; blue: N; gray: C. **e** Details of the side (left) and the top (right) views of the arrangement of four $\mathbf{M_3}$ in the helix (monomers within the black rectangle in **d**). H-bonds between the monomers are shown as dashed black lines. **f** Top: equilibrated snapshot of a $\mathbf{M_3}$ pre-assembled fiber after 1 µs of MD simulation. The system corresponds to a full helical turn with a pitch of ~12 nm (opaque), forming an infinite helicoidal fiber through the periodic boundaries (periodic images shown in transparency). Bottom: space-filling model of $\mathbf{M_3}$ polymer demonstrating relative arrangement of two monomer stacks (gray and blue).

displayed a z-displacement of ca. 4.1–4.5 nm, which corresponds to the average fiber width observed for the $\mathbf{M_5}$ homopolymer (Supplementary Figs. 42, 43).

Structure of the fibers. Having demonstrated how LSP allows us to control the length of well-defined fibers, we set out to understand the structure of these self-assemblies. In AFM images of $\mathbf{M_3}^{\mathbf{Polymer}}$ (Fig. 4b, g, h, i) we observed individual fibers with a height profile of ca. 3.1 nm. The diameter of the fibers is therefore significantly larger than the calculated length of monomer $\mathbf{M_3}$ (ca. 2.3 nm), suggesting that several one-dimensional filaments combine to form the final structure. In the ATR-IR spectrum of $\mathbf{M_3}^{\mathbf{Polymer}}$, we observed characteristic stretching frequencies for hydrogen-bonded amides at 3302 cm^{-1} and 1633 cm^{-1} as well as an intense C – F stretching band at 1018 cm^{-1}, that is not present in non-polymerizable $\mathbf{MeM_3}$ (Supplementary Figs. 44, 45). Analysis of the crystal structure of precursor compound **2** revealed that in the solid state this compound class stacks via dipole-dipole interactions between all-cis $C_6H_6F_5$ groups, and hydrogen bonding between carbamates (Supplementary Fig. 57). Most importantly, the crystal packing features pairs of neighboring stacks, which are arranged in an antiparallel fashion, which presumably serves to cancel the large macrodipoles. Taken together, we conclude from this data that the polymer contains separate stacks of the self-complementary all-cis $C_6H_6F_5$ (dipole-dipole) and amide (H bonding) motifs.

To probe the crystallinity of the organic fibers, we performed electron diffraction using transmission electron microscopy (TEM) on a circular region with a diameter of ca. 5 µm. A diffraction ring is clearly visible (Fig. 6a), unambiguously demonstrating the long-range order within the organic fibers. The radial-integrated intensity profile of the diffraction pattern (Supplementary Fig. 46) reveals a lattice distance of 4.8 Å. By correlating the fiber morphology (Fig. 6b) with the selected-area electron diffraction pattern (Fig. 6c), we found that the direction of the Bragg reflections coincides with the long axis of the organic fibers; the molecular stacking direction is parallel to the fiber elongation direction, leading to the significant size anisotropy of the organic fibers. The too high sensitivity toward electron irradiation precluded further structural elucidation via high-resolution TEM imaging (Supplementary Fig. 47).

As experimentally observed, the formation of fibers is a complex process, which is challenging to investigate in silico at the molecular level. By running MD simulations of a molecular system containing 150 initially disassembled $\mathbf{M_3}$ monomers, we could observe that the free energy barrier for $\mathbf{M_3}$ folding-unfolding can be effectively crossed (unfolding), while this event

may be facilitated when several monomers interact non-covalently. This indicates that the monomers can efficiently explore the previously discussed FES (Fig. 3d) during self-assembly (Supplementary Fig. 48a). Although the formation of persistent ordered assemblies could not be observed during classical MD simulations, we could obtain important qualitative insights into the key monomer-monomer interactions during the polymerization process. Especially, the inter-monomer H-bonding between amide-carbonyl groups and the stacking of the pentafluorocyclohexanes emerge as dominant interactions (Supplementary Fig. 48b). In order to study the assembly of (unfolded) $\mathbf{M_3}$ into fibers, we tested two possible self-assembled configurations, where the $\mathbf{M_3}$ monomers are respectively arranged into stacks in parallel or antiparallel fashion. We then compared these fibers' structures from the point of view of their dynamic stability. A parallel axial $\mathbf{M_3}$ stacking is stabilized by the H-bonds between the monomers and the dipole-dipole interactions between the pentafluorocyclohexane dipoles. However, the solvophilic properties of such a parallel stack are not well balanced, because the resulting assembly has an implicit amphiphilic character, with all solvophilic tails oriented on one side and all solvophobic heads on the other side. An antiparallel axial $\mathbf{M_3}$ stacking still allows for a favorable hydrogen-bonding between the monomers while at the same time it guarantees a more uniform solvophilicity of the fiber. In both cases, single filaments were found unstable in the solvent during MD simulations. This suggested that higher scale self-assembly of these into hierarchical fibers composed of multiple filaments is a likely event, consistent with experimental evidence obtained by AFM (vide supra).

We investigated various possible hierarchical arrangements of $\mathbf{M_3}$ stacks. The configuration that demonstrated the highest stability is that reported in Fig. 6, where two antiparallel $\mathbf{M_3}$ stacks (blue and cyan arrows in Fig. 6d) combine to form a helical superstructure. This proposed structure for the assembly is stabilized via H-bonds between the amides and stacking of pentafluorocyclohexane dipoles (Fig. 6e), while at the same time providing an optimized interaction with the solvent (and conceptually the cancellation of the two macrodipole moments). Preformed antiparallel $\mathbf{M_3}$ stacks were seen to torque spontaneously during MD simulations in the solvent. Deeper modeling studies demonstrated that the most favorable tilting angle corresponds to a helical pitch of ~10–15 nm. Such $\mathbf{M_3}$ helices were found stable for over 1 μs of MD simulation (Supplementary Fig. 49b–d). The equilibrated helix structure has an average diameter consistent with that measured experimentally (Supplementary Fig. 50: ~3.1 nm). Within the equilibrated helix, the stacking distance between the antiparallel $\mathbf{M_3}$ dimers is ~5 Å, which is in very good agreement with the ~4.8 Å determined experimentally (Fig. 6a, c).

Starting from our $\mathbf{M_3}$ fiber model, we conducted an analogous investigation on a $\mathbf{M_5}$ homopolymer model (Supplementary Fig. 51). Also in this case, the $\mathbf{M_5}$ fiber model showed high stability during 1 μs of MD simulation. The equilibrated $\mathbf{M_5}$ fiber model showed a helical pitch of ~10–15 nm, and overall similar structure to that of $\mathbf{M_3}$ fiber. Next, we built $\mathbf{M_3}$-$\mathbf{M_5}$ copolymer models that we compared between them, and with the $\mathbf{M_3}$ and $\mathbf{M_5}$ homopolymers. In particular, we compared three copolymer models starting from a helical conformation with 12 nm of pitch, where 48 monomers of $\mathbf{M_3}$ and 48 monomers of $\mathbf{M_5}$ are arranged into segregated Blocks (Fig. 7a, top), into segregated intertwining Columns (Fig. 7a, middle), or are distributed in Random fashion in the copolymer (Fig. 7a, bottom). All three copolymer models were pre-equilibrated and simulated via 1 μs of MD. We calculated the monomer-monomer interaction energies between the monomers in the copolymer structures, and compared these with the energy of the same number of $\mathbf{M_3}$ and $\mathbf{M_5}$ monomers separated into two $\mathbf{M_3}$ and $\mathbf{M_5}$ homopolymers. While $\Delta E > 0$ values indicate that from an energetic point of view the intermixing of monomers is unfavored, such event is favored entropically in the real system. In particular, monomer mixing in Blocks configuration shows a very similar energy than two separated $\mathbf{M_3}$ and $\mathbf{M_5}$ homopolymers ($\Delta E = +0.34$ kcal/mol), while mixing them in Columns or Random fashion appears to be more energetically unfavorable (ΔE of $+1.84$ and $+2.72$ kcal/mol respectively). However, it is worth noting that these ΔE values (expressed per $\mathbf{M_3}$-$\mathbf{M_5}$ couple) are quite small. This suggests that in this case the entropic tendency to $\mathbf{M_3}$-$\mathbf{M_5}$ mixing is dominant during self-assembly, and that in the real systems the monomers likely intermix in the fibers in a more/less blocky/random fashion. On the contrary, a complete segregation in separated $\mathbf{M_3}$ and $\mathbf{M_5}$ homopolymers, as well as a homogeneous 1:1 $\mathbf{M_3}$: $\mathbf{M_5}$ intermixing in the fibers appear to be unfavorable from the entropic point of view.

From a structural point of view, comparing the behavior of the fibers during the MD runs we observed that the Blocks model is more persistent than the Columns and Random models. Shown in Fig. 7b, the Blocks preserves the starting fiber length (green), while the random fiber evolves toward a more distorted/bent conformation (purple). To gain a deeper knowledge on the internal structural dynamics of these assemblies, we used a high-dimensional analysis based on the Smooth Overlap of Atomic Position (SOAP) vectors[71], as agnostic fingerprints capable of capturing structural and dynamic differences/similarities in the atomic environments in supramolecular polymers[72,73] and soft complex molecular systems[74]. We use a set of five SOAP centers in the $\mathbf{M_3}$ and $\mathbf{M_5}$ monomers in the fiber models (Supplementary Fig. 52), one in the center of the fluorinated ring, one in the amide, and three in the terminal alkyl groups of the monomers (details in Supplementary Information). The SOAP analysis allowed us to classify the local environments that surround these sites based on their local structural and dynamic features. We use a Principal Component Analysis (PCA) to reduce the dimensionality of the SOAP vectors (Fig. 7d: PCA projections along the first two PCA components, PC1 and PC2, for all simulated systems). In particular, the first three components of the PCA retain up to 86% of the system fluctuations/complexity, and were used for the analyses.). We used the Probabilistic Analysis of Molecular Motifs (PAMM)[72,75] unsupervised clustering method to identify the dominant macroclusters in the systems: different colors in the PCAs of Fig. 7e indicate structurally/dynamically different domains/motifs within the assembly as identified by the PAMM-SOAP analysis. By coloring the beads accounted in the SOAP analysis based on the clusters to which these belong (Fig. 7e), we can observe that the red and blue colored clusters correspond to the cyclohexane ring and to the amide respectively (see also Fig. 7c). The other three clusters (Fig. 7e: gray, cyan and green) correspond to the tails of the monomers, and to the surface of the fibers (see Fig. 7c). Performing the SOAP-PAMM analysis on the second half of the MD trajectories sampled every 100 ps allows us monitor the transitions of the sites between different clusters (dynamic change of colors). From the frequency of these transitions, we can then estimate transition probabilities (Fig. 7f: which divided by the time-lapse between the analyzed MD snapshots, provide the transition rates), which are indicative of the dynamics of the different domains within the fibers. This analysis demonstrates how in the time explored by the MD simulations the core of the fibers is substantially static compared to the fibers' surface. In fact, the absence of arrows between the red and blue macroclusters of Fig. 7f indicates that the domains of the stacked fluorinated cyclohexanes and of the amide groups is very persistent and quite static. On the other hand, the dynamic

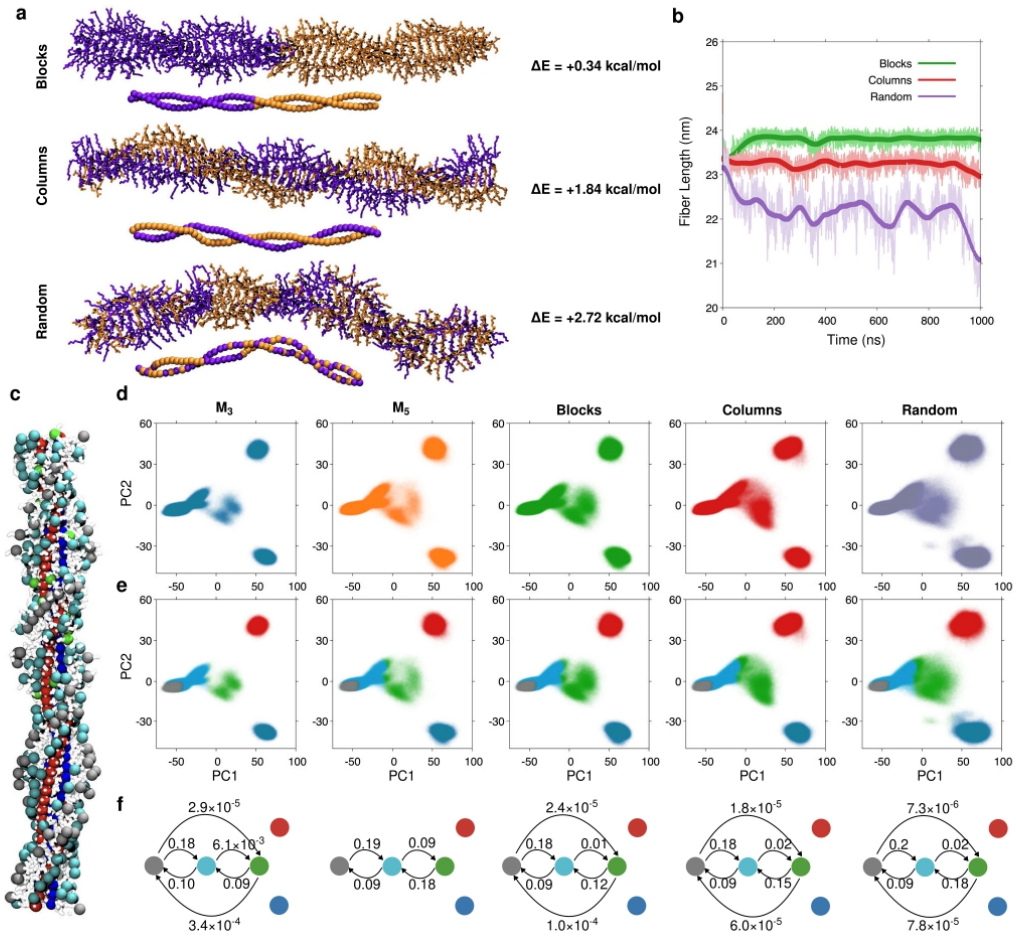

Fig. 7 Structure and dynamics of supramolecular block copolymers. a Equilibrated MD snapshots of $\mathbf{M_3}$-$\mathbf{M_5}$ copolymers models where the $\mathbf{M_3}$ (in orange) and $\mathbf{M_5}$ monomers (violet) are arranged in blocks (top), into segregated $\mathbf{M_3}$ and $\mathbf{M_5}$ intertwining columns (middle), or randomly mixed in the fiber (bottom). The arrangements of the fluorinated cyclohexane centers are shown below the MD fibers' snapshots. The energies of the different $\mathbf{M_3}$-$\mathbf{M_5}$ mixing schemes relative to completely segregated $\mathbf{M_3}$ and $\mathbf{M_5}$ homopolymers (ΔE) are reported beside each equilibrated copolymer model. **b** Length of the Blocks (in green), Columns (red) and Random (violet) copolymer models as a function of MD simulation time. **c** Structure of the Blocks fiber colored based on the clusters (molecular motifs) identified by the SOAP-PAMM analysis: fluorinated cyclohexane and amide groups in blue and red, the alkyl side chains of the monomers in gray, green and cyan[66,67]. **d** PCAs of the SOAP vectors for $\mathbf{M_3}$ and $\mathbf{M_5}$ homopolymers, and for Blocks, Columns and Random copolymers (left-to-right). **e** Unsupervised PAMM clustering of the PCA data (**d**): different colored clusters indicate different local structural/dynamic motifs in the fibers. The closer and more interconnected are the colors (e.g., gray, cyan, green surface sites), the more dynamic is the interconnection between them (e.g., indicative of a dynamic surface). Separated clusters identify static, ordered, and persistent domains in the fiber (e.g., red and blue clusters, indicative of a relatively static fiber backbone). **f** Schematic representation of the dynamic transitions between the clusters estimated from the MD: the higher are the transition probabilities (numbers associated to the transition arrows), the more dynamic is the exchange between the clusters. No arrows indicate no exchange. The results show that these fibers have an intrinsic dynamic diversity: with a dynamic surface, and a static and ordered backbone.

interconnection between gray, cyan and green clusters (Fig. 7f) shows that in the same time-lapse there is dynamics on the surface of these fibers. The rich dynamic nature of these fibers is reminiscent of the innate dynamic diversity seen for also in other supramolecular polymers in solution[72,76]. Also, the growing interconnection between gray, cyan and green clusters going from left-to-right in Fig. 7f indicate that the surface of the fibers becomes more dynamic and disordered going from homopolymers to increased $\mathbf{M_3}$- $\mathbf{M_5}$ mixing within the copolymers.

In conclusion, we describe a new type of building block for supramolecular polymerization. We were able to demonstrate that monomers comprising facially polarized fluorocyclohexanes engage in intramolecular hydrogen bonding, dipole-dipole and CH···π interactions, leading to dormant states, which enable seeded LSP. We were able to make use of this kinetically controlled process to prepare self-assembled nanofibers of controlled length as well as supramolecular A-B-A block copolymers. To the best of our knowledge, this is the first report

on supramolecular block copolymers synthesized from kinetically trapped monomers rather than off-pathway aggregates. The monomers reported herein differ from the state-of-the art in LSP by their simplicity, the lack of extended π-systems or metal centres, and the facile variation of side chains. For this reason, we envisage that fluorinated cyclohexanes may play a vital role in progress on LSP. Future work will focus on the synthesis of more complex block copolymers and an exploration of ferroelectric properties[77].

Data availability

All data generated and analyzed during this study are included in this article and its Supplementary Information files. Crystallographic data have been deposited at the Cambridge Crystallographic Data Centre (CCDC) as CCDC 2010482 and CCDC 2071404 and can be obtained free of charge from the CCDC via https://www.ccdc.cam.ac.uk/.

Received: 14 December 2020; Accepted: 23 April 2021;
Published online: 25 May 2021

References

1. Matyjaszewski, K. Advanced materials by atom transfer radical polymerization. *Adv. Mater.* **30**, 1706441 (2018).
2. Lutz, J. F., Lehn, J.-M., Meijer, E. W. & Matyjaszewski, K. From precision polymers to complex materials and systems. *Nat. Rev. Mater.* **1**, 16024 (2016).
3. Szwarc, M. 'Living' polymerization. *Nature* **178**, 1168–1169 (1956).
4. Mitchell, V. D. & Jones, D. J. Advances toward the effective use of block copolymers as organic photovoltaic active layers. *Polym. Chem.* **9**, 795–814 (2018).
5. Stefik, M., Guldin, S., Vignolini, S., Wiesner, U. & Steiner, U. Block copolymer self-assembly for nanophotonics. *Chem. Soc. Rev.* **44**, 5076–5091 (2015).
6. Cabral, H., Miyata, K., Osada, K. & Kataoka, K. Block copolymer micelles in nanomedicine applications. *Chem. Rev.* **118**, 6844–6892 (2018).
7. Aida, T., Takemura, A., Fuse, M. & Inoue, S. Synthesis of a novel amphiphilic porphyrin carrying water-soluble polyether side chains of controlled chain length. Formation of a cofacial molecular assembly in aqueous media. *J. Chem. Soc. Chem. Commun*. 391–393 (1988).
8. Fouquey, C. & Lehn, J.-M. Molecular recognition directed self-assembly of supramolecular liquid crystalline polymers from complementary chiral components. *Adv. Mater.* **2**, 254–257 (1990).
9. Sijbesma, R. P. et al. Reversible polymers formed from self-complementary monomers using quadruple hydrogen bonding. *Science* **278**, 1601–1604 (1997).
10. Aida, T., Meijer, E. W. & Stupp, S. I. Functional supramolecular polymers. *Science* **335**, 813–817 (2012).
11. Webber, M. J., Appel, E. A., Meijer, E. W. & Langer, R. Supramolecular biomaterials. *Nat. Mater.* **15**, 13–26 (2016).
12. Dumele, O., Chen, J., Passarelli, J. V. & Stupp, S. I. Supramolecular Energy Materials. *Adv. Mater.* **32**, 1907247 (2020).
13. Ogi, S., Sugiyasu, K., Manna, S., Samitsu, S. & Takeuchi, M. Living supramolecular polymerization realized through a biomimetic approach. *Nat. Chem.* **6**, 188–195 (2014).
14. Matern, J., Dorca, Y., Sánchez, L. & Fernández, G. Revising complex supramolecular polymerization under kinetic and thermodynamic control. *Angew. Chem. Int. Ed.* **58**, 16730–16740 (2019).
15. Wagner, W., Wehner, M., Stepanenko, V., Ogi, S. & Würthner, F. Living supramolecular polymerization of a perylene bisimide dye into fluorescent J-aggregates. *Angew. Chem. Int. Ed.* **56**, 16008–16012 (2017).
16. Sarkar, A. et al. Self-sorted, random, and block supramolecular copolymers via sequence controlled, multicomponent self-assembly. *J. Am. Chem. Soc.* **142**, 7606–7617 (2020).
17. Greciano, E. E., Matarranz, B. & Sánchez, L. Pathway complexity versus hierarchical self-assembly in N-annulated perylenes: structural effects in seeded supramolecular polymerization. *Angew. Chem. Int. Ed.* **57**, 4697–4701 (2018).
18. Greciano, E. E. & Sánchez, L. Seeded supramolecular polymerization in a three-domain self-assembly of an N-annulated perylenetetracarboxamide. *Chem. Eur. J.* **22**, 13724–13730 (2016).
19. Jarrett-Wilkins, C. et al. Living supramolecular polymerisation of perylene diimide amphiphiles by seeded growth under kinetic control. *Chem. Eur. J.* **24**, 15556–15565 (2018).
20. Ma, X. et al. Fabrication of chiral-selective nanotubular heterojunctions through living supramolecular polymerization. *Angew. Chem. Int. Ed.* **55**, 9539–9543 (2016).
21. Ghosh, G., Dey, P. & Ghosh, S. Controlled Supramolecular Polymerization of π-Systems. *Chem. Commun.* **56**, 6757–6769 (2020).
22. Wang, H. et al. Living supramolecular polymerization of an aza-BODIPY dye controlled by a hydrogen-bond-accepting triazole unit introduced by click chemistry. *Angew. Chem. Int. Ed.* **59**, 5185–5192 (2020).
23. Helmers, I., Ghosh, G., Albuquerque, R. Q. & Fernández, G. Pathway and length control of supramolecular polymers in aqueous media via a hydrogen bonding lock. *Angew. Chem. Int. Ed.* **60**, 4368–4376 (2021).
24. Valera, J. S., Gómez, R. & Sánchez, L. Tunable energy landscapes to control pathway complexity in self-assembled N-heterotriangulenes: living and seeded supramolecular polymerization. *Small* **14**, 1702437 (2018).
25. Aliprandi, A., Mauro, M. & De Cola, L. Controlling and imaging biomimetic self-assembly. *Nat. Chem.* **8**, 10–15 (2016).
26. Wan, Q., To, W. P., Yang, C. & Che, C. M. The metal–metal-to-ligand charge transfer excited state and supramolecular polymerization of luminescent pincer Pd^{II}–isocyanide complexes. *Angew. Chem. Int. Ed.* **57**, 3089–3093 (2018).
27. Mishra, A. et al. Biomimetic temporal self-assembly via fuel-driven controlled supramolecular polymerization. *Nat. Commun.* **9**, 1295 (2018).
28. Jain, A., Dhiman, S., Dhayani, A., Vemula, P. K. & George, S. J. Chemical fuel-driven living and transient supramolecular polymerization. *Nat. Commun.* **10**, 450 (2019).
29. Endo, M. et al. Photoregulated living supramolecular polymerization established by combining energy landscapes of photoisomerization and nucleation-elongation processes. *J. Am. Chem. Soc.* **138**, 14347–14353 (2016).
30. Chakraborty, A., Ghosh, G., Pal, D. S., Varghese, S. & Ghosh, S. Organobase triggered controlled supramolecular ring opening polymerization and 2D assembly. *Chem. Sci.* **10**, 7345–7351 (2019).
31. Fukui, T., Sasaki, N., Takeuchi, M. & Sugiyasu, K. Living supramolecular polymerization based on reversible deactivation of a monomer by using a 'dummy' monomer. *Chem. Sci.* **10**, 6770–6776 (2019).
32. Pal, A. et al. Controlling the structure and length of self-synthesizing supramolecular polymers through nucleated growth and disassembly. *Angew. Chem. Int. Ed.* **54**, 7852–7856 (2015).
33. Wang, X., Manners, I. & Winnik, M. A. Cylindrical block copolymer micelles and co-micelles of controlled length and architecture. *Science* **317**, 644–647 (2007).
34. Hudson, Z. M. et al. Tailored hierarchical micelle architectures using living crystallization-driven self-assembly in two dimensions. *Nat. Chem.* **6**, 893–898 (2014).
35. Qiu, H. et al. Uniform patchy and hollow rectangular platelet micelles from crystallizable polymer blends. *Science* **352**, 697–701 (2016).
36. Tian, J. et al. Tailored self-assembled photocatalytic nanofibres for visible-light-driven hydrogen production. *Nat. Chem.* **12**, 1150–1156 (2020).
37. Qiu, H., Hudson, Z. M., Winnik, M. A. & Manners, I. Multidimensional hierarchical self-assembly of amphiphilic cylindrical block comicelles. *Science* **347**, 1329–1332 (2015).
38. Li, X., Gao, Y., Boott, C. E., Winnik, M. A. & Manners, I. Non-covalent synthesis of supermicelles with complex architectures using spatially confined hydrogen-bonding interactions. *Nat. Commun.* **6**, 8127 (2015).
39. Gilroy, J. B. et al. Monodisperse cylindrical micelles by crystallization-driven living self-assembly. *Nat. Chem.* **2**, 566–570 (2010).
40. He, Y. et al. Uniform biodegradable fiber-like micelles and block comicelles via "living" crystallization-driven self-assembly of poly(l-lactide) block copolymers: the importance of reducing unimer self-nucleation via hydrogen bond disruption. *J. Am. Chem. Soc.* **141**, 19088–19098 (2019).
41. Finnegan, J. R. et al. Extending the scope of "living" crystallization-driven self-assembly: well-defined 1D micelles and block comicelles from crystallizable polycarbonate block copolymers. *J. Am. Chem. Soc.* **140**, 17127–17140 (2018).
42. He, X. et al. Complex and hierarchical 2D assemblies via crystallization-driven self-assembly of poly(l-lactide) homopolymers with charged termini. *J. Am. Chem. Soc.* **139**, 9221–9228 (2017).
43. Xu, J., Zhou, H., Yu, Q., Manners, A. & Winnik, M. A. Competitive self-assembly kinetics as a route to control the morphology of core-crystalline cylindrical micelles. *J. Am. Chem. Soc.* **140**, 2619–2628 (2018).
44. Jin, X.-H. et al. Long-range exciton transport in conjugated polymer nanofibers prepared by seeded growth. *Science* **360**, 897–900 (2018).
45. Ogi, S., Stepanenko, V., Sugiyasu, K., Takeuchi, M. & Würthner, F. Mechanism of self-assembly process and seeded supramolecular polymerization of perylene bisimide organogelator. *J. Am. Chem. Soc.* **137**, 3300–3307 (2015).
46. Ogi, S., Matsumoto, K. & Yamaguchi, S. Seeded polymerization through the interplay of folding and aggregation of an amino-acid-based diamide. *Angew. Chem. Int. Ed.* **57**, 2339–2343 (2018).
47. Fukaya, N., Ogi, S., Kawashiro, M. & Yamaguchi, S. Hydrophobicity-driven folding and seeded polymerization of cystine-based dimeric diamides in aqueous media. *Chem. Commun.* **56**, 12901–12904 (2020).
48. Choi, H., Ogi, S., Ando, N. & Yamaguchi, S. Dual trapping of a metastable planarized triarylborane π-system based on folding and Lewis acid − base

complexation for seeded polymerization. *J. Am. Chem. Soc.* **143**, 2953–2961 (2021).
49. Ogi, S. et al. Seeded polymerization of an amide-functionalized diketopyrrolopyrrole dye in aqueous media. *Chem. Eur. J.* **25**, 7303–7307 (2019).
50. Kang, J. et al. C5 - symmetric chiral corannulenes: desymmetrization of bowl inversion equilibrium via 'intramolecular' hydrogen-bonding network. *J. Am. Chem. Soc.* **136**, 10640–10644 (2014).
51. Kang, J. et al. A rational strategy for the realization of chain-growth supramolecular polymerization. *Science* **347**, 646–651 (2015).
52. Keddie, N. S., Slawin, A. M. Z., Lebl, T., Philp, D. & O'Hagan, D. All-cis 1,2,3,4,5,6-hexafluorocyclohexane is a facially polarized cyclohexane. *Nat. Chem.* **7**, 483–488 (2015).
53. Wiesenfeldt, M. P., Nairoukh, Z., Li, W. & Glorius, F. Hydrogenation of fluoroarenes: direct access to all-cis-(multi)fluorinated cycloalkanes. *Science* **357**, 908–912 (2017).
54. Shyshov, O., Siewerth, K. A. & von Delius, M. Evidence for anion-binding of all-cis hexafluorocyclohexane in solution and solid state. *Chem. Commun.* **54**, 4353–4355 (2018).
55. Pratik, S. M., Nijamudheen, A. & Datta, A. Janus all-cis-1,2,3,4,5,6-hexafluorocyclohexane: a molecular motif for aggregation-induced enhanced polarization. *ChemPhysChem* **17**, 2373–2381 (2016).
56. Ogi, S., Stepanenko, V., Thein, J. & Würthner, F. Impact of alkyl spacer length on aggregation pathways in kinetically controlled supramolecular polymerization. *J. Am. Chem. Soc.* **138**, 670–678 (2016).
57. Barducci, A., Bussi, G. & Parrinello, M. Well-tempered metadynamics: a smoothly converging and tunable free-energy method. *Phys. Rev. Lett.* **100**, 020603 (2008).
58. Cormanich, R. A., Keddie, N. S., Rittner, R., O'Hagan, D. & Bühl, M. Particularly strong C-H···π interactions between benzene and all-cis 1,2,3,4,5,6-hexafluorocyclohexane. *Phys. Chem. Chem. Phys.* **17**, 29475–29478 (2015).
59. Vantomme, G. et al. Tuning the length of cooperative supramolecular polymers under thermodynamic control. *J. Am. Chem. Soc.* **141**, 18278–18285 (2019).
60. Das, A. et al. Supramolecular copolymers: structure and composition revealed by theoretical modeling. *J. Am. Chem. Soc.* **139**, 7036–7044 (2017).
61. Hendrikse, S. I. S. et al. Elucidating the ordering in self-assembled glycocalyx mimicking supramolecular copolymers in water. *J. Am. Chem. Soc.* **141**, 13877–13886 (2019).
62. Adelizzi, B. et al. Supramolecular block copolymers under thermodynamic control. *J. Am. Chem. Soc.* **140**, 7168–7175 (2018).
63. Kitamoto, Y. et al. One-shot preparation of topologically chimeric nanofibers via a gradient supramolecular copolymerization. *Nat. Commun.* **10**, 4578 (2019).
64. Zhang, W. et al. Supramolecular linear heterojunction composed of graphite-like semiconducting nanotubular segments. *Science* **334**, 340–343 (2011).
65. Adelizzi, B. et al. Long-lived charge-transfer state from B—N frustrated Lewis pairs enchained in supramolecular copolymers. *J. Am. Chem. Soc.* **142**, 16681–16689 (2020).
66. Wagner, W., Wehner, M., Stepanenko, V. & Würthner, F. Supramolecular block copolymers by seeded living polymerization of perylene bisimides. *J. Am. Chem. Soc.* **141**, 12044–12054 (2019).
67. Jung, S. H., Bochicchio, D., Pavan, G. M., Takeuchi, M. & Sugiyasu, K. A Block supramolecular polymer and its kinetically enhanced stability. *J. Am. Chem. Soc.* **140**, 10570–10577 (2018).
68. Wan, Q., To, W. P., Chang, X. & Che, C. M. Controlled synthesis of Pd^{II} and Pt^{II} supramolecular copolymer with sequential multiblock and amplified phosphorescence. *Chem* **6**, 945–967 (2020).
69. Fukui, T. et al. Control over differentiation of a metastable supramolecular assembly in one and two dimensions. *Nat. Chem.* **9**, 493–499 (2017).
70. Wehner, M. & Würthner, F. Supramolecular polymerization through kinetic pathway control and living chain growth. *Nat. Rev. Chem.* **4**, 38–53 (2020).
71. Bartók, A. P., Kondor, R. & Csányi, G. On representing chemical environments. *Phys. Rev. B* **87**, 184115 (2013).
72. Gasparotto, P., Bochicchio, D., Ceriotti, M. & Pavan, G. M. Identifying and tracking defects in dynamic supramolecular polymers. *J. Phys. Chem. B* **124**, 589–599 (2020).
73. De Marco, A. L., Bochicchio, D. & Pavan, G. M. Controlling the exchange pathways in dynamic supramolecular polymers by controlling their defects. *ChemRxiv*, https://doi.org/10.26434/chemrxiv.13655864.v1 (2021).
74. Capelli, R., Gardin, A., Empereur-mot, C., Doni, G. & Pavan, G. M. A. A data-driven dimensionality reduction approach to compare and classify lipid force fields. *ChemRxiv*, https://doi.org/10.26434/chemrxiv.14039834.v2 (2021).
75. Gasparotto, P., Meißner, R. H. & Ceriotti, M. Recognizing local and global structural motifs at the atomic scale. *J. Chem. Theory Comput.* **14**, 486–498 (2018).
76. Bochicchio, D., Salvalaglio, M. & Pavan, G. M. Into the dynamics of a supramolecular polymer at submolecular resolution. *Nat. Commun.* **8**, 147 (2017).
77. Tayi, A. S., Kaeser, A., Matsumoto, M., Aida, T. & Stupp, S. I. Supramolecular ferroelectrics. *Nat. Chem.* **7**, 281–294 (2015).

Acknowledgements

M.v.D. is grateful for financial support from the European Research Council (ERC) under the European Union's Horizon 2020 research and innovation program (grant agreement no. 802428 - SUPRANET), the DFG (TRR234, no. 364549901), the University of Ulm and the DAAD (PhD fellowship to O.S.). G.M.P. acknowledges the funding received by the Swiss National Science Foundation (SNSF grants IZLIZ2_183336) and by the ERC under the European Union's Horizon 2020 research and innovation program (grant agreement no. 818776 - DYNAPOL). The authors also acknowledge the computational resources provided by the Swiss National Supercomputing Center (CSCS) and by CINECA. H.Q. and U.K. acknowledge the funding from the DFG in SFB1415 (no. 417590517). Prof. P. Bäuerle and Dr. E. Mena-Osteritz are acknowledged for access to equipment and support with AFM. We thank Lionel Kroner for recording single-crystal X-ray diffraction data. Dr. U. Werz is acknowledged for NOE NMR measurements. We thank Prof. Boris Mizaikoff and Diellza Bajrami for the help with transmission mode FT-IR measurements. Prof. A. Kühne is acknowledged for valuable suggestions.

Author contributions

O. S. and M.v.D. conceived the original idea. O.S. developed the molecular design and devised and supervised the experimental work. O.S. and S.V.H. carried out all syntheses and characterization studies. L.P., A.G., D.B., and G.M.P. developed the molecular models, performed and analyzed the molecular simulations. H.Q. and U.K. performed transmission electron microscopy studies. M.v.D. directed the project. All authors contributed to the discussion and the preparation of the paper.

Competing interests

The authors declare no competing interests.

Additional information

Supplementary information The online version contains supplementary material available at https://doi.org/10.1038/s41467-021-23370-y.

Correspondence and requests for materials should be addressed to G.M.P. or M.v.D.

Peer review information *Nature Communications* thanks Anja Palmans and the other, anonymous, reviewer(s) for their contribution to the peer review of this work.

Reprints and permission information is available at http://www.nature.com/reprints

Publisher's note Springer Nature remains neutral with regard to jurisdictional claims in published maps and institutional affiliations.

Open Access This article is licensed under a Creative Commons Attribution 4.0 International License, which permits use, sharing, adaptation, distribution and reproduction in any medium or format, as long as you give appropriate credit to the original author(s) and the source, provide a link to the Creative Commons license, and indicate if changes were made. The images or other third party material in this article are included in the article's Creative Commons license, unless indicated otherwise in a credit line to the material. If material is not included in the article's Creative Commons license and your intended use is not permitted by statutory regulation or exceeds the permitted use, you will need to obtain permission directly from the copyright holder. To view a copy of this license, visit http://creativecommons.org/licenses/by/4.0/.

© The Author(s) 2021

Supporting Information for

Living Supramolecular Polymerization of Fluorinated Cyclohexanes

Oleksandr Shyshov[1], Shyamkumar Vadakket Haridas[1], Luca Pesce[2], Haoyuan Qi[3,4], Andrea Gardin[6], Davide Bochicchio[2,5], Ute Kaiser[3], Giovanni M. Pavan[2,6]* & Max von Delius[1]*

[1]Institute of Organic Chemistry, University of Ulm, Albert-Einstein-Allee 11, 89081 Ulm, Germany. Email: max.vondelius@uni-ulm.de

[2]Department of Innovative Technologies, University of Applied Sciences and Arts of Southern Switzerland, Polo Universitario Lugano - Campus Est, Via la Santa 1, CH-6962 Lugano - Viganello, Switzerland

[3]Central Facility of Electron Microscopy, Electron Microscopy Group of Materials Science, University of Ulm, 89081 Ulm, Germany.

[4]Center for Advancing Electronics Dresden (cfaed) and Faculty of Chemistry and Food Chemistry, Technical University of Dresden, 01069 Dresden, Germany.

[5]Department of Physics, Università degli studi di Genova, Via Dodecaneso 33, 16100 Genova, Italy.

[6]Department of Applied Science and Techology, Politecnico di Torino, Corso Duca degli Abruzzi 24, 10129 Torino, Italy. Email: giovanni.pavan@polito.it

Supplementary Methods

General experimental methods

All commercially available reagents were purchased from Sigma Aldrich, Alfa Aesar, Acros Organics, ABCR or TCI and were used without further purification unless otherwise stated. Hydrogenation reactions were carried out in a 150mL Roth HighPressure Autoclave. NMR spectra were recorded on a BrukerAvance 400 (^{1}H: 400 MHz; ^{13}C: 101 MHz; ^{19}F: 377 MHz), a BrukerAvance 500 (^{1}H: 500 MHz; ^{13}C: 125 MHz) spectrometers at 295 K and referenced to the residual solvent peak (^{1}H: chloroform-*d*, 7.26 ppm; acetone-d_6, 2.05 ppm; DMSO-d_6, 2.5 ppm; cyclohexane-d_{12}, 1.38 ppm; ^{13}C: chloroform-*d*, 77.00 ppm; acetone-d_6, 206.68 ppm, DMSO-d_6, 39.52 ppm). Coupling constants (J) are denoted in Hz and chemical shifts (δ) in ppm. Multiplicities are denoted as follows: s = singlet, d = doublet, t = triplet, m = multiplet, br = broad. Mass spectra were obtained on a Bruker SolariX (HRMS-ESI^{+}, solvent: acetonitrile) instrument. CD spectra were measured in a 1 mm quartz cuvette on Jasco J-810 CD spectrometer equipped with Julabo F12 temperature controller. A Bandelin Sonorex was used as an "ultrasonic bath" (US bath). Single-crystal diffraction analysis data was collected at 150 K with a Rigaku/Oxford instruments Supernova. Atomic force microscopy (AFM) was performed on a NanoScope IIIa device (Veeco Instruments, Santa Barbara, CA) in tapping mode under air. Commercial antimony doped silicon tips (Type RTESPA-150) were used with a nominal tip radius of 8 nm and a spring constant of 6 N m^{-1} at a resonance frequency of 150 kHz. Transmission Fourier transform infrared spectroscopic analyses (FT-IR) was performed on a Bruker Tensor II IR spectrometer equipped with transmission compartment using a liquid cell with KBr windows and 1 mm path length. ATR-IR analyses was performed using Bruker Alpha II spectrometer. TEM experiments were performed on an image-side aberration-corrected FEI Titan 80-300 operated at 300kV. The microscope is equipped with a CEOS hexapole aberration-corrector , which corrects the geometrical axial aberrations up to the 3rd-order. Data acquisition was conducted on a Gatan UltraScan CCD camera. Electron diffraction was conducted under both nano-beam diffraction mode and selected-area electron diffraction mode. Due to the high beam sensitivity of the organic fibers, we applied low-dose conditions during data acquisition, and the electron dose was limited in the range of 0.1 - 0.5 e^{-}/Å^{2}. For sample preparation, the organic fibers, obtained using a [**M$_3$**]/[**M$_3^{Seed}$**] 100/1 (v/v) ratio, were 100x time diluted with cyclohexane. Subsequently, 10 µL of the diluted solution was drop-casted on to a holey carbon TEM grid. The grid was left in ambiance for c.a. 1 h before TEM investigation. Dynamic light scattering (DLS) was performed using Malvern Instruments Zetasizer Nano ZS, UK at 293 K with a scattering angle 173° and wavelength λ = 633 nm.

Procedure for M_3^{Seed} preparation:

M_3^{Seed} solution was obtained by applying sonication to a Cyclohexane/$CHCl_3$ (84:16 v/v) solution of **M3** and ***Me*M3** (molar ratio: 3:1; total concentration: 1.2 mM) for 20 minutes at 273 K in a round-bottom flask tightly closed with glass stopcock. M_3^{Seed} was used for further experiments immediately.

General procedure for seeded LSP

A 1.2 mM solution of **M3** in 84:16 v/v cyclohexane/chloroform in was added to a 1 mm quartz cuvette and annealed for 40 sec at 323 – 328 K to ensure complete depolymerisation. After this treatment spontaneous polymerization does not occur for >3 h. The monomer solution was placed into a CD spectropolarimeter with the temperature set to 293 K and thermostated for 10 min. A defined volume of an M_3^{Seed} solution was added and the cuvette content was homogenized by turning the cuvette upside down 5 – 10 times and placed back into the CD spectropolarimeter at 293 K.

Notes: 1) For every experiment we prepared fresh M_3^{Seed} solutions (old solutions can be depolymerized as described above); 2) M_3^{Seed} solution was always kept at 273 K.

AFM studies on supramolecular polymers

Samples of supramolecular polymers for AFM were prepared by spin-coating (8000 rpm) on the silicon wafer immediately after 100-fold dilution with cyclohexane. Dilution is necessary to prevent severe bundling. AFM images were recorded for several different areas of the substrate. AFM data was processed using WSxM 5.0 software.[1] Images were analyzed using the ImageJ software, developed at the US National Institute of Health.[2] Lengths of all separate unbundled fibers were used for statistics. In every case, we measured approximately 200 fibers (Supplementary Table 1). Weight-averaged length (L_w) and number-averaged length (L_n) for n objects were calculated according to equations S1 and S2.

$$L_w = \frac{\sum_{i=1}^{n} N_i L_i^2}{\sum_{i=1}^{n} N_i L_i} \qquad \text{(S1)}$$

$$L_n = \frac{\sum_{i=1}^{n} N_i L_i}{\sum_{i=1}^{n} N_i} \qquad \text{(S2)}$$

The length distribution was characterized by the polydispersity index (PDI) according to:

$$PDI = \frac{L_w}{L_n} \qquad \text{(S3)}$$

General procedure for preparation of supramolecular block copolymer by seeded LSP

A 1.2 mM solution of $\mathbf{M_5}$ in 93:7 v/v cyclohexane/chloroform was added to a 1 mm quartz cuvette and was annealed for 40 sec at 323 – 328 K to ensure complete depolymerisation. The monomer solution was placed in a CD spectropolarimeter with temperature set to 293 K and thermostated for 10 min. A defined volume of $\mathbf{M_3^{Seed}}$ solution was added and the cuvette content was homogenized by turning the cuvette upside down 5 – 10 times and placed back into CD spectropolarimeter at 293 K.

Notes: 1) For every experiment we prepared fresh $\mathbf{M_3^{Seed}}$ solutions (old solutions can be depolymerized as described above); 2) $\mathbf{M_3^{Seed}}$ solution was always kept at 273 K.

Living supramolecular polymerization

To provide evidence for the living nature of supramolecular polymerization we performed a multicycle dilution experiment. 20 μL of $\mathbf{M_3^{Seed}}$ solution was added to 200 μL of $\mathbf{M_3}$ solution at 293 K, polymerization occurred and was completed within 60 seconds. 100 μL of the obtained polymer solution was added to 100 μL of $\mathbf{M_3}$ solution. This procedure was repeated for two more cycles (Supplementary Fig. 36a). Since after each cycle, the initial concentration of $\mathbf{M_3^{Seed}}$ was diluted by half, the rate of polymerization decreases by half as well (Supplementary Fig. 36b). The rates of polymerization can be fitted according to exponential equation $y = A*(1/2)^{x-1}$, where x is the number of cycles (Supplementary Fig. 36c). These results clearly indicate that the number of active termini does not change during polymerization.

To demonstrate the living nature of supramolecular block copolymers, to 1 volume of $\mathbf{M_5}$-$\mathbf{M_3}$-$\mathbf{M_5}$ (obtained with $[\mathbf{M_5}]/[\mathbf{M_3^{Seed}}]$ = 3:1 (v/v) ratio) block copolymer we added 0.5 volumes of $\mathbf{M_3}$ (1.2 mM, 84:16 cyclohexane/chloroform v/v, 293 K) and investigate length distribution using AFM (Supplementary Fig. 40b).

Thermodynamics of polymerization

To obtain thermodynamic data, we studied thermal depolymerisation of polymers, which proceeds under thermodynamic control unlike the kinetically controlled, cooling-induced polymerization. The heating curves of the polymers, obtained upon cooling of the polymer solution, have unusual kinks presumably due to fast kinetics of polymerization leading to defects in the molecular packing and presence of different polymorphs in the same sample (for example those that form during spontaneous polymerization). Therefore, we prepared polymers via seeded growth under kinetic control, using different initial concentrations of the monomer and constant monomer/seed ratio ($[\mathbf{M_3}]/[\mathbf{M_3^{Seed}}]$

50/1). The obtained polymer solutions were cooled down to 275 K and heating CD curves were recorded (Supplementary Fig. 53).

Obtained heating curves had non-sigmoidal shapes with clear transitions at T_e. The molar fraction of aggregated molecules (α_{agg}) was calculated according to the equation S4, where CD_{agg} and CD_{mono} are CD intensities of fully aggregated (at the lowest temperature) and monomeric states (at the highest temperature). The plot of α_{agg} versus temperature (Supplementary Fig. 54) provides heating curves which can be fitted according to the cooperative model proposed by Meijer and co-workers (equation S5) in which h_e is the molecular enthalpy release during elongation, T_e and T are elongation temperature and absolute temperature respectively.[3]

$$\alpha_{agg} = 1 - \frac{CD_{agg} - CD(T)}{CD_{agg} - CD_{mono}} \qquad \text{(S4)}$$

$$\alpha = \alpha_{SAT}\left[1 - exp\left(\frac{-h_e}{RT_e^2}(T - T_e)\right)\right] \qquad \text{(S5)}$$

The standard values of enthalpy ($\Delta H°$), entropy ($\Delta S°$) and Gibbs free energy were obtained using the van`t Hoff plot (Supplementary Fig. 55).

Synthesis and characterization data

All-*cis* 2,3,4,5,6-pentafluorocyclohexan-1-ol (1)



1

A 25 mL Schlenk flask was charged with all-cis 1,2,3,4,5-pentafluoro-6-methoxycyclohexane[4] (168 mg, 0.83 mmol, 1 equiv.) and 8 mL of anhydrous CH_2Cl_2. Butane-1-thiol (0.75 g, 0.89 mL, 8.31 mmol, 10 equiv.) and anhydrous $AlCl_3$ (406 mg, 2.91 mmol, 3.5 equiv.) were added subsequently and the reaction mixture was stirred for 14 hours at room temperature. The reaction mixture was filtered through silica pad, the first fraction was washed with hexane to remove the thiol, second with acetone. The acetone fraction was concentrated and the crude material was purified by flash column chromatography (CH_2Cl_2/acetone 8:2) to give **1** (129 mg, 83%) as a colourless solid.

^{1}H NMR (400 MHz, acetone-d_6, 295 K): δ 5.51 - 4.77 (m, 5H), 3.98 (t, 1H).

^{19}F NMR (377 MHz, acetone-d_6, 295 K): δ -211.20 (br s, 2F), -217.5 (m, 2F), -217.63 (m, 1F).

^{13}C NMR (101 MHz, acetone-d_6, 295 K): δ 91.70 (m), 89.73(m), 87.52 (m), 85.63 (m), 66.82 (m).

HRMS (ESI$^-$): *m/z* = 248.9728 $[M+CH_3COO]^-$ (calculated 249.0556 for $C_8H_{10}F_5O_3^-$).

General procedure compounds S1 – S3



S1, n = 0
S2, n = 1
S3, n = 2

In a 100 mL round-bottom flask corresponding Boc-aminoacid (25 mmol, 1 equiv.), 2,3,4,5,6-pentafluorophenol (28 mmol, 1.12 equiv.) and few crystals of 4-dimethylaminopyridine were dissolved in 30 mL of CH_2Cl_2. EDC (28 mmol, 1.12 equiv.) was added and the reaction mixture was stirred 12h at room temperature. The reaction mixture was diluted with 70 mL of CH_2Cl_2 and washed with water (4*30 mL) and brine (30mL). The organic phase was dried over magnesium sulfate and evaporated to afford the target compounds, which were used for the next step without purification.

Perfluorophenyl 3-((tert-butoxycarbonyl)amino)propanoate (S1)

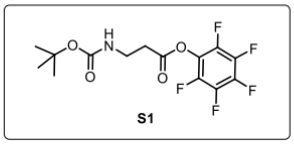

S1

Crude yield: 100%, brownish solid.

^{1}H NMR (400 MHz, $CDCl_3$, 295 K): δ 5.05 (br, 1H), 3.50 (q, J = 6.2 Hz, 2H), 2.91 (t, J = 6.1 Hz, 2H), 1.43 (s, 9H).

^{19}F NMR (377 MHz, $CDCl_3$, 295 K): δ -151.58 – -152.93 (m, 2F), -157.86 (t, J = 21.6 Hz, 2F), -162.03 – -162.68 (m, 2F).

^{13}C NMR (101 MHz, $CDCl_3$, 295 K): δ 168.34, 155.84, 142.44 – 142.06 (m), 141.21 – 140.40 (m), 140.36 – 139.56 (m), 139.27 – 138.9 (m), 138.65 – 137.96 (m), 137.04 – 136.34 (m), 79.85, 35.94, 33.83, 28.20.

HRMS (ESI$^+$): *m/z* = 378.0727 $[M+Na]^+$ (calculated 378.0741 for $C_{14}H_{14}F_5NO_4Na^+$).

Perfluorophenyl 4-((tert-butoxycarbonyl)amino)butanoate (S2)

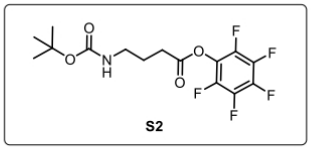

Crude yield: 98%, white solid.

^{1}H NMR (400 MHz, $CDCl_3$, 295 K): δ 4.67 (br, 1H), 3.25 (q, J = 6.6 Hz, 2H), 2.72 (t, J = 7.4 Hz, 2H), 1.96 (p, J = 7.0 Hz, 2H), 1.44 (s, 9H).

^{19}F NMR (377 MHz, $CDCl_3$, 295 K): δ -151.03 – -154.44 (m, 2F), -157.64 (dt, J = 33.6, 15.1 Hz, 2F), -161.98 (q, J = 20.6, 17.3 Hz, 1F).

^{13}C NMR (101 MHz, $CDCl_3$, 295 K): δ 169.30, 156.20, 142.63 – 141.99 (m), 140.95 – 140.41 (m), 140.04 – 139.59 (m), 139.37 – 138.78 (m), 138.39 – 137.96 (m), 136.85 – 136.24 (m), 77.36, 39.70, 30.72, 28.49, 25.46.

HRMS (ESI$^+$): *m/z* = 392.0884 $[M+Na]^+$ (calculated 392.0897 for $C_{15}H_{16}F_5NO_4Na^+$).

Perfluorophenyl 5-((tert-butoxycarbonyl)amino)pentanoate (S3)

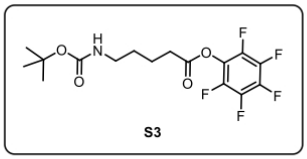

Crude yield: 100%, brown solid.

^{1}H NMR (400 MHz, $CDCl_3$, 295 K): δ 4.57 (br, 1H), 3.18 (q, J = 6.7 Hz, 2H), 2.70 (t, J = 7.3 Hz, 2H), 1.80 (tt, J = 7.5 Hz, 6.2 Hz, 2H), 1.61 (dq, J = 10.4 Hz, 7.1 Hz, 2H) 1.44 (s, 9H).

^{19}F NMR (377 MHz, $CDCl_3$, 295 K): δ -152.75 (dd, J = 21.9 Hz, 4.9 Hz, 2F), -158 (t, J = 21.6 Hz, 1F), -162.29 (q, J = 22.9, 18.1 Hz, 1F).

^{13}C NMR (101 MHz, $CDCl_3$, 295 K): δ 169.25, 156.03, 142.63 – 142.02 (m), 141.03 – 139.55 (m), 139.53 – 137.57 (m), 137.04 – 136.25 (m), 79.32, 39.87, 32.81, 29.27, 28.34, 21.84.

HRMS (ESI$^+$): *m/z* = 406.1055 $[M+Na]^+$ (calculated 406.1054 for $C_{16}H_{18}F_5NO_4Na^+$).

All-*cis* 2,3,4,5,6-pentafluorocyclohexyl acetate (Ref_2)

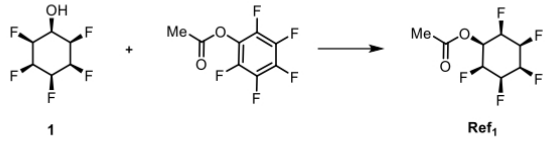

1 **Ref_1**

In a 10 mL round-bottom flask pentafluorophenyl acetate (150 mg, 0.66 mmol, 2.5 equiv.) and **1** (50 mg, 0.26 mmol, 1 equiv.) were dissolved in 1 mL of dry DMF and 1 mL of triethylamine. Reaction mixture was stirred at 120 °C until **1** was consumed (ca. 2 – 3 hours). Solvents were removed under reduced pressure and the crude material was purified by flash column chromatography (gradient elution CH_2Cl_2 to CH_2Cl_2/acetone 8:2) to afford all-cis 2,3,4,5,6-pentafluorocyclohexyl acetate (56 mg, 92%) as a colourless crystalline solid.

^{1}H NMR (400 MHz, acetone-d_6, 295 K): δ 5.60 – 4.86 (m, 6H), 2.15 (s, 3H).

^{19}F NMR (377 MHz, acetone-d_6, 295 K): δ -211.48 (br s, 2F), -215.92 (br s, 2F), -217.86 (br s, 1F).

^{13}C NMR (101 MHz, acetone-d_6, 295 K): δ 170.55, 90.15 – 88.28 (m), 87.95 – 86.28 (m), 86.9 – 84.51 (m), 68.10 – 67.25 (m), 20.91.

HRMS (ESI$^-$): *m/z* = 267.0216 $[M + Cl]^-$ (calculated 267.0217 for $C_8H_{10}F_5O_3Cl^-$).

General procedure compounds 2 - 4

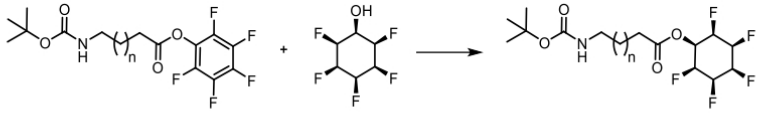

S1, n = 0
S2, n = 1
S3, n = 2

1

2, n = 0
3, n = 1
4, n = 2

In a 10 mL round-bottom flask pentafluorophenyl ester **S1** – **S3** (7.7 mmol, 1.9 equiv.) and **1** (4 mmol, 1 equiv.) were dissolved in 3 mL of dry DMF and 2 mL of triethylamine. The reaction mixture was stirred at 120 °C until **1** was completely consumed (ca. 2 - 3 hours). Solvents were removed under reduced pressure and the crude material was purified by flash column chromatography (gradient elution CH_2Cl_2 to CH_2Cl_2/acetone 8:2).

All-*cis* 2,3,4,5,6-pentafluorocyclohexyl 3-((tert-butoxycarbonyl)amino)propanoate (2)

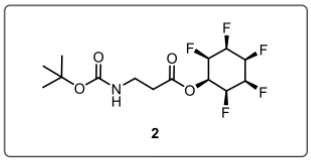

Yield: 95%, white solid.

^{1}H NMR (400 MHz, acetone-d_6, 295 K): δ 6.07 (br, 1H), 5.59 – 4.78 (m, 6H), 3.39 (q, J = 6.5 Hz, 2H), 2.66(t, J = 6.8 Hz, 2H), 1.39 (s, 9H).

^{19}F NMR (377 MHz, acetone-d_6, 295 K): δ -211.47 (br s, 2F), -215.84 (br s, 2F), -217.81 (br s, 1F).

^{13}C NMR (101 MHz, acetone-d_6, 295 K): δ 171.81, 156.97, 89.88 – 88.62 (m), 88.30 – 86.26 (m), 86.17 – 84.46 (m), 79.31, 68.34 – 67.22 (m), 37.45, 35.68, 29.0.

HRMS (ESI$^+$): *m/z* = 400.0938 $[M + K]^+$ (calculated 400.0950 for $C_{14}H_{20}F_5NO_4K^+$).

All-*cis* 2,3,4,5,6-pentafluorocyclohexyl 4-((tert-butoxycarbonyl)amino)butanoate (3)

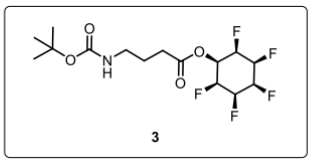

Yield: 100%, white solid.

^{1}H NMR (400 MHz, DMSO-d_6, 295 K): δ 6.88 (t, J = 5.8 Hz, 1H), 5.61 – 4.82 (m, 6H), 2.96 (q, J = 6.5 Hz, 2H), 2.48 – 2.38 (m, 2H), 1.66 (p, J = 7.2 Hz, 2H), 1.37 (s, 9H).

^{19}F NMR (377 MHz, DMSO-d_6, 295 K): δ -210.13 (br s, 2F), -214.63 (br s, 2F), -216.85 (br s, 1F).

^{13}C NMR (101 MHz, DMSO-d_6, 295 K): δ 177.61, 155.68, 88.42 – 87.00 (m), 86.55 – 84.89 (m), 84.29 – 82.92 (m), 77.55, 66.41 – 65.47 (m), 30.59, 28.25, 27.68, 24.80.

HRMS (ESI$^+$): *m/z* = 398.1371 $[M + Na]^+$ (calculated 398.1392 for $C_{15}H_{22}F_5NO_4Na^+$).

All-*cis* 2,3,4,5,6-pentafluorocyclohexyl 5-((tert-butoxycarbonyl)amino)pentanoate (4)

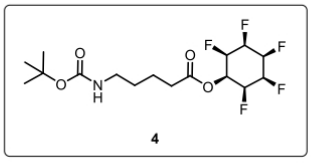

Yield: 92%, white solid.

^{1}H NMR (500 MHz, acetone-d_6, 295 K): δ 5.93 (br, 1H), 5.71 – 4.76 (m, 6H), 3.08 (t, J = 6.2 Hz, 2H), 2.49 (t, J = 7.4 Hz, 2H), 1.80 – 1.61 (m, 2H), 1.55 (p, J = 7.1 Hz, 2H), 1.39 (s, 9H).

^{19}F NMR (377 MHz, acetone-d_6, 295 K): δ -211.46 (br s, 2F), -215.92 (br s, 2F), -217.85 (br s, 1F).

^{13}C NMR (126 MHz, acetone-d_6, 295 K): δ 173.35, 157.22, 89.86 – 88.66 (m), 88.25 – 86.41 (m), 86.41 – 84.90 (m), 78.90, 68.27 – 67.38, 41.09, 40.96, 29.18, 23.28, 16.22.

HRMS (ESI$^+$): *m/z* = 412.1514 $[M + Na]^+$ (calculated 412.1523 for $C_{16}H_{24}F_5NO_4Na^+$).

Synthesis of S9

(S)-6-((tert-butyldimethylsilyl)oxy-4-methylhexanal (S4)

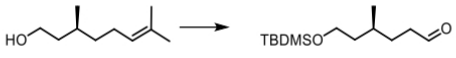

S4

A 250 mL round-bottom flask was charged with β-S-(-)citronellol (3 g, 19.2 mmol, 1 equiv.), 90 mL of dioxane and 30 ml of water. OsO_4 (96 mg, 0.38 mmol, 0.02 equiv.), $NaIO_4$ (16.4 g, 76.6 mmol, 4 equiv.) and 2,6-lutidine (4.38 ml, 4.1 g, 38 mmol, 2 equiv.) were added subsequently and the reaction mixture was stirred at room temperature. When all starting material was consumed, the reaction mixture was extracted with CH_2Cl_2. The organic phase was dried over magnesium sulfate, passed through a short celite pad and solvents were removed under reduced pressure. The brown oil, obtained after evaporation, was dissolved in 50 mL of CH_2Cl_2. TBDMSCl (4.3 g, 28 mmol, 1.5 equiv.) and imidazole (1.9 g, 28 mmol, 1.5 equiv.) was added and the reaction mixture was stirred for 12h at room temperature. The reaction mixture was transferred into a separatory funnel and washed with water (100 mL). The organic phase was dried over magnesium sulfate. The solvent was removed under reduced pressure and the residue was purified by flash column chromatography (petroleum ether/ethyl acetate 9:1) to give **S4** (2.6 g, 55% two steps) as a colourless oil.

^{1}H NMR (400 MHz, $CDCl_3$, 295 K): δ 9.77 (t, J = 1.9 Hz, 1H), 3.89 – 3.44 (m, 3H), 2.48 – 2.40 (m, 3H), 1.75 – 1.41 (m, 6H), 1.40 – 1.29 (m. 2H), 0.91 – 0.90 (m, 3H), 0.88 (s, 9H), 0.04 (s, 6H).

^{13}C NMR (101 MHz, $CDCl_3$, 295 K): δ 202.86, 61.04, 41.65, 39.49, 29.14, 28.93, 25.92, 19.33, 18.29, -5.32, -5.35.

HRMS (ESI$^+$): *m/z* = 245.1910 $[M+H]^+$ (calculated 245.1931 for $C_{13}H_{29}O_2Si^+$).

(S)-6-((tert-butyldimethylsilyl)oxy-4-methylhexan-1-ol (S5)

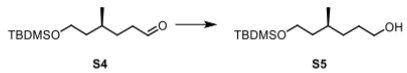

S4 S5

In a 250 mL round-bottom flask **S4** (2.6 g, 10.6 mmol, 1 equiv.) was dissolved in MeOH (100 mL) and $NaBH_4$ (401 mg, 10.6 mmol, 1 equiv.) was added at 0 ºC. The reaction mixture was allowed to warm up to room temperature and was stirred at room temperature until all starting material was consumed. MeOH was evaporated under reduced pressure. The residue was dissolved in 100 mL of water and extracted with ethyl acetate (3*50 mL). The organic phase was washed with brine and dried over $MgSO_4$. The solvent was removed under reduced pressure and the crude material was purified by flash column chromatography (8:2 petroleum ether: ethyl acetate) to give **S5** (2.15 g, 82%) as a colourless oil.

^{1}H NMR (400 MHz, $CDCl_3$, 295 K): δ 3.71 – 3.55 (m, 4H), 1.68 – 1.43 (m, 5H), 1.43 – 1.28 (m, 2H), 1.23 – 1.12 (m, 1H), 0.93 – 0.85 (m, 12H), 0.04 (s, 6H).

^{13}C NMR (101 MHz, $CDCl_3$, 295 K): δ 63.29, 61.34, 39.81, 32.97, 30.19, 29.26, 25.94, 19.63, 18.31, -5.29, -5.31.

HRMS (ESI^+): *m/z* = 247.2090 $[M+H]^+$ (calculated 247.2093 for $C_{13}H_{31}SiO_2^+$).

(S)-tert-butyl((6-iodo-3-methylhexyl)oxy)dimethylsilane (S6)

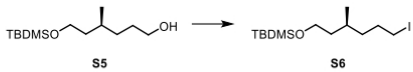

S5 S6

A 250 mL flask was charged with **S5** (2.15 g, 8.74 mmol, 1 equiv.) and dissolved in dry acetonitrile (50 mL). Triphenylphosphine (3 g, 11.4 mmol, 1.3 equiv.), iodine (3.1 g, 12.2 mmol, 1.4 equiv.) and imidazole (0.9 g, 13.1 mmol, 1.5 equiv.) were added subsequently under nitrogen atmosphere at 0 ºC. The reaction mixture was stirred for 10 minutes at 0 °C and for 2 h at room temperature. The reaction mixture was concentrated under reduced pressure and 100 mL of petroleum ether was added. The precipitate was filtered off and the mother liquor was passed through a silica pad to obtain **S6** (1.96 g, 63%) as colourless oil.

^{1}H NMR (400 MHz, $CDCl_3$, 295 K): δ 3.70 – 3.58 (m, 2H), 3.21 – 3.11 (m, 2H), 1.94 – 1.73 (m, 2H), 1.65 – 1.49 (m, 2H), 1.46 – 1.29 (m, 2H), 1.29 – 1.17 (m, 1H), 0.93 – 0.83 (m, 12H), 0.04 (s, 6H).

^{13}C NMR (101 MHz, $CDCl_3$, 295 K): δ 61.16, 39.67, 37.87, 31.14, 28.70, 25.95, 25.86, 19.61, 18.30, 7.37, -5.27, -5.30.

HRMS (ESI^+): *m/z* = 357.1100 $[M+H]^+$ (calculated 357.1105 for $C_{13}H_{30}ISiO^+$).

(S)-tert-butyl((6-buthylthio)-3-methylhexyl)oxy)dimethylsilane (S7)

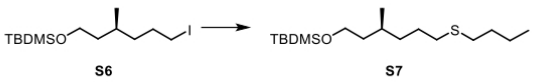

S6 **S7**

In a 100 ml round-bottom flask butane-1-thiol (594mg, 6.6 mmol, 1.2 equiv.) was dissolved in dry DMF (25 mL). Cs_2CO_3 (2.15g, 6.6 mmol, 1.2 equiv.), tetrabutylammonium iodide (2.4g, 6.6 mmol, 1.2 equiv.) were added and stirred for 1 h at room temperature under N_2 atmosphere. The reaction mixture was cooled to 0 °C and **S6** (1.96 g, 5.5 mmol, 1 equiv.) was added dropwise. The reaction mixture was stirred for 2 h at room temperature and water (100 mL) was added. The reaction mixture was extracted with ethylacetate (3x50 mL). The organic phase was washed with water, brine and dried over $MgSO_4$. The filtrate was concentrated under reduced pressure and the crude material was purified by flash column chromatography (petroleum ether/ethyl acetate 95:5) to give **S7** (1.4 g, 80%) as a colourless oil.

^{1}H NMR (400 MHz, $CDCl_3$, 295 K): δ 3.71 – 3.55 (m, 2H), 2.49 (dd, J = 9.3, 7.9, 6.3, 1.8 Hz, 4H), 1.72 – 1.48 (m, 6H), 1.47 – 1.28 (m, 4H), 1.27 – 1.14 (m, 1H), 0.97 – 0.80 (m, 16H), 0.04 (s, 6H).

^{13}C NMR (101 MHz, $CDCl_3$, 295 K): δ 61.30, 39.80, 36.34, 32.42, 31.81, 29.18, 27.17, 25.95, 22.02, 19.60, 18.30, 13.69, -5.30.

HRMS (ESI^+): *m/z* = 319.2480 $[M+H]^+$ (calculated 319.2491 for $C_{17}H_{39}OSSi^+$).

(S)-6-(butylthio)-3-methylhexan-1-ol (S8)

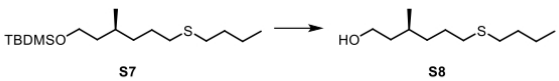

S7 **S8**

S7 (1.4 g, 4.4 mmol, 1 equiv.) was dissolved in 30 mL THF. TBAF (1 M solution in THF, 4.84 mL, 4.8 mmol, 1.1 equiv.) was added at 0 °C and the reaction mixture was stirred at room temperature for 12 h. The solvent was removed under reduced pressure and water (75 mL) was added. The reaction

mixture was extracted with ethylacetate (3*50 mL). The organic phase was washed with brine and dried over $MgSO_4$. The solvent was removed under reduced pressure and the crude material was purified by flash column chromatography (ethyl acetate/petroleum ether 20:80) to give **S8** (898 mg, 100%) as a colourless oil.

^{1}H NMR (400 MHz, $CDCl_3$, 295 K): δ 3.67 (qt, J = 10.6, 6.6 Hz, 2H), 2.49 (dtd, J = 7.9, 4.7, 2.4 Hz, 4H), 1.68 – 1.49 (m, 4H), 1.47 – 1.32 (m, 6H), 1.28 – 1.17 (m, 1H), 0.95 – 0.85 (m, 7H).

^{13}C NMR (101 MHz, $CDCl_3$, 295 K): δ 60.98, 39.77, 36.15, 32.33, 31.82, 31.76, 29.12, 26.99, 22.00, 19.50, 13.67.

HRMS (ESI$^-$): *m/z* = 205.1621 $[M+H]^+$ (calculated 205.1626 for $C_{11}H_{25}OS^+$).

(S)-butyl(6-iodo-4-methylhexyl)sulfide (S9)

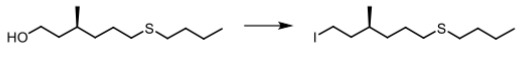

S8 **S9**

This compound was prepared following the same procedure as for **S6** to give **S9** (450 mg, 30%) as colourless oil.

^{1}H NMR (400 MHz, $CDCl_3$, 295 K): δ 3.25 (ddd, J = 9.6, 8.3, 5.7 Hz, 1H), 3.16 (ddd, J = 9.6, 8.0, 7.3 Hz, 1H), 2.55 – 2.44 (m, 4H), 1.86 (dddd, J = 13.5, 8.2, 7.3, 5.1 Hz, 1H), 1.71 – 1.50 (m, 6H), 1.47 – 1.34 (m, 3H), 1.23 (dddd, J = 13.2, 10.2, 7.7, 5.6 Hz, 1H), 0.97 – 0.85 (m, 6H).

^{13}C NMR (101 MHz, $CDCl_3$, 295 K): δ 40.64, 35.29, 33.48, 32.26, 31.82, 31.73, 26.86, 21.97, 18.60, 13.67, 5.08.

HRMS (ESI$^+$): *m/z* = 315.0626 $[M+H]^+$ (calculated 315.0638 for $C_{11}H_{24}IS^+$).

General procedure compounds S10 – S12

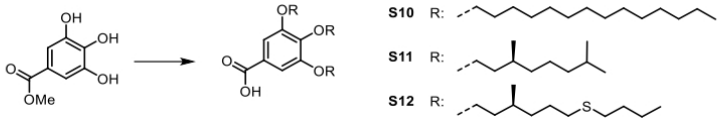

A 250 mL round-bottom flask was charged with 3,4,5-trihydroxymethylbenzoate (10 mmol, 1 equiv.), the corresponding alkyl halide (35 mmol, 3.5 equiv.), a spatula tip of potassium iodide and 100 mL of dry DMF. Anhydrous Cs_2CO_3 (42 mmol, 4.2 equiv.) was added and the reaction mixture was stirred at 130 °C until all starting material was consumed (NMR control). The solvent was removed under reduced pressure. The residue was suspended in 150 mL of water and extracted with CH_2Cl_2 (4*75 mL). The combined organic phase was dried over magnesium sulfate and evaporated under reduced pressure. To the residue were added 50 mL of MeOH, 150 mL of water and sodium hydroxide (0.15 mol, 15 equiv.). The reaction mixture was refluxed until all starting material was consumed (TLC control), cooled down to room temperature, carefully acidified with concentrated hydrochloric acid to pH 1 and extracted with CH_2Cl_2. The organic phase was dried over magnesium sulfate and the solvent was removed under reduced pressure. The crude material was purified by flash column chromatography (petroleum ether/ethyl acetate 9:1).

3,4,5-tris(tetradecyloxy)benzoic acid (S10)

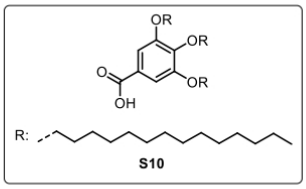

Yield: 87%, orange oil.

^{1}H NMR (400 MHz, $CDCl_3$, 295 K): δ 7.33 (s, 2H), 4.06 – 4.0 (m, 6H), 1.82 (p, J = 6.7 Hz, 4H), 1.74 (p, J = 6.9 Hz, 2H), 1.48 (p, J = 7.1 Hz, 6H), 1.27 (m, 66H), 0.88 (t, J = 6.7 Hz, 9H).

^{13}C NMR (101 MHz, $CDCl_3$, 295 K): δ 171.95, 152.82, 143.10, 123.61, 108.48, 73.53, 69.14, 31.93, 30.32, 29.75, 29.71, 29.67, 29.64, 29.56, 29.39, 29.38, 29.26, 26.07, 26.04, 22.69, 14.12.

HRMS (ESI$^+$): *m/z* = 759.6863 $[M + H]^+$ (calculated 759.6867 for $C_{49}H_{91}O_5^+$).

3,4,5-tris(((S)-3,7-dimethyloctyl)oxy)benzoic acid (S11)

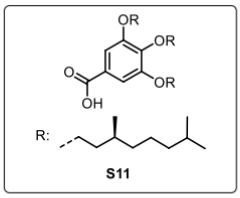

Yield: 85%, orange oil.

^{1}H NMR (400 MHz, $CDCl_3$, 295 K): δ 7.34 (s, 2H), 4.15 – 4.20 (m, 6H), 1.92 – 1.79 (m, 3H), 1.76 – 1.67 (m, 3H), 1.67 – 1.57 (m, 2H), 1.57 – 1.47 (m, 4H), 1.39 – 1.22 (m, 9H), 1.22 – 1.08 (m, 9H), 0.95 (d, J = 6.6 Hz, 6H), 0.93 (d, J = 6.6 Hz, 3H), 0.87 (dd, J = 6.6, 2.3 Hz, 18H).

^{13}C NMR (101 MHz, $CDCl_3$, 295 K): δ 171.71, 152.88, 143.19, 123.62, 108.55, 77.20, 71.79, 67.52, 39.36, 39.27, 37.48, 37.33, 36.28, 29.86, 29.64, 27.98, 24.73, 22.69, 22.59, 19.59, 19.57.

HRMS (ESI^+): *m/z* = 591.4982 $[M + H]^+$ (calculated 591.4989 for $C_{37}H_{67}O_5^+$).

Compound S12

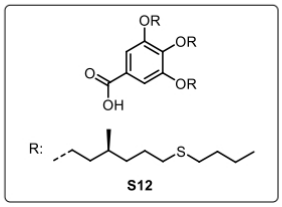

Yield: 98%, orange oil.

^{1}H NMR (400 MHz, $CDCl_3$, 295 K): δ 7.32 (s, 2H), 4.12 – 4.00 (m, 6H), 2.58-2.43 (m, 12H), 1.95 – 1.80 (m, 3H), 1.80 – 1.69 (m,3H), 1.69 – 1.49 (m, 17H), 1.49 – 1.35 (m, 10H), 1.35 – 1.21 (m, 7H), 1.01 – 0.86 (m, 19H).

^{13}C NMR (101 MHz, $CDCl_3$, 295 K): δ 170.77, 152.79, 142.94, 123.60, 108.46, 77.20, 71.54, 67.34, 37.20, 36.50, 36.28, 36.15, 32.51, 32.43, 31.91, 31.89, 31.81, 29.67, 29.40, 27.17, 22.04, 19.51, 19.45, 13.71, 1.01.

HRMS (ESI^-): *m/z* = 727.4475 $[M - H]^-$ (calculated 727.4469 for $C_{40}H_{71}O_5S_3^-$).

General procedure compounds S13 – S15

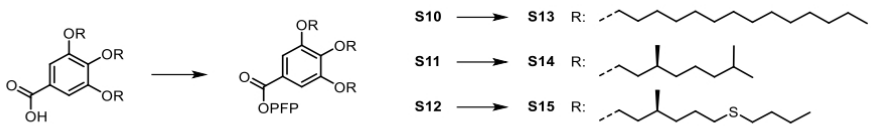

Acid **S10** – **S12** (11 mmol, 1 equiv.), 2,3,4,5,6-pentafluorophenol (13.2 mmol, 1.2 equiv.) and few crystals of DMAP were dissolved in 40 mL of CH_2Cl_2. EDC (13.2 mmol, 1.2 equiv.) was added. The

reaction mixture was stirred at room temperature overnight, diluted with 100 mL of CH_2Cl_2 and washed with water (4*75 mL). The organic phase was dried over magnesium sulfate and evaporated to give the title compound, which was used for the next step without further purification.

Pentafluorophenyl 3,4,5-tris(tetradecyloxy)benzoate (S13)

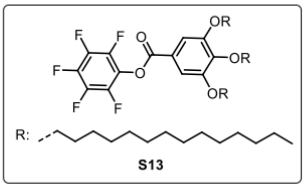

S13

Crude yield: 96%, colourless solid.

^{1}H NMR (400 MHz, $CDCl_3$, 295 K): δ 7.39 (s, 2H), 4.09 – 4.0 (m, 6H), 1.83 (p, J = 6.8 Hz, 4H), 1.79 – 1.70 (p, J = 6.9 Hz, 2H), 1.48 (p, J = 7.4 Hz, 6H), 1.40 – 1.18 (m, J = 8.9 Hz, 74H), 0.88 (t, J = 6.7 Hz, 9H).

^{19}F NMR (377 MHz, $CDCl_3$, 295 K): δ -152.23 – -153.02 (m, 2F), -158.39 (t, *J* = 22.3 Hz, 1F), -162.55 – -162.87 (m, 2F).

^{13}C NMR (101 MHz, $CDCl_3$, 295 K): δ 171.25, 162.45, 153.12, 144.02, 143.09 – 142.16 (m), 141.15 – 139.78 (m), 139.63 – 138.57 (m), 137.33 – 136.32 (m), 121.01, 109.05, 73.68, 72.98, 69.32, 64.67, 31.93, 30.34, 29.70, 29.63, 29.56, 29.37, 29.25, 26.06, 22.69, 14.11.

Pentafluorophenyl 3,4,5-tris(((S)-3,7-dimethyloctyl)oxy)benzoate (S14)

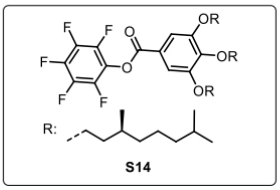

S14

Crude yield: 90%, orange oil.

^{1}H NMR (400 MHz, $CDCl_3$, 295 K): δ 7.40 (s, 2H), 4.16 – 4.03 (m, 6H), 1.93 – 1.80 (m, 3H), 1.76 - 1.68 (m, 3H), 1.67 – 1.58 (m, 2H), 1.58 – 1.47 (m, 4H), 1.38 – 1.23 (m, 9H), 1.21 – 1.10 (m, 9H), 0.95 (d, J = 6.5 Hz, 6H), 0.92 (d, J = 6.6 Hz, 3H), 0.85 (dd, J = 6.6, 1.3 Hz, 18H).

^{19}F NMR (377 MHz, $CDCl_3$, 295 K): δ -151.60 – -152.27 (m, 2F), -157.66 (t, *J* = 21.7 Hz, 2F), -162.01 (td, J = 22.5, 5.1 Hz, 1F).

^{13}C NMR (101 MHz, $CDCl_3$): δ 162.47, 153.11, 143.93, 142.98 – 142.08 (m), 141.21 – 139.94 (m), 139.57 – 138.83 (m), 137.19 – 136.26 (m), 125.46, 121.03, 108.94, 77.20, 71.89, 67.58, 39.33, 39.23, 37.45, 37.30, 36.21, 29.79, 29.58, 27.98, 24.73, 22.69, 22.58, 19.55.

Compound S15

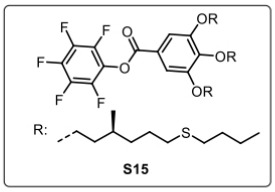

Crude yield: 88%, orange oil.

^{1}H NMR (400 MHz, $CDCl_3$, 295 K): δ 7.39 (s, 2H), 4.15 – 4.01 (m, 6H), 2.57 – 2.43 (m, 14H), 1.95 – 1.80 (m, 3H), 1.80 – 1.70 (m, 4H), 1.69 – 1.50 (m, 17H), 1.50 – 1.35 (m, 11H), 1.34 – 1.22 (m, 4H), 1.02 – 0.86 (m, 21H).

^{19}F NMR (377 MHz, $CDCl_3$, 295 K): δ -151.76 – -152.42 (m, 2F), -157.65 (t, J = 21.7 Hz, 1F), -162.00 (td, J = 22.6, 5.1 Hz, 2F).

^{13}C NMR (101 MHz, $CDCl_3$, 295 K): δ 162.41, 153.05, 143.83, 142.85 – 142.43 (m), 140.36 – 139.82 (m), 139.54 – 183.91 (m), 137.08 – 136.24 (m), 121.14, 108.99, 106.56, 71.70, 67.48, 37.18, 36.47, 36.29, 36.24, 36.19, 36.11, 32.50, 32.42, 31.91, 31.81, 31.79, 29.64, 29.38, 27.16, 27.13, 22.03, 22.02, 19.50, 19.43, 13.70, 13.68.

General procedure compounds M_1 – M_5

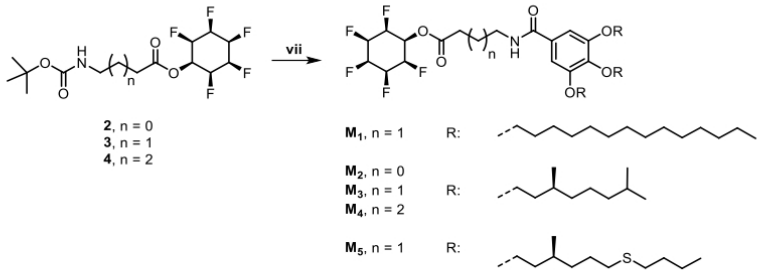

To a suspension of compound **2 - 4** (2 mmol, 1 equiv.) in 2 mL of anhydrous CH_2Cl_2 was added 2 mL of TFA at 0 °C. The reaction mixture was stirred at room temperature until all starting material was consumed. CH_2Cl_2 and TFA were removed under vacuum. Pentafluorophenyl ester **S13** – **S15** (4 mmol, 2 equiv.), 5 mL of DMF and triethylamine 3 mL were added subsequently and the reaction mixture was stirred at room temperature overnight. After removal of solvents under reduced pressure the crude material was purified by flash column chromatography (CH_2Cl_2 to CH_2Cl_2/acetone 8:2) to yield the title compound.

Comments on reaction conditions, side products and purification:

1. DMF is needed to completely dissolve starting materials containing all-*cis* $C_6H_6F_5$ group and to prevent gelation which sometimes can happen if DCM alone is used as a solvent.
2. To completely remove pentafluorophenol from the reaction mixture, sometimes two purifications by flash column chromatography are needed.
3. For the linker based on γ-aminobutyric acid approximately 13% of butyrolactam was formed as a side product.

Compound M_1

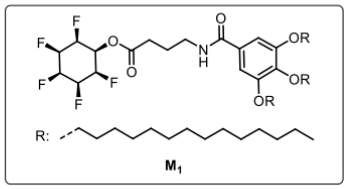

Yield: 71%, colourless solid.

^{1}H NMR (400 MHz, $CDCl_3$, 295 K): δ 6.95 (s, 2H), 6.38 (br s, 1H), 5.52 – 4.22 (m, 5H), 4.03 - 3.92 (m, 6H), 3.50 (q, J = 6.5 Hz, 2H), 2.58 (t, J = 7.0 Hz, 2H), 2.00 (p, J = 6.8 Hz, 2H), 1.83 – 1.65 (m, 7H), 1.51 – 1.39 (m, 7H), 1.38 – 1.16 (m, 66H), 0.88 (t, J = 6.7 Hz, 9H).

^{19}F NMR (377 MHz, $CDCl_3$, 295 K) mixture of conformers: δ -209.83 (br s, 2F), -210.66, -211.73, -215.95 (d, *J* = 26.2 Hz, 2F), -215.78, -216.83 (br s, 1F).

^{13}C NMR (101 MHz, $CDCl_3$, 295 K): δ 172.24, 167.52, 153.10, 141.06, 129.14, 105.43, 87.79 – 86.82 (m), 85.92 – 84.55 (m), 83.76 – 82.73 (m), 73.50, 69.28, 66.47 – 65.85, 38.89, 31.92, 31.17, 30.31, 29.73, 29.65, 29.58, 29.42, 29.36, 26.08, 24.73, 22.68, 14.10.

HRMS (ESI^+): *m/z* = 1016.7679 $[M+H]^+$ (calculated 1016.7706 for $C_{59}H_{103}F_5NO_6^+$).

Compound M_2

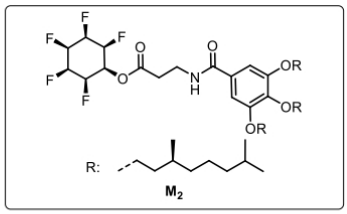

Yield: 64%, glassy colourless solid.

^{1}H NMR (400 MHz, $CDCl_3$, 295 K): δ 6.96 (s, 2H), 6.77 (br s, 1H), 5.45 – 4.38 (m, 5H), 4.08 – 3.93 (m, 6H), 3.73 (q, J = 6.1 Hz, 2H), 2.79 (t, J = 5.8 Hz, 2H), 1.89 – 1.75 (m, 3H), 1.74 – 1.63 (m, 3H), 1.63 – 1.45 (m, 6H), 1.38 – 1.20 (m, 10H), 1.20 – 1.04 (m, 9H), 0.94 – 0.89 (m, 9H), 0.86 (d, J = 6.5 Hz, 18H).

^{19}F NMR (377 MHz, $CDCl_3$, 295 K) mixture of conformers: δ -207.32 (br s, 2F), -208.13 (br s, 1F), -209.13 (br s, 0.5F), -212.01 – -212.60 (m, 2F), -213.01 (br s, 1F), -214.25 (s. 0.5F).

^{13}C NMR (126 MHz, $CDCl_3$, 295 K): δ 170.74, 167.48, 153.06, 140.94, 128.96, 105.34, 88.17 – 86.63 (m), 86.63 – 84.12 (m), 84.05 – 81.71 (m), 71.73, 67.43, 66.60 – 66.03 (m), 39.32, 39.24, 37.48, 37.35, 37.31, 36.35, 35.46, 34.57, 29.77, 29.65, 27.94, 24.70, 24.67, 22.66, 22.56, 19.51, 19.42.

HRMS (ESI$^+$): *m/z* = 872.5128 $[M+K]^+$ (calculated 872.5230 for $C_{46}H_{75}F_5NKO_6^+$).

Compound M$_3$

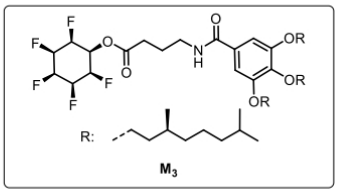

M$_3$

Yield: 87%, glassy colourless solid.

^{1}H NMR (500 MHz, $CDCl_3$, 295 K): δ 6.97 (s, 2H), 6.41 (t, J = 5.9 Hz, 1H), 5.47 – 4.37 (m, 6H), 4.09 – 3.92 (m, 6H), 3.49 (q, J = 6.6 Hz, 2H), 2.57 (t, J = 7.0 Hz, 2H), 1.99 (p, J = 6.9 Hz, 2H), 1.90 – 1.76 (m, 3H), 1.75 - 1.64 (m, 4H), 1.63 – 1.56 (m, 7H), 1.38 – 1.21 (m, 10H), 1.21 – 1.08 (m, 10H) 0.95 – 0.89 (m, 9H), 0.86 (d, J = 6.6 Hz, 20H).

^{19}F NMR (377 MHz, $CDCl_3$, 295 K) mixture of conformers: δ -208.81 (br s, 2F), -209.62, -210.64, -214.94, -215.97 (br s, 1F).

^{13}C NMR (126 MHz, $CDCl_3$, 295 K): δ 172.21, 167.56, 153.12, 141.08, 129.17, 105.45, 87.84 – 86.73, 86.20 – 84.41, 84.11 – 82.60, 83.38, 77.20, 71.74, 67.58, 66.49 – 65.97, 39.33, 39.24, 38.93, 37.48, 37.35, 37.31, 36.37, 31.18, 29.79, 29.66, 27.95, 24.71, 22.67, 22.57, 19.52, 19.47.

HRMS (ESI$^+$): *m/z* = 848.5829 $[M+H]^+$ (calculated 848.5822 for $C_{47}H_{79}F_5NO_6^+$).

Compound M$_4$

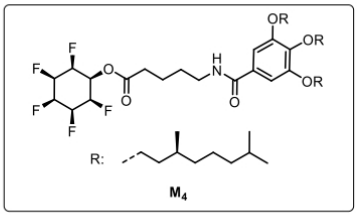

M$_4$

Yield: 26%, glassy colourless solid.

^{1}H NMR (400 MHz, acetone-d_6, 295 K): δ 7.76 (s, 1H), 7.22 (s, 2H), 5.59 – 4.86 (m, 8H), 4.14 – 3.93 (m, 6H), 3.44 – 3.31 (m, 3H), 2.58 – 2.44 (m, 3H), 2.56 – 2.45 (m, 3H), 1.92 – 1.46 (m, 20H), 1.44 – 1.25 (m, 11H), 1.25 – 1.09 (m, 10H), 0.98 – 0.94 (m, 9H), 0.90 – 0.85 (m, 19H).

^{19}F NMR (377 MHz, acetone-d_6, 295 K): δ -211.44 (br s, 2F), -215.89 (br s, 2F), -217.85 (br s, 1F).

^{13}C NMR (101 MHz, acetone-d_6, 295 K): δ 173.31, 167.43, 154.29, 141.93, 131.46, 107.09, 101.42, 90.01 – 88.59, 88.11 – 86.68, 86.12 – 84.65, 72.34, 68.10 – 67.44, 40.66, 40.56, 40.45, 40.33, 38.76, 38.63, 37.80, 34.51, 34.29, 31.03, 29.25, 26.06, 23.56, 23.46, 23.15, 20.60, 20.40.

HRMS (ESI$^+$): *m/z* = 884.5575 $[M+Na]^+$ (calculated 884.5803 for $C_{48}H_{80}F_5NNaO_6^+$).

Compound M_5

Yield: 23%, glassy colourless solid.

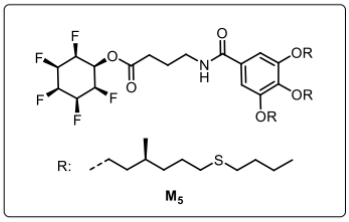

M_5

^{1}H NMR (500 MHz, $CDCl_3$, 295 K): δ 6.96 (s, 2H), 6.25 (br s, 1H), 5.48 – 4.35 (m, 6H), 4.10 – 3.95 (m, 6H), 3.53 (q, J = 6.5 Hz, 2H), 2.60 (t, J = 7.2 Hz, 2H), 2.54 - 2.44 (m, 12H), 2.02 (p, J = 6.8 Hz, 2H), 1.91 – 1.79 (m, 4H), 1.77 – 1.68 (m, 4H), 1.68 – 1.52 (m, 16H), 1.51 – 1.35 (m, 11H), 1.35 – 1.21 (m, 6H), 0.98 – 0.94 (m, 8H), 0.z94 – 0.89 (m, 11H).

^{19}F NMR (377 MHz, $CDCl_3$, 295 K) mixture of conformers: δ -209.48 (br s, 2F), -210.32, -211.32, -214.77 (d, J = 24 Hz, 2F), -215.53, -216.53 (br s, 1F).

^{13}C NMR (126 MHz, $CDCl_3$, 295 K): δ 172.26, 167.44, 153.06, 141.05, 129.27, 105.54, 87.55 – 86.43 (m), 86.15 – 84.15 (m), 84.11 – 82.73 (m), 71.49, 67.49, 66.49 – 65.77, 38.87, 37.20, 36.52, 36.26, 36.12, 32.53, 32.45, 31.91, 31.82, 31.22, 29.64, 29.43, 27.17, 24.74, 22.03, 19.49, 19.45, 13.69.

HRMS (ESI$^-$): *m/z* = 1020.5067 $[M+Cl]^-$ (calculated 1020.5075 for $C_{50}H_{84}F_5NS_3O_6Cl^-$).

Synthesis of *Me*M$_3$

Methyl 4-((tert-butoxycarbonyl)(methylamino)butanoate (S17)



S17

A 100 mL heat gun-dried Schlenk flask was charged with γ-(Boc-amino)butyric acid (2 g, 9.9 mmol, 1 equiv.), methyl iodide (6 mL, 99 mmol, 10 equiv.) and 40 mL of dry DMF under argon. NaH (2.36 g of 60% (w%) solution in mineral oil, 60 mmol, 6 equiv.) was added at 0 °C, the reaction mixture was stirred at this temperature for 2 h and ice bath was removed and reaction was stirred at room temperature overnight. Excess of NaH was carefully quenched with water, 50 mL of concentrated aqueous solution of ammoniac was added. The reaction mixture was diluted with 150 mL of water and extracted with ethyl acetate (4*50 mL). The combined organic phase was washed with water (3*50 mL) and brine. The organic phase was dried over sodium sulfate and evaporated under reduced pressure to give **S17** (2.2 g, 97%) as yellowish oil ,which was used for the next step without purification.

^{1}H NMR (400 MHz, $CDCl_3$, 295 K): δ 3.64 (s, 3H), 3.22 (t, J = 7.1 Hz, 2H), 2.81 (s, 3H), 2.29 (t, J = 7.4 Hz, 2H), 1.81 (p, J = 7.3 Hz, 2H), 1.42 (s, 9H).

^{13}C NMR (101 MHz, $CDCl_3$, 295 K): δ 173.52, 155.69, 79.29, 51.57, 51.51, 48.02, 47.57, 37.02, 33.95, 32.68, 31.86, 30.99, 29.96, 29.63, 29.29, 28.35, 27.02, 23.08, 22.98, 22.62, 19.66, 17.15, 14.05.

HRMS (ESI$^+$): *m/z* = 254.1364 $[M+Na]^+$ (calculated 254.1368 for $C_{11}H_{21}NO_4Na^+$).

Compound S18

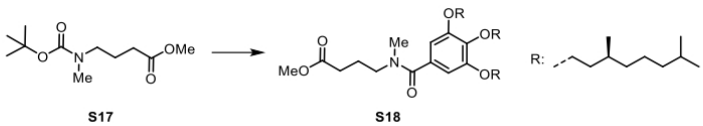

S17 **S18**

S17 (254 mg, 1.1 mmol, 1 equiv.) was dissolved in CH_2Cl_2 (1 mL) and TFA (1 mL) was added. The reaction mixture was stirred for 30 minutes and the solvent was removed under vacuum. To the obtained solid material **S14** (1g, 1.32 mmol, 1.2 equiv), few crystals of DMAP, CH_2Cl_2 (2 mL) and TEA (1 mL) were added subsequently. The reaction mixture was stirred for 12h at room temperature.

The solvent was removed under reduced pressure and the crude material was purified by flash column chromatography (petroleum ether/ethyl acetate 8:2) to give **S18** (515 mg, 67%) as a colourless oil.

^{1}H NMR (400 MHz, $CDCl_3$, 295 K): δ 6.56 (s, 2H), 4.05 – 3.09 (m, 6H), 3.75 – 3.20 (m, 5H), 3.10 – 2.92 (br, 3H), 2.62 – 2.08 (br, 2H), 2.08 – 1.94 (br, 1H), 1.94 – 1.75 (m, 4H), 1.74 – 1.45 (m, 10H), 1.39 – 1.20 (m, 10H), 1.20 – 1.08 (m, 10H), 0.92 (d, J = 6.6 Hz, 6H), 0.91 (d, J = 6.6 Hz, 3H), 0.86 (d, J = 6.7 Hz, 18H).

^{13}C NMR (101 MHz, $CDCl_3$, 295 K): δ 171.72, 153.08, 139.11, 130.94, 105.46, 105.06, 77.21, 71.66, 67.48, 51.67, 39.33, 39.23, 37.48, 37.30, 36.32, 29.79, 29.64, 27.95, 24.70, 22.68, 22.57, 19.51.

HRMS (ESI^+): *m/z* = 704.5808 $[M+H]^+$ (calculated 704.5829 for $C_{43}H_{78}NO_6^+$).

Compound *Me*M$_3$

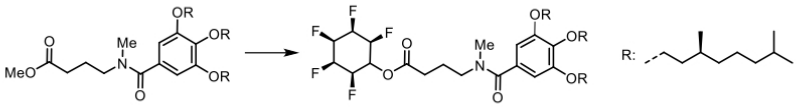

S18 (1.1 g, 1.38 mmol, 1 equiv.) and sodium hydroxide (1 g, 25 mmol, 18 equiv.) were refluxed in 25 ml of water/methanol (3:1) mixture until all starting material was consumed. The reaction mixture was acidified at 0 °C to pH=1 with a concentrated aqueous solution of hydrochloric acid and extracted with CH_2Cl_2 (3*50 mL). The organic phase was dried over anhydrous sodium sulfate and evaporated under reduced pressure. The obtained orange oil was dissolved in 50 mL of CH_2Cl_2. Pentafluorophenol (305 mg, 1.66 mmol, 1.2 equiv.), few crystals of DMAP and EDC (312 mg, 1.66 mmol, 1.2 equiv.) were added subsequently and the reaction mixture was stirred overnight at room temperature. 100 mL of water were added and extracted with CH_2Cl_2 (4*50 mL). Organic phase was dried over anhydrous sodium sulfate and solvent was removed under reduced pressure. To the residue **1** (201 mg, 1.06 mmol, 0.77 equiv.), 1 mL of dry DMF and 1 mL of TEA were added. The reaction mixture was stirred at 120 °C for 4 h after which solvents were removed and crude material was purified via flash column chromatography (gradient elution CH_2Cl_2 to CH_2Cl_2/acetone 8:2) to give ***Me*M$_3$** (870 mg, 65%) as a colourless solid.

^{1}H NMR (500 MHz, $CDCl_3$, 295 K): δ 6.58 (s, 2H), 5.44 – 4.30 (m, 5H), 4.10 – 3.87 (m, 6H), 3.69 – 3.28 (m, 2H), 3.14 – 2.92 (m, 3H), 2.68 – 2.26 (m, 2H), 2.10 – 1.77 (m, 5H), 1.77 – 1.66 (m, 3H),

1.66 – 1.49 (m, 6H), 1.42 – 1.24 (m, 9H), 1.25 – 1.11 (m, 9H), 0.93 (d, J = 6.6 Hz, 6H), 0.92 (d, J = 6.6 Hz, 3H), 0.87 (d, J = 6.6 Hz, 17H).

^{19}F NMR (377 MHz, $CDCl_3$, 295 K): δ -210.26 (d, J = 93.3 Hz, 2F), -211.18, -212.36, -215.75 (br s, 2F), -216.43, -217.12 (br s, 1F).

^{13}C NMR (126 MHz, $CDCl_3$, 295 K): δ 171.67, 153.18, 139.34, 131.56, 131.10, 105.55, 104.75, 87.63 – 86.68 (m), 86.02 – 84.59 (m), 83.91 – 83.05 (m), 71.75, 66.97 – 65.95 (m), 50.20, 46.10, 39.35, 39.30, 39.28, 39.25, 39.20, 37.51, 37.42, 37.34, 37.25, 36.34, 32.80, 30.78, 29.96, 29.82, 29.72, 27.96, 24.71, 22.68, 22.60, 22.57, 19.54, 19.49.

HRMS (ESI^+): *m/z* = 862.5955 $[M+H]^+$ (calculated 862.5984 for $C_{48}H_{81}F_5NO_6^+$).

Synthesis of Ref$_2$

Cyclohexyl 4-((tert-butoxycarbonyl)amino)butanoate (S19)

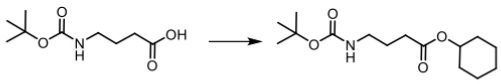

S19

γ-(Boc-amino)butyric acid (470 mg, 2.3 mmol, 1 equiv.), cyclohexanol (481 µL, 4.6 mmol, 2 equiv.) and few crystals of DMAP were dissolved in CH_2Cl_2. EDC (441 mg, 2.3 mmol, 1 equiv.) was added and the reaction mixture was stirred overnight at room temperature. The reaction mixture was diluted with ethyl acetate (50 mL), washed with water (3*25mL) and brine (2*25 mL). The organic phase was dried over sodium sulfate and evaporated under reduced pressure. Excess of cyclohexanol was distilled off under vacuum to give **S19** (450 mg, 69%) as a colourless oil.

^{1}H NMR (400 MHz, $CDCl_3$, 295 K): δ 4.74 (td, J = 8.9, 4.1 Hz, 1H), 4.63 (br, 1H), 3.16 (q, J = 6.6 Hz, 2H), 2.32 (t, J = 7.3 Hz, 2H), 1.87 – 1.75 (m, 4H), 1.75 – 1.64 (m, 2H), 1.59 – 1.49 (m, 1H), 1.43 (s, 9H), 1.40 – 1.16 (m, 5H).

^{13}C NMR (101 MHz, $CDCl_3$, 295 K): δ 172.72, 155.90, 79.17, 77.21, 72.72, 39.98, 32.04, 31.61, 28.39, 25.34, 23.74.

HRMS (ESI^+): *m/z* = 593.3778 $[2M+Na]^+$ (calculated 593.3772 for $C_{30}H_{54}N_2O_8Na^+$).

Compound Ref$_2$

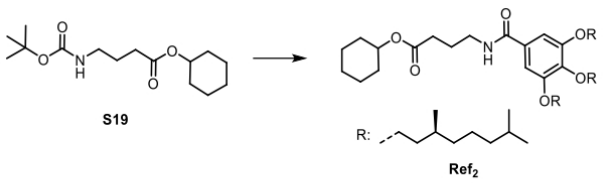

S19 (450 mg, 1.58 mmol, 1 equiv.) was stirred in 1 mL of CH_2Cl_2/TFA (1:1 v/v) mixture for 30 min. Solvent was removed under reduced pressure. **S14** (1.5 g, 1.9 mmol, 1.2 equiv.), few crystals of DMAP, 1 mL of CH_2Cl_2 and 1 mL of TEA were added subsequently and the reaction mixture was stirred overnight at room temperature. Solvent was removed under reduced pressure and crude material was purified by flash column chromatography (petroleum ether/ethyl acetate 8:2) to yield **Ref$_2$** (684 mg, 57%) as yellow oil, which solidified upon standing.

^{1}H NMR (400 MHz, $CDCl_3$, 295 K): δ 7.00 (s, 2H), 6.69 (t, J = 5.4 Hz, 1H), 4.74 (td, J = 8.9, 4.1 Hz, 1H), 4.21 – 3.86 (m, 6H), 3.50 (q, J = 6.3 Hz, 2H), 2.45 (t, J = 6.8 Hz, 2H), 1.96 (p, J = 6.7 Hz, 2H), 1.91 – 1.76 (m, 5H), 1.75 – 1.65 (m, 5H), 1.64 – 1.57 (m, 2H), 1.57 – 1.46 (m, 5H), 1.45 – 1.21 (m, 16H), 1.21 – 1.09 (m, 9H), 0.94 (d, J = 6.6 Hz, 6H), 0.91 (d, J = 6.7 Hz, 3H), 0.86 (d, J = 6.6 Hz, 9H).

^{13}C NMR (101 MHz, $CDCl_3$, 295 K): δ 173.68, 167.47, 153.06, 140.97, 129.17, 105.44, 76.12, 73.15, 71.70, 67.53, 40.11, 39.35, 39.26, 37.49, 37.35, 37.30, 36.38, 32.65, 31.58, 29.83, 29.64, 27.98, 25.29, 24.73, 24.19, 23.73, 22.70, 22.59, 19.54.

HRMS (ESI$^+$): *m/z* = 758.6307 $[M+H]^+$ (calculated 758.6299 for $C_{47}H_{84}NO_6^+$).

N-butyl-3,4,5-tris(((S)-3,7-dimethyloctyl)oxy)benzamide (Ref$_3$)

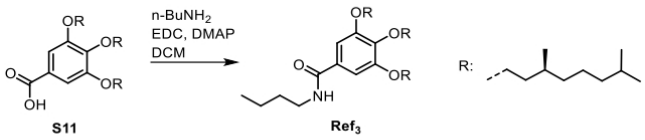

S11 (180 mg, 0.31 mmol, 1 equiv.), butan-1-amine (61 µL, 0.62 mmol, 2 equiv.) and few crystals of DMAP were dissolved in 10 mL of CH_2Cl_2. EDC (116 mg, 0.62 mmol, 2 equiv.) was added. The reaction mixture was stirred at room temperature overnight, diluted with 50 mL of CH_2Cl_2 and washed with water (4*50 mL). The organic phase was dried over magnesium sulfate and evaporated.

Crude material was purified by flash column chromatography to give **Ref$_3$** (160 mg, 81%) as a colouress oil.

^{1}H NMR (400 MHz, $CDCl_3$, 295 K): δ 6.95 (s, 2H), 6.01 (t, J = 5.8 Hz, 1H), 4.09 – 3.94 (m, 6H), 3.43 (q, J = 7.2 Hz, 2H), 1.91 – 1.76 (m, 3H), 1.76 – 1.65 (m, 2H), 1.65 – 1.55 (m, 4H), 1.55 – 1.46 (m, 3H), 1.46 – 1.36 (m, 2H), 1.36 – 1.20 (m, 7H), 1.20 – 1.07 (m, 9H), 0.99 – 0.89 (m, 12H), 0.86 (d, J = 6.6 Hz, 18H).

^{13}C NMR (101 MHz, $CDCl_3$, 295 K): δ 167.42, 153.09, 141.05, 129.90, 105.63, 71.70, 67.69, 39.88, 39.35, 39.26, 37.49, 37.33, 37.30, 36.38, 31.82, 29.82, 29.64, 27.97, 24.72, 24.70, 22.69, 22.60, 22.58, 20.17, 19.57, 19.54, 13.79.

HRMS (ESI^+): *m/z* = 668.5596 $[M+Na]^+$ (calculated 668.5588 for $C_{41}H_{75}NNaO_4^+$)

Computational Methods

Parametrization

The molecular models of the molecules **M$_2$**, **M$_3$**, **M$_4$** and ***Me*M$_3$** herein studied, along with the solvent composed by cyclohexane and chloroform were parametrized by using the General Amber Force Field (GAFF),[5] and the partial charges were modelled by using the AM1-BCC method.[6] These parameters were extracted by using the software Antechamber.[7]

Molecular dynamics setup

All the simulation herein performed, were run on GROMACS-2018.6[8] patched with plumed-2.5.[9] All systems were simulated for 1 μs of MD at the temperature of 293 K and pressure of 1 atm in explicit TIP3P water molecules[10] in periodic boundary NPT conditions (constant N: number of particles, P: pressure and T: temperature), employing the v-rescale thermostat[11] and the Berendsen barostat (semi-isotropic barostat during the study of fiber stability).[12] A timestep of 2 fs was used in the MD simulations. The electrostatic interactions were treated using particle mesh Ewald (PME).[13] The cutoff lengths of the real summation and of the VdW were set to 1.0 nm. The dynamics of the hydrogens was constrained using the LINCS algorithm.[14] All the systems studied were simulated with a solvent composition 84:16 cyclohexane:chloroform.

While for the studies of conformations and self-assembly the systems after being minimized were equilibrated with short runs followed by the 1μs MD simulation, the MD simulations of the preformed fibers were performed by first pre-equilibrating the "tails" of the monomers, by keeping restrained the atoms of the "core" (Supplementary Fig. 25b) for 10ns. After this it followed 1μs of MD as production run.

Metadynamics

In this work, we employed metadynamics (MetaD) simulations[15] to enhance the exploration of the conformational space of the single monomers. We used two collective variables (CV): CV1, monitoring the orientation of the pentafluorocyclohexane moiety (F_5-CHX) with respect to the amide moiety, and CV2, controlling the opening of the "core" of the monomer. CV2 is defined as the radius of gyration of the heavy atoms of the "core", while CV1 is defined as the difference between two distances (d_{FsH} and d_{HsO}, in Supplementary Fig. 25c). d_{FsH} is the distance between geometrical center of the fluorides and the amide nitrogen, while d_{HsO} is the distance between the geometrical center of the F_5-CHX-hydrogens and the amide-oxygen. Small values of CV2 indicate that the monomer core is closed, while large values indicate that the core is open. Positive values of CV1 indicate that the system tends to orient F_5-CHX-hydrogens toward the oxygen, while negative values show that the fluorides are closer to the amide group. These metadynamics calculations were performed in its well-tempered variant (WT-MetaD), which allows to obtain a smoother convergence of the system.[16] During the WT-MetaD run, the bias was deposited along CV1 and CV2 in the form of Gaussian-shaped kernels of height *0.8* kJ/mol and σ equal to 0.02 and 0.01 nm along CV1 and CV2 respectively while the deposition rate was *1* ps^{-1}. The bias factor of this WT-MetaD run was set to 15.

Intrinsic structural dynamics of the fiber

In order to deeper investigate on the dynamic of the **M3** and **M5** monomers within the fibers, we performed an unsupervised machine-learning analysis that allowed us to classify the arrangement, order and dynamics of the **M3** and **M5** monomers within the fiber in a robust, abstract and high-dimensional way. The configuration of each monomer from MD trajectory was classified according to its molecular environment by means of a Smooth Overlap of Atomic Positions (SOAP),[17] an approach that encodes the atomic/molecular environment of each molecule as a rotationally invariant representation (SOAP vectors). The SOAP vectors of each molecule were computed, considering five centers, defined as the center of the cyclohexane, the center of the amide for M3 and M5, the alkyl centers in the three tails on **M3** (Supplementary Fig. 52a), and the sulfurs atoms on **M5** (Supplementary Fig. 52b) that occupy the equivalent position of the alkyl moieties in **M3**. Based on this description, the behavior of each monomer in the system is represented (and simplified) by the movements and behaviors of these five centers, which are monitored and characterized by the SOAP vectors. This approach was previously demonstrated to be capable of providing remarkably rich insights into the internal structure and dynamics of supramolecular polymers.[18] We carried out this SOAP analysis with the Python package *DScribe*,[19] setting the input parameters as r_{cut} = 60Å, n_{max} = 5, l_{max} = 5, and leaving the other parameters as default.

The SOAP centers could then be classified into different states by applying a clustering algorithm to the SOAP dataset, to obtain the most probable states in the multidimensional descriptor space. First, we reduced the high-dimensional SOAP features via principal component analysis (PCA) by retaining only the first three components. This approach reduced the computational cost for the processing of the data, while maintaining a high level of accuracy (up to ~86% of the information preserved). Linear PCA dimensionality reduction was performed using the Python package *Scikit-Learn*.[20] At this point, we performed unsupervised clustering of the dimensionally reduced dataset by applying the density-based clustering scheme Probabilistic Analysis of Molecular Motifs (PAMM),[18, 21, 22] which allowed us to classify all possible arrangements of the SOAP centers in the monomers within the fiber during the MD trajectories. The different clusters detected by the PAMM method are represented by different colors and are projected onto the first two PCA components. The obtained microclusters were then merged into dominant macroclusters (see references 18, 21 and 22 for details), in order to obtain a relevant classification with a more direct interpretation in terms of the structural features within the aggregate (Figs. 7c,e). In fig. 7c we can observe the labelling of each center included in the SOAP analysis. From this we can understand that the red-labelled SOAP centers are related to the cyclohexane centers while the blue-labelled SOAP centers are related to the center of the amide – these identify the backbone of the fibers. The other three macroclusters (gray, cyan and green colored) are related to the SOAP centers located on the tails,and are indicative of the fibers' surface. In particular, the green centers are localized in closer proximity of the fiber center, while the cyan ones represent an intermediate layer, and the gray ones identify the most external ones.

Finally, as described in detail in a previous work,[18] the time evolution of this clustering of SOAP centers states, and their dynamic interconversion along the MD trajectory allowed us to retrieve the probability of transition among different states, thus providing a clear picture of the intrinsic dynamics of the fiber. The transition probabilities reported in Fig. 7f of the main text were obtained with this methodology. The rates for the transitions between them can be then simply estimated by dividing these transition probabilities by the timelapse between the analysed snapshots (the examined snapshots are distant in time 0.1 ns from each other in our case.

Supplementary Figures

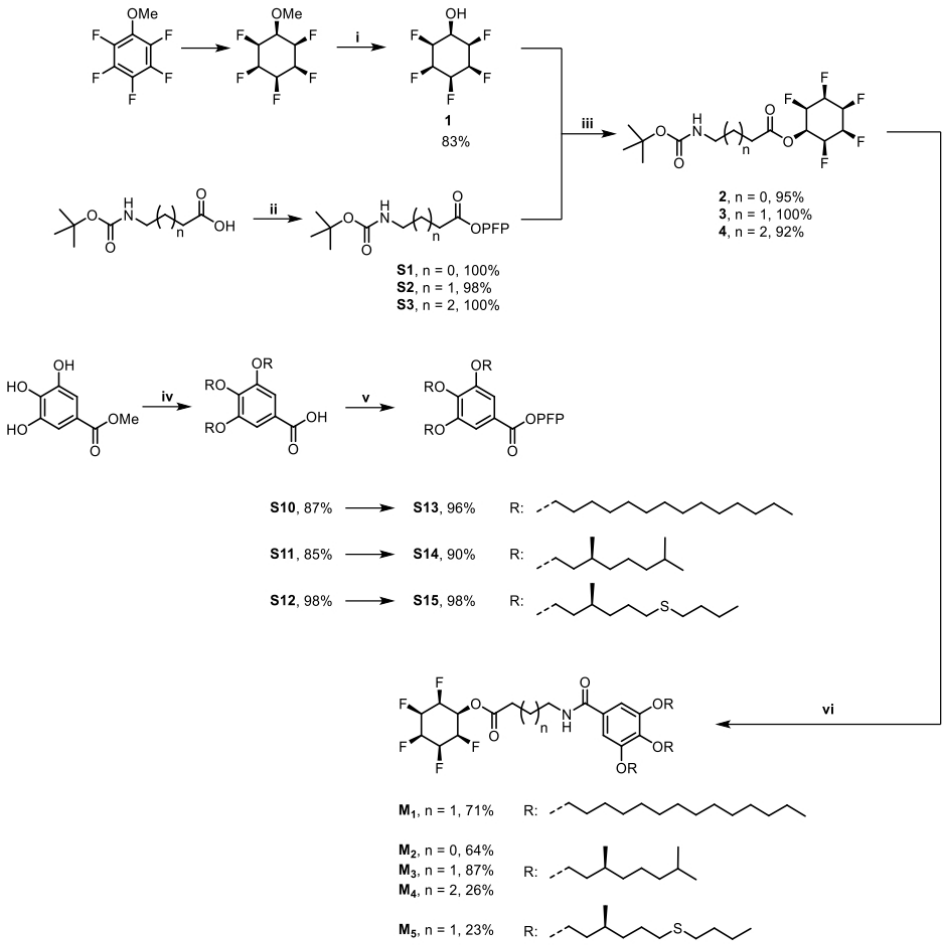

Supplementary Figure 1 | Overview on the synthesis of monomers $\mathbf{M_1 - M_5}$. Reaction conditions: (i) n-BuSH, $AlCl_3$, CH_2Cl_2, room temperature, 14h; (ii) 2,3,4,5,6-pentafluorophenol (PFPOH), EDC, DMAP, CH_2Cl_2, room temperature, 12h; (iii) DMF, TEA, 120 °C, 2h; (iv) 1) R-X, Cs_2CO_3, KI, DMF, 120 °C, 3h; 2) NaOH, MeOH, H_2O; (v) PFPOH, EDC, DMAP, CH_2Cl_2, room temperature, 12h; (vi) 1) TFA, CH_2Cl_2, 0 °C, 2h; 2) CH_2Cl_2, DMAP, TEA, room temperature, 12h.

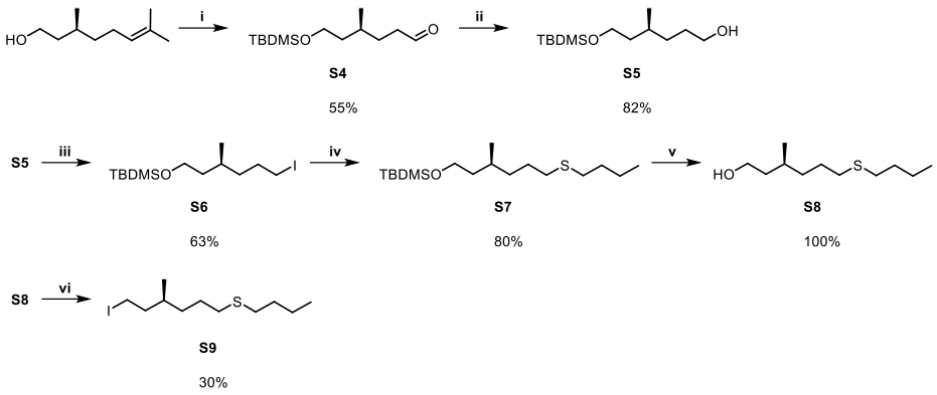

Supplementary Figure 2 | Overview on synthesis of **S9**. Reaction conditions: (i) 1) OsO_4, $NaIO_4$, 1,4-dioxane, H_2O, room temperature, 24h; 2) TBDMSCl, imidazole, CH_2Cl_2, room temperature, 12h; (ii) $NaBH_4$, MeOH, 0 °C to room temperature, 12h; (iii) I_2, PPh_3, imidazole, acetonitrile, 0 °C to room temperature, 2h; (iv) n-BuSH, Cs_2CO_3, TBAI, DMF, 0 °C to room temperature, 2h; (v) TBAF, THF, 0 °C to room temperature, 12h; (vi)) I_2, PPh_3, imidazole, acetonitrile, 0 °C to room temperature, 2h.

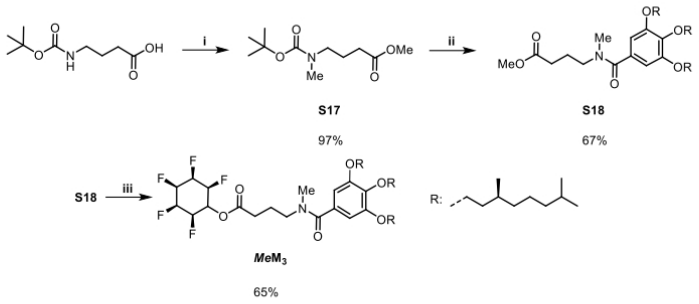

Supplementary Figure 3 | Overview on synthesis of ***Me*M3.** Reaction conditions: (i) MeI, NaH, DMF, 0 °C to room temperature, 12 h; (ii) 1) TFA, CH_2Cl_2, room temperature, 30 min; 2) **S14**, CH_2Cl_2, TEA, room temperature, 12 h; (iii) 1) NaOH, THF, H_2O, reflux, 8 h; 2) PFPOH, EDC, DMAP, CH_2Cl_2, room temperature, 12 h; 3h) **1**, DMF, TEA, 120 °C, 4 h.

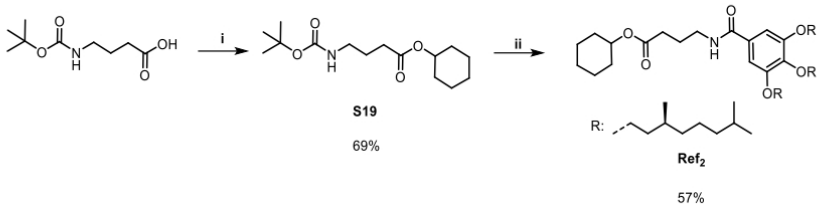

Supplementary Figure 4 | Overview on synthesis of **Ref2**. Reaction conditions: (i) Cyclohexanol, EDC, DMAP, CH_2Cl_2, room temperature, 12 h; (ii) 1) TFA, CH_2Cl_2, 0 °C, 2h; 2) CH_2Cl_2, DMAP, TEA, room temperature, 12h.

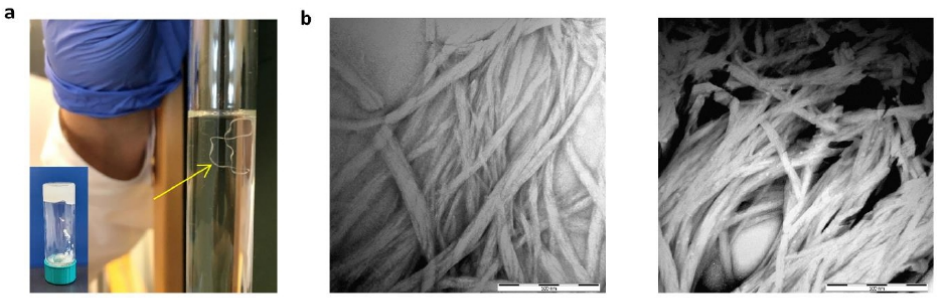

Supplementary Figure 5 | a, Fibers of $\mathbf{M_1}$ growing on the solvent-air interface inside a test tube after flash column chromatography. Inset shows a gel formed by 2 wt.% solution of $\mathbf{M_1}$ in $CHCl_3$. **b**, TEM images of $\mathbf{M_1}$ fibers on a carbon-coated copper grid, negatively stained with uranyl acetate (scale bars: 500 nm).

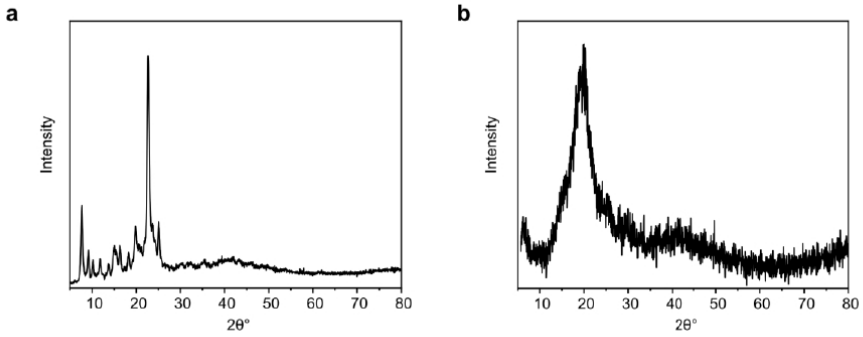

Supplementary Figure 6 | a, PXRD pattern for $\mathbf{M_1}^{\mathbf{Polymer}}$ fibers obtained from 20 mM solution in $CHCl_3$. **b**, PXRD pattern for $\mathbf{M_3}^{\mathbf{Polymer}}$ fibers obtained from 1.2 mM solution in cyclohexane/chloroform 84:16 v/v via seeded growth. In both cases, solvents were removed under vacuum at 273 K and polymers were finely grinded in a mortar prior to measurement.

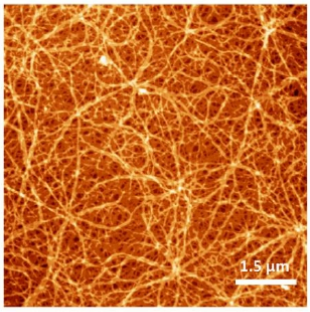

Supplementary Figure 7 | AFM height image of a cooled solution of $\mathbf{M_3}$ (275 K, 1.2 mM, cyclohexane/chloroform 84:16 v/v) spin-coated on a silicon wafer.

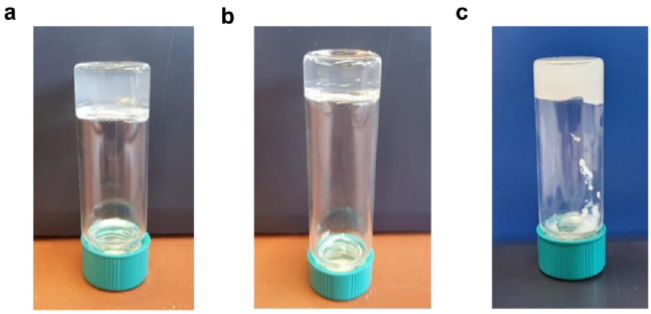

Supplementary Figure 8 | a, Gel of **M3** (5 mM, cyclohexane/chloroform 84:16 v/v, 293 K). **b**, Gel of **M5** (5 mM cyclohexane/chloroform 95:5 v/v 293 K). **c**, Gel of **M1** (17 mM in $CHCl_3$ 293 K).

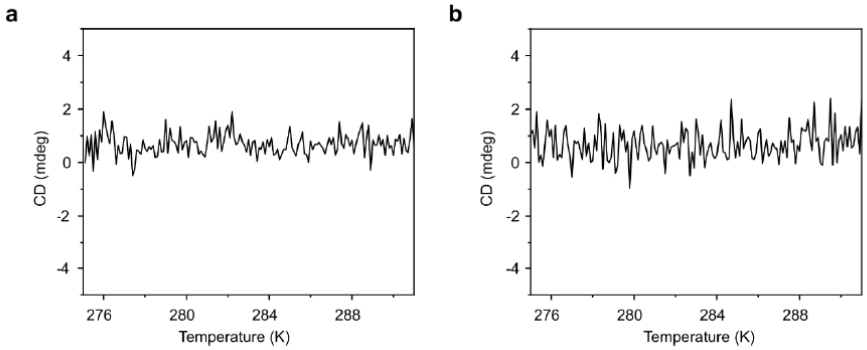

Supplementary Figure 9 | Plots of ellipticity at 260 nm against temperature for the cooling of (**a**) **Ref2** and (**b**) ***Me*M3**. Conditions: 1.2 mM, $CH/CHCl_3$ (84:16 v/v), 0.5 K min^{-1}.

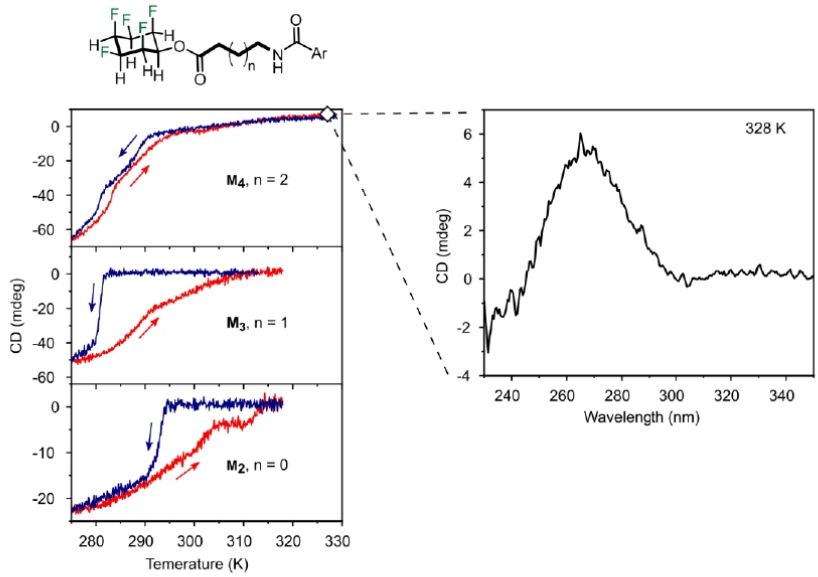

Supplementary Figure 10 | CD signal (260 nm) recorded for cooling (blue lines) and heating (red lines) of 1.2 mM solutions of $\mathbf{M_4}$, $\mathbf{M_3}$ and $\mathbf{M_2}$ in cyclohexane/chloroform mixture (84:16 v/v) at a rate of 0.5 K min^{-1} and CD spectrum of $\mathbf{M_4}$ (1.2 mM, cyclohexane/chloroform 84:16 v/v) at 328 K.

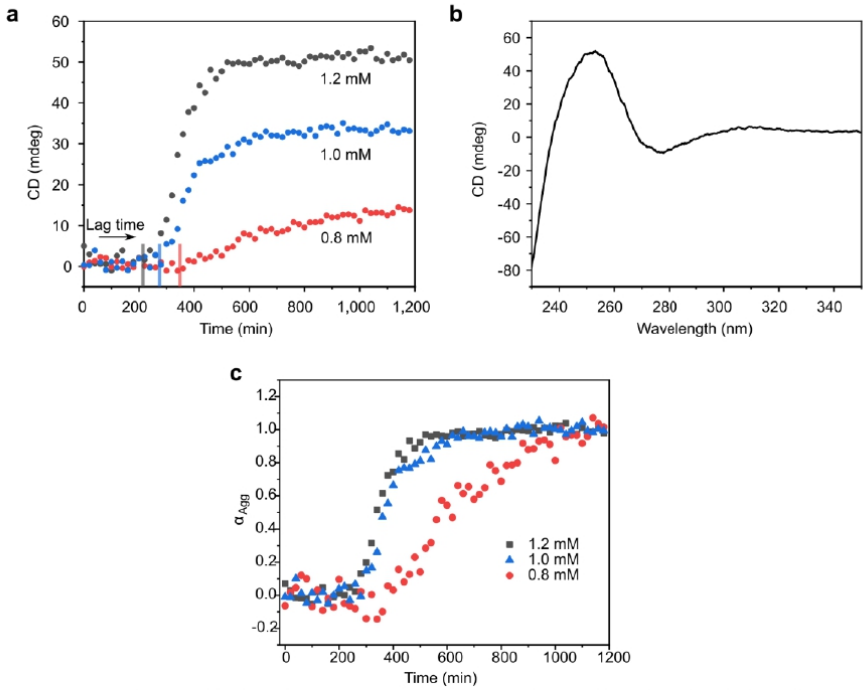

Supplementary Figure 11 | **a**, Time-course change of the CD signal (252 nm) for different concentrations of **M3** in cyclohexane/chloroform 84:16 (v/v) mixture at 293 K. **b**, CD spectrum of fully-aggregated 1.2 mM solution of **M3** in cyclohexane/chloroform 84:16 (v/v) mixture at 293 K. **c**, Normalized time-course change of the CD signal. Spontaneous polymerization of **M3** in cyclohexane/chloroform 84:16 (v/v) mixture occurs after a lag time and exhibits a sigmoidal transition. The lag time of the spontaneous polymerization depends on the initial concentration of **M3**, namely the time lag becomes shorter upon increasing the initial concentration of **M3**. This result indicates that no off-pathway aggregates are involved into kinetic stabilization of **M3**. Interestingly, during spontaneous polymerization at 293 K, we observed the formation of a different polymorph, which we did never observe in the seeded living polymerization.

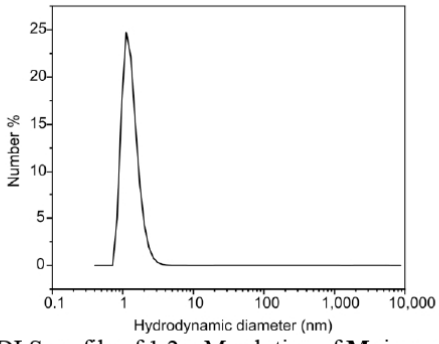

Supplementary Figure 12 | DLS profile of 1.2 mM solution of **M3** in cyclohexane/chloroform 84:16 (v/v) mixture at 293 K.

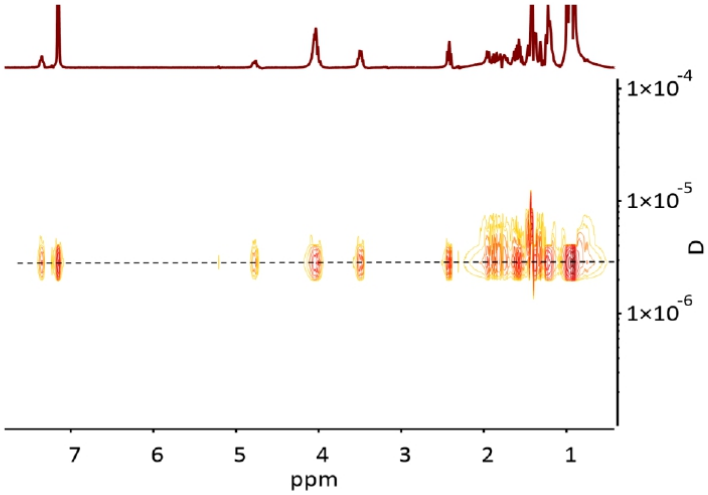

Supplementary Figure 13 | DOSY NMR of **Ref$_2$** (20 mM) in cyclohexane-d_{12}/chloroform-*d* 84:16 v/v mixture at 295 K. Diffusion coefficients are represented in $cm^2\ s^{-1}$. Black dotted line corresponds to D = $2.9\times10^{-10}\ m^2\ s^{-1}$.

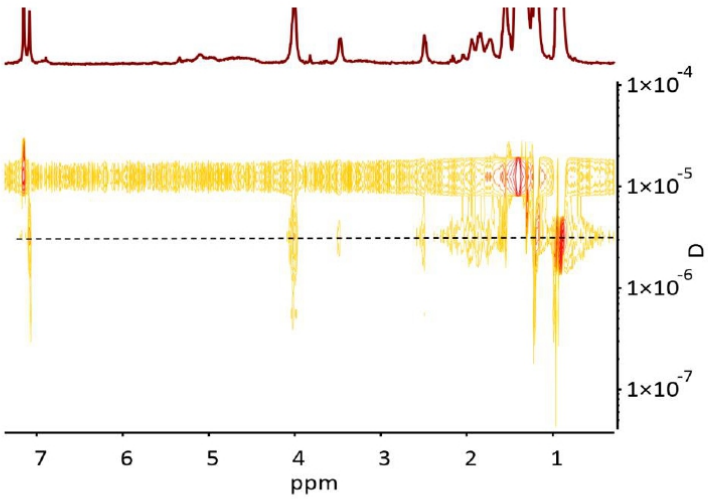

Supplementary Figure 14 | DOSY NMR of **M$_3$** (1.2 mM) in cyclohexane-d_{12}/chloroform-*d* 84:16 v/v mixture at 295 K. Diffusion coefficients are represented in $cm^2\ s^{-1}$. Black dotted line corresponds to D = $3.3\times10^{-10}\ m^2\ s^{-1}$. Please note not all signals can be clearly seen at this concentration due to limited resolution of the NMR machine.

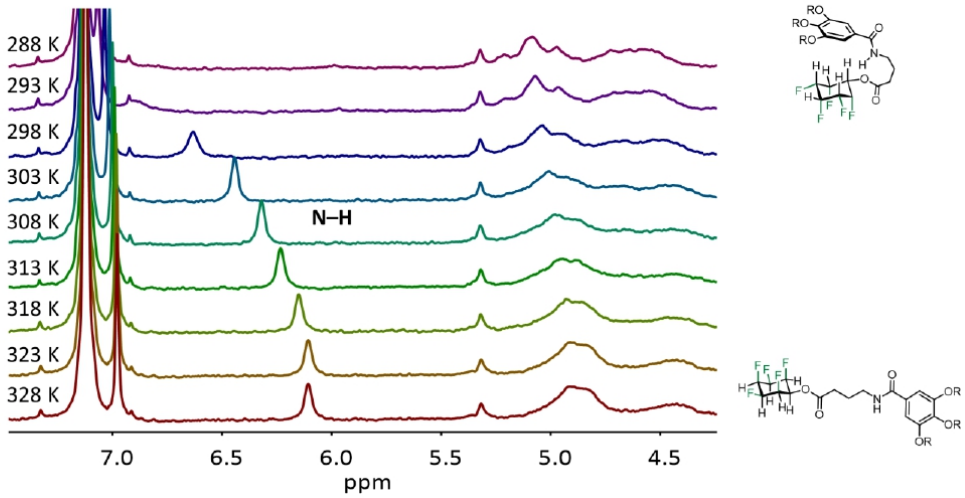

Supplementary Figure 15 | Partial VT ^{1}H NMR (500 MHz) spectra of **M$_3$** (1.2 mM) in cyclohexane-d_{12}/chloroform-*d* 84:16 v/v mixture.

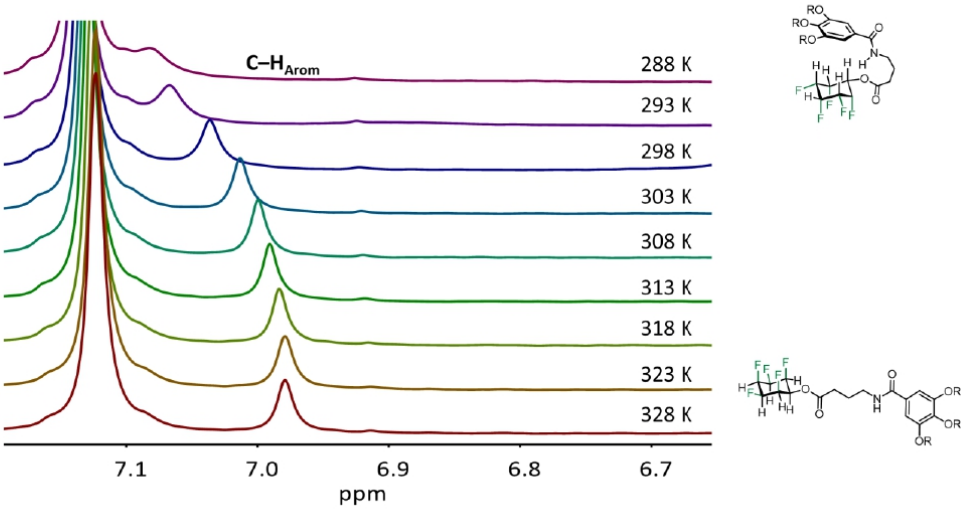

Supplementary Figure 16 | Partial VT ^{1}H NMR (500 MHz) spectra of **M$_3$** (1.2 mM) in cyclohexane-d_{12}/chloroform-*d* 84:16 v/v mixture. Aromatic region.

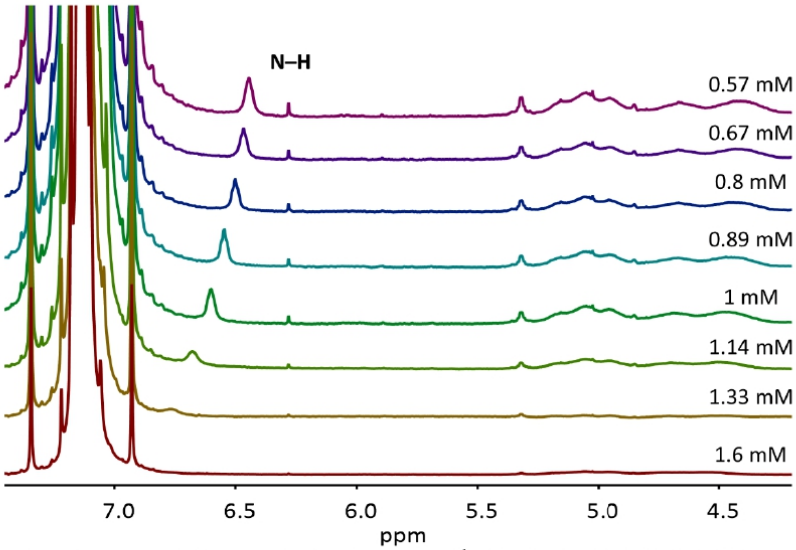

Supplementary Figure 17 | Concentration dependent ^{1}H NMR (400 MHz, 295 K) spectra of **M₃** in cyclohexane-d_{12}/chloroform-d 84:16 v/v mixture. Small changes of δ(N–H) were observed indicating low aggregation in solution.

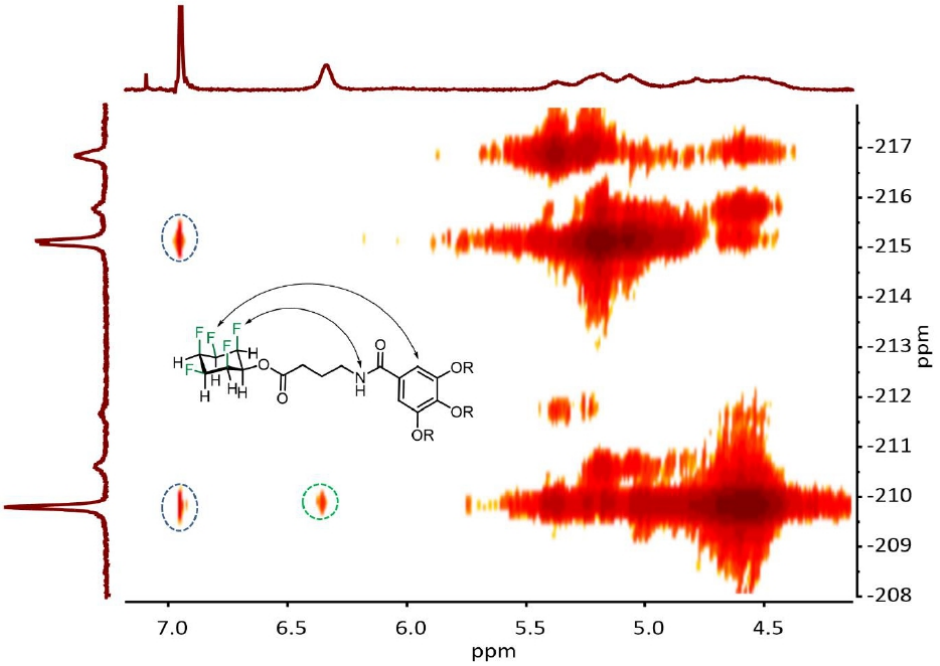

Supplementary Figure 18 | ^{1}H-^{19}F HOESY spectrum of 35 mM solution of **M₁** in $CDCl_3$ at 295 K.

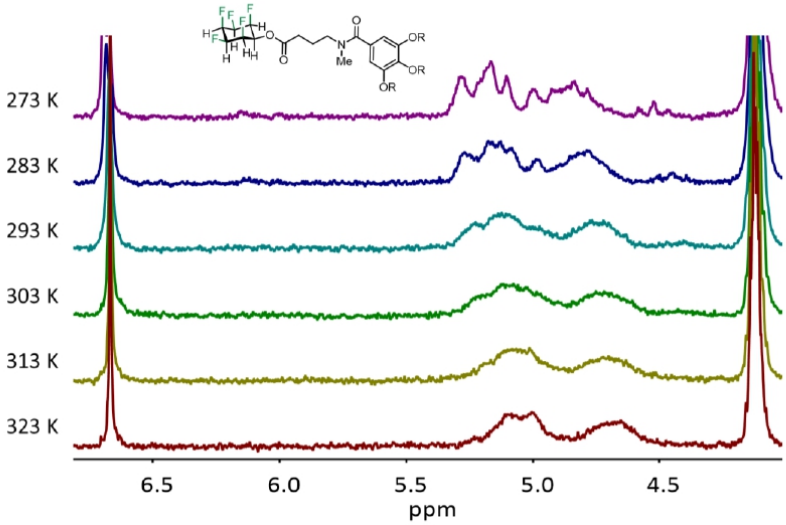

Supplementary Figure 19 | Partial VT ^{1}H NMR (500 MHz, 295 K) spectra of **MeM$_3$** (1.2 mM) in cyclohexane-d_{12}/chloroform-*d* 84:16 v/v mixture.

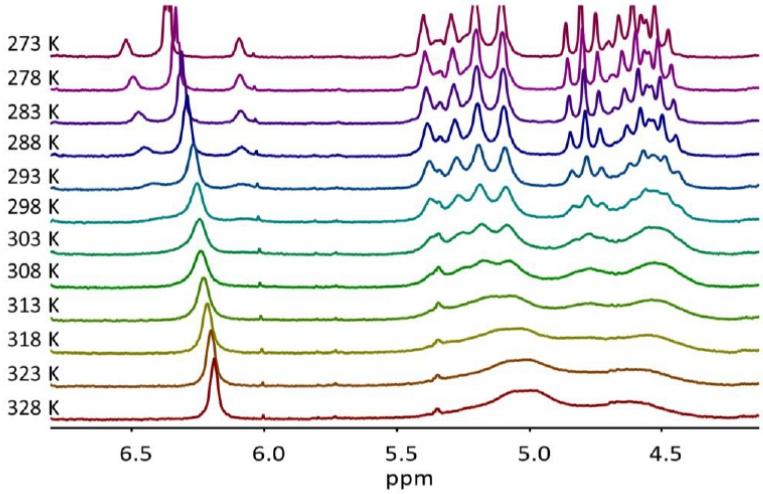

Supplementary Figure 20 | Partial VT ^{1}H NMR (500 MHz) spectra of **M$_3$** (15 mM) in chloroform-*d*.

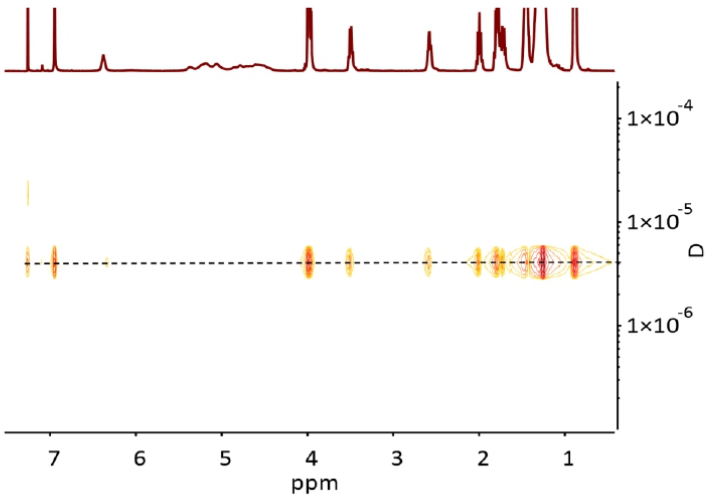

Supplementary Figure 21 | DOSY NMR of **M_1** (25 mM) in $CDCl_3$ at 295 K. Diffusion coefficient are represented in $cm^2\ s^{-1}$. Black dotted line corresponds to $D = 4.2\times10^{-10}\ m^2\ s^{-1}$.

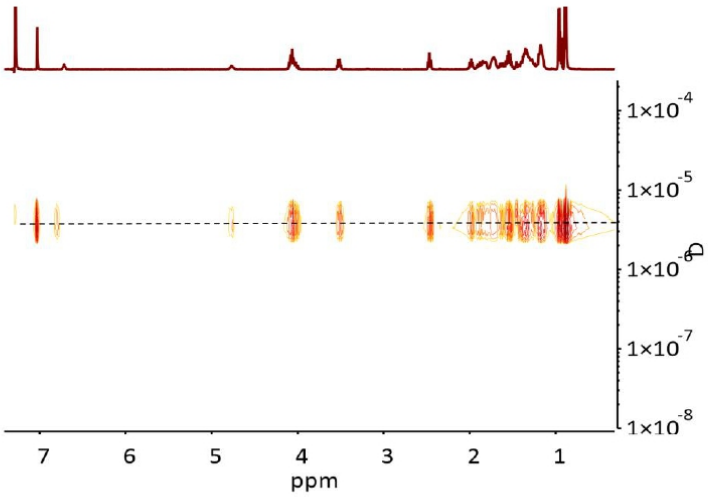

Supplementary Figure 22 | DOSY NMR of **Ref_2** (25 mM) in $CDCl_3$ at 295 K. Diffusion coefficient are represented in $cm^2\ s^{-1}$. Black dotted line corresponds to $D = 4\times10^{-10}\ m^2\ s^{-1}$.

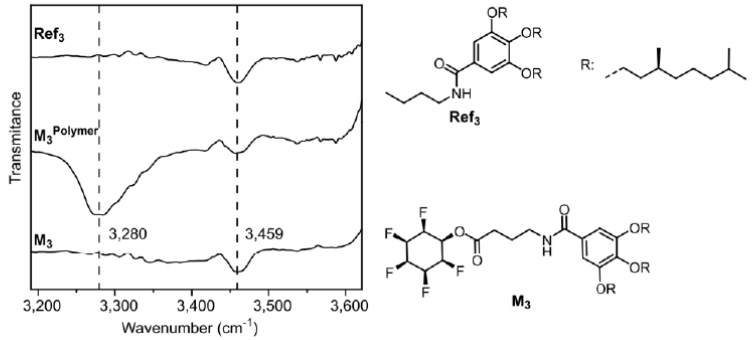

Supplementary Figure 23 | FT-IR spectra of N-H stretching vibration of 1.2 mM solutions (cyclohexane/chloroform 84:16 v/v) of **Ref3**, **M3Polymer**, obtained via seeded growth, and **M3**. The vibration at 3280 cm^{-1} corresponds to intermolecularly hydrogen bonded amide.

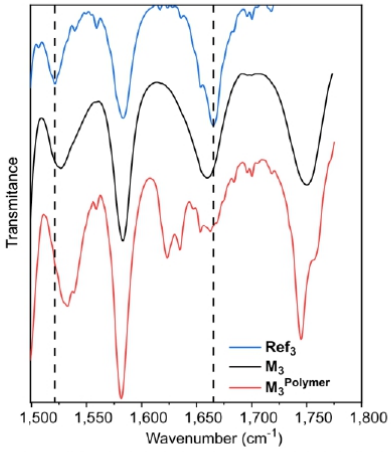

Supplementary Figure 24 | FT-IR spectra of the amide I (dashed line at 1665 cm^{-1}, C=O stretching vibration) and amide II (dashed line at 1521 cm^{-1}, NH in plane bend and the CN stretching vibration) of 1.2 mM solutions (cyclohexane/chloroform 84:16 v/v) of **Ref3**, **M3Polymer**, obtained via seeded growth, and **M3**. The small shift is observed for both amide bends for **M3** and **M3Polymer** in comparison to **Ref3**, lacking all-*cis* $C_6H_6F_5$ group. The shift of amide I band can be a result of CH···π interaction between all-*cis* $C_6H_6F_5$ group and aromatic ring, which directly influences the conjugation between the amide and aromatic ring.

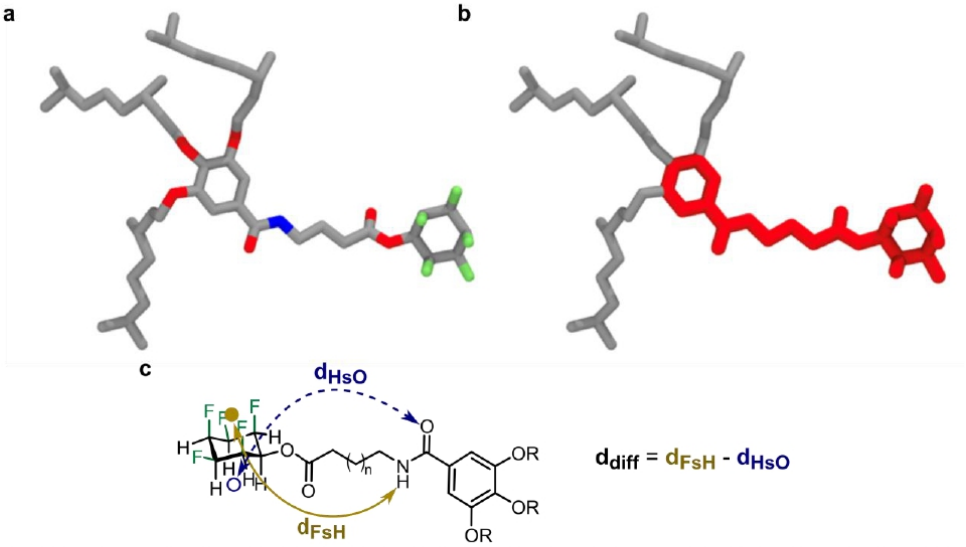

Supplementary Figure 25 | a, Licorice representation of $\mathbf{M_3}$ monomer (hydrogen atoms have been ommited for clarity). **b**, Partition of $\mathbf{M_3}$ monomer into "core" (in red) and "tails" (grey). The radius of gyration of the monomer core is used to define CV2 used in the WT-MetaD simulations. **c**, CV1 is defined as difference between d_{FsH} and d_{HsO} distances. Distances are measured between the centres of mass of the cyclohexane fluorides and the amidic hydrogen (d_{FsH}) and the centres of mass of the cyclohexane hydrogens and the amidic oxygen (d_{HsO}).

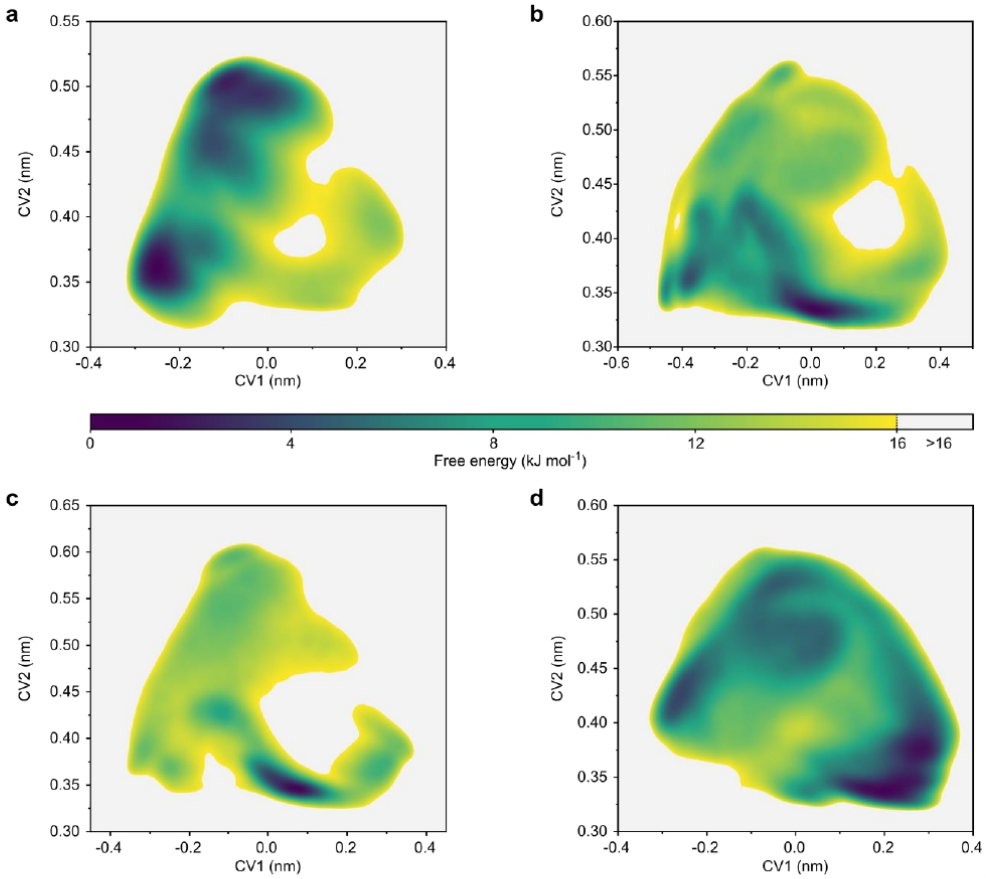

Supplementary Figure 26 | Free energy surface of the monomers **M₂** (**a**), **M₃** (**b**), **M₄** (**c**) and ***Me*M₃** (**d**) conformational space estimated by MetaD enhancing the sampling along the difference of the distances between pentafluorocyclohexyl-Hs and amide oxygen and between the pentafluorocyclohexyl-Fs and the amide-nitrogen (abscissa, except for the case of ***Me*M₃** where the methyl-carbon was considered), and the radius of gyration of the core of each monomer (ordinate).

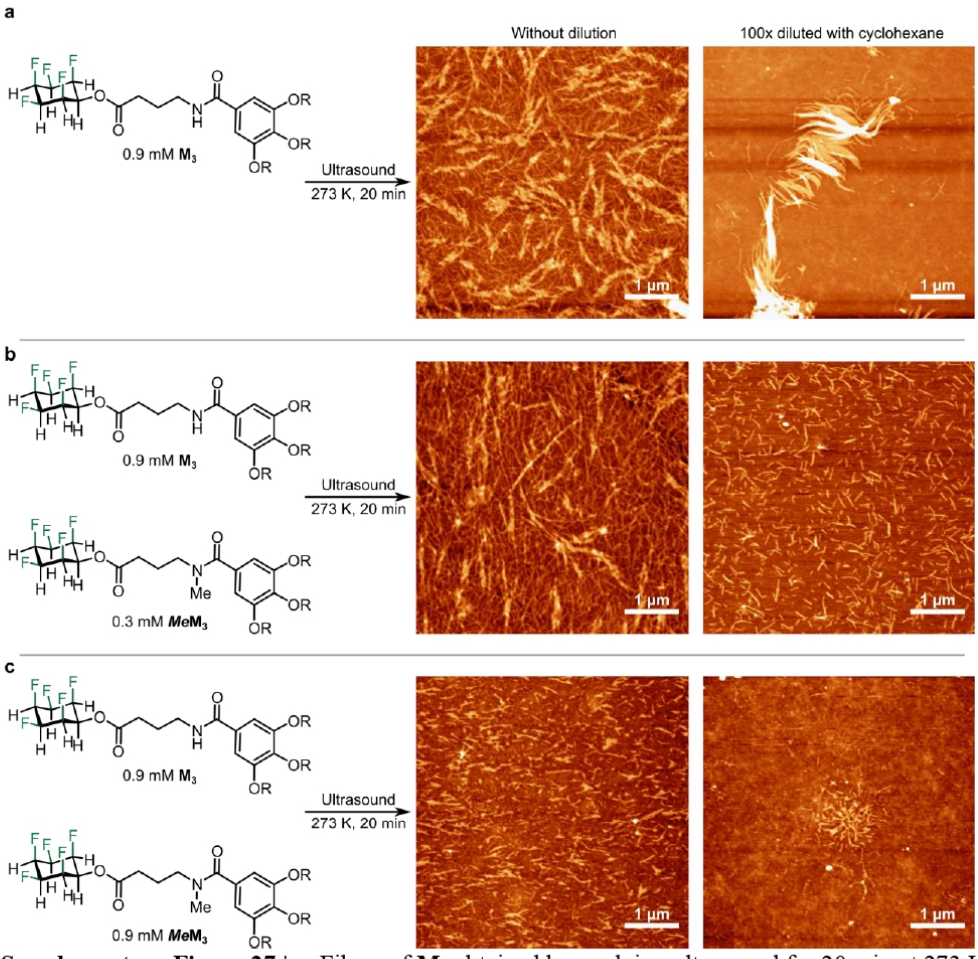

Supplementary Figure 27 | a, Fibers of **M3** obtained by applying ultrasound for 20 min at 273 K to 0.9 mM solution of **M3** in cyclohexane/chloroform mixture 84:16 (v/v). AFM height images of fibers spin-coated on the silicon wafer directly from the solution (without dilution) and diluted 100x with cyclohexane. In former case, most of the material is deposited in the form of bundles of long non-uniform (ca. 1 µm) fibers. **b**, $\mathbf{M3}^{\mathbf{Seed}}$ obtained by applying ultrasound for 20 min at 273 K to the mixture of **M3** (0.9 mM) and ***Me*M3** (0.3 mM) in cyclohexane/chloroform solvent mixture 84:16 (v/v). AFM height images show well-defined short fibers after dilution. **c**, Fibers of **M3** obtained by applying ultrasound for 20 min at 273 K to the mixture of **M3** (0.9 mM) and ***Me*M3** (0.9 mM) in cyclohexane/chloroform solvent mixture 84:16 (v/v). AFM height images of fibers spin-coated on the silicon wafer indicate the formation of aggregates with poorly defined morphology. In all cases, AFM samples were prepared in an identical way, using the same substrate (silicone).

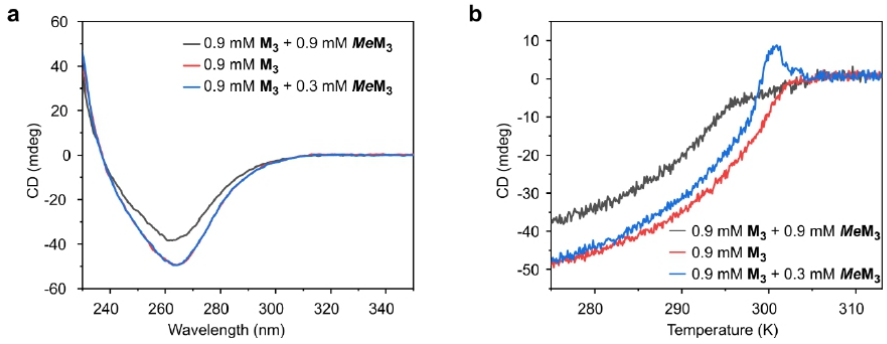

Supplementary Figure 28 | a, CD spectra (84:16 v/v cyclohexane/chloroform, 275 K) of "seeds" obtained by 1) sonication of 0.9 mM solution of **M₃** for 20 min at 273 K (red line); 2) sonication of the mixture of ***Me*M₃** (0.3 mM) and **M₃** (0.9 mM) for 20 min at 273 K (blue line); 3) sonication of the mixture of ***Me*M₃** (0.9 mM) and **M₃** (0.9 mM) for 20 min at 273 K (black line). **b**, Melting CD curves (260 nm, 84:16 v/v cyclohexane/chloroform, 0.5 K/min) of "seeds" obtained by 1) sonication of 0.9 mM solution of **M₃** for 20 min at 273 K (red line); 2) sonication of the mixture of ***Me*M₃** (0.3 mM) and **M₃** (0.9 mM) for 20 min at 273 K (blue line); 3) sonication of the mixture of ***Me*M₃** (0.9 mM) and **M₃** (0.9 mM) for 20 min at 273 K (black line).

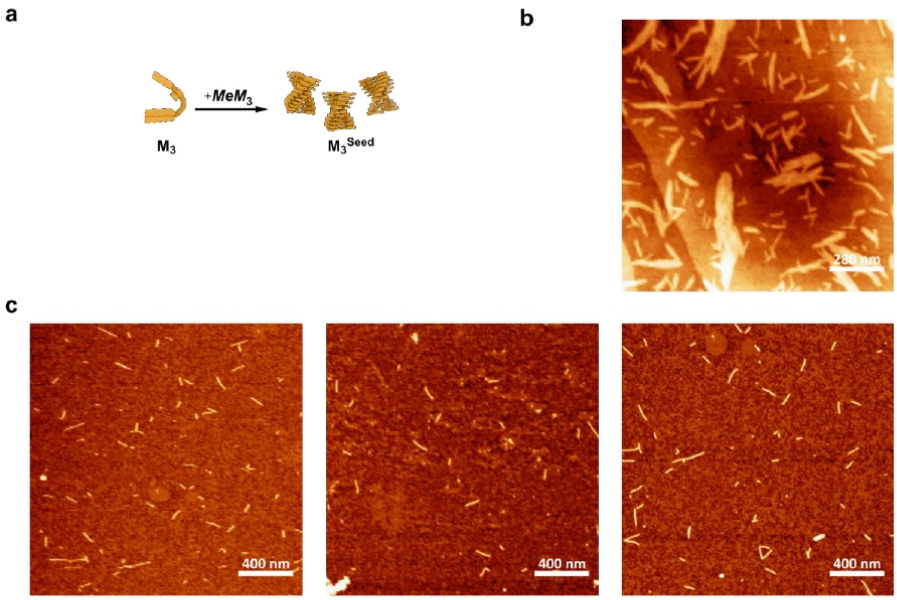

Supplementary Figure 29 | a. Schematic illustration of **M₃^{Seed}** preparation. **b.** AFM height image of **M₃^{Seed}**, spin-coated (1 µL, 8000 rpm) on a HOPG wafer before 100x dilution with cyclohexane (scale bar 280 nm). **c.** Representative AFM height images of **M₃^{Seed}**, spin-coated on a silicon wafer after 100x dilution with cyclohexane.

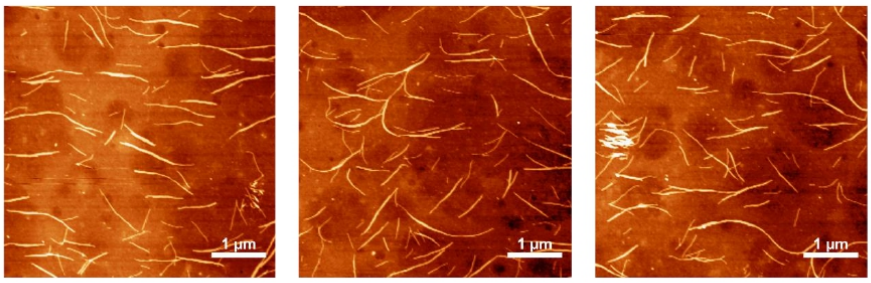

Supplementary Figure 30 | AFM height images of supramolecular polymers obtained using "seeds" obtained by sonication of 0.9 mM solution of **M3** (84:16 v/v cyclohexane/chloroform) for 20 min at 273 K. **M3**/**Seed** = 3:1.

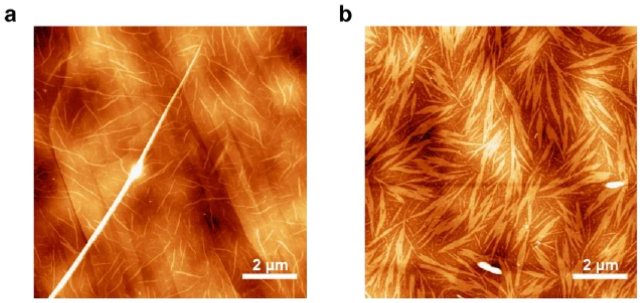

Supplementary Figure 31 | AFM height images of $\mathbf{M_3}^{\mathbf{Polymer}}$ obtained with 5:1 [**M3**]/[$\mathbf{M_3}^{\mathbf{Seed}}$] (v/v) ratio spin-coated (<1 µL, 8000 rpm) before 100x dilution on (**a**) HOPG and (**b**) silicon wafers.

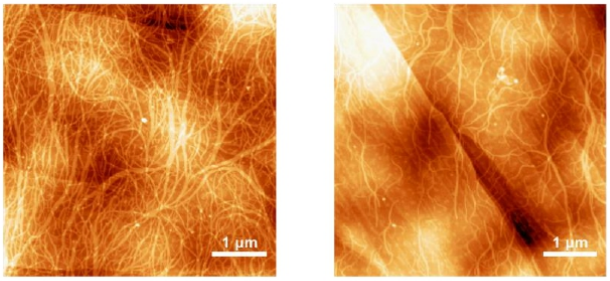

Supplementary Figure 32 | AFM height images of $\mathbf{M_3}^{\mathbf{Polymer}}$ obtained with 10:1 [**M3**]/[$\mathbf{M_3}^{\mathbf{Seed}}$] (v/v) ratio spin-coated (<1 µL, 8000 rpm) before 100x dilution on HOPG.

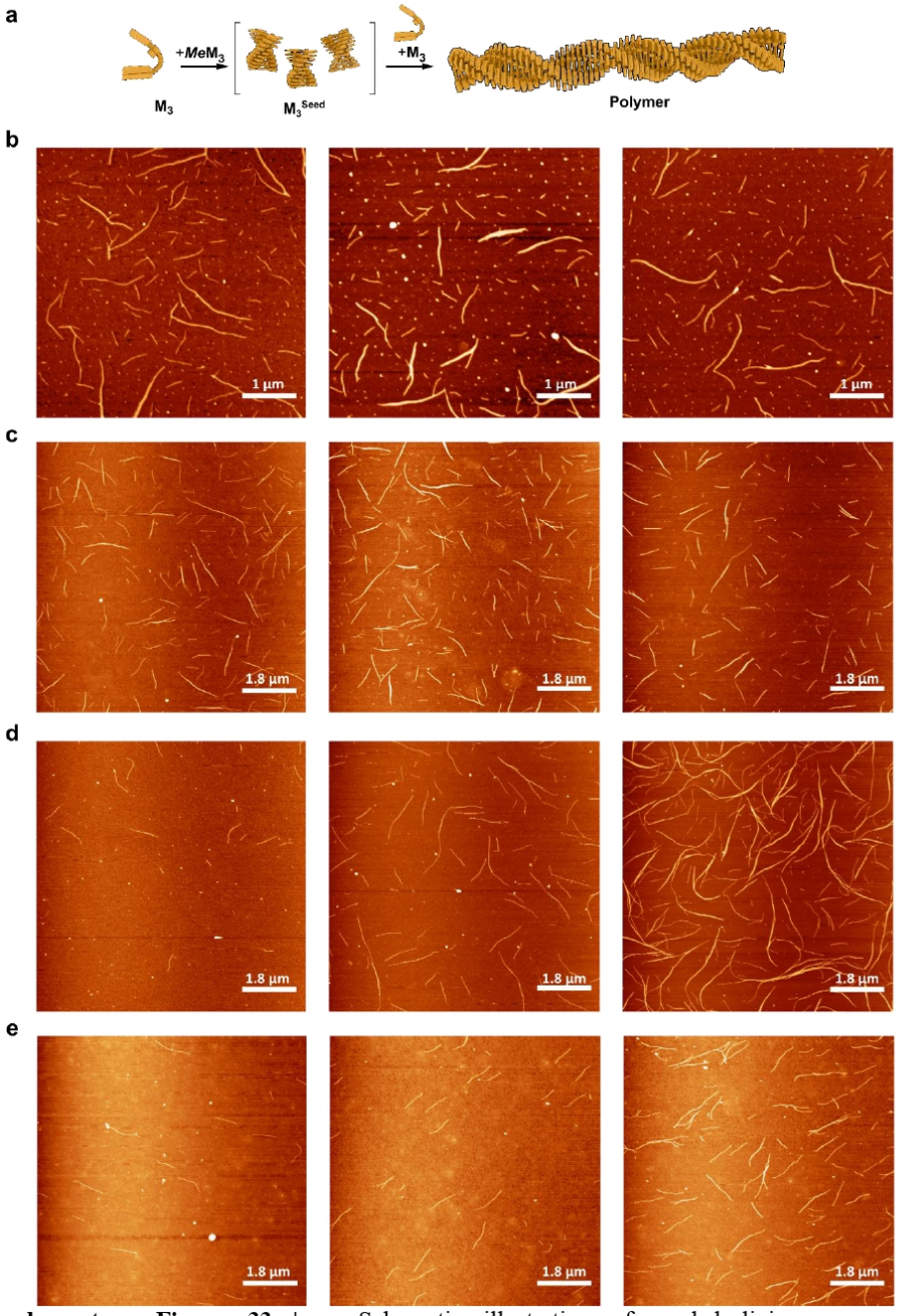

Supplementary Figure 33 | **a**, Schematic illustration of seeded living supramolecular polymerization. AFM height images of $\mathbf{M_3}^{\mathbf{Polymer}}$ obtained with (**b**) 3:1 (**c**) 5:1, (**d**) 7:1 and (**e**) 10:1 [$\mathbf{M_3}$]/[$\mathbf{M_3}^{\mathbf{Seed}}$] (v/v) ratio.

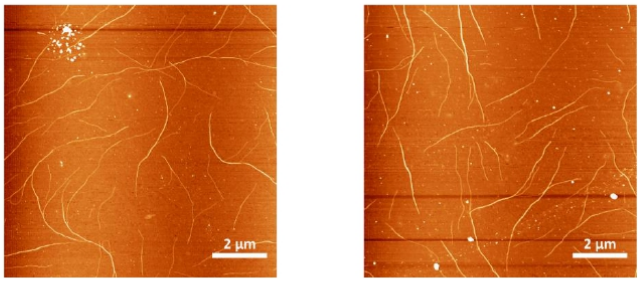

Supplementary Figure 34 | AFM height images of supramolecular polymers obtained with 20:1 [$\mathbf{M_3}$]/[$\mathbf{M_3^{Seed}}$] ratio.

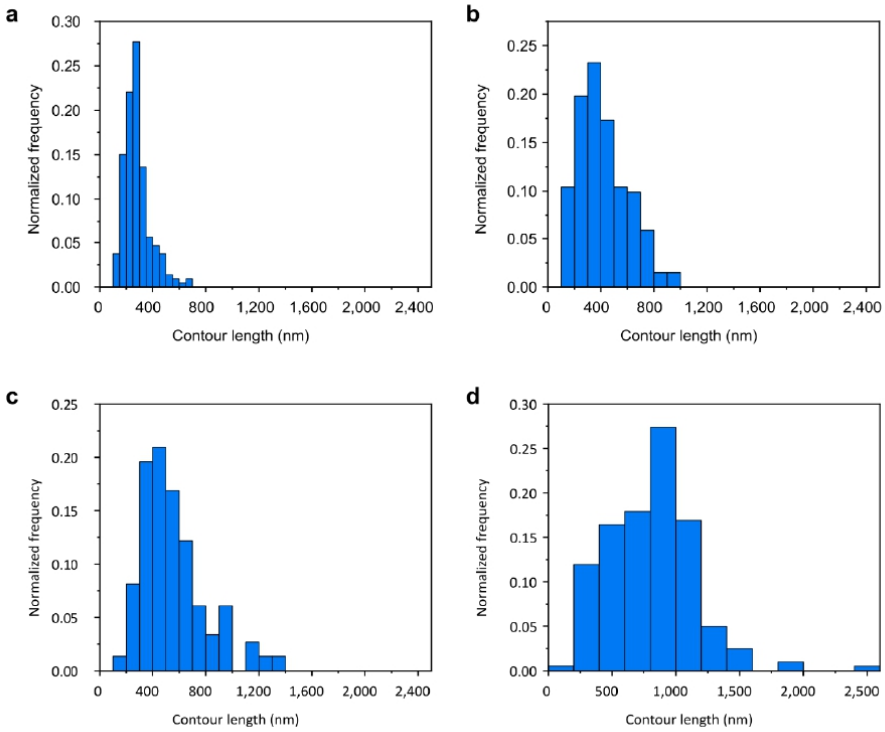

Supplementary Figure 35 | Contour length distribution obtained from AFM images of supramolecular polymers obtained with different [$\mathbf{M_3}$]/[$\mathbf{M_3^{Seed}}$] ratios: (**a**) 3:1; (**b**) 5:1; (**c**) 7:1; (**d**) 10:1 v/v.

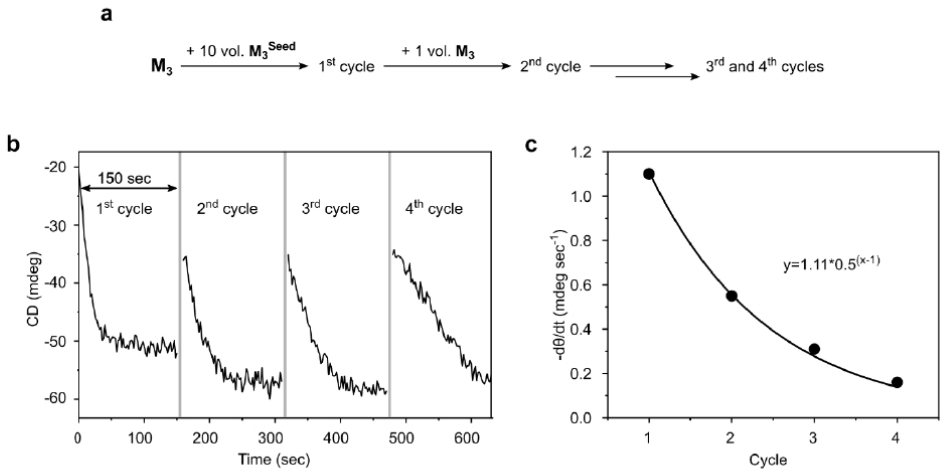

Supplementary Figure 36 | a, Schematic illustration of the experiment used to investigate the living character of the supramolecular polymerization of **M3**. **b**, Time-dependent CD (260 nm) changes during each polymerization cycle. **c**, Rate of polymerization as a function of the cycle number.

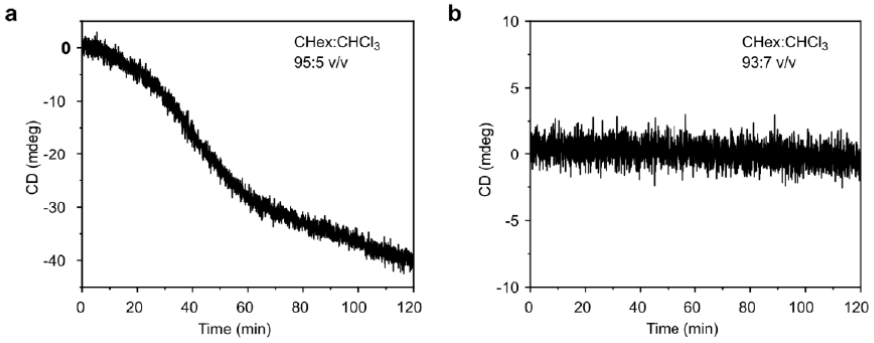

Supplementary Figure 37 | Time development of the CD signal (260 nm) of **M5** in (**a**) cyclohexane/chloroform 95:5 (v/v) and (**b**) cyclohexane/chloroform 93:7 (v/v) at 293 K. In cyclohexane/chloroform 95:5 (v/v) spontaneous polymerization starts in <10 min whereas in cyclohexane/chloroform 93:7 (v/v) monomer remains in a molecularly dissolved state for >1 h which is enough to carry out seeded living supramolecular polymerization. If necessary kinetic stability can be increased by increasing the fraction of chloroform.

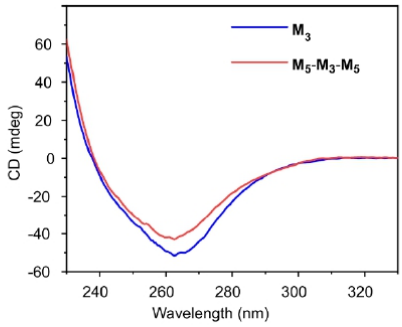

Supplementary Figure 38 | Blue - CD spectrum of $\mathbf{M_3}$ homopolymer (c_{tot} = 1.2 mM, 84:16 v/v cyclohexane/chloroform, 293 K, [$\mathbf{M_3}$]/[$\mathbf{M_3^{Seed}}$] = 50:1 v/v). Red - CD spectrum of $\mathbf{M_5}$-$\mathbf{M_3}$-$\mathbf{M_5}$ supramolecular block copolymer (c_{tot} = 1.2 mM, 293 K, [$\mathbf{M_5}$]/[$\mathbf{M_3^{Seed}}$] = 3:1 v/v).

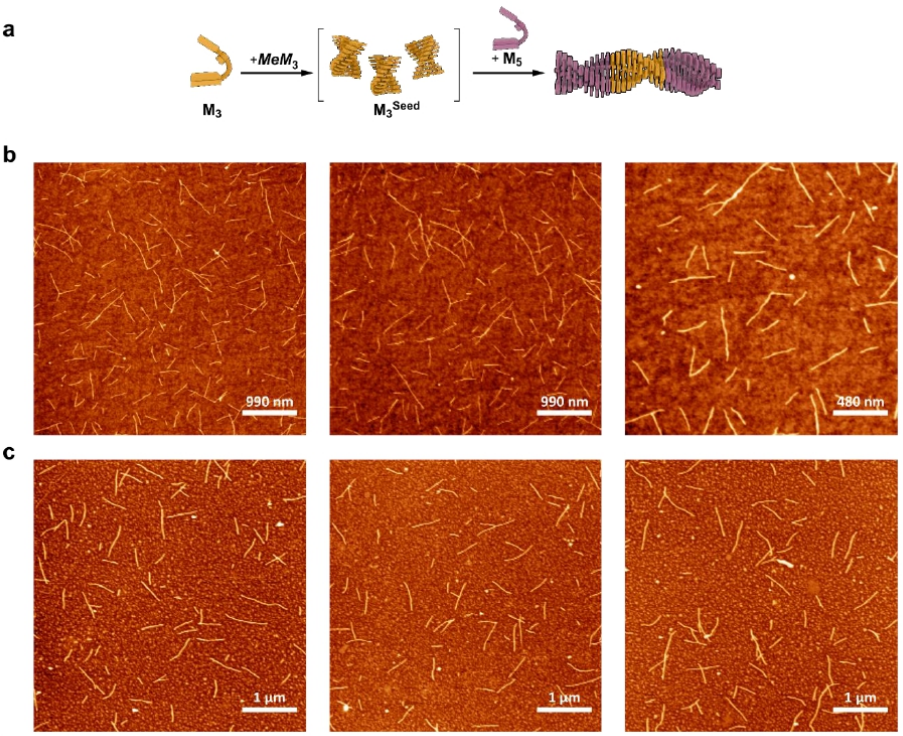

Supplementary Figure 39 | **a**, Schematic illustration of the experiment. Solution of $\mathbf{M_5}$ (1.2 mM, cyclohexane/chloroform 93:7 v/v) was seeded with $\mathbf{M_3^{Seed}}$ at 293 K. AFM height images of $\mathbf{M_5}$-$\mathbf{M_3}$-$\mathbf{M_5}$ supramolecular block copolymer obtained with (**b**) 3:1 and (**c**) 5:1 [$\mathbf{M_5}$]/[$\mathbf{M_3^{Seed}}$] (v/v) ratio**.** The values for the $\mathbf{M_3}$-$\mathbf{M_3}$-$\mathbf{M_3}$ homopolymer obtained with 3:1 [$\mathbf{M_3}$]/[$\mathbf{M_3^{Seed}}$] (v/v) ratio were 316 nm, 282 nm and 1.12. The values for the $\mathbf{M_3}$-$\mathbf{M_3}$-$\mathbf{M_3}$ homopolymer obtained with 5:1 [$\mathbf{M_3}$]/[$\mathbf{M_3^{Seed}}$] (v/v) ratio were 499 nm, 418 nm and 1.19.

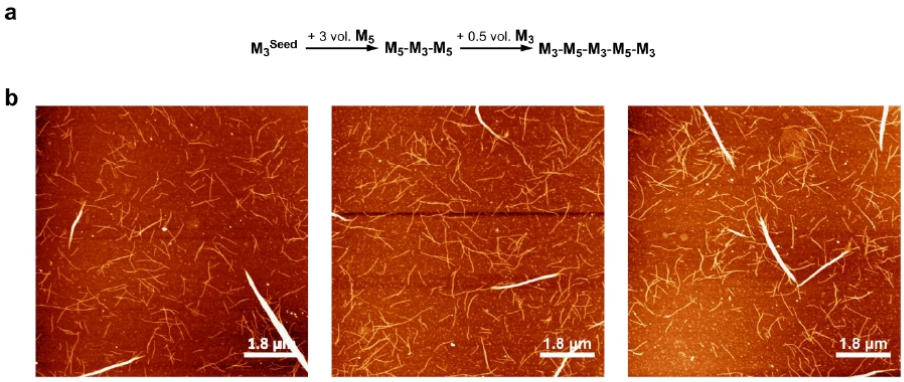

Supplementary Figure 40 | **a**, Schematic illustration of the experiment. Solution of $\mathbf{M_5}$ (1.2 mM, cyclohexane/chloroform 93:7 v/v) was seeded with $\mathbf{M_3^{Seed}}$ at 293 K with [$\mathbf{M_5}$]/[$\mathbf{M_3^{Seed}}$] = 3:1 (v/v). To 1 volume of the obtained block copolymer (**BAB**) solution were added 0.5 volume of $\mathbf{M_3}$ (1.2 mM, cyclohexane/chloroform 93:7 v/v) to obtain **ABABA** copolymer. **b**, AFM height images of **ABABA** supramolecular block copolymer.

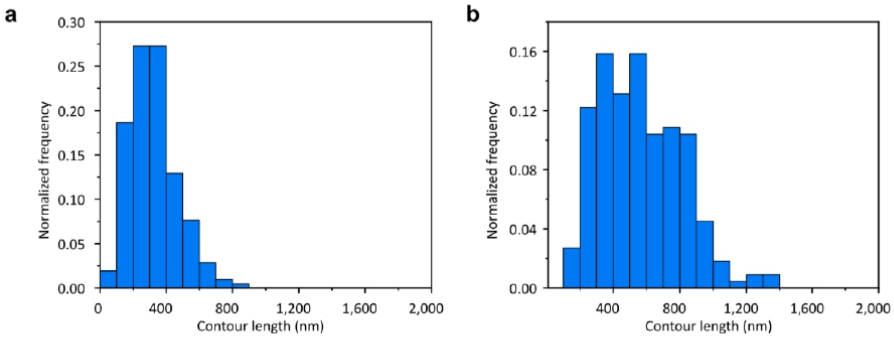

Supplementary Figure 41 | Contour length distribution obtained from AFM images of supramolecular polymers. **a** $\mathbf{M_5}$-$\mathbf{M_3}$-$\mathbf{M_5}$ supramolecular block copolymer obtained with [$\mathbf{M_5}$]/[$\mathbf{M_3^{Seed}}$] = 3:1 (v/v). **b** $\mathbf{M_3}$-$\mathbf{M_5}$-$\mathbf{M_3}$-$\mathbf{M_5}$-$\mathbf{M_3}$ obtained with [$\mathbf{M_5}$-$\mathbf{M_3}$-$\mathbf{M_5}$]/[$\mathbf{M_3}$] = 2:1 (v/v). The weight-average length (L_w), number-average length (L_n) and PDI (L_w/L_n) are 673 nm, 566 nm and 1.19.

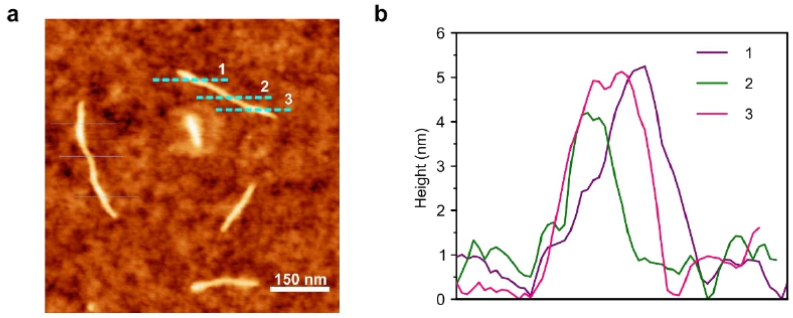

Supplementary Figure 42 | AFM height image of $\mathbf{M_5}$-$\mathbf{M_3}$-$\mathbf{M_5}$ supramolecular block copolymer obtained with [$\mathbf{M_5}$]/[$\mathbf{M_3}^{\mathbf{Seed}}$] = 3:1 (v/v) ratio spin-coated on the silicon wafer and cross-section analyses along blue dashed lines 1 – 3.

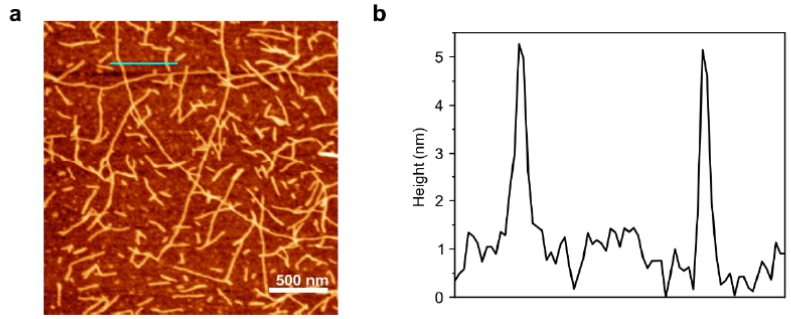

Supplementary Figure 43 | AFM height image of $\mathbf{M_5}$ homopolymer obtained by sonication for 60 sec of 1.2 mM solution of $\mathbf{M_5}$ (93:7 cycholexane/chloroform v/v, rt.) spin-coated on the silicon wafer and cross-section analyses along the blue line.

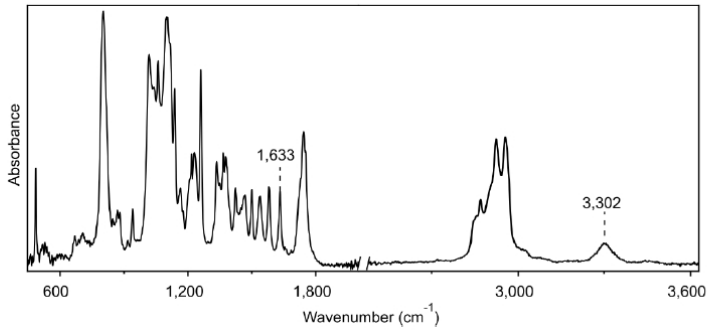

Supplementary Figure 44 | ATR-IR spectrum of $\mathbf{M_3}^{\mathbf{Polymer}}$.

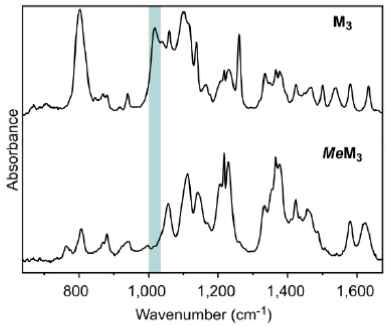

Supplementary Figure 45 | Partial ATR-IR spectra of ***Me*M3** and the supramolecular polymer of **M3**. In the case of $\mathbf{M_3}^{\mathbf{Polymer}}$ new strong C–F stretching band appears at 1018 cm^{-1} (highlighted in blue).

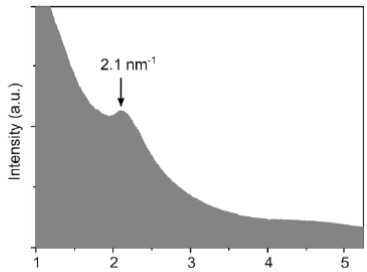

Supplementary Figure 46 | Radial-integrated intensity profile of the electron diffraction pattern shown in Fig. 5a. The diffraction ring is located at 2.1 nm^{-1}, corresponding to a lattice distance of 4.8 Å in the real space.

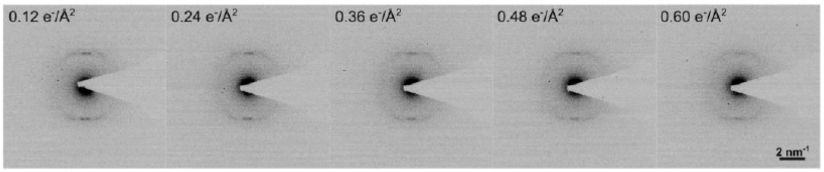

Supplementary Figure 47 | Electron dose series analysis. The selected-area electron diffraction patterns were acquired at the same position with an increasingly accumulated electron dose. With a

total electron dose of 0.12 $e^-/Å^2$, the diffraction spots remained sharp and readily visible. However, with an accumulated electron dose of 0.60 $e^-/Å^2$, only diffusive intensity could be observed, indicating substantial structural disintegration of the organic fibers.

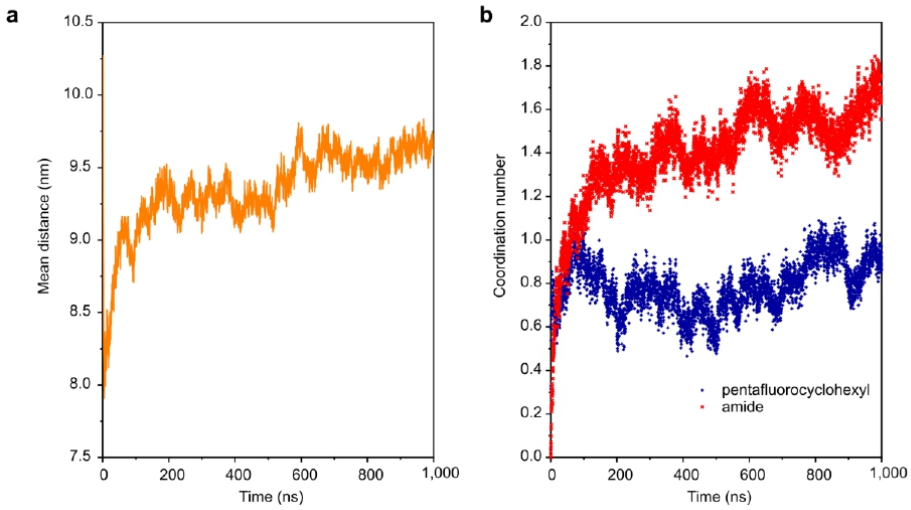

Supplementary Figure 48 | Self-assembly of 150 $\mathbf{M_3}$ monomers in solution. (a) Time evolution of the mean distance between the center of the benzene and the center of the cyclohexane groups of each $\mathbf{M_3}$ monomer during the MD simulation. (b) Time evolution of the coordination number between the amide (red) and pentafluorocyclohexyl (blue) groups of the $\mathbf{M_3}$ monomers during self-assembly.

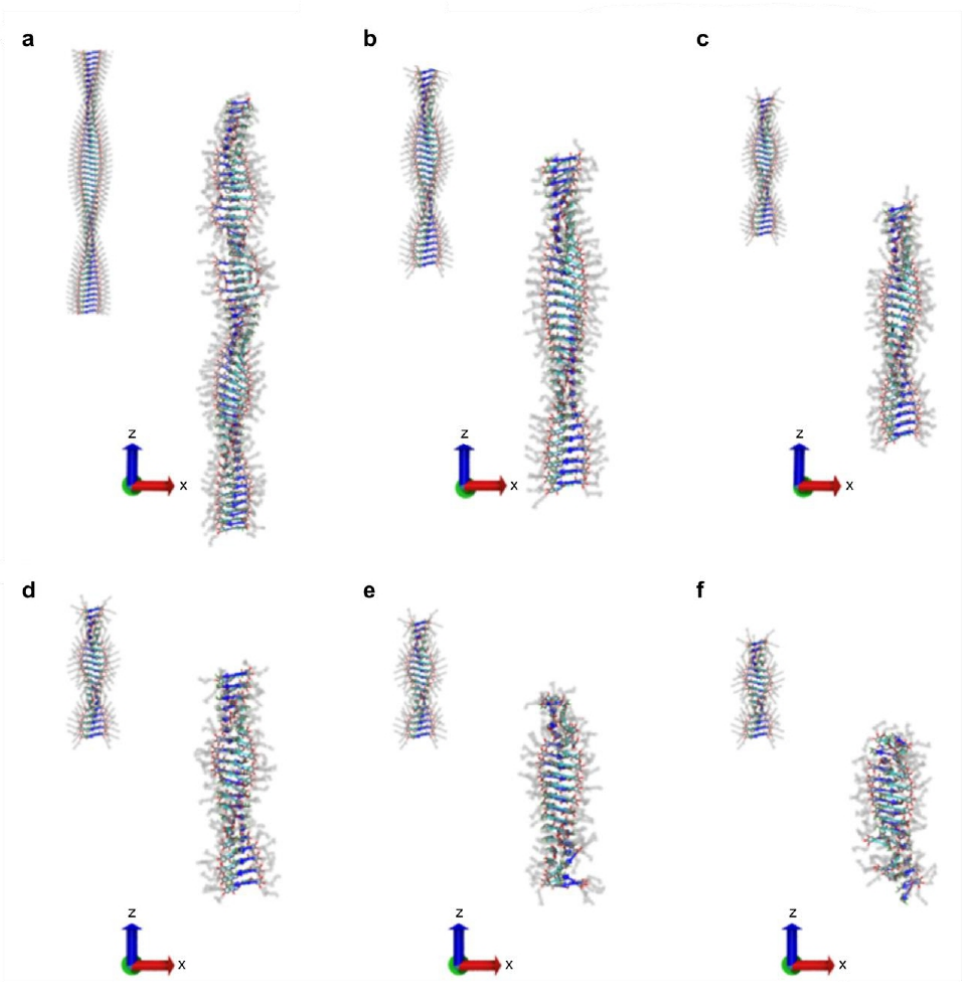

Supplementary Figure 49 | Atomistic models of preformed helical assemblies (top-left of each panel) of $\mathbf{M_3}$ which are relaxed during 1μs of MD simulations (last equilibrated MD frame shown as zoomed at the bottom right of each panel). The starting configurations for the assemblies are prepared starting from the same dimeric units and changing in each system the initial torsion between them (helical pitch) along the fibers to ~24 (**a**), ~15 (**b**), ~12 (**c**), ~10 (**d**), ~9 (**e**), and ~7.5 nm (**f**). The structures (starting and equilibrated) are shown at atomistic level showing the heavy atoms (licorice representation), overlaid by blue and cyan arrows that connect the benzene group (tail) to the pentafluorocyclohexyl (head) columns of monomers. Alkyl chains are shown in transparency.

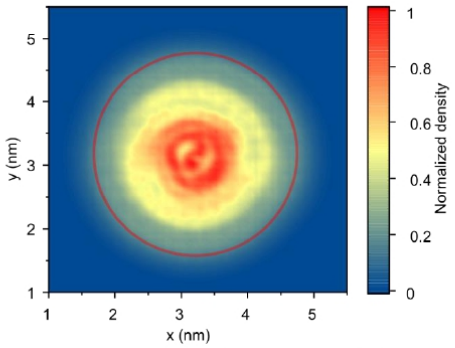

Supplementary Figure 50 | Normalized atom distribution of the average *xy* section of the $\mathbf{M_3}^{\mathbf{Polymer}}$ fiber (*z* being the main fiber axis). High densities are colored in red, while low densities are green/blue. The red circle indicates the experimental estimation of the fiber thickness.

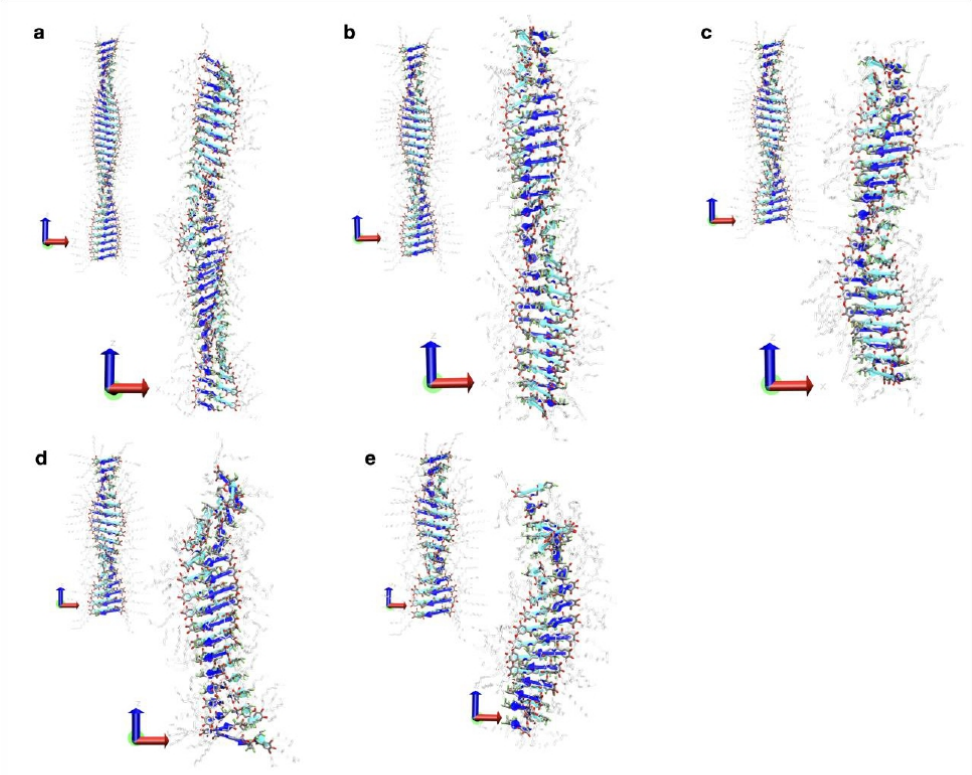

Supplementary Figure 51 | Atomistic models of preformed helical assemblies (top-left of each panel) of $\mathbf{M_5}$ which are relaxed during 1μs of MD simulations (last equilibrated MD frame shown as zoomed at the bottom right of each panel). The starting configurations for the assemblies are prepared starting from the same dimeric units and changing in each system the initial torsion between them (helical pitch) along the fibers to ~15 (**a**), ~12 (**b**), ~10 (**c**), ~9 (**d**), and ~7.5 nm (**e**). The structures (starting and equilibrated) are shown at atomistic level showing the heavy atoms (licorice representation), overlaid by blue and cyan arrows that connect the benzene group (tail) to the pentafluorocyclohexyl (head) columns of monomers. Solvophilic chains are shown in transparency.

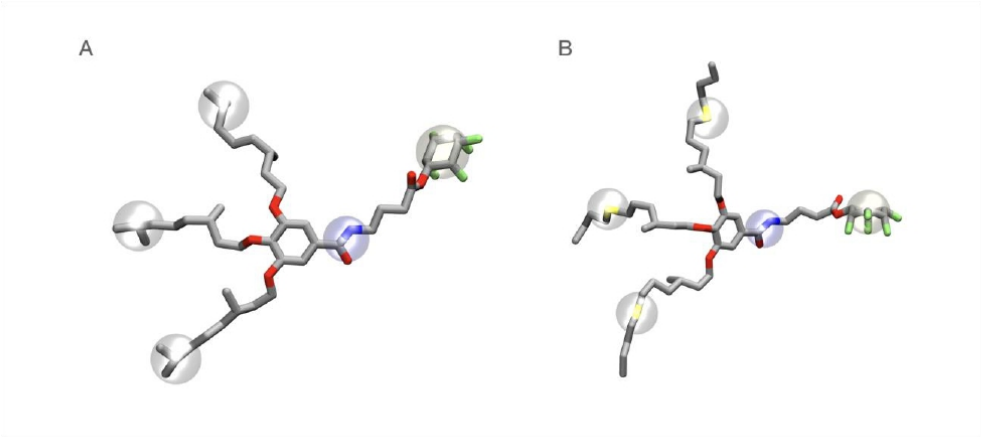

Supplementary Figure 52 | Localization of the SOAP centers (transparent spheres) on the **M3** (panel A) and **M5** (panel B) monomers. Colour code: green: F; red: O; blue: N; grey: C.

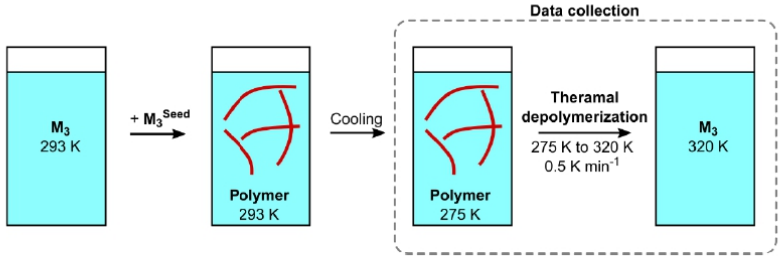

Supplementary Figure 53 | Schematic illustration of the experimental design used to investigate thermodynamic parameters of supramolecular polymerization.

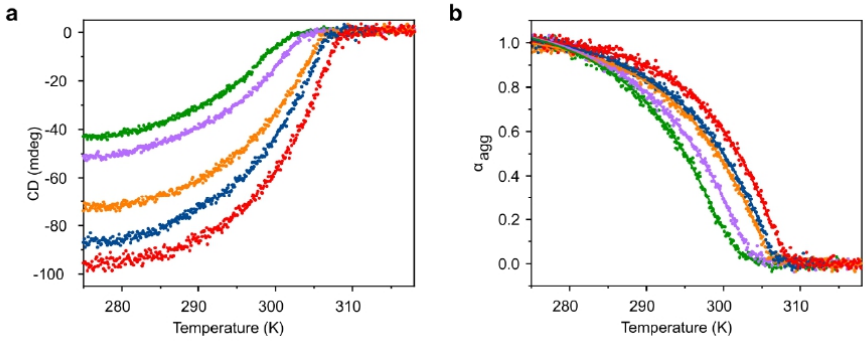

Supplementary Figure 54 | **a**, Changes of the CD signal (260 nm) of $\mathbf{M_3^{Polymer}}$ during heating at different total concentration of the **M3**. Conditions: cyclohexane/chloroform 84:16 (v/v), 0.5 K min^{-1}. Color code: red, c = 1.6 mM; blue, c = 1.4 mM; yellow, c = 1.2 mM; pink, c = 1.0 mM; green, c = 0.8 mM. **b**, Temperature-dependent degree of aggregation. Solid lines represent fit according to the cooperative model.

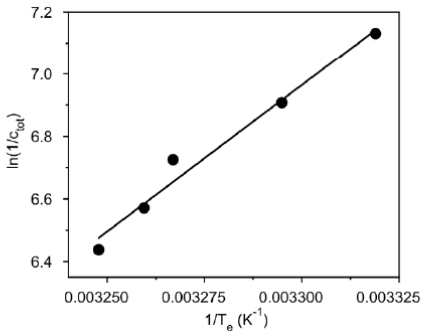

Supplementary Figure 55 | van't Hoff plot obtained from plotting the natural logarithm of $1/c_{tot}^{-1}$ as a function of $1/T_e^{-1}$.

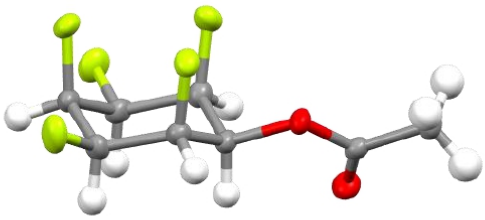

Supplementary Figure 56 | Crystal structure of all-*cis* 2,3,4,5,6-pentafluorocyclohexyl acetate. Thermal ellipsoids are shown at the 50% probability level. Single crystals all-*cis*-2,3,4,5,6-pentafluorocyclohexyl acetate (**Ref1**) were obtained by slow evaporation of its solution in $CHCl_3$/acetone 9:1 (v/v). The cif-file was deposited in the Cambridge Structural Database under identifier CCDC 2010482.

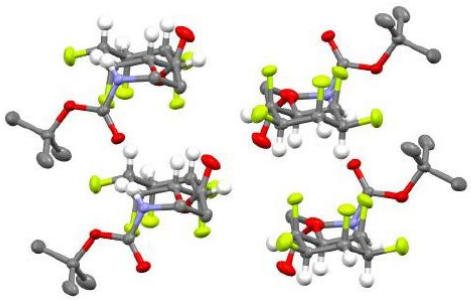

Supplementary Figure 57 | Crystal structure and packing of **2**. Thermal ellipsoids are shown at the 50% probability level. Non-cyclohexane hydrogens have been omitted for clarity. Single crystals of

compound **2** were obtained by slow evaporation of its solution in acetone. The cif-file was deposited in the Cambridge Structural Database under identifier CCDC 2071404.

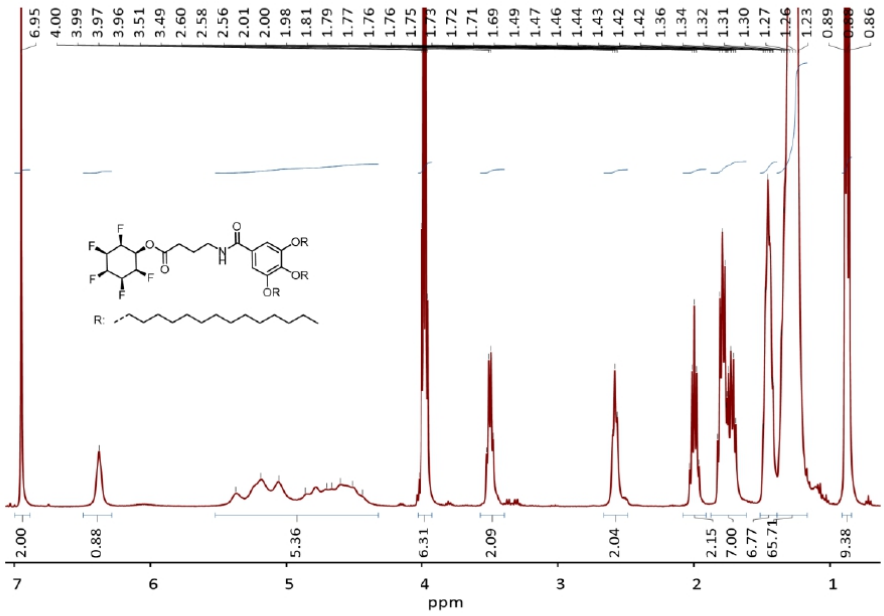

Supplementary Figure 58 | ^{1}H NMR (400 MHz) spectrum of **M$_1$** in $CDCl_3$ at 295 K.

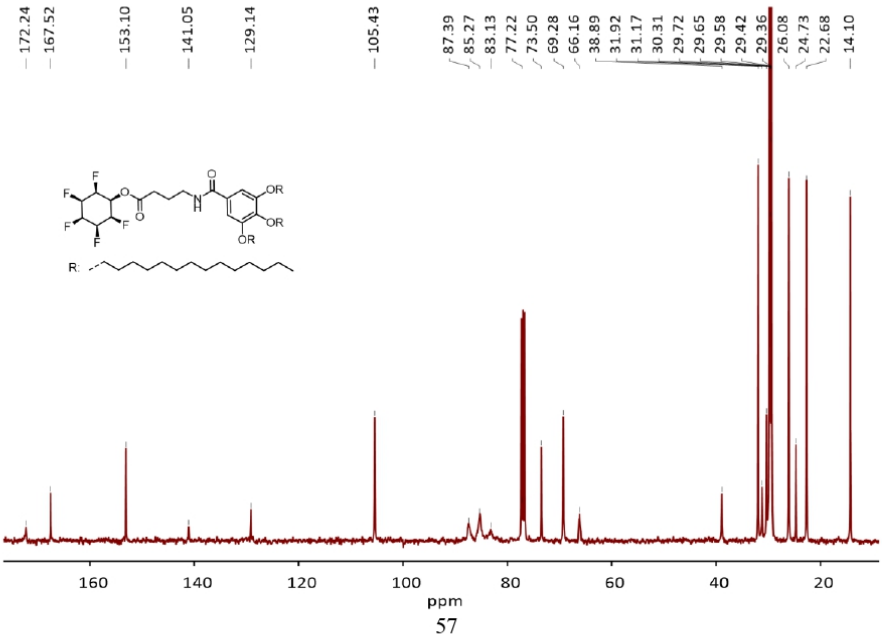

Supplementary Figure 59 | ^{13}C NMR (101 MHz) spectrum of **M_1** in $CDCl_3$ at 295 K.

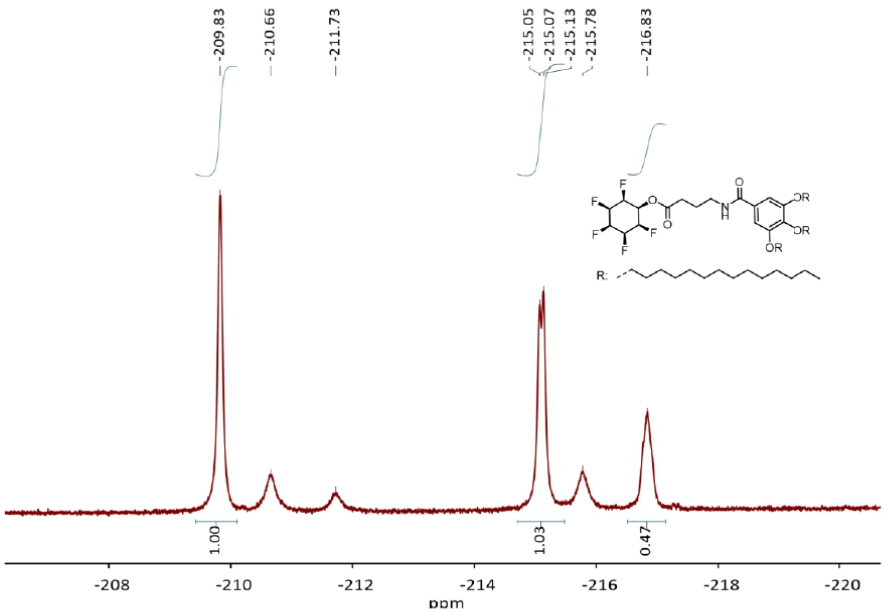

Supplementary Figure 60 | ^{19}F NMR (377 MHz) spectrum of **M_1** in $CDCl_3$ at 295 K.

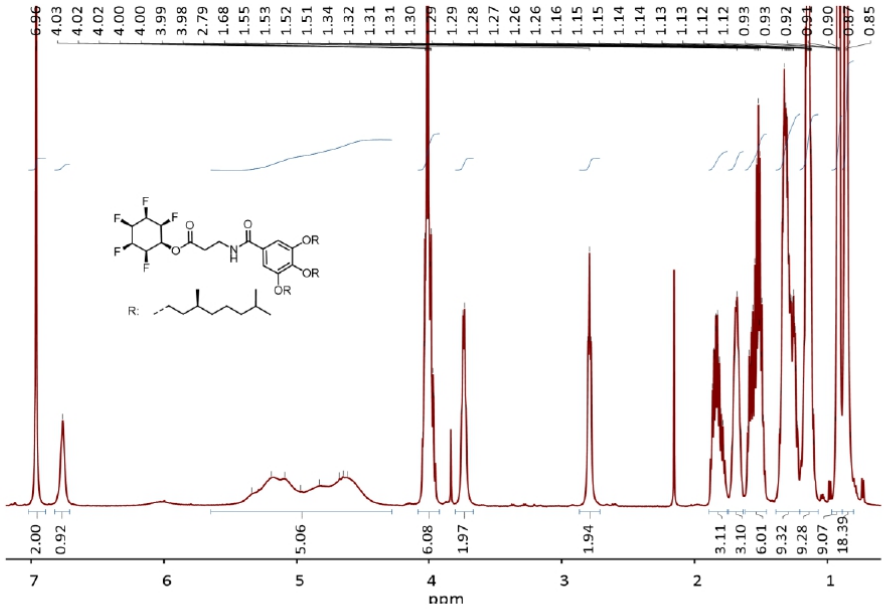

Supplementary Figure 61 | ^{1}H NMR (400 MHz) spectrum of **M_2** in $CDCl_3$ at 295 K.

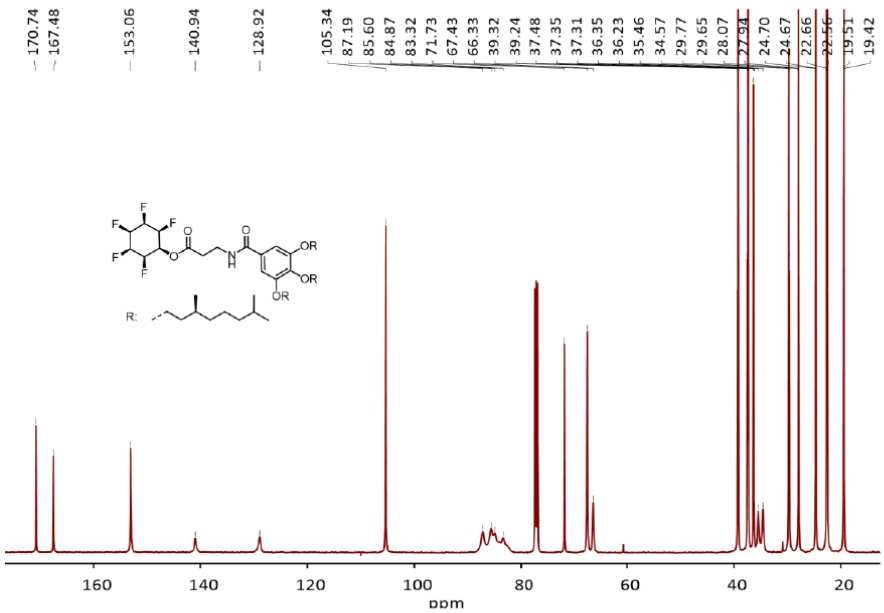

Supplementary Figure 62 | ^{13}C NMR (126 MHz) spectrum of **M₂** in $CDCl_3$ at 295 K.

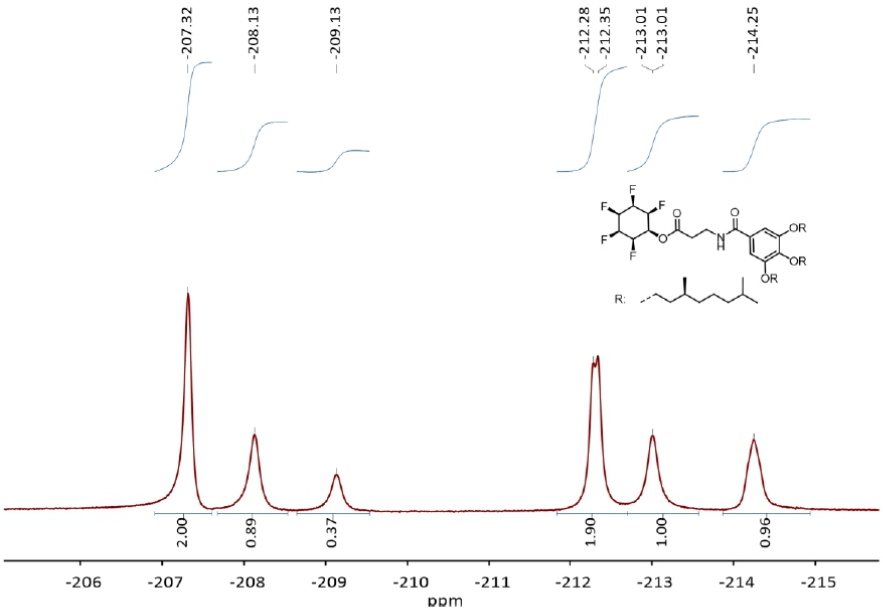

Supplementary Figure 63 | ^{19}F NMR (377 MHz) spectrum of **M₂** in $CDCl_3$ at 295 K.

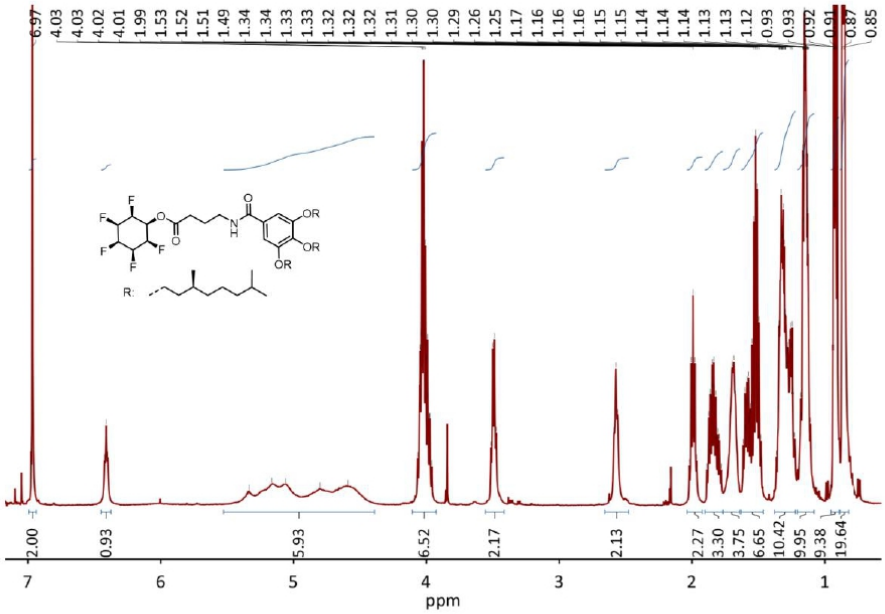

Supplementary Figure 64 | ^{1}H NMR (500 MHz) spectrum of **M3** in $CDCl_3$ at 295 K.

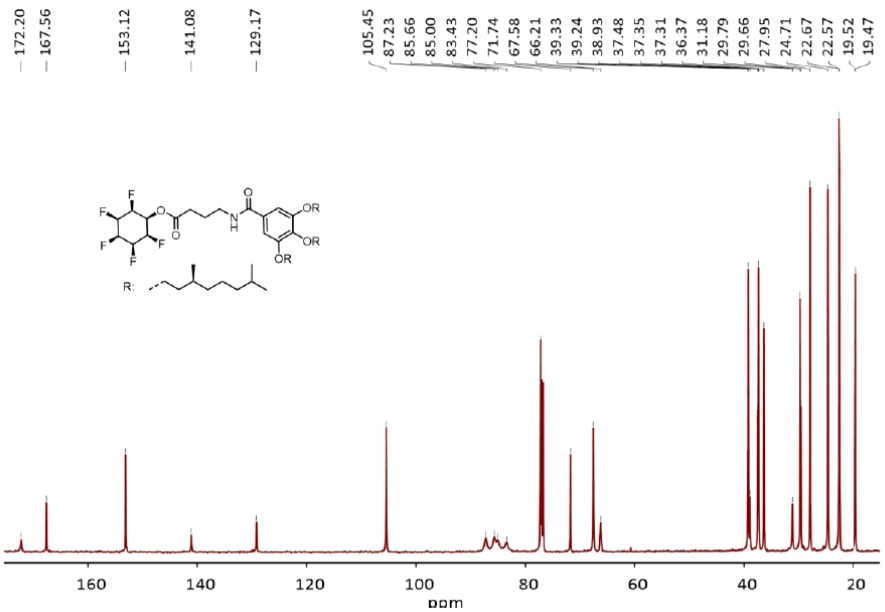

Supplementary Figure 65 |.^{13}C NMR (126 MHz) spectrum of **M3** in $CDCl_3$ at 295 K.

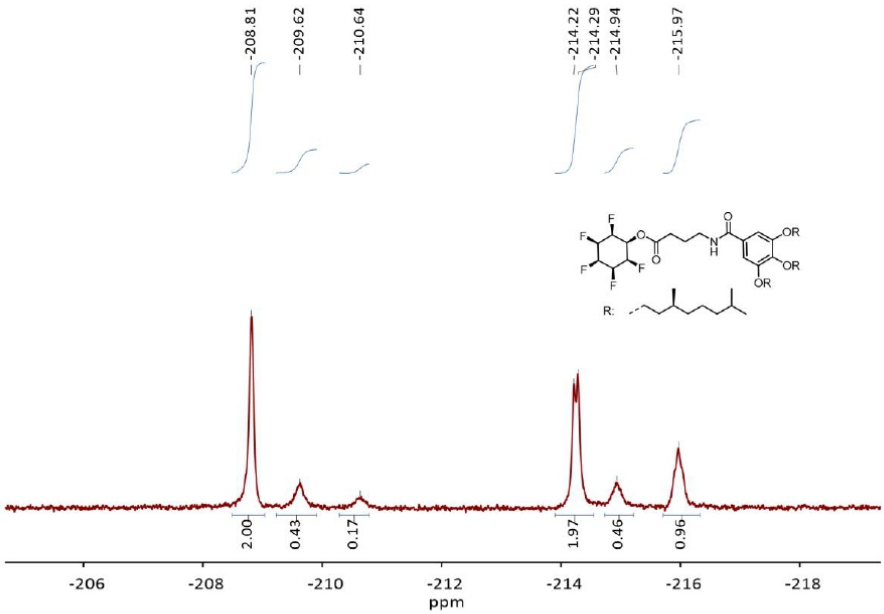

Supplementary Figure 66 | ^{19}F NMR (377 MHz) spectrum of **M3** in $CDCl_3$ at 295 K.

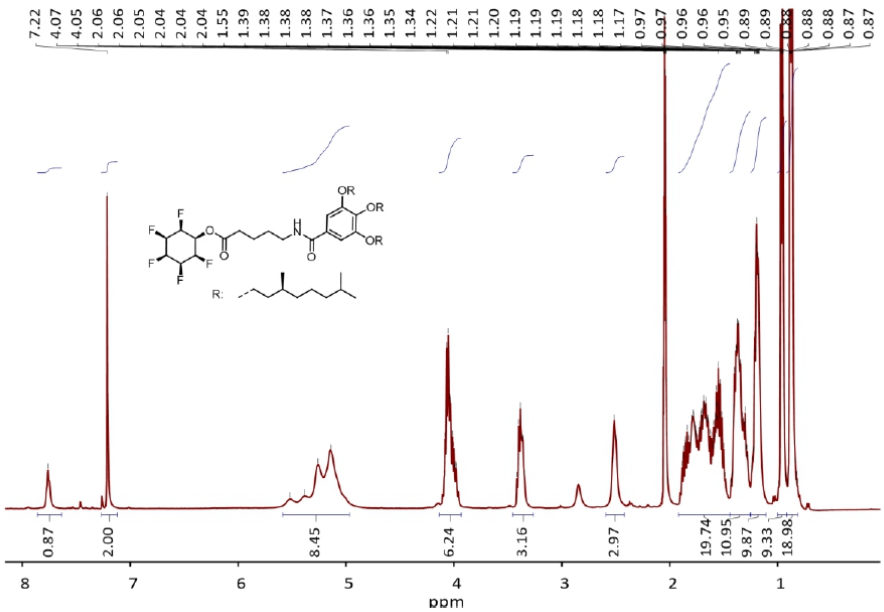

Supplementary Figure 67 | ^{1}H NMR (400 MHz) spectrum of **M4** in acetone-d_6 at 295 K.

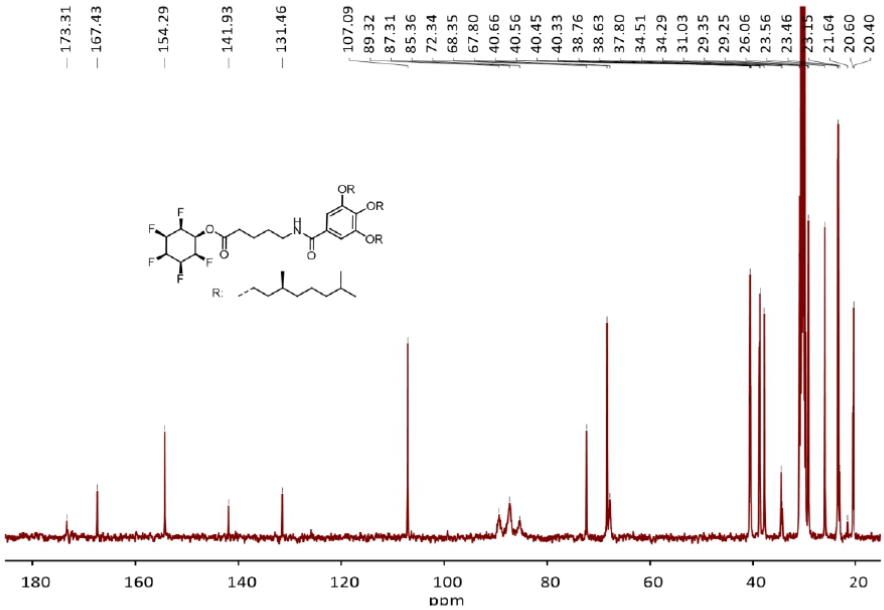

Supplementary Figure 68 | ^{13}C NMR (101 MHz) spectrum of **M4** in acetone-d_6 at 295 K.

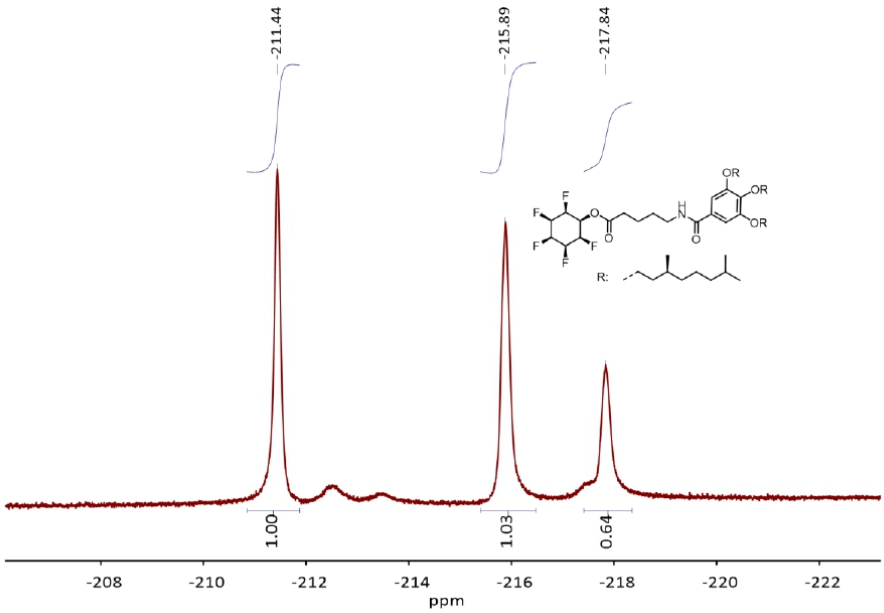

Supplementary Figure 69 | ^{19}F NMR (377 MHz) spectrum of **M4** in acetone-d_6 at 295 K.

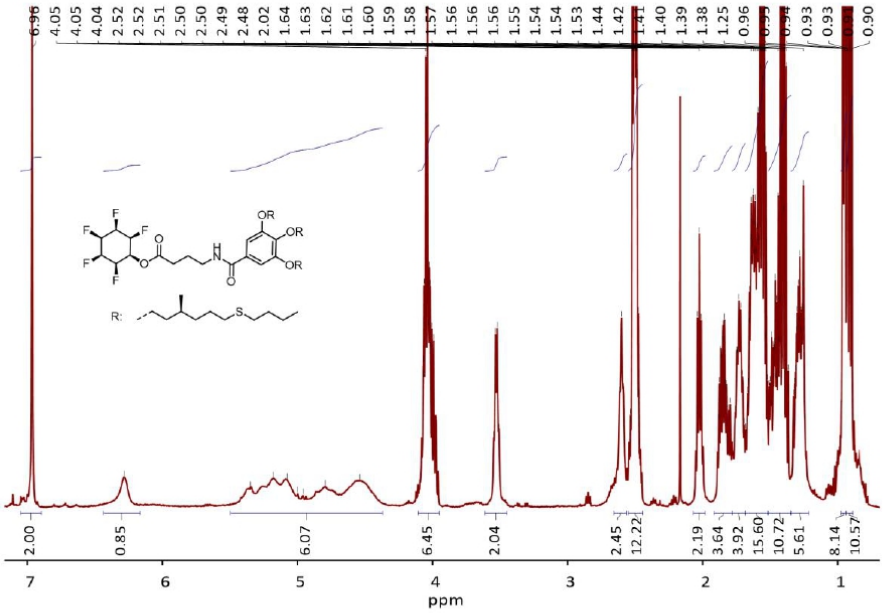

Supplementary Figure 70 | ^{1}H NMR (500 MHz) spectrum of **M5** in $CDCl_3$ at 295 K.

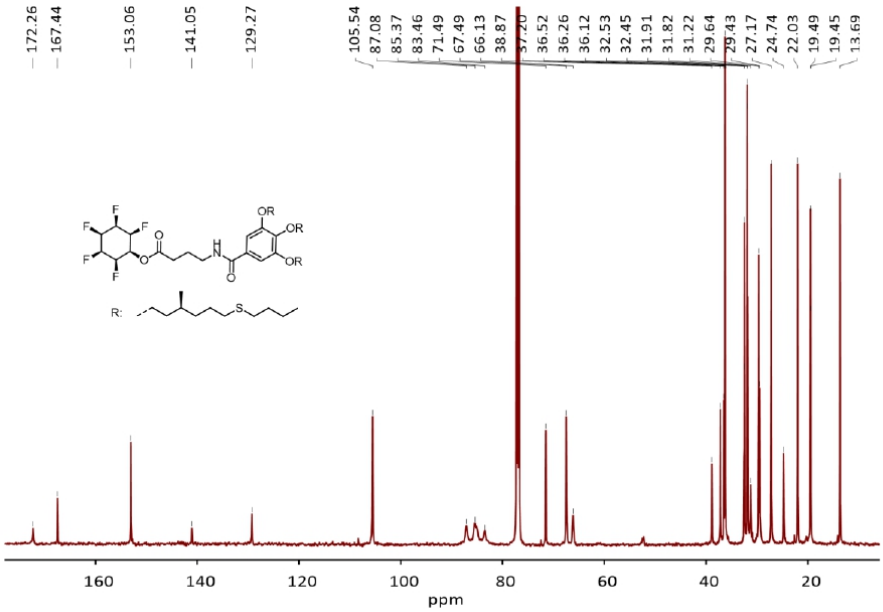

Supplementary Figure 71 | ^{13}C NMR (126 MHz) spectrum of **M5** in $CDCl_3$ at 295 K.

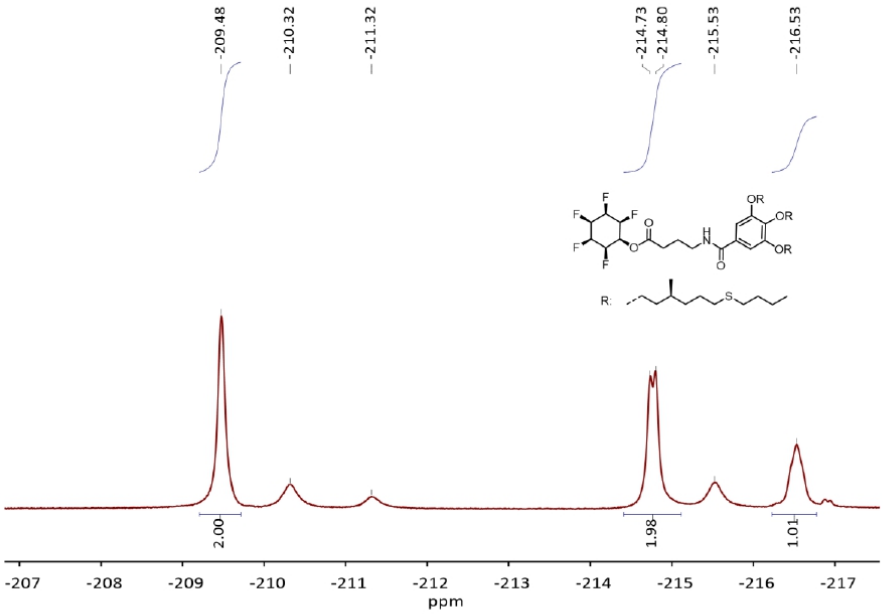

Supplementary Figure 72 | ^{19}F NMR (377 MHz) spectrum of **M$_5$** in $CDCl_3$ at 295 K.

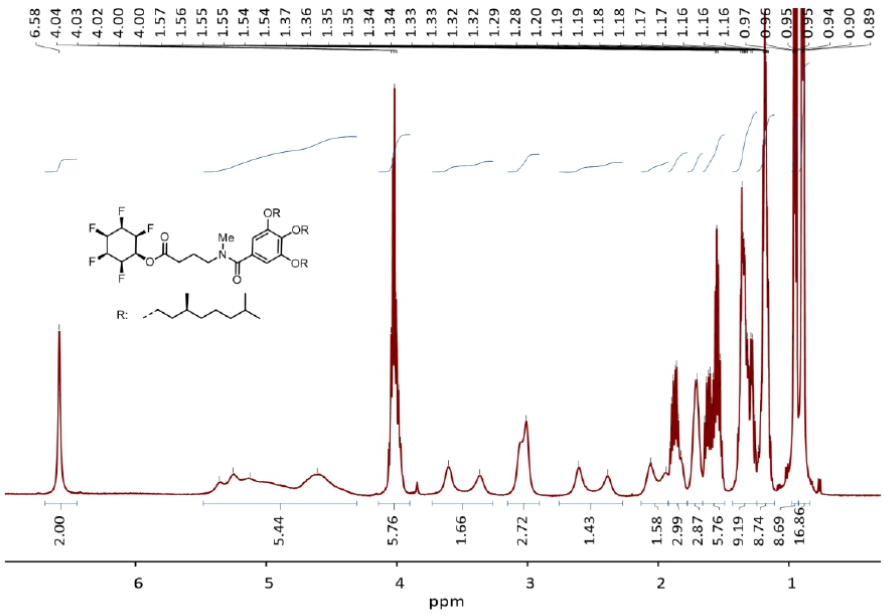

Supplementary Figure 73 | ^{1}H NMR (500 MHz) spectrum of ***Me*M$_3$** in $CDCl_3$ at 295 K.

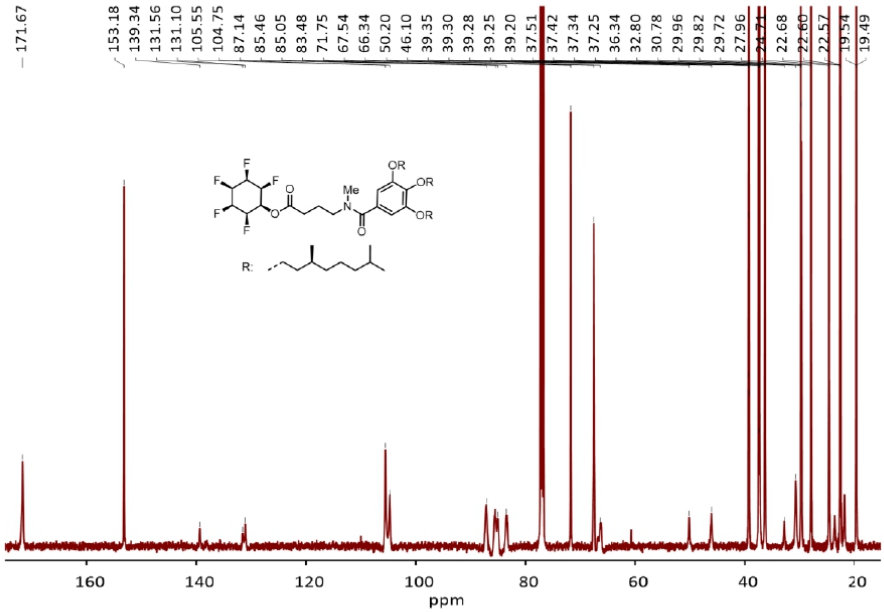

Supplementary Figure 74 |. ^{13}C NMR (126 MHz) spectrum of ***Me*M$_3$** in $CDCl_3$ at 295 K.

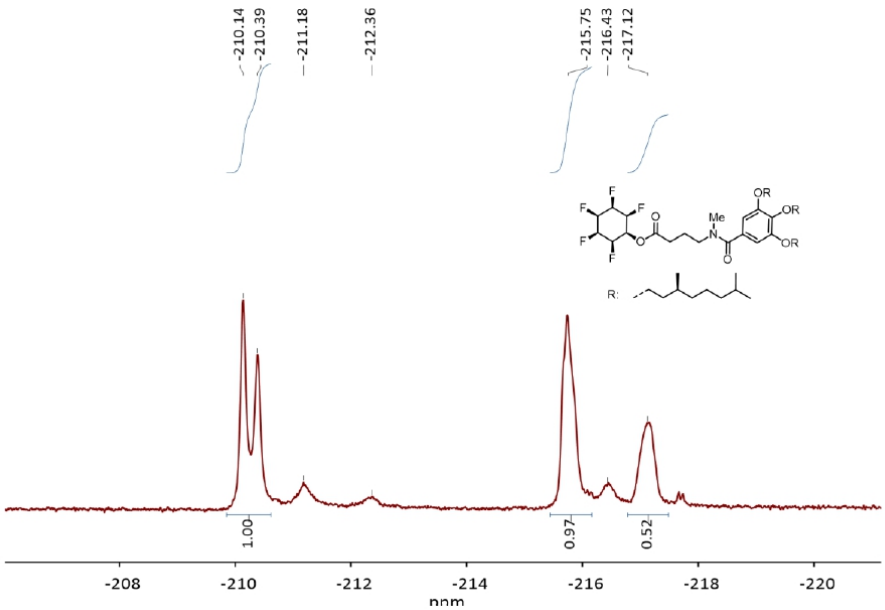

Supplementary Figure 75 |. ^{19}F NMR (377 MHz) spectrum of ***Me*M$_3$** in $CDCl_3$ at 295 K.

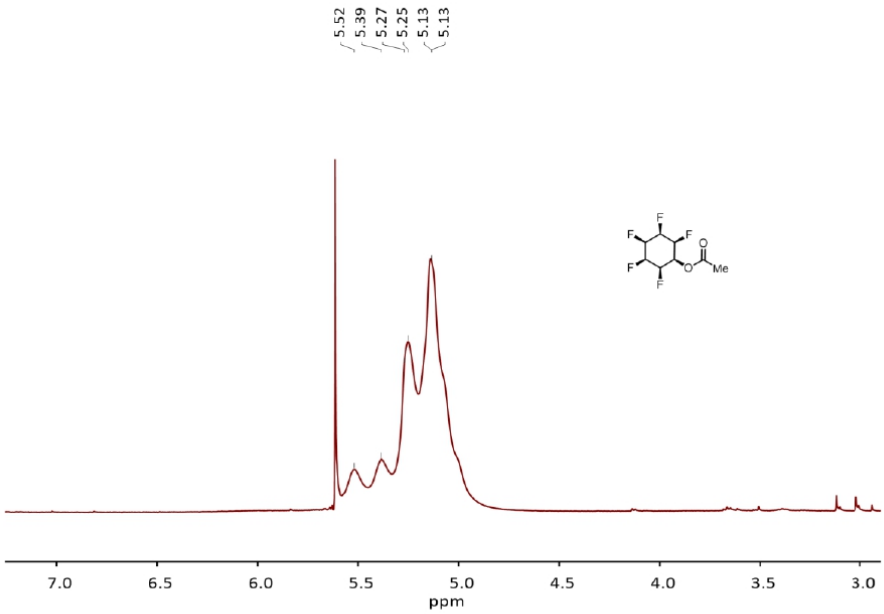

Supplementary Figure 76 | ^{1}H NMR (400 MHz) spectrum of **Ref$_1$** in acetone-d_6 at 295 K.

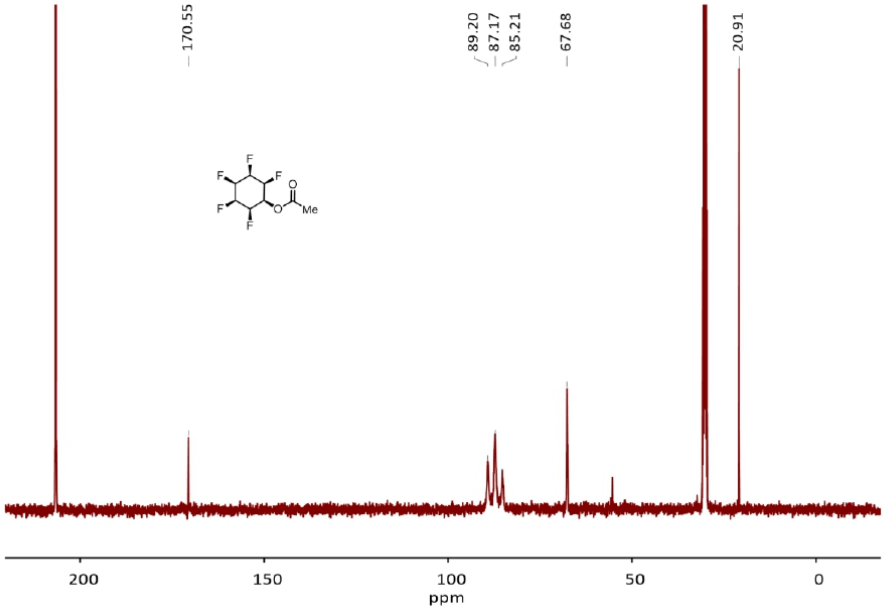

Supplementary Figure 77 | ^{13}C NMR (101 MHz) spectrum of **Ref$_1$** in acetone-d_6 at 295 K.

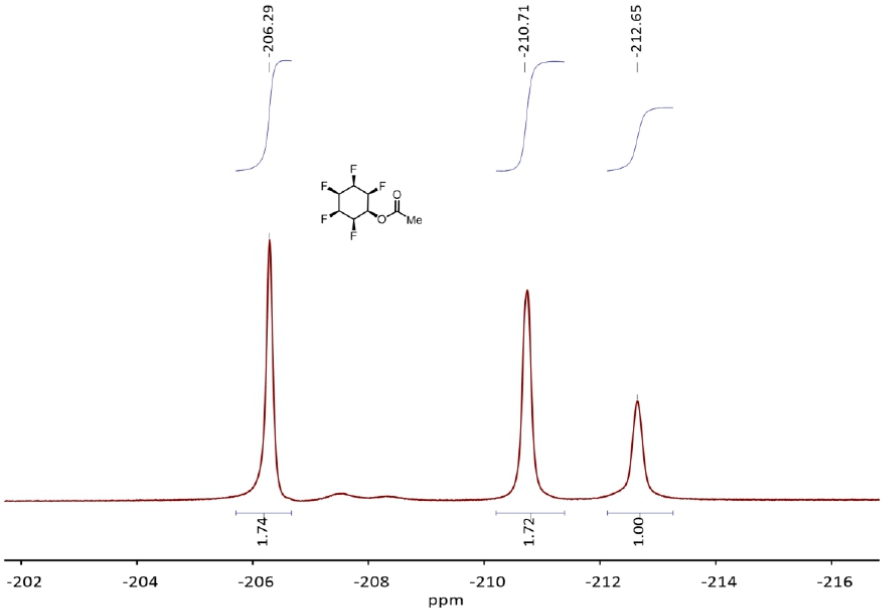

Supplementary Figure 78 | ^{19}F NMR (377 MHz) spectrum of **Ref$_1$** in acetone-d_6 at 295 K.

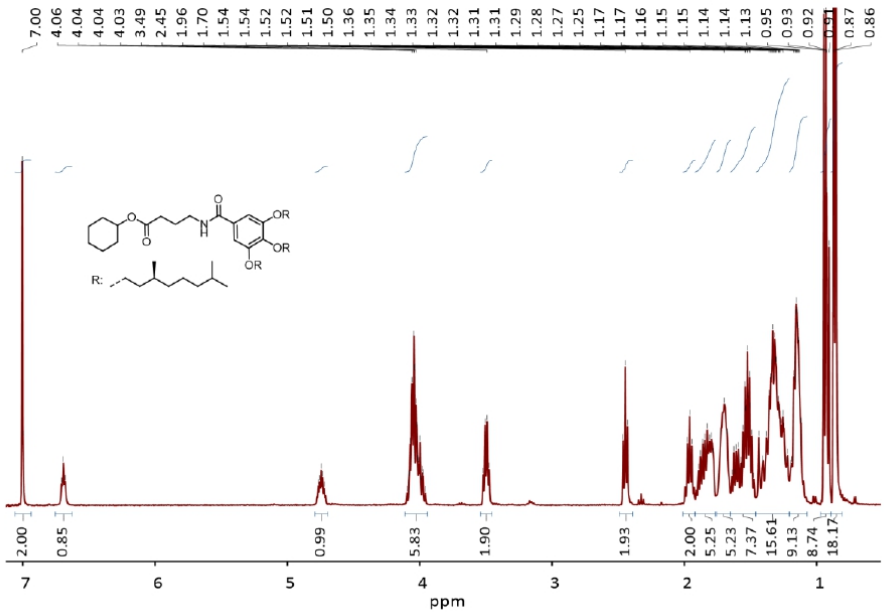

Supplementary Figure 79 | ^{1}H NMR (400 MHz) spectrum of **Ref$_2$** in $CDCl_3$ at 295 K.

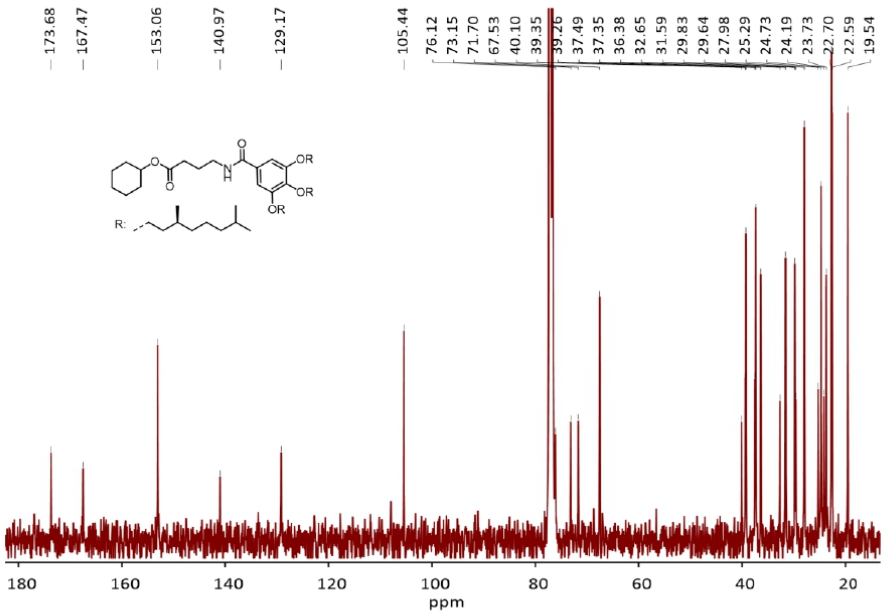

Supplementary Figure 80 | ^{13}C NMR (101 MHz) spectrum of **Ref$_2$** in $CDCl_3$ at 295 K.

Supplementary Tables

Supplementary Table 1 | Weight-averaged length (L_w), number-averaged length (L_n) and PDI (L_w/L_n) obtained by measuring lengths of n separate unbundled fibers obtained with different [**M3**]/[**M3**$^{\mathbf{Seed}}$] ratios.

[**M3**]/[**M3**$^{\mathbf{Seed}}$] (v/v)	n	L_w, (nm)	L_n, (nm)	PDI (L_w/L_n)
M3$^{\mathbf{Seed}}$	216	83	70	1.19
3/1	213	317	282	1.12
5/1	203	499	418	1.19
7/1	148	552	664	1.20
10/1	201	956	809	1.18

Supplementary Table 2 | Thermodynamic parameters of polymerization obtained by fitting the temperature dependent degree of aggregation (α_{agg}) according to the cooperative model.

Conc. (M)	α_{SAT}	h_e (kJ mol^{-1})	T_e (K)
0.8×10^{-3}	1.12	-70.6	301.3
1.0×10^{-3}	1.12	-67.0	303.5
1.2×10^{-3}	1.05	-74.0	306.1
1.4×10^{-3}	1.07	-73.5	306.8
1.6×10^{-3}	1.04	-86.2	307.9

Supplementary Table 3 | Thermodynamic parameters obtained by van`t Hoff analyses.

$\Delta H°$ (kJ mol^{-1})	$\Delta S°$ (J mol^{-1} K^{-1})	ΔG^{293} (kJ mol^{-1})
-77.9	-199	-19.6

Supplementary Table 4 | Crystal data and structure refinement for OSH19054.[23-25]

Identification code	OSH19054
Empirical formula	$C_{10.67}H_{12}F_{6.67}O_{2.67}$
Formula weight	309.54
Temperature/K	150.00(14)
Crystal system	monoclinic
Space group	$P2_1/c$
a/Å	6.5607(2)
b/Å	9.2352(4)
c/Å	14.4625(6)
α/°	90
β/°	92.224(4)
γ/°	90

Volume/Å^3	875.61(6)
Z	3
ρ_{calc}g/cm^3	1.761
μ/mm^{-1}	1.746
F(000)	472.0
Crystal size/mm^3	0.294 × 0.141 × 0.092
Radiation	CuKα (λ = 1.54184)
2Θ range for data collection/°	11.37 to 147.8
Index ranges	-7 ≤ h ≤ 7, -11 ≤ k ≤ 11, -9 ≤ l ≤ 17
Reflections collected	3327
Independent reflections	1709 [R_{int} = 0.0296, R_{sigma} = 0.0303]
Data/restraints/parameters	1709/0/137
Goodness-of-fit on F^2	1.046
Final R indexes [I>=2σ (I)]	R_1 = 0.0368, wR_2 = 0.0970
Final R indexes [all data]	R_1 = 0.0407, wR_2 = 0.1011
Largest diff. peak/hole / e Å^{-3}	0.29/-0.23

Supplementary Table 5 | Fractional atomic coordinates (×10^4) and equivalent isotropic displacement parameters (Å^2×10^3) for OSH19054. U_{eq} is defined as 1/3 of the trace of the orthogonalised U_{IJ} tensor.

Atom	*x*	*y*	*z*	U(eq)
F001	-481.3(14)	2835.2(11)	2422.6(7)	27.9(3)
F002	3396.5(14)	1541.9(10)	2559.1(7)	26.7(2)
F003	1050.3(15)	1954.0(11)	4113.5(7)	30.1(3)
F004	-1247.6(15)	4429.3(13)	3972.4(7)	35.2(3)
F005	2574.4(16)	3675.2(14)	1308.6(7)	37.1(3)
O006	5296.2(17)	2082.4(12)	4202.0(7)	22.5(3)
O007	5889.8(19)	3470.7(13)	5462.7(9)	29.5(3)
C008	6148(2)	2352.1(18)	5057.1(11)	22.3(3)

C009	567(2)	4128.3(17)	2603.0(11)	23.3(4)
C00A	4109(2)	3230.8(17)	3782.7(11)	21.4(3)
C00B	4080(2)	2943.9(18)	2745.6(11)	22.3(3)
C00C	714(2)	4408.1(19)	3632.9(12)	24.5(4)
C00D	1989(2)	3309.2(18)	4173.1(11)	23.9(4)
C00E	7373(3)	1098.3(19)	5404.1(12)	26.4(4)
C00F	2707(2)	4028.4(19)	2240.8(11)	25.2(4)

Supplementary Table 6 | Anisotropic displacement parameters ($Å^2 \times 10^3$) for OSH19054. The anisotropic displacement factor exponent takes the form: $-2\pi^2[h^2a^{*2}U_{11}+2hka^*b^*U_{12}+\ldots]$.

Atom	**U_{11}**	**U_{22}**	**U_{33}**	**U_{23}**	**U_{13}**	**U_{12}**
F001	21.2(5)	27.6(5)	34.2(5)	-1.4(4)	-7.1(4)	-4.4(4)
F002	30.0(5)	22.1(5)	27.7(5)	-4.2(4)	-4.4(4)	2.4(4)
F003	25.6(5)	27.8(5)	37.2(6)	8.7(4)	3.3(4)	-3.0(4)
F004	20.1(5)	44.1(7)	41.7(6)	-3.6(5)	4.4(4)	8.0(4)
F005	35.5(6)	51.6(7)	24.1(5)	9.6(5)	1.0(4)	7.8(5)
O006	22.0(6)	19.7(6)	25.1(6)	-2.0(4)	-7.4(4)	2.8(4)
O007	32.6(7)	24.5(6)	30.9(6)	-6.3(5)	-5.7(5)	0.5(5)
C008	18.4(7)	22.9(8)	25.4(8)	-0.7(6)	-3.0(6)	-3.2(6)
C009	18.4(8)	20.1(8)	31.0(8)	3.7(7)	-4.5(6)	-0.7(6)
C00A	17.6(7)	18.1(7)	28.1(8)	-0.4(6)	-4.5(6)	1.2(6)
C00B	18.2(7)	22.0(8)	26.8(8)	0.5(6)	0.3(6)	-1.3(6)
C00C	16.1(7)	23.9(8)	33.5(9)	-3.3(7)	-0.2(6)	1.8(6)
C00D	21.5(8)	25.4(8)	24.6(8)	-2.0(6)	-0.8(6)	1.7(7)
C00E	26.7(8)	26.4(8)	25.6(8)	-0.1(7)	-6.2(6)	1.4(7)
C00F	22.9(8)	26.0(8)	26.8(8)	6.2(7)	0.2(6)	-0.5(7)

Supplementary Table 7 | Bond lengths for OSH19054.

Atom	Atom	Length/Å	Atom	Atom	Length/Å
F001	C009	1.3974(18)	C008	C00E	1.486(2)
F002	C00B	1.3932(18)	C009	C00C	1.511(2)
F003	C00D	1.3959(19)	C009	C00F	1.521(2)
F004	C00C	1.3954(18)	C00A	C00B	1.522(2)
F005	C00F	1.386(2)	C00A	C00D	1.523(2)
O006	C008	1.3602(19)	C00B	C00F	1.515(2)
O006	C00A	1.4362(19)	C00C	C00D	1.513(2)
O007	C008	1.203(2)			

Supplementary Table 8 | Bond angles for OSH19054.

Atom	Atom	Atom	Angle/°	Atom	Atom	Atom	Angle/°
C008	O006	C00A	116.46(12)	F002	C00B	C00F	109.88(13)
O006	C008	C00E	111.23(14)	C00F	C00B	C00A	110.12(13)
O007	C008	O006	122.68(15)	F004	C00C	C009	108.93(13)
O007	C008	C00E	126.08(15)	F004	C00C	C00D	109.06(13)
F001	C009	C00C	110.02(13)	C009	C00C	C00D	114.04(13)
F001	C009	C00F	109.76(13)	F003	C00D	C00A	109.96(13)
C00C	C009	C00F	108.97(13)	F003	C00D	C00C	109.63(13)
O006	C00A	C00B	105.86(12)	C00C	C00D	C00A	109.56(13)
O006	C00A	C00D	111.51(13)	F005	C00F	C009	108.97(13)
C00B	C00A	C00D	113.39(13)	F005	C00F	C00B	109.07(14)
F002	C00B	C00A	110.13(13)	C00B	C00F	C009	114.44(13)

Supplementary Table 9 | Hydrogen atom coordinates (Å×10^4) and isotropic displacement parameters (Å^2×10^3) for OSH19054.

Atom	*x*	*y*	*z*	U(eq)
H009	-165.09	4929.39	2294.33	28
H00A	4810.49	4151.25	3907.19	26
H00B	5468.72	3046.35	2527.76	27
H00C	1326.36	5365.6	3734.74	29
H00D	2107.5	3606.85	4823.42	29
H00E	6568.07	520.21	5803.61	40
H00F	8564.47	1442.42	5742.65	40
H00G	7779.56	522.07	4890.39	40
H00H	3343.35	4985.67	2301.6	30

Supplementary Table 10 | Crystal data and structure refinement for SVH21029.[23-25]

Identification code	SVH21029
Empirical formula	$C_{18.67}H_{26.67}F_{6.67}N_{1.33}O_{5.33}$
Formula weight	481.75
Temperature/K	150.00(14)
Crystal system	monoclinic
Space group	$P2_1/c$
a/Å	5.04730(10)
b/Å	16.0606(3)
c/Å	20.3828(3)
α/°	90
β/°	94.174(2)
γ/°	90

Volume/Å^3	1647.90(5)
Z	3
ρ_{calc}g/cm^3	1.456
μ/mm^{-1}	1.250
F(000)	752.0
Crystal size/mm^3	0.744 × 0.121 × 0.097
Radiation	Cu Kα (λ = 1.54184)
2Θ range for data collection/°	7.014 to 145.902
Index ranges	-4 ≤ h ≤ 6, -19 ≤ k ≤ 19, -25 ≤ l ≤ 24
Reflections collected	10365
Independent reflections	3218 [R_{int} = 0.0274, R_{sigma} = 0.0217]
Data/restraints/parameters	3218/0/220
Goodness-of-fit on F^2	1.038
Final R indexes [I>=2σ (I)]	R_1 = 0.0365, wR_2 = 0.0926
Final R indexes [all data]	R_1 = 0.0396, wR_2 = 0.0952
Largest diff. peak/hole / e Å^{-3}	0.25/-0.20

Supplementary Table 11 | Fractional atomic coordinates (×10^4) and equivalent isotropic displacement parameters (Å^2×10^3) for SVH21029. U_{eq} is defined as 1/3 of the trace of the orthogonalised U_{IJ} tensor.

Atom	***x***	***y***	***z***	**U(eq)**
F001	5552.1(15)	8843.5(5)	4229.8(4)	34.0(2)
F002	4348.2(17)	7192.2(6)	4574.4(4)	40.0(2)
F003	3969.3(16)	7678.0(6)	3284.4(4)	39.8(2)
F004	2519.5(19)	9304.1(6)	3136.4(4)	44.2(2)
O005	3395.3(19)	8475.3(7)	5386.0(5)	36.2(3)
F006	406(2)	6554.6(6)	3724.6(6)	53.0(3)
O007	7227.1(18)	7257.5(6)	6799.7(5)	34.1(2)

O008	4067.3(19)	6288.9(6)	6492.6(6)	39.7(3)
O009	433(2)	9346.8(8)	5773.7(5)	46.3(3)
N00A	2837(2)	7551.0(7)	6761.9(5)	24.3(2)
C00B	2479(3)	8976.7(8)	5851.0(6)	26.1(3)
C00C	4308(3)	8971.2(8)	6465.3(6)	28.0(3)
C00D	4915(3)	7045.6(8)	6692.1(6)	26.7(3)
C00E	1776(3)	8399.0(9)	4779.7(6)	27.6(3)
C00F	3213(3)	8402.5(8)	6986.0(6)	25.6(3)
C00G	2831(3)	8976.1(8)	4270.4(6)	26.5(3)
C00H	1376(3)	8821.5(8)	3603.3(6)	26.7(3)
C00I	1758(3)	7486.5(9)	4587.1(7)	32.4(3)
C00J	1386(3)	7920.1(9)	3388.7(7)	29.2(3)
C00K	295(3)	7384.5(9)	3914.8(7)	32.3(3)
C00L	5973(3)	5621.1(9)	6361.9(9)	38.8(4)
C00M	7753(3)	5438.7(11)	6976.6(8)	43.5(4)
C00N	7511(4)	5860.7(12)	5780.2(8)	48.1(4)
C	4163(4)	4885.2(13)	6195.7(17)	87.4(10)

Supplementary Table 12 | Anisotropic displacement parameters ($Å^2 \times 10^3$) for SVH21029. The anisotropic displacement factor exponent takes the form: $-2\pi^2[h^2a^{*2}U_{11}+2hka^*b^*U_{12}+\ldots]$.

Atom	**U_{11}**	**U_{22}**	**U_{33}**	**U_{23}**	**U_{13}**	**U_{12}**
F001	21.4(4)	43.5(5)	36.7(4)	-2.7(3)	-0.8(3)	-2.9(3)
F002	37.5(5)	36.7(5)	44.8(5)	1.8(4)	-4.1(4)	14.4(4)
F003	28.5(4)	56.3(6)	34.9(4)	-16.5(4)	5.2(3)	6.4(4)
F004	48.0(5)	52.1(6)	32.1(4)	12.1(4)	0.5(4)	-15.7(4)
O005	29.2(5)	56.5(7)	22.5(5)	-6.6(4)	-1.2(4)	15.3(5)

F006	54.9(6)	26.1(5)	76.3(7)	-11.2(4)	-6.7(5)	-3.2(4)
O007	17.6(5)	34.2(5)	50.1(6)	-4.1(4)	0.7(4)	-3.3(4)
O008	19.0(5)	26.9(5)	72.8(8)	-11.9(5)	0.2(5)	-0.1(4)
O009	48.3(7)	51.2(7)	38.3(6)	-10.2(5)	-5.1(5)	26.3(6)
N00A	19.1(5)	24.5(5)	29.4(6)	-1.3(4)	1.2(4)	-3.2(4)
C00B	30.2(7)	24.0(6)	24.7(6)	2.4(5)	5.7(5)	-0.2(5)
C00C	32.1(7)	26.6(7)	25.0(6)	0.0(5)	1.2(5)	-5.6(5)
C00D	21.7(6)	27.2(7)	30.9(7)	0.0(5)	1.4(5)	-2.3(5)
C00E	22.3(6)	38.6(7)	21.9(6)	-1.9(5)	1.1(5)	7.9(5)
C00F	28.7(7)	26.6(6)	21.5(6)	-1.1(5)	2.8(5)	-1.7(5)
C00G	23.6(6)	26.1(6)	29.3(7)	-4.2(5)	-1.4(5)	3.0(5)
C00H	25.1(6)	30.5(7)	24.3(6)	3.6(5)	0.6(5)	-1.9(5)
C00I	29.8(7)	32.8(7)	35.1(7)	7.1(6)	4.5(6)	3.4(6)
C00J	22.4(6)	37.2(8)	27.6(6)	-8.3(5)	-0.6(5)	2.1(5)
C00K	27.5(7)	24.6(7)	44.3(8)	-4.5(6)	-0.1(6)	-0.8(5)
C00L	21.8(7)	29.4(7)	64.7(10)	-9.7(7)	0.0(6)	4.0(6)
C00M	45.2(9)	39.8(8)	47.3(9)	11.9(7)	14.8(7)	12.1(7)
C00N	47.3(10)	60.0(11)	35.5(8)	-5.8(7)	-6.7(7)	21.2(8)
C	33.5(10)	37.1(10)	191(3)	-45.4(14)	0.6(13)	2.3(8)

Supplementary Table 13 | Bond lengths for SVH21029.

Atom	**Atom**	**Length/Å**	**Atom**	**Atom**	**Length/Å**
F001	C00G	1.3984(15)	N00A	C00F	1.4499(17)
F002	C00I	1.3921(16)	C00B	C00C	1.5005(18)
F003	C00J	1.3918(16)	C00C	C00F	1.5334(18)

F004	C00H	1.3852(15)	C00E	C00G	1.5168(19)
O005	C00B	1.3508(16)	C00E	C00I	1.517(2)
O005	C00E	1.4362(15)	C00G	C00H	1.5179(17)
F006	C00K	1.3903(16)	C00H	C00J	1.5125(19)
O007	C00D	1.2200(16)	C00I	C00K	1.517(2)
O008	C00D	1.3416(16)	C00J	C00K	1.510(2)
O008	C00L	1.4777(17)	C00L	C00M	1.516(2)
O009	C00B	1.1922(17)	C00L	C00N	1.514(3)
N00A	C00D	1.3418(17)	C00L	C	1.517(2)

Supplementary Table 14 | Bond angles for SVH21029.

Atom	**Atom**	**Atom**	**Angle/°**	**Atom**	**Atom**	**Atom**	**Angle/°**
C00B	O005	C00E	116.89(10)	F004	C00H	C00J	109.07(11)
C00D	O008	C00L	120.98(11)	C00J	C00H	C00G	113.83(11)
C00D	N00A	C00F	121.24(11)	F002	C00I	C00E	110.17(12)
O005	C00B	C00C	111.15(11)	F002	C00I	C00K	110.02(12)
O009	C00B	O005	122.82(12)	C00E	C00I	C00K	109.35(11)
O009	C00B	C00C	125.99(12)	F003	C00J	C00H	109.53(11)
C00B	C00C	C00F	110.50(11)	F003	C00J	C00K	110.09(11)
O007	C00D	O008	125.94(12)	C00K	C00J	C00H	109.34(11)
O007	C00D	N00A	123.84(12)	F006	C00K	C00I	109.18(12)
O008	C00D	N00A	110.23(11)	F006	C00K	C00J	108.91(12)
O005	C00E	C00G	109.32(11)	C00J	C00K	C00I	113.66(11)
O005	C00E	C00I	107.30(11)	O008	C00L	C00M	110.22(13)
C00G	C00E	C00I	114.14(11)	O008	C00L	C00N	109.53(13)

N00A	C00F	C00C	112.91(10)	O008	C00L	C	102.49(12)
F001	C00G	C00E	110.03(10)	C00M	C00L	C	110.20(18)
F001	C00G	C00H	109.58(10)	C00N	C00L	C00M	112.92(13)
C00E	C00G	C00H	110.02(11)	C00N	C00L	C	110.98(18)
F004	C00H	C00G	108.99(11)				

Supplementary Table 15 | Hydrogen atom coordinates (Å×10^4) and isotropic displacement parameters (Å^2×10^3) for SVH21029.

Atom	***x***	***y***	***z***	**U(eq)**
H00A	1253.05	7366.43	6671.96	29
H00B	4496.99	9532.87	6637.4	34
H00C	6049.77	8776.5	6363.04	34
H00E	-41.61	8567.42	4856.47	33
H00D	4430.7	8406.61	7376.79	31
H00F	1525.26	8622.25	7106.31	31
H00G	2542.01	9554.4	4401	32
H00H	-473.63	8998.63	3624.3	32
H00I	835.79	7166.26	4910.54	39
H00J	264.93	7857.98	2978.49	35
H00K	-1571.1	7534.43	3950.1	39
H00L	9074.81	5867.11	7037.81	65
H00M	8608.66	4910.22	6930.36	65
H00N	6704.14	5423.41	7350.78	65
H00O	6298.22	6045.43	5425.37	72
H00P	8483.78	5386.81	5640.47	72
H00Q	8727.87	6301.82	5905.82	72

HA	3142.73	4763.01	6563.43	131
HB	5215.32	4408.84	6099.13	131
HC	2984.34	5018.15	5819.23	131

Supplementary Discussion

Discussion on NMR experiments

***Me*M$_3$** shows broadening of cyclohexane resonances at ca. 5.5 – 4.5 ppm similar to **M$_3$** (Supplementary Fig. 19). Therefore, the broadening of cyclohexane resonances (5.5 – 4.5 ppm) in **M$_3$** can not be due to the formation of aggregates with intermolecular N-H hydrogen bonds (since no N-H hydrogen bonding is possible for ***Me*M$_3$**). It indicates that for both compounds, broadened proton resonances for cyclohexane moiety are due to ring flipping of cyclohexane, which is generally slower for all-*cis* fluorinated cyclohexanes,[26] and slow equilibrium between multiple folded states in solution as evident from corresponding FESs (Supplementary Fig. 26b and d). To further address this point we performed VT-NMR measurements in chloroform (Supplementary Fig. 20), in which **M$_3$** does not polymerize but folds, as evident from HOESY measurements (Supplementary Fig. 18). In this case similar broadening of cyclohexane resonances (ca. 5.5 – 4.5 ppm) to **M$_3$** in cyclohexane/chloroform (84:16 v/v) is observed. Cyclohexane resonances become sharp only at low temperatures (< 293 K) confirming that in cyclohexane-d_{12}/chloroform-*d* (84:16 v/v) broadening is due to the slow cyclohexane ring flipping and the formation of multiple folded states.

Close values of the diffusion coefficients for **M$_1$** and **Ref$_2$** (reference compound that can neither fold nor form aggregates in solution) (Supplementary Figs. 21 and 22) clearly demonstrate that in chloroform **M$_1$** exists in a molecularly dissolved state therefore broadening of cyclohexane and NH resonances can not be attributed to the formation of oligomeric species.

Discussion on seed preparation

During our initial attempts to prepare **M$_3^{Seed}$** we noticed that sonication of a 0.9 mM solution (cyclohexane/chloroform 84:16 v/v) at 273 K for 20 min did not lead to homogeneous seeds with low polydispersity, and instead long (ca. 1 μm) bundled fibers were obtained as indicated by AFM (Supplementary Fig. 27). Moreover, the obtained seeds did not provide reliable reproducibility and length control during seeded living supramolecular polymerization. Therefore, we decided to use ***Me*M$_3$** as an auxiliary during seed preparation. ***Me*M$_3$** – a semi monotopic monomer that does not polymerize, but could form complexes with **M$_3$**. Complexation reduces the concentration of available **M$_3$**, which can no longer be incorporated into polymer chains. This effect is called "sequestration" and it is one of the ways to control the length of cooperative supramolecular polymers.[27] Shorter polymers can be better homogenized when ultrasound is applied. AFM studies on seeds obtained by sonication of 0.9 mM solutions of **M$_3$** (84:16 cyclohexane/chloroform, 20 min, 273 K) with different amounts of ***Me*M$_3$** added revealed that the addition of ***Me*M$_3$** has a pronounced effect on the size of

seeds. We discovered that sonication of **M3** and ***Me*M3** in 3:1 mol/mol ratio (c_{tot} = 1.2 mM, cyclohexane/chloroform 84:16 v/v, 273 K, 20 min) leads to the formation of small fibers with relatively low PDI. Using equimolar amounts of **M3** and ***Me*M3** (0.9 mM each) resulted in more amorphous aggregates (Supplementary Fig. 27). Thermal depolymerization, studied by CD, also revealed decreasing thermal stability and the degree of aggregation of "seeds" when the equivalence of ***Me*M3** increases (Supplementary Fig. 28) as expected for the formation of **M3**-***Me*M3** dimers.[27] We also attempted to carry out seeded LSP using "seeds" obtained without ***Me*M3**, however AFM revealed formation of non-uniform fibers with higher tendency to bundle (Supplementary Fig. 30).

Supplementary References

1. Horcas, I., Fernandez, R., Gomez-Rodriguez, J. M., Colchero, J., Gomez-Herrero, J. & Baro, A. M. WSXM: A software for scanning probe microscopy and a tool for nanotechnology. *Rev. Sci. Instrum.* **78**, 013705 (2007).
2. Rasband, W.S., ImageJ, U. S. National Institutes of Health, Bethesda, Maryland, USA, https://imagej.nih.gov/ij/, 1997-2018.
3. (a) Smulders, M. M. J., Nieuwenhuizen, M. M. L., de Greef, T. F. A., van der Shoot, P., Schenning, A. P. H. J. & Meijer, E. W. How to Distinguish Isodesmic from Cooperative Supramolecular Polymerization. *Chem. Eur. J.*, **16**, 362 – 367, (2010); (b) Jonkheijm, P., van der Schoot, P., Schenning, A. P. H. J. & Meijer, E. W. Probing the Solvent-Assisted Nucleation Pathway in Chemical Self-Assembly. *Science* **313**, 80-83 (2006).
4. Shyshov, O., Siewerth, K. A. & von Delius, M. Evidence for anion-binding of all-cis hexafluorocyclohexane in solution and solid state. *Chem. Commun.* **54**, 4353-4355 (2018).
5. Wang, J., Wolf, R. M., Caldwell, J. W., Kollman, P. A. & Case, D. A. Development and testing of a general AMBER force field. *J. Comput. Chem.* **25**, 1157-1174 (2004).
6. Jakalian, A., Bush, B. L., Jack, D. B. & Bayly, C. I. Fast, efficient generation of high-quality atomic charges. AM1-BCC model: I. Method. *J. Comput. Chem.* **21**, 132-146 (2000); (b) Jakalian, A., Jack, D. B. & Bayly, C. I. Fast, efficient generation of high-quality atomic charges. AM1-BCC model: II. Parametrization and validation, *J. Comput. Chem.* **23**, 1623-1641 (2002).
7. Wang, J., Wang, W., Kollman, P. A. & Case, D. A. Automatic atom type and bond type perception in molecular mechanical calculations, *J. Mol. Graph. Model.* **25**, 247260 (2006)
8. Hess, B., Kutzner, C., van der Spoel, D. & Lindahl, E. GROMACS 4: Algorithms for Highly Efficient, Load-Balanced, and Scalable Molecular Simulation. *J. Chem. Theory Comput.* **4**, 435–447 (2008).
9. Tribello, G. A., Bonomi, M., Branduardi, D., Camilloni, C. & Bussi, G. PLUMED 2: New feathers for an old bird. *Comput. Phys. Commun.* **185**, 604–613 (2014).
10. Jorgensen, W. L., Chandrasekhar, J., Madura, J. D., Impey, R. W. & Klein, M. L. Comparison of Simple Potential Functions for Simulating Liquid Water. *J. Chem. Phys.* **79**, 926–935 (1983).
11. Bussi, G., Donadio, D. & Parrinello, M. Canonical Sampling through Velocity Rescaling. *J. Chem. Phys.* **126**, 014101 (2007).
12. Berendsen, H. J. C., Postma, J. P. M., van Gunsteren, W. F., DiNola, A. & Haak, J. R. Molecular dynamics with coupling to an external bath. *J. Chem. Phys.* **81**, 3684–3690 (1984).
13. Essmann, U., Perera, L., Berkowitz, M. L., Darden, T., Lee, H. & Pedersen, L. G. A smooth particle mesh Ewald method. *J. Chem. Phys.* **103**, 8577–8593 (1995).
14. Hess, B., Bekker, H., Berendsen, H. & Fraaije, J. LINCS: A linear constraint solver for molecular simulations. *J. Comput. Chem.* **18**, 1463–1472 (1998).

15. Laio, A. & Parrinello, M. Escaping Free-Energy Minima. *Proc. Natl. Acad. Sci. USA* **99**, 12562–12566 (2002).
16. Barducci, A., Bussi, G. & Parrinello, M. Well-Tempered Metadynamics: A Smoothly Converging and Tunable Free-Energy Method. *Phys. Rev. Lett.* **100**, 020603 (2008).
17. Bartók, A. P., Kondor, R. & Csányi, G. On representing chemical environments. *Phys. Rev. B* **87**, 184115 (2013).
18. Gasparotto, P., Bochicchio, D., Ceriotti, M. & Pavan, G. M. Identifying and tracking defects in dynamic supramolecular polymers. *J. Phys. Chem. B* **124**, 589–599 (2020).
19. Himanen, L. et al. DScribe: Library of descriptors for machine learning in materials science. *Comp. Phys. Commun.* **247**, 106949 (2020).
20. Pedregosa, F. et al. Scikit-learn: machine learning in Python. *J. Mach. Learn Res.* **12**, 2825–2830 (2011).
21. Gasparotto, P. & Ceriotti, M. Recognizing molecular patterns by machine learning: an agnostic structural definition of the hydrogen bond. *J. Chem. Phys.* **141**, 174110 (2014).
22. Gasparotto, P., Meißner, R. H. & Ceriotti, M. Recognizing local and global structural motifs at the atomic scale. *J. Chem. Theory Comput.* **14**, 486–498 (2018).
23. Dolomanov, V., Bourhis, L. J., Gildea, R. J., Howard, J. A. K. & Puschmann, H. *J. Appl. Cryst.,* **42**, 339-341 (2009).
24. Scheldrick, G. M. *Acta. Cryst*. **A71**, 3-8 (2015).
25. Scheldrick, G. M. *Acta. Cryst*. **C71**, 3-8 (2015).
26. Keddie, N. S., Slawin, A. M. Z., Lebl, T., Philp, D. & O'Hagan, D. All-cis 1,2,3,4,5,6-hexafluorocyclohexane is a facially polarized cyclohexane. *Nat. Chem.* **7**, 483–488 (2015).
27. (a) Vantomme, G. et al. Tuning the Length of Cooperative Supramolecular Polymers under Thermodynamic Control. *J. Am. Chem. Soc.* **141**, 18278-18285 (2019); (b) Weyandt, E. et al. *Org. Mat.* **2**, 129-142 (2020).

References

[1] R. H. DeWolfe, *Synthesis* **1974**, 153–172.
[2] A. Pinner, *Ber. Dtsch. Chem. Ges.* **1883**, *16*, 352–363.
[3] A. Pinner, *Ber. Dtsch. Chem. Ges.* **1883**, *16*, 1643–1655.
[4] A. W. Williamson, *J. Chem. Soc. London* **1852**, *4*, 229–239.
[5] E. R. Alexander, H. M. Busch, *J. Am. Chem. Soc.* **1952**, *74*, 554–555.
[6] H. Stetter, *Chem. Ber.* **1988**, *642*, 639–642.
[7] J. F. Mike, A. J. Makowski, M. Jeffries-EL, *Org. Lett.* **2008**, *10*, 4915–4918.
[8] T. H. Fife, *Acc. Chem. Res.* **1972**, *5*, 264–272.
[9] M. Selva, F. Trotta, P. Tundo, *J. Chem. Soc. Perkin Trans. 2,* **1992**, *3*, 519–522.
[10] A. E. Tschitschibabin, *Ber. Dtsch. Chem. Ges.* **1904**, *37*, 850–853.
[11] G. Bastug, C. Eviolitte, I. E. Markó, *Org. Lett.* **2012**, *14*, 3502–3505.
[12] A. L. Chauvin, S. A. Nepogodiev, R. A. Field, *J. Org. Chem.* **2005**, *70*, 960–966.
[13] D. O'Hagan, *Chem. Soc. Rev.* **2008**, *37*, 308–319.
[14] J. A. K. Howard, V. J. Hoy, D. O'Hagan, G. T. Smith, *Tetrahedron* **1996**, *52*, 12613–12622.
[15] J. D. Dunitz, R. Taylor, *Chem. Eur. J.* **1997**, *3*, 89–98.
[16] L. Hunter, P. Kirsch, A. M. Z. Slawin, D. O'Hagan, *Angew. Chem. Int. Ed.* **2009**, *48*, 5457–5460.
[17] M. Burns, S. Essafi, J. R. Bame, S. P. Bull, M. P. Webster, S. Balieu, J. W. Dale, C. P. Butts, J. N. Harvey, V. K. Aggarwal, *Nature* **2014**, *513*, 183–188.
[18] A. J. Durie, A. M. Z. Slawin, T. Lebl, P. Kirsch, D. O'Hagan, *Chem. Commun.* **2011**, *47*, 8265–8267.
[19] A. J. Durie, A. M. Z. Slawin, T. Lebl, P. Kirsch, D. O'Hagan, *Chem. Commun.* **2012**, *48*, 9643–9645.
[20] N. S. Keddie, A. M. Z. Slawin, T. Lebl, D. Philp, D. O'Hagan, *Nat. Chem.* **2015**, *7*, 483–488.
[21] M. P. Wiesenfeldt, Z. Nairoukh, W. Li, F. Glorius, *Science* **2017**, *357*, 908-912
[22] Y. Wei, B. Rao, X. Cong, X. Zeng, *J. Am. Chem. Soc.* **2015**, *137*, 9250–9253.
[23] *Ferroelectric - Applications* (ed.: M. Lallart), InTech, Rijeka, Croatia, **2011**.
[24] J. F. Scott, *Science* **2007**, *315*, 954–959.
[25] J. Li, Y. Liu, Y. Zhang, H. L. Cai, R. G. Xiong, *Phys. Chem. Chem. Phys.* **2013**, *15*, 20786–20796.
[26] S. Horiuchi, Y. Tokura, *Nat. Mater.* **2008**, *7*, 357–366.
[27] A. S. Tayi, A. Kaeser, M. Matsumoto, T. Aida, S. I. Stupp, *Nat. Chem.* **2015**, *7*, 281–294.
[28] H. Kawai, *Jpn. J. Appl. Phys.* **1969**, *8*, 975–976.
[29] M. S. Q. M. Zhang, V. Bharti, G. Kavarnos, in *Encycl. Smart Mater. Vol. 1-2* (Ed.: M. Schwartz), New York, **2002**, pp. 807–825.
[30] S. M. Pratik, A. Nijamudheen, A. Datta, *J. Phys. Chem. C,* **2017**, *121*, 1752–1762.
[31] R. A. Cormanich, N. S. Keddie, R. Rittner, D. O'Hagan, M. Bühl, *Phys. Chem. Chem. Phys.* **2015**, *17*, 29475–29478.
[32] W. M. Sun, B. L. Ni, D. Wu, J. M. Lan, C. Y. Li, Y. Li, Z. R. Li, *Organometallics* **2017**, *36*, 3352–3359.
[33] B. E. Ziegler, M. Lecours, R. A. Marta, J. Featherstone, E. Fillion, W. S. Hopkins, V.

Steinmetz, N. S. Keddie, D. O'Hagan, T. B. McMahon, *J. Am. Chem. Soc.* **2016**, *138*, 7460–7463.
[34] M. J. Lecours, R. A. Marta, V. Steinmetz, N. Keddie, E. Fillion, D. O'Hagan, T. B. McMahon, W. S. Hopkins, *J. Phys. Chem. Lett.* **2017**, *8*, 109–113.
[35] J. W. Larson, T. B. McMahon, *J. Am. Chem. Soc.* **1985**, *107*, 766–773.
[36] S. M. Pratik, A. Nijamudheen, A. Datta, *ChemPhysChem* **2016**, 2373–2381.
[37] B. Dietrich, J. M. Lehn, J. P. Sauvage, *Tetrahedron Lett.* **1969**, *10*, 2885–2888.
[38] P. T. Corbett, J. Leclaire, L. Vial, K. R. West, J. L. Wietor, J. K. M. Sanders, S. Otto, *Chem. Rev.* **2006**, *106*, 3652–3711.
[39] A. Herrmann, *Chem. Soc. Rev.* **2014**, *43*, 1899–1933.
[40] V. Berl, I. Huc, J.-M. Lehn, A. DeCian, J. Fischer, *Eur. J. Org. Chem.* **1999**, *1999*, 3089–3094.
[41] Y. Jin, C. Yu, R. J. Denman, W. Zhang, *Chem. Soc. Rev.* **2013**, *42*, 6634–6654.
[42] M. Fujita, N. Fujita, K. Ogura, K. Yamaguchi, *Nature* **1999**, *400*, 52–55.
[43] M. Yoshizawa, M. Tamura, M. Fujita, *Science* **2006**, *312*, 251–255.
[44] R. Zhu, I. Regeni, J. J. Holstein, B. Dittrich, M. Simon, S. Prévost, M. Gradzielski, G. H. Clever, *Angew. Chem. Int. Ed.* **2018**, *57*, 13652–13656.
[45] F. J. Rizzuto, L. K. S. von Krbek, J. R. Nitschke, *Nat. Rev. Chem.* **2019**, *3*, 204–222.
[46] N. J. Cookson, J. J. Henkelis, R. J. Ansell, C. W. G. Fishwick, M. J. Hardie, J. Fisher, *Dalt. Trans.* **2014**, *43*, 5657–5661.
[47] W. J. Ramsay, F. T. Szczypiński, H. Weissman, T. K. Ronson, M. M. J. Smulders, B. Rybtchinski, J. R. Nitschke, *Angew. Chem. Int. Ed.* **2015**, *54*, 5636–5640.
[48] K. Yazaki, M. Akita, S. Prusty, D. K. Chand, T. Kikuchi, H. Sato, M. Yoshizawa, *Nat. Commun.* **2017**, *8*, 15914.
[49] D. Samanta, J. Gemen, Z. Chu, Y. Diskin-Posner, L. J. W. Shimon, R. Klajn, *Proc. Natl. Acad. Sci. U. S. A.* **2018**, *115*, 9379–9384.
[50] F. J. Rizzuto, J. R. Nitschke, *Nat. Chem.* **2017**, *9*, 903–908.
[51] D. Fujita, K. Suzuki, S. Sato, M. Yagi-Utsumi, Y. Yamaguchi, N. Mizuno, T. Kumasaka, M. Takata, M. Noda, S. Uchiyama, K. Kato, M. Fujita, *Nat. Commun.* **2012**, *3*, 1093.
[52] M. D. Pluth, R. G. Bergman, K. N. Raymond, *J. Am. Chem. Soc.* **2008**, *130*, 11423–11429.
[53] H. Takezawa, K. Shitozawa, M. Fujita, *Nat. Chem.* **2020**, *12*, 574–578.
[54] T. Furusawa, M. Kawano, M. Fujita, *Angew. Chem. Int. Ed.* **2007**, *119*, 5819–5821.
[55] D. Fujita, Y. Ueda, S. Sato, N. Mizuno, T. Kumasaka, M. Fujita, *Nature* **2016**, *540*, 563–566.
[56] D. MacDowell, J. Nelson, *Tetrahedron Lett.* **1988**, *29*, 385–386.
[57] M. Mastalerz, *Acc. Chem. Res.* **2018**, *51*, 2411–2422.
[58] T. Tozawa, J. T. A. Jones, S. I. Swamy, S. Jiang, D. J. Adams, S. Shakespeare, R. Clowes, D. Bradshaw, T. Hasell, S. Y. Chong, C. Tang, S. Thompson, J. Parker, A. Trewin, J. Bacsa, A. M. Z. Slawin, A. Steiner, A. I. Cooper, *Nat. Mater.* **2009**, *8*, 973–978.
[59] N. Giri, M. G. Del Pópolo, G. Melaugh, R. L. Greenaway, K. Rätzke, T. Koschine, L. Pison, M. F. C. Gomes, A. I. Cooper, S. L. James, *Nature* **2015**, *527*, 216–220.
[60] M. Cesario, C. O. Dietrich-Buchecker, J. Guilhem, C. Pascard, J.-P. Sauvage, *J. Chem. Soc. Chem. Commun.* **1985**, 244–247.
[61] N. Ponnuswamy, F. B. L. Cougnon, J. M. Clough, G. D. Pantoş, J. K. M. Sanders, *Science* **2012**, *338*, 783–785.
[62] C. D. Meyer, C. S. Joiner, J. F. Stoddart, *Chem. Soc. Rev.* **2007**, *36*, 1705–1723.

[63] L. Vial, R. F. Ludlow, J. Leclaire, R. Pérez-Fernández, S. Otto, *J. Am. Chem. Soc.* **2006**, *128*, 10253–10257.
[64] V. A. Bloomfield, *Biopolymers* **1997**, *44*, 269–282.
[65] K. N. Houk, A. G. Leach, S. P. Kim, X. Zhang, *Angew. Chem. Int. Ed.* **2003**, *42*, 4872–4897.
[66] E. A. Katayev, G. D. Pantos, M. D. Reshetova, V. N. Khrustalev, V. M. Lynch, Y. A. Ustynyuk, J. L. Sessler, *Angew. Chem. Int. Ed.* **2005**, *44*, 7386–7390.
[67] P. Frei, R. Hevey, B. Ernst, *Chem. Eur. J.* **2019**, *25*, 60–73.
[68] B. A. Katz, J. Finer-Moore, R. Mortezaei, D. H. Rich, R. M. Stroud, *Biochemistry* **1995**, *34*, 8264–8280.
[69] I. Huc, J. M. Lehn, *Proc. Natl. Acad. Sci. U. S. A.* **1997**, *94*, 2106–2110.
[70] M. S. Congreve, D. J. Davis, L. Devine, C. Granata, M. O'Reilly, P. G. Wyatt, H. Jhoti, *Angew. Chem. Int. Ed.* **2003**, *42*, 4479–4482.
[71] A. Bugaut, J. J. Toulmé, B. Rayner, *Angew. Chem. Int. Ed.* **2004**, *43*, 3144–3147.
[72] B. Klekota, B. L. Miller, *Tetrahedron* **1999**, *55*, 11687–11697.
[73] C. Karan, B. L. Miller, *J. Am. Chem. Soc.* **2001**, *123*, 7455–7456.
[74] M. Hochgürtel, H. Kroth, D. Piecha, M. W. Hofmann, C. Nicolau, S. Krause, O. Schaaf, G. Sonnenmoser, A. V. Eliseev, *Proc. Natl. Acad. Sci. U. S. A.* **2002**, *99*, 3382–3387.
[75] Y. Zhang, M. Barboiu, *Chem. Rev.* **2016**, *116*, 809–834.
[76] H. Guo, Y. Han, W. Zhao, J. Yang, L. Zhang, *Nat. Commun.* **2020**, *11*, 2037.
[77] M. Röttger, T. Domenech, R. Van Der Weegen, A. Breuillac, R. Nicolaÿ, L. Leibler, *Science* **2017**, *356*, 62–65.
[78] P. R. Christensen, A. M. Scheuermann, K. E. Loeffler, B. A. Helms, *Nat. Chem.* **2019**, *11*, 442–448.
[79] R. C. Brachvogel, M. von Delius, *Chem. Sci.* **2015**, *6*, 1399–1403.
[80] A. M. Vibhute, A. Vidyasagar, S. Sarala, K. M. Sureshan, *Chem. Commun.* **2012**, *48*, 2448–2450.
[81] J. Zhou, G. Yu, F. Huang, *Chem. Soc. Rev.* **2017**, *46*, 7021–7053.
[82] P. A. Gale, J. T. Davis, R. Quesada, *Chem. Soc. Rev.* **2017**, *46*, 2497–2519.
[83] H. Löw, E. Mena-Osteritz, M. von Delius, *Chem. Sci.* **2018**, *9*, 4785–4793.
[84] R. W. Taft, *J. Am. Chem. Soc.* **1952**, *74*, 2729–2732.
[85] R. C. Brachvogel, F. Hampel, M. von Delius, *Nat. Commun.* **2015**, *6*, 7129.
[86] R. C. Brachvogel, H. Maid, M. von Delius, *Int. J. Mol. Sci.* **2015**, *16*, 20641–20656.
[87] H. Löw, E. Mena-Osteritz, M. von Delius, *Chem. Commun.* **2019**, *55*, 11434–11437.
[88] T. F. A. De Greef, M. M. J. Smulders, M. Wolffs, A. P. H. J. Schenning, R. P. Sijbesma, E. W. Meijer, *Chem. Rev.* **2009**, *109*, 5687–5754.
[89] R. P. Sijbesma, F. H. Beijer, L. Brunsveld, B. J. B. Folmer, J. H. K. K. Hirschberg, R. F. M. Lange, J. K. L. Lowe, E. W. Meijer, *Science* **1997**, *278*, 1601–1604.
[90] N. M. Matsumoto, R. P. M. Lafleur, X. Lou, K. C. Shih, S. P. W. Wijnands, C. Guibert, J. W. A. M. van Rosendaal, I. K. Voets, A. R. A. Palmans, Y. Lin, E. W. Meijer, *J. Am. Chem. Soc.* **2018**, *140*, 13308–13316.
[91] M. M. J. Smulders, A. P. H. J. Schenning, E. W. Meijer, *J. Am. Chem. Soc.* **2008**, *130*, 606–611.
[92] S. K. Yang, S. C. Zimmerman, *Isr. J. Chem.* **2013**, *53*, 511–520.
[93] T. Aida, A. Takemura, M. Fuse, S. Inoue, *J. Chem. Soc. Chem. Commun.* **1988**, *26*, 391–393.
[94] R. F. Pasternack, C. Fleming, S. Herring, P. J. Collings, J. DePaula, G. DeCastro, E. J.

Gibbs, *Biophys. J.* **2000**, *79*, 550–560.
[95] T. E. Kaiser, V. Stepanenko, F. Würthner, *J. Am. Chem. Soc.* **2009**, *131*, 6719–6732.
[96] T. E. Kaiser, H. Wang, V. Stepanenko, F. Würthner, *Angew. Chem. Int. Ed.* **2007**, *119*, 5637–5640.
[97] F. Würthner, *Acc. Chem. Res.* **2016**, *49*, 868–876.
[98] F. Würthner, S. Yao, U. Beginn, *Angew. Chem. Int. Ed.* **2003**, *42*, 3247–3250.
[99] S. Yao, U. Beginn, T. Gress, M. Lysetska, F. Würthner, *J. Am. Chem. Soc.* **2004**, *126*, 8336–8348.
[100] G. Fernández, M. Stolte, V. Stepanenko, F. Würthner, *Chem. Eur. J.* **2013**, *19*, 206–217.
[101] K. Ohga, Y. Takashima, H. Takahashi, Y. Kawaguchi, H. Yamaguchi, A. Harada, *Macromolecules* **2005**, *38*, 5897–5904.
[102] A. Winter, U. S. Schubert, *Chem. Soc. Rev.* **2016**, *45*, 5311–5357.
[103] S. I. A. Cohen, R. Cukalevski, T. C. T. Michaels, A. Šarić, M. Törnquist, M. Vendruscolo, C. M. Dobson, A. K. Buell, T. P. J. Knowles, S. Linse, *Nat. Chem.* **2018**, *10*, 523–531.
[104] A. K. Buell, *Biochem. J.* **2019**, *476*, 2677–2703.
[105] C. Revenu, R. Athman, S. Robine, D. Louvard, *Nat. Rev. Mol. Cell Biol.* **2004**, *5*, 635–646.
[106] L. D. B. Evans, G. P. Stafford, S. Ahmed, G. M. Fraser, C. Hughes, *Proc. Natl. Acad. Sci. U. S. A.* **2006**, *103*, 17474–17479.
[107] J. Matern, Y. Dorca, L. Sánchez, G. Fernández, *Angew. Chem. Int. Ed.* **2019**, *58*, 16730–16740.
[108] S. Ogi, K. Sugiyasu, S. Manna, S. Samitsu, M. Takeuchi, *Nat. Chem.* **2014**, *6*, 188–195.
[109] A. Aliprandi, M. Mauro, L. De Cola, *Nat. Chem.* **2016**, *8*, 10–15.
[110] W. Wagner, M. Wehner, V. Stepanenko, S. Ogi, F. Würthner, *Angew. Chem. Int. Ed.* **2017**, *56*, 16008–16012.
[111] G. Ghosh, P. Dey, S. Ghosh, *Chem. Commun.* **2020**, *56*, 6757-6769.
[112] H. Kar, G. Ghosh, S. Ghosh, *Chem. Eur. J.* **2017**, *23*, 10536–10542.
[113] A. Chakraborty, G. Ghosh, D. S. Pal, S. Varghese, S. Ghosh, *Chem. Sci.* **2019**, *10*, 7345–7351.
[114] D. S. Pal, H. Kar, S. Ghosh, *Chem. Commun.* **2018**, *54*, 928–931.
[115] C. Jarrett-Wilkins, X. He, H. E. Symons, R. L. Harniman, C. F. J. Faul, I. Manners, *Chem. Eur. J.* **2018**, *24*, 15556–15565.
[116] J. S. Valera, R. Gómez, L. Sánchez, *Small* **2018**, *14*, 1–9.
[117] H. Wang, Y. Zhang, Y. Chen, H. Pan, X. Ren, Z. Chen, *Angew. Chem. Int. Ed.* **2020**, *59*, 5185–5192.
[118] S. Ogi, N. Fukaya, Arifin, B. B. Skjelstad, Y. Hijikata, S. Yamaguchi, *Chem. Eur. J.* **2019**, *25*, 7303–7307.
[119] S. Ogi, V. Stepanenko, K. Sugiyasu, M. Takeuchi, F. Würthner, *J. Am. Chem. Soc.* **2015**, *137*, 3300–3307.
[120] S. Ogi, V. Stepanenko, J. Thein, F. Würthner, *J. Am. Chem. Soc.* **2016**, *138*, 670–678.
[121] J. Kang, D. Miyajima, T. Mori, Y. Inoue, Y. Itoh, T. Aida, *Science* **2015**, *347*, 646–651.
[122] J. Kang, D. Miyajima, Y. Itoh, T. Mori, H. Tanaka, M. Yamauchi, Y. Inoue, S. Harada, T. Aida, *J. Am. Chem. Soc.* **2014**, *136*, 10640–10644.
[123] S. Ogi, K. Matsumoto, S. Yamaguchi, *Angew. Chem. Int. Ed.* **2018**, *57*, 2339–2343.
[124] M. Endo, T. Fukui, S. H. Jung, S. Yagai, M. Takeuchi, K. Sugiyasu, *J. Am. Chem. Soc.* **2016**, *138*, 14347–14353.

[125] Q. Wan, W. P. To, C. Yang, C. M. Che, *Angew. Chem. Int. Ed.* **2018**, *57*, 3089–3093.
[126] A. Jain, S. Dhiman, A. Dhayani, P. K. Vemula, S. J. George, *Nat. Commun.* **2019**, *10*, 450.
[127] A. Mishra, D. B. Korlepara, M. Kumar, A. Jain, N. Jonnalagadda, K. K. Bejagam, S. Balasubramanian, S. J. George, *Nat. Commun.* **2018**, *9*, 1295.
[128] T. Fukui, N. Sasaki, M. Takeuchi, K. Sugiyasu, *Chem. Sci.* **2019**, *10*, 6770–6776.
[129] M. Wehner, F. Würthner, *Nat. Rev. Chem.* **2020**, *4*, 38–53.
[130] B. Adelizzi, N. J. Van Zee, L. N. J. De Windt, A. R. A. Palmans, E. W. Meijer, *J. Am. Chem. Soc.* **2019**, *141*, 6110–6121.
[131] X. Wang, I. Manners, M. A. Winnik, *Science* **2007**, *644*, 644–648.
[132] J. B. Gilroy, T. Gädt, G. R. Whittell, L. Chabanne, J. M. Mitchels, R. M. Richardson, M. A. Winnik, I. Manners, *Nat. Chem.* **2010**, *2*, 566–570.
[133] Z. M. Hudson, C. E. Boott, M. E. Robinson, P. A. Rupar, M. A. Winnik, I. Manners, *Nat. Chem.* **2014**, *6*, 893–898.
[134] H. Qiu, Z. M. Hudson, M. A. Winnik, I. Manners, *Science* **2015**, *347*, 1329–1332.
[135] X. Li, Y. Gao, C. E. Boott, M. A. Winnik, I. Manners, *Nat. Commun.* **2015**, *6*, 8127.
[136] W. Zhang, W. Jin, T. Fukushima, A. Saeki, S. Seki, T. Aida, *Science* **2011**, *334*, 340-343.
[137] A. Pal, M. Malakoutikhah, G. Leonetti, M. Tezcan, M. Colomb-Delsuc, V. D. Nguyen, J. Van Der Gucht, S. Otto, *Angew. Chem. Int. Ed.* **2015**, *54*, 7852–7856.
[138] S. H. Jung, D. Bochicchio, G. M. Pavan, M. Takeuchi, K. Sugiyasu, *J. Am. Chem. Soc.* **2018**, *140*, 10570–10577.
[139] W. Wagner, M. Wehner, V. Stepanenko, F. Würthner, *J. Am. Chem. Soc.* **2019**, *141*, 12044–12054.
[140] A. Sarkar, R. Sasmal, C. Empereur-mot, D. Bochicchio, S. V. K. Kompella, K. Sharma, S. Dhiman, B. Sundaram, S. S. Agasti, G. M. Pavan, S. J. George, *J. Am. Chem. Soc.* **2020**, *142*, 7606–7617.
[141] Q. Wan, W. P. To, X. Chang, C. M. Che, *Chem* **2020**, *6*, 945–967.
[142] G. Ashkenasy, T. M. Hermans, S. Otto, A. F. Taylor, *Chem. Soc. Rev.* **2017**, *46*, 2543–2554.
[143] J. Li, P. Nowak, S. Otto, *J. Am. Chem. Soc.* **2013**, *135*, 9222–9239.
[144] S. Hiraoka, K. Harano, M. Shiro, M. Shionoya, *Angew. Chem. Int. Ed.* **2005**, *44*, 2727–2731.
[145] S. O. J. M. A. Carnall, C. A. Waudby, A. M. Belenguer, M. C. A. Stuart, J. J.-P. Peyralans, *Science* **2010**, *327*, 1502–1507.
[146] I. A. Riddell, M. M. J. Smulders, J. K. Clegg, Y. R. Hristova, B. Breiner, J. D. Thoburn, J. R. Nitschke, *Nat. Chem.* **2012**, *4*, 751–756.
[147] S. Zarra, D. M. Wood, D. A. Roberts, J. R. Nitschke, *Chem. Soc. Rev.* **2015**, *44*, 419–432.
[148] A. R. Stefankiewicz, M. R. Sambrook, J. K. M. Sanders, *Chem. Sci.* **2012**, *3*, 2326–2329.
[149] J. F. Ayme, J. E. Beves, C. J. Campbell, D. A. Leigh, *Angew. Chem. Int. Ed.* **2014**, *53*, 7823–7827.
[150] J. K. Clegg, J. Cremers, A. J. Hogben, B. Breiner, M. M. J. Smulders, J. D. Thoburn, J. R. Nitschke, *Chem. Sci.* **2013**, *4*, 68–76.
[151] I. A. Riddell, Y. R. Hristova, J. K. Clegg, C. S. Wood, B. Breiner, J. R. Nitschke, *J. Am. Chem. Soc.* **2013**, *135*, 2723–2733.
[152] W. Meng, B. Breiner, K. Rissanen, J. D. Thoburn, J. K. Clegg, J. R. Nitschke, *Angew. Chem. Int. Ed.* **2011**, *50*, 3479–3483.

[153] S. Freye, J. Hey, A. Torras-Galán, D. Stalke, R. Herbst-Irmer, M. John, G. H. Clever, *Angew. Chem. Int. Ed.* **2012**, *51*, 2191–2194.
[154] S. Freye, R. Michel, D. Stalke, M. Pawliczek, H. Frauendorf, G. H. Clever, *J. Am. Chem. Soc.* **2013**, *135*, 8476–8479.
[155] S. Löffler, J. Lübben, L. Krause, D. Stalke, B. Dittrich, G. H. Clever, *J. Am. Chem. Soc.* **2015**, *137*, 1060–1063.
[156] R. Zhu, J. Lübben, B. Dittrich, G. H. Clever, *Angew. Chem. Int. Ed.* **2015**, *54*, 2796–2800.
[157] R. Custelcean, *Chem. Soc. Rev.* **2014**, *43*, 1813–1824.
[158] B. Fuchs, A. Nelson, A. Star, J. F. Stoddart, S. Vidal, *Angew. Chem. Int. Ed.* **2003**, *42*, 4220–4224.
[159] S. Otto, R. L. E. Furlan, J. K. M. Sanders, *Science* **2002**, *297*, 590–593.
[160] S. Otto, S. Kubik, *J. Am. Chem. Soc.* **2003**, *125*, 7804–7805.
[161] H. Y. Au-Yeung, F. B. L. Cougnon, S. Otto, G. D. Pantoş, J. K. M. Sanders, *Chem. Sci.* **2010**, *1*, 567–574.
[162] J. A. Berrocal, R. Cacciapaglia, S. Di Stefano, *Org. Biomol. Chem.* **2011**, *9*, 8190–8194.
[163] Y. Zhang, Y. M. Legrand, A. van der Lee, M. Barboiu, *Eur. J. Org. Chem.* **2016**, *2016*, 1825–1828.
[164] O. Shyshov, R. C. Brachvogel, T. Bachmann, R. Srikantharajah, D. Segets, F. Hampel, R. Puchta, M. von Delius, *Angew. Chem. Int. Ed.* **2017**, *56*, 776–781.
[165] W. R. R. W. E. von Doering, *Angew. Chem. Int. Ed.* **1963**, *2*, 115–122.
[166] A. Ault, *J. Chem. Educ.* **2001**, *78*, 924–927.
[167] F. Scholz, D. Himmel, F. W. Heinemann, P. V R Schleyer, K. Meyer, I. Krossing, *Science* **2013**, *341*, 62–64.
[168] K. K. Larson, M. He, J. F. Teichert, A. Naganawa, J. W. Bode, *Chem. Sci.* **2012**, *3*, 1825–1828.
[169] J. F. Teichert, D. Mazunin, J. W. Bode, *J. Am. Chem. Soc.* **2013**, *135*, 11314–11321.
[170] X. Wang, O. Shyshov, M. Hanževački, C. M. Jäger, M. von Delius, *J. Am. Chem. Soc.* **2019**, *141*, 8868–8876.
[171] R. De Stephanis, J. Giménez, E. Carpinelli, C. Gutierrez-Exposito, A. Cañadas, *Mar. Pollut. Bull.* **2013**, *69*, 206–214.
[172] M. R. Gregory, *Philos. Trans. R. Soc. B Biol. Sci.* **2009**, *364*, 2013–2025.
[173] V. Tournier, C. M. Topham, A. Gilles, B. David, C. Folgoas, E. Moya-Leclair, E. Kamionka, M. L. Desrousseaux, H. Texier, S. Gavalda, M. Cot, E. Guémard, M. Dalibey, J. Nomme, G. Cioci, S. Barbe, M. Chateau, I. André, S. Duquesne, A. Marty, *Nature* **2020**, *580*, 216–219.
[174] "Bioplastics market data 2017," can be found under https://www.european-bioplastics.org/market/**.**
[175] R. A. Gross, B. Kalra, *Science* **2002**, *297*, 803–807.
[176] A. Anjum, M. Zuber, K. M. Zia, A. Noreen, M. N. Anjum, S. Tabasum, *Int. J. Biol. Macromol.* **2016**, *89*, 161–174.
[177] M. Winnacker, *Eur. J. Lipid Sci. Technol.* **2019**, *121*, 1–9.
[178] P. Ortmann, I. Heckler, S. Mecking, *Green Chem.* **2014**, *16*, 1816–1827.
[179] F. Stempfle, P. Ortmann, S. Mecking, *Chem. Rev.* **2016**, *116*, 4597–4641.
[180] E. H. Cordes, H. G. Bull, *Chem. Rev.* **1974**, *74*, 581–603.
[181] J. Heller, J. Barr, *Biomacromolecules* **2004**, *5*, 1625–1632.
[182] M. J. L. Tschan, N. S. Leong, R. Todd, J. Everson, A. P. Dove, *Angew. Chem. Int. Ed.*

2017, *56*, 16664–16668.
[183] T. Haider, O. Shyshov, O. Suraeva, I. Lieberwirth, M. Von Delius, F. R. Wurm, *Macromolecules* **2019**, *52*, 2411–2420.
[184] P. D. Beer, P. A. Gale, *Angew. Chem. Int. Ed.* **2001**, *40*, 486–516.
[185] L. Chen, S. N. Berry, X. Wu, E. N. W. Howe, P. A. Gale, *Chem* **2020**, *6*, 61–141.
[186] N. H. Evans, P. D. Beer, *Angew. Chem. Int. Ed.* **2014**, *53*, 11716–11754.
[187] G. Nie, Y. Sun, F. Zhang, M. Song, D. Tian, L. Jiang, H. Li, *Chem. Sci.* **2015**, *6*, 5859–5865.
[188] L. Qin, A. Hartley, P. Turner, R. B. P. Elmes, K. A. Jolliffe, *Chem. Sci.* **2016**, *7*, 4563–4572.
[189] C. F. Chow, P. Y. Ho, W. L. Wong, Y. J. Lu, Q. Tang, C. B. Gong, *Chem. Sci.* **2017**, *8*, 3812–3820.
[190] M. Zurro, S. Asmus, S. Beckendorf, C. Mück-Lichtenfeld, O. G. Mancheño, *J. Am. Chem. Soc.* **2014**, *136*, 13999–14002.
[191] A. J. Plaunt, K. M. Harmatys, W. R. Wolter, M. A. Suckow, B. D. Smith, *Bioconjug. Chem.* **2014**, *25*, 724–737.
[192] M. C. Etter, M. Zia-Ebrahimi, Z. Urbañczyk-Lipkowska, T. W. Panunto, *J. Am. Chem. Soc.* **1990**, *112*, 8415–8426.
[193] G. T. G. Cavallo, P. Metrangolo, R. Milani, T. Pilati, A. Priimagi, G. Resnati, *Chem. Rev.* **2016**, *116*, 2478–2601.
[194] R. O. Ramabhadran, Y. Liu, Y. Hua, M. Ciardi, A. H. Flood, K. Raghavachari, *J. Am. Chem. Soc.* **2014**, *136*, 5078–5089.
[195] J. L. Sessler, M. J. Cyr, V. Lynch, E. McGhee, J. A. Ibers, *J. Am. Chem. Soc.* **1990**, *112*, 2810–2813.
[196] P. A. Gale, J. L. Sessler, V. Král, V. Lynch, *J. Am. Chem. Soc.* **1996**, *118*, 5140–5141.
[197] V. H. Dalvi, P. J. Rossky, *Proc. Natl. Acad. Sci. U. S. A.* **2010**, *107*, 13603–13607.
[198] O. Shyshov, K. A. Siewerth, M. von Delius, *Chem. Commun.* **2018**, *54*, 4353–4355.
[199] Y. Liu, A. Sengupta, K. Raghavachari, A. H. Flood, *Chem* **2017**, *3*, 411–427.
[200] W. Zhang, H. L. Zhuang, L. Fan, L. Gao, Y. Lu, *Sci. Adv.* **2018**, *4*, 4410
[201] E. Schwartz, M. Koepf, H. J. Kitto, R. J. M. Nolte, A. E. Rowan, *Polym. Chem.* **2011**, *2*, 33–47.
[202] E. Weyandt, M. F. J. Mabesoone, L. N. J. de Windt, E. W. Meijer, A. R. A. Palmans, G. Vantomme, *Org. Mater.* **2020**, *02*, 129–142.
[203] O. Shyshov, V. H. Shyamkumar, L. Pesce, H. Qi, A. Gardin, D. Bochicchio, U. Kaiser, G. M. Pavan, M. von Delius, Living Supramolecular Polymerization of Fluorinated Cyclohexanes, *Nat. Chommun.* **2021**, *12*, 3134.

List of Publications

1. **O. Shyshov**, V. H. Shyamkumar, L. Pesce, H. Qi, D. Gardin, D. Bochicchio, U. Kaiser, G. M. Pavan, M. von Delius, Living supramolecular polymerization of fluorinated cyclohexanes, *Nat. Commun.* **2021**, 12, 3134.
2. B. Balakrishna, A. Puthiyedath, S. B. Beil, K. Cao, S. Gsänger, J. V. Fernandez, **O. Shyshov**, O. Martin, F. Hauke, A. Hirsch, B. Meyer, U. Kaiser, D. M. Guldi, M. von Delius, Dynamic covalent formation of concave disulfide macrocycles around single-walled carbon nanotubes, *Angew. Chem. Int. Ed.* **2020**, 59, 18774-18785.
3. Y. Xu, S. Gsänger, M. B. Minameyer, I. Imaz, D. Maspoch, **O. Shyshov**, F. Schwer, X. Ribas, T. Drewello, B. Meyer, M. von Delius, Highly Strained, Radially π-Conjugated Porphyrinylene Nanohoops, *J. Am. Chem. Soc.* **2019**, 141, 18500-18507.
4. X. Wang, **O. Shyshov**, M. Hanževački, C. Jäger, M. von Delius, Ammonium Complexes of Orthoester Cryptands are Inherently Dynamic and Adaptive, *J. Am. Chem. Soc.* **2019**, 141, 8868-8876.
5. T. Haider, **O. Shyshov**, O. Suraeva, I. Lieberwirth, M. von Delius, F. Wurm, Long-Chain Polyorthoesters as Degradable Polyethylene Mimics, *Macromolecules*, **2019**, 52, 2411-2420.
6. **O. Shyshov**, K. A. Siewerth, M. von Delius, Evidence for anion-binding of all-cis hexafluorocyclohexane in solution and solid state, *Chem. Commun.* **2018**, 54, 4353-4355.
7. **O. Shyshov***, R. Brachvogel*, T. Bachmann, R. Srikantharajah, D. Segets, F. Hampel, R. Puchta, M. von Delius, Adaptive Behaviour of Dynamic Orthoester Cryptands, *Angew. Chem. Int. Ed.* **2017**, 56, 776-781 (*equal contribution).

List of Talks and Conference Contributions

Talks

1. Tag der Organischen Chemie, University of Stuttgart, Stuttgart, Germany, 11/10/2019;
2. OC-Sommer-Symposium 2019, University of Ulm, Ulm, Germany, 12/07/2019;

Poster Presentations

1. CEMSupra 2019, Tokyo, Japan, 9/12 – 10/12 2019: poster presentation;
2. ISMSC 2019, Lecce, Italy, 2/6 – 6/6 2019: poster presentation;
3. SupraChem 2019, Würzburg, Germany, 24/2 – 26/2 2019: poster presentation;
4. Ulm-Erlangen Symposium, 10/7 – 11/7/2017: poster presentation;
5. 3rd ERC Grantees Conference: “Frontiers in Chemistry”, Zandvoort, Netherlands, 31/8 – 2/9 2016, poster presentation;

Curriculum Vitae

OLEKSANDR SHYSHOV

Education and Research Experience

9/2015 – present	PhD student, University of Ulm, Germany (from 1/7/2016), University of Erlangen-Nürnberg, Germany (from 1/9/2015 to 29/6/2016) Supervisor: Prof. Dr. Max von Delius Thesis title: "Facially polarized cyclohexanes and orthoesters as building blocks in host-guest architectures and functional materials"
9/2019	Research internship Institute of Biomolecules Max Mousseron, France with Dr. Sébastien Ulrich
10/2014 – 7/2015	Master of Science in Chemistry, University of Nice Sophia-Antipolis, France and V. N. Karazin Kharkiv National University, Ukraine.
1/2015 – 7/2015	Work on Master thesis, Institute of Chemistry of Nice, UMR 7272 CNRS, Team "Bioactive molecules" Supervisors: Prof. Dr. Nadia Patino and Prof. Dr. Stéphane Azoulay Master thesis: "Towards the synthesis of Panicein A, natural compound with anticancer activity"
9/2010 – 6/2014	Bachelor of Science in Chemistry (with distinction), V. N. Karazin Kharkiv National University, Ukraine

Awards and Scholarships

Awards	Springer poster prize at SupraChem 2019, Würzburg, Germany, 2019; Advanced Science poster prize at 3rd ERC Grantees Conference, Zandvoort, Netherlands, 2016; Winner of National Ukrainian Olympiads in Chemistry: 2008 – 2nd place, 2009 – 3rd place, 2010 – 3rd place.
Scholarships	2017 – present DAAD Doctoral Scholarship; 2014 – 2015 French Government Scholarship.

Acknowledgments

I would like to thank Prof. von Delius for giving me the opportunity to work in his group, for his mentorship during my PhD studies, for financial support, for teaching me how to write papers, proposals and presenting research, and for not coming into the lab and telling me what to do allowing me to work independently in peace.

I would like to thank previous and past members of the Delius group: René, Fabian F., Michael, Xiang, Bala, Youzhi, Tobias, Tanya, Lucia, Lizzy, Fabian Sch., Fabian St., Selina, Jie, Julian, Jing, Yev, Janina, Andreas, Simon, Jan. Particularly I would to thank Oleg for his help with proofreading of my thesis and for numerous scientific discussion which, although often made me want to puke, led to some scientific improvements.

I would like to thank my numerous bachelor and projects student: André, Selina, Philipp, Sarah, Pascal, Nikhil, Benjamin, Maren, Kevin, Amelie.

Prof. P. Bäuerle and Dr. E. Mena-Osteritz are acknowledged for access to equipment and support with AFM. Dr. U. Werz is acknowledged for his assistance with NMR measurements. Mr. Tontsch is acknowledged for his technical genius and weird sense of humour.

I would like to express my gratitude to all my collaborators who provided indispensable research input significantly improving our studies: Prof. F. Wurm, Dr. T. Haider, Dr. Pesce, Dr. D. Bochicchio, Prof. G. Pavan, Prof. C. Jäger, Prof. U. Kaiser, Dr. H. Qi, Dr. Ulrich, M. Coste.

I would like to thank the DAAD for financing my graduate studies.

Finally I would like to thank my family for support.

Statement

Die vorliegende Arbeit entstand im Zeitraum von September 2015 bis September 2020 zunächst am Institut für organische Chemie der FAU-Erlangen-Nürnberg und danach am Instituten für Organische Chemie II und IUniversität Ulm (durchgehend jedoch im Arbeitskreis von Prof. Dr. Max von Delius). Hiermit erkläre ich, dass ich die vorliegende Arbeit selbstständig angefertigt und keine anderen als die angegebenen Quellen und Hilfsmittel benutzt sowie die wörtlich oder inhaltlich übernommenen Stellen als solche kenntlich gemacht und die Satzung der Universität Ulm zur Sicherung guter wissenschaftlicher Praxis in der aktuell gültigen Fassung vom 08.03.2012 beachtet habe.

Ulm, September 2020

Oleksandr Shyshov